


Fall 2014

Quantum mechanics in complex systems

Ross Douglas Hoehn
Purdue University

Follow this and additional works at: https://docs.lib.purdue.edu/open_access_dissertations

 Part of the [Atomic, Molecular and Optical Physics Commons](#), [Biophysics Commons](#), and the [Chemistry Commons](#)

Recommended Citation

Hoehn, Ross Douglas, "Quantum mechanics in complex systems" (2014). *Open Access Dissertations*. 287.
https://docs.lib.purdue.edu/open_access_dissertations/287

This document has been made available through Purdue e-Pubs, a service of the Purdue University Libraries. Please contact epubs@purdue.edu for additional information.

PURDUE UNIVERSITY
GRADUATE SCHOOL
Thesis/Dissertation Acceptance

This is to certify that the thesis/dissertation prepared

By Ross Douglas Hoehn

Entitled QUANTUM MECHANICS IN COMPLEX SYSTEMS

For the degree of Doctor of Philosophy

Is approved by the final examining committee:

Sabre Kais

Chair

David H. Thompson

Adam Wasserman

Lyudmila Slipchenko

To the best of my knowledge and as understood by the student in the *Research Integrity and Copyright Disclaimer (Graduate School Form 20)*, this thesis/dissertation adheres to the provisions of Purdue University's "Policy on Integrity in Research" and the use of copyrighted material.

Approved by Major Professor(s): Sabre Kais

Approved by: R. E. Wild

Head of the Graduate Program

10-10-2014

Date

QUANTUM MECHANICS IN COMPLEX SYSTEMS

A Dissertation

Submitted to the Faculty

of

Purdue University

by

Ross Douglas Hoehn

In Partial Fulfillment of the

Requirements for the Degree

of

Doctor of Philosophy

December 2014

Purdue University

West Lafayette, Indiana

For my family, friends and mentors.

ACKNOWLEDGMENTS

This opportunity affording, I would like to express my deepest gratitude to all those individuals who have supported me morally and academically throughout my stay at Purdue University. My works, herein contained, are only possible because of their assistance.

My gratitude is primarily directed toward both Prof. Sabre Kais, my academic advisor, and Prof. Emer. Jurgen Honig. You have both displayed qualities necessary for the nurturance of future scientists: patience, which I have taxed; enthusiasm, on which I have fed; steadfastness, from which I have sampled and joy in achievement, which has motivated me throughout my works. I would also like to thank my primary collaborators: Prof. Emer David Nichols, Prof. Mohammed Fayez Al Rez, Prof. Jixiang Wang, Prof. Timothy Zweir, Dr. Harmut Neven and Mr. Nathaniel Kidwell. I would also like to thank both of my excellent undergraduate research students: Mr. Nicholas Mack and Ms. Ashley Schreder; both are fully capable of achieving that to which they aspire.

I would also like to thank all of my committee members: Prof. David Thompson, Prof. Lyudmila Slipchenko and Prof. Adam Wasserman for their encouragement and valued comments. Extended gratitude should be given to Prof. Thompson as it was in his lab that I first experienced the cultures of research and academia.

I would like to acknowledge the professors under whom I had the pleasure of working during my period as teaching assistant; Prof. Steven Adelman and Prof. Garth Simpson. I would like to thank all previous and current members of theoretical chemistry division at Purdue University, particularly Dr. Marcleo Carignano, Dr.

Edwin Antillon, Dr. Anmer Daskin, Dr. Winton Moy, Dr. Qi Wei, Dr. Jing Zhu, Mr. Martin Mosquera and Mr. Shu-hao Yeh.

Last but not the least; I would like to thank my family. My mother, Cinda Hoehn, my father, Steve Hoehn, and stepmother, Margery Hoehn for supporting me during my more stressful periods. Finally, I would like to acknowledge my dear friends Ms. Elizabeth Cohen and Mr. Paul Geraci for their support this past two years.

TABLE OF CONTENTS

	Page
LIST OF TABLES	viii
LIST OF FIGURES	ix
ABSTRACT	xv
1 INTRODUCTION	1
1.1 Dimensional Scaling	1
1.2 IETS	7
1.2.1 Olfaction and Luca	7
1.2.2 History of IETS	9
1.2.3 Measurements	10
1.2.4 Map to Proteins	14
1.3 Quantum Tic-Tac-Toe	17
1.4 The Organization of the Thesis	20
1.5 References	24
2 RELATIVISITIC CORRECTIONS TO DIMENSIONAL SCALING	35
2.1 Introduction	35
2.2 Non-Relativistic Methodology	38
2.2.1 The Relativistic Mass Gauge	39
2.2.2 Trajectory Corrections	40
2.2.3 1-D Particle in a Box	43
2.2.4 Dressed Atomic Potential under Consideration	47
2.3 Methodology for D=3 Calculations	49
2.4 Dimensional Scaling: Calculations and Considerations	54
2.4.1 Methodology	54
2.4.2 Planar Infinite-D Hamiltonian	56
2.5 Results and Discussion	60
2.6 Comments on Elliptical and Circular Polarizations	71
2.7 Conclusion	73
2.8 Acknowledgments	73
2.9 References	75

	Page
3 DRUG EFFICACY PREDICTION BY QUANTUM PROCESSES	78
3.1 Introduction	78
3.2 Inelastic Electron Tunneling Mechanics	81
3.2.1 Point Dipole Approximation	89
3.2.2 Polarizability	91
3.2.3 Orientation	94
3.2.4 Docking Geometry	96
3.3 Mapping the Models	98
3.4 Results	103
3.5 Experiment	110
3.6 Conclusions	116
3.7 Acknowledgements	117
3.8 References	118
4 TEACHING QUANTUM MECHANICS THROUGH QUANTUM GAMES	123
4.1 Introduction	123
4.2 Physical Concepts and Game Play	125
4.2.1 Board	125
4.2.2 General Structure of the Game	128
4.2.3 Exercises	133
4.3 Probability Amplitude, Sign Symmetry and Probability Density	135
4.4 The Inner Product, Normalization and Overlap	138
4.5 Hilbert Space and Basis Functions	140
4.6 Change of Basis, Projectors and Observations	145
4.7 Separability and Entanglement	149
4.8 Density Matrix and Concurrence	150
4.9 Conclusions	154
4.10 Acknowledgments	155
4.11 References	156
APPENDICES	
A MODELING OF CELLULAR REGENERATION VIA ATOMATON MODEL	159
A.1 Abstract	159
A.2 Introduction	159
A.3 Algorithm	163
A.4 Results and Discussion	171
A.5 Conclusions	180
A.6 Present and Future Directions	180
A.6.1 Indtroduction	180

	Page
A.6.2 Algorithm	182
A.6.2.1 Fluid Dynamics	182
A.6.3 Cellular Automata	189
A.7 References	193
B PATENT APPLICATION	198
VITA	229
PUBLICATIONS	230
IN SUBMISSION	308

LIST OF TABLES

Table	Page
2.1 The below table displays the differences present when relativistic considerations are undertaken for these multiply-charge ions. The Non-Relativistic values were taken from[14].	66
2.2 Results of Mulliken Population Analysis, note that there are four outer orbitals the table contains one of the four values.	70
3.1 Numerical Values for calculations of the geometric alterations and optimized geometry variants of the formate ions. This table contains displacements of the first three modes	100
3.2 Numerical Values for calculations of the geometric alterations and optimized geometry variants of the formate ions. This table contains displacements of the final three modes	101
3.3 Numerical Values for calculations of the geometric alterations and optimized geometry variants of the formate ions. This table contains the partial charges of all atoms for each geometric arrangement	102
3.4 Table contains the SI indexes for several 5-HT _{2A} agonists. The procedure was applied to the total spectra, and several sections of 1000cm ⁻¹ which march with an overlapping pattern and shifted by 500cm ⁻¹ . The region of interest is also performed with a calculated SI for the region of 1500±100cm ⁻¹	108
Appendix Table	
A.1 Table contains constants of motion for cells used within calculations, also includes references for values.	166
A.2 Table containing all of the initial to final state turning probabilities. . . .	170
A.3 Table containing experimental run data concerning the levels of hypoxia and duration of hypoxia to which cells are exposed.	185

LIST OF FIGURES

Figure	Page
1.1 Cartoon displaying the competing processes during IETS where V is potential energy and F_e is the Fermi Level. Path A is radiative [101, 99], requiring the tunneling electron to spontaneously lose energy to meet the energy of the conductive band. Path B shows the electron losing energy via a non-radiative process; it is implicit that the energy lost is to a normal mode of a deposited molecule within the gap - such is our case.	12
1.2 Detection of IETS mechanism within laboratory experiments. i shows the relationship between applied potential and the current across the gaps. ii the current's derivative with respect to the applied field. iii the current's impulse with respect to applied field, note that this is the quantity used in an experimental IETS apparatus.	13
1.3 The layout of the game board for either classical or quantum Tic-Tac-Toe. This figure also displays the enumeration scheme that is used throughout this paper.	21
2.1 Non-relativistic effective potential for a 1D particle in a box under different laser intensity, measured by α_0	45
2.2 Relativistic corrections to the effective potential for different laser fields.	46
2.3 Effective potential for two alternating electric fields superposed along \hat{e}_x and \hat{e}_z , respectively, with different colors.	48
2.4 Contour Plots of Dressed Potential for (clockwise) $\alpha_0=0, 25, 100, 50$. Note both the shift in regime as α_0 grows and the key below the plots for the interpretation of the intensity of the contours.	50
2.5 Three Dimensional Plots of the Potential Energy, V_{dres}^{HFFT} , as a function of x and z coordinates for the case $\alpha_0=100$. Left and Right of above are two different angles of same surface.	51
2.6 Top: Probability distribution for H^- , a two electron system. Bottom: Probability distribution for He^- , a three electron system	53

Figure	Page
2.7 Plots of both molecular energies and binding energy for (clockwise): \mathcal{H}_{DA} with non-relativistic trajectory; \mathcal{H}_{DA} , relativistic trajectory; \mathcal{H}_P , relativistic trajectory; and \mathcal{H}_P with non-relativistic trajectory. All may be read as Yellow:Binding Energy; Blue:Hydrogen Energy; Purple:H ⁻ Energy . . .	57
2.8 The above displays the relationship between the system's geometry with respect to the electrons and the coordinates use in Eq. (2.40)	61
2.9 Above are plots of the binding energies of, from left to right and top to bottom: H ⁻ , H ⁻² , He ⁻ , He ⁻² and He ⁻³	62
2.10 Energies for the hydrogen atom energies scaling with the applied field intensity, α . The blue curve are the findings using \mathcal{H}_P while the purple are those points generated with UHF SCF calculations.	63
2.11 Plots of binding energy comparisons for (clockwise):comparison plot of \mathcal{H}_{DA} versus \mathcal{H}_P , non-relativistic trajectory; \mathcal{H}_P with relativistic trajectory m_0 and m_r , differences value of Hydrogen energy between use of m_0 and m_r ; and a comparison of relativistic trajectory (both m_0 and m_r) with non-relativistic trajectory both using \mathcal{H}_P	64
2.12 Plots of binding energy for the H ⁻ (left) and He ⁻ (right) systems. Top, Non-Normalized plots of the calculation data showing agreement between the methods. Bottom, -B.E./B.E. _{max} to emphasis the qualitative similarity between the methods as they share minima for the B.E. curves. . . .	67
2.13 Top Row: Plots of the Probabiltiy Distribution for the corrected (left) and non-corrected (right) H ⁻ system, directly below is a superimposition of the trajectory upon the the probabilty density function plot to emphasis their relation. Bottom Row: Contour Plots of the H ⁻ system, both corrected (left) and non-corrected (right), note the different scales on the vertical (z) axis and the more diffuse behavior of the corrected system.	69
2.14 The electronic elliptical contribution can be seen as the function whose major axis lies in the z-direction (vertical) and the magnetic contribution has an orthogonal orientation.	72
2.15 Within the above plot, the total trajectory can be seem, the amplitude of the major and minor axes are mediated in value between those from the electronic and magnetic components and the orientation is set off by an angle whose value respects the same coefficients as the relative amplitudes. 74	74

Figure	Page
3.1 Cartoon displaying the competing processes during IETS where V is potential energy and F_e is the Fermi Level. Path A is radiative [65, 63], requiring the tunneling electron to spontaneously lose energy to meet the energy of the conductive band. Path B shows the electron losing energy via a non-radiative process; it is implicit that the energy lost is to a normal mode of a deposited molecule within the gap - such is our case.	83
3.2 A cartoon displaying the physical relations and significance of variables within the problem. e^- is the tunneling electron with vector displacement of \vec{r} and Z_e is the partial charge associated with a molecular mode with displacement \vec{R} , and d is the distance between the two plates.	84
3.3 a) A cartoon schematic of the formate ion within its gap, distance parameters d and a are shown within the figure for clarity. b) The IETS spectra of the formate ion taken from[cite], provided as reference.	85
3.4 A display of the normal modes associated with the formate ion. Also included are a unit vector indicator as to the direction of displacement and the magnitude is shown beside it. Distances are in <i>a.u.</i> Frequencies are also displayed in cm^{-1} beneath the mode to which it belongs.	90
3.5 The percent relative error between variations of the interaction potential given in Eq. 3.4 and Eq. 3.19a. This was completed for several values of θ to emphasize the angular dependence stemming from projection operations in terms eliminated through approximation.	92
3.6 The blue line shows the IETS of the formate ion; the maroon line shows the spectra where the interaction potential given Eq. 3.4 is replaced by the interaction potential between the electron and the molecular dipole. The two plots have been scaled so to be comparable.	95
3.7 Effects of orientation of the molecule within the gap. Rotational axes are noted in Subfigure (a). Subfigure (b) and (c) show the IETS for the formate ion as it is rotated by the X- and Y-axis, respectively.	97
3.8 Effects of alterations of the geometry of a system on the IETS. Subfigure (a) shows cartoons of the geometries of concern: optimized geometry, symmetric alteration and asymmetric alteration, respectively. Subfigure (b) shows the IETS of the formate ion variants	99
3.9 IETS of Serotonin to be compared throughout the discussion. Here the abscissa has units of wavenumber and the ordinate has units proportional to tunneling probability; this conversion holds for all following IET Spectrum.	105

Figure	Page
3.10 The IETS of several known 5-HT _{2A} agonists and the square of the tunneling PDF reflected below the energy axes. The Spectral Similarity index of each plot given in the inlay.	106
3.11 The IETS of DOC (Blue) is plotting alongside a scaled, discrete density of states for the vibrational modes of DOC. The scaling factor is given in the inlay. Note the enhanced number of states associated with 1500cm ⁻¹ region	109
3.12 Plots of the isotopologues of oxygen with the DOC molecules. The isotope exchanges has no effect on the region in question.	111
3.13 (a) The tunneling spectra of several DOX class agonists as well as their structures. (b) The inverse of the median effective concentration for the DOX class agonists plotted against the tunneling probability within the region in question.	112
3.14 (a) The tunneling spectra of several 2C-X class agonists as well as their structures. (b) The inverse of the median effective concentration for the 2C-X class agonists plotted against the tunneling probability within the region in question.	113
3.15 IETS of several deuterium-isotopologues of DAM-57. Yellow highlights have been given to the energy region which is assumed to be the active energy region for inelastic tunneling transfer.	115
4.1 The layout of the game board for either classical or quantum Tic-Tac-Toe. This figure also displays the enumeration scheme that is used throughout this paper.	126
4.2 The Bloch Sphere represented pictographically. Where a spin can be described through a superposition, linear-combination, of the two observable states Spin-up and Spin-down.	129
4.3 The effect of measurement on the system of cyclic entanglement can yield, at minimum, a pair of classical states corresponding to the state in which X ₃ was observed.	131
4.4 The measurement on a specific board can have observable ramifications even for game pieces that are not members of the cyclic entanglement; these pieces are referred to as dangling markers.	132
4.5 Board (a) shows a series of classical markers; by their nature of classical markers any wave function describing one is linearly independent with any other markers wave function. Board (b) shows a series of Spooky Markers. The wave function describing this series of moves reveals that these partials are linearly independent with each other.	136

Figure	Page
4.6 Boards that can be used during class exercises. (a) is a board giving a brief pair of exercises that can be used to enforce the concept of normalization as the student integrates the board over each of the markers and then the pair of Spooky Markers. (b) is a board yielding several exercises that can be used as a means of both enforcing the concept of overlap and allow the student to numerically evaluation the overlap integral of Gaussian-type functions.	141
4.7 Boards displaying several possible exercises. Board A is a brief series of exercises for the expansion of moves in terms of basis functions. Board B yields several possible exercises for the topics of normalization and overlap.	142
4.8 A board presenting possible exercises that may be used to introduce the mathematics of observations of moves in several different basis.	147
4.9 Board (a) shows a pair of moves placed in such a way were the overall wave function of the board is separable; this can be shown through an expansion of the product of the wave functions for each Spooky Marker and then the subsequent concretion back to the original product, completed in discussion. Board (b) displays a pair of moves whose total board wave function is inseparable, there exist members of the product expansion who are exclusionary to other members, seen in discussion.	151
Appendix Figure	
A.1 Schematic representation of the architecture of a blood vessel. The composite structure is described within the body of the section.	162
A.2 Algorithmic map for the discrete model used herein. Note sections of same color work together in a unified purpose describing a single facet of the program or cell behavior.	167
A.3 A schematic representation of the directional states within Markov Chain Analysis with their vector and θ_d state designations.	169
A.4 Figures showing the dependency of the confluence behavior on several variables: (a) initial seeding geometry, (b) motility parameters, (c) velocity parameters. Note, the definite impact parameter and geometric alterations have upon both the logistic and setting phases of colony growth. This comes about as the motility time increase dampens the effect of the initial division within the system causing, for smaller μ_τ an earlier logistic phase and setting phase on-set. The difference in the geometric confluence behaviors was highlighted for emphasis.	173

Figure	Page
A.5 Initial seeding geometry is varied in Subfigures a, b, and c. The behaviors are: (a) attempted divisions within the system, (b) cells which are in the Mobile Phase, and (c) cells which are in the Stationary Phase. It should be made clear that the number of cells which could possibly attempt division within the system is upper bound by the number of cells within the Stationary Phase, thus the relationship shown in Figures a, b and c. It is important to note that (a) is attempted divisions, and should be compared to the corresponding confluence plot for perspective. In Subfigures d, e and f motility time is varied and labeled are the lowest and highest values of μ_τ , the values in between increase in increments of 2. These behaviors are: (d) attempted divisions within the system, (e) cells which are in the Mobile Phase and (f) cells which are in the Stationary Phase.	174
A.6 Plots of effective behaviors displaying influence of: Row 1, different initial seeding conditions; Row 2, different values of μ_τ ; and Row 3, different values of c_v . Plots (a), (c) and (e) show the number of collisions within the system; Plots (b), (d) and (f) are of the effective average velocity of the cells. Note, (a) shows the depletion of collision count near the setting phase as more cells are being influenced by contact inhibition and becoming stationary. In (b) the drastic difference in initial effective velocity between the seeding cases at constant c_v . (d) and (f) displays the overall trending behavior is uniform in all cases, just varying time-scales. (e) shows the limiting dependence of the system behavior on c_v as the velocity approaches the motility parameter.	177
A.7 Four simulations under our model, starting left: Stationary Centroid; Motile Centroid; Random Seeding; Wound Closing. The first row is the initial seeding condition, the second is the system at 20 % coverage and subsequent rows are at increments of 10 % more coverage.	179
A.8 A schematic representation of the overall algorithm used during the second phase of simulations.	183
A.9 A schematic representation of the cell specific portion of the algorithm used during the second phase of simulations.	184
A.10 A schematic representation of disagreement between the fluid dynamic computational grid and the cellular automaton grid.	188
A.11 Visualizations of the solution space for the vascular system. a) the solution space with grid-skeleton. b) computational mesh points for fluid mechanics. c) visualization of fluid diffusion within mesh environment. . .	190
A.12 An example of a three dimensional Markov Turner for the vector definitions within a discrete automaton system.	191

ABSTRACT

Hoehn, Ross Douglas. Ph.D., Purdue University, December 2014. Quantum Mechanics in Complex Systems. Major Professor: Sabre Kais.

This document should be considered in its separation; there are three distinct topics contained within and three distinct chapters within the body of works. In a similar fashion, this abstract should be considered in three parts. Firstly, we explored the existence of multiply-charged atomic ions by having developed a new set of dimensional scaling equations as well as a series of relativistic augmentations to the standard dimensional scaling procedure and to the self-consistent field calculations. Secondly, we propose a novel method of predicting drug efficacy in hopes to facilitate the discovery of new small molecule therapeutics by modeling the agonist-protein system as being similar to the process of Inelastic Electron Tunneling Spectroscopy. Finally, we facilitate the instruction in basic quantum mechanical topics through the use of quantum games; this method of approach allows for the generation of exercises with the intent of conveying the fundamental concepts within a first year quantum mechanics classroom. Furthermore, not to be mentioned within the body of the text, yet presented in appendix form, certain works modeling the proliferation of cell types within the confines of man-made lattices for the purpose of facilitating artificial vascular transplants.

In Chapter 2, we present a theoretical framework which describes multiply-charged atomic ions, their stability within super-intense laser fields, also lay corrections to the systems due to relativistic effects. Dimensional scaling calculations with relativistic

corrections for systems: H , H^- , H^{2-} , He , He^- , He^{2-} , He^{3-} within super-intense laser fields were completed. Also completed were three-dimensional self consistent field calculations to verify the dimensionally scaled quantities. With the aforementioned methods the system's ability to stably bind 'additional' electrons through the development of multiple isolated regions of high potential energy leading to nodes of high electron density is shown. These nodes are spaced far enough from each other to minimize the electronic repulsion of the electrons, while still providing adequate enough attraction so as to bind the excess electrons into orbitals. We have found that even with relativistic considerations these species are stably bound within the field. It was also found that performing the dimensional scaling calculations for systems within the confines of laser fields to be a much simpler and more cost-effective method than the supporting D=3 SCF method. The dimensional scaling method is general and can be extended to include relativistic corrections to describe the stability of simple molecular systems in super-intense laser fields.

Chapter 3, we delineate the model, and aspects therein, of inelastic electron tunneling and map this model to the protein environment. G protein-coupled receptors (GPCRs) constitute a large family of receptors that sense molecules outside of a cell and activate signal transduction pathways inside the cell. Modeling how an agonist activates such a receptor is important for understanding a wide variety of physiological processes and it is of tremendous value for pharmacology and drug design. Inelastic electron tunneling spectroscopy (IETS) has been proposed as the mechanism by which olfactory GPCRs are activated by an encapsulated agonist. In this note we apply this notion to GPCRs within the mammalian nervous system using ab initio quantum chemical modeling. We found that non-endogenous agonists of the serotonin receptor share a singular IET spectral aspect both amongst each other and with the serotonin molecule: a peak that scales in intensity with the known agonist activities. We propose an experiential validation of this model by utilizing lysergic acid dimethylamide (DAM-57), an ergot derivative, and its isotopologues in which

hydrogen atoms are replaced by deuterium. If validated our theory may provide new avenues for guided drug design and better in silico prediction of ecacies.

Our final chapter, explores methods which may be explored to assist in the early instruction in quantum mechanics. The learning of quantum mechanics is contingent upon an understanding of the physical significance of the mathematics that one must perform. Concepts such as normalization, superposition, interference, probability amplitude and entanglement can prove challenging for the beginning student. This paper outlines several class exercises that use a non-classical version of tic-tac-toe to instruct several topics in an undergraduate quantum mechanics course. Quantum tic-tac-toe (QTTT) is a quantum analogue of classical tic-tac-toe (CTTT) benefiting from the use of superposition in movement, qualitative (and later quantitative) displays of entanglement and state collapse due to observation. QTTT can be used for the benefit of the students understanding in several other topics with the aid of proper discussion.

1. INTRODUCTION

1.1 Dimensional Scaling

Many Body interactions are something which has troubled computational methodologies within quantum mechanics since inception; throughout the years the physical and chemical communities have made great advances in the field of electronic structure theory to help account for these electron-electron interaction through variational practices such as the Hartree Fock Method or Density Functional Theory. The alternative method to the aforementioned is a Dimensional Scaling treatment pioneered by Herschbach [1], discussed in[2, 3, 4, 5, 6], and is briefly introduced here for the central force problem[2]. We shall firstly note that the overall procedures is given in four general steps; these being:

1. Formulate the problem to a general dimensionality, a D -dimensional form.
2. Transform the D -dimensional form to a suitably scaled space which allows for the removal of major dimensional dependency associated with the quantity of concern.
3. Evaluate the newly scaled quantity at several special dimensions (namely, $D \rightarrow \infty$, $D \rightarrow 1$, $D \rightarrow 2$). At these dimensions computation of the quantity becomes very easy.
4. Obtain an approximate value for the $D=3$ system by repeating the dimensional evaluations and relating these special D values to $D=3$ solutions. This is complete in many cases by some form of interpolation or extrapolation.

Moving on to the central force example, the time-independent Schrodinger Equation for the simple central force problem in D-dimensions:

$$[-\frac{1}{2}\nabla_D^2 + V(r)]\Psi_D = \epsilon_D\Psi_D. \quad (1.1)$$

If we were to employ polar coordinates to the above we would require:

$$r \equiv [\sum_{k=1}^D x_k^2]^{\frac{1}{2}} \quad (1.2a)$$

$$\nabla_D^2 = \frac{1}{r^{D-1}} \frac{\partial}{\partial r} (r^{D-1} \frac{\partial}{\partial r}) - \frac{L_{D-1}^2}{r^2}. \quad (1.2b)$$

Where Eq.(1.2a) gives the definition of the radial coordinate in a generic D-scaled space, and Eq.(1.2b) is the polar Laplacian in this D-scaled space, L_D^2 is the term which retains all angular dependencies. These angular and radial terms shall be dealt with in a divide and conquer treatment reminiscent to the radial and angular terms of the Rigid Rotor/Harmonic Oscillator approximations for the simple diatomic. We first write the wave function in D-dimensions to be the product: $\Psi_D = r^l \mathcal{Y}(\Omega_{D-1})$, where all radial dependencies are in the r^l term and the D-1 remaining angular dimensions are described through $\mathcal{Y}(\Omega_{D-1})$. Now solving the angular terms for the form Eq.(1.3), and the recognizing that the $V(r)$ term in Eq.(1.1) can be set to equal magnitude as the ϵ_D term, thus making Eq.(1.1) reduce to the Laplace equation shown in Eq.(1.4).

$$L_{D-1}^2 \mathcal{Y}(\Omega_{D-1}) = C \mathcal{Y}(\Omega_{D-1}) \quad (1.3)$$

$$\nabla_D^2 r^l \mathcal{Y}(\Omega_{D-1}) = 0 \quad (1.4a)$$

$$\{l(l + D - 2) - C\} r^{l-2} \mathcal{Y}(\Omega_{D-1}) \quad (1.4b)$$

This means: $C=l(l + D - 2)$; and the Hamiltonian Operator in Eq.(1.1) is now of the form:

$$\hat{H}_D = -\frac{1}{2}K_{D-1}(r) + \frac{l(l + d - 2)}{2r^2} + V(r). \quad (1.5)$$

In the above, $K_{D-1}(r)$ is the single non-angular term from the polar Laplacian in Eq.(1.2b). We may now pass the system through a unit Jacobian, making: $J_D|\Psi_D|^2 =$

Φ_D , J_D is the radial part of the unit Jacobian and is of the form: $r^{(D-1)}$. This would mean, $\Psi_D = r^{-\frac{1}{2}(D-1)}\Phi_D$. All leading to the form of K_{D-1} seen here:

$$K_{D-1}(r)=r^{-\frac{1}{2}(D-1)}\left\{\frac{\partial^2\Phi_D}{\partial r^2}-\frac{D-1}{2}\frac{D-3}{2}\frac{\Phi_D}{r^2}\right\} \quad (1.6)$$

Reassembling all the above, and placing them appropriately back into Eq.(1.1), one shall -after menial simplification- get:

$$\left\{-\frac{1}{2}\frac{\partial^2}{\partial r^2} + \frac{\Lambda(\Lambda + 1)}{2r^2} + V(r)\right\}\Phi_D = \epsilon_D\Phi_D. \quad (1.7)$$

Eq.(1.7) is the radial, D-scaled form of Eq. (1.1), where the only dimensional dependencies lay within the Λ terms as: $\Lambda = l + \frac{1}{2}(D - 3)$. This procedure allows for the generation of a simple minimization problem for the hydrogen atom and delivers the ground state energy to be *a.u.* (Hartree), which is in great agreement with other, more standard, computational approaches.

The dimensional scaling approach has been shown to work well for a number of problems and under various degrees of complexity in small quantum systems. The procedure did well in its infancy to describe simple 3-body problems[7, 8] as well as harmonic oscillators[9]. Small quantum mechanical systems such as 2-electron molecules[10], homo- and hetero-nuclear diatomics[11, 12] and their ions[13] as well as a hydride[14] have all been completed. Chemical binding[15] as well as bound systems under quasistationary conditions[16] have been completed, including systems acting without the imposition of the Born-Oppenheimer Approximation[17, 18]. Non-quantum mechanical problems have also been approached, such as the derivation of the Virial coefficients[19] and random walks[20, 21]. Finally, this procedure has also been used to find appropriate functionals for density functional theory[22, 23]. The generation of stable, multiply-charged atomic ions via exposure to super-intense laser fields is a topic which challenges preconceived notions for ionic atoms and is, therefore, of fundamental importance in atomic and molecular physics[24, 25, 26]. Over the past decades, advancements in spectroscopic methods have yielded verification of mono-charged Calcium and Strontium atomic anions[27, 28] and various gas-phase

poly-charged molecular ions[29, 30, 31] . However without the large charge volume which is provided by the heavy atoms -above- or small molecules it is unlikely that species would be able to bind more than one excess electron; this can be noted by the relative stability of O^{-2} in the liquid-phase, yet it's instability within the gas-phase[29]. Theoretical works have developed an absolute upper-limit to the number of electrons which may be bound to a atomic center[32]: $N_c \geq 2Z$, with N_c being the number of electrons and Z being the Coulomb charge of the nucleus. Within the context of Lieb's frameworks, Hydrogen would therefore be disallowed any excess electrons beyond that which yields the Hydride state, thusly H^{2-} is unstable[33, 34]. Supporting theoretical works have come later[35, 36] -some including implementation of finite-sized scaling[36]- and have conclusively determined at gas-phase, dianionic atoms are unstable. It has been shown that stable, multiply-charged atomic ions may be developed within extremely strong laser fields on the order of 10^{16} W/cm² and above[37, 38]. Within the field, the electron density - still being bound to the nucleus - has been found to be nodal in nature as the Coulomb potential splinters under the influence of the field into distinct, localized regions whose positions are governed by the field parameters of the laser. This phenomenon is most easily - and best- discussed within the context of the Krammers Henneberger (KH) reference frame, electron centric frame, where the electron is treated as the stationary body and the nucleus traverses the path of the applied field; in this context the local nodes of electron density are located at the turning points on the path of the nucleus. These are the location at which the angular velocity of the nucleus decreases and thus spends more time in a local area - thus generating a greater pull in that area. Within these nodal regions, the bound electrons maintain a great enough distance from one and another to minimize their Coulomb repulsion while also giving each a center with which to bind. In this field, the electrons which intuition tells us would be completely ionized- are capable of stably binding into multiply-charged atomic ions. The field strength allows one to manipulate the location and pull of the nodal centers , thus generating a method of control over the potential and therefore establishing

the ability to push the electrons into and past their most stable state by means of manipulating laser parameters, frequency and intensity. The contained theoretical works are concerned with High-Frequency Floquet Theory (HFFT) which allows for a time-independent treatment of the coupling of the static Coulomb potential with a time-varying electromagnetic field. This is possible by exploiting highly oscillatory fields in which the electrons would be prohibited from coupling with the periodic nature of the field due to extremely short periods (large frequencies) of oscillation, thus the system's electrons would feel a period average of the applied potential coupled with the static Coulomb potential, again this is best discussed within the KH frame. This time-average allows generation of the aforementioned nodal structure and therefore permits the stability of the subsequent states and allows the system to forgo autoionization. The above discussed methodology was introduced to atomic systems by Pont et al[39], van Duijn et al[40], and was used again by Wei et al[38, 41, 42, 37] to describe non-relativistic, multiply-charged atomic ions. Herein we shall propose a framework utilizing HFFT as a backbone for applying relativistic corrections to atomic ions in a time-independent manner. Consideration within the non-relativistic cases lies no longer with both the mass and the magnetic coupling, but with the time dependent electric field coupling with the system's Coulomb potential; this work was performed by Wei et al[38, 41, 42, 37] and produced stably bound multiply-charged ions for small atomic centers utilizing the field parameter (α_0), discussed later, and finding detachment energies on orders of 0.1eV to 1.0 eV. The enclosed works, here, expound upon this by adding the necessary relativistic corrections to the previous framework. A free electron within an oscillating electric field shall undergo oscillatory motions which are governed by a coupling to the field; the electron is said to be 'quivering' with a motion defined by a trajectory, $\vec{\alpha}_0(t)$, and a quiver amplitude, α_0 . A bound electron within the same situation shall feel a new potential which is a stacking of the applied field and the Coulomb potential of the central charge; the total potential for the system is said to be a Coulomb potential dressed by the laser, denoted as a dressed potential, V_{dres} . Mass -as a fundamental- is conceptualized in two

different manners within physics, these being the rest mass and the relativistic mass. Rest mass, or invariant mass, is for a specific body a constant, measurable quantity denoted m_0 . In opposition to the rest mass is the variant quantity: relativistic mass, m_r . The relativistic mass depends upon the velocity of the observer. The variant nature of m_r is a correction to the rest mass which accounts for a non-zero kinetic energy for the measured system. This means that the relativistic mass increases in magnitude as the velocity of the system increases, and shall reach infinite mass as the system reaches the speed of light. We are now called to introduce the concept of ponderomotive energy, U_p ; this being the cycle average kinetic energy of a quivering electron, i.e. electron undergoing oscillatory motion due to an external field and also qualifying under the dipole approximation. This is quantity discussed in context of such systems by Joachain, Dörr and Klystra[43]. An evolved form of this statement is used within these works:

$$m_r = m^{dressed} = m_e \left(1 + 2 \frac{U_p}{m_e c^2}\right)^{\frac{1}{2}} \quad (1.8a)$$

$$= m_e (1 + 2q)^{\frac{1}{2}}. \quad (1.8b)$$

As can be seen, the quantity q begins to shift the mass and becomes the dominant factor within the expression as it approaches unity[44]. The form of Eq. (2.3b) was found by Brown and Kibble[45] and later verified by Eberly and Sleeper[46] via the Hamilton-Jacobi equation.

Three dimensional calculations which describe our systems were executed as a mean of verifying the simpler Dimensional Scaling approach discussed later. The methodology consisted of unrestricted Hartree-Fock (UHF) utilizing the Pople-Nesbot equations -which allow for the accommodation of basis sets- to complete calculations for a series of total electron counts, N , per single value of the field intensity parameter, α_0 . The orbital centers were selected to satisfy the above curve and to coincide with the "hottest" locations displayed within the contour plots of potential energy. A basis set was selected which allowed for significant description of both polarized and diffuse phenomenon residing on small centers. Overlap and kinetic integrals were

performed with variations on the integrals described by McMurchie and Davidson in their seminal paper here[47]. Numerical integration methods were appropriate for the more challenging, non-analytic potential integrals. For this reason two-centered integral includes the cost of shifting the coordinate-origin to the center of the product Gaussian as defined by[48]. The four-centered integrals needed for the self-consistency were generated by exploiting the axillary function defined by Boyes[49].

1.2 IETS

Quantum activity within biological systems and information theory applied therein have drawn much recent attention [50, 51, 52, 54, 55]. Examples of systems that exploit such phenomenon are: quantum coherence and entanglement in photosynthetic complexes [56, 57, 53, 58, 59, 60, 61, 62, 63, 64], quantum mutations [65, 66], information theory and thermodynamics of cancers [67, 68], the avian magnetic compass [69, 70, 71, 72], tunneling behavior in the antioxidant breakdown of catechols present in green tea [73], enzymatic action[74], olfaction[75], and genetic coding [76]. G Protein-Coupled Receptors (GPCR) are the target for the greatest portion of modern therapeutic small molecule medications[77]. Predictability of pharmacological efficacy for new drugs prior to a complex total synthesis can be aided by pharmacophore modeling, crystal structure or a homology model. The theory of protein/agonist binding has been described through variants of the Lock and Key model, originally proposed by Fischer[78] and the extensions thereof[79]. Although this theory has provided insight into changes of free energy associated with the formation of the activated complex, it has not manifested sufficient capacity for the prediction ligand activity or a mechanism by which the agonist activates the system.

1.2.1 Olfaction and Luca

The Lock and Key description has essentially been the model by which odorant activation in sensory proteins has been thought to occur. This model lacks - as it

did with generic protein agonist binding - the predictive ability desired by the perfumery community [80]. In support of this theory a complex system was devised to explain how many unique atomistic signals from distinct receptor proteins are collected and decoded by the olfactory bulb and transformed into a single signal that can be properly interpreted [81, 82, 83]. Other models that have been put forward to account for odorant binding and prediction include those of Dyson and Wright [84], who first proposed a vibrational theory of olfaction and based their works upon the odorant activating several receptors, each of which detect a certain portion of the total stimulant pattern of the molecule. It is the collective detected pattern that yields the specific response associated with the odorant. The theory was expanded upon to include scents generated through the blend of two or more molecules [85] and explanations of chiral behaviors in olfaction [86]. Early models attempting to account for predictability of agonist classification beyond shape were those of odorant binding [87, 84]; these works proposed a vibrational theory of activation and effect. Vibrational theories were eventually disregarded for reasons that include a lack of conceived mechanism and the inability of the protein (which is vibrating) to detect the continuum of thermally-activated, classical vibrations of the odorant. Several studies have been conducted to determine which molecular facets are considered, neutral or unnoticed by the olfactory system, including configurational isomerism [81], stereoisomerism [88, 89, 90, 91], isotopisms [92], odor blending [93] and structural analogies [75]. A recently suggested a theory of olfactory activation consisting of a physical mechanism closely resembling Inelastic Electron Tunneling Spectroscopy (IETS) [75, 94, 80]. Turin contends that the earlier vibrational theory of olfaction was valid, yet lacked a specific physical mechanism of action. As the system lacked the necessary radiation source for photo-absorption mechanisms and the proper mechanism should require consideration of all normal modes within the molecule, the physical mechanism that most closely resembles the considerations of the proposed system is Inelastic Electron Tunneling Spectroscopy (IETS). Within his works, Turin demonstrated the viability of his theory across several classes of odorants with several

examples per class. The theory was examined and the plausibility of the time scales of the phenomenon has since been verified through consideration of Marcus theory governing rates and kinetic viability [95]. Electron tunneling rates for the olfaction system have been calculated and support the theory [97]. Furthermore, eigenvalue spectral analysis of odorant molecules has shown a high correlation between the vibrations and odorant classification [96]. Experiments have been performed using *Drosophila melanogaster*, the common fruit fly, in an effort to give merit to Turin's theory. *D. melanogaster* displayed, in both trained and untrained simulations, a sensitivity to the deuteration of several compounds [92, 98]. One compound used within this set of experiments was acetophenone (ACP). It was found that untrained flies were attracted to ACP in preference to unscented air. Progressive deuteration of the hydrogens of ACP yielded compounds which were found to be progressively more aversive to the flies. Observations of *D. melanogaster*'s ability to discern between specific isotope analogues provides a degree of evidential support consistent with Turin's theory of mechanical excitation.

1.2.2 History of IETS

Inelastic Electron Tunneling Spectroscopy is a well-founded experimental method utilizing a simplistic laboratory set-up that can deliver the vibrational spectra of an analyte. The mechanism of action is semi-classical and not optical, particular selection rules are derivable with IETS [99] but in general this method allows for forbidden transitions, thus all vibrational modes are addressable [100]. The method is implemented by the application of a potential across a two-plate junction with a spatial separation between the plates. High energy electrons from the valence band of one plate will tunnel across the junction into the conduction band of the other. When the tunneling process occurs in the absence of analyte molecules, the process is elastic in nature and electron energy is maintained throughout the process, thus the electrons energy must be respective of the energy between the valence and conductance band.

1.2.3 Measurements

The IETS mechanism relies on a field driven electron transfer across an insulating gap situated between two conductive metal plates. The driving field promotes electrons to tunnel from the donor site on one side of the gap to the acceptor site on the other side, this being the elastic process. As the intensity of the driving field is increased, the electrons may donate a quanta of energy to a molecule situated within the gap along their path, this being the inelastic process. As the interaction is between the electron and a single atom of the molecule, the contribution to the conductivity found through this calculation must be repeated and summed over all atoms within the molecule. This secondary conductive path promotes an enhancement to the current across the gap. The donated quanta of energy is equal to a quanta accepted by the molecules vibrational or electronic transitions. There exist several other mechanisms by which electrons are conveyed across the gap including elastic transfer, inelastic transfer, 2^{nd} order elastic transfer as well as subsequent and less contributing modes of transport including modes displaying photon emission[101, 102]. Theoretical descriptions of this mechanism were introduced by Kirtley et al[103] and later elucidated by Phillips and Adkins[104]. As the electrons tunnel through the barrier they may undergo several processes including: elastic transfer, inelastic transfer, 2^{nd} order elastic transfer and subsequent less contributing modes of transfer. The inelastic modes of transport are facilitated through interaction between the tunneling electron and a deposited molecule within the gap[102]; the tunneling electron donates of quanta of energy to the deposited molecule. In the case where there are a non-continuum of acceptor and donor energy levels, the donation of energy from the electron to the molecule must obey Fermis Golden Rule. The quanta of energy is typically in the range of vibrations for IETS, although electronic excitations have also been achieved experimentally[105]. The electronic interaction between the ligand and the molecule treats each atom of the molecule separately; each atom is assigned a partial charge, Z , and sits at its equilibrium positions, R , it vibrates with a displacement u . The interaction potential is that of an electron and single dipole. Depositing

an analyte molecule onto the electron source plate, as the tunneling electrons enter the gap they may interact with the deposited analyte molecules; in doing so they are effectively given a springboard, shortening their tunneling path. This interaction comes at a cost of energy; the electron will lose energy to the analyte molecule, where the amount of lost energy is equal to that of a vibrational mode of the molecule. This process may be seen in Figure 3.1. This method has been well described theoretically [106, 107, 108] and expanded to include such considerations as molecular orientation [109] and short-ranged higher harmonics [110]. Here we shall review aspects of the theoretical description of the elastic process as seen in [103, 104].

The most fundamental expression describing electromagnetic interactions between an electron and a charged dipole is [111]:

$$V = \frac{z_i (-z_j) e^2}{4\pi\epsilon_0} \frac{1}{|r_j - r_i|} + \frac{z_i z_j e^2}{4\pi\epsilon_0} \frac{1}{|r_j + p_j - r_i|} \quad (1.9)$$

Where r_i is the location of the electron providing a field $z_i e^2$ and r_j is location of a single side of the dipole where both ends provide a field with the magnitude $z_j e^2$; the second term describes the remaining, oppositely charged side of the dipole at a distance p_j from r_j . This is typically repressed through a Taylor Series expansion concerning the denominator.

After the series expansion, the point dipole approximation is typically employed; this approximation states that the distance between the charge and the dipole is much greater than the displacement between the dipole termini. Under the point dipole approximation all but the leading terms of the expansion drop due to minimal contribution. It is important to note that it has been suggested that the spatial dimensions of the activation site within this class of proteins is to be on the order of 15\AA [97]. This suggested dimension of, when compared to order of magnitude of the normal mode displacement vector, does not meet the criteria for the point dipole approximation.

Inelastic electron tunneling, a method for obtaining information about the vibrational modes of a molecule, does not rely on the interactions between the molecular dipole and the field of the electron [104, 103]. The interaction potential, Eq. 3.4,

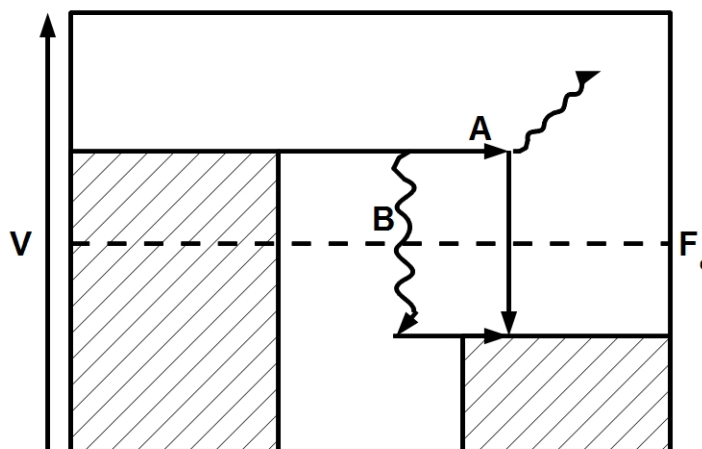


Figure 1.1. Cartoon displaying the competing processes during IETS where V is potential energy and F_e is the Fermi Level. Path A is radiative [101, 99], requiring the tunneling electron to spontaneously lose energy to meet the energy of the conductive band. Path B shows the electron losing energy via a non-radiative process; it is implicit that the energy lost is to a normal mode of a deposited molecule within the gap - such is our case.

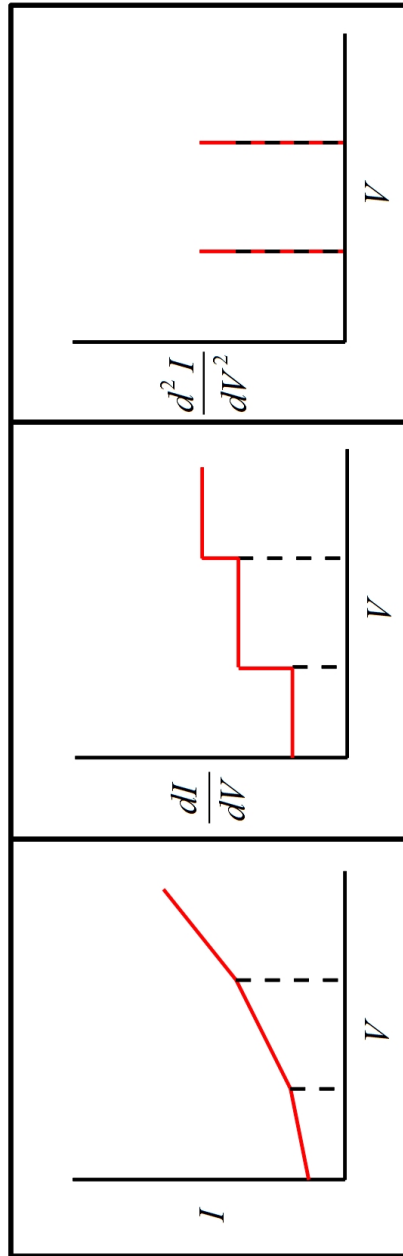


Figure 1.2. Detection of IETS mechanism within laboratory experiments. i shows the relationship between applied potential and the current across the gaps. ii the current's derivative with respect to the applied field. iii the current's impulse with respect to applied field, note that this is the quantity used in an experimental IETS apparatus.

describes the interaction between an electron and a single oscillating dipole, representing a single vibrating atom within the molecule; this interaction depends neither upon the polarizability of the system nor the change in net dipole. The single-dipole nature of the potential requires a summation over the atoms within the molecule to account for each independent electron-atom interaction. The coherent motion of two atoms within a molecule may allow for the generation of a phase factor that helps account for the roughly equal intensities of IR- and Raman-associated modes within IETS.

1.2.4 Map to Proteins

In 1991 a class of genes was discovered that encodes for proteins responsible for olfaction[113]. These proteins are a specific subtype of G-Protein Coupled Receptor (GPCR). GPCRs are prevalent throughout living organisms, with roles that include the synaptic recognition of neurotransmitters within the central nervous system. GPCRs can have many more functions in physiology, yet the principle concern of this paper is an examination of the viability of Turin's theory in cases involving protein-agonist binding within the CNS and as a predictor of intrinsic efficacy as defined within [114]. Herein we will examine the IETS spectra of chemical species that are known endogenous agonists, as well as some synthetic agonists for serotonin (5-HT) type receptors (specifically the 5-HT_{2A} subtype). The 5-HT_{2A} receptor is specifically cited as a receptor whose activation is associated with human hallucinogenic responses [115, 116]. The serotonin molecule has been adequately vibrationally studied, with a wealth of docking studies to determine its agonist acceptability in light of the Lock and Key model, yet this receptor has yet to be crystallized in an activated state, an advance that would yield important information for future calculations and theory development [117]. A small examination of the viability of the theory in the case of antagonist molecules is also undertaken here, as well as a proposed set of molecules that could be employed in the experimental validation of this (general) expansion of

the theory. The activation of G-Protein Coupled Receptors (GPCRs) governs many physiological activities examples of which include: olfaction[118], central nervous system regulation[119] and maintaining circadian rhythm[120]. Roughly half of all modern small molecule therapeutics target this class of proteins[112] and roughly 50% of all human encoded GPCR genes encode for olfaction alone[121]. Understanding the mechanism by which GPCRs are activated is paramount to applications within both the pharmaceutical and the flavor/scent industries. The theory of protein/agonist binding has been described through variants of the Lock and Key model, originally proposed by Fischer[78] and the extensions thereof[79]. Although this theory has provided insight into changes of free energy associated with the formation of the activated complex, it has not manifested sufficient capacity for the prediction ligand activity or a mechanism by which the agonist activates the system. We focus on an initial examination of the viability of the vibrational theory of protein activation in cases involving protein-agonist binding within the central nervous system and as a predictor of intrinsic efficacy as defined within [114]. Activation of the 5-HT_{1A} and 5-HT_{2A} receptors is implicated as being associated with human hallucinogenic responses [115, 116]. Specifically discussing the activation of olfactory proteins under the odotope theory, the volatile odorant molecule is hypothetically capable of maintaining something akin to its optimized geometry within the activation site[122]. This is due to the fact that only certain sections of the molecule are being determined at once suggestive of a soft or partial docking; it could be rationalized that the molecule only loosely enters and is never fully enveloped by the activation site. This rationalization would be countered by docking studies of the OR1A1, OR1A2 and OR1G1 human olfactory receptors that do show envelopment of the ligands which dock with the protein[123, 124].

Full ligand envelopment can lead to geometric alterations of the ligand during the docking as the protein-agonist complex reaches its energy minimum states. The alteration of ligand geometry can lead to attenuations in both the modal displacements and the partial charges, which for our example system can roughly generate a

10% alteration by displacement or a 5% alteration by partial charge (where partial charge was calculated through NBO analysis) in the tunneling intensity if the molecular geometry group is maintained. Moreover, these attenuations alter the potential interaction between the electron and the dipole through the dot product present in several terms of the non-approximated interaction potential Eq. 3.19 (line 1) as well as the standard interaction potential Eq. 3.4.

Orientation effects within IETS intensity calculations have been described as being of such importance as to practically be a selection rule for this type of vibrational characterization [103, 99, 109]. Interaction potentials used within early formulations of IETS calculations rely on the coupling strength of the electron within the donor site to atomic harmonic oscillators, and did not include any dynamic interactions within the system. More dynamic formulations exist to deal with that rather minute contribution of inelastic tunneling contributions to the current through molecular junctions, such as greens functions approaches. It should be noted that in these cases the inelastic contribution is to the molecular conductance and is attributed to vibronic alteration of electronic levels within the molecule this second-order coupling (electron-vibrational state-electronic state) is why the inelastic contribution is minute in these cases [125]. Application of the IETS model for the protein environment requires mapping several aspects of the IETS methodology to the biological system. The two-plate setup of the tunneling junction represent the walls of the receptor site; more explicitly, under electron transfer the valance and conductance bands within the juncture become specific HOMOs and LUMOs of the residues making the walls of the receptor. This dictates that energy transition detectable by the protein should be the energy difference between electronic levels of residue side-chains or any bound cofactors such as a metal ion. This alteration of IETS also localizes the source of tunneling electrons to a single residue side-chain; the implication is that electrons are not capable of uniformly tunneling through the molecule. This lack of uniformity suggests that the act of tunneling is localized to regions of the agonist molecule and that not all local oscillators of a specific mode fully contribute to the current

enhancement. Secondly, unlike the experimental IETS procedure, the analyte is not deposited upon a surface, being encapsulated by the active site. There is no externally applied potential within the receptor site which would have allowed for the scanning of energies; yet, it has been suggested that an ionic cofactor, likely a calcium ion, could provide this driving field. The implication of this is that the receptor is set to test the vibrational-assisted enhancement to the electron tunneling rate at a specific energy. The electrostatic interactions which govern docking orientation would be a means of orienting the endogenous agonists in such a way that the tunneling junction is appropriately aligned for maximized electron transfer across the atoms responsible for the inelastic contribution. Non-endogenous agonists would align with residues in a manner which may place energetically appropriate modes in proximity of the tunneling junction, thus allow for the activation of the receptor.

1.3 Quantum Tic-Tac-Toe

A student's first excursion into quantum mechanics can be both overwhelming and daunting, even to an upper division science student. Understanding such concepts as wave functions, overlap integrals and probability amplitudes are vital in mastering the subsequent material within the course. A typical first semester course in quantum mechanics focuses on the Schrödinger Picture and Equation[126, 127, 128]. Herein we present an outline covering several exercises using Quantum Tic-Tac-Toe (QTTT), presented originally by Allen Goff[129, 130, 131], as a means of introducing and enforcing early topics in an introductory quantum mechanics course. The exercises presented here allow for introduction and discussion of: probability amplitude, probability density, normalization, overlap, the inner product, and separability of states. QTTT can be used as an approachable, fun and intuitive means of introducing these topics. It is the hope of the authors that this tool could act as a companion throughout instruction; after the students have been taught the game, the instructor can use it as a stepping stone to new topics and as an avenue for intuitive exercises. For an

introduction to the game, please see these papers[132, 129, 130, 131]. Other quantum games exist[133, 134, 135] and their introduction into the classroom as teaching tools and metaphors is strongly encouraged and will be pursued in future works by this author. We have generated instructor-guided inquiry exercises[136, 137] as if the classroom was broken-up into groups of two students per group. We present specific board examples as a means of discussion and instructional guidance examples, as introductory courses have been shown to benefit from strong instructor guidance[138]. A more natural exercise would be allowing the students (post-instruction on the rules and teaching a specific phenomenon) to play the game and come across these phenomenon on their own in an inductive learning style similar to a lab exercise[139, 140, 141, 142]. QTTT could also be used as a continuing-themed homework exercise as it can be used to exemplify many of the introductory topics in quantum mechanics. In this manner these exercises are akin to lab exercises in that they exploit elements of inductive learning[139, 140, 141, 142] and guided inquiry[136, 137]. Classical Mechanics whose approach was developed based on Newtons new mathematics was contemporaneously formulated alongside calculus. Both topics moved from academic investigation into high school classrooms, and in the case of Newtonian Mechanics earlier still. Quantum mechanics, developed in the twentieth century, was required to adequately describe such experimental phenomena as black-body radiation, the photoelectric effect, and the atomic spectrum of hydrogen. The development of quantum mechanics has led to description of phenomena such as the superposition principle, the ability of an unobserved quantum object to exist in a superposition of multiple states simultaneously; entanglement, spooky action at a distance where the state of one system affects that of another without a direct observable relationship connecting them; and interference, as matter exists in both particle and wave form within quantum theory matter interactions present wave phenomenon such as diffraction and the properties of constructive and destructive matter-wave addition. Just as a rudimentary understanding, at minimum, of classical mechanics became necessary for so many fields, an introduction into the concepts of quantum mechanics is of growing importance.

Furthermore, computational chemistry methods are of vital importance in areas such as materials science and drug design due to their predictive capacities, which may aid researchers in the prevention of generating failed targets. During the advent of quantum mechanics two schools of thought began to emerge: the Schrodinger Picture and the Heisenberg Picture[143]. The numerical results and physical significance taken from these schools are the same, they differ in where the time-dependency is exhibited (operators vs states). From the Heisenberg picture, Born and Heisenberg generated the matrix methods that are prevalent in modern computation chemistry[144, 145]; methods such as: Hartree-Fock method, Density Functional Theory, and Configuration Interaction methods.

Discussion of basis-set methods is something that is normally avoided in undergraduate level courses. This paper provides discussion and exercises by which topics in matrix methods can be approached in undergraduate level courses or as an early assessment or introduction to computational methods in a graduate level course. We also briefly discuss density matrices so that we may introduce entanglement and concurrence to the students. We have chosen to introduce entanglement as it has proved to be a vital element in the future studies of quantum computing[146, 147] and quantum biology[148, 149].

Topics which we later broach within the terms of quantum games include all of the following. The fundamental quantity within the Schrodinger picture of quantum mechanics, the wave function, $\Psi(x)$. $\Psi(x)$, describing the total system energy of a particle[150]. Dependent topics such as probability amplitude, sign symmetry and probability density follow. The handling of inner product spaces, normalization and overlap of spatial wave functions. We also present the matrix formulations which are typically avoided until later in a students pursuit of quantum mechanics[128], due to the preferable *Anschaulichkeit* of the Schrodinger equation)[143]. Topics such as Hilbert spaces, basis functions, change of basis and vector spanning, although relegated to later in the students career, are extensively used in quantum chemistry methods[151, 126, 127, 152]. Separability and entanglement are approached through

the inseparability of wave functions [153, 154, 155]. We also introduce the measurement of concurrence, yielding a quantitative measurement of pair-wise entanglement of particles within our system; the method was developed by Wootters[156, 157]. The calculation of concurrence is a brief five-step process[155]:

1. Construction of a Density Matrix: $\rho = |\psi\rangle\langle\psi|$.
2. Construction of a Flipped Density Matrix: $\tilde{\rho}$.
3. Product Matrix: $\rho\tilde{\rho}$.
4. Determine the Eigenvalues of $\rho\tilde{\rho}$: $\lambda_1, \lambda_2, \lambda_3 \dots$
5. Calculate Concurrence: $C = \max[0, \sqrt{\lambda_1} - \sqrt{\lambda_2} - \sqrt{\lambda_3} - \dots]$

Instruction in the concepts discussed above hinges on the design of the Classical Tic-Tac-Toe board and how it relates to the Quantum Tic-Tac-Toe board. Both are square and are divided into nine square subspaces. These subspaces will be referred to as principal squares and will each carry a number to denote the particular square being referenced. The numbering pattern of the principal squares on the board is shown in Figure 4.1. A complete discussing the game play will be undertaken in the chapter concerning this material and requires such a sufficient amount of concepts, vocabulary and rules that we shall terminate introduction here.

1.4 The Organization of the Thesis

This whole thesis is divided into three research directions: Dimensional Scaling for the search for multiply-charged ions; Inelastic Electron Tunneling Spectroscopy as a possible, novel mechanism for protein activation; and the use of Quantum Tic-Tac-Toe as a method of instructing an introductory quantum mechanics audience. Chapters 2-4 each focus, respectively, on a single of the aforementioned topics. Works were completed on cellular regeneration, these are presented within the attached

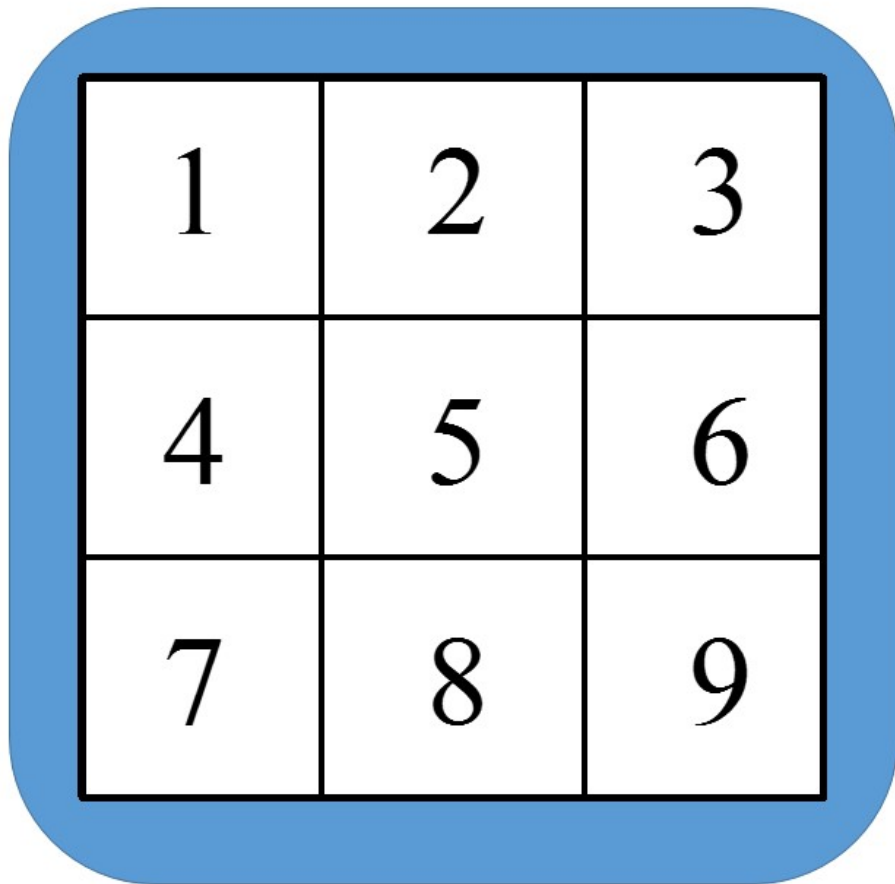


Figure 1.3. The layout of the game board for either classical or quantum Tic-Tac-Toe. This figure also displays the enumeration scheme that is used throughout this paper.

Appendices, as well as the patent documents pertaining to the Protein Activation project.

In Chapter 2, we progress through the dimensional scaling procedure. We begin by emphasizing the importance of the search for multi-charged ions within the gas phase, both dressed and undressed (in terms of an externally applied electromagnetic field). Some discussion is given to the known limits of excess charges to such species. After an introduction of several of the possible relativistic corrections applied to the system, we perform a particle in a box example using the pseudo-potential introduced through a relativistic ally inspired field trajectory. Following this, a description of both the 3-dimensional methods and the D-dimensional methods employed; this all followed by a presentation of results and a discussion of the lack of need to conduct the calculations for circular and elliptically polarized light.

Chapter 3 covers a suggested method of protein activation through the application of an inelastic method of tunneling for an electron through the docked agonist. We provide an introduction to this topic through a literature review of similar theories as well as previous theories surrounding this topic. A discussion of Inelastic Electron Tunneling Spectroscopy (IETS) is undertaken and several facets of the computation are discussed. A mapping between the proposed problem and method are discussed. We move on to introduce the spectral imagine method employed in the search for appropriate spectral signatures in probing this possible mechanism. We finally divulge results which are suggestive of this mechanism for two classes of serotonin agonists and propose an experiment which may be used to evaluate this theory.

Chapter 4 introduces a selection of material which can be covered in the standard first and second semester quantum mechanics course. We begin through a minor discussion to frame the importance of developing new methods and perspectives in which to frame introductory quantum mechanical instruction. We present the design of the game and quickly begin to define the topics inherent to the game which may be used to facilitate instruction. Section-by-section, thereafter, we present an array of topics and how to approach these topics within the confines of the game.

There are two Appendices provided. The first is, almost, a chapter unto itself concerning information surrounding a pair of cellular regeneration projects performed. These projects were time consuming, yet did not fall into the prevue of this thesis and as such were added as an Appendix. The second Appendix is material submitted to the United States Patent Office concerning the findings presented within Chapter 3 of this thesis. This material was generate by myself and the Purdue University Office of Technology Commercialization within the Purdue Research Foundation. This material lead to a provisional patent encompassing the material; the designation for the patent is PN: 62/037,457. This thesis is concluded with my Vita as well as a collection of my publications but in print and in submission.

1.5 References

- [1] D. R. Herschbach. Dimensional interpolation for two-electron atoms. *J. Chem. Phys.* 84, 838 (1986).
- [2] D. Herschbach, J. Aver, and O. Goscinkis, *Dimensional Scaling in Chemical Physics* (Kluwer Academic Publishers, 1993) p. 480.
- [3] A. Svidzinsky, G. Chen, S. Chin, and et al. Bohr model and dimensional scaling analysis of atoms and molecules. *Int. Rev. Phys. Chem.* 27, 665 (2008).
- [4] S. Kais and D. R. Herschbach. The $1/Z$ expansion and renormalization of the large dimension limit for many electron atoms. *J. Chem. Phys.* 100, 4367 (1993).
- [5] M. Dunn, T. C. Germann, D. Z. Goodson, C. A. Traynor, J. D. Morgan, D. K. Watson, and D. R. Herschbach. A linear algebraic method for exact computation of the coefficients of the $1/D$ expansion of the Schrödinger equation. *J. Chem. Phys.* 101, 5987 (1994).
- [6] J. Avery, D. Z. Goodson, and D. R. Herschbach. Dimensional Scaling and the Quantum Mechanical Many-body Problem. *Theor. Chim. Acta* 81, 1 (1991).
- [7] A. V. Sergeev. $1/D$ expansions for analytic three-body problems. *Sov. J. Nucl. Phys.* 50, 589 (1989).
- [8] J. Avery, in *Structure and Dynamics of Atoms and Molecules: Conceptual Trends*, J.-L. Calais and E. S. Kryachko, eds. (Kluwer Academic, Dordrecht, 1995), p. 135. Review, large- D limit for 3-particle systems.
- [9] A. A. Belov, Yu. E. Lozovik, and A. Gonzalez. First-order $1/D$ for electrons in a harmonic oscillator potential. *Phys. Lett. A* 142, 389 (1989).
- [10] Sabre Kais, T. C. Germann, and D. R. Herschbach. Corresponding states for $D=3$ and large- D potential curves of two-electron molecules. *J. Phys. Chem.* 98, 11015 (1994).
- [11] R. Bleil, A. Faliks, M. Miletic, and S. Kais. D -renormalization for homonuclear diatomic molecules. *J. Chem. Phys.* (1995).
- [12] R. Bleil and S. Kais. D -renormalization for heteronuclear diatomic and polyatomic molecules. *Int. J. Quantum Chem.* (1995).
- [13] V. S. Popov and A. V. Sergeev. Analytic results for $1/D$ expansion for H_2^+ . *Phys. Lett. A* 172, 193 (1993).
- [14] D. K. Watson and D. Z. Goodson. $1/D$ expansion for hydride ion improved by Z -variation. *Phys. Rev. A* 51, R5 (1995).

- [15] S. M. Sung and J. M. Rost. Chemical binding in the large-D limit. *J. Phys. Chem.* 97, 2479 (1993).
- [16] S. Kais and D. R. Herschbach. D-scaling for quasistationary states. *J. Chem. Phys.* 98, 3990 (1993).
- [17] C. A. Traynor and D. Z. Goodson. D-scaling without the Born-Oppenheimer approximation. *J. Phys. Chem.* 97, 2464 (1993).
- [18] J. M. Cohen and D. Z. Goodson. D-scaling for H_2^+ without Born-Oppenheimer approximation. *J. Chem. Phys.* (in press, 1995).
- [19] D. R. Herschbach. Review including D-interpolation of virial coefficients. *Proc. Am. Phil. Soc.* 137, 532 (1993).
- [20] C. M. Bender, S. Boettcher, and L. Mead. Random walk on a D-dimensional spherical lattice. *J. Math Phys.* 35, 368 (1994).
- [21] C. M. Bender, S. Boettcher, and M. Moshe. Spherically symmetric random walks in noninteger D. *J. Math. Phys.* 35, 4941 (1994).
- [22] S. Kais, D. R. Herschbach, N. C. Handy, C. W. Murray, and G. J. Laming. Density functionals and D-renormalization for exactly solvable Hooke's law atom. *J. Chem. Phys.* 99, 417 (1993).
- [23] S. M. Valone. D-scaling for constrained search energy density functionals. *Int. J. Quantum Chem.* 49, 591 (1994).
- [24] M. Gavrilin. Atomic stabilization in superintense laser fields. *J. Phys. B* 35, R147 (2002).
- [25] M. Gavrilin, *Atoms in Intense Laser Fields* (Academic Press, NY, 1992).
- [26] J. H. Eberly and K. C. Kulander. Atomic Stabilization by Super-Intense Lasers. *Science* 262, 1229 (1993).
- [27] D. J. Pegg, J. S. Thompson, R. N. Compton, and G. D. Alton. Evidence for a stable negative ion of calcium. *Phys. Rev. Lett.* 59, 2267 (1987).
- [28] D. Berkovits, E. Boaretto, S. Ghelberg, O. Heber, and M. Paul. Electron Affinity of Strontium. *Phys. Rev. Lett.* 75, 414 (1995).
- [29] M. K. Scheller, R. N. Compton, and L. S. Cederbaum. Gas-Phase Multiply Charged Anions. *Science* 270, 1160 (1995).
- [30] J. Simons. Theoretical Study of Negative Molecular Ions. *Ann. Rev. Phys. Chem.* 62, 107 (2011).

- [31] J. Simons. Molecular Anions. *J. Phys. B* 112, 6401 (2008).
- [32] E. H. Lieb. Bound on the maximum negative ionization of atoms and molecules. *Phys. Rev. A* 29, 3018 (1984).
- [33] K. H. Chang, R. D. McKeown, R. G. Milner, and J. Labrenz. Search for long-lived doubly charged negative atomic ions. *Phys. Rev. A* 35, 3949 (1987).
- [34] D. R. Bates, in *Negative Ions: Structure and Spectra, Advances In Atomic, Molecular, and Optical Physics*, Vol. 27, edited by S. D. Bates and B. Bederson (Academic Press, 1990) pp. 1–80.
- [35] A. V. Sergeev and S. Kais. Variational principle for critical parameters of quantum systems. *J. Phys. A* 32, 6891 (1999).
- [36] P. Serra and S. Kais. Finite size scaling for critical conditions for stable dipole-bound anions. *Chem. Phys. Lett.* 372, 205 (2003).
- [37] Q. Wei, S. Kais, and D. Herschbach. Dimensional scaling treatment of stability of atomic anions induced by superintense, high-frequency laser fields. *J. Chem. Phys.* 127, 094301 (2007).
- [38] Q. Wei, S. Kais, and N. Moiseyev. New stable multiply charged negative atomic ions in linearly polarized superintense laser fields. *J. Chem. Phys.* 124, 201108 (2006).
- [39] M. Pont, N. R. Walet, M. Gavrilu, and C. W. McCurdy. Dichotomy of the Hydrogen Atom in Superintense, High-Frequency Laser Fields. *Phys. Rev. Lett.* 61, 939 (1988).
- [40] E. van Duijn, M. Gavrilu, and H. G. Muller. Multiply Charged Negative Ions of Hydrogen Induced by Superintense Laser Fields. *Phys. Rev. Lett.* 77, 3759 (1996).
- [41] Q. Wei, S. Kais, and N. Moiseyev. Frequency-dependent stabilization of He^- by a superintense laser field. *Phys. Rev. A* 76, 013407 (2007).
- [42] Q. Wei, S. Kais, and D. Herschbach. Dimensional scaling treatment of stability of simple diatomic molecules induced by superintense, high-frequency laser fields. *J. of Chem. Phys.* 129, 214110 (2008).
- [43] C. Joachain, M. Dorr, and N. Kylstra, in *High-Intensity Laser-Atom Physics, Advances In Atomic, Molecular, and Optical Physics*, Vol. 42, edited by B. Bederson and H. Walther (Academic Press, 2000) pp. 225–286.
- [44] C. J. Joachain and N. J. Kylstra. Relativistic Effects in Laser-Atom Interactions. *Physica Scripta* 68, C72+ (2003).

- [45] L. S. Brown and T. W. B. Kibble. Interaction of Intense Laser Beams with Electrons. *Phys. Rev.* 133, A705 (1964).
- [46] J. H. Eberly and A. Sleeper. Trajectory and Mass Shift of a Classical Electron in a Radiation Pulse. *Phys. Rev.* 176, 1570 (1968).
- [47] L. E. McMurchie and E. R. Davidson. One- and two-electron integrals over cartesian gaussian functions. *J. Comp. Phys.* 26, 218 (1978).
- [48] A. Szabo and N. S. Ostlund, *Modern quantum chemistry: introduction to advanced electronic structure theory* (Dover Publications, 1996) p. 480.
- [49] S. F. Boys. *Electronic Wave Functions. I. A General Method of Calculation for the Stationary States of Any Molecular System.* Royal Society of London Proceedings Series A 200, 542 (1950).
- [50] M. Arndt, T. Juffmann and V. Vedral. Quantum physics meets biology. *HFSP J.* 3, 386 (2009)
- [51] P. C. W. Davies. Does quantum mechanics play a non-trivial role in life? *BioSystems.* 78, 69-79 (2004)
- [52] P. Ball. The dawn of quantum biology. *Nature.* 474(7351), 272-274 (2011)
- [53] S. Kais. ENTANGLEMENT, ELECTRON CORRELATION, AND DENSITY MATRICES. *Advances in Chemical Physics.* 134, 493-535 (2007)
- [54] S. F. Huelga and M. B. Plenio. Vibrations, Quanta and Biology. *Contemporary Physics.* 54, 181 (2013)
- [55] S. Lloyd, M. Mohseni, A. Shabani and H. Rabitz. The quantum Goldilocks effect: on the convergence of timescales in quantum transport. arXiv:1111.4982 [quant-ph]. (2011)
- [56] G. S. Engel, T. R. Calhoun, E. L. Read, T.-K. Ahn, T. Mancal, Y.-C. Cheng, R. Blankenship and G. R. Fleming. Evidence for wavelike energy transfer through quantum coherence in photosynthetic systems. *Nature.* 446, 782-76 (2007)
- [57] G. R. Fleming, S. F. Huelga and M. B. Plenio. Focus on quantum effects and noise in biomolecules. *New Journal of Physics.* 13, 115002 (2011)
- [58] S.-H. Yeh, J. Zhu and S. Kais. Population and coherence dynamics in light harvesting complex II (LH2). *J. Chem. Phys.* 137(8), 084110 (2012)
- [59] M. Sarovar, A. Ishizaki, G. R. Fleming and et al. Quantum entanglement in photosynthetic light-harvesting complexes. *NATURE PHYSICS.* 6(6), 462-467 (2010)

- [60] J. Zhu, S. Kais, A. Aspuru-Guzik and et al. Multipartite quantum entanglement evolution in photosynthetic complexes. *J. Chem. Phys.* 137(7), 074112 (2012)
- [61] T. Fujita, J. C. Brookes, S. K. Saikin and A. Aspuru-Guzik. Memory-assisted exciton diffusion in the chlorosome light-harvesting antenna of green sulfur bacteria. *J Phys Chem Lett.* 3, 2357-2361 (2012)
- [62] A. Shabani, M. Mohseni, H. Rabitz and S. Lloyd. Efficient estimation of energy transfer efficiency in light-harvesting complexes. arXiv:1103.3823 [quant-ph] (2012)
- [63] E. Collini, C. Y. Wong, K. E. Wilk, P. M. G. Curmi, P. Brumer and G. D. Scholes. Vibrations, Coherently wired light-harvesting in photosynthetic marine algae at ambient temperature. *Nature.* 463, 782-76 (2010)
- [64] A. Olaya-Castro and G. D. Scholes. Vibrations, Energy transfer from Forster-Dexter theory to quantum coherent light-harvesting. *Int. Nat. Revs. in Phys. Chem.* 30, 49-77 (2011)
- [65] J. McFadden. *Quantum Biology.* Norton Publishing (2001)
- [66] J. McFadden and J. Al-Khalili. A quantum mechanical model of adaptive mutations. *BioSystems.* 50, 203-211 (1999)
- [67] R. Remacle, N. Kraychenko-Balasha, A. Levitzki and R. D. Levine. Information-theoretic analysis of phenotype changes in early stages of carcinogenesis. *PNAS.* 107(22), 10324-9 (2010)
- [68] T. G. Graeber, J. R. Heath, B. J. Skaggs, M. E. Phelps, R. Remacle and R. D. Levine. Maximal entropy inference of oncogenicity from phosphorylation signaling. *PNAS.* 107(13), 6112-7 (2010)
- [69] D. Heyers, M. Manns, H. Luksch, O. Gunturkun and H. Mouritsen. A Visual Pathway Links Brain Structures Active during Magnetic Compass Orientation in Migratory Birds. *PLOS ONE.* 9, e937 (2007)
- [70] K. Maeda, K. B. Henbest, K. Cintolesi, et al. Chemical compass model of avian magnetoreception. *NATURE.* 453(7193), 387-U38 (2008)
- [71] J. A. Pauls, Y. T. Zhang, G. P. Berman and S. Kais. Quantum coherence and entanglement in the avian compass. *Phys. Rev. E.* 87(6), 062704 (2013)
- [72] J. M. Cai and M. B. Plenio. Chemical Compass Model for Avian Magnetoreception as a Quantum Coherent Device. *PRL.* 111, 230503 (2013)
- [73] I. Tejero, N. Gonzalez-Garcia, A. Gonzalez-Lafont and J. M. Lluch. Tunneling in Green Tea: Understanding the Antioxidant Activity of Catechol-Containing Compounds. A Variational Transition-State Theory Study. *Journal of the American Chemical Society.* 129, 5846-5854 (2007)

- [74] M. Garcia-Viloca, J. Gao, M. Karplus and D. G. Truhlar. How enzymes work: analysis by modern rate theory and computer simulations. *Science*. 303, 186-195 (2004)
- [75] L. Turin. A Method for the Calculation of Odor Character from Molecular Structure. *Journal of Theoretical Biology*. 216, 3, 367-385 (2002).
- [76] A. Patel. Why genetic information processing could have a quantum basis. *J. Biosci.* 26, 145-151 (2001)
- [77] A. Christopoulos. Allosteric binding sites on cell surface receptors: novel targets for drug discovery. *Nat Rev Drug Discov.* 1, 198-210 (2002)
- [78] E. Fischer. Einfluss der Configuration auf die Wirkung der Enzyme. *Ber. Dt. Chem. Ges.* 27, 2985-2993 (1894).
- [79] D. E. Koshland. Application of a Theory of Enzyme Specificity to Protein Synthesis. *Proc. Natl. Acad. Sci.* 44, 98-104 (1958).
- [80] L. Turin and F. Yoshii. *Handbook of Olfaction and Gustation*. Marcel Dekker, Inc. (2003).
- [81] K. Mori, H. Nagao and Y. Yoshihara. The Olfactory Bulb: Coding and Processing of Odor Molecule Information. *Science*. 286, 5440, 711-715 (1999).
- [82] C. Linster, B. A. Johnson, D. Yue, A. Morse, Z. Xu, E. E. Hingco, Y. Choi, M. Choi, A. Messiha and M. Leon. Perceptual Correlates of Neural Representations Evoked by Odorant Enantiomers. *The Journal of Neuroscience*. 21, 9837-9843 (2001).
- [83] H. Hamana, J. Hirono, M. Kizumi and T. Sato. Sensitivity-dependent Hierarchical Receptor Codes for Odors. *Chem. Senses*. 28, 87-104 (2003).
- [84] R.H. Wright. Odor and molecular vibration: Neural coding of olfactory information. *Journal of Theoretical Biology*. 64, 3, 473 - 502 (1977).
- [85] R.H. Wright. Molecular vibration and odour blending. *Chemical Senses*. 8, 103-106 (1983).
- [86] R.H. Wright. Odor and molecular vibration: optical isomers. *Chemical Senses*. 1, 3, 35-37 (1978).
- [87] G. M. Dyson. Some aspects of the vibration theory of odor. *Perfumery and Essential Oil Record*. 19, 456-459 (1928)
- [88] G. F. Russel and J. I. Hill. Order Differences between Enantiomeric Isomers. *Science, New Series*. 172, 1043-1044 (1971).

- [89] M. Taniguchi, M. Kashiwayanagi and K. Kurihara. Quantitative analysis on odor intensity and quality of optical isomers in turtle olfactory system. *American Journal of Physiology - Regulatory, Integrative and Comparative Physiology*. 262, R99-R104 (1992).
- [90] M. Laska. Olfactory discrimination Ability of Human Subjects for Enantiomers with an Isopropenyl Group at the Chiral Center. *Chem. Senses*. 29, 143-152 (2004).
- [91] Y. Sugawara, C. Hara, T. Aoki, N. Sugimoto and T. Masujima. Odor Distinctiveness between Enantiomers of Linalool: Difference in Perception and Responses Elicited by Sensory Test and Forehead Surface Potential Wave Measurement. *Chem. Senses*. 25, 77-84 (2000).
- [92] M. I. Franco, L. Turin A. Mershin and E. M. C. Skoulakis. Molecular vibration-sensing component in *Drosophila melanogaster* olfaction. *PNAS*. (2001).
- [93] A. Keller and L. B. Vosshall. A psychophysical test of the vibration theory of olfaction. *Nature Neuroscience*. 7, 337-338 (2004).
- [94] L. Turin. A Spectroscopic Mechanism for Primary Olfactory Reception. *Chemical Senses*. 21, 6, 773-791 (1996).
- [95] J. C. Brookes, F. Hartoutsiou, A. P. Horsfield and A. M. Stoneham. Could Humans Recognize Odor by Phonon Assisted Tunneling?. *Phys. Rev. Lett.* 98, 3, 038101 (2007).
- [96] S.-Y. Takane, J. B. O. Mitchell. A structure-odour relationship study using EVA descriptors and hierarchical clustering. *Org. Biolol. Chem.* 2, 3250-3255 (2004)
- [97] I. A. Solov'yov, P.-Y. Chang and K. Schulten. Vibrationally assisted electron transfer mechanism of olfaction: myth or reality? *Phys. Chem. Chem. Phys.* 14, 13861-13871 (2012)
- [98] E. R. Bittner, A. Madalan, A. Czader and R. Greg. Quantum origins of molecular recognition and olfaction in *drosophila*. *J. Chem. Phys.* 137, 22A551 (2012).
- [99] J. Lambe and R. C. Jaklevic. Molecular Vibration Spectra by Inelastic Electron Tunneling. *Phys. Rev.* 165(3), 821-832 (1968)
- [100] K. W. Hipps and U. Mazur. Inelastic Electron Tunneling Spectroscopy. *Handbook of Vibrational Spectroscopy*. Wiley (2001)
- [101] J. Lambe and S. L. McCarthy. Light Emission from Inelastic Electron Tunneling. *Phys. Rev. Lett.* 37(14), 923-925 (1976)

- [102] M. Reed. Inelastic Electron Tunneling Spectroscopy. *MaterialsToday*. 11, 46 (2008)
- [103] J. Kirtley, D. J. Scalapino and P. K. Hansma. Theory of vibrational mode intensities in inelastic electron tunneling spectroscopy. *Phys. Rev. B*. 14, 3177-3184 (1976)
- [104] W. A. Phillips and C. J. Adkins. A theory for the intensities of inelastic electron-tunnelling spectra. *Philosophical Magazine Part B*. 52, 739-750 (1985)
- [105] S. K. Khanna and J. Lambe. Inelastic Electron Tunneling Spectroscopy. *Science*. 220, 1345 (1983)
- [106] A. K. Sleigh, M. E. Taylor, C. J. Adkins and W. A. Phillips. Top-electrode and roughening effects in electron tunnelling spectroscopy. *Journal of Physics: Condensed Matter*. 1, 1107 (1989)
- [107] C. J. Adkins, W. A. Phillips. Inelastic electron tunnelling spectroscopy. *Journal of Physics C: Solid State Physics*. 18, 1313 (1985)
- [108] A. K. Sleigh, W. A. Phillips, C. J. Adkins and M. E. Taylor. A quantitative analysis of the inelastic electron tunnelling spectrum of the formate ion. *Journal of Physics C: Solid State Physics*. 19, 6645 (1986)
- [109] J. Kirtley and J. T. Hall. Theory of intensities in inelastic-electron tunneling spectroscopy orientation of adsorbed molecules. *Phys. Rev. B*. 22, 848-856 (1980)
- [110] J. Kirtley and P. Soven. Multiple-scattering theory of intensities in inelastic electron tunneling spectroscopy. *Phys. Rev. B*. 19, 1812-1817 (1979)
- [111] H. W. Wyld. *Mathematical Methods for Physics*. Westview Press (1987)
- [112] D. Filmore. It's a GPCR world. *Modern Drug Discovery*. 24-28 (2004)
- [113] L. Buck and R. Axel. A novel multigene family may encode odorant receptors: a molecular basis for odor recognition. *Cell*. 65, 175-187 (1991).
- [114] J. D. Urban, et al. Functional Selectivity and Classical Concepts of Quantitative Pharmacology. *Journal of Pharmacology and Experimental Therapeutics*. 320, 1, 1-13 (2007).
- [115] D. E. Nichols. Hallucinogens. *Pharmacology & Therapeutics*. 101, 2, 131-181 (2004).
- [116] D. E. Nichols and C. D. Nichols. Serotonin Receptors. *Chem. Rev.* 108, 1614-1641 (2008).

- [117] K. Karuppiah, M. Malini, D. Bhattacharya, M. M. Panicker and R. Sowdhamini. Molecular modeling and docking studies of human 5-hydroxytryptamine 2A (5-HT_{2A}) receptor for the identification of hotspots for ligand binding. *Mol. BioSyst.* 5, 12, 1877-1888 (2009).
- [118] I. Gailard, S. Rouquier and D. Giorgi. Olfactory receptors. *Cell. Mol. Life Sci.* 61, 456-69 (2004)
- [119] D. Hoyer, D. E. Clarke, J. R. Fozard, P. R. Hartig, G. R. Martin, E. J. Mylecharrane, P. R. Saxena and P. P. Humphery. International Union of Pharmacology classification of receptors for 5-hydroxytryptamine (Serotonin). *Pharmacol. Rev.* 46, 157-203 (1994)
- [120] S. M. Reppert. Melatonin Receptors: Molecular Biology of a New Family of G Protein-Coupled Receptors. *J Biol Rhythms. Rev.* 12, 528-531 (1997)
- [121] Y. Niimura and M. Nei. Evolution of olfactory receptor genes in the human genome. *PNAS.* 100, 12235-40 (2003)
- [122] A. Rinaldi. The scent of life. The exquisite complexity of the sense of smell in animals and humans. *EMBO Rep.* 8, 629-633 (2007)
- [123] K. Schmiedeberg, E. Shirokova, H-P. Weber, B. Schilling, W. Meyerhof and D. Krautwurst. Structural determinants of odorant recognition by the human olfactory receptors OR1A1 and OR1A2. *J. Struct. Biol.* 159, 400-412 (2007)
- [124] G. Launay, S. Teletchea, F. Wade, E. Pajot-Augy, J. F. Gibrat and G. Sanz. Automatic modeling of mammalian olfactory receptors and docking of odorants. *Protein Eng. Des. Sel.* 25(8), 377-86 (2012)
- [125] M. Galperin, M. A. Ratner and A. Nitzan. Inelastic Electron Tunneling Spectroscopy in Molecular Junctions: Peaks and Dips. *arXiv.* 1-41 (2004)
- [126] A. Messiah. *Quantum Mechanics*, Dover, 1999
- [127] A. Messiah. *Quantum Mechanics Volume II*, Dover, 1999
- [128] D. A. McQuarrie J. D. Simon. *Physical Chemistry: A Molecular Approach*, 1st ed., University Science Books, 1997
- [129] Goff, A.; Lehmann, D.; Seigel, J. Quantum TicTaToe as Metaphor for Quantum Physics. *AIP Conf. Proc.* 2004, 699, 1152.
- [130] Goff, A. Quantum Tic-Tac-Toe: A Teaching Metaphor for Superposition in Mechanics. *Am. J. Phys.* 2006, 74, 962.
- [131] Goff, A.; Lehmann, D.; Siegel, J. Quantum Tic-Tac-Toe, Spooky-Coins Magic-Envelopes, as Metaphors for Relativistic Quantum Physics. *AIAA Pap.* 2002, No. AIAA-2002-3763.

- [132] Hoehn, R.; Kais, S. Using Quantum Games to Teach Quantum Mechanics, Part 1. *J. Chem. Educ.*, 91, 417, 2014
- [133] Leaw, J. N.; Cheong, S. A. Strategic Insights from Playing Quantum Tic-Tac-Toe. *J. Phys. A: Math. Theor.* 2010, 43, 455304.
- [134] Meyer, D. A. Quantum Strategies. *Phys. Rev. Lett.* 1999, 82 (5), 10521055.
- [135] Schmidt, A. G. M.; da Silva, L. Quantum Russian Roulette. *Physica A* 2013, 392, 400410.
- [136] Domin, D. A Review of Laboratory Instruction Styles. *J. Chem. Educ.* 1999, 76, 543547.
- [137] Prince, M. J.; Felder, R. M. Inductive Teaching and Learning Methods: Definitions, Comparisons, And Research Bases. *J. Eng. Educ.* 2006, 95, 123138.
- [138] Kirschner, P. A.; Sweller, J.; Clark, R. E. Why Minimal Guidance during Instruction Does Not Work: An Analysis of the Failure of Constructivist, Discovery, Problem-Based, Experiential and Inquiry Based Teaching. *Educ. Psychol.* 2006, 41, 7586.
- [139] Briggs, M.; Long, G.; Owens, K. Qualitative Assessment of Inquiry-Based Teaching Methods. *J. Chem. Educ.* 2011, 88, 1034 1040.
- [140] Spencer, J. New Approaches to Chemistry Teaching. *J. Chem. Educ.* 2006, 83, 538533.
- [141] Farrell, J. J.; Moog, R. S.; Spencer, J. N. A Guided Inquiry General Chemistry Course. *J. Chem. Educ.* 1999, 76, 570574.
- [142] Ditzler, M. A.; Ricci, R. W. Discovery Chemistry: Balancing Creativity and Structure. *J. Chem. Educ.* 1994, 71, 685688.
- [143] Beller, M. The Conceptual and the Anecdotal History of Quantum Mechanics. *Found. Phys.* 1996, 26 (4), pp545557.
- [144] Born, M.; Heisenberg, W.; Jordan, P.; Zur Quantenmechanik, I. *I. Z. Phys.* 1936, 35 (89), pp557615.
- [145] Hilbert, D.; Ewald, W. B.; Hallett, M.; Majer, U.; Sieg, W. David Hilbert's Lectures on the Foundations of Mathematics and Physics, 1891-1933; Springer: New York, 2004; Volume 5.
- [146] Feynman, R. P. Simulating Physics with Computers. *Int. J. Theor. Phys.* 1982, 21, 6/7.

- [147] Lloyd, S. Universal Quantum Simulators. *Science* 1996, 273 (5278), 10731078.
- [148] Zhu, J.; Kais, S.; Aspuru-Guzik, A.; Rodrigues, S.; Brock, B.; Love, P. J. Multipartite Quantum Entanglement Evolution in Photosynthetic Complexes. *J. Chem. Phys.* 2012, 137, 074112.
- [149] Gauger, E. M.; Rieper, E.; Morton, J. J. L.; Benjamin, S. C.; Vedral, V. Sustained Quantum Coherence and Entanglement in the Avian Compass. *Phys. Rev. Lett.* 2011, 106, 040503.
- [150] Schrodinger, E. An Undulatory Theory of the Mechanics of Atoms and Molecules. *Phys. Rev.* 1926, 28 (6), 10491070.
- [151] Szabo, A.; Ostlund, N. S. *Modern Quantum Chemistry: Introduction to Advanced Electronic Structure Theory*; Dover Publications: Mineola, NY, 1996.
- [152] Levine, I. N. *Quantum Chemistry*, 5th ed.; Prentice Hall: Upper Saddle River, NJ. 2000.
- [153] Schrodinger, E. Discussion of Probability Relations between Separated Systems. *Math. Proc. Cambridge Philos. Soc.* 1935, 31, 555-563, DOI: 10.1017/S0305004100013554.
- [154] Schrodinger, E. Probability Relations between Separated Systems. *Math. Proc. Cambridge Philos. Soc.* 1936, 32, 446-452, DOI: 10.1017/S0305004100019137.
- [155] Kias, S. Entanglement, Electron Correlation and Density Matrices. *Adv. Chem. Phys.* 2007, 134, 493-535.7
- [156] Hill, S.; Wootters, W. K. Entanglement of a Pair of Quantum Bits. *Phys. Rev. Lett.* 1997, 78 (26), 5022-5025.
- [157] Wootters, W. K. Entanglement of Formation and Concurrence. *Quantum Inf. Comput.* 2001, 1 (1), 27-44.

2. RELATIVISTIC CORRECTIONS TO DIMENSIONAL SCALING

2.1 Introduction

The generation of stable, multiply-charged atomic ions via exposure to super-intense laser fields is a topic which challenges preconceived notions for ionic atoms and is, therefore, of fundamental importance in atomic and molecular physics[1, 2, 3]. Over the past decades, advancements in spectroscopic methods have yielded verification of mono-charged Calcium and Strontium atomic anions[4, 5] and various gas-phase poly-charged molecular ions[6, 7, 8]. However without the large charge volume which is provided by the heavy atoms -above- or small molecules it is unlikely that species would be able to bind more than one excess electron; this can be noted by the relative stability of O^{-2} in the liquid-phase, yet its instability within the gas-phase[6]. Theoretical works have developed an absolute upper-limit to the number of electrons which may be bound to a atomic center[9]: $N_e \geq 2Z$, with N_e being the number of electrons and Z being the Coulomb charge of the nucleus. Within the context of Lieb's frameworks, Hydrogen would therefore be disallowed any excess electrons beyond that which yields the Hydride state, thusly H^{2-} is unstable[10, 11]. Supporting theoretical works have come later[12, 13] -some including implementation of finite-sized scaling[13]- and have conclusively determined at gas-phase, dianionic atoms are unstable.

It has been shown that stable, multiply-charged atomic ions may be developed within extremely strong laser fields on the order of 10^{16} W/cm² and above[14, 15]. Within the field, the electron density - still being bound to the nucleus - has been found to be nodal in nature as the Coulomb potential splinters under the influence of the field into distinct, localized regions whose positions are governed by the field

parameters of the laser. This phenomenon is most easily - and best- discussed within the context of the Krammers Henneberger (KH) reference frame, electron centric frame, where the electron is treated as the stationary body and the nucleus traverses the path of the applied field; in this context the local nodes of electron density are located at the turning points on the path of the nucleus. These are the location at which the angular velocity of the nucleus decreases and thus spends more time in a local area - thus generating a greater pull in that area. Within these nodal regions, the bound electrons maintain a great enough distance from one and another to minimize their Coulomb repulsion while also giving each a center with which to bind. In this field, the electrons -which intuition tells us would be completely ionized- are capable of stably binding into multiply-charged atomic ions. The field strength allows one to manipulate the location and pull of the nodal centers , thus generating a method of control over the potential and therefore establishing the ability to push the electrons into and past their most stable state by means of manipulating laser parameters, frequency and intensity.

The contained theoretical works are concerned with High-Frequency Floquet Theory (HFFT) which allows for a time-independent treatment of the coupling of the static Coulomb potential with a time-varying electromagnetic field. This is possible by exploiting highly oscillatory fields in which the electrons would be prohibited from coupling with the periodic nature of the field due to extremely short periods (large frequencies) of oscillation, thus the system's electrons would feel a period average of the applied potential coupled with the static Coulomb potential, again this is best discussed within the KH frame. This time-average allows generation of the aforementioned nodal structure and therefore permits the stability of the subsequent states and allows the system to forgo autoionization. The above discussed methodology was introduced to atomic systems by Pont et al[16], van Duijin et al[17], and was used again by Wei et al[15, 18, 19, 14] to describe non-relativistic, multiply-charged atomic ions. Herein we shall propose a framework utilizing HFFT as a backbone for applying relativistic corrections to atomic ions in a time-independent manner.

The procedure enclosed is not only a search for the stability of multiply-charged ions, but also that in concert with an explicit utilization and validation of the Dimensional Scaling procedure and the fourth-fold installment in such works. Multiple electrons in bound state configurations under either either the Dirac or Klein-Gordon equations are both open questions in Dimensional Scaling, and thus we resort such augmentations to the Time Independent Schrodinger Equation at the large-dimensional limit as most relativistic effects can be appended to the Schrodinger Equation through first-order Perturbation Theory.

Also, Kaminski had proposed a relativistic Kramers-Henneberger frame based on the three-dimensional Dirac equation[20], which however, is rather impractical for numerical purposes as the electron momenta appear in the argument of the potential of the KH-transformed Hamiltonian. Krstic also discussed the relativistic corrections starting from Dirac equation and showed the same orbital corrections as used in our work[21], although we present it in a phenomenological way. Protopapas et al.[22] discussed the relativistic mass shift effects from Klein-Gordon equation in stabilization with respect to the non-relativistic prediction and demonstrated in KH frame the feasibility of using the the relativistic effective mass.

To derive the atom-intense laser interaction directly from Dirac equation is a demanding work both theoretically and numerically; and, as of yet, the use of such method in a search for stable multiply-charged ions is open. The most sensible way is to start from Schoedinger equation by including the relativistic corrections in a perturbative way. Physically, the main relativistic corrections in atom-laser interactions include the magnetic component of the laser field, the relativistic mass shift, the invalidity of the dipole approximation and spin and retardation effects. The effects of retardation, the dipole approximation and spin have been shown by Latinne to be small in general[23].

2.2 Non-Relativistic Methodology

Consideration within the non-relativistic cases lies no longer with both the mass and the magnetic coupling, but with the time dependent electric field coupling with the system's Coulomb potential; this work was performed by Wei et al[15, 18, 19, 14] and produced stably bound multiply-charged ions for small atomic centers utilizing the field parameter (α_0), discussed later, and finding detachment energies on orders of 0.1eV to 1.0 eV. The enclosed works, here, expound upon this by adding the necessary relativistic corrections to the previous framework. A free electron within an oscillating electric field shall undergo oscillatory motions which are governed by a coupling to the field; the electron is said to be 'quivering' with a motion defined by a trajectory, $\vec{\alpha}_0(t)$, and a quiver amplitude, α_0 . A bound electron within the same situation shall feel a new potential which is a stacking of the applied field and the Coulomb potential of the central charge; the total potential for the system is said to be a Coulomb potential dressed by the laser, denoted as a dressed potential, V_{dres} .

Under the auspices of HFFT, introduced above and here[16], by applying a highly oscillatory laser field with an extremely short period the electrons will lack the ability to oscillate synchronously with the the applied field. In this manner, the potential felt by the electrons is a period average of the oscillatory field, this new potential is a dressed potential under the HFFT approximation, V_{dres}^{HFFT} . In all cases addressed within this paper the laser-coordinates are: laser fired in y-direction, electronic component linearly polarized in the z-direction, and the magnetic component in the x-direction

The situation of the dressed potential, V_{dres}^{HFFT} , is a time independent problem as the field has been period averaged, due to this the full Hamiltonian can be treated within the Time Independent Schrodinger Equation (TISE):

$$\epsilon_i \Psi_i = \hat{H} \Psi_i = \frac{-\hbar^2}{2m_e} \nabla^2 \Psi_i + V_{dres}^{HFFT} \Psi_i. \quad (2.1)$$

Accurate solutions to the equation are difficult for systems of more than one electron due to many-body interactions, but approximate solutions can be obtained in a

self-consistent method (SCF) through Hartree-Fock (RHF/UHF), Density Functional Theory (DFT), or post-Hartree-Fock Methods.

2.2.1 The Relativistic Mass Gauge

Mass -as a fundamental- is conceptualized in two different manners within physics, these being the rest mass and the relativistic mass. Rest mass, or invariant mass, is for a specific body a constant, measurable quantity denoted m_0 . In opposition to the rest mass is the variant quantity: relativistic mass, m_r . The relativistic mass depends upon the velocity of the observer. The variant nature of m_r is a correction to the rest mass which accounts for a non-zero kinetic energy for the measured system. This means that the relativistic mass increases in magnitude as the velocity of the system increases, and shall reach infinite mass as the system reaches the speed of light.

This portrayal of the mass shall be implemented within the Time Independent Schrodinger Equation (TISE) for the enclosed work, we shall now need to express alterations to the rest mass in terms of the system's laser parameters.

We are now called to introduce the concept of ponderomotive energy, U_p ; this being the cycle average kinetic energy of a quivering electron, i.e. electron undergoing oscillatory motion due to an external field and also qualifying under the dipole approximation. This is quantity discussed in context of such systems by Joachain, Dörr and Klystra[24].

$$U_P = \frac{e^2 \mathcal{E}_0^2}{4m_e \omega^2} \quad (2.2)$$

In the above, \mathcal{E}_0 is the peak strength of the electric field, ω is the angular frequency of the applied field and both e and m_e retain their conventional meanings: of magnitude of electron charge and electron mass, respectively. This quantity aides in the evolution of the rest mass to the relativistic mass as:

$$m_r = m^{dressed} = m_e \left(1 + 2 \frac{U_P}{m_e c^2}\right)^{\frac{1}{2}} \quad (2.3a)$$

$$= m_e (1 + 2q)^{\frac{1}{2}}. \quad (2.3b)$$

As can be seen, the quantity q begins to shift the mass and becomes the dominant factor within the expression as it approaches unity[25]. The form of Eq. (2.3b) was found by Brown and Kibble[26] and later verified by Eberly and Sleeper[27] via the Hamilton-Jacobi equation.

Below we shall discuss the above mass concept as it applies to the TISE for one electron (which can then be generalized to N electrons), these lines shall be discussed stepwise.

$$Eq.(1) \rightarrow \frac{-\hbar^2}{2m_e(1+2q)^{\frac{1}{2}}} \nabla^2 \Psi_i + V \Psi_i \quad (2.4)$$

$$\rightarrow \frac{-\hbar^2}{2m_e(1+2\frac{e^2\alpha^2\omega^2}{4m_e^2c^2})^{\frac{1}{2}}} \nabla^2 \Psi_i + V \Psi_i \quad (2.5)$$

$$\rightarrow \frac{-\hbar^2}{2(1+2.66 \times 10^{-5} \alpha^2 \omega^2)^{\frac{1}{2}}} \nabla^2 \Psi_i + V \Psi_i \quad (2.6)$$

The first line, Eq. (2.4), shows the form of the TISE as it appears accounting for the mass gauge, which is tuned by the quantity q . Secondly, we have introduced and employed the field coefficient, $\alpha = \frac{\mathcal{E}_0}{\omega^2}$, as a means of defining q in terms of known laser parameters. Lastly, we express all quantities in $\hbar=m_e=1$ units (atomic units), this allows us to maintain the relativistic alterations as a unitless multiplier, Eq. (3.6). As the multiplier which transforms invariant mass to relativistic mass is a unitless quantity, the resultant energies from the final line, Eq. (3.6), shall be in Hartree E_H , as they would if one ignored the mass gauge entirely. In all cases considered within this paper the potential function, V , shall be dressed under HFFT, making $V=V_{dres}^{HFFT}$

2.2.2 Trajectory Corrections

High-Frequency Floquet Theory (HFFT) was first introduced to similar systems by Pont et al[16], relies on the frequency of the externally applied electromagnetic field to be so quickly oscillating so as even the electrons are incapable of coupling their motions to the field. In this manner the D -dimensional dressed Coulomb potential

-which is in essence a time-dependent problem is simplified to a time-independent problem:

$$V_{dres}^{HFFT} = \frac{Z}{2\pi} \int_0^{2\pi} \left(\frac{d(\omega t)}{\sqrt{\sum_i^D (x_i + \alpha_i)^2}} \right). \quad (2.7)$$

To apply the above period average to a system one must develop an interest in the trajectory, $\vec{\alpha}(t)$, of the laser's path as its components are required in the above averaging as α_i along with the i^{th} Cartesian component, x_i . Earlier works[14, 15, 18, 19] have concentrated upon non-relativistic systems, and thus the laser trajectory is equivalent to the path taken by a free electron undergoing influence by a time-dependent external electric field (or laser field where no magneto-coupling is considered); the up and down oscillatory motion of the electric field governs the trajectory of the electron, seen in Eq.(2.8), where the polarization is as discussed in §A.

$$\vec{\alpha}(t) = \langle \alpha_x, \alpha_y, \alpha_z \rangle \quad (2.8a)$$

$$= \langle 0, 0, \alpha_0 \cos(\omega t) \rangle. \quad (2.8b)$$

Now concerning ourselves with the electronic-magnetic coupling within relativistic regimes; this shall be described analogously to the non-relativistic case above by the path taken by a free electron in an electromagnetic field now with the electronic-magneto coupling accounted. Within a plane-wave laser field, the electron classical trajectory can be obtained analytically. For a linearly polarized laser field, the non-zero field components can be written as:

$$E_z = E_0 \cos \eta, \quad (2.9)$$

$$cB_x = E_0 \cos \eta, \quad (2.10)$$

where $\eta = \omega t - ky$ is the phase of the field. By using Newton-Lorentz equation,

$$\frac{d\vec{P}}{dt} = -e(\vec{E} + \vec{v} \times \vec{B}), \quad (2.11)$$

we have,

$$\begin{aligned}\frac{d\vec{P}}{dt} &= \left\{ \frac{dP_x}{dt}, \frac{dP_y}{dt}, \frac{dP_z}{dt} \right\} \\ &= \{-eE_0\beta_x \cos\eta, 0, -eE_0(1 - \beta_z)\cos\eta\}\end{aligned}\quad (2.12)$$

$$m_e c^2 \frac{d\gamma}{dt} = -eE_0 \cos\eta \cdot v_x, \quad (2.13)$$

where $\gamma = \sqrt{1 + \vec{P}^2/(m_e^2 c^2)}$ is the Lorentz factor. For an electron initially at rest, from Eqs.(2.12-2.13), we obtain:

$$\begin{aligned}\vec{P} &= \{P_x, P_y, P_z\} \\ &= \left\{ \frac{e^2 E_0^2}{2m_e c \omega^2} \sin^2\eta, 0, -\frac{eE_0}{\omega} \sin\eta \right\}\end{aligned}\quad (2.14)$$

From the above an electron's trajectory can be acquired,

$$\vec{\alpha} = \left\{ -\frac{c}{8\omega} Q_0^2 \sin(2\eta), 0, \frac{c}{\omega} Q_0 \cos\eta \right\}. \quad (2.15)$$

Where $Q_0 = eE_0/(m_e \omega c)$ and electron drift motion has been neglected. Within dipole approximation,

$$\vec{\alpha} = \left\{ 0, -\frac{c}{8\omega} Q_0^2 \sin(2\omega t), \frac{c}{\omega} Q_0 \cos(\omega t) \right\}, \quad (2.16)$$

which means:

$$\begin{aligned}\frac{d^2 \vec{\alpha}}{dt^2} &= \{\ddot{\alpha}_x, \ddot{\alpha}_y, \ddot{\alpha}_z\} \\ &= \left\{ \frac{1}{2} c \omega Q_0^2 \sin(2\omega t), 0, -c \omega Q_0 \cos(\omega t) \right\}.\end{aligned}\quad (2.17)$$

Eq. (2.17) tells us that we can approximately take the above relativistic trajectory as an equivalent one for the electron moving in the following effective electric fields,

$$\vec{E} = \left\{ \frac{\omega m_e c}{2e} Q_0^2 \sin(2\omega t), 0, -\frac{\omega m_e c}{e} Q_0 \cos(\omega t) \right\}, \quad (2.18)$$

which will be used in HK theory. In atomic units, the trajectory can be written as,

$$\vec{\alpha} = \{-\alpha_0^2 \alpha_f \sin(2\omega t), 0, \alpha_0 \cos(\omega t)\} \quad (2.19)$$

By comparing with the non-relativistic trajectory, we have an extra oscillation motion along the laser propagation direction, which comes from the magnetic coupling,

also introduced is the fine structure constant which mediates the magnetic-electronic coupling term, α_f . This results in the famous figure-8 motion. To illustrate the effects of this correction in HK effective potential, we will first take a 1-D box potential as an example in the following section.

It should be noted that the KH expansion[28] committed to allow for this above expressions was developed by Gilary et al[29]. In our previous work[15] it was seen that the higher order terms, those with the leading ω^{-2} , provided additional stability such that a system with a bound state under the dis-inclusion of the higher ordered terms would still be bound under the inclusion of said terms. The total value of the potential scales with respect to α_0 in a similar manner and thus the same arguments contained within the above reference hold here. Inclusion of the mass gauge provides a small alteration to the system, but in a destabilizing manner; thus bound states and their limitations under the methods of this paper are of a more conservative estimation.

2.2.3 1-D Particle in a Box

For simplicity, we take the 1-D box potential as follows,

$$V(z) = \begin{cases} \pi, & |z| \leq 1, \\ 0, & \text{elsewhere.} \end{cases} \quad (2.20)$$

Then the HK effective potential can be acquired analytically by the following integration.

$$V_{eff}(z) = \frac{1}{2\pi} \int_0^{2\pi} V(z + \alpha_0 \cos(\Omega)) d\Omega. \quad (2.21)$$

When $0 \leq \alpha_0 \leq \frac{1}{2}$,

$$V_{eff}(z) = \begin{cases} \arccos \left[\frac{-z+1}{\alpha_0} \right], & -\alpha_0 \leq z \leq -1 + \alpha_0, \\ \arccos \left[\frac{z-1}{\alpha_0} \right], & 1 - \alpha_0 \leq z \leq 1 + \alpha_0, \\ \pi, & -1 - \alpha_0 \leq z \leq 1 - \alpha_0, \\ 0, & \text{elsewhere.} \end{cases} \quad (2.22)$$

When $\alpha_0 \geq \frac{1}{2}$,

$$V_{eff}(z) = \begin{cases} \arccos \left[-\frac{z+1}{\alpha_0} \right], & -\alpha_0 \leq z \leq 1 - \alpha_0, \\ \arccos \left[\frac{z-1}{\alpha_0} \right], & 1 - \alpha_0 \leq z \leq -1 + \alpha_0, \\ \arccos \left[\frac{z-1}{\alpha_0} \right], & -1 + \alpha_0 \leq z \leq 1 + \alpha_0, \\ 0, & \text{elsewhere.} \end{cases} \quad (2.23)$$

Fig.2.1 shows how the box potential is modified by the external laser field. It is clear to see that as the laser intensity increases above certain value, the original potential will evolve into a double well. Moreover, the two wells will become more separate and more shallow if α_0 is further increased. This indicates two important features for the ground state in this potential. Firstly, the electrons will become less bound or the potential might have higher ground state energy. Secondly, if we have two electrons in this effective potential, they will have more space in which to avoid each other, which means the electron repulsion energy will tend to be smaller for un-paired electrons. Hence the final ground state energy for multi-electron systems should depend upon the competition of these two factors.

Once we introduce the relativistic corrections to the electron trajectory, the effective potential along z -axis will becomes:

$$V_{eff}(z) = \frac{1}{2\pi} \int_0^{2\pi} d\Omega \left(\sqrt{(z + \alpha_0 \cos \Omega)^2 + (x + \alpha_0^2 \alpha^2 \sin^2 2\Omega)^2 + y^2} \right)^{-1}, \quad (2.24)$$

in which the integral will be calculated numerically. From Fig.(2.2), it is interesting to note that, when α_0 is large enough, for example $\alpha_0 = 10$ as in Fig.2.2(b), the effective potential will have three local minima. Qualitatively, this should result from the relativistic figure-8 motions, which helps the electron maintain a position nearer the orbit center for a greater period of time. Another characteristic is that the three separate minima become much shallower for higher laser intensity. These drastic changes over the effective potential will be expected to have influences over the many-electron states bound by the potential. It seems that the relativistic effect provides us another way to engineer the potential. Based upon the observations over Eq.(2.24), we can even think about using lasers with different colors superposed

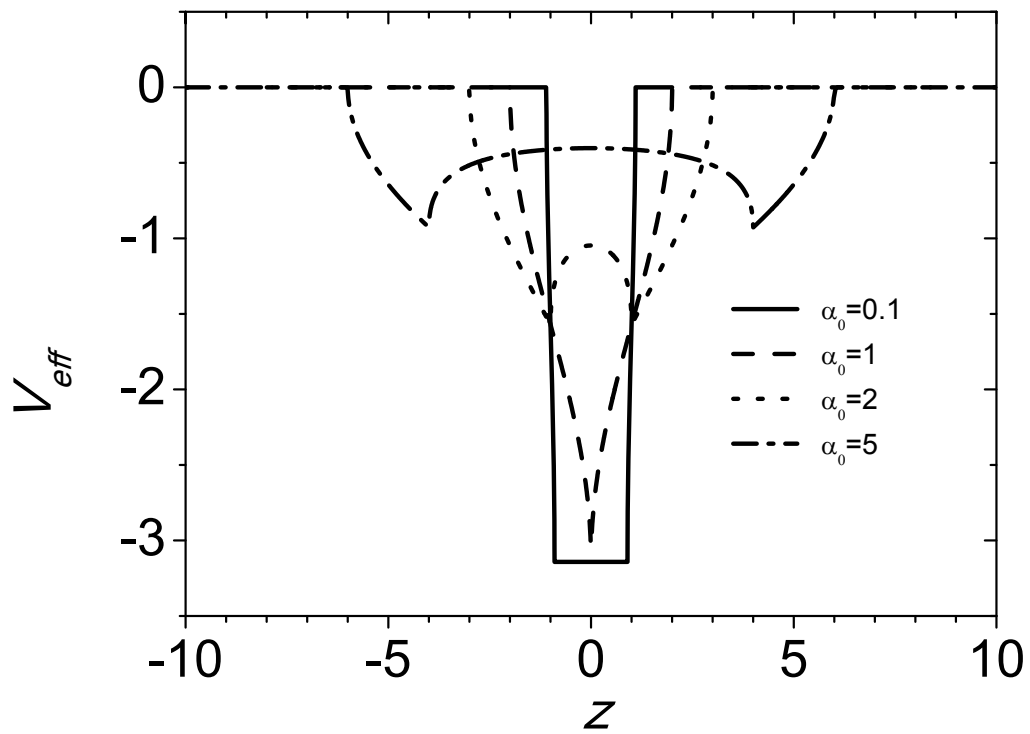


Figure 2.1. Non-relativistic effective potential for a 1D particle in a box under different laser intensity, measured by α_0 .

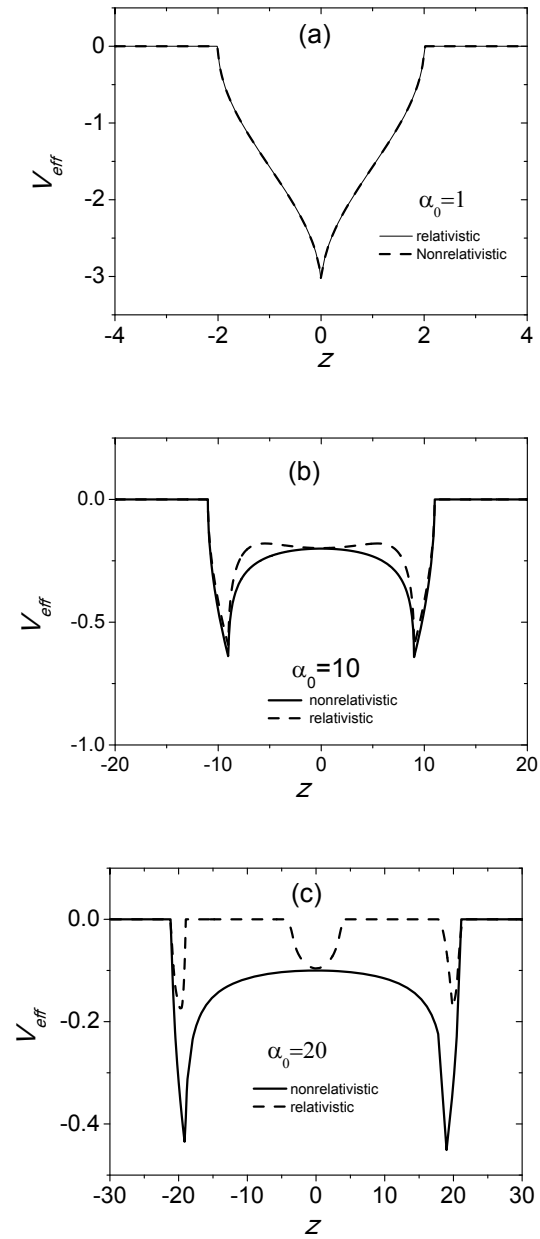


Figure 2.2. Relativistic corrections to the effective potential for different laser fields.

together to have more freedoms modifying the effective potentials. Fig. 2.3 shows us one example with two alternating electric fields as follows,

$$\vec{\alpha}(t) = \alpha_0 \cos(\omega t) \hat{e}_x + \alpha_1 \sin(4\omega t) \hat{e}_z. \quad (2.25)$$

2.2.4 Dressed Atomic Potential under Consideration

Beginning with the spherically symmetric Coulomb potential, the applied external fields shall morphologically alter this potential to conform to the trajectory discussed in § B. In doing this there are three main regimes in which the potential may exist: firstly, the spherical; secondly, the pseudo-linear; and finally, the parametric. The potential only exists within the spherical regime when there is no applied external field, as the field begins to evolve the coupling of the external field and the Coulomb potential becomes apparent with the electric field component dominating; this creates a regime where the system maintains an almost linear behavior as if there were no relativistic correction to the trajectory. Distortion of the pure linear nature exists but is a small effect compared to the primary electric effect.

As the intensity of applied field increases the magnitude of the magnetic field begins to compensate for the dampening effect of the fine structure constant, α_f ; as this takes place, the magnetic contributions to the field coupling begin to dominate the system, whose character now exhibits the hourglass figure of the parametric regime. Figure 2.4 shows a series of contour plots of the potential energy plotted in the x-z directions for a series of field intensities, α_0 ; the behavior of the system and its development through the previously discussed regimes should be obvious. A three-dimensional plot of the potential energy surface for $\alpha_0 = 100$ is also enclosed as Fig. 2.5, this plot only considers displacements in the spatial x-z directions for reasons introduced in § A, where the vertical axis describes the magnitude of the potential energy at this x-z location.

This potential is ideal for attempting to develop multiply-charged ionic system from small nuclei, as it maintains a potential well at the center of the systems along

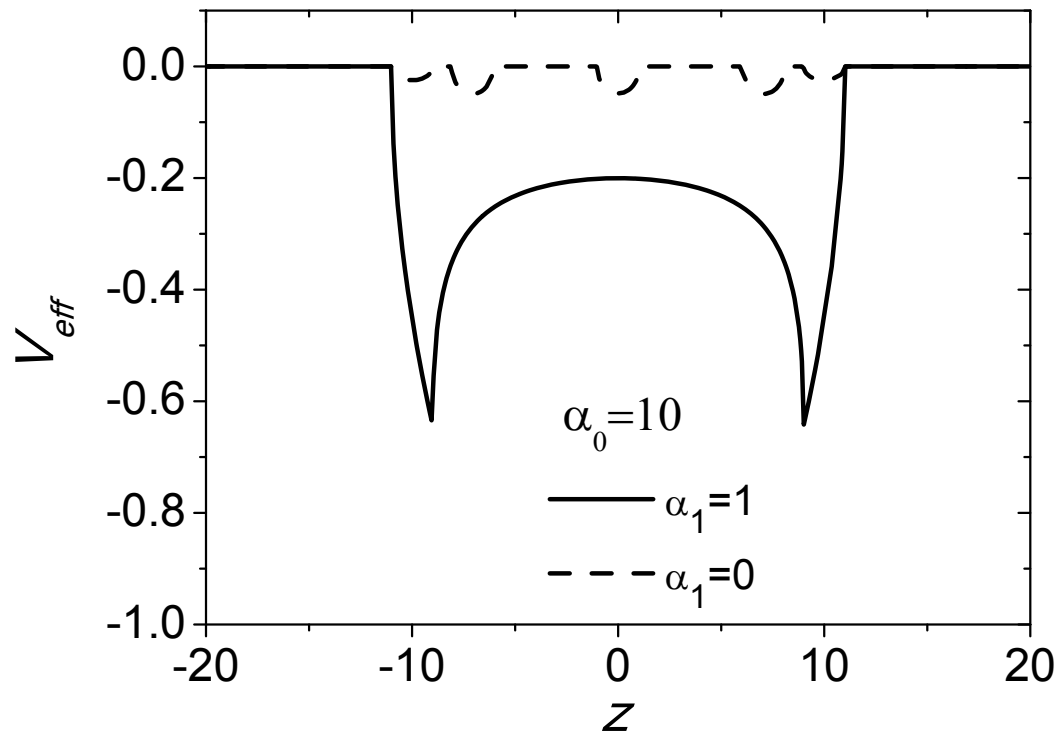


Figure 2.3. Effective potential for two alternating electric fields superposed along \hat{e}_x and \hat{e}_z , respectively, with different colors.

with four other locations along the parametric trajectory; this allows bound electrons to attach to the individual potential wells while maintaining a large enough distance from each other to minimize electron-electron repulsions.

2.3 Methodology for D=3 Calculations

Three dimensional calculations which describe our systems were executed as a mean of verifying the simpler Dimensional Scaling approach discussed later. The methodology consisted of unrestricted Hartree-Fock (UHF) utilizing the Pople-Nesbot equations -which allow for the accommodation of basis sets- to complete calculations for a series of total electron counts, N , per single value of the field intensity parameter, α_0 . The calculations were dependent both upon appropriate choice of basis set and upon the locations selected as the centers for these basis sets; for the determinations of the locations of probable electron density we deferred both to 'exact' locations of the electrons from the limit $D \rightarrow \infty$ calculations and to contour plots of the potentials for a given field intensity value, see Figure 2.4 for an example. Upon discerning from the above information the locations of the psuedo-centers within the system-space, a basis set was selected which could describe these nodes. There exist, at minimum, 5 distinct nodes of electron density within the system, these being at the center coexisting with the origin of our coordinates systems- and at four psuedo-centers residing upon the parametric curve described by the relativistic trajectory used within the HFFT Potential.

$$\begin{pmatrix} x \\ y \\ z \end{pmatrix} = \begin{pmatrix} -(\frac{\alpha_0^2}{\alpha_f})\sin(2t) \\ 0 \\ \alpha_0\cos(t) \end{pmatrix} \quad (2.26)$$

The orbital centers were selected to satisfy the above curve and to coincide with the "hottest" locations displayed within the contour plots of potential energy. A basis set was selected which allowed for significant description of both polarized and diffuse phenomenon residing on small centers. The centers of potential electron density which

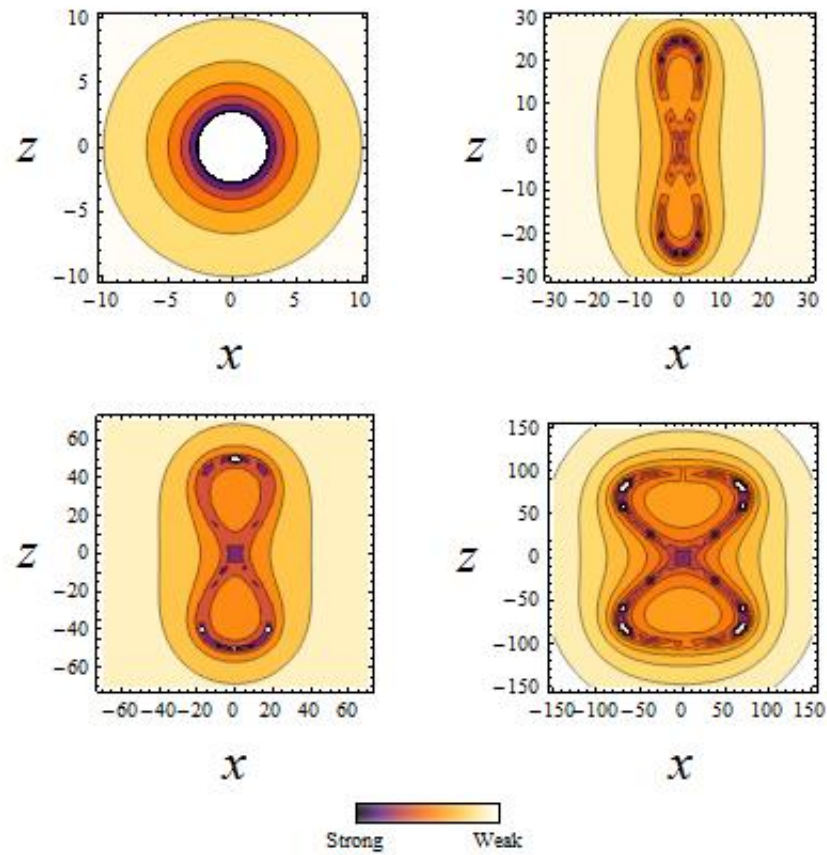


Figure 2.4. Contour Plots of Dressed Potential for (clockwise) $\alpha_0=0$, 25, 100, 50. Note both the shift in regime as α_0 grows and the key below the plots for the interpretation of the intensity of the contours.

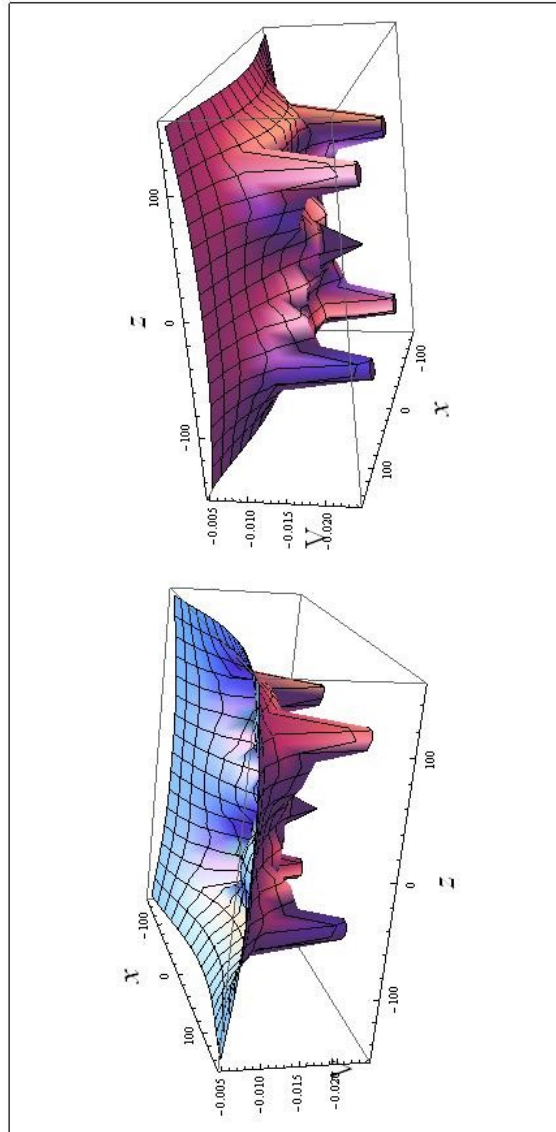


Figure 2.5. Three Dimensional Plots of the Potential Energy, V_{dres}^{HFFT} , as a function of x and z coordinates for the case $\alpha_0=100$. Left and Right of above are two different angles of same surface.

do not reside at origin were described by basis sets optimized to describe the atom of the nucleus at the system's origin, i.e. all five centers on hydrogen use a hydrogen-fit basis set. Overlap and kinetic integrals were performed with variations on the integrals described by McMurchie and Davidson in their seminal paper here[30]. Numerical integration methods were appropriate for the more challenging, non-analytic potential integrals. A global adaptive method was applied to the system which performs admirably with Gaussian functions placed at the coordinate origin; but as the method relies on sampling points within the equation-space to find non-zero areas of the function, Gaussians placed distances away from the origin were sometimes so small relative to the distance from origin as to be invisible. For this reason two-centered integral includes the cost of shifting the coordinate-origin to the center of the product Gaussian as defined by[31]:

$$\begin{aligned}
 & \phi_{1s}^{GF}(\alpha_A, r-R_A) \times \phi_{1s}^{GF}(\alpha_B, r-R_B) \\
 &= \exp\{-(\alpha_A(r-R_A) + \alpha_B(r-R_B))\} \\
 &= \exp\{-\alpha_A\alpha_B(\alpha_A+\alpha_B)^{-1}|R_A-R_B|^2\} \times \\
 & \quad \phi_{1s}^{GF}(\alpha_A+\alpha_B, r-R_P).
 \end{aligned} \tag{2.27}$$

In this way the chosen method of numerical integration was capable of adequately describing the three-dimensional potential energy integrals. Single electron cases were verified prior to enacting the self-consistent field calculations, as the energies of the single electron system may be revealed as the eigenvalues of the canonically orthogonalized H^{core} matrix alone, $H_{\mu,\nu}^{core} = T_{\mu,\nu} + V_{\mu,\nu}$. The four-centered integrals needed for the self-consistency were generated by exploiting the auxiliary function defined by Boyes[32]. The calculations for the multi-electron energies were performed self-consistently with a convergence set to six decimals of accuracy, as chemical accuracy is defined as $1.6mE_H$, this set limit should suffice.

A plot of the square of the linear combination of atomic orbitals which comprised the set describing the appropriate eigenvalue yields semblance to the wave function of the system, whose probability density ($|\Psi|^2$) is shown in Figure 2.6 for H^- and for He^- , a two and a three electron case. It should be noted, as the D=3, UHF calculations

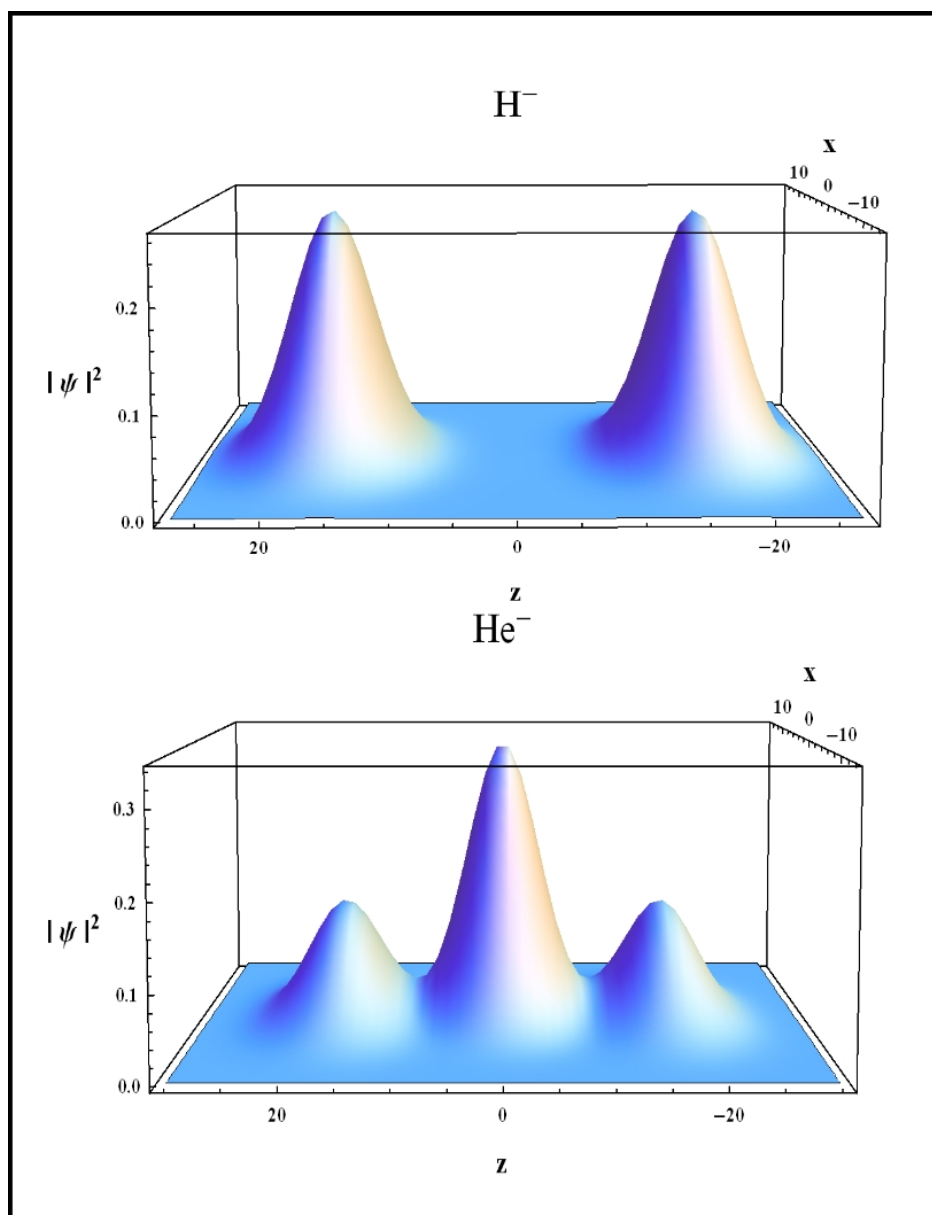


Figure 2.6. Top: Probability distribution for H^- , a two electron system. Bottom: Probability distribution for He^- , a three electron system

were employed to verify the results of the Dimensional Scaling approach, that the locations of electron density shown in the aforementioned probability density plots speak to the validity of the Dimensional Scaling approach as the locations of the delta functions, see discussion provided in Results Section, which describe the seemingly stationary locations of the electrons in the limit of $D \rightarrow \infty$ calculations are very near those locations of highest probability density for finding electrons given by the $D=3$ calculations. Three-dimensional verification was performed for both the H^- and He^- species, as the regions of high potential energy become very delocalized for the remaining high-field species. Aside from the high level of delocalization prohibiting the species from being described sufficiently with an appropriate number of Gaussians, the potential also spans a region of space on the order of 100 Bohr radii, yet optimized Gaussian basis sets for atomic centers span an order of 1-10 Bohr radii; this prohibits overlap for these species forcing the use of more and more Gaussians. This acts prohibitively as the matrices required for UHF calculations are $n \times n$, where n scales as the number of centers by the number of basis contractions; this obviously limits the achievable intensities applied to systems which can be calculated in this manner, especially on stand alone machines.

2.4 Dimensional Scaling: Calculations and Considerations

2.4.1 Methodology

Many Body interactions are something which has troubled computational methodologies within quantum mechanics since inception; throughout the years the physical and chemical communities have made great advances in the field of electronic structure theory to help account for these electron-electron interaction through variational practices such as the Hartree Fock Method or Density Functional Theory. The alternative method to the aforementioned is a Dimensional Scaling treatment pioneered by Herschbach [33], discussed in [34, 35, 36, 37, 38], and is briefly introduced here for

the central force problem[34]. Given the TISE for the simple central force problem in D-dimensions:

$$[-\frac{1}{2}\nabla_D^2 + V(r)]\Psi_D = \epsilon_D\Psi_D. \quad (2.28)$$

If we were to employ polar coordinates to the above we would require:

$$r \equiv [\sum_{k=1}^D x_k^2]^{\frac{1}{2}} \quad (2.29a)$$

$$\nabla_D^2 = \frac{1}{r^{D-1}} \frac{\partial}{\partial r} (r^{D-1} \frac{\partial}{\partial r}) - \frac{L_{D-1}^2}{r^2}. \quad (2.29b)$$

Where Eq.(2.29a) gives the definition of the radial coordinate in a generic D-scaled space, and Eq.(2.29b) is the polar Laplacian in this D-scaled space, L_D^2 is the term which retains all angular dependencies. These angular and radial terms shall be dealt with in an divide and conquer treatment reminiscent to the radial and angular terms of the Rigid Rotor/Harmonic Oscillator approximations for the simple diatomic. We first write the wave function in D-dimensions to be the product: $\Psi_D = r^l \mathcal{Y}(\Omega_{D-1})$, where all radial dependencies are in the r^l term and the D-1 remaining angular dimensions are described through $\mathcal{Y}(\Omega_{D-1})$. Now solving the angular terms for the form Eq.(2.30), and the recognizing that the V(r) term in Eq.(2.28) can be set to equal magnitude as the ϵ_D term, thus making Eq.(2.28) reduce to the Laplace equation shown in Eq.(2.31).

$$L_{D-1}^2 \mathcal{Y}(\Omega_{D-1}) = C \mathcal{Y}(\Omega_{D-1}) \quad (2.30)$$

$$\nabla_D^2 r^l \mathcal{Y}(\Omega_{D-1}) = 0 \quad (2.31a)$$

$$\{l(l + D - 2) - C\} r^{l-2} \mathcal{Y}(\Omega_{D-1}) \quad (2.31b)$$

This means: $C=l(l + D - 2)$; and the Hamiltonian Operator in Eq.(2.28) is now of the form:

$$\hat{H}_D = -\frac{1}{2}K_{D-1}(r) + \frac{l(l + d - 2)}{2r^2} + V(r). \quad (2.32)$$

In the above, $K_{D-1}(r)$ is the single non-angular term from the polar Laplacian in Eq.(2.29b). We may now pass the system through a unit Jacobian, making: $J_D|\Psi_D|^2 =$

Φ_D , J_D is the radial part of the unit Jacobian and is of the form: $r^{(D-1)}$. This would mean, $\Psi_D = r^{-\frac{1}{2}(D-1)}\Phi_D$. All leading to the form of K_{D-1} seen here:

$$K_{D-1}(r)=r^{-\frac{1}{2}(D-1)}\left\{\frac{\partial^2\Phi_D}{\partial r^2}-\frac{D-1}{2}\frac{D-3}{2}\frac{\Phi_D}{r^2}\right\} \quad (2.33)$$

Reassembling all the above, and placing them appropriately back into Eq.(2.28), one shall -after menial simplification- get:

$$\left\{-\frac{1}{2}\frac{\partial^2}{\partial r^2} + \frac{\Lambda(\Lambda+1)}{2r^2} + V(r)\right\}\Phi_D = \epsilon_D\Phi_D. \quad (2.34)$$

Eq.(2.34) is the radial, D-scaled form of Eq. (2.28), where the only dimensional dependencies lay within the Λ terms as: $\Lambda = l + \frac{1}{2}(D-3)$. The above leads to the minimization problem defined by the Hamiltonian discussed in §B.

2.4.2 Planar Infinite-D Hamiltonian

Prior works published[19, 14] have also described systems both by infinite dimensional limit and then verified with three dimensional self consistent methods. The dimensional scaled Hamiltonian presented in previous works was diatomic in nature and of the form[39]:

$$\begin{aligned} \mathcal{H}_{DA} = & \frac{1}{2} \sum_{i=1}^N \frac{1}{\rho_i^2} + \sum_{i=1}^N V(\rho_i, z_i) \\ & + \sum_{i=1}^N \sum_{j=i+1}^{N-1} \frac{1}{\sqrt{(z_i - z_j)^2 + \rho_i^2 + \rho_j^2}} \end{aligned} \quad (2.35)$$

and relied on previous works in which D-scaled Hamiltonians for diatomic systems were constructed, these diatomic Hamiltonians are also of the form above, and denoted \mathcal{H}_{DA} .

Hamiltonians of this form are applicable to the previous works as those non-relativistic systems, this is due to the consideration in absence of the second degree of symmetry breaking in the linear potential systems.

The diatomic-based Hamiltonian performed well on linear systems, but when attempting to use the above described Hamiltonian on a relativistically corrected trajectory, it was found that the equation behaved erratically with a smoothly evolving

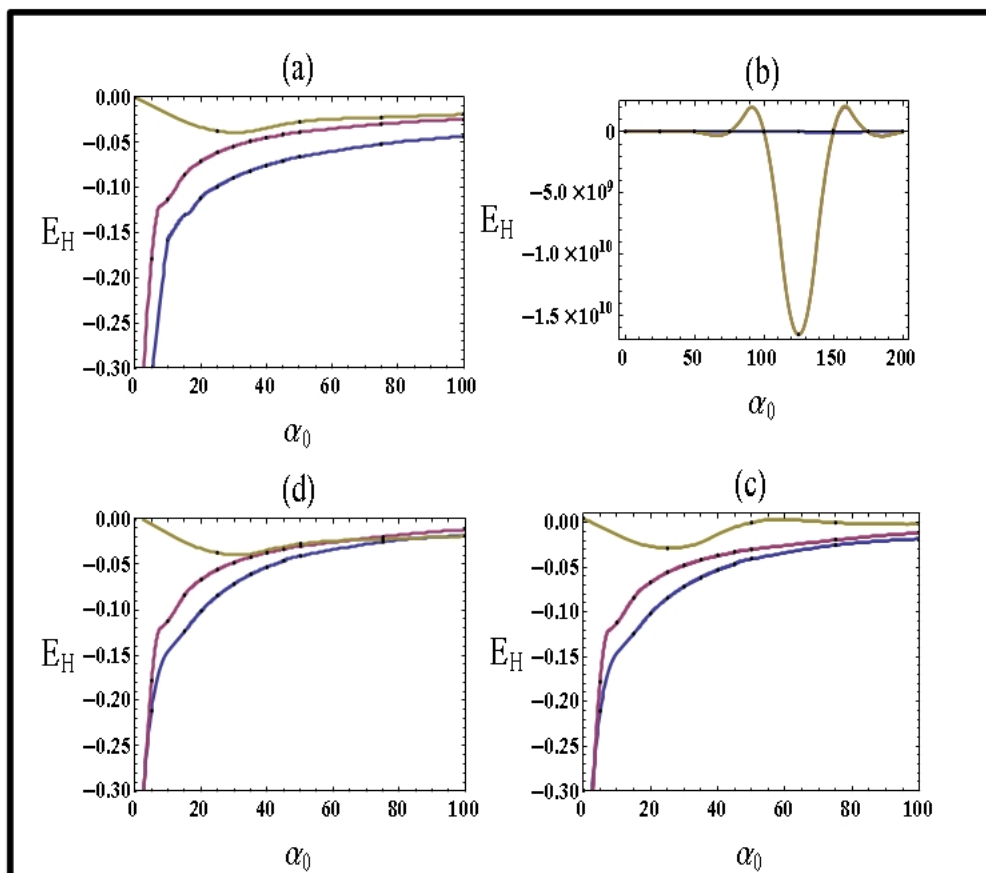


Figure 2.7. Plots of both molecular energies and binding energy for (clockwise): \mathcal{H}_{DA} with non-relativistic trajectory; \mathcal{H}_{DA} , relativistic trajectory; \mathcal{H}_P , relativistic trajectory; and \mathcal{H}_P with non-relativistic trajectory. All may be read as Yellow:Binding Energy; Blue:Hydrogen Energy; Purple: H^- Energy

intensity as seen in Figure 2.7, and was in disagreement with the early 3-D calculations. Although this Hamiltonian does not work well, overall it was found to be in good agreement while the potential was in the spherical and pseudo-linear regimes, failing only as the system approached and entered the parametric regime.

As dimensionally scaled Hamiltonians are not unique in nature, they are not singular in form. We relied on arguments based on the breaking of spherical and then cylindrical symmetries to generate the followed assumed Hamiltonian for systems with broken radial and cylindrical symmetries, yet maintaining three orthogonal planes of symmetry.

As the dimensional-scaled, single electron central force problem yields as it's Hamiltonian \mathcal{H}_{CF} ,

$$\mathcal{H}_{CF} = \frac{1}{2r^2} + V(r). \quad (2.36)$$

One can see from above the spherical nature of all terms within the Hamiltonian, as the potential is radial. This equation predicts the ground state Hydrogen energy to be at $-\frac{1}{2}E_H$, exactly where it should be, and predicts the inter-atomic distance between the electron and the proton to be 1 in units of R_{Bohr} . If one were to alter the above potential to conform with either the relativistic or non-relativistic cases discussed in this paper, the energies obtained would possess no physical significance and would overall behave similarly to the diatomic equation with the relativistic trajectory. The addition of multiple electrons to the spherical symmetric problem yields :

$$\begin{aligned} \mathcal{H}_{CF} = & \frac{1}{2} \sum_{i=1}^N \frac{1}{r_i^2} + \sum_{i=1}^N V(r_i) \\ & + \sum_{i=1}^N \sum_{j=i+1}^{N-1} \frac{1}{\sqrt{r_i + r_j}}. \end{aligned} \quad (2.37)$$

Now we examine the diatomic case shown in Eq. (2.35). This equation has been designed to allow for potential which are of a cylindrical nature, as it must for a diatomic system. Reevaluating the equation in Cartesian coordinates yields:

$$\begin{aligned} \mathcal{H}_{DA} = & \frac{1}{2} \sum_{i=1}^N \frac{1}{x_i^2 + y_i^2} + \sum_{i=1}^N V(x_i, y_i, z_i) \\ & + \sum_{i=1}^N \sum_{j=i+1}^{N-1} \frac{1}{\sqrt{(z_i - z_j)^2 + x_i^2 + x_j^2 + y_i^2 + y_j^2}}. \end{aligned} \quad (2.38)$$

Reevaluation of the spherically symmetrical case in Cartesian coordinates gives:

$$\begin{aligned} \mathcal{H}_{CF} = & \frac{1}{2} \sum_{i=1}^N \frac{1}{x_i^2 + y_i^2 + z_i^2} + \sum_{i=1}^N V(x_i, y_i, z_i) \\ & + \sum_{i=1}^N \sum_{j=i+1}^{N-1} \frac{1}{\sqrt{x_i^2 + x_j^2 + y_i^2 + y_j^2 + z_i^2 + z_j^2}}. \end{aligned} \quad (2.39)$$

As can be seen from the above, the orthogonal coordinate which is being cleaved from spherical symmetry has been removed from the kinetic evaluation and have been treated as a difference in the electron-electron term. Continuing to use Cartesian coordinates, as it is this coordinate system which makes the relations apparent, we can move to an equation where the x-coordinate is now allowed to deviate from radial symmetry. This again would remove the symmetry breaking coordinate from the kinetic term and utilize it as a difference in the electron-electron term. This Hamiltonian is shown in Eq. (2.40). It's energies completely agree with those of the the radial and cylindrical cases, and by allowing this symmetry breaking in the x-coordinate can be use for the potential discussed in Section II §E.

This Planar Hamiltonian, \mathcal{H}_P :

$$\begin{aligned} \mathcal{H}_P = & \frac{1}{2} \sum_{i=1}^N \frac{1}{y_i^2} + \sum_{i=1}^N V(x_i, y_i, z_i) \\ & + \sum_{i=1}^N \sum_{j=i+1}^{N-1} \frac{1}{\sqrt{(z_i - z_j)^2 + (x_i - x_j)^2 + y_i^2 + y_j^2}} \end{aligned} \quad (2.40)$$

was found to allow -but not require- the breaking of symmetry, as it was applied to the previously discussed linear systems and had extremely good agreement, shown

in Figure 2.7. The relation between the Cartesian coordinates used in the above and the geometry of the system is shown in Figure 2.8. When applied to our system, containing the corrected trajectory, this new Hamiltonian performs both smoothing with smoothly evolving trajectories- as seen in Figure 2.11. This planar Dimensional Scaled Hamiltonian was capable of adequate description of the system in all three of the regimes discussed earlier. We also verified the findings of the \mathcal{H}_P by calculation of the energy of the hydrogen atom and scaling with the field intensity while comparing these calculations with UHF SCF calculations, Fig. 2.10.

2.5 Results and Discussion

We shall concern ourselves with a discussion of the binding energies (B.E.) for the following species: H^- , H^{-2} , He^- , He^{-2} , He^{-3} ; where the B.E. is the negative of the detachment energy for a single 'excess' electron shown in Eq. (2.41), where N signifies the number of electrons for a species.

$$B.E. = E_H(N) - E_H(N - 1) \quad (2.41)$$

Figure 2.9 Displays the binding energies for the two species, $Z=1$ and $Z=2$. From this figure we can see a clear maximum binding energy for the H^- species (top left) at, roughly, $\alpha_0 = 10$; this energy shows a stability of the second electron of 0.047 Hartree (1.28 eV). Also shown in Figure 2.9 the B.E. curve for H^{2-} (top right), showing a stable binding of 0.00012 Hartree (0.0033eV). This, the B.E. of H^{2-} , reaches it's minimal value asymptotically with increasing α_0 implying the addition of any further electrons will not be allowed; this fact was verified by performing the requisite minimization, and if the mass gauge was not applied to the system the number of allowed additional electrons would increase unrealistically and seemingly without bound as the laser intensity is increased.

The middle, left plot in Figure 2.9 shows the binding of a third electron to Helium at α_0 equals, roughly, 10 again; the binding energy for this species at it's greatest magnitude is extrapolated to be 0.057 Hartree (1.55 eV). The second 'additional'

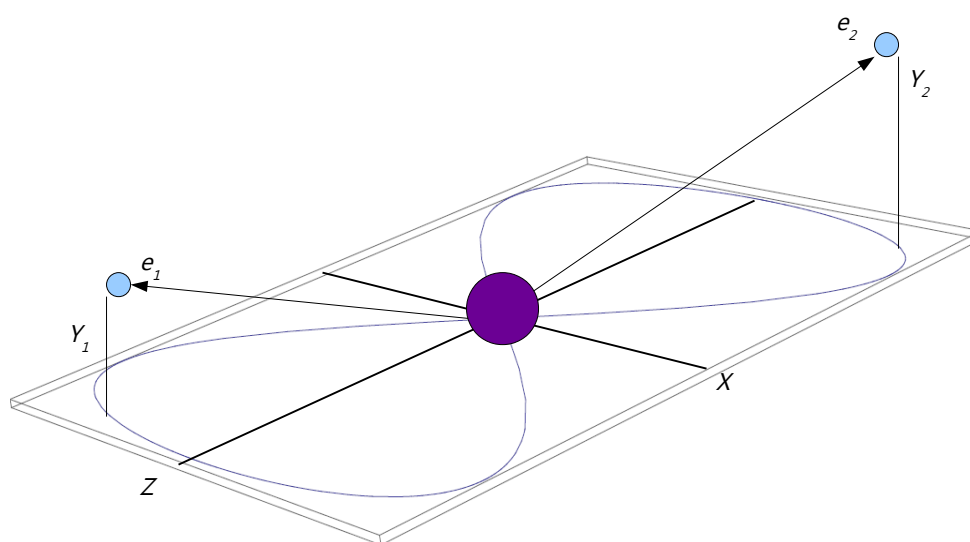


Figure 2.8. The above displays the relationship between the system's geometry with respect to the electrons and the coordinates use in Eq. (2.40)

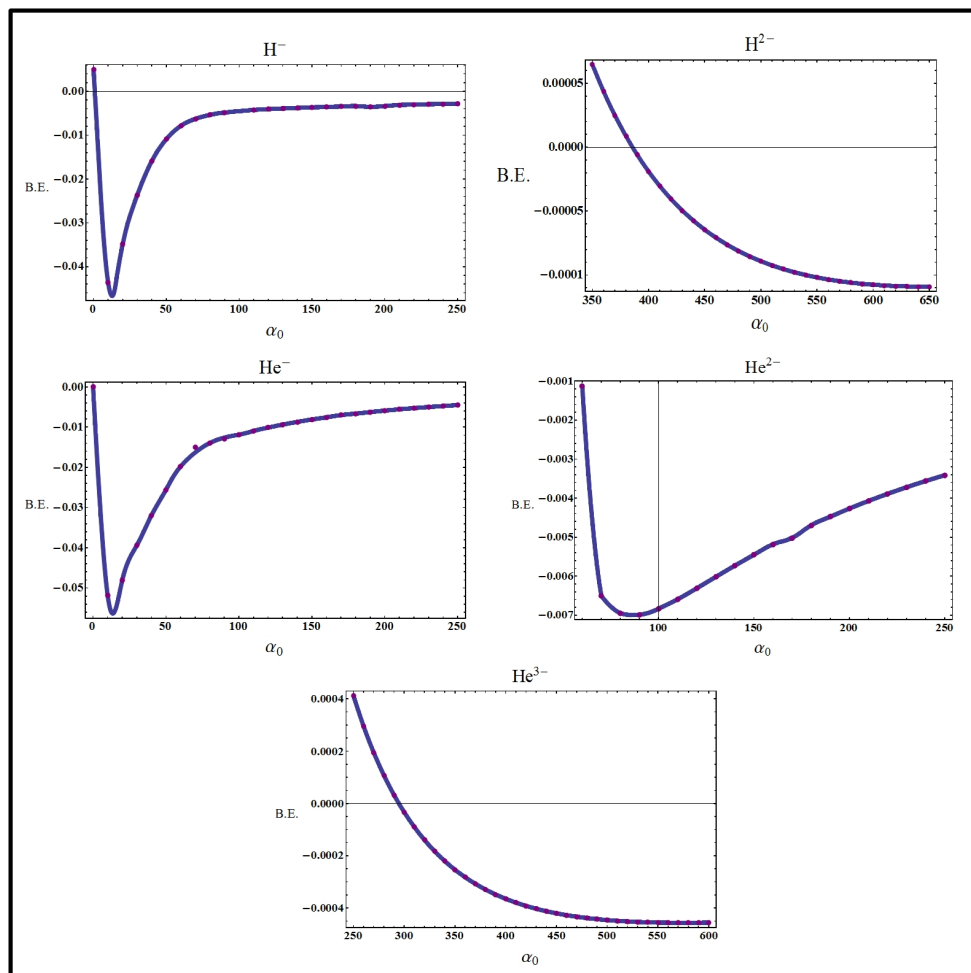


Figure 2.9. Above are plots of the binding energies of, from left to right and top to bottom: H^- , H^{2-} , He^- , He^{2-} and He^{3-} .

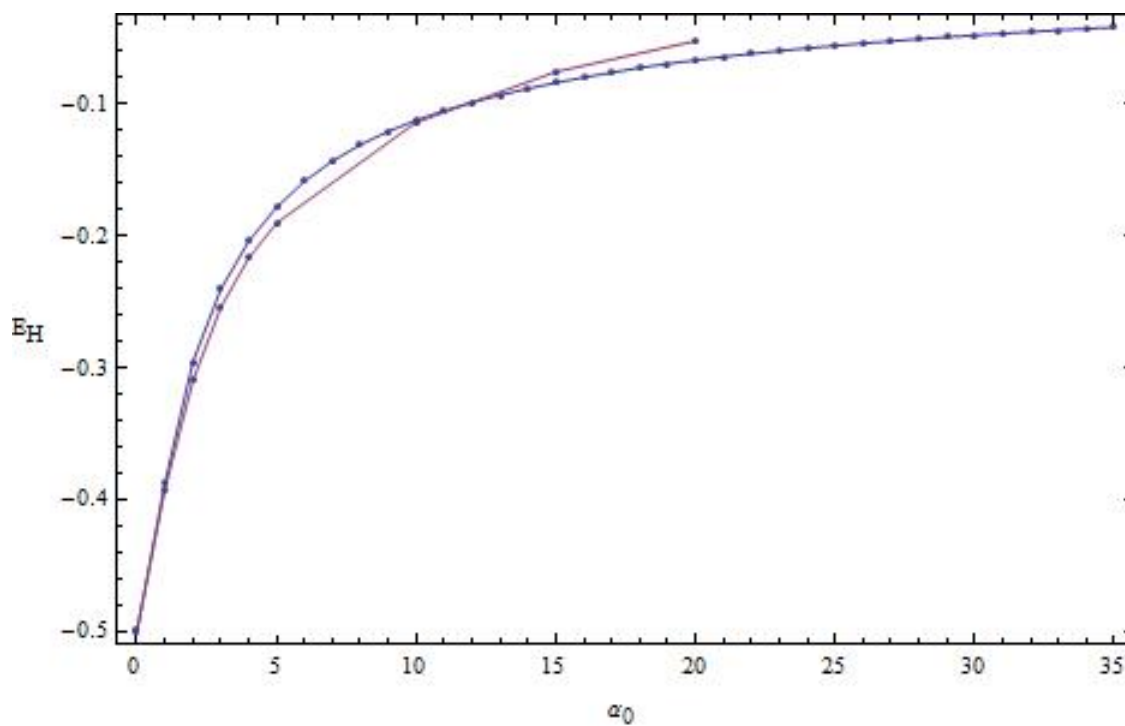


Figure 2.10. Energies for the hydrogen atom energies scaling with the applied field intensity, α . The blue curve are the findings using \mathcal{H}_P while the purple are those points generated with UHF SCF calculations.

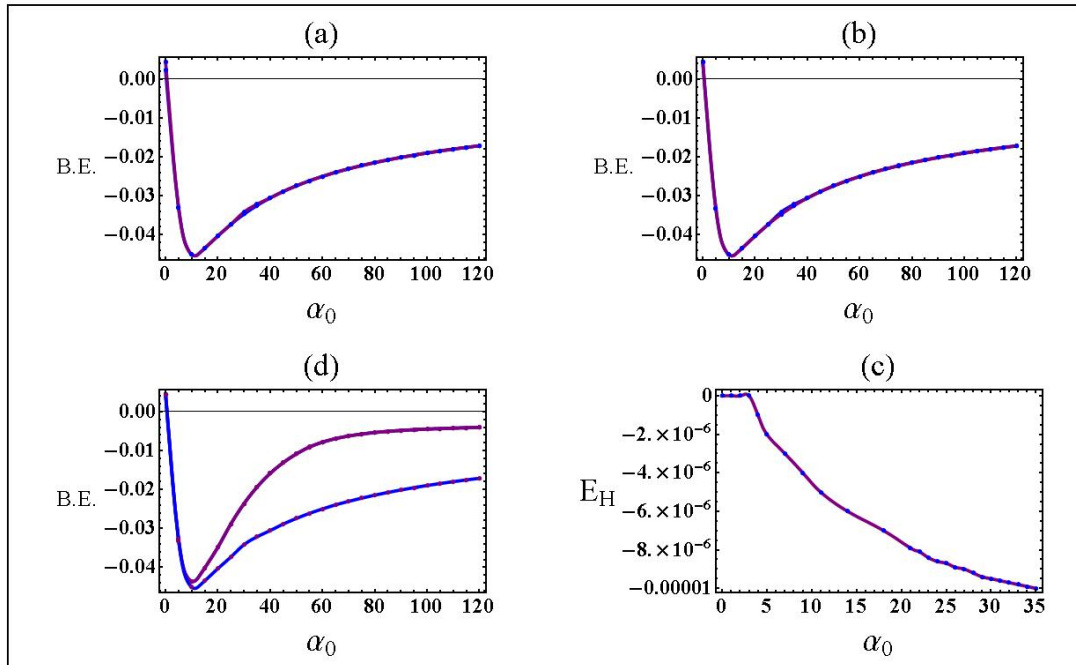


Figure 2.11. Plots of binding energy comparisons for (clock-wise): comparison plot of \mathcal{H}_{DA} versus \mathcal{H}_P , non-relativistic trajectory; \mathcal{H}_P with relativistic trajectory m_0 and m_r , differences value of Hydrogen energy between use of m_0 and m_r ; and a comparison of relativistic trajectory (both m_0 and m_r) with non-relativistic trajectory both using \mathcal{H}_P .

electron to Helium (middle right) is most stable at $\alpha_0=90$, with a B.E. of 0.007 Hartree (0.19 eV). The fifth and final electron which can stable bind to a $Z=2$ center (bottom center) is, similarly to the H^{2-} species, a terminal binding who reaches an asymptotic stability with increasing alpha, the B.E. is 0.0004 Hartree (0.011 eV).

Of the two relativistic corrections accounted for in the above framework, the trajectory is the paramount addition. An examination of Figures 2.11 and 2.7 shall be required for the subsequent discussions. The introduction of the planar Large-D Hamiltonian, \mathcal{H}_P , for the systems was a boom which aligns itself in agreement with the previous works -see Figure 2.11 a and compare plots a and c in Figure 2.7- and yet out preforms the previous equation when this relativistic trajectory is introduced, to see this compared plots b and c in Figure 2.7.

By comparing plots a and d of Figure 2.7 it can be seen that the raw energies and the binding energies between the non-relativistic trajectory (plotted with \mathcal{H}_{DA}) and the relativistic trajectory are not extreme. This can be verified and more clearly seen by examination of Figure 2.11 c, wherein both the non-relativistic and relativistic binding energies are shown; although the energies become quite different with increasing α_0 , the field intensity which yields the most stable binding energy is same and the most stable binding energy deviates only in the thousandth of a Hartree. Consideration of the mass gauge for this system provides a very slight correction within the values of α_0 examined here; where although these values of α_0 indicate laser field strengths on the order of atomic units and greater (in competition with the Coulomb potential of the center) they are in no way strong enough to generate quivering electron masses, m_r , which deviate significantly from the invariant mass, m_0 . Due to this, the deviation of the binding energies due to consideration of m_r over m_0 is also slightly less than breath-taking, this can be seen in Figure 2.11b and again impressed by examination of the deviation of the raw energies of Hydrogen in Figure 2.11d. To be gleaned from this is that within the examined field strengths, m_r deviates very little from m_0 , but more significant is the fact that the overall consideration of relativistic effects does destabilize the system, but not by an appreciable amount.

Table 2.1

The below table displays the differences present when relativistic considerations are undertaken for these multiply-charge ions. The Non-Relativistic values were taken from [14].

Species	D= ∞				D=3			
	Non-Relativistic		Relativistic		Non-Relativistic		Relativistic	
	α_0^{max}	BE (eV)	α_0^{max}	BE (eV)	α_0^{max}	BE (eV)	α_0^{max}	BE (eV)
H ⁻	10	-1.2	12	-1.17	17	-1.1	12	-0.98
H ²⁻	500	-0.019	∞	-0.003	400	-0.026	-----	-----
He ⁻	12	-1.4	12	-1.46	26	-1.2	14	-1.03
He ²⁻	160	-0.14	85	-0.19	180	-0.12	-----	-----

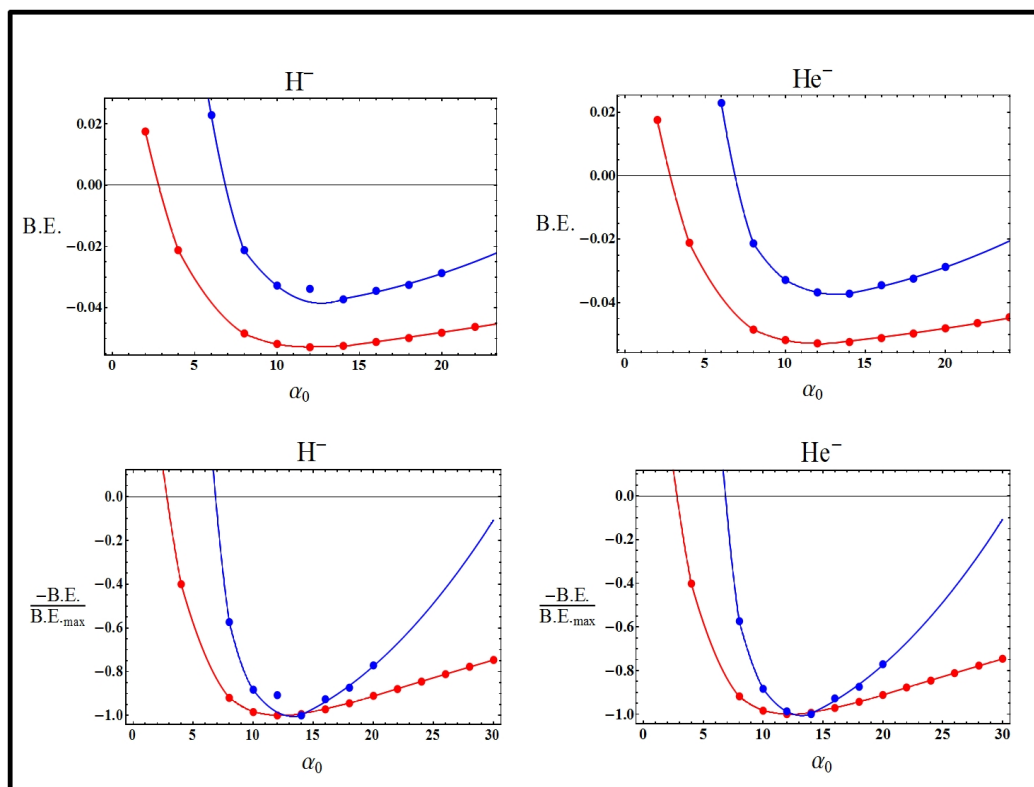


Figure 2.12. Plots of binding energy for the H^- (left) and He^- (right) systems. Top, Non-Normalized plots of the calculation data showing agreement between the methods. Bottom, $-\text{B.E.}/\text{B.E.}_{\max}$ to emphasize the qualitative similarity between the methods as they share minima for the B.E. curves.

Figure 2.13 helps emphasize the differences between the corrected and non-corrected systems. The top level of the figure is the probability density, $|\psi|^2$, of corrected (left) and non-corrected (right), the density in the outer orbital centers is lower due to a more diffuse spread of probability density at these locations compared to the non-corrected. The mid-level of the plot is the negative probability density, superimposed on the probability density function is the trajectory of the system which it describes. Below all else is a contour plot of each system, again emphasis is merited on the more diffuse spread in the corrected system due to the evolution of the parametric trajectory as opposed to the linear oscillating trajectory of the non-corrected system.

Figure 2.12 shows a plot of the B.E. For the H^- (left) and He^- (right) systems from both the SCF (blue) and D-Scaled (red) methods. The lower B.E. plots in Fig. 2.12 have been normalized to the minimum value to show the tight agreement between the qualitative assessment of the scaling procedure and the SCF method. The Dimensionally Scaled minimization problem bore 'exact' position of the electrons as $(x_1, y_1, z_1; \alpha_0) = (4.1660 \times 10^{-10}, 5.4461, -12.2387; 20)$ for the $Z=1, N=1$ system and $(x_1, y_1, z_1; x_2, y_2, z_2; \alpha_0) = (6.4472 \times 10^{-8}, 5.0386, 16.5852; -6.4472 \times 10^{-8}, 5.0386, -16.5852; 20)$ for the $Z=1, N=2$ system; these localized electron positions are similarly predictable as they attempt to bind to regions where the angular velocity of the nucleus is lowest in the KH Frame; these locations would most notably be the $\frac{\pi}{4}$'s the trajectory. With a single electron the central point of the parametric curve, set a origin in our calculations, binds the electron strongly; as more electrons are introduced they are situated at locations which minimize the electron-electron repulsion of the system. A Mulliken population analysis of the systems shows that the orbitals about the central charge typically possess a smaller number of electrons, except in the $N=3$ (and assumably the $N=5$ case); the results of such population assessments can be seen in Table 2.2. In this way we are able to verify not only the energetic behavior of the D-Scaled Hamiltonian but its treatment of the electrons in space.

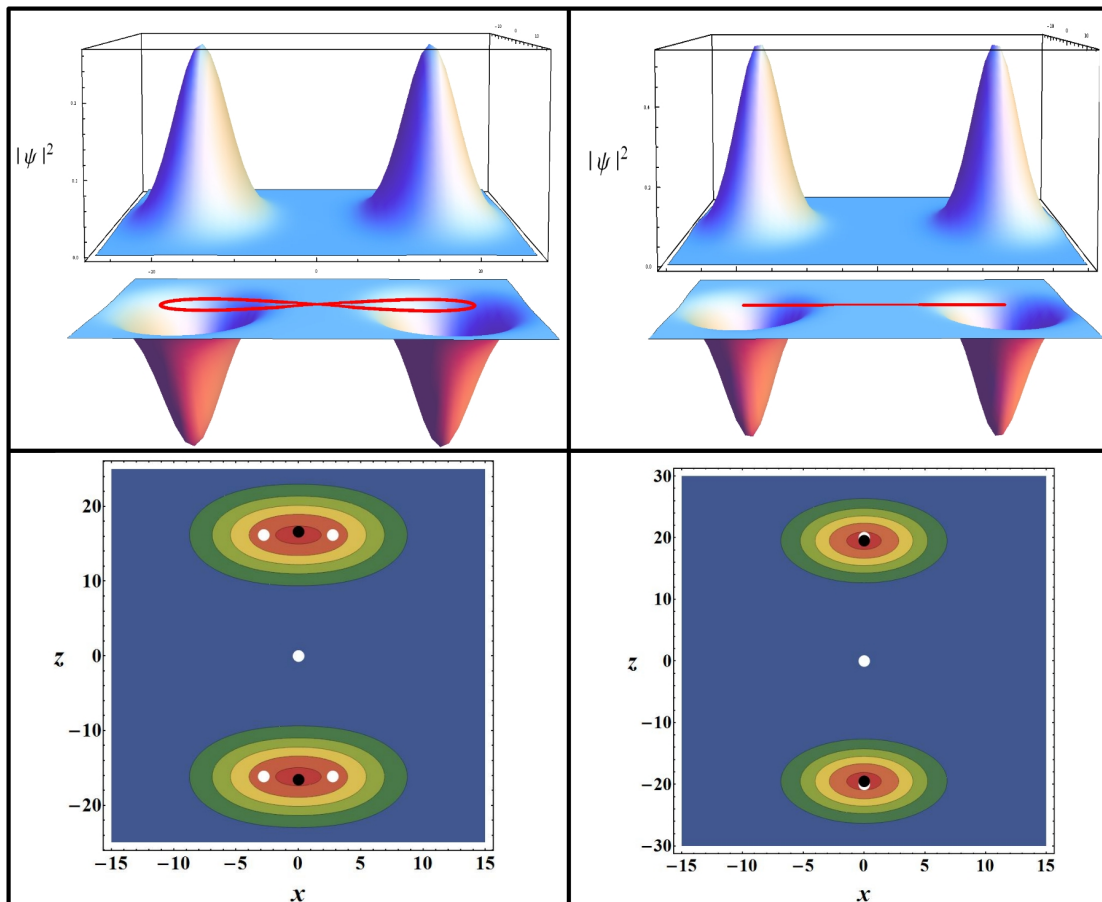


Figure 2.13. Top Row: Plots of the Probability Distribution for the corrected (left) and non-corrected (right) H^- system, directly below is a superimposition of the trajectory upon the the probability density function plot to emphasis their relation. Bottom Row: Contour Plots of the H^- system, both corrected (left) and non-corrected (right), note the different scales on the vertical (z) axis and the more diffuse behavior of the corrected system.

Table 2.2

Results of Mulliken Population Analysis, note that there are four outer orbitals the table contains one of the four values.

Species	Inner Orbital Population	Outer Orbital Population (each)	Total Electron Count (N)
H	0.01645	0.24576	1
H ⁻	0.000524	0.49987	2
He	0.000432	0.499892	2
He ⁻	1.00001	0.499999	3

2.6 Comments on Elliptical and Circular Polarizations

Within the above concern was only given to the relativistically corrected linear polarized light, this is because similar corrections placed on elliptical polarized light yield no new -or interesting- phenomenon. Following similar mathematics as to achieve an analogous relativistically considered trajectory would consider the electronic coupling as before and consider a minor weighted coupling to the magnetic field, as in the linear case before. An elliptically polarized laser fired in the y-direction with the electronic major (minor) axis oriented in the x(z)-direction yields the trajectories

$$\vec{\alpha}_{\vec{E},Elliptical}(t) = \{\epsilon_1 \cos(\phi), 0, \epsilon_2 \sin(\phi)\} \quad (2.42)$$

$$\vec{\alpha}_{\vec{B},Elliptical}(t) = \{-\beta_2 \sin(\phi), 0, \beta_1 \cos(\phi)\}. \quad (2.43)$$

Within Eqs. (2.42-2.43) the amplitude in each the major and minor axis is denoted by the subscript 1 and 2, respectively, and the ϵ and β are the coefficients of the electronic and magnetic components. The trajectory generated by both the above biases applied to free particle merely generates a new ellipse with a major and minor amplitude mediated between those of the above and tilted by an angle respective to the coefficients.

$$\vec{\alpha} = \{\epsilon_1 \cos(t) - \beta_2 \sin(t), 0, \epsilon_2 \sin(\phi) + \beta_1 \cos(\phi)\}. \quad (2.44)$$

This can be seen graphically in Fig. 2.14 which displays the individual electronic and magnetic trajectories and then in Fig. 2.15 which displays the combined trajectory which would be followed by a free particle traveling within this electromagnetic field.

If this scheme is applied to a circularly polarized field the same mathematics will appear but the coefficients within the trajectories will be reduced to $\epsilon_1 = \epsilon_2 = \epsilon$ and $\beta_1 = \beta_2 = \beta$. This will yield the same uninteresting phenomenon, but merely present it as the mediate of two circles with no change in the orientation angle as there is no unique point of reference on a circle.

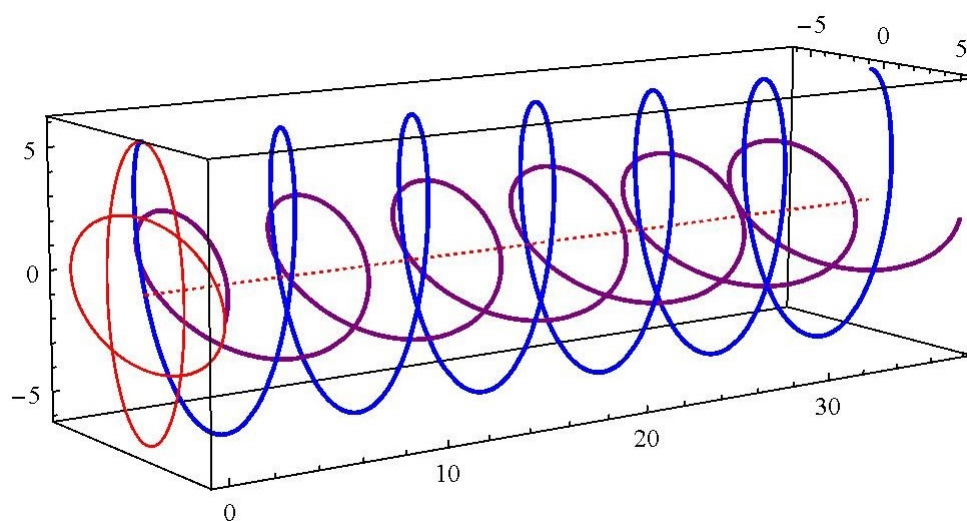


Figure 2.14. The electronic elliptical contribution can be seen as the function whose major axis lies in the z -direction (vertical) and the magnetic contribution has an orthogonal orientation.

2.7 Conclusion

It has been shown that even under conditions of relativity multiply-charge atomic ions should still be achievable within the confines of an intense laser field. The stability of several atomic-anions has been found and discussed, some ions are on the order of an entire electron volt more stable than the ionized system. The importance of the general dimensional scaling procedure was verified not only via the energetics, but with a comparison of the 'exact' locations of the electrons as predicted by Dimensional Scaling as they compare to the probability densities from the standard SCF procedure. These species were found to be stable and should, therefore, be experimentally realizable. Stability of simple molecular systems in super-intense laser fields have been previously discussed here[40, 41, 42]. This dimensionally scaled framework with relativistic corrections yields itself easily to a description of molecules and molecular ions within the confines of super-intense laser fields, which shall be undertaken next.

2.8 Acknowledgments

We would like to thank the Army Research Offices for funding this project. Jiaxiang Wang would like to thank NSF-China for the support by Grant No. 10974056. We would also like to thank Prof. Dudley Herschbach of stimulating discussion of the materials within this paper.

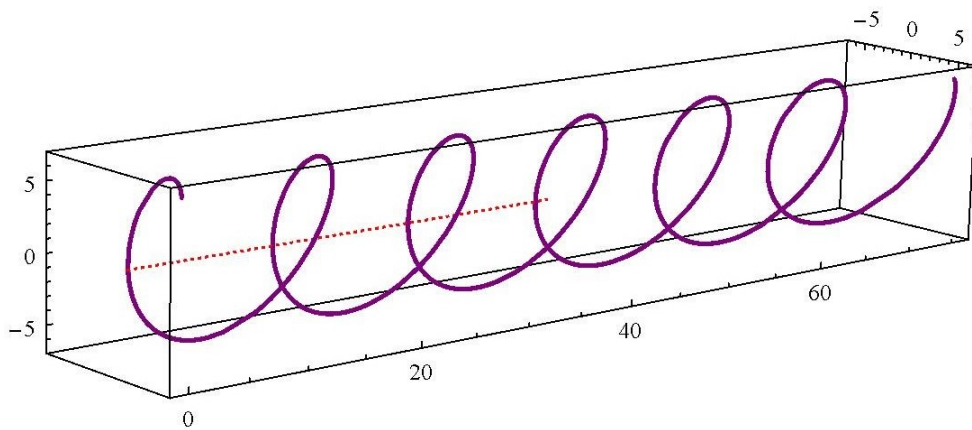


Figure 2.15. Within the above plot, the total trajectory can be seen, the amplitude of the major and minor axes are mediated in value between those from the electronic and magnetic components and the orientation is set off by an angle whose value respects the same coefficients as the relative amplitudes.

2.9 References

- [1] M. Gavrilă. Atomic stabilization in superintense laser fields. *J. Phys. B* 35, R147 (2002).
- [2] M. Gavrilă, *Atoms in Intense Laser Fields* (Academic Press, NY, 1992).
- [3] J. H. Eberly and K. C. Kulander. Atomic Stabilization by Super-Intense Lasers. *Science* 262, 1229 (1993).
- [4] D. J. Pegg, J. S. Thompson, R. N. Compton, and G. D. Alton. Evidence for a stable negative ion of calcium. *Phys. Rev. Lett.* 59, 2267 (1987).
- [5] D. Berkovits, E. Boaretto, S. Ghelberg, O. Heber, and M. Paul. Electron Affinity of Strontium. *Phys. Rev. Lett.* 75, 414 (1995).
- [6] M. K. Scheller, R. N. Compton, and L. S. Cederbaum. Gas-Phase Multiply Charged Anions. *Science* 270, 1160 (1995).
- [7] J. Simons. Theoretical Study of Negative Molecular Ions. *Ann. Rev. Phys. Chem.* 62, 107 (2011).
- [8] J. Simons. Molecular Anions. *J. Phys. B* 112, 6401 (2008).
- [9] E. H. Lieb. Bound on the maximum negative ionization of atoms and molecules. *Phys. Rev. A* 29, 3018 (1984).
- [10] K. H. Chang, R. D. McKeown, R. G. Milner, and J. Labrenz. Search for long-lived doubly charged negative atomic ions. *Phys. Rev. A* 35, 3949 (1987).
- [11] D. R. Bates, in *Negative Ions: Structure and Spectra, Advances In Atomic, Molecular, and Optical Physics, Vol. 27*, edited by S. D. Bates and B. Bederson (Academic Press, 1990) pp. 1–80.
- [12] A. V. Sergeev and S. Kais. Variational principle for critical parameters of quantum systems. *J. Phys. A* 32, 6891 (1999).
- [13] P. Serra and S. Kais. Finite size scaling for critical conditions for stable dipole-bound anions. *Chem. Phys. Lett.* 372, 205 (2003).
- [14] Q. Wei, S. Kais, and D. Herschbach. Dimensional scaling treatment of stability of atomic anions induced by superintense, high-frequency laser fields. *J. Chem. Phys.* 127, 094301 (2007).
- [15] Q. Wei, S. Kais, and N. Moiseyev. New stable multiply charged negative atomic ions in linearly polarized superintense laser fields. *J. Chem. Phys.* 124, 201108 (2006).
- [16] M. Pont, N. R. Walet, M. Gavrilă, and C. W. McCurdy. Dichotomy of the Hydrogen Atom in Superintense, High-Frequency Laser Fields. *Phys. Rev. Lett.* 61, 939 (1988).
- [17] E. van Duijn, M. Gavrilă, and H. G. Muller. Multiply Charged Negative Ions of Hydrogen Induced by Superintense Laser Fields. *Phys. Rev. Lett.* 77, 3759 (1996).

- [18] Q. Wei, S. Kais, and N. Moiseyev. Frequency-dependent stabilization of He^- by a superintense laser field. *Phys. Rev. A* 76, 013407 (2007).
- [19] Q. Wei, S. Kais, and D. Herschbach. Dimensional scaling treatment of stability of simple diatomic molecules induced by superintense, high-frequency laser fields. *J. of Chem. Phys.* 129, 214110 (2008).
- [20] J. Z. Kaminski. Relativistic generalisation of the Kroll-Watson formula. *J. Phys. A* 18, 3365 (1985).
- [21] P. S. Krstic and M. H. Mittleman. Bound states of atomic hydrogen in a laser field beyond the nonrelativistic dipole approximation. *Phys. Rev. A* 42, 4037 (1990).
- [22] C. H. Keitel, M. Protopapas and P. L. Knight. Relativistic mass shift effects in adiabatic intense laser field stabilization of atoms. *J. Phys. B* 29, L591 (1996).
- [23] C. J. Joachain, O. Latinne and M. Dorr. Atomic Hydrogen in a Superintense High-Frequency Field: Testing the Dipole Approximation. *Europhys. Lett.* 26, 333 (1994).
- [24] C. Joachain, M. Dorr, and N. Kylstra, in *High-Intensity Laser-Atom Physics, Advances In Atomic, Molecular, and Optical Physics*, Vol. 42, edited by B. Bederson and H. Walther (Academic Press, 2000) pp. 225 - 286.
- [25] C. J. Joachain and N. J. Kylstra. Relativistic Effects in Laser-Atom Interactions. *Physica Scripta* 68, C72+ (2003).
- [26] L. S. Brown and T. W. B. Kibble. Interaction of Intense Laser Beams with Electrons. *Phys. Rev.* 133, A705 (1964).
- [27] J. H. Eberly and A. Sleeper. Trajectory and Mass Shift of a Classical Electron in a Radiation Pulse. *Phys. Rev.* 176, 1570 (1968).
- [28] W. C. Henneberger. Perturbation Method for Atoms in Intense Light Beams. *Phys. Rev. Lett.* 21, 838 (1968).
- [29] I. Gilary and N. Moiseyev. Alternative Representation of Time-Dependent Hamiltonians with Application to Laser-Driven Systems. *Phys. Rev. A* 66, 063415 (2002).
- [30] L. E. McMurchie and E. R. Davidson. One- and two-electron integrals over cartesian gaussian functions. *J. Comp. Phys.* 26, 218 (1978).
- [31] A. Szabo and N. S. Ostlund, *Modern quantum chemistry: introduction to advanced electronic structure theory* (Dover Publications, 1996) p. 480.
- [32] S. F. Boys. *Electronic Wave Functions. I. A General Method of Calculation for the Stationary States of Any Molecular System.* Royal Society of London Proceedings Series A 200, 542 (1950).
- [33] D. R. Herschbach. Dimensional interpolation for two-electron atoms. *J. Chem. Phys.* 84, 838 (1986).

- [34] D. Herschbach, J. Avery, and O. Goscinkis, *Dimensional Scaling in Chemical Physics* (Kluwer Academic Publishers, 1993) p. 480.
- [35] A. Svidzinsky, G. Chen, S. Chin, and et al. Bohr model and dimensional scaling analysis of atoms and molecules. *Int. Rev. Phys. Chem.* 27, 665 (2008).
- [36] S. Kais and D. R. Herschbach. The $1/Z$ expansion and renormalization of the large dimension limit for many electron atoms. *J. Chem. Phys.* 100, 4367 (1993).
- [37] M. Dunn, T. C. Germann, D. Z. Goodson, C. A. Traynor, J. D. Morgan, D. K. Watson, and D. R. Herschbach. A linear algebraic method for exact computation of the coefficients of the $1/D$ expansion of the Schrödinger equation. *J. Chem. Phys.* 101, 5987 (1994).
- [38] J. Avery, D. Z. Goodson, and D. R. Herschbach. Dimensional Scaling and the Quantum Mechanical Many-body Problem. *Theor. Chim. Acta* 81, 1 (1991).
- [39] C. Tsipis, V. Popov, D. Herschbach, and J. Avery, *New Methods in Quantum Theory* (Kluwer Academic Publishing, 1996) pp. 3354.
- [40] N. A. Nguyen and T.-T. Nguyen-Dang. Molecular dichotomy within an intense high-frequency laser field. *J. Chem. Phys.* 112, 1229 (2000).
- [41] T. Yasuike and K. Someda. HeHe chemical bonding in high-frequency intense laser fields. *J. Phys. B* 37, 3149 (2004).
- [42] B. Rotenberg, R. Taieb, V. Veniard, and A. Maquet. H₂⁺ in intense laser field pulses: ionization versus dissociation within moving nucleus simulations. *J. Phys. B* 35, L397 (2002).

3. DRUG EFFICACY PREDICTION BY QUANTUM PROCESSES

3.1 Introduction

Attention has recently been given to a theory governing the activation of G-Protein Coupled Receptors (GPCRs) within the olfactory cavity by means of an electron transfer process across the activation site of the protein. This theory prescribes similar mechanisms to those governing Inelastic Electron Tunneling Spectroscopy (IETS), a method of spectroscopic determination based on molecular vibrational and electronic transitions. This theory has been used to reassert odorant compounds within their known odor classes; agreement was established, possibly bolstering the applicability of this theory. There are several facets within the framework of IETS theory that should be further considered and included in future works within this topic. Herein we elucidate several considerations and to what degree these influence calculations: dimensions of the activation site, orientation effects of the odorant within the site, modulation of the geometry of docked ligands, and the importance of both Infrared and Raman active modes.

Prediction of the behaviors of a bound agonist within the active site of a protein is of major interest in fields surrounding taste/scent, pharmaceuticals and of drug design. Inelastic Electron Tunneling Spectroscopy (IETS) has been proposed as a mechanism by which olfactory G-Protein Coupled Receptors (GPCRs) are activated by an encapsulated agonist. Herein we apply this notion to GPCRs within the mammalian nervous system. We have noted that non-endogenous agonists of the Serotonin receptor share a singular IET spectral aspect both amongst each other and also with the serotonin molecule; this peak roughly scales in intensity with the known activities of known agonist activity. We conclude by proposing an experiential validation of this

model by utilizing Lysergic Acid Dimethylamide (DAM-57), an ergot derivative, and its isotopologues. If validated this theory may provide new avenues for guided drug design and better *in silico* prediction of efficacies.

Quantum activity within biological systems is a topic that has drawn a great deal of attention recently[1, 2, 3]. Examples of systems that exploit such phenomenon are: the avian magnetic compass [5, 6, 7], quantum mutations [9, 10], entanglement in photosynthetic complexes [13, 14, 15, 16, 17], tunneling behavior in the antioxidant breakdown of catechols present in green tea [18], enzymatic action[19], olfaction[20], and genetic coding [21].

The activation of GPCRs govern many physiological activities examples of which include olfaction, central nervous system regulation and maintaining circadian rhythm. Roughly half of all modern small molecule therapeutics target this class of proteins and 50% of all human encoded GPCR genes encode for olfaction alone. Understanding the mechanism by which activation of this class of proteins is achieved is paramount to applications within both the pharmaceutical and the flavor/scent industries. G Protein-Coupled Receptors (GPCR) are the target for the greatest portion of modern therapeutic small molecule medications[22]. Predictability of pharmacological efficacy for new drugs prior to a complex total synthesis can be aided by pharmacore modeling or with either crystal structure or a homology model. The theory of protein/agonist binding has been described through variants of the Lock and Key model, originally proposed by Fischer[23] and the extensions thereof[24]. Although this theory has provided insight into changes of free energy associated with the formation of the activated complex, it has not manifested sufficient capacity for the prediction ligand activity or a mechanism by which the agonist activates the system.

Early models attempting to account for odorant binding and the prediction of odor classification include those of Dyson[25] and Wright [26], who proposed a vibrational theory of olfaction. These theories were expanded upon to include scents generated through the blend of two or more molecules [27] and explanations of chiral behaviors in olfaction [28]. Vibrational theories were eventually disregarded for reasons

that include a lack of conceived mechanism and the inability of the protein (which is vibrating) to detect the continuum of thermally-activated, classical vibrations of the odorant. Recently, Turin suggested a theory of olfactory activation consisting of a physical mechanism closely resembling Inelastic Electron Tunneling Spectroscopy (IETS) [20, 29, 30]. Turin demonstrated the viability of his theory across several classes of odorants with several examples per class. The plausibility of time scales associated with this process was verified through Marcus theory[31]. Electron tunneling rates for the olfaction system have been calculated and support the theory [32]. Furthermore, eigenvalue spectral analysis of odorant molecules has shown a high correlation between the vibrations and odorant classification [33].

Genes encoding Olfactory Receptor (OR) proteins, a specific subtype of GPCR, were discovered in the early 1990's[34]. GPCRs are prevalent throughout living organisms and have many functions in physiology; with roles that include the synaptic recognition of neurotransmitters within the central nervous system (CNS). The primary focus of this paper is an initial examination of the viability of a recently proposed vibrational theory of protein activation in cases involving protein-agonist binding within the CNS and as a predictor of intrinsic efficacy as defined within [35]. Activation of the 5-HT_{1A} and 5-HT_{2A} receptors is implicated as being associated with human hallucinogenic responses [36, 37]. A recent resurgence of interest for a vibrational-based theory of protein activation has occurred, featuring IETS as its possible means of detecting the vibrational modes of the bound ligand. The IETS mechanism relies on a field driven electron transfer across an insulating gap situated between two conductive metal plates. The driving field promotes electrons to tunnel from the donor site on one side of the gap to the acceptor site on the other side; this is the elastic process. As the intensity of the driving field is increased, the electrons may donate a quanta of energy to a molecule situated within the gap along their path. This exchange of energy must be equal to a quanta accepted by the molecules vibrational or electronic transitions. This secondary mechanism provides a new path which enhances the current across the gap. There exist several other mechanisms by which

electrons are conveyed across the gap including elastic transfer, inelastic transfer, 2^{nd} order elastic transfer as well as subsequent and less contributing modes of transport. The theoretical description of this mechanism was introduced by Scalapino, Hansma and Kirtley and later elucidated by Phillips and Adkins.

As a means to exemplify the effects of several factors on the measurable IETS intensities, we have selected as our example system the formate ion. This ionic system is both small and simple enough to allow for easily observed emphasis of effects of the IETS mechanism discussed within this paper as it possesses a very tractable number of vibrational modes and a simple geometry. This example also has the added benefit of being a classical example within the IETS theory and experimental literature. We will then present a qualitative discussion of the relationship between the IETS model and the protein-agonist complex. Following this, we will discuss the IETS of several 5-HT_{1A} and 5-HT_{2A} agonists, and how these correlate with efficacy of these molecules. We conclude with a proposed set of molecules that could be employed in an experimental validation of the vibrational theory's applicability in the CNS.

3.2 Inelastic Electron Tunneling Mechanics

Inelastic Electron Tunneling Spectroscopy is a well-founded experimental method utilizing a simplistic laboratory set-up that can deliver the vibrational spectra of an analyte. The mechanism of action is semi-classical and not optical, particular selection rules are derivable with IETS [63] but in general this method allows for forbidden transitions, thus all vibrational modes are addressable[64]. The method is implemented by the application of a potential across a two-plate junction with a spatial separation between the plates. High energy electrons from the valence band of one plate will tunnel across the junction into the conduction band of the other. When the tunneling process occurs in the absence of analyte molecules, the process is elastic in nature and electron energy is maintained throughout the process, thus the electrons energy must be respective of the energy between the valence and conductance

band/ Depositing an analyte molecule onto the electron source plate, as the tunneling electrons enter the gap they may interact with the deposited analyte molecules; in doing so they are effectively given a springboard, shortening their tunneling path. This interaction comes at a cost of energy; the electron will lose energy to the analyte molecule, where the amount of lost energy is equal to that of a vibrational mode of the molecule. This process may be seen in Figure 3.1. This method has been well described theoretically [66, 67, 38] and expanded to include such considerations as molecular orientation [68] and short-ranged higher harmonics [69].

Here we shall review the theoretical description of the elastic process as seen in [40, 39]. Calculations of Inelastic Electron Tunneling rates have been performed in various ways throughout the literature. Typically the Barden Transfer Hamiltonian method is employed to allow for the calculation of the elastic contribution from the tunneling wavefunctions across the barrier sides. The WKB approximation is used to describe the wavefunction of the tunneling electrons from each side; the following are the evanescent wavefunctions describing an electron traversing a gap of length d defined by two conductive plates of area L^2 :

$$\varphi_1 = \left(\frac{A}{L}\right) e^{ik_{\parallel} \cdot r} e^{-\alpha_0 z} \quad (3.1)$$

$$\varphi_2 = \left(\frac{A}{L}\right) e^{ik'_{\parallel} \cdot r} e^{-\alpha_0(d-z)} \quad (3.2)$$

From the above it should be noted that L is the dimension of the square plate. $k_{parallel}$ and k'_{\parallel} are the momentum parallel to the surfaces. Similarly, A is a collection of constants forming the normalization for our system, α_0 is the decay rate of the evanescent wave in the z^{th} direction and assuming cylindrical symmetry the wave vectors in the \hat{x} and \hat{y} directions are identical and are combined into the radial wave vector k_{\parallel} , noting that this is the wave vector components parallel to the plate surface. The anatomy of this system is given in Figure 3.2. As a reference, a cartoon description of the formate ion within the gap is given in Figure 3.3a and the experimentally resolved spectra for this system is in Figure 3.3b.

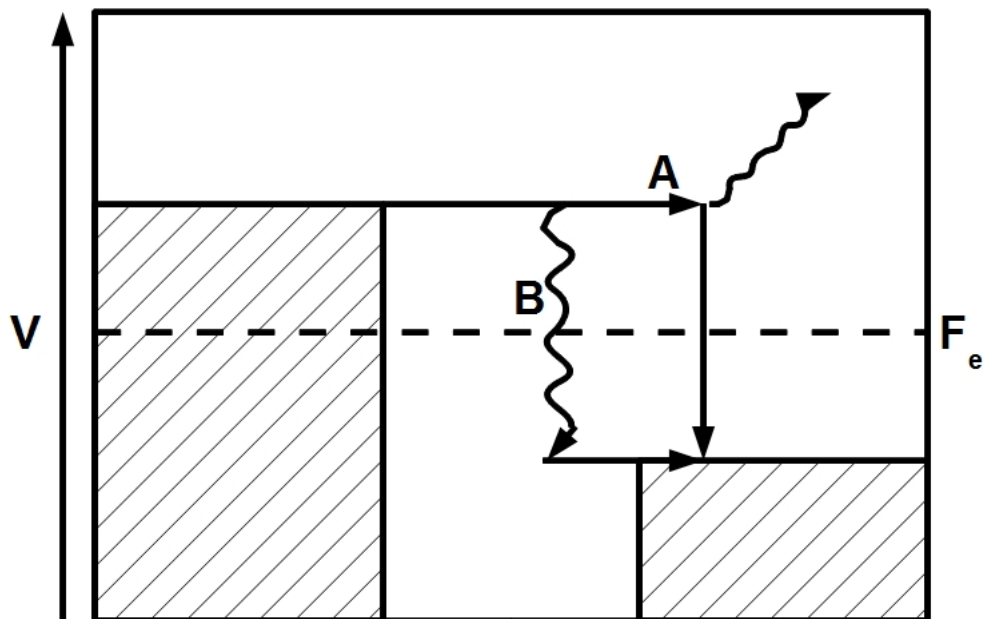


Figure 3.1. Cartoon displaying the competing processes during IETS where V is potential energy and F_e is the Fermi Level. Path A is radiative [65, 63], requiring the tunneling electron to spontaneously lose energy to meet the energy of the conductive band. Path B shows the electron losing energy via a non-radiative process; it is implicit that the energy lost is to a normal mode of a deposited molecule within the gap - such is our case.

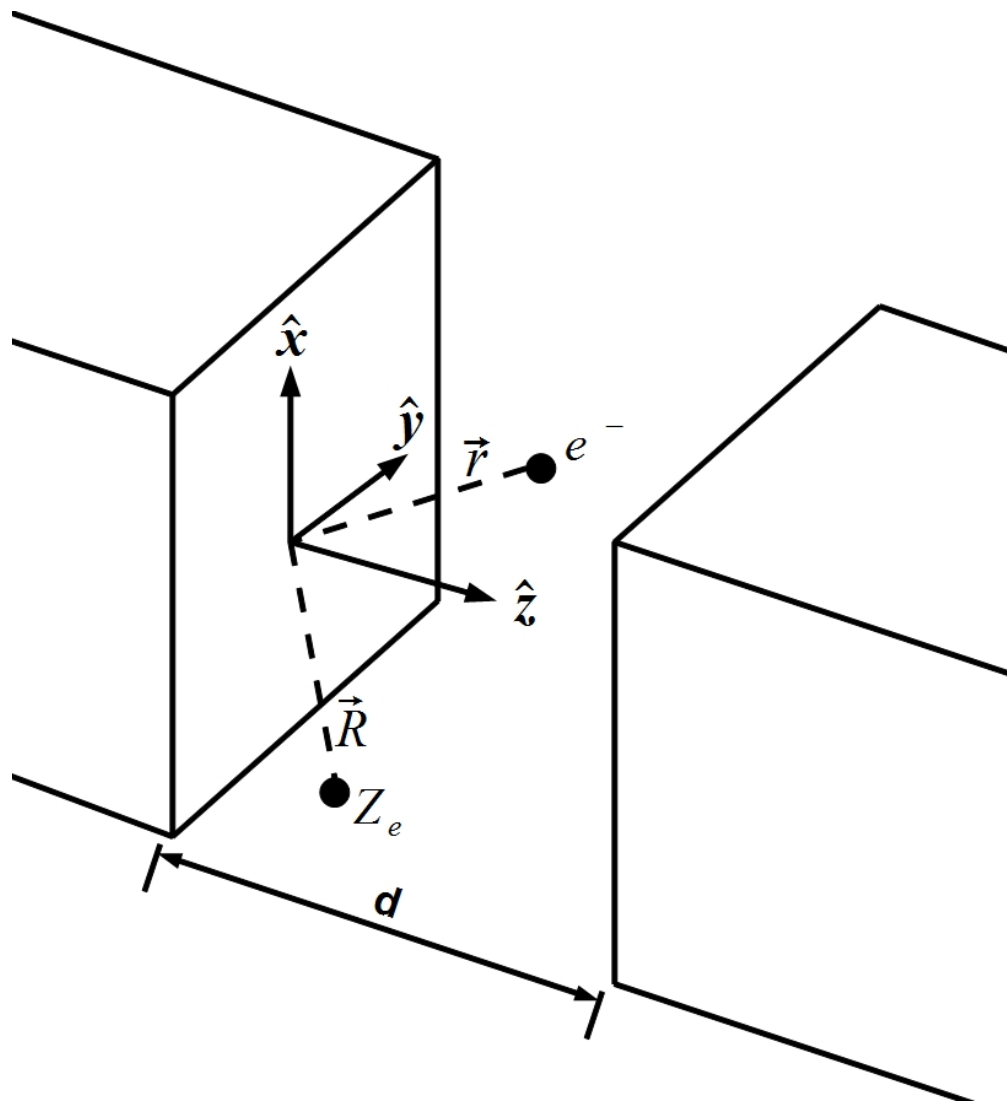


Figure 3.2. A cartoon displaying the physical relations and significance of variables within the problem. e^- is the tunneling electron with vector displacement of \vec{r} and Z_e is the partial charge associated with a molecular mode with displacement \vec{R} , and d is the distance between the two plates.

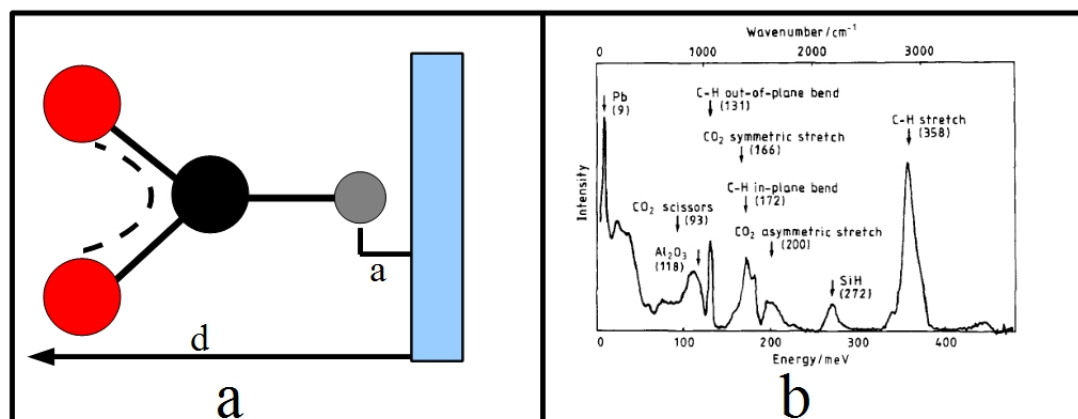


Figure 3.3. a) A cartoon schematic of the formate ion within its gap, distance parameters d and a are shown within the figure for clarity. b) The IETS spectra of the formate ion taken from [cite], provided as reference.

As the electrons tunnel through the barrier they may undergo several processes including: elastic transfer, inelastic transfer, 2nd order elastic transfer and subsequent less contributing modes of transfer. The inelastic modes of transport are facilitated through interaction between the tunneling electron and a deposited molecule within the gap; the tunneling electron donates of quanta of energy to the deposited molecule. The donation of energy from the electron to the molecule must obey Fermis Golden Rule:

$$T_{i \rightarrow f} = \frac{2\pi}{\hbar} \left| \langle \varphi_2 | \hat{U} | \varphi_1 \rangle \right|^2 \delta(E_f - E_i \pm \hbar\omega) \quad (3.3)$$

Where $T_{i \rightarrow f}$ is the probability of an electron transferring from state i to state f , with the stationary state wavefunctions φ_i and φ_f ; \hat{U} is the interaction potential to be discussed and δ is the Kronecker delta function depending on the energies of the states and the quanta absorbed by the deposited molecule. The quanta of energy is typically in the range of vibrations for IETS, although electronic excitations have also been achieved experimentally. The electronic interaction between the ligand and the molecule treats each atom of the molecule separately; each atom is assigned a partial charge, Z , and sits at its equilibrium positions, R , it vibrates with displacement u . The interaction potential is that of an electron and single dipole:

$$\hat{U}(r, \theta, z) = \left(\frac{Ze^2}{4\pi\epsilon_0\epsilon_r} \right) \frac{u \cdot (R - r)}{(|R - r|^3)} \quad (3.4)$$

As the interaction is between the electron and a single atom of the molecule, the contribution to the conductivity found through this calculation must be repeated and summed over all atoms within the molecule. We shall use the wave functions in Eq. 3.4 to attain the average value of the current for the system, via the elastic current operator, \hat{M}_e . To determine the contribution to the conductivity of any mode of transport, one must first calculate the tunneling matrix element. In the case of the elastic mode the tunneling matrix element, M_e , is calculated as the overlap of the wavefunctions from the donor and acceptor sites over the volume of the gap since this mechanism does not require interaction with the deposited molecule. The calculation

of the tunneling matrix element for the inelastic transport to the contribution utilizes the both donor and acceptor wavefunctions and the interaction potential:

$$\langle \psi_i | \hat{M}_e | \psi_f \rangle = M_e = \left(\frac{A^2}{L^2} \right) \int_0^L dS e^{i\mathbf{q}\cdot\mathbf{r}} \left(\frac{\hbar^2 \alpha_0}{m} \right) e^{-\alpha_0 d} \quad (3.5)$$

$$= \left(\frac{A^2 \hbar^2 \alpha_0}{m} \right) \cdot e^{-\alpha_0 d}, \quad (3.6)$$

where \mathbf{q} is the difference between \mathbf{k}'_{\parallel} and \mathbf{k}_{\parallel} . The inelastic process for a single specified normal mode is governed by the following interaction potential:

$$U(r') = \frac{Z_e e^2}{4\pi \epsilon_0 \epsilon_r} \cdot \frac{\mathbf{u} \cdot (\mathbf{R} - \mathbf{r})}{(|\mathbf{R} - \mathbf{r}|)^3}, \quad (3.7)$$

where all symbols retain their standard definitions, including ϵ_r being the permittivity of the generic real media, \mathbf{r} and \mathbf{R} are made clear by Figure 3.2 and \mathbf{u} is the vector representing the displacement of the atom within the molecule with partial charge Z_e . This potential allows us to calculate the inelastic contributions in a manner similarly to the above:

$$M_{in} = \left(\frac{A^2}{L^2} \right) e^{-\alpha_0 d} e^{i\mathbf{q}\cdot\mathbf{R}} \int_0^\infty \int_0^{2\pi} \int_0^d r e^{i\mathbf{q}\cdot\mathbf{r}} U(r, \theta, z) dz d\theta dr. \quad (3.8)$$

Where the integral in Equation 3.8 can be performed analytically for cases where the vector directions of \mathbf{u} are either parallel or perpendicular to the plate surfaces. For \mathbf{u} along the z direction (parallel to gap):

$$M_{in}^z = M_0 \frac{1}{qd} (e^{-q\alpha_0} - e^{-q(d-\alpha_0)}) ; \quad (3.9)$$

and for \mathbf{u} parallel to the plates:

$$M_{in}^x = iM_0 \frac{1}{qd} \{ (1 - e^{-q\alpha_0}) + (1 - e^{-q(d-\alpha_0)}) \}. \quad (3.10)$$

Where, in both the above, the quantity M_0 is given by:

$$M_0 = e^{i\mathbf{q}\cdot\mathbf{R} - \alpha_0 d} \left(\frac{A^2 Z e^2 u d}{L^2 2\epsilon_0 \epsilon_r} \right). \quad (3.11)$$

The decay constants for each of ψ_i and ψ_f should conform with the statement:

$$E_c - E = \frac{\hbar^2}{2m} (\alpha^2 - k_{\parallel}^2) \quad (3.12)$$

where E is the energy of the tunneling electron, E_c is the energy of the conductive band and m is the mass of the electron (effective mass is typically used). The above yields two unique decay constants consistent with the difference in electron energies at the conduction band and during tunneling. With these two unique decay constants we must append a factor of

$$e^{(\alpha_i+\alpha_f)d/2}e^{(\alpha_i-\alpha_f)z} \quad (3.13)$$

to our matrix elements due to the difference in α 's. Carrying this factor through we note there is a depletion of tunneling probability equivalent to:

$$e^{-q^2/4(\alpha_0d)}; \quad (3.14)$$

and finally placing this into an expression for the relative conductivities associated with the inelastic and elastic processes, $\frac{\Delta\sigma}{\sigma_e}$, and finally including a 2-D density of states representative of the plate surface areas:

$$\frac{\Delta\sigma}{\sigma_e} = \left\{ \frac{1}{M_e} \right\}^2 \int_0^\infty (M_{in}^z)^2 e^{-q^2/4(\alpha_0/d)} \left(\frac{qL^2}{2\pi} \right) dq. \quad (3.15)$$

The above allows us to make the statement:

$$\frac{\Delta\sigma}{\sigma_e} \propto Z_e^2 u_z^2, \quad (3.16)$$

as those quantities on the R.H.S. of Eq. 3.15 are the only quantities dependent on molecular characteristics and thus are featured in Eq. 3.16. As the elastic tunneling process occurs with or without the presence of the analyte molecules, the experimental observable is the ratio between the known elastic contribution, $\sigma_e = M_e^2$, to the current at a given applied potential (found through a zeroing process with a non-deposited gap) and the deposited gap current at the same potential; this ratio quantity is denoted as $\frac{\Delta\sigma}{\sigma_e}$. Armed with the above, the IETS intensity for a given active mode j can be approximated by[20, 38]:

$$I_j = \sum_{i=1}^N I_{i,j} = \sum_{i=1}^N q_i^2 (\Delta x_{i,j})^2, \quad (3.17)$$

where the sum is over all atoms within the molecule, q_i is the partial charge of atom i , and $\Delta x_{i,j}$ is the Cartesian displacement of atom i in mode j . This is a

simplification through elimination of all constants within the calculation, it is taken as arbitrary units but is proportional to the strict calculation through multiplication of a constant. Figure 3.4 is provided as a useful reference for subsequent sections; it gives the normal modes of the formate ion for association with the intensities and spectra below. Within this figure, the displacements in *a.u.*, the directional unit vector and the frequency in cm^{-1} are all given; oxygens are depicted in red, carbon in black and hydrogen in grey.

3.2.1 Point Dipole Approximation

The most fundamental expression for the interaction between an electron and a charged dipole is given here:

$$V = \frac{z_i (-z_j) e^2}{4\pi\epsilon_0} \frac{1}{|r_j - r_i|} + \frac{z_i z_j e^2}{4\pi\epsilon_0} \frac{1}{|r_j + p_j - r_i|} \quad (3.18)$$

Where r_i is the location of the electron providing a field $z_i e^2$ and r_j is location of a single side of the dipole where both ends provide a field with the magnitude $z_j e^2$; the second term describes the remaining, oppositely charged side of the dipole at a distance p_j from the other end. Recollection of the terms yields the expression in Eq. 8a, and a subsequent Taylor series expansion for the denominator yields Eq. 3.19 line 2.

$$V = \frac{-z_i z_j e^2}{4\pi\epsilon_0} \left(\frac{1}{r_{ij}} - \frac{1}{\sqrt{r_{ij}^2 + 2\vec{r}_{ji} \cdot \vec{p}_j + p_j^2}} \right) \quad (3.19a)$$

$$\cong z_j z_i e^2 4\pi\epsilon_0 r_{ji} \left(\frac{2\vec{r}_{ji} \cdot \vec{p}_j}{r_{ji}^2} + \frac{1}{2} \frac{p_j^2}{r_{ji}^2} - \frac{3}{8} \left(\frac{2\vec{r}_{ji} \cdot \vec{p}_j}{r_{ji}^2} + \frac{p_j^2}{r_{ji}^2} \right)^2 \right) \quad (3.19b)$$

After the series expansion, the point dipole approximation is typically employed; this approximation states that the distance between the charge and the dipole is much greater than the displacement between the dipole termini, $r_{ji} \gg p_j$. Under the point

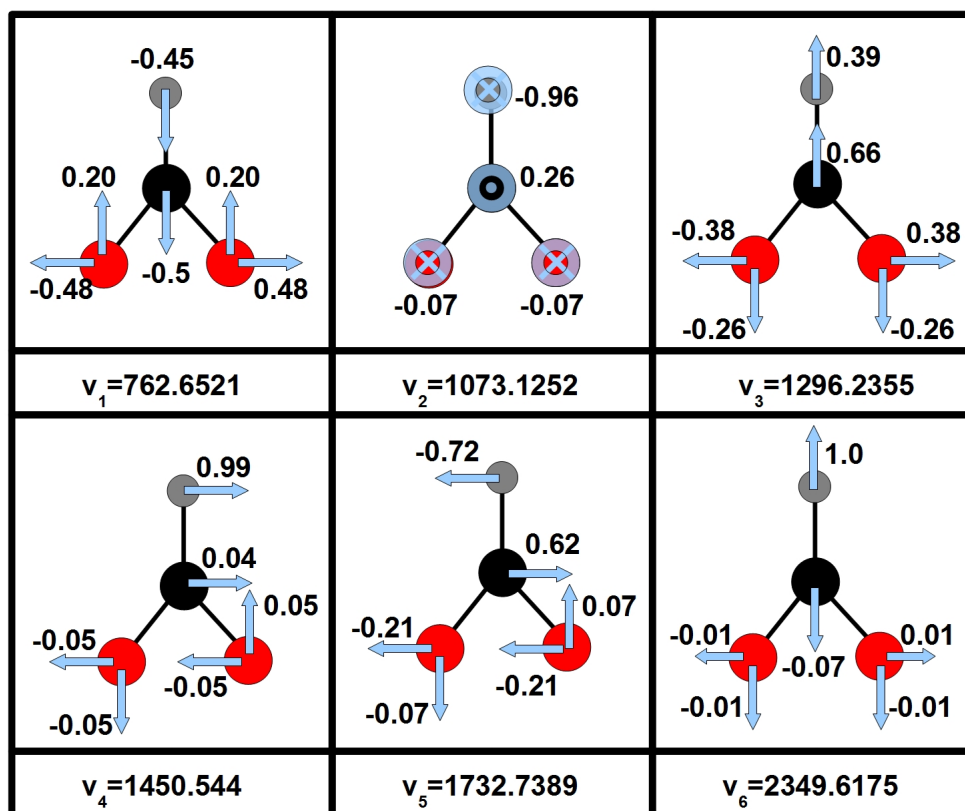


Figure 3.4. A display of the normal modes associated with the formate ion. Also included are a unit vector indicator as to the direction of displacement and the magnitude is shown beside it. Distances are in *a.u.* Frequencies are also displayed in cm^{-1} beneath the mode to which it belongs.

dipole approximation all but the leading terms of Eq. 3.19 line 1 drop due to minimal contribution, seen in Eq. 3.20.

$$V \approx \frac{z_j e}{4\pi\epsilon_0} \frac{\vec{r}_{ji} \cdot \vec{\mu}_j}{r_{ji}^3} = \frac{z_j z_i e^2}{4\pi\epsilon_0} \frac{\vec{r}_{ji} \cdot \vec{u}_j}{r_{ji}^3} \quad (3.20)$$

It is important to note that the spatial dimensions of the activation site within this class of proteins has been suggested to be roughly 15\AA . The suggested dimensions of the active site, when compared to that of the displacement vector, does not meet the criteria for the point dipole approximation. Considering at the system is possibly inappropriate for application of the point dipole approximation, comparing the numerical values for the tunneling matrix elements as calculated by Eq. 3.8 using the interaction potential Eq. 3.4 and the more complete form of the interaction potential in Eq. 3.19 line 1. Figure 3.5 shows the relative error associated with using the point dipole approximation with the spatial scale of the active site; it should be noted that the error associated with this misuse of the approximated potential is peaked in the range of the active site length scale. As the point dipole approximation eliminates terms which are dependent upon the projection, $r_{ji} \cdot p_j$, there exists an angular dependence on the magnitude of the tunneling matrix element. This angular dependence can be observed in Figure 3.5, and is due to the projector in terms eliminated during application of the point dipole approximation; the magnitude of the relative error is proportional to the cosine of the angle, and then we observe an oscillatory component to the θ dependence.

3.2.2 Polarizability

As a method for obtaining information about the vibrational modes of a molecule, IETS does not rely on the interactions between the molecular dipole and the field of the electron. The interaction potential, Eq. 3.4, is that between an electron and a single oscillating dipole, representative of a vibrating atom within the molecule. This interaction does not depend upon the polarizability of the system nor the change in

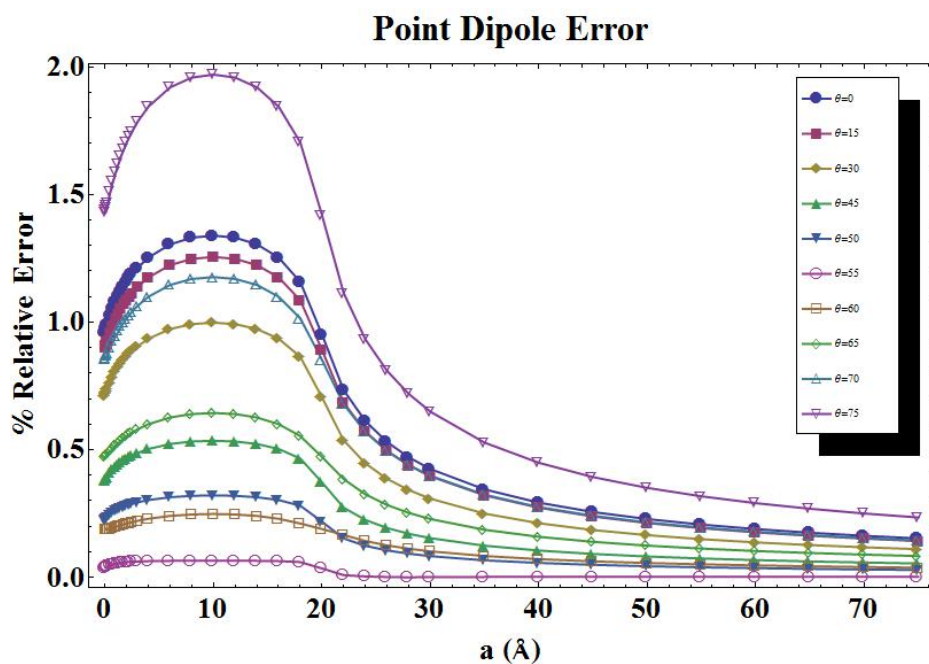


Figure 3.5. The percent relative error between variations of the interaction potential given in Eq. 3.4 and Eq. 3.19a. This was completed for several values of θ to emphasize the angular dependence stemming from projection operations in terms eliminated through approximation.

net dipole. The single-dipole nature of the potential requires a summation over the atoms within the molecule to account for all possible interactions.

The ratio given in Eq. 3.16 is characteristic of the enhancement to the conductivity due to single atom motions. If this were the only responsible contribution to 1st order inelastic conduction than the symmetric modes, corresponding to Raman transitions, would not appear in IETS, yet they do and with roughly the same magnitude as Infrared active modes.

$$\frac{\Delta\sigma}{\sigma_e} \propto \int_0^\infty M_A M_B e^{-q^2 d^2 \alpha_0} F(qb) q dq = I_{AB}(a, d) Z_A Z_B u_A u_B \quad (3.21)$$

The above describes the contribution to the conductivity enhancement due to the coherent motion of two atoms. Eq. 3.21 contains a phase factor, $F(qb)$, which is generated through the addition of matrix elements. The advent of this phase factor comes from the addition of the $e^{iq \cdot R}$ terms seen within Eq. 3.8. If the two atoms are identical and their distance from the nearest barrier is the same, the form of the phase factor becomes: $(u_1 + u_2 e^{iq \cdot b})$. In the case that the displacements of each atoms are of equal magnitude and the same direction, $u_1 = u_2$ (IR active), the phase factor becomes $\cos^2(q \cdot b/2)$. In the case of Raman active modes, $u_1 = -u_2$, the phase factor simplifies to $\sin^2(q \cdot b/2)$.

It has been shown through experiment that both IR and Raman modes are active within IETS and scale roughly equally. Yet some works within this field authors have chosen to couple the oscillating dipole associated with an entire molecular mode, this would generate the intensities associated with the infrared vibrations of the molecule but not contributions associated with Raman active modes.

Figure 3.6 shows the effects of including intensity contributions of the Raman active modes (standard IETS), blue plot. Beside the blue plot, we have provided the intensity expected if the coupling mechanism were to be only with the molecular dipole moment. The two plots are scaled to each other for convenience of comparison. It is clear to note, by comparison between the blue plot of Figure 3.6 and the experimental

plot given in Figure 3.3, that the inclusion of Raman mode associated intensities has delivered a better approximation to experiment.

3.2.3 Orientation

When considering the charge-dipole interaction potentials it is clear that the leading (point-dipole) term as well as any subsequent terms rely on the projection of the harmonic displacement vector for a specific atomic oscillator $(j), u_j$, onto the charge-dipole vector, r_{ji} . This projection is of paramount importance within the calculation of the coupling within these systems as it effectively modulates the power of the denominator.

Orientation effects within IETS intensity calculations have been described as being of such importance as to practically be a selection rule for this type of vibrational characterization. Interaction potentials used within early formulations of IETS calculations has relied on the coupling strength of the electron within the donor site to atomic harmonic oscillators, and did not include any dynamic interactions within the system. More dynamic formulations exist to deal with that rather minute contribution of inelastic tunneling contributions to the current through molecular junctions, such as greens functions approaches. It should be noted that in these cases the inelastic contribution is to the molecular conductance and is attributed to vibronic alteration of electronic levels within the molecule this second-order coupling (electron-vibrational state-electronic state) is why the inelastic contribution is minute in these cases.

In maintaining the simplicity of static calculations, one cannot ignore the contributions to the interaction potential from the vector projection. To emphasize the importance of this interaction we have plotted the IETS of the formate ion; in Figure 3.7a you can see the three angular parameters. The red rotation about the red (z) axis does not alter the spectrum of the formate ion as the calculations set the origin of the tunneling junction along this axis and thus this rotation does not alter the projection of the electron onto any molecular modes, merely which component possesses

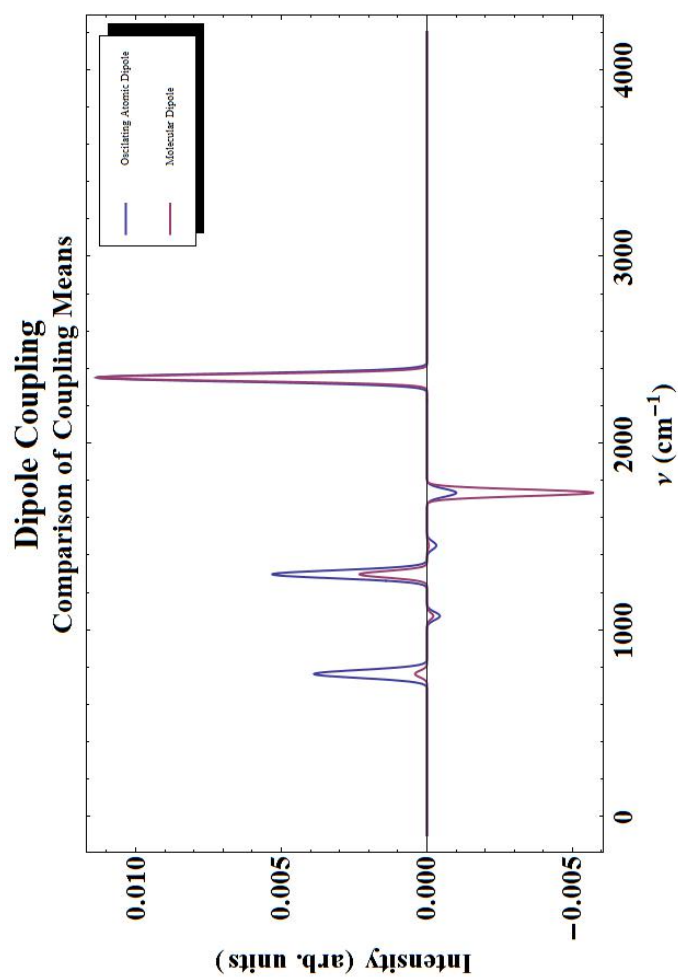


Figure 3.6. The blue line shows the IETS of the formate ion; the maroon line shows the spectra where the interaction potential given Eq. 3.4 is replaced by the interaction potential between the electron and the molecular dipole. The two plots have been scaled so to be comparable.

the projection; it should be clearly stated that this is a facet of the formate ion, not of IETS. Rotation about the green (y) and blue (x) axes will alter the projections, the effects can be seen in Figure 3.7b for rotation about the x-axis and Figure 3.7c for rotation about the y-axis. Furthermore, without having calculated these orientation effects one can never achieve modes where the rate of inelastic tunneling is lower than the rate of the elastic process.

3.2.4 Docking Geometry

Specifically discussing the activation of olfactory proteins under the odotope theory, the volatile odorant molecule is hypothetically capable of maintaining something akin to its optimized geometry within the activation site. This fact is due to the fact that only certain sections of the molecule are being determined at once, it could be rationalized that the molecule only loosely enters and is never fully enveloped by the activation site. This rationalization would be countered by docking studies of the OR1A1, OR1A2 and OR1G1 human olfactory receptors that do show envelopment of the ligands which dock with the protein.

Full ligand envelopment can lead to geometric alterations of the ligand during the docking. The alteration of ligand geometry can lead to attenuations in both the modal displacements and the partial charges, which for our example system can roughly generate a 10% by displacement or a 5% by partial charge (where partial charge was calculated through NBO analysis) alteration in the IETS intensity if the molecular geometry group is maintained. Moreover, these attenuations alter the potential interaction between the electron and the dipole through the dot product present in several terms of the non-approximated interaction potential Eq. 8a as well as the standard interaction potential Eq. 3.4.

Figure 3.8a shows the geometry and alignment within the gap of the formate ion as well as variations on the bond angles. Fig. 3.8ai is the optimized for of the ion, Fig. 3.8aaii is has altered both O-C-H bond angles equally (maintaining both σ planes)

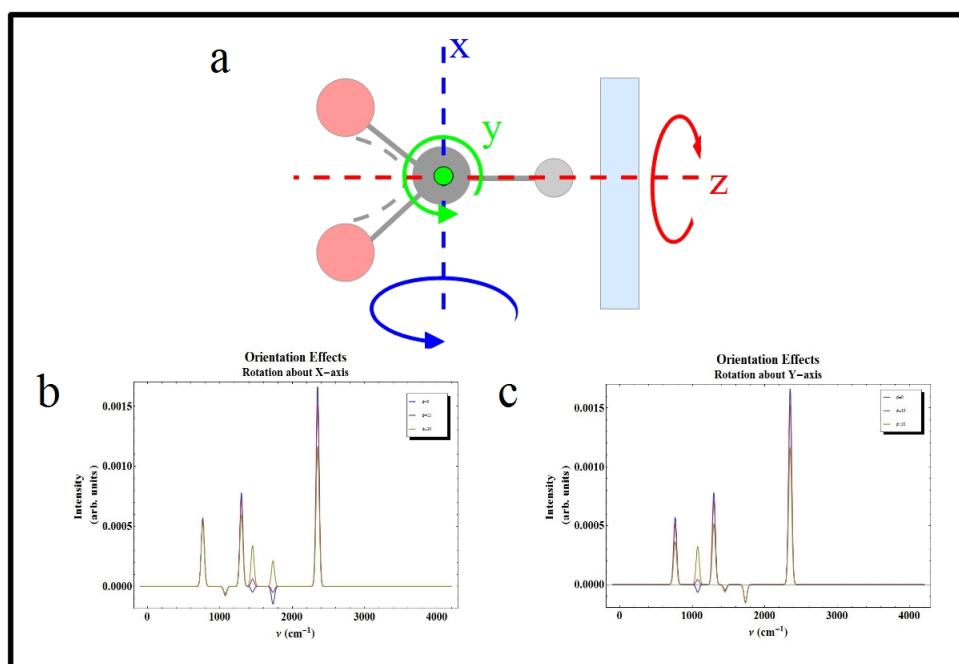


Figure 3.7. Effects of orientation of the molecule within the gap. Rotational axes are noted in Subfigure (a). Subfigure (b) and (c) show the IETS for the formate ion as it is rotated by the X- and Y-axis, respectively.

and Fig. 6a_{iii} has altered only one of the O-C-H bond angles (maintaining only the σ plane bisecting all bonds). The alterations in the frequencies, displacements and partial charges are shown in Table 3.3. Figure 3.8b gives the IETS for the variations of the formate ion. For obvious reasons the frequencies are slightly displaced, and the introduction of asymmetry in the oxygen pairs movement eliminates much of their non-canceling contribution.

3.3 Mapping the Models

Application of the IETS model for the protein environment requires mapping several aspects of the IETS methodology to the biological system. The two-plate setup of the tunneling junction represent the walls of the receptor site; more explicitly, under electron transfer the valance and conductance bands within the juncture become specific HOMOs and LUMOs of the residues making the walls of the receptor. This dictates that energy transition detectable by the protein should be the energy difference between electronic levels of residue side-chains. This alteration of IETS also localizes the source of tunneling electrons to a single residue side-chain; the implication is that electrons are not capable of uniformly tunneling through the molecule. This lack of uniformity suggests that the act of tunneling is localized to regions of the agonist molecule and that not all local oscillators of a specific mode contribute to the current enhancement.

Secondly unlike the experimental IETS procedure, the analyte is not deposited upon anything within the activation site; the agonist is encapsulated by the active site. There is no externally applied potential within the receptor site which would have allowed for the scanning of energies; yet, it has been suggested that an ionic cofactor, likely a calcium ion, could provide this driving field. The implication of this is that the receptor is set to test the vibrational-assisted enhancement to the electron tunneling rate at a specific energy. The electrostatic interactions which govern docking orientation would be a means of orienting the endogenous agonists in

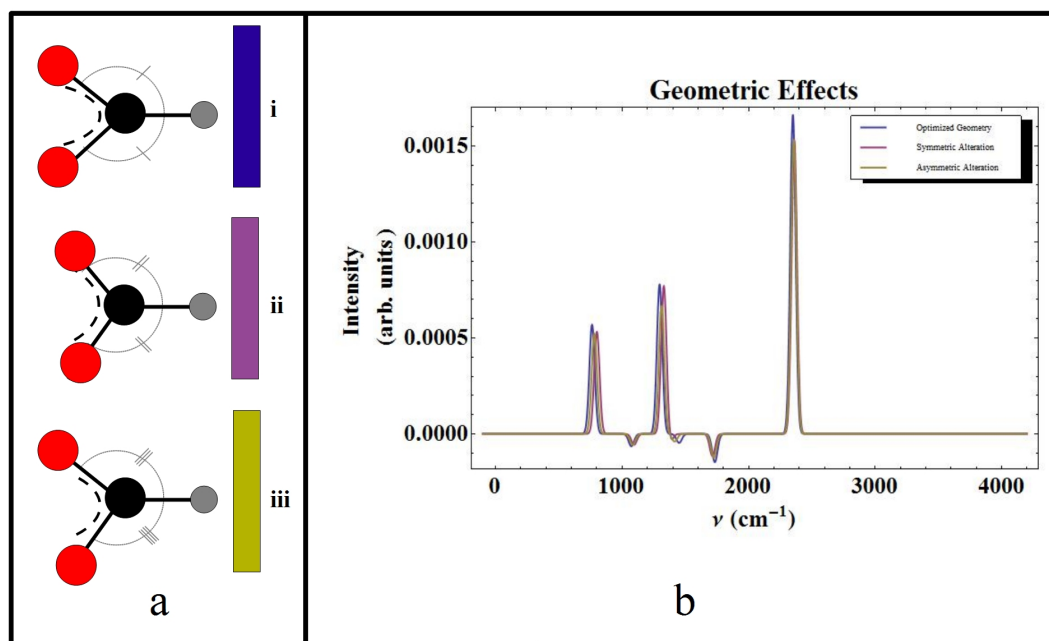


Figure 3.8. Effects of alterations of the geometry of a system on the IETS. Subfigure (a) shows cartoons of the geometries of concern: optimized geometry, symmetric alteration and asymmetric alteration, respectively. Subfigure (b) shows the IETS of the formate ion variants

Table 3.1
 Numerical Values for calculations of the geometric alterations and optimized geometry variants of the formate ions. This table contains displacements of the first three modes

	Displacement (\AA) (x, y, z)						C		H
	Mode 1		Mode 2		Mode 3		O_α	O_β	
	Asymm. Variant	(0.01, -0.5, 0)	(0.04, -0.45, 0)	(0, 0, 0.24)	(0, 0, -0.97)	(-0.02, 0.61, 0)	(-0.29, 0.41, 0)		
	(0.48, 0.21, 0)	(-0.48, 0.2, 0)	(0, 0, -0.06)	(0, 0, -0.06)	(0.37, -0.26, 0)	(-0.34, -0.23, 0)			
Optimized	(0, 0, -0.51)	(0, 0, -0.45)	(0.23, 0, 0)	(-0.97, 0, 0)	(0, 0, 0.62)	(0, 0, 0.48)			
	(0, 0.48, 0.21)	(0, -0.48, 0.21)	(-0.06, 0, 0)	(-0.06, 0, 0)	(0, 0.37, -0.25)	(0, -0.37, -0.25)			
Symm. Variant	(0, 0, -0.5)	(0, 0, -0.45)	(0.26, 0, 0)	(-0.96, 0, 0)	(0, 0, 0.66)	(0, 0, 0.39)			
	(0, 0.48, 0.2)	(0, -0.48, 0.2)	(-0.07, 0, 0)	(-0.07, 0, 0)	(0, 0.38, -0.26)	(0, -0.38, -0.26)			

Table 3.2
 Numerical Values for calculations of the geometric alterations and optimized geometry variants of the formate ions. This table contains displacements of the final three modes

		Displacement (\AA) (x, y, z)						C		H	
		Mode 4		Mode 5		Mode 6		O_{α}		O_{β}	
Asymm. Variant	(0.04, 0.02, 0)	(0.99, 0.03, 0)	(0.59, 0.01, 0)	(-0.75, -0.05, 0)	(0, -0.07, 0)	(-0.02, 1, 0)					
	(-0.04, 0.05, 0)	(-0.06, -0.07, 0)	(-0.2, 0.08, 0)	(-0.2, -0.08, 0)	(0, 0, 0)	(-0.01, -0.01, 0)					
Optimized	(0, 0.05, 0)	(0, 0.99, 0)	(0, 0.56, 0)	(0, -0.78, 0)	(0, 0, -0.07)	(0, 0, 1)					
	(0, -0.05, 0.06)	(0, -0.05, -0.06)	(0, -0.18, 0.08)	(0, -0.18, -0.08)	(0, 0, 0)	(0, 0, 0)					
Symm. Variant	(0, 0.04, 0)	(0, 0.99, 0)	(0, 0.62, 0)	(0, -0.72, 0)	(0, 0, -0.07)	(0, 0, 1)					
	(0, -0.05, 0.05)	(0, -0.05, -0.05)	(0, -0.21, 0.07)	(0, -0.21, -0.07)	(0, 0.01, -0.01)	(0, -0.01, -0.01)					

Table 3.3

Numerical Values for calculations of the geometric alterations and optimized geometry variants of the formate ions. This table contains the partial charges of all atoms for each geometric arrangement

Partial Charges				
	C	H	O _α	O _β
Asymm. Variant	0.39379	0.03396	-0.71387	-0.71387
Optimized	0.42841	0.00053	-0.71447	-0.71447
Symm. Variant	0.43839	-0.00863	-0.71261	-0.71714

such a way that the tunneling junction is appropriately aligned for maximized electron transfer. Non-endogenous agonists would align with residues in a manner which may place energetically appropriate modes in proximity of the tunneling junction, thus activating the receptor.

3.4 Results

Generation of tunneling spectra is completed through the procedure described in [20, 38], and expressed in Eq. 3.17 within the Appendix. This procedure was adapted from earlier IETS literature[39, 40] and similarly uses arbitrary units for the tunneling intensity. Our spectral procedure was validated by comparison of the spectra of the formate ion, which is prevalent through experimental and theoretical literature in IETS. These arbitrary units are proportional to the conductance enhancement, as well as the enhancement to the Coulombic interaction probability during tunneling. Necessary information for implementing Eq. 3.17 was collected through quantum chemical calculations. Computations were performed using Density Functional theory at 6-311G level of theory; expanded pseudopotential correlation consistent 5-zeta basis was used for large atoms where necessary. DFT was chosen both due to its high accuracy in transition dipole frequencies and to avoid encroaching error associated with dissimilarity between analyte and parameter molecules in semi-empirical methods. Vibrational calculations utilize reduced modal displacements; proportional to the Cartesian displacement through $\sqrt{\mu}$, μ is the mode's reduced mass. Natural bond order calculations yield the partial charges, q_i in Eq 3.17. Scaled Kronecker delta functions are plotted at the absorbance frequency of the mode; these functions were convolved with Gaussian functions possessing a FWHM of 25 cm^{-1} , representing a very narrow thermal distribution. 25cm^{-1} was selected to be conservative and yet allow for peak additions while avoiding over estimations of peak breadth.

An examination of the endogenous agonist, 5-HT, is given in Figure 3.9. The main spectral features are (quantities are in cm^{-1}): the OH stretch at 3700; NH_2 bend at

1700; coherent ring motions appear at both 1500 and 1150; and indole bending at 530. For reasons discussed below, we will focus our discussion on tunneling in the 1500 cm^{-1} region. Working within Turins theory, this implies that these motions assist in the tunneling and that the tunneling source and sink are in proximity to these motions. Docking studies of homology modeled 5-HT_{2A} show that the moieties discussed above are local to F339, F340, S159 and L229 residues [41, 42, 43, 44], meaning that one of these residues assist in the tunneling.

Assessment of vibrational bands for 2A agonists that could be associated with protein activation under Turins vibrational theory is of primary import. Also agonists of a particular protein would share a single IET feature associated with the electron transfer. We selected several known 5-HT_{2A} agonists and generated the IETS for each. LSD, was selected as it possesses a high potential for activation of serotonin receptors within the cortical interneurons[45]. DOI (2,5-dimethoxy-4-Iodo-amphetamine) was selected due to its high selective for the 2A-subtype receptor [46]. The remaining selected molecules are members of the 2C-X (4-X-2,5-dimethoxyphenethylamine) class of psychedelic phenethylamines. All compounds selected are known hallucinogens [47, 48, 49] some first characterized by Alexander Shulgin in the compendia works PiHKAL and TiHKAL[50, 51].

Figure 3.10 shows the IETS of the selected molecules (above the axis). The selection of candidate peaks was performed using a spectral similarity index (SI), similar to that used for comparison of mass spectra [52], over the entire spectra and then over local regions. The SI is calculated by:

$$SI = 1 - \sqrt{\frac{|a_i - b_i|}{N}} \quad (3.22)$$

Where N is a normalization constant (the numerator performed for spectra b); b_i is the value of the spectra being analyzed at discrete location i and a is the spectra being compared against. LSD, as the most potent agonist, was selected as the reference spectra for SI calculations. The SIs associated with each of the IETS are given in Table A.1; the SI is given for the overall spectrum and followed by regional SI's calculated

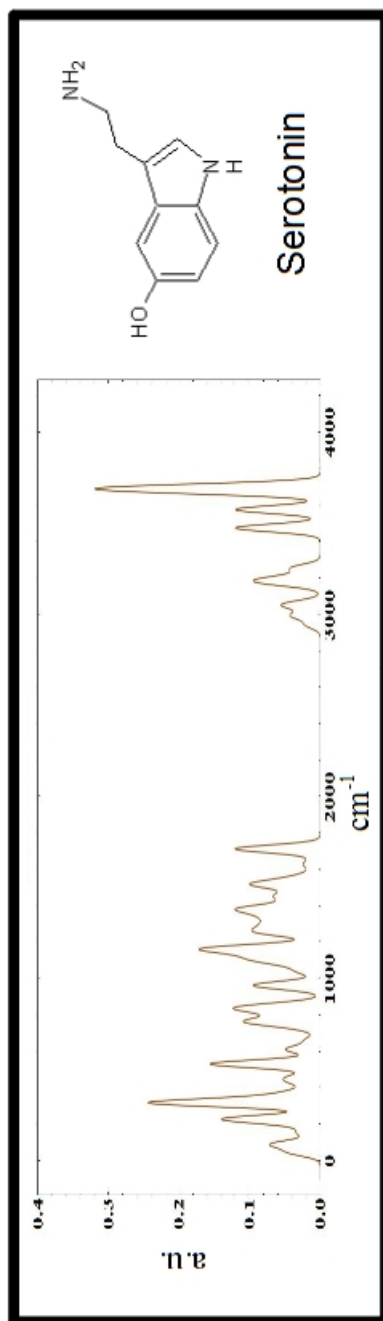


Figure 3.9. IETS of Serotonin to be compared throughout the discussion. Here the abscissa has units of wavenumber and the ordinate has units proportional to tunneling probability; this conversion holds for all following IET Spectrum.

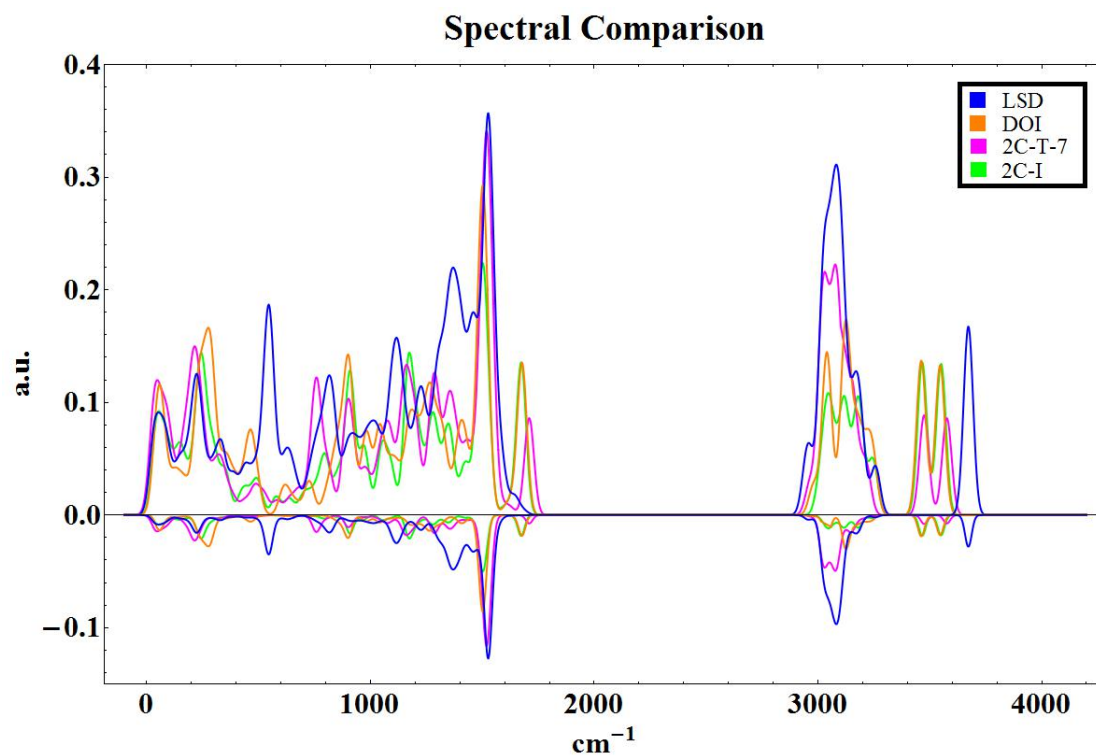


Figure 3.10. The IETS of several known 5-HT_{2A} agonists and the square of the tunneling PDF reflected below the energy axes. The Spectral Similarity index of each plot given in the inlay.

for spans of 1000cm^{-1} with 500cm^{-1} steps, to emphasize the possible region associated with activation the final column shows the SI of each compound for $1500\pm 100\text{cm}^{-1}$. Regions with large ranges of no intensity have SI's inflated by this spectral facet, these regions have been disincluded within the table. When disincluding these regions, the SI for the region spanning $1000\text{-}2000\text{cm}^{-1}$ shows enhanced values, and includes the peak at 1500cm^{-1} . The final column of the table gives the SI for a 100cm^{-1} region about this peak to emphasis this heavily shared spectral feature. As a means of reducing the minor aspects within the tunneling PDF, we choose to square the function to exaggerate those energy ranges which exhibit large tunneling amplitudes within the spectra, shown in Figure 3.10 below the energy axis. Application of the SI to the square of the spectra showed similar results (not shown), yet with the expected enhancement of the SI values. The only universally shared spectral aspect were the peaks at 1500cm^{-1} .

In the next few sections we have selected DOC (2,5-dimethoxy-4-C-amphetamines) as a prototypical molecule for discussion, this selection was based on its fairly tractable number of modes, simple geometry, symmetry and similarities to other agonists. Energy regions associated with an assisted electron transfer would benefit from a large density of vibrational states; implying a greater number of possible states to interact with in this energy range. Figure 3.11 shows both the IETS and scaled density of states for DOC; the spectral feature at 1500cm^{-1} exhibits an enhanced number of vibrational states.

In §3.5 we propose an isotopologue series for DAM-57; the series is of variants are deuterated functional groups altering the character in the 1500cm^{-1} region. We verified that isotopologues of other atoms do not to alter tunneling character in this region. Figure 3.12 shows the isotope effects within several groups of the molecule. Fig. 3.12 a) shows the effects of replacing the oxygens with ^{18}O 's, this results in little alteration near 1500cm^{-1} ; substitution of the halide has similar results, with differences appearing at much lower energies. Fig. 3.12 b) displays the effects of deuterating the hydrogens on the methoxys, this show a large attenuation of the

Table 3.4

Table contains the SI indexes for several 5-HT_{2A} agonists. The procedure was applied to the total spectra, and several sections of 1000 cm^{-1} which march with an overlapping pattern and shifted by 500 cm^{-1} . The region of interest is also performed with a calculated SI for the region of 1500 \pm 100 cm^{-1}

	Spectral Range (cm^{-1})						
	0-4200	0-1000	500-1500	1000-2000	3000-4000	1400-1600	
LSD	1	1	1	1	1	1	
DAM-57	0.89019	0.87090	0.85286	0.87048	0.86997	0.85726	
2C-I	0.81664	0.81792	0.75492	0.76284	0.78236	0.70693	
2C-T-7	0.83977	0.81371	0.77398	0.80550	0.81748	0.79913	
DOI	0.81903	0.80415	0.76196	0.77684	0.78614	0.71396	
Aleph-2	0.83233	0.82218	0.77757	0.79102	0.80063	0.77539	
DMT	0.84620	0.82282	0.78969	0.80327	0.85075	0.75394	
Mescaline	0.82280	0.80003	0.74899	0.77347	0.80797	0.76743	
Quipazine	0.82353	0.80820	0.77809	0.79677	0.77694	0.72653	
Benzylpiperazine	0.82135	0.79383	0.76929	0.79990	0.79270	0.72390	

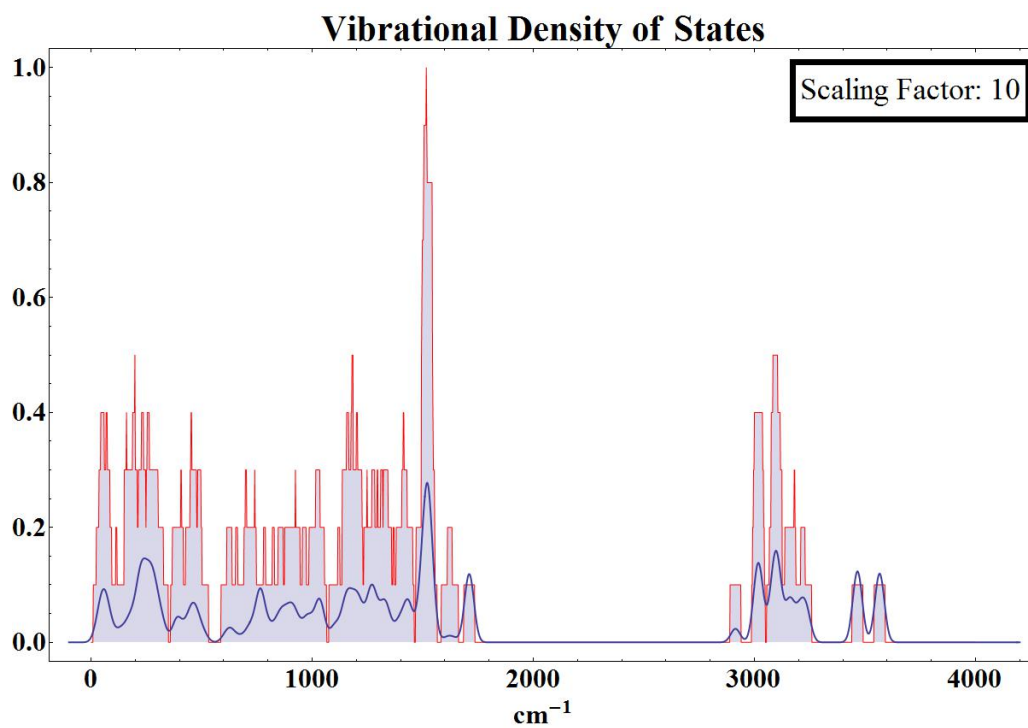


Figure 3.11. The IETS of DOC (Blue) is plotting alongside a scaled, discrete density of states for the vibrational modes of DOC. The scaling factor is given in the inlay. Note the enhanced number of states associated with 1500cm⁻¹ region

tunneling intensity; finally, Fig. 3.12 c) shows the effect of selectively deuterating different functional groups.

The integral of the tunneling probability was taken for $1500 \pm 35\text{cm}^{-1}$ and compared to known EC50 data for compounds shown to activate 5-HT_{2A}. The effective concentrations of several phenethylamines were taken from [53] and compared to the local integrals of the tunneling PDF. This comparison exposes a possible correlation to the inverse of the EC50 data. Results for the 1500cm^{-1} region are shown in Figures 3.13 and 3.14 for the DOI class and 2C-X class molecules computed, respectively. Figures 3.13a and 3.14a give the IETS for each molecule, Fig. 3.13b and 3.14b compare the integral values to the known EC50s.

As tunneling is a highly local process where the interaction potential falls-off as r^{-3} for non-parallel displacements. Modes not local to the electron donor/acceptor sites cannot contribute to the electron transfer responsible for protein activation. Particular modes in 2C-T-2 and in Aleph-2 reside within the thioether (roughly 5 angstrom from the ring system); due to the non-locality of these oscillators, tunneling probability should be examined after removing these contributions from the spectra. Figures 3.13a and 3.14a present the IETS of 2C-T-2 and Aleph-2 both considering and disregarding these contributions; excess contribution to the integral due to these modes shown in orange of Fig. 3.13b and 3.14b. After the correction for non-local motion, the integrals are in fair agreement with the inverse EC50.

3.5 Experiment

Experimental evidence surrounding Turn's theory has been contentious; earlier findings suggest that both the lake whitefish and the American cockroach can identify isotopologues of amino acids and pheromones, respectively [54, 55]. Recent experiments using the common fruit fly present both naive bias to and potential for trained aversion towards isotopologues of acetophenone [56], and reposte [57]. Human testing of the vibrational theory of olfaction has been camped with the recent works show-

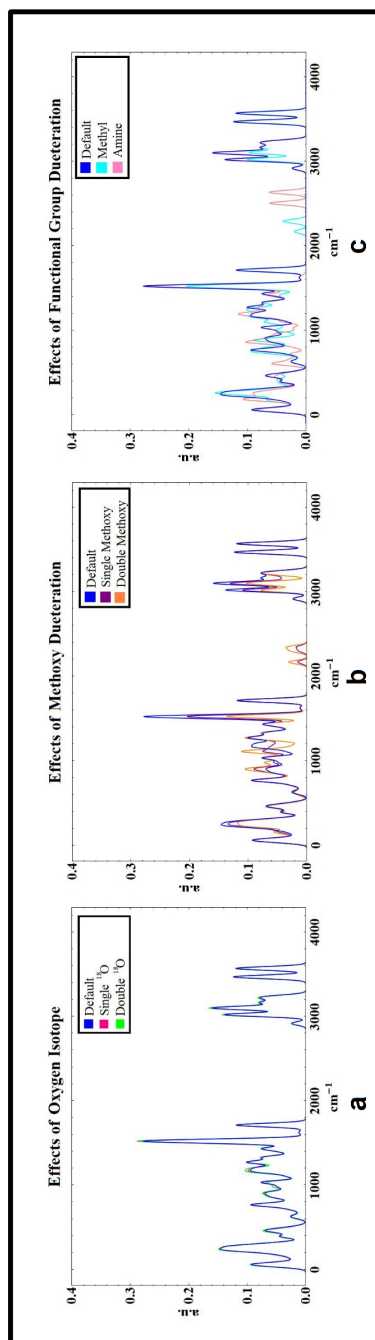


Figure 3.12. Plots of the isotopologues of oxygen with the DOC molecules. The isotope exchanges has no effect on the region in question.

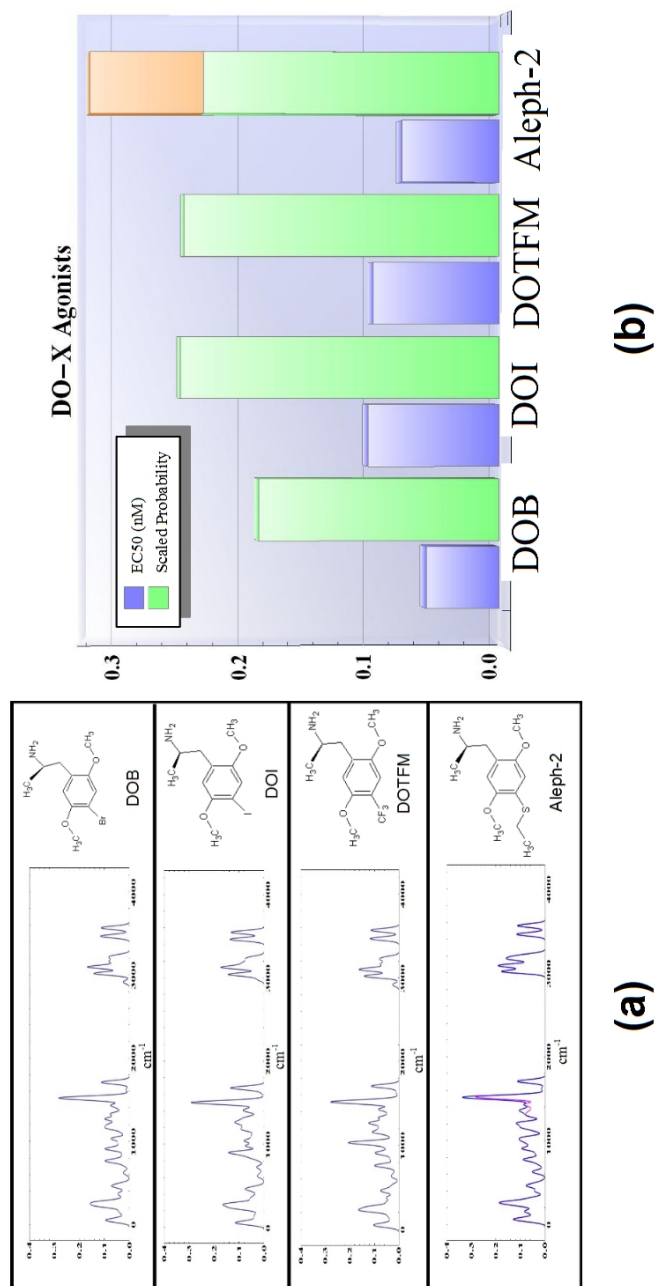


Figure 3.13. (a) The tunneling spectra of several DOX class agonists as well as their structures. (b) The inverse of the median effective concentration for the DOX class agonists plotted against the tunneling probability within the region in question.

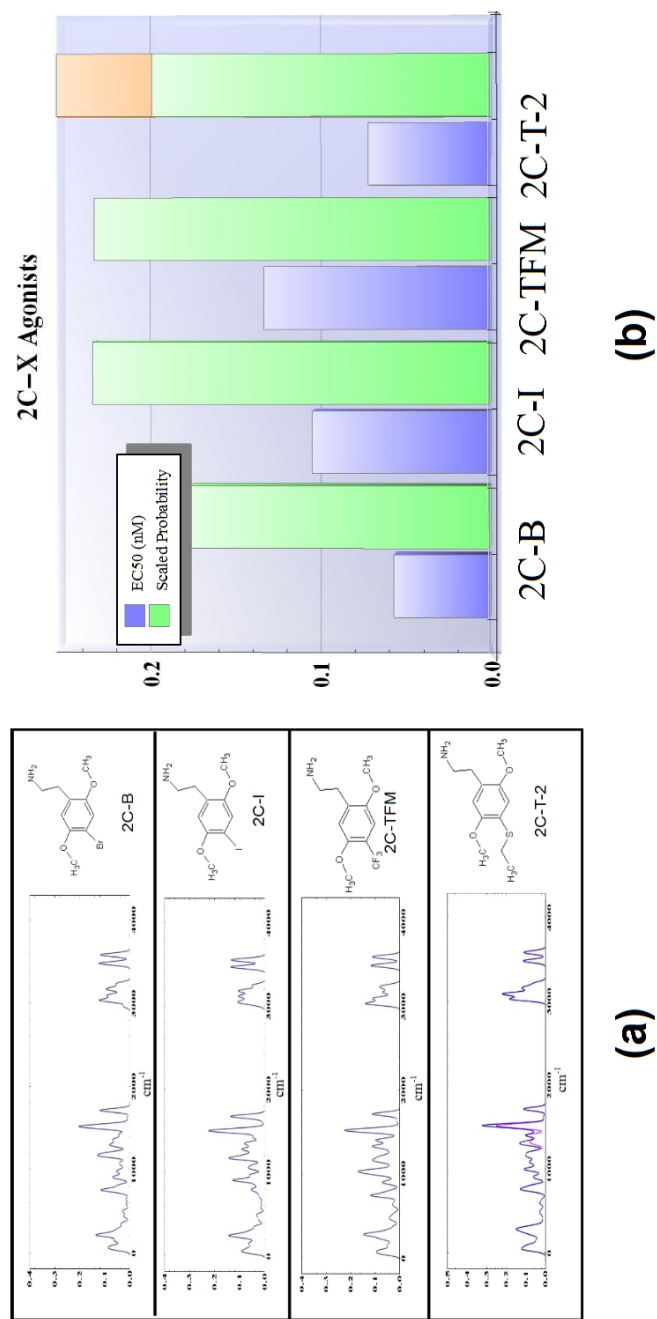


Figure 3.14. (a) The tunneling spectra of several 2C-X class agonists as well as their structures. (b) The inverse of the median effective concentration for the 2C-X class agonists plotted against the tunneling probability within the region in question.

ing that naive human subjects cannot discern between deuterated acetophenone[58]; while another study[59] confirmed the first, while suggesting that human subjects can discern between deuterated variants of musk odorants. This theory has led to works with the intent to possibly identify the characteristic vibrations associated with particular odors[60].

For the benefit of possibly validating this theory we propose a series of isotopologues for the ergine derivative DAM-57 (N,N-dimethyllysergamide). DAM-57 is a mild halucenogen with activity at the 5-HT_{2A} receptor; this implies that the above discussed peak for the 2C-X, DOX and Azapirones families should be the prospective active peak for DAM-57. Any predictability afforded in the following discussion should also analogously apply if one were to perform this experiment with LSD, as it is the diethyl amide analogue of DAM-57. Figure 3.15 shows the tunneling spectra for various isotope labeled DAM-57 variants. Each spectra is accompanied by a molecular structure conveying which of the hydrogen have undergone isotope exchange; the possible energy region responsible for serotonin-class activation is highlighted in yellow.

Using 1500 cm^{-1} as a central point, and recalling the applied FWHM was 25cm^{-1} , the peaks contributing to the tunneling intensity at 1500 cm^{-1} are those modes resonating at $1500 \pm 50\text{ cm}^{-1}$. Modes within that range have motions associated with (in order of contribution): stretching of the amide methyl hydrogen; stretching of the phenyl and indole hydrogens; and bending of the methyl hydrogen of the tertiary amine.

Discussing the series of spectra we will begin with the deuteriation of the three phenyl hydrogens (DAM-57-i); this deuteriation yields a marginal attenuation in the intensity of the 1500 cm^{-1} peak, implying a small overall change in the tunneling probability in this energy regime. DAM-57-ii displays a reduction in the 3700 cm^{-1} region; this peak being caused by the N-H stretch shifts its weight to 2700 cm^{-1} . The deuteriation of the indole amine results in almost no change of character near the active region. Pro-deuteriation of the hydrogen on a single amide methyl (DAM-

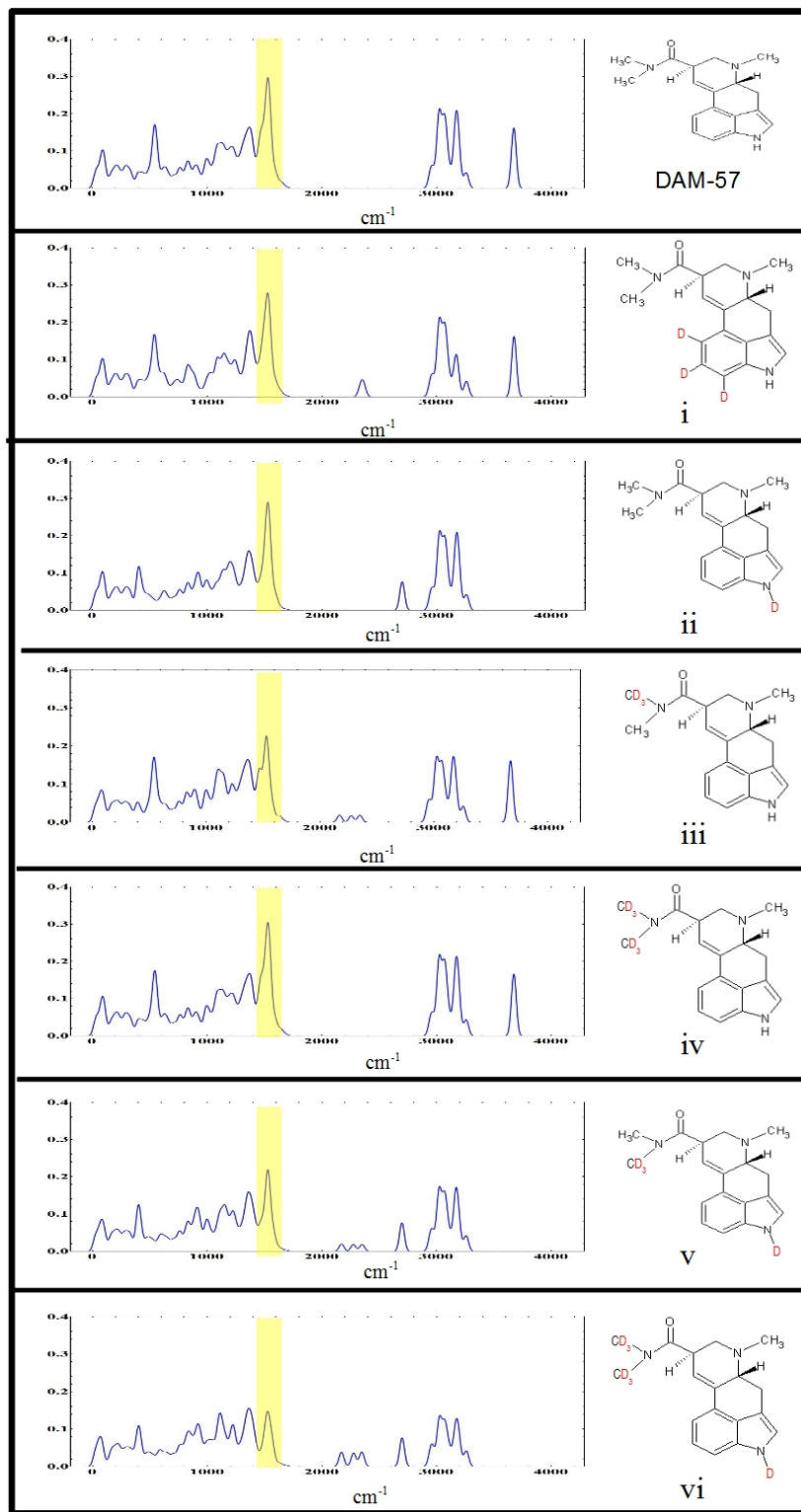


Figure 3.15. IETS of several deuterium-isotopologues of DAM-57. Yellow highlights have been given to the energy region which is assumed to be the active energy region for inelastic tunneling transfer.

57-iii) significantly decreases the tunneling intensity in the 1500 cm^{-1} region. Continued deuteration of the amide system (DAM-57-vi), reduces the peak to roughly one-half the intensity of pro-protium DAM-57. DAM-57-vi and DAM-57-v, moiety co-deuteration scenarios, present very small alterations of the peak intensity when compared to DAM-57-iii and DAM-57-vi

Under Turins vibrational theory, a conclusion which may be drawn from the isotopologues of DAM-57 is that the deuteration of the amide side chains should dampen the activity of the molecule within the CNS. This conclusion is supported by a pair of facts concerning the relative activity between DAM-57 and LSD. The flexible ethyl amide of LSD has been found to be essential to its high activity [37, 61, 36, 62], and that the methyl analogue (DAM-57) is far less potent. Also, the tunneling probability within the 1600 cm^{-1} region is very depleted compared to that of LSD. Utilizing these facts, it could be predicted that further depletion of the tunneling probability within this region should continue to diminish the molecules ability to activate the receptor. The intensity of the tunneling spectra is roughly is more than one-third smaller, and the probability density of tunneling is roughly tenthed this implies an extreme loss of activity associated with deuteration of the amide side-chains.

3.6 Conclusions

The feasibility of tunneling electrons being the mechanism behind the activation of has been the subject of recent works. The mechanism by which the electron interacts with a bound ligand has been proposed as being IETS; for future works in this direction it is important to consider a more complete description of the IETS model including considerations of the angular dependence between the mode and tunneling vector, alterations in the ligand geometry due to docking and the importance of choosing an appropriate interaction potential considering the confines of the activation site. These facets of the full static IETS calculations have been explored here and these authors iterate their importance. Future works should not only consider the

aspects discussed within this paper, as these aspects are mandatory consideration, but could also explore mode coupling of residue chains within the activation site itself or thermal line broadening at biological temperatures.

We have reapplied Turins vibrational theory for activation of olfactory receptors to general GPCRs and have focused on the 5-HT_{1A} and 5-HT_{2A} receptor. We first examined the IETS of a series of isotopologues used within an experiment to validate the vibrational theory of olfaction, and showed possible alterations in the tunneling probabilities which could account for the behaviors observed within the experiment. We initially identified possible characteristic peaks through evaluation of a spectral similarity index of several known potent partial agonists of the 5-HT_{2A} receptor, as data on hydrogen isotopologues for endogenous neurotransmitters are rare. We present a comparison of the rate of tunneling within an energy range, and compare these probabilities to the EC50 data for these compounds with good agreement. A brief discussion of the theoretical implications of the locality of the atomic oscillators to the electron donor-acceptor sites and the density of states of the agonist are provided. We conclude by proposing an experiment comprised of a series of isotopologues which could determine the viability of Turins vibrational theory within the GPCRs of the CNS.

3.7 Acknowledgements

This work is supported by the NSF Centers for Chemical Innovation: Quantum Information for Quantum Chemistry, CHE-1037992

3.8 References

- [1] Juffmann, T.; Arndt, M.; Vedral, V. Quantum physics meets biology. *HFSP J.*, 3:386, 2009.
- [2] Davies, P. C. W. Does quantum mechanics play a non-trivial role in life? *BioSystems*, 78:69-79, 2004.
- [3] Ball, P. The dawn of quantum biology. *NATURE*, 474:272-274, June 2011.
- [4] Huelga, S. F.; Plenio, M. B. Vibrations, quanta and biology. *Contemporary Physics*, 54:181, 2013.
- [5] Heyers, D.; Manns, M.; Luksch, H.; Gntzkn, O.; Mouritsen, H. A visual pathway links brain structures active during magnetic compass orientation in migratory birds. *PLoS ONE*, 2(9):e937, 09 2007.
- [6] Maeda, K.; Henbest, K. B.; Cintolesi, F.; et al. Chemical compass model of avian magnetoreception. *NATURE*, 453:387-U38, May 2008.
- [7] Pauls, J. A.; Zhang, Y. T. ; Berman, G. P. ; Kais, S. Quantum coherence and entanglement in the avian compass. *Phys. Rev. E*, 87:062704, Jun 2013.
- [8] Cai, J. M.; Plenio, M. B. Chemical compass model for avian magnetoreception as a quantum coherent device. *PRL*, 111:230503, 2013.
- [9] McFadden, J.;. *Quantum Biology*. Norton Publishing, 2001.
- [10] McFadden, J.; Al-Khalili, J. A quantum mechanical model of adaptive mutations. *BioSystems*, 50:203-211, 1999.
- [11] Remacle, R.; Kravchenko-Balasha, N.; Levitzki, A.; Levine, R. D. Information-theoretic analysis of phenotype changes in early stages of carcinogenesis. *PNAS*, 107:10324-9, 2010.
- [12] Graeber, T.G.; Heath, J. R.; Skaggs, B. J. ; Phelps, M. E.; Remacle, R.; Levine, R. D. Maximal entropy inference of oncogenicity from phosphorylation signaling. *PNAS*, 107:6112-7, 2010.
- [13] Fleming, G. R.; Huelga, S. F.; Plenio, M. B. Focus on quantum effects and noise in biomolecules. *New Journal of Physics*, 13(11): 115002, 2011. URL <http://stacks.iop.org/1367-2630/13/i=11/a=115002>.
- [14] Kais, S. Entanglement, electron correlation, and density matrices. *Advances in Chemical Physics*, 134:493-535, 2007.
- [15] Yeh, S.-H.; Zhu, J.; Kais, S. Population and coherence dynamics in light harvesting complex ii (lh2). *J. Chem. Phys.*, 137:084110, Aug 2012.
- [16] Sarovar, M.; Ishizaki, A.; Fleming, G. R.; et al. Quantum entanglement in photosynthetic light-harvesting complexes. *NATURE PHYSICS*, 6:462467, Jun 2010.
- [17] Zhu, J.; Kais, S.; Aspuru-Guzik, A.; et al. Multipartite quantum entanglement evolution in photosynthetic complexes. *J. Chem. Phys.*, 137:074112, Aug 2012.

- [18] Tejero, I.;Gonzalez-Garcia, N.; Gonzlez-Lafont, A.; Lluch, J. M. Tunneling in green tea: understanding the antioxidant activity of catechol-containing compounds. a variational transition-state theory study. *Journal of the American Chemical Society*, 129(18):5846-5854, 2007.
- [19] Gao, J.; Karplus, M.; Garcia-Viloca, M.; Truhlar, D. G. How enzymes work: analysis by modern rate theory and computer simulations. *Science*, 303:186-195, 2004.
- [20] TURIN, L. A method for the calculation of odor character from molecular structure. *Journal of Theoretical Biology*, 216(3):367-385, 2002. ISSN 0022-5193.
- [21] Patel, A. Why genetic information processing could have a quantum basis. *J. Biosci.*, 26: 145-151, 2001.
- [22] Christopoulos, A. Allosteric binding sites on cell surface receptors: novel targets for drug discovery. *Nat. Rev. Drug Discov.*, 1: 198-210, 2002.
- [23] Fischer, E. Einuess der con_guration auf die Wirkung der Enzyme. *Ber. Dt. Chem. Ges.*, 27 : 2985 – 2993, 1894.
- [24] Koshland, D. E. Application of a theory of enzyme specificity to protein synthesis. *Proc. Natl. Acad. Sci.*, 44:98-104, 1958.
- [25] Dyson, G. M. Some aspects of the vibration theory of odor. *Perfumery and Essential Oil Record*, 19:456-459, 1928.
- [26] Wright, R. H. Odor and molecular vibration: Neural coding of olfactory information. *Journal of Theoretical Biology*, 64(3):473-502, 1977. ISSN 0022-5193.
- [27] Wright, R. H. Molecular vibration and odour blending. *Chemical Senses*, 8:103-106, 1983.
- [28] Wright, R. H. Odor and molecular vibration: optical isomers. *Chemical Senses*, 3(1):35-37, 1978.
- [29] Turin, L. A spectroscopic mechanism for primary olfactory reception. *Chemical Senses*, 21(6):773-791, 1996. doi:10.1093/chemse/21.6.773.
- [30] Turin, L.; Yoshii, F. *Handbook of Olfaction and Gustation*. Marcel Dekker, Inc., 2003.
- [31] Brookes, J. C.; Hartoutsiou, F.; Horsfield, A. P. ; Stoneham, A. M.; Could humans recognize odor by phonon assisted tunneling? *Phys. Rev. Lett.*, 98:038101, Jan 2007.
- [32] Solovyov, I. A.; Changwb, P.-Y.; Schulten, K. Vibrationally assisted electron transfer mechanism of olfaction: myth or reality? *Phys. Chem. Chem. Phys.*, 14:13861-13871, Oct 2012.
- [33] Takane S.-Y.; Mitchell, J. B. O. A structure-odour relationship study using eva descriptors and hierarchical clustering. *Org. Biolol. Chem.*, 2:3250-3255, 2004.
- [34] Buck, L.; Alex, R. A novel multigene family may encode odorant receptors: a molecular basis for odor recognition. *Cell*, 65:175-187, 1991.

- [35] Urban, J. D.; Clarke, W. P.; Zastrow, M. V.; et al. Functional selectivity and classical concepts of quantitative pharmacology. *Journal of Pharmacology and Experimental Therapeutics*, 320(1):1-13, 2007.
- [36] Nichols, D. E. Hallucinogens. *Pharmacology Therapeutics*, 101(2):131-181, 2004. ISSN 0163-7258.
- [37] Nichols, D. E.; Nichols, C. D. Serotonin receptors. *Chem. Rev.*, 108:1614-1641, 2008.
- [38] Sleight, A. K.; Phillips, W. A.; Adkins, C. J.; Taylor, M. E. A quantitative analysis of the inelastic electron tunnelling spectrum of the formate ion. *Journal of Physics C: Solid State Physics*, 19(33):6645, 1986.
- [39] Phillips, W. A.; Adkins, C. J. A theory for the intensities of inelastic electron-tunnelling spectra. *Philosophical Magazine Part B*, 52(3): 739-750, 1985.
- [40] Kirtley, J.; Scalapino, D. J.; Hansma, P. K. Theory of vibrational mode intensities in inelastic electron tunneling spectroscopy. *Phys. Rev. B*, 14:3177-3184, Oct 1976.
- [41] Braden, M. R.; Nichols, D. E. Assessment of the roles of serines 5.43(239) and 5.46(242) for binding and potency of agonist ligands at the human serotonin 5-HT_{2A} receptor. *MOLECULAR PHARMACOLOGY*, 72:1200-1209, 2007.
- [42] Choudhary, M. S.; Scahs, N.; Uluer, A.; et al. Differential ergoline and ergopeptide binding to 5-hydroxytryptamine_{2A} receptors: Ergolines require an aromatic residue at position 340 for high affinity binding. *MOLECULAR PHARMACOLOGY*, 47:450-457, 1995.
- [43] Braden, M. R.; Parrish, J. C.; Naylor, J. C.; Nichols, D. E. Molecular interaction of serotonin 5-HT_{2A} receptor residues phe339 and phe340 with superpotent n-benzyl phenethylamine agonists. *MOLECULAR PHARMACOLOGY*, 70:1956-1964, 2006.
- [44] Chambers, J. J.; Nichols, D. E. A homology-based model of the human 5-HT_{2A} receptor derived from an in silico activated G-protein coupled receptor. *Journal of Computer-Aided Molecular Design*, 16:511-520, 2002.
- [45] Marek, G. J.; Aghajanian, G. K. LSD and the phenethylamine hallucinogen DOI are potent partial agonists at 5-HT_{2A} receptors on interneurons in rat piriform cortex. *JPET*, 278(3):1373-1382, 1996.
- [46] Knight, A. R.; Misra, A.; Quirk, K.; Benwell, K.; Revell, D.; Kennett, G.; Bickerdike, M. Pharmacological characterisation of the agonist radioligand binding site of 5-HT_{2A}, 5-HT_{2B} and 5-HT_{2C} receptors. *Naunyn-Schmiedeberg's Arch Pharmacol*, 370:114-123, 2004.
- [47] Delliou, D. 4-bromo-2,5-dimethoxyamphetamine: Psychoactivity, toxic effects and analytical methods. *Forensic Science International*. 21:259-267, 1983
- [48] Maurer, H. H. Chemistry, pharmacology, and metabolism of emerging drugs of abuse. *Ther. Drug. Monit.*, 32:544-549, Oct 2010.
- [49] Iez-Maeso, J. G.; Weisstaub, N. V.; Zhou, M.; et al. Hallucinogens recruit specific cortical 5-HT_{2A} receptor-mediated signaling pathways to affect behavior. *Neuron*, 52:439-452, Feb 2007.

- [50] Shulgin, A.; Shulgin, A. PiHKAL: A Chemical Love Story. Transform Press, 1991.
- [51] Shulgin, A.; Shulgin, A. TiHKAL: The Continuation. Transform Press, 1997.
- [52] Wan, K. X.; Vidavsky, I.; Gross, M. L. Comparing similar spectra: From similarity index to spectral contrast angle. *J Am Soc Mass Spectrom*, 13:85-88, 2002.
- [53] Braden, M. R. Towards a biophysical understanding of hallucinogen action. Thesis Purdue University, 2007.
- [54] Hara, J. Olfactory discrimination between glycine and deuterated glycine by fish. *Experientia*, 33:6189, 1977.
- [55] Havens, B. R.; Melone, C. D. The application of deuterated sex pheromone mimics of the american cockroach (*periplaneta americana*, l.), to the study of wright's vibrational theory of olfaction. *Dev. Food. Sci.*, 37:497-524, 1995.
- [56] Franco, M. I.; Turin, L.; Merzhinov, A.; Skoulakis, E. M. C. Molecular vibration-sensing component in *drosophila melanogaster* olfaction. *PNAS*, 2011.
- [57] Hettinger, T. P. Olfaction is a chemical sense, not a spectral sense. *PNAS*, 108(31):E349, 2011.
- [58] Keller, A.; Vosshall, L. B. A psychophysical test of the vibration theory of olfaction. *NATURE NEUROSCIENCE*, 7, 2004.
- [59] Gane, S.; Georganakis, D.; Maniati, K.; Vamvakias, M.; Ragoussis, N; Skoulakis, E. M. C.; Turin, L. Molecular vibration-sensing component in human olfaction. *PLO ONE*, 8:e55780, Jan 2013.
- [60] Haffenden, L. J. W.; Yaylayan, V. A.; Fortin, J. Investigation of vibrational theory of olfaction with various labelled benzaldehydes. *Food Chem.*, 73:67-72, 2001.
- [61] Kanagarajadurai, K.; Malini, M.; Bhattacharya, A.; Panicker, M. M.; Sowdhamini, R. Molecular modeling and docking studies of human 5-hydroxytryptamine 2a (5-ht2a) receptor for the identification of hotspots for ligand binding. *Mol. BioSyst.*, 5 : 1877 – 1888, 2009.
- [62] Bayar, S.; Saglam, S.; Ustundag, H. F. Experimental and theoretical studies of the vibrational spectrum of 5-hydroxytryptamine. *Journal of Molecular Structure: THEOCHEM*, 726:225-232, 2005. ISSN 0166-1280.
- [63] Lambe, J.; Jaklevic, R. C. Molecular vibration spectra by inelastic electron tunneling. *Phys. Rev.*, 165(3):821-832, 1968
- [64] Hipps, K. W.; Mazur, U. Inelastic Electron Tunneling Spectroscopy. *Handbook of Vibrational Spectroscopy*. Wiley, 2001
- [65] Lambe, J.; McCarthy, S. L. Light emission from inelastic electron tunneling. *Phys. Rev. Lett.*, 30(14):923-925, 1976
- [66] Sleight, A. K.; Taylor, M. E.; Adkins, C. J.; Phillips, W. A. Top-electrode and roughening effects in electron tunnelling spectroscopy. *Journal of Physics: Condensed Matter*, 1(6):1107, 1989

- [67] Adkins, C. J.; Phillips W. A. Inelastic electron tunnelling spectroscopy. *Journal of Physics C: Solid State Physics*, 18(7):1313, 1985.
- [68] Kirtley, J.; Hall, J. T. Theory of intensities in inelastic-electron tunneling spectroscopy orientation of adsorbed molecules. *Phys. Rev. B*, 22:848-856, Jul 1980.
- [69] Kirtley, J.; and Soven, P.; Multiple-scattering theory of intensities in inelastic electron tunneling spectroscopy. *Phys. Rev. B*, 19:1812-1817, Feb 1979.

4. TEACHING QUANTUM MECHANICS THROUGH QUANTUM GAMES

4.1 Introduction

Classical Mechanics whose approach was developed based on Newtons new mathematics was contemporaneously formulated alongside calculus. Both topics moved from academic investigation into high school classrooms, and in the case of Newtonian Mechanics earlier still. Quantum mechanics, developed in the twentieth century, was required to adequately describe such experimental phenomena as black-body radiation, the photoelectric effect, and the atomic spectrum of hydrogen. The development of quantum mechanics has led to description of phenomena such as the superposition principle, the ability of an unobserved quantum object to exist in a superposition of multiple states simultaneously; entanglement, spooky action at a distance where the state of one system affects that of another without a direct observable relationship connecting them; and interference, as matter exists in both particle and wave form within quantum theory matter interactions present wave phenomenon such as diffraction and the properties of constructive and destructive matter-wave addition. Just as a rudimentary understanding, at minimum, of classical mechanics became necessary for so many fields, an introduction into the concepts of quantum mechanics is of growing importance.

A students first excursion into quantum mechanics can be both overwhelming and daunting, even to an upper division science student. Understanding such concepts as wave functions, overlap integrals and probability amplitudes are vital in mastering the subsequent material within the course. A typical first semester course in quantum mechanics focuses on the Schrdinger Picture and Equation[1, 2, 3]. Herein we present an outline covering several exercises using QTTT, presented by Allen Goff[4, 5, 6], as

a means of introducing and enforcing early topics in an introductory quantum mechanics course. The exercises presented here allow for introduction and discussion of: probability amplitude, probability density, normalization, overlap, the inner product, and separability of states. It is the belief of the authors that QTTT can be used as an approachable, fun and intuitive means of introducing these topics. It is the hope of the authors that this tool could act as a companion throughout instruction; after the students have been taught the game, the instructor can use it as a stepping stone to new topics and as an avenue for intuitive exercises.

The exercise enclosed, as well as other similar exercises, have been used to assist the understanding of various audiences in anything from a brief understanding of concepts necessary to quantum computing to furthering a students understanding of topics in their quantum mechanics classroom. Much of this material was used to introduce high school science teachers to topics contained within a seminar the authors had given in quantum computing technology. The bulk of the material was used as supplemental material and assignments in an undergraduate quantum mechanics classroom to great avail with students who did not grasp some early concepts within the course.

Furthermore, computational chemistry methods are of vital importance in areas such as materials science and drug design due to their predictive capacities, which may aid researchers in the prevention of generating failed targets. During the advent of quantum mechanics two schools of thought began to emerge: the Schrodinger Picture and the Heisenberg Picture[7]. The numerical results and physical significance taken from these schools are the same, they differ in where the time-dependency is exhibited (operators vs states). From the Heisenberg picture, Born and Heisenberg generated the matrix methods that are prevalent in modern computation chemistry[8, 9]; methods such as: Hartree-Fock method, Density Functional Theory, and Configuration Interaction methods.

Discussion of basis-set methods is something that is normally avoided in undergraduate level courses. This paper provides discussion and exercises by which topics

in matrix methods can be approached in undergraduate level courses or as an early assessment or introduction to computational methods in a graduate level course. This paper is the second in a series[10]; for an introduction to the game, please see these papers[10, 4, 5, 6].

We also briefly discuss density matrices so that we may introduce entanglement and concurrence to the students. We have chosen to introduce entanglement as it has proved to be a vital element in the future studies of quantum computing[11, 12] and quantum biology[13, 14].

4.2 Physical Concepts and Game Play

4.2.1 Board

The CTTT board is square and is divided into nine square subspaces. These subspaces will be referred to as principal squares and will each carry a number to denote the particular square being referenced. The numbering pattern of the principal squares on the board is shown in Figure 4.1. Prior to discussing the game play, some vocabulary and concepts should be introduced. The following four elements are underlying physical concepts that are necessary for game play and thus their use is weaved within the description of the game.

- "Spooky Marker" : Named after Einsteins reference to entanglement and hidden variable interactions as spooky action at a distance [15]. This is a direct consequence to the system being completely described through a finite number of basis functions of an observable. A coupled pair of electrons exist within a 0-spin state; that is to say that the wavefunction of the pair is of the form: $\psi = \frac{1}{\sqrt{2}} (|\uparrow\downarrow\rangle + |\downarrow\uparrow\rangle)$. If one observes the state of a single electron within the pair, well say its in the up-state, that observer incidentally knows the state of the other spin within the pair. Like CTTT markers, the Spooky Marker represents a single move of a single

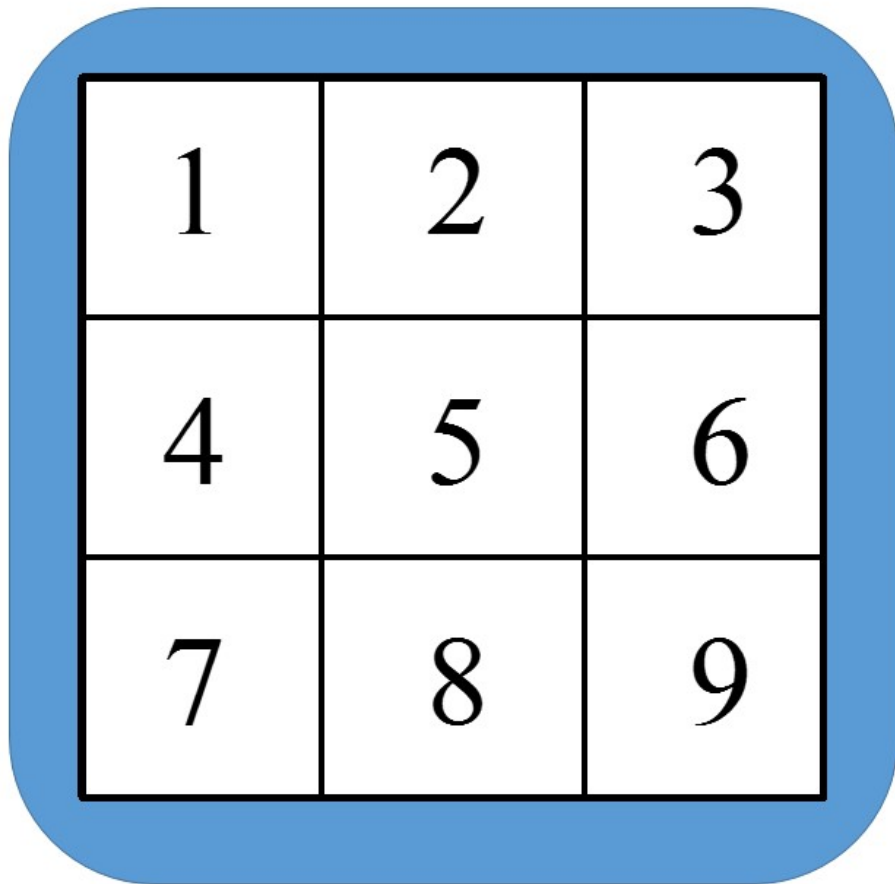


Figure 4.1. The layout of the game board for either classical or quantum Tic-Tac-Toe. This figure also displays the enumeration scheme that is used throughout this paper.

player during one turn, yet a Spooky Marker exists within two separate principal squares simultaneously.

- "Superposition" : As players have placed a pair of Spooky Markers that represents their move for that turn, this move can be said to exist as a superposition of the states (board positions) in which it may exist. This harkens back to the concept of the Bloch sphere, Fig 4.2, in which a given spin may exist within the up-spin state or the down-spin state as well as any state generated by a weighted linearly combination of these two. If Alice places Spooky Markers for her first move into Squares 1 and 5, then the state of that move is the superposition of the two states: Square 1 and Square 5. All player moves within QTTT are superposition moves. A typical teaching example of this is the superposition of spins separated through observation in the Stern-Gerlach[16, 17, 18] experiments, which are typically discussed in introductory quantum mechanics courses. A further example, to which the students may have already been exposed, is the superposition of ammonia states by tunneling; the students may have discussed this already in their organic chemistry course with reference to nitrogen inversions[19] and the topic can be expounded through a discussion of the MASER problem[20].
- "Cyclic Entanglement" : Entanglement is the correlation between parts of a system - induced through an interaction and maintained in separation - which is independent of factors such as position and momentum[21]. In QTTT this would consist of a group of Spooky Markers whose board positions are all self-referencing; as an example: Alices first move (X_1) exists in both Squares 1 and Square 5; Bobs first move (O_2) exists both within Square 5 and Square 7; and Alices second move (X_3) is within both Square 7 and Square 1. In this way the possible states of these moves are dependent upon each other in a similar fashion as to the spin states of paired electrons. The cyclic reference here is that X_1 shares Principal Square 1 with X_3 , X_3 shares principal square 7 with O_2 and finally O_2 shares principal

square 5 with X_1 ; this can be represented by: $X_1 \xrightarrow{1} X_3 \xrightarrow{7} O_2 \xrightarrow{5} X_1$. This series of moves is shown in Figure 4.3 and will be made clearer in the sample game.

- "State Collapse" : A quantum system may exist in a superposition of several states. Only one subordinate state is observed when the state of the system is measured. An example of this would be a doublet spin system; the state of the single electron would be a superposition of up-spin and down-spin yet when observed a single electron will present only either an up-spin or a down-spin state. When a state collapse occurs through observation within the game Spooky Markers collapse into CTTT marks.

4.2.2 General Structure of the Game

The general structure of the game is similar to that of CTTT. The few caveats and expansions to the rules can be most easily fleshed-out through an example game. Game play begins as Alice places her first pair of Spooky Markers on the board; any such move within the game will be denoted by $|\psi_i^\eta\rangle_j$, where η represents the player to whom the marker belongs and will thus take on the values X or O, i denotes the turn when this marker was placed and j is the location on the board where the marker was placed. She places her markers in principal squares 1 and 5. This means that her first move, $|\psi_1^X\rangle$, is a super position with the form: $|\psi_1^X\rangle = \frac{1}{\sqrt{2}} (|\varphi_1^X\rangle_1 + |\varphi_1^X\rangle_5)$. Let us now have Bob place his markers in principal squares 5 and 7; unlike the classical tic-tac-toe game, the placement of a Spooky Marker in QTTT does not prevent either player from placing subsequent markers in a particular square. Alice retorts with markers in principal squares 7 and 1. With this last move our game board is now consistent with that in Figure 4.3. It can now be seen that the state of each of the Spooky Markers is a linear combination of the two squares that it occupies and each position within this linear combination is a position within a linear combination describing another Spooky Marker. In Figure 4.3 it can now be seen that we have generated a Cyclic Entanglement between markers placed for ψ_1^X , ψ_2^O and ψ_3^X through their possible states (Squares 1, 5 and 7).

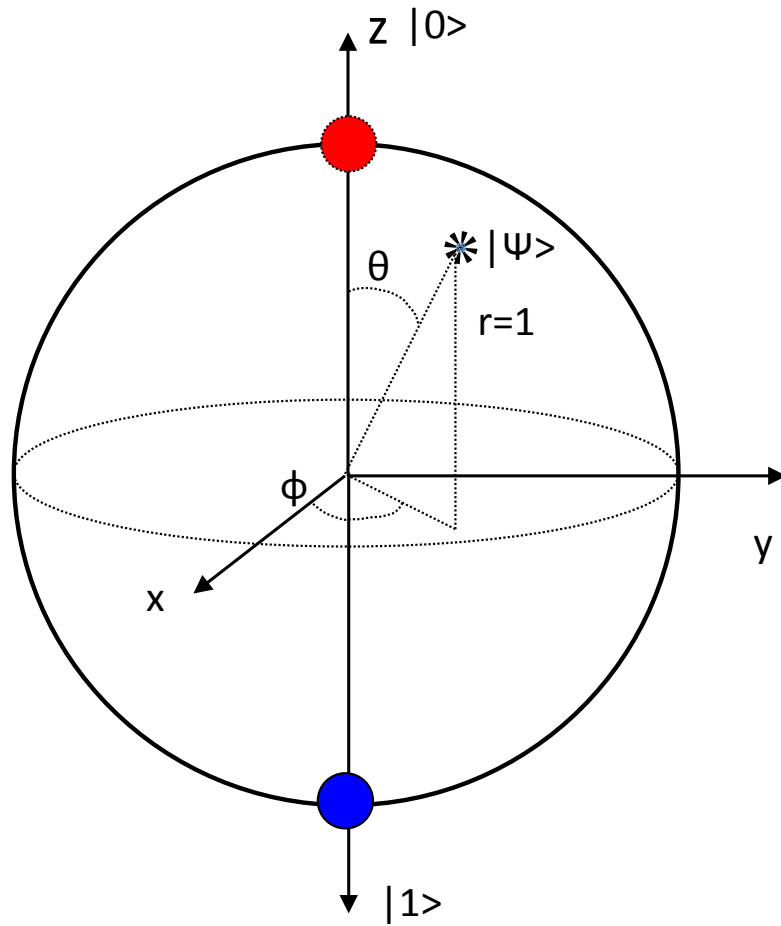


Figure 4.2. The Bloch Sphere represented pictographically. Where a spin can be described through a superposition, linear-combination, of the two observable states Spin-up and Spin-down.

As a cyclic entanglement has been generated it is time for a player to make an observation on the system that will cause a state collapse of our Spooky Markers into Classical Markers. As Alice's last move was that which sealed the cyclic entanglement it will be Bob's right to decide in which way the states will collapse; this reciprocation of closure and observation was developed in hope to generate a fair game, although it was an ad hoc rule implemented for the sake of fair game play (a more quantum mechanically accurate rule would be flipping a coin to decide the collapse). When an observation is made on the system the states of the markers involved with the cyclic entanglement will collapse. Unlike a Spooky Marker, when a Classical Marker occupies a board position no other marker (neither classical nor quantum) may occupy that position.

The two possible pathways that an observation could take are also shown in Figure 4.3. We will first state completely the logic of the upper path and then that of the lower path. If Bob chooses that Alice's most recent move, $|\psi_3^X\rangle = \frac{1}{\sqrt{2}} (|\psi_3^X\rangle_1 + |\psi_3^X\rangle_7)$, should be observed in Square 7 this would imply that the only state that $|\psi_2^O\rangle = \frac{1}{\sqrt{2}} (|\psi_2^O\rangle_5 + |\psi_2^O\rangle_7)$ could take is that of Square 5 and thus the only state $|\psi_1^X\rangle = \frac{1}{\sqrt{2}} (|\psi_1^X\rangle_1 + |\psi_1^X\rangle_5)$ can manifest is that of Square 1; all this due to the fact that this observation turns these Spooky Markers into Classical Markers and thus exclusively occupy their site.

If Bob had chosen the other path, ψ_3^X would collapse in Square 1 forcing ψ_1^X in Square 1 and finally ψ_2^O in Square 5. The lower board is that which would occur if Bob chose to observe ψ_3^X in Square 1. It should also be noted that if a situation arises consistent with Figure 4.4 there exist a pair (or more) of Spooky Markers that are entangled with the cycle without both of its states being enveloped by the cycle. In these cases the observation will also effect a collapse upon the "dangling" marker; the subsequent collapse of dangling markers can also be seen in Figure 4.4.

Game play will continue in this manner until one of the players has generated a three-in-a-row consisting of only Classical Markers. It is possible that two players will simultaneously win the game through the same observation. When this occurs the

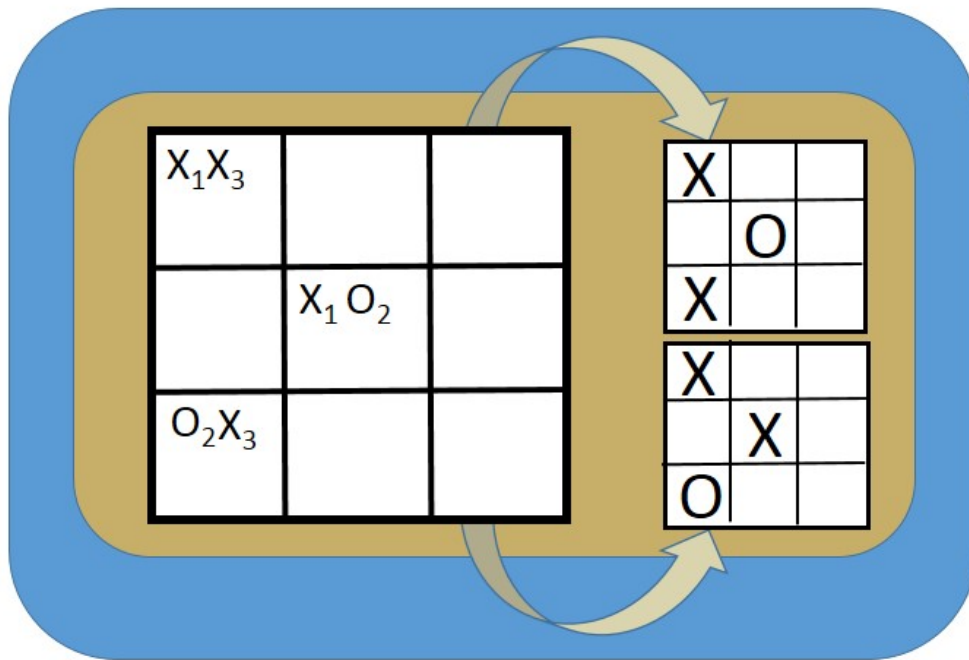


Figure 4.3. The effect of measurement on the system of cyclic entanglement can yield, at minimum, a pair of classical states corresponding to the state in which X_3 was observed.

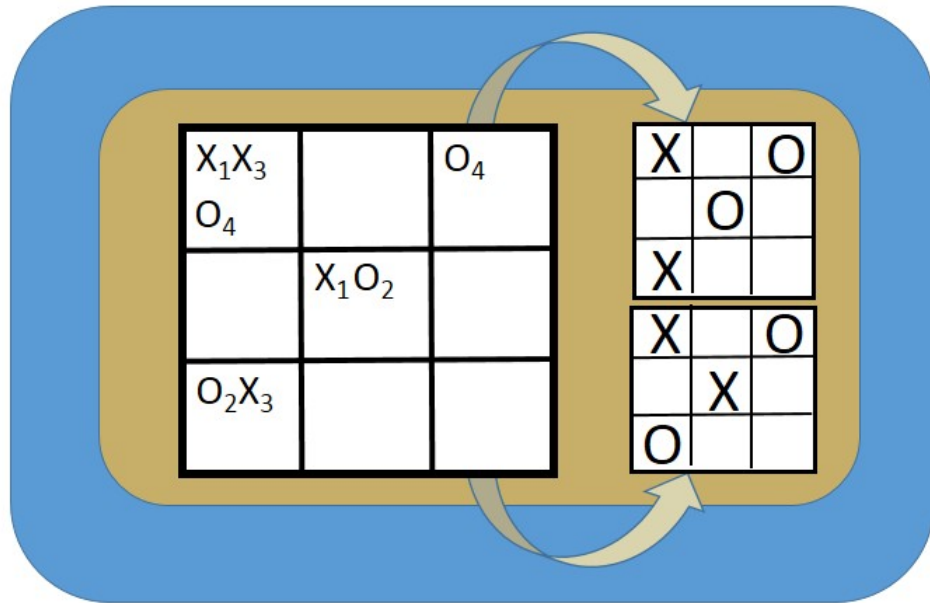


Figure 4.4. The measurement on a specific board can have observable ramifications even for game pieces that are not members of the cyclic entanglement; these pieces are referred to as dangling markers.

player with the most recent Spooky Makers generating one of their winning Classical Markers, loses; which is, in a way, to say first in, first out. When playing a volley of games Goff does propose that the winning player during a simultaneous victory be awarded 1 point and the loser $\frac{1}{2}$ point.

4.2.3 Exercises

We present the following work as an instructor-guided inquiry exercise[22, 23] as if the classroom was broken-up into groups of two students per group. We present specific board examples as a means of discussion and instructional guidance examples, as introductory courses have been shown to benefit from strong instructor guidance[24]. A more natural exercise would be allowing the students (post-instruction on the rules and teaching a specific phenomenon) to play the game and come across these phenomenon on their own in an inductive learning style similar to a lab exercise[25, 26, 27, 28]. QTTT could also be used as a continuing-themed homework exercise as it can be used to exemplify many of the introductory topics in quantum mechanics.

It was found that introducing the game rules and running a small example game can take up to 15 minutes, whereas the average time to play a single game is roughly 4 minutes. In the experience of these authors, the use of quantum tic-tac-toe lowers the level of fear associated with introducing these early concepts, as it both builds student confidence and gives them a foothold on the material through a familiar mechanic. Students took to the game enthusiastically, and divorced of the quantum mechanical concepts learning the game rules comes quickly. The most difficult part in learning the game is recognizing the closed loops; it is suggested that the instructor select a student to act as a representative for all the students as the class plays against the instructor for a game; this method seems to reveal the present thought processes of the students which can benefit instruction. These authors also found that the notions to be discussed within the following sections of this paper benefitted from

introduction through QTTT as they are, at times, the canaries in the coal mine for student understanding of quantum mechanics.

We will maintain the use of Alice as Player X and Bob as Player O, which is appropriate as the assumed groups are of two players. Player names, Alice and Bob, were purposefully chosen as discussion of pairs entangled particles uses the notation particles A and B; from this notation observers at each end of the system are often referred to as Alice (for A) and Bob (for B)[21].

Herein we will provide a series of example exercises focusing on the matrix methods commonly used within computational chemistry. The exercises presented here are not encompassing, and thus this paper is meant to inspire the instructor to use the tools of CTTT and QTTT in any way applicable to their classroom. Introduction of the game to audience with undergraduate-level of understanding in science has taken roughly 15 minutes; extending this topic to a graduate level course should take less time. The average length of time to play a single game is 4 minutes. Students seem to take to the game enthusiastically. Instruction in the topics below have not been tested using quantum games, unlike those in the previous paper; but benefit to both concept and clarity is expected.

Again, these exercises are intended to be used in inquiry-based, classroom and take-home capacities. These authors have found that assigning these types of problems after a degree of strong instructional guidance and discussion of topics is best[24]. These methods allows the student to explore these new topics after a framework has been laid, which affords an exploration with confidence due to the students pre-existing intuition for several aspects of both CTTT and QTTT. In this manner these exercises are akin to lab exercises in that they exploit elements of inductive learning[25, 26, 27, 28] and guided inquiry[22, 23].

4.3 Probability Amplitude, Sign Symmetry and Probability Density

The fundamental quantity within the Schrödinger picture of quantum mechanics is the wave function, $\Psi(x)$. $\Psi(x)$ are the solutions to the second order differential wave equation describing the total system energy of a particle[29]. The use of either QTTT or CTTT does not lend itself to the introduction of the Schrödinger Equation as there are no intuitive nor appropriate methods for the student to connect game play to energy. Yet use of QTTT has proven beneficial in the explanation and discussion of several properties of the wavefunction, especially topics such as normalization and sign symmetry of the probability amplitude.

Wave functions, as stated by the first postulate of quantum mechanics[1], show how the state of their system evolves in time. The use of Gaussian-type functions in the description of moves lends itself immediately as a means of emphasizing the sign invariance of the probability density. We will begin by defining:

$$g_i^\eta(x, y) = \alpha e^{-\frac{(x-\mu_i^x)^2 + (y-\mu_i^y)^2}{2\alpha^2}} \quad (4.1)$$

Where i denotes the board space in which the Gaussian function resides ($i \in [1, 9]$), α is the normalization constant of the function, η denotes which players move is described by the Gaussian, μ is the full width at half max of the Gaussian function and $x_{[0,i]}$ is the center of the board square i . Defining each board square to be of unit length then: $\mu_i^x \in (0.5, 1.5, 2.5)$; $\mu_i^y \in (0.5, 1.5, 2.5)$; $\sigma = 0.2$; and $\alpha = \frac{1}{\sigma\sqrt{2\pi}}$. In this scheme the center of the 5th board square would be: $(\mu_5^x, \mu_5^y) = (1.5, 1.5)$. By using Gaussian functions to represent the wavefunction describing a players move, we afforded an opportunity to teach the Gaussian integrals that are vital in quantum chemistry[30] while exploiting the ease of the integral forms[31]. Students seem to take to this introduction to the use of Gaussian functions more so than a typical introduction in atomic or molecular calculations. This may be due to the less intimidating or esoteric application.

One could assign to Alice a normalized wave function that is a Gaussian-type function for her pieces with a negative (-) leading sign and to Bob a Gaussian-type

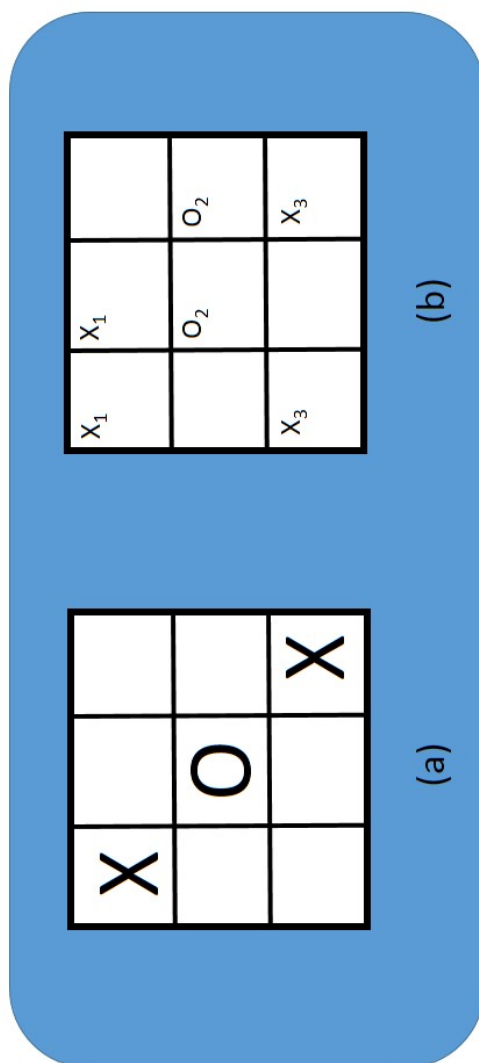


Figure 4.5. Board (a) shows a series of classical markers; by their nature of classical markers any wave function describing one is linearly independent with any other markers wave function. Board (b) shows a series of Spooky Markers. The wave function describing this series of moves reveals that these partials are linearly independent with each other.

wave function with positive (+) leading sign. Beginning a classical game of TTT, allow both Alice and Bob to make their first move. Both players will recognize that the X and O represent game pieces, yet they have opposing signs. This will frame a discussion of the sign invariance of the wave function. During this discussion, these authors have found it appropriate to emphasize that it is the magnitude of the functions displacement from zero that is of significance and draw an analogue to waves in fluids while pointing out that the Laplacian term of the Schrödinger Equation is used to describe fluid waves as well.

As these probability amplitudes can differ in both sign and complexity (real vs. imaginary), it is here that these authors have introduced the magnitude (in fact, the squared magnitude) to the students as the valuable and physically interpretable quantity. As the function is possibly complex, one should remind the student that magnitude of a general complex number is given by: $|z| = \sqrt{z \cdot z^*}$ and that the wave function acts in a similar fashion. We may now introduce the probability density, $|\Psi|^2$, of the system as the physical quantity.

In both the quantum and classical analogues of tic-tac-toe, the system could either be described through a series of single player's moves, $|\psi_i^\eta\rangle$, or the total state of the board, Ψ . In terms of the classical game each move represents a complete particle on the board. These single particles each inhabit a principal square within the board, in this manner any function describing a specific particle would be linearly independent of a function describing another. This example can be seen in Figure 4.5(a); this linearly independent set of moves can be described through the following function for the total state of the board:

$$\Psi = |\psi_1^X\rangle_1 |\psi_2^O\rangle_5 |\psi_3^X\rangle_9 \quad (4.2)$$

Similarly, a Spooky Marker represents a single particle that exists in two different board square simultaneously and the moves seen in Figure 4.5(b) can be described through a total board wave function:

$$\begin{aligned}\Psi &= |\psi_1^X\rangle |\psi_2^O\rangle |\psi_3^X\rangle \\ &= \frac{1}{\sqrt{8}} (|\varphi_1^X\rangle_1 + |\varphi_1^X\rangle_2) (|\varphi_2^O\rangle_5 + |\varphi_2^O\rangle_6) (|\varphi_3^X\rangle_7 + |\varphi_3^X\rangle_9)\end{aligned}\quad (4.3)$$

We reserve explaining the factor of $\frac{1}{\sqrt{8}}$ to the student until later.

Our decision to use Gaussian functions lends itself to instruction of these introductory concepts through CTTT alone; this allows the instructor to choose to reserve the use of QTTT for times when it is more comprehensible to the student and more necessary for the course material. The instructor can choose to show that a classical game piece is representable by a Gaussian function that can be of either sign. Both signs equally represent a particle and lead to a properly signed (+) probability density for the system. At this point it is also at the instructors discretion to employ imaginary exponents in the Gaussian functions to show a properly signed magnitude for the probability density, and proving the need for taking the complex conjugate of the wave function.

4.4 The Inner Product, Normalization and Overlap

Extending the discussions framed within the previous section allows for the introduction of the inner product whose general form is:

$$\langle \Psi(\tilde{\tau}) | \Psi(\tilde{\tau}) \rangle = \int^{\Omega_e} \Psi^*(\tilde{\tau}) \Psi(\tilde{\tau}) d\tilde{\tau}, \quad (4.4)$$

where $\tilde{\tau}$ refers to all coordinates within the function, and Ω_e is the bounds of the space defined by a specific problem. The inner product may be exercised within the confines of the game in ways that exemplify its two early uses: the normalization and the overlap.

Many early students beginning their studies in quantum mechanics find that the first hurdle to their understanding is normalization. We have used this game and

presented methods to successfully introduce this topic to students who are struggling in their undergraduate quantum mechanics course; the authors feel that the student benefits from the initial removal of the concept from atomic and molecular systems. This allows the student to understand the concept intuitively, learn the mathematical statement and then transplant all of this back into quantum mechanics. Starting with the boards expressed in Figure 4.6, we have used a series of exercises to test the students comprehension of normalization.

Students, from experience, recognize that when a classical marker is placed in a square of the game board the marker is completely contained within that space, and does not exist within any other space on the board. In an effort to prove that which the student already knows we can perform the following inner product using the wave function for just the X in Figure 4.6(a):

$$\langle \psi^X(\tilde{\tau}) | \psi^X(\tilde{\tau}) \rangle_{5,5} = \int^{\Omega_e} (g_5(x, y))^* g_5(x, y) dx dy \quad (4.5)$$

The inner product will be evaluated three times for Figure 4.6(a). For the first evaluation of Eq. 4.4 we shall define $\Omega_e = \Omega_{Board}$; in this instance the students intuition that the marker is somewhere within the board is verified through the value of the integral being 1; thus permitting the student to solve for α by following intuition. We can further impress upon the student this point by the reevaluation of Eq. 4.4 with $\Omega_e = \Omega_5$ and then again with $\Omega_e = \Omega_9$. The first of these evaluations again leads the student to accept that the marker is exactly where they think it should be, in square 5. The later of these two exercises merely shows the student that the marker that is not in square 9 is, in fact, not in square 9.

Shifting focus to evaluations of Eq. 4.3 on the board shown in Figure 4.6(a); we can now generate the linear combination, $\psi_1^X = \frac{1}{\sqrt{2}} (|\varphi_1^X\rangle_1 + |\varphi_1^X\rangle_4)$, and describing the state of Spooky Marker in a manner consistent with Eq. 4.3. Reverting to Dirac

notation and the students intuition we can complete the following simplifications and evaluations with $\Omega_e = \Omega_{Board}$:

$$\begin{aligned}
 \langle \psi_1^X | \psi_1^X \rangle &= \frac{1}{\sqrt{4}} (\langle \varphi_1^X |_1 + \langle \varphi_1^X |_4) (|\varphi_1^X \rangle_1 + |\varphi_1^X \rangle_4) \\
 &= \frac{1}{2} (\langle \varphi_1^X | \varphi_1^X \rangle_{1,1} + \langle \varphi_1^X | \varphi_1^X \rangle_{1,4} + \langle \varphi_1^X | \varphi_1^X \rangle_{4,1} + \langle \varphi_1^X | \varphi_1^X \rangle_{4,4}) \quad (4.6) \\
 &= \frac{1}{2} (1 + 0 + 0 + 1) = 1
 \end{aligned}$$

The students by now have recognized that a Spooky Marker has the same weight as a classical marker in the totality of the board. These authors also chose to commit the inner product of the Spooky Marker in Figure 4.6 with $\Omega_e = \Omega_4$, revealing that Square 4 contains half of the Spooky Marker.

In a similar fashion the instructor can impress both the meaning and mechanism of the overlap integral onto the student through exercises definable on game boards. Here, the use of the Spooky Marker in this exercise is highlighted as they are capable of overlapping with other Spooky Markers. The provided board and marker combinations in Figure 4.6 hold the potential for a variety of exercises for the student.

4.5 Hilbert Space and Basis Functions

The matrix formulation is typically avoided in early quantum mechanics courses geared towards undergraduate students[3], where preference is given to the Schrodinger equation due to the *Anschaulichkeit* of the latter (which has historically been the primary positive aspect of this formulation)[7]. Although matrix formulations have been relegated to graduate-level courses, they are extensively used in quantum chemistry methods[30, 1, 2, 32].

We have begun by introducing the game briefly and then we define a clear and finite set of basis vectors spanning the space of the game board. This set can be used as a means of formulating a vector describing any particular move within the game. Noting as a sensible preliminary to further discussion that the basis that spans

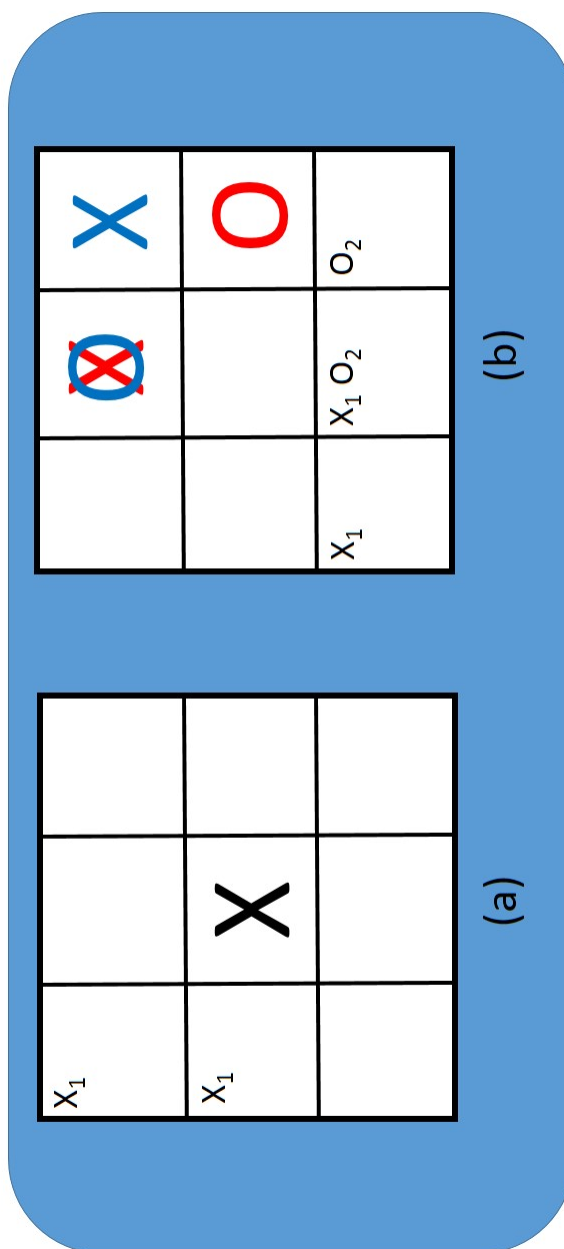


Figure 4.6. Boards that can be used during class exercises. (a) is a board giving a brief pair of exercises that can be used to enforce the concept of normalization as the student integrates the board over each of the markers and then the pair of Spooky Markers. (b) is a board yielding several exercises that can be used as a means of both enforcing the concept of overlap and allow the student to numerically evaluate the overlap integral of Gaussian-type functions.

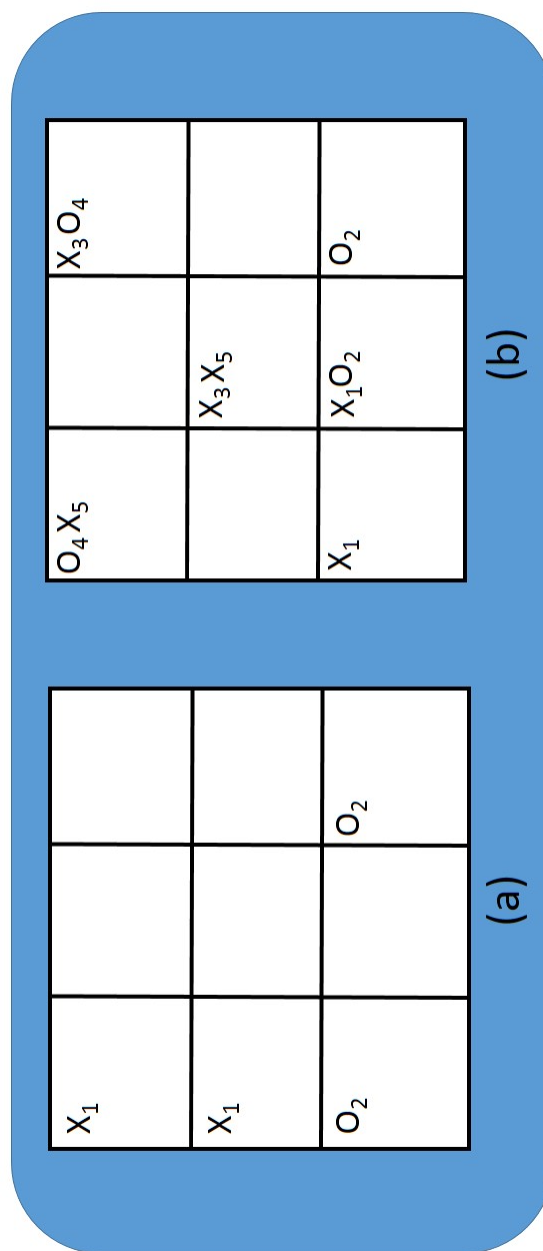


Figure 4.7. Boards displaying several possible exercises. Board A is a brief series of exercises for the expansion of moves in terms of basis functions. Board B yields several possible exercises for the topics of normalization and overlap.

and describes the spaces on board is the set of nine basis vectors conforming to the completeness relation:

$$\sum_i^9 |\varphi_i\rangle \langle \varphi_i| = I_9 \quad (4.7)$$

by noting that $|\varphi_i\rangle$ is the i^{th} dimensional principle Cartesian vector where each dimension in the vector is representative of a principal square on the board. Each player's move can be described as a column vector constructed of weighted basis vectors spanning the totality of possible (finite) states within the board:

$$|\psi\rangle = \sum_{i=1}^9 v_i |\varphi_i\rangle \quad (4.8)$$

In this manner, the move X_1 shown in Figure 4.7(a) can be described in the aforementioned manner and is given by either of the following equivalent statements:

$$\begin{aligned} \psi_1^X &= \frac{1}{\sqrt{2}} \begin{pmatrix} 1 \\ 0 \\ 0 \\ 0 \\ 0 \\ 0 \\ 0 \\ 0 \\ 0 \end{pmatrix} + 0 \begin{pmatrix} 0 \\ 1 \\ 0 \\ 0 \\ 0 \\ 0 \\ 0 \\ 0 \\ 0 \end{pmatrix} + 0 \begin{pmatrix} 0 \\ 0 \\ 1 \\ 0 \\ 0 \\ 0 \\ 0 \\ 0 \\ 0 \end{pmatrix} + \frac{1}{\sqrt{2}} \begin{pmatrix} 0 \\ 0 \\ 0 \\ 1 \\ 0 \\ 0 \\ 0 \\ 0 \\ 0 \end{pmatrix} + 0 \begin{pmatrix} 0 \\ 0 \\ 0 \\ 0 \\ 1 \\ 0 \\ 0 \\ 0 \\ 0 \end{pmatrix} + 0 \begin{pmatrix} 0 \\ 0 \\ 0 \\ 0 \\ 0 \\ 1 \\ 0 \\ 0 \\ 0 \end{pmatrix} + 0 \begin{pmatrix} 0 \\ 0 \\ 0 \\ 0 \\ 0 \\ 0 \\ 1 \\ 0 \\ 0 \end{pmatrix} + 0 \begin{pmatrix} 0 \\ 0 \\ 0 \\ 0 \\ 0 \\ 0 \\ 0 \\ 1 \\ 0 \end{pmatrix} + 0 \begin{pmatrix} 0 \\ 0 \\ 0 \\ 0 \\ 0 \\ 0 \\ 0 \\ 0 \\ 1 \end{pmatrix} \\ &= \frac{1}{\sqrt{2}} s_1 + 0s_2 + 0s_3 + \frac{1}{\sqrt{2}} s_4 + 0s_5 + 0s_6 + 0s_7 + 0s_8 + 0s_9 \end{aligned} \quad (4.9)$$

Noting that the coefficients provide weight to each basis vector we may now represent the probability amplitude of a particle in a board space defined by the basis vector (s_i) .

We can now easily show students the importance of normalization in a method apart from the use of integrals. In this manner the student is exposed to the material

from several vantages (as they have seen the overlap integral method in earlier courses and coursework), this allows the student to achieve a full perspective and decide which picture they find most insightful. The student need only to recognize that a single classical move represents a single particle placed within the board, thus the following statement makes the connection between common sense and quantum mechanics:

$$\sum_{i=1}^9 |v_i|^2 = 1 \quad (4.10)$$

where the evaluation, at this point, can be shown to the student as the dot product of two vectors(in this case is X_1 from Figure 4.7):

$$\langle \psi_1^X | \psi_1^X \rangle = \left(\frac{1}{\sqrt{2}} \quad 0 \quad 0 \quad \frac{1}{\sqrt{2}} \quad 0 \quad 0 \quad 0 \quad 0 \quad 0 \right) \begin{pmatrix} \frac{1}{\sqrt{2}} \\ 0 \\ 0 \\ \frac{1}{\sqrt{2}} \\ 0 \\ 0 \\ 0 \\ 0 \\ 0 \end{pmatrix} \quad (4.11)$$

Just as the mathematics of normalization and overlap are nearly identical in the Schrödinger picture, so it is in the Heisenberg picture. The act of describing the overlap integral of two moves in vector notation can be performed for the pair of

Spooky Marker moves seen in Figure 4.7(b) and yields the same solution as the use of the Gaussian functions presented in [10]:

$$\langle \psi_1^X | \psi_2^O \rangle = \left(0 \quad 0 \quad 0 \quad 0 \quad 0 \quad 0 \quad \frac{1}{\sqrt{2}} \quad \frac{1}{\sqrt{2}} \quad 0 \right) \begin{pmatrix} 0 \\ 0 \\ 0 \\ 0 \\ 0 \\ 0 \\ 0 \\ 0 \\ \frac{1}{\sqrt{2}} \\ \frac{1}{\sqrt{2}} \end{pmatrix} \quad (4.12)$$

We have now shown the student how to describe a move, normalization and overlap integral within the matrix formulation; now we may guide our discussions into the direction of observables in quantum mechanics.

4.6 Change of Basis, Projectors and Observations

The student - now being able to describe both the board and the individual moves in terms of vector spaces - is prepared to start making observations within those spaces. We should first introduce the concept of change of basis. To the student the phrase, there are two sides to every story, may be trite but is exemplary in the description of basis for a vector space. The phrase merely implores the listener to look at the problem in another perspective this is the fundamental concept in change of basis.

We have until now described our vectors through a weighted sum of Cartesian basis vectors (which will be shorthand by the s-basis for site-basis). At this point let us introduce a new basis by which to describe our system. Victory in both classical and quantum versions Tic-Tac-Toe can be obtained through generating a 3-in-a-row on

any of the three vertical columns defined by the board. We shall define a normalized set of spanning vectors starting with a 3-in-a-row in each of the columns:

$$\begin{pmatrix} \frac{1}{\sqrt{3}} & 0 & 0 & \frac{1}{\sqrt{2}} & 0 & 0 & -\frac{1}{\sqrt{6}} & 0 & 0 \\ 0 & \frac{1}{\sqrt{3}} & 0 & 0 & \frac{1}{\sqrt{2}} & 0 & 0 & -\frac{1}{\sqrt{6}} & 0 \\ 0 & 0 & \frac{1}{\sqrt{3}} & 0 & 0 & \frac{1}{\sqrt{2}} & 0 & 0 & -\frac{1}{\sqrt{6}} \\ \frac{1}{\sqrt{3}} & 0 & 0 & -\frac{1}{\sqrt{2}} & 0 & 0 & -\frac{1}{\sqrt{6}} & 0 & 0 \\ 0 & \frac{1}{\sqrt{3}} & 0 & 0 & -\frac{1}{\sqrt{2}} & 0 & 0 & -\frac{1}{\sqrt{6}} & 0 \\ 0 & 0 & \frac{1}{\sqrt{3}} & 0 & 0 & -\frac{1}{\sqrt{2}} & 0 & 0 & -\frac{1}{\sqrt{6}} \\ \frac{1}{\sqrt{3}} & 0 & 0 & 0 & 0 & 0 & \sqrt{\frac{2}{3}} & 0 & 0 \\ 0 & \frac{1}{\sqrt{3}} & 0 & 0 & 0 & 0 & 0 & \sqrt{\frac{2}{3}} & 0 \\ 0 & 0 & \frac{1}{\sqrt{3}} & 0 & 0 & 0 & 0 & 0 & \sqrt{\frac{2}{3}} \end{pmatrix}, \quad (4.13)$$

that will be referred to as the Victory basis (v-basis). V-basis was defined by generating the vector describing the three-in-a-row along the columns of a board; the subsequent vectors can be solved for analytically or by any canonical orthogonalization method. The v-basis is not the only other basis that could be defined that spans our board, so we would encourage the reader to form any basis that is appropriate for their class.

We are capable of constructing a matrix from these basis that will allow for vectors from one basis to be transformed to the other basis[33]. The creation of such a matrix (P) is a simple matter of defining the target basis vectors, B' , in terms of the source basis, B , and constructing a matrix from these definitions. Consider a pair of basis sets, B and B' , each spanning the space of a problem and consisting of vectors u and w in basis B as well as u' and w' in B' :

$$u = \begin{pmatrix} a \\ b \end{pmatrix} \text{ and } w = \begin{pmatrix} c \\ d \end{pmatrix}, \quad (4.14)$$

where the vector elements are found from:

$$u = au' + bw' \text{ and } w = cu' + dw'. \quad (4.15)$$

$X_1 O_2$		O_2
X		
X_1		

Figure 4.8. A board presenting possible exercises that may be used to introduce the mathematics of observations of moves in several different basis.

These allow the construction of our P matrix:

$$P = \begin{pmatrix} a & c \\ b & d \end{pmatrix}. \quad (4.16)$$

whose properties are such that: $Pv = v'$. Following this standard method, we can define a P' matrix allowing the translation from site basis to victory basis. This matrix is identical to that of Eq. 4.13.

We can now use the column vectors of the P' matrix to start making observations on our system. We will begin by defining a projection operator, $\hat{\Xi} = |v\rangle\langle v|$. Using the first column vector of our P matrix to generate P' and then employ that operator within $\langle\psi|\hat{\Xi}|\psi\rangle$. We will make our observation on the three moves shown in Figure 4.8. Starting with the classical marker, we can see that our observation of its state made with the projector defined from the first vector of the victory basis would be:

$$\langle\psi^X|v_1\rangle\langle v_1|\psi^X\rangle = \frac{1}{3}. \quad (4.17)$$

The value of $\frac{1}{3}$ for the observation is due to the weight of the Spooky Marker within the vector space of v_1 being $\frac{1}{3}$; when summing over all the spanning vectors of the basis the student is able to recover the total density of the Marker, 1. Completing the same act for the Spooky Markers of $\langle\psi_1^X|$, we get the numerical value of $\frac{2}{3}$ because the Spooky Marker pair has greater weight within v_1 than has the classical Marker of Figure 4.8.

When we complete the final example in Figure 4.8, that of $\langle\psi_2^O|$, we can see the observation is $\frac{1}{6}$, which is to say half that of the previous two measurements because this time the particles are only half within the space of the measurement, v_1 . The sum over all the vectors within the basis yields a density of 1, but the sum over v_1 , v_2 and v_3 yield $\frac{1}{2}$; this value is due to only have of the superposition defining the state being within the region of the basis defined by these vectors.

As we have now made a measurement, we may begin defining a density matrix for our system and show the student how they can make their first measurement of entanglement.

4.7 Separability and Entanglement

If an instructor wishes to introduce the concept of entanglement within the course, as we did, they may do so by introducing the most fundamental necessity for entanglement: inseparability of wave functions[34, 35, 36]. To this end, a series of moves can be shown to the student, such as those seen in Figure 4.9. As the game hinges on the generation of the entangled cycles through generation of inseparable states through marker placement, this is a great opportunity to forge into this topic.

It can be shown that the moves in Figure 4.9 are linearly independent as the series of moves fails to generate a state whose collapse into classicality is forbidden. This is clarified by example, observe Figure 4.9(a); this series of moves can be described by the following expression for the wave function of the board (Ψ):

$$\begin{aligned}
 \Psi &= \psi_1^X \psi_2^O \\
 &= \frac{1}{\sqrt{2}} (|\varphi_1^X\rangle_1 + |\varphi_1^X\rangle_5) \frac{1}{\sqrt{2}} (|\varphi_2^O\rangle_6 + |\varphi_2^O\rangle_9) \\
 &= \frac{1}{\sqrt{4}} (|\varphi_1^X\rangle_1 |\varphi_2^O\rangle_6 + |\varphi_1^X\rangle_1 |\varphi_2^O\rangle_9 + |\varphi_1^X\rangle_5 |\varphi_2^O\rangle_6 + |\varphi_1^X\rangle_5 |\varphi_2^O\rangle_9)
 \end{aligned} \tag{4.18}$$

Here we pointed out to the students that the density of Particle X is not cohabiting with any fraction of the density of Particle O; this indicates that the classically collapsed state of Particle X has no effect on the classically collapsed state of Particle O. The expanded total state expression seen in equality 3 of Eq. 4.6 can be recollected back into equality 2 - this state function can be said to display the property of separability imbued on systems comprised of states that are linearly independent of each other. This linear independence is forfeit if density fractions of the two particles share the same state (or position on the board), as seen in Figure 4.9(b) and whose functional description is here:

$$\begin{aligned}
 \Psi &\neq \psi_1^X \psi_2^O \\
 &= \frac{1}{\sqrt{3}} (|\varphi_1^X\rangle_1 |\varphi_2^O\rangle_5 + |\varphi_1^X\rangle_1 |\varphi_2^O\rangle_9 + |\varphi_1^X\rangle_5 |\varphi_2^O\rangle_9)
 \end{aligned} \tag{4.19}$$

It is clearly noted that the expanded form of the states describing the board in Eq. 4.18 does not include states that are forbidden on the board, noted by the loss of the

$|\varphi_1^X\rangle_5 |\varphi_2^O\rangle_5$ state which is classically forbidden. Due to the loss of this mathematical state the expression cannot be recollected as a product of the two individual moves - this is referred to as inseparability of functions and is a fundamental property for systems who possess and exhibit entanglement. Similarly, individual electrons can be in the $|\uparrow\rangle$ state or the $|\downarrow\rangle$ state; yet when in a coupled pair the electron system can only be in the $|\uparrow\downarrow\rangle$ state or the $|\downarrow\uparrow\rangle$ state, noting the loss of the $|\uparrow\uparrow\rangle$ state and the $|\downarrow\downarrow\rangle$ state.

4.8 Density Matrix and Concurrence

Now, let us begin to show the student how one can make a measurement of entanglement. Entanglement is the correlation between parts of a system - induced through an interaction and maintained in separation - which is independent of factors such as position and momentum[21]. Entanglement was introduced by Schrödinger[34, 35] and was the focus of the famous EPR paper[15]. We will do this by measuring the concurrence, which gives us a measurement of pair-wise entanglement of particles within our system; the method was developed by Wootters[37, 38]. The calculation of concurrence is a brief five-step process[36]:

1. Construction of a Density Matrix: $\rho = |\psi\rangle \langle\psi|$.
2. Construction of a Flipped Density Matrix: $\tilde{\rho}$.
3. Product Matrix: $\rho\tilde{\rho}$.
4. Determine the Eigenvalues of $\rho\tilde{\rho}$: $\lambda_1, \lambda_2, \lambda_3 \dots$
5. Calculate Concurrence: $C = \max[0, \sqrt{\lambda_1} - \sqrt{\lambda_2} - \sqrt{\lambda_3} - \dots]$

Let us start by generating a density matrix for our system; this is typically done by generating and subsequently diagonalizing the Hamiltonian matrix for the system, but we have no energies associated with our board or moves so we will choose marker location as our observable. Let us construct an observation matrix, \mathcal{O} , by using the

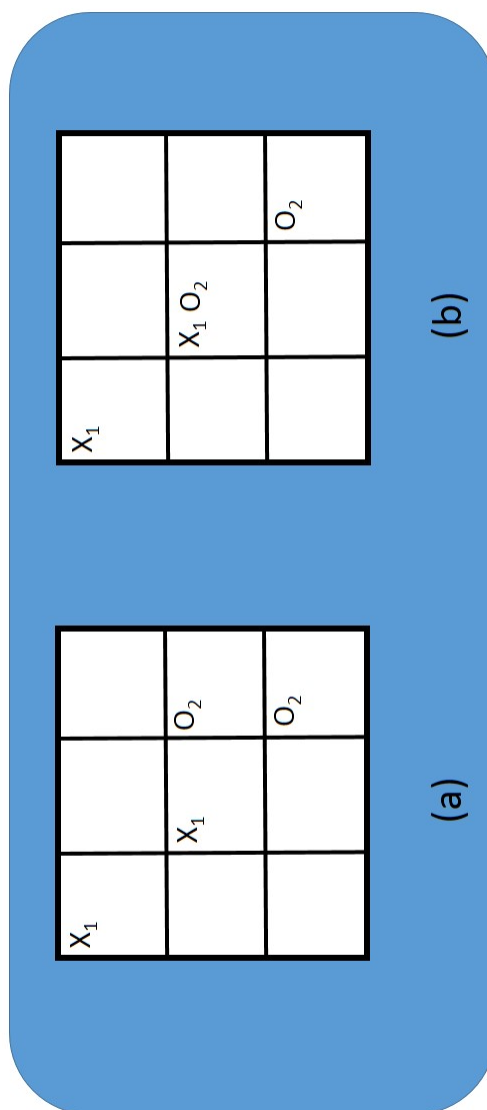


Figure 4.9. Board (a) shows a pair of moves placed in such a way were the overall wave function of the board is separable; this can be shown through an expansion of the product of the wave functions for each Spooky Marker and then the subsequent concretion back to the original product, completed in discussion. Board (b) displays a pair of moves whose total board wave function is inseparable, there exist members of the product expansion who are exclusionary to other members, seen in discussion.

site basis for the board and a projector, $|\psi_1^X\rangle\langle\psi_1^X|$, described by the Spooky Markers seen in Figure 4.7(a):

$$|\psi_1^X\rangle = \begin{pmatrix} \frac{1}{\sqrt{2}} \\ 0 \\ 0 \\ \frac{1}{\sqrt{2}} \\ 0 \\ 0 \\ 0 \\ 0 \\ 0 \end{pmatrix} \quad (4.20)$$

$$\begin{aligned} \mathcal{O}_{i,j} &= \langle\psi_i|\psi_1^X\rangle\langle\psi_1^X|\psi_j\rangle \\ &= \langle s_i|\psi_1^X\rangle\langle\psi_1^X|s_j\rangle \end{aligned} \quad (4.21)$$

This allows us to generate a general observation matrix over the space of the board, not unlike a Hamiltonian matrix generated with a finite basis set.

This matrix, \mathcal{O} , will be of the form:

$$\mathcal{O} = \begin{pmatrix} \frac{1}{2} & 0 & 0 & \frac{1}{2} & 0 & 0 & 0 & 0 & 0 \\ 0 & 0 & 0 & 0 & 0 & 0 & 0 & 0 & 0 \\ 0 & 0 & 0 & 0 & 0 & 0 & 0 & 0 & 0 \\ \frac{1}{2} & 0 & 0 & \frac{1}{2} & 0 & 0 & 0 & 0 & 0 \\ 0 & 0 & 0 & 0 & 0 & 0 & 0 & 0 & 0 \\ 0 & 0 & 0 & 0 & 0 & 0 & 0 & 0 & 0 \\ 0 & 0 & 0 & 0 & 0 & 0 & 0 & 0 & 0 \\ 0 & 0 & 0 & 0 & 0 & 0 & 0 & 0 & 0 \\ 0 & 0 & 0 & 0 & 0 & 0 & 0 & 0 & 0 \end{pmatrix} \quad (4.22)$$

Now we may construct a density matrix from the above. We will first diagonalize the \mathcal{O} matrix and select the state of the system we will use for the generation of the density matrix. We will use the first eigenvectors of the system, the vector

corresponding to the eigenvalue of 1. This vector may be seen in Eq. 4.23 as it is being used to generate the density matrix:

$$\rho = |\mathcal{O}_1\rangle \langle \mathcal{O}_1| = \begin{vmatrix} \frac{1}{2} & & \frac{1}{2} \\ 0 & \rangle \langle & 0 \\ 0 & & 0 \\ \frac{1}{\sqrt{2}} & & \frac{1}{\sqrt{2}} \end{vmatrix} \quad (4.23)$$

In generating ρ , we can note that most of the space in which this system lives is superfluous and thus we can reduce the space of our calculations into a 4×4 region; this simplification yields a ρ :

$$\rho = \begin{pmatrix} \frac{1}{2} & 0 & 0 & \frac{1}{2} \\ 0 & 0 & 0 & 0 \\ 0 & 0 & 0 & 0 \\ \frac{1}{2} & 0 & 0 & \frac{1}{2} \end{pmatrix} \quad (4.24)$$

From the above we may now start to generate the spin-flip density matrix, $\tilde{\rho}$, for this state of the system. The generation of $\tilde{\rho}$ is completed by:

$$\tilde{\rho} = (\sigma_y \otimes \sigma_y) \rho (\sigma_y \otimes \sigma_y) \quad (4.25)$$

where ρ is the density matrix discussed above and the σ_y is the y^{th} Pauli spin matrix. The use of the Kronecker product (\otimes) on the series of Pauli spin matrices is to generate a rotation matrix in the same dimensions of the system. As our ρ is a 4×4 matrix, the Kronecker product of two Pauli spin matrices is sufficient to generate a four dimensional rotation matrix for our system. Following the above procedural step our $\tilde{\rho}$ happens to, again, generate:

$$\tilde{\rho} = \begin{pmatrix} \frac{1}{2} & 0 & 0 & \frac{1}{2} \\ 0 & 0 & 0 & 0 \\ 0 & 0 & 0 & 0 \\ \frac{1}{2} & 0 & 0 & \frac{1}{2} \end{pmatrix} \quad (4.26)$$

Armed with both ρ and $\tilde{\rho}$ we can now complete the fourth procedural step: finding the Eigenvalues of the $\rho\tilde{\rho}$ matrix-product:

$$\rho\tilde{\rho} = \begin{pmatrix} \frac{1}{2} & 0 & 0 & \frac{1}{2} \\ 0 & 0 & 0 & 0 \\ 0 & 0 & 0 & 0 \\ \frac{1}{2} & 0 & 0 & \frac{1}{2} \end{pmatrix} \quad (4.27)$$

with Eigenvalues $1, 0, 0, 0$. Using these Eigenvalues within the expression for concurrence: $C = \max [0, \sqrt{1} - \sqrt{0} - \sqrt{0} - \sqrt{0}]$. This would yield a concurrence of 1; this is the maximum value that the concurrence can yield for pair-wise entanglement. The value implies that the two parts of the Spooky Marker are maximally entangled. This is a sensible finding as these markers are entangled (as per the rules) and unencumbered by interaction with other markers.

4.9 Conclusions

In summary we have presented a series of exercises that may be used during introductory quantum mechanics and physics courses. These exercises have through the experience of these authors aided students in their understanding of quantum mechanics by providing a degree of intuition to the mathematics of the topic. This intuition provided by both classical and quantum versions of a childrens game with which most student have had some experience has, to the authors experience, benefited the instruction simple topics within the course, especially normalization and simple statements described through the use of wavefunctions. Furthermore. By exploiting the game we have found this method lowers the degree of fear some students possess toward quantum mechanics. It is the hope of these authors that utilizing such intuitive examples may become as widely accepted as has the use of the Particle in a Box problem. These authors also hope that the armory of quantum games used in the classroom will be expanded to include other versions of tic-tac-toe[39] and furthered to a larger variety of games[6, 40]. For use by the students or practice for

the instructor a playable online version that includes an AI player can be found at <http://www.paradigmpuzzles.com/QT3Play.htm>.

We have herein presented an introduction to the possible uses of both classical and quantum Tic-Tac-Toe as a means of instruction in the matrix methods of quantum chemistry. These authors have also found that a brief introduction in quantum entanglement is beneficial to students and have presented a brief series of exercise using QTTT as a means of intruding entanglement. It is the experience of these authors that students can benefit from their previous experience in CTTT in the teaching of quantum mechanical topics. Students also further their knowledge of these topics through learning and exercising with QTTT. Other quantum games exist[39, 40, 41] and their introduction into the classroom as teaching tools and metaphors is encouraged.

4.10 Acknowledgments

This work is supported by the NSF Centers for Chemical Innovation: Quantum Information for Quantum Chemistry, CHE-1037992. The authors would also like to thank Prof. George Bodner of Purdue University for critical reading.

4.11 References

- [1] A. Messiah. Quantum Mechanics, Dover, 1999
- [2] A. Messiah. Quantum Mechanics Volume II, Dover, 1999
- [3] D. A. McQuarrie J. D. Simon. Physical Chemistry: A Molecular Approach, 1st ed., University Science Books, 1997
- [4] Goff, A.; Lehmann, D.; Seigel, J. Quantum TicTaToe as Metaphor for Quantum Physics. AIP Conf. Proc. 2004, 699, 1152.
- [5] Goff, A. Quantum Tic-Tac-Toe: A Teaching Metaphor for Superposition in Mechanics. Am. J. Phys. 2006, 74, 962.
- [6] Goff, A.; Lehmann, D.; Siegel, J. Quantum Tic-Tac-Toe, Spooky- Coins Magic-Envelopes, as Metaphors for Relativistic Quantum Physics. AIAA Pap. 2002, No. AIAA-2002-3763.
- [7] Beller, M. The Conceptual and the Anecdotal History of Quantum Mechanics. Found. Phys. 1996, 26 (4), pp545557.
- [8] Born, M.; Heisenberg, W.; Jordan, P.; Zur Quantenmechanik, I. I. Z. Phys. 1936, 35 (89), pp557615.
- [9] Hilbert, D.; Ewald, W. B.; Hallett, M.; Majer, U.; Sieg, W. David Hilbert's Lectures on the Foundations of Mathematics and Physics, 1891 1933; Springer: New York, 2004; Voume 5.
- [10] Hoehn, R.; Kais, S. Using Quantum Games to Teach Quantum Mechanics, Part 1. J. Chem. Educ., 91, 417, 2014
- [11] Feynman, R. P. Simulating Physics with Computers. Int. J. Theor. Phys. 1982, 21, 6/7.
- [12] Lloyd, S. Universal Quantum Simulators. Science 1996, 273 (5278), 10731078.
- [13] Zhu, J.; Kais, S.; Aspuru-Guzik, A.; Rodrigues, S.; Brock, B.; Love, P. J. Multipartite Quantum Entanglement Evolution in Photosynthetic Complexes. J. Chem. Phys. 2012, 137, 074112.
- [14] Gauger, E. M.; Rieper, E.; Morton, J. J. L.; Benjamin, S. C.; Vedral, V. Sustained Quantum Coherence and Entanglement in the Avian Compass. Phys. Rev. Lett. 2011, 106, 040503.
- [15] Einstein, A.; Podolsky, B.; Rosen, N. Can Quantum-Mechanical Description of Physical Reality Be Considered Complete? Phys. Rev. 1935, 47 (10), 777780.

- [16] Stern, O. Ein Weg zur experimentellen Prufung der Richtungsquantelung im Magnetfeld. *Z. Phys.* 1921, 7, 249253.
- [17] Gerlach, W.; Stern, O. Das magnetische Moment des Silberatoms. *Z. Phys.* 1922, 9, 353355.
- [18] Bernstein, J. The Stern Gerlach Experiment. 2010, arXiv:1007.2435v1. arXiv.com e-Print archive.
- [19] Loudon, M. *Organic Chemistry*, 4th ed.; Oxford University Press: New York, 2002; pp 3738.
- [20] Feynman, R.; Leighton, R.; Sands, M. *The Feynman Lectures on Physics*; Addison-Wesley: Reading, MA, 1964; p 1966, 3 volumes; Library of Congress Catalog Card No. 63-20717.
- [21] Nielsen, M. A.; Chuang, I. L. *Quantum Computation and Quantum Information* (Cambridge Series on Information and the Natural Sciences); Cambridge University Press: New York, 2004.
- [22] Domin, D. A Review of Laboratory Instruction Styles. *J. Chem. Educ.* 1999, 76, 543547.
- [23] Prince, M. J.; Felder, R. M. Inductive Teaching and Learning Methods: Definitions, Comparisons, And Research Bases. *J. Eng. Educ.* 2006, 95, 123138.
- [24] Kirschner, P. A.; Sweller, J.; Clark, R. E. Why Minimal Guidance during Instruction Does Not Work: An Analysis of the Failure of Constructivist, Discovery, Problem-Based, Experiential and Inquiry Based Teaching. *Educ. Psychol.* 2006, 41, 7586.
- [25] Briggs, M.; Long, G.; Owens, K. Qualitative Assessment of Inquiry-Based Teaching Methods. *J. Chem. Educ.* 2011, 88, 1034 1040.
- [26] Spencer, J. New Approaches to Chemistry Teaching. *J. Chem. Educ.* 2006, 83, 538533.
- [27] Farrell, J. J.; Moog, R. S.; Spencer, J. N. A Guided Inquiry General Chemistry Course. *J. Chem. Educ.* 1999, 76, 570574.
- [28] Ditzler, M. A.; Ricci, R. W. Discovery Chemistry: Balancing Creativity and Structure. *J. Chem. Educ.* 1994, 71, 685688.
- [29] Schrodinger, E. An Undulatory Theory of the Mechanics of Atoms and Molecules. *Phys. Rev.* 1926, 28 (6), 10491070.
- [30] Szabo, A.; Ostlund, N. S. *Modern Quantum Chemistry: Introduction to Advanced Electronic Structure Theory*; Dover Publications: Mineola, NY, 1996.

- [31] McMurchie, L. E.; Davidson, E. R. One-and Two-Electron Integrals over Cartesian Gaussian Functions. *J. Comput. Phys.* 1978, 26, 218.
- [32] Levine, I. N. *Quantum Chemistry*, 5th ed.; Prentice Hall: Upper Saddle River, NJ. 2000.
- [33] Schneider, H.; Baker, G. P. *Matrices and Linear Algebra*, 2nd ed.; Dover Publishing: New York, 1989.
- [34] Schrodinger, E. Discussion of Probability Relations between Separated Systems. *Math. Proc. Cambridge Philos. Soc.* 1935, 31, 555–563, DOI: 10.1017/S0305004100013554.
- [35] Schrodinger, E. Probability Relations between Separated Systems. *Math. Proc. Cambridge Philos. Soc.* 1936, 32, 446–452, DOI: 10.1017/S0305004100019137.
- [36] Kias, S. Entanglement, Electron Correlation and Density Matrices. *Adv. Chem. Phys.* 2007, 134, 493–535.7
- [37] Hill, S.; Wootters, W. K. Entanglement of a Pair of Quantum Bits. *Phys. Rev. Lett.* 1997, 78 (26), 5022–5025.
- [38] Wootters, W. K. Entanglement of Formation and Concurrence. *Quantum Inf. Comput.* 2001, 1 (1), 27–44.
- [39] Leaw, J. N.; Cheong, S. A. Strategic Insights from Playing Quantum Tic-Tac-Toe. *J. Phys. A: Math. Theor.* 2010, 43, 455304.
- [40] Meyer, D. A. Quantum Strategies. *Phys. Rev. Lett.* 1999, 82 (5), 1052–1055.
- [41] Schmidt, A. G. M.; da Silva, L. Quantum Russian Roulette. *Physica A* 2013, 392, 400–410.

APPENDICES

APPENDIX A. MODELING OF CELLULAR REGENERATION VIA ATOMATON MODEL

A.1 Abstract

Cellular agent-based models are a technique that can be easily adapted to describe nuances of a particular cell type. Within we have concentrated on the cellular particularities of the human Endothelial Cell, explicitly the effects both of anchorage dependency and of heightened scaffold binding on the total confluence time of a system. By expansion of a discrete, homogeneous, asynchronous cellular model to account for several states per cell (phases within a cell's life); we accommodate and track dependencies of confluence time and population dynamics on these factors. Increasing the total motility time, analogous to weakening the binding between lattice and cell, affects the system in unique ways from increasing the average cellular velocity; each degree of freedom allows for control over the time length the system achieves logistic growth and confluence. These additional factors may allow for greater control over behaviors of the system. Examinations of system's dependence on both seed state velocity and binding are also enclosed.

A.2 Introduction

Guided tissue regeneration for the purpose of implantation, or strictly in vivo growth, is an exciting multidisciplinary field which joins cell biology, immunology, material science and biotechnology engineering [1, 2]. Both in vivo and in vitro studies have been conducted towards such ends; these studies include cartilage, vascular tissues [3, 4] and many others. Chief in these studies is not only concern for the

particularities of the specific cell type and the cell's physics [5], but the behavior of the scaffold due both to the material properties and the structural organization of the material [6, 7, 8]. Cells interact with the scaffolding in several ways including pore induced motility limitations (both statistical and steric) and these behaviors govern the biophysical properties of the final tissue [9, 10, 11].

Scaffolds provide several degrees of freedom affording the manipulation of geometry, post-implant properties and proliferation behavior during incubation; this being exemplified in the scaffold's deterministic influence on cellular specialization [11]. Prospective scaffolding types include both biological (fibrin, collagen, chitosan) [12, 13, 14] and synthetic (polyactic acid, polyglycolic acid, and poly-lactic-glycolic acid, etc.) [15, 16, 17] scaffolding materials; each, of course, possessing unique characteristics. These materials can be functionally tailored for specific cell attachments through biomedical surface modifications and through addition of growth factors both of which can provide improvements and guidance to system behavior [18, 19, 20]. Cell-scaffold interactions such as guided migration and adhesion can have profound effects on the rate of formation of an implantable tissue [21, 22, 23].

As *in vitro* (worse yet *in vivo*) studies do take time, as well as ample consideration and cost, it is natural to attempt to simulate the behavior of systems prior to synthesis or bioreactor application, in this capacity *in silico* studies can prove to be an invaluable first step in a study. On this front there are several theoretical methods being used on cellular systems, including: continuum models based both on Fisch-Kolmogorov equation and mass conservation statements [24, 25, 26, 27, 28, 29]; Finite Element solutions to Continuity equations [30]; Control Network models [31]; and discrete automaton models [32, 33, 34, 35]. Other models incorporate aspects of both discrete -for cell behavior- and continuum models -nutrient/waste handling- these being hybrid models [36, 37]. Models have been developed to simulate specific instances in cellular biology such as stem cell differentiation [38], interactions within heterogeneous cell populations [39], and a great many concentrating on tumor growth [40, 41], invasion [42] and their relation to angiogenesis [43]. As a means

of simulation, the discrete cellular automaton/agent model was used in our work to capture the global consequences of highly specific cellular activities. Cellular automaton/agent models have been used to model vaccine populations [32], endothelial cells [34, 35], epidermal wound closures [21], etc. Such a model has been shown adequate in description of real systems [44] and has been shown capable of describing specialized cellular behaviors [45]. Discrete models for proliferation and mobility can be designed to explicitly exemplify the behavior and consequences of that behavior in specific cells types. This gives the agent-based models some definite advantages over continuity models in adequately describing specific behaviors of particular cell types. It is the ability to address individual cells which gives discrete models advantage in the generation of simulations describing the creation of endothelial monolayers.

Human vascular structure is comprised of three tissue layers surrounding the transport tube(lumen) these layers are: tunica intima, inner most layer of endothelial cells; tunica media, populated with smooth muscle cells that maintain blood pressure by dilating the vessel; and tunica adventitia which is a region dominated by matrix and fibroblastic cells. This structure can be seen in Fig. A.1. Human Endothelial Cells form highly confluent monolayers comprising the inner most strata of the composite vascular structure [46]; the endothelium is responsible for regulating the passage of waste and nutrients between the blood stream on one side and the surrounding tissues on the opposing side [47, 48] chiefly benefiting from vascular Smooth Muscle Cells (v-SMCs) and fibroblast cells [49]. A further responsibility of this monolayer is to release of heparan sulfate [35], which acts as a cofactor in the inhibition of the cascading coagulation of blood and reduces turbulent forces. Defective endothelium can lead to thrombosis [50, 51] and proliferation of smooth muscles cells through the endothelium and into the lumen, leading to atherosclerosis [52].

H-ECs exhibit the properties of contact inhibition and anchorage dependency, where Anchorage dependent cells require specific binding to surfaces; this effect modulates the proliferation, motility and effects cellular apoptosis [53]. Contact inhibition describes the tendencies of cells to inhibit the division and motility of neighboring

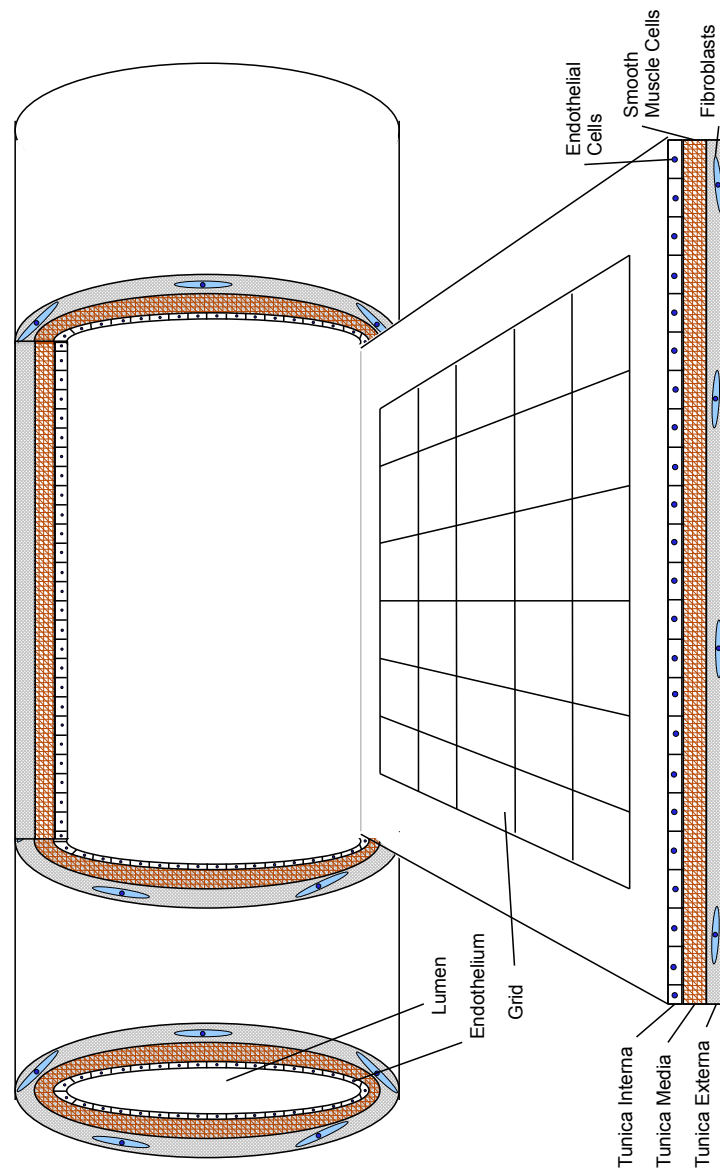


Figure A.1. Schematic representation of the architecture of a blood vessel. The composite structure is described within the body of the section.

cells in a confluent structure [9, 45, 54]. It is this behavior which governs the density at which the continued proliferation of the colony cease and incorporates a density dependent change in cell size; cells in highly confluent regions take on more regular geometry to allow for a more confluent packing [9, 55, 56]. Bonding of cells to extracellular matrix can alter the proliferation and the migration behavior of a macro-cluster of cells [57, 58] through contact guidance, exemplified in the proliferation and motility of carcinoma cells along collagen connective tissues [53].

A.3 Algorithm

As the cellular automata/agent model is amply defined in other publications [34, 35], and expanded [37, 9, 36], we shall emphasize the modifications built into our model a final time while briefly describing the algorithmic procedure. Allowing for a two-phase life cycle we have achieved the following: collapsing all motility into a single phase; all division into a single phase; and introduced parameter which functionally behaves like binding coefficients. The inclusion of blackout helps account for the further effects in short-ranged, foot-lengthening locomotion behavior of cells on a surface [59] and aides in maintaining physiological consistency in an asynchronous model. We address motility as the central means by which to model EC growth during cellular random walks [60]; herein we concentrate on the effects of cellular anchoring onto scaffold sites and thus generate differential motility and division behaviors due to the effects of anchorage dependent behaviors. Each free space within the system which can be unoccupied, or occupied by a cell or agent, this being consistent with the procedure presented in previous works [45, 35, 44]. Within our model, there are two possible states for the occupied automaton: occupied by a mobile phase cell, or occupied by a stationary phase cell. The occupancy - and state information shall be stored within a state vector which will be uniquely assigned to each agent and stored within a master list. The elements of the site vector will at least convey position,

$\nu_1 = (x_{site}; y_{site}; z_{site})$, site index, $\nu_2 = i_{site}$, occupancy status, $\nu_3 = 1, 2$ if occupied, else $\nu_3 = 0$.

If $\nu_3 = 0$, the information required for the automaton is position and index. If ν_3 is 1, the site contains a mobile cell and has the state vector:

$$\nu_{Mobile}^{site} = |position_{site}; index_{site}; 1; c_v; m_\tau; p_\tau; \theta_d\rangle; \quad (\text{A.1})$$

the values of the fourth through seventh components are: c_v , the value of the cellular speed; p_τ , the persistence time, is the amount of time a particular type of cell spends traveling in a single direction before pausing or turning in the absence of interaction from other cells; m_τ , the total motility time, is the total amount of time an anchorage dependent cell spends in the Mobile Phase while still in the presence of a scaffold; θ_d is the discrete vectorized direction which the cell is traveling along the matrix. The Stationary Phase vector would be:

$$\nu_{Stationary}^{site} = |position_{site}; index_{site}; 2; d_\tau\rangle; \quad (\text{A.2})$$

where d_τ is the time prior to cell's next division. It should be noted that both newly placed daughter cells will enter life in the Mobile Phase.

The values associated with the physiological constants used within our simulations are presented in Table A.1. Observed quantities are used as the average value about which to construct either a Poisson or a Gamma distribution and then we select values about the average conforming to the distribution's cumulative distribution function (exemplified by Poisson):

$$F(x|\lambda) = e^{-\lambda} \sum_{i=0}^{\lfloor x \rfloor} \frac{\lambda^i}{i!}. \quad (\text{A.3})$$

Where λ is the mean parameter controlling the shape of the distribution, and x is the variable of the distribution. Random numbers for cell velocity, motility time, etc. are constructed for individual automaton around the experimentally observed value. These values are set normal to the average velocity so that all constants reference uniform time-steps:

$$\bar{c}_{norm} = \bar{c} * (\bar{c}_v)^{-1}, \quad (\text{A.4})$$

where \bar{c}_v is the average value of the cellular velocity which all system time steps are set in reference, \bar{c} represents any other time-based average value used within our calculations and \bar{c}_{norm} is the time-step adapted version of \bar{c} .

Randomly selected values allow for the creation of a diverse population of cells each with unique associated quantities. Using statistical values bears the caveat that simulation data is accurate only in a statistical nature i.e. any derived quantities are averages themselves and should take on experimental values as the samples sets approaches the large number limit. The time step size is .5h, as this allows several steps in a persistent direction, and a length of evolution time prior to changes in the phase of the cell-cycle; similar size time step justifiably employed in [45]. All evolutions are completed in an asynchronous manner - this allows for use of the previously mentioned Black-out List for the description of anchorage dependent locomotion and helps guarantee a more stable mathematical solution as well as allowing for unique differences in singular automaton to take greater part in the system's evolution. The system is designed to enforce a Moore neighborhood for the cells, and confluence is reached when no neighboring locations are vacant. Once the value of each cell has been updated for time-step t , $t = t + 1$. This shall be repeated until confluence is reached; confluence is checked for at the end of each time-step. The initialization, and algorithmic structure for the system can be seen in Figure A.2.

The probabilities associated with direction-of-travel are found via Markov chain analysis and provided within Table A.2 [61, 49, 62]; these values are slightly augmented from the reference values to generate symmetry under counter-rotation - as an anisotropy was not introduced into our system. There exists an elevated chance that the cell enters into the $\theta_d = 0$ state - this is a pausing, or waiting, state. Figure A.3 displays a device conveying the appropriate unit vectors for cellular locomotion with origin being the cell's present position. As the p_r counter reaches zero for a Mobile Phase cell they prepare to turn, it must be verified that the cell's progression

Table A.1

Table contains constants of motion for cells used within calculations, also includes references for values.

Constants	Symbol	Value	Cell Type
Persistence Time	p_{τ}	8h	hm-EC
Motility Time ¹⁰	m_{τ}	2h	CHOC
Cell Speed ¹³	c_v	28.2microm/h	BPAAE
Division Time ⁸	d_{τ}	17h	BPAAE
Mesh Size ¹³	m_s	30micro m	BPAAE

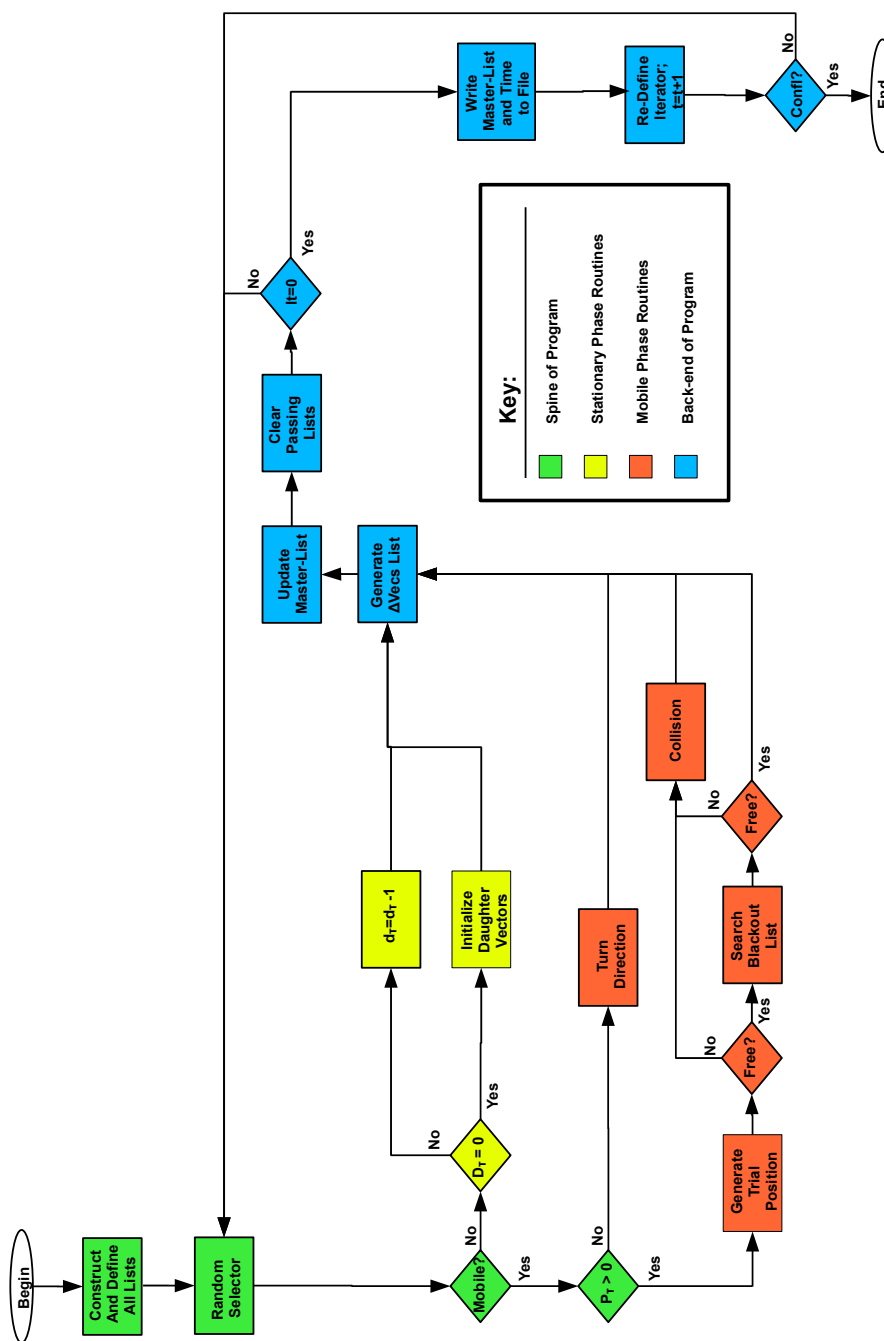


Figure A.2. Algorithmic map for the discrete model used herein. Note sections of same color work together in a unified purpose describing a single facet of the program or cell behavior.

towards its new site does not cross the path of a cell which has already begun to move. These motile-cell paths are held within the blackout list. If the cell does not cross the path of other cells it evolves normally; if it crosses paths or the target site is occupied then the mobile cell of interest undergoes collision.

To be modeled is a two-dimensional region of scaffold-binding surface on which h-ECs can migrate and proliferate. The algorithm begins by defining and then dissecting the entire 2-D solution space by a regular, rectangular grid; intersections on the gridded solution space define the geometry of the $l \times l$ lattice, where the side length l is equal to a cellular radius, r_c . Thus for a cell whose $r_c = 30 \mu\text{meter}$, a 10×10 mesh would be equivalent to a $300 \times 300 \text{ micron}^2$ area of lattice. Periodic boundaries conditions were imposed to emulate the mechanics of an infinite lattice. Four seeding conditions will be employed: random spraying, motile centroid (MC), stationary centroid (SC), and wound closure. The random seeding and wound healing conditions are well known. Both the translational seeding cases rely on the conveyance of a preformed confluent colony of a predefined size (relative to the solution space) to be transferred into the solution-space; these conditions vary only in the state which the cells are transferred as: mobile phase for cellular translation, and stationary for cell plus lattice translation.

The overall algorithm can, alternatively, be described through a series of steps organized within a list structure, such as:

- From *master list*, a random vector is selected (*master list* contains only the indices for every agent), this vector is passed to the subsequent decision structure.
- If the cell is found to be in the Stationary Phase ($v_3 = 2$), this biologically signifies that it is bound to a location within the Extracellular Matrix (ECM); coming with this loss of mobility, the cell experiences an accelerated division rate.
 - If d_τ is greater than zero, the cell must wait before it is capable of division - thus $d_\tau^{t+1} = d_\tau^t - 1$.

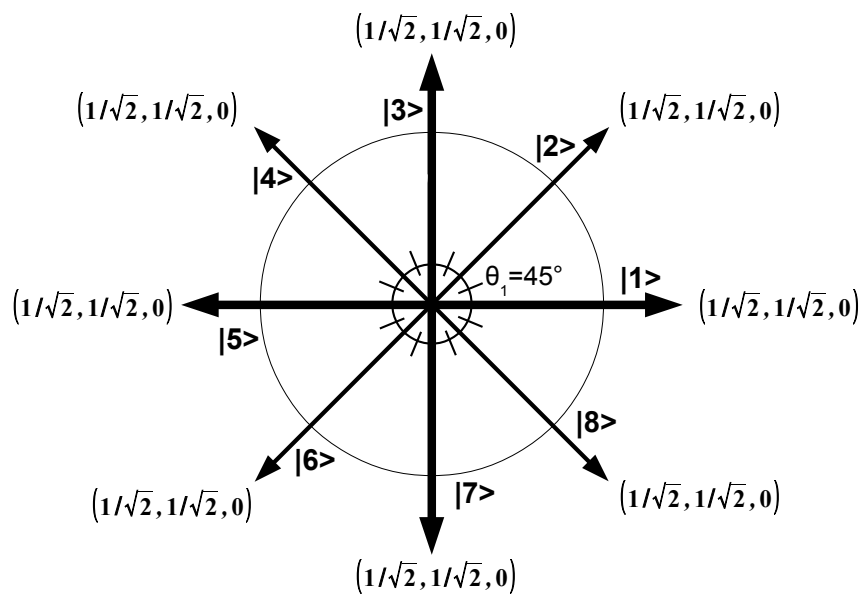


Figure A.3. A schematic representation of the directional states within Markov Chain Analysis with their vector and θ_d state designations.

Table A.2

Table containing all of the initial to final state turning probabilities.

Instance Used	$\rightarrow f\rangle$ States									
	0	1	2	3	4	5	6	7	8	
Initial Direction	0.4300	0.0712	0.0712	0.0712	0.0712	0.0712	0.0712	0.0712	0.0712	0.0712
Turning	0.4300	0.0300	0.1000	0.0800	0.0600	0.0600	0.0600	0.0600	0.0800	0.1000
Collision	0.1000	0.0033	0.1500	0.0033	0.1500	0.2900	0.1500	0.1500	0.0033	0.1500

- If $d_{\tau} \leq 0$, the cell is prepared to divide; in this case, all possible locations for a daughter cell are scouted for availability.
- If several acceptable daughter locations are found, one is selected at random; if no daughter locations are available, the cell does not divide and the division counter is reset to account for contact inhibition.
- The cell is in the Mobile Phase of its life-cycle, $v_3 = 1$.
 - If $p_{\tau} = 0$, the cell would initiate the turning procedure. The probability for each possible vector state of the c_v relative to the present state is found through Markov Chain Analysis
 - * When turning the vector is re-comprised it's assigned a new value for each p_{τ} , c_v and θ_d (direction) each selected randomly from the Poisson distribution.
 - $p_{\tau} \neq 0$, this cell is in the Mobile Phase and is moving. We call both the c_v and the θ_d values of the particular agent to construct a vector describing the motion of the cell, moved to *trial location*.
 - * All motile-cell paths are held within a passing list *blackout*. If the motile vector doesn't cross any member of *blackout* and *trail location*'s $v_3 = 0$, then the cell is allowed to update its position while $p_{\tau}^{t+1} = p_{\tau}^t - 1$ and $m_{\tau}^{t+1} = m_{\tau}^t - 1$.
- The initial randomly selected index is removed from master, and another is randomly selected.

A.4 Results and Discussion

Herein we have modeled and discussed the dependence on surface binding of proliferation as a means of simulating the behavior of anchorage-dependent cells within

the confines of a scaffolding. Figure A.4 displays the systematic evolution toward confluence and dependence on extension of the overall motility time (length of time in the motile-phase) in an initially random .32 percent seeded scenario. In the limiting case where the cell's motile-phase life time is set to zero, the system experiences similar growth to the exponential/logarithmic growth curves, displaying the contact dependence as asymptotic growth near the ends of both the logistic and setting phases. As the total motility time increases, the behavior trends to a general decrease in motility stemming from the management of division times due to by anchorage-dependency; similarly, increases in motility on the proliferation behavior have been shown [34]. Discussion of Figure A.4 should include mention of first derivatives of the emerging cell count curves for the system - within the high motility time case. The rate of new cell generation levels-off near confluence as contact-inhibition inhibits division; whereas the leveling behavior of the system near initialization is due to motility and division times acting to delay growth prior to the first wave of daughter cells. Note should be given to cases where the scaffold binding is weak, here the system spends extended time with relatively high mobility and doesn't attain to any extent the behaviors associated with the anchored cells exemplified here by divisions.

Figure A.4 displays the dependence of confluence on both the initial geometry of the system and on the average cell speed. The geometric dependence is most obvious when noting the initially stationary; this difference is generated in the system's initial seeding, as the advantage of a quick initial division affects total confluence time. Figure A.4c shows the effects of altering the cells average velocity at constant motility time; the difference between runs is small, yet the same characteristic behaviors such as changing of motility time are present.

Dependence of confluence time on the seeding geometry is shown in Figure A.5a; the number of cells which are attempting to undergo division. The behavior to note here is that the stationary centroid case has an elevated number of cells attempting division at a very early time which supports the inferences made from the confluence times. The behaviors of the remaining geometries are seemingly identical. In both

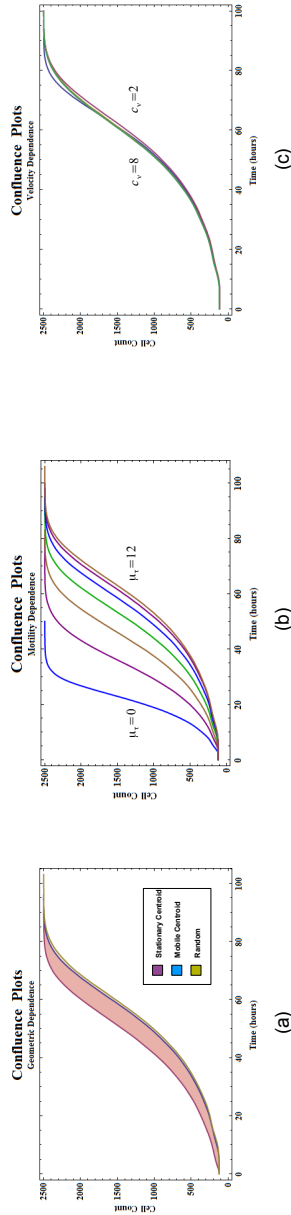


Figure A.4. Figures showing the dependency of the confluence behavior on several variables: (a) initial seeding geometry, (b) motility parameters, (c) velocity parameters. Note, the definite impact parameter and geometric alterations have upon both the logistic and setting phases of colony growth. This comes about as the motility time increase dampens the effect of the initial division within the system causing, for smaller μ_τ an earlier logistic phase and setting phase on-set. The difference in the geometric confluence behaviors was highlighted for emphasis.

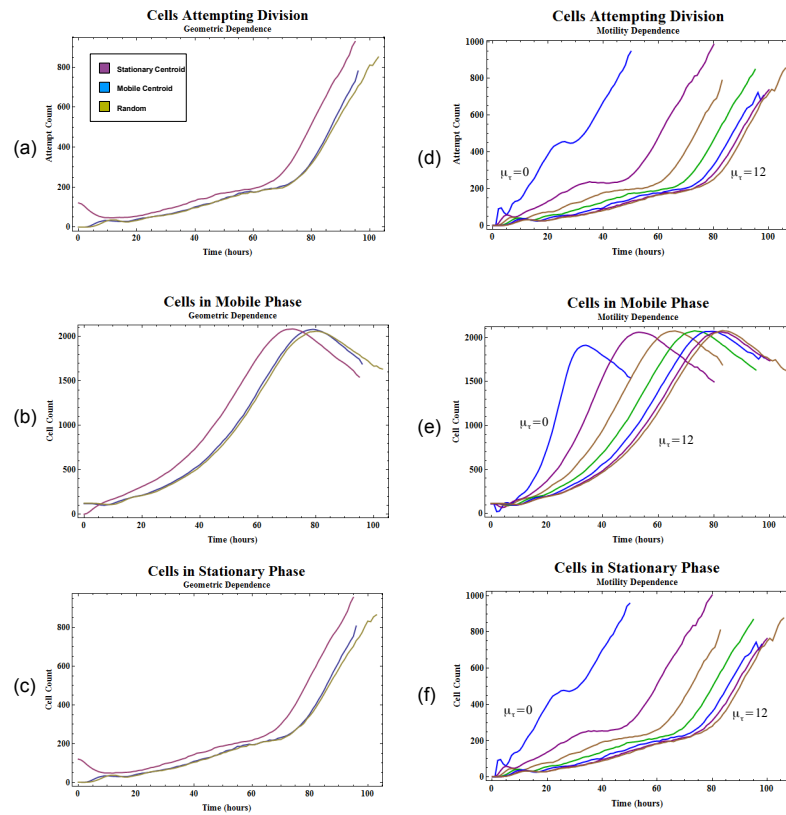


Figure A.5. Initial seeding geometry is varied in Subfigures a, b, and c. The behaviors are: (a) attempted divisions within the system, (b) cells which are in the Mobile Phase, and (c) cells which are in the Stationary Phase. It should be made clear that the number of cells which could possibly attempt division within the system is upper bound by the number of cells within the Stationary Phase, thus the relationship shown in Figures a, b and c. It is important to note that (a) is attempted divisions, and should be compared to the corresponding confluence plot for perspective. In Subfigures d, e and f motility time is varied and labeled are the lowest and highest values of μ_τ , the values in between increase in increments of 2. These behaviors are: (d) attempted divisions within the system, (e) cells which are in the Mobile Phase and (f) cells which are in the Stationary Phase.

Figure A.5b and c there is a reciprocal behavior in the number of cells in each phase which is due to the initial seeding conditions; seen in a high initial population in the Mobile (Stationary) Phase for the random and mobile centroid (stationary case).

The behavior during the evolution of the system with varying μ_τ is shown in Figure A.5. Figure A.5d shows division attempts, note that the smaller μ_τ is the larger the number of cells attempting division. Smaller μ_τ increases the rate of cells beginning division. The system undergoes beats in population dynamics due to variations in constants while the system size is small. As evolution time increases the statistical nature of the parameter selection begins to wash-out this beating due to random value selection off of already random values causing a broadening and dampening of division. The overall decline in the number of cells in the Mobile Phase is due to the lack of available space within the scaffold at later times in the evolution forcing a sedentary behavior in all cells due to contact inhibition.

Figure A.6 Row 1 shows the number of collisions undergone by cells within the system and Row 2 the effective velocity of the average cell within the system; the effective velocity is the average cell velocity considering colliding, waiting and stationary cells; the average effective velocity is computed as:

$$\bar{c}_{eff.} = \frac{\sum_i^{N_{mob.}} \sqrt{(x_f - x_i)^2 + (y_f - y_i)^2 + (z_f - z_i)^2}}{N_T(t)}; \quad (\text{A.5})$$

where N_{mob} is the number of cells in the Mobile Phase and $N_T(t)$ is the total number of cells within the system at time t . The effective velocity of cells falls off as confluence is reached due to a lessening of available space within the system. After the first beat in population increase the majority of differences between initial seeding conditions becomes minimal. Figure A.6c and d, the number of collisions in the mobile centroid case are initially elevated for steric reasons; the systematic μ_τ dependence is clearly comprehensible as the less mobile the cells within the system the fewer collisions in which each cell may participate. Figure A.6e shows behaviors which are similar to the aforementioned μ_τ dependence, as the cell travels faster it is capable of colliding more often. The overall shape of the curves speaks to anchorage dependence

within the system - as the cells become more packed there is less space in which to move. Figure A.6b shows the effects of seeding condition on effective velocity; the random seeding trial has the least initial steric restraint which presents itself in a large initial effective velocity, whereas the initial effective velocity of the stationary centroid case is zero. Figure A.6d and f show the effect of motility time and cell speed on the effective velocity; the less mobile the cells within the system, the smaller the effective velocity. With an increasing μ_τ the number of cells within the Mobile Phase is increased, this increase manifests itself in a larger effective velocity; the variation of cell velocity alone does not affect the rate at which population is increased within the system and this is manifest in the same limiting confluence time for all velocities, subfigure f.

The simulations of the four initial conditions were devised with a specific purpose in application. Implantation of non-motile phase cells would be analogous to placing a small cutting of already confluent occupied scaffold and allowing the resident cells to proliferate onto and through a new matrix; whereas the motile-phase implantation would be caused by the growth of a colony in media without the presence of a binding surface, and then incorporating the colony as a whole onto the artificial scaffolding. The random seeding distribution is seeding of the matrix by randomly "spraying" cultured cells onto the scaffolding. Wound closure models the closure of a wound within a vessel where the wound is considered infinitely long, but finitely wide - thus presence of walls yield cells required to heal (as this simulation does not incorporate the processes of generating basement membrane, the healing time frame is unrealistic without consideration of the application of an artificial basement membrane which could stunt the healing vessel). The stationary and motile runs reach 90% confluence in an average time of roughly 66 hours and 74.5 hours, respectively. That the stationary centroid condition primes the cells in the Stationary Phase means that the system will divide sooner than the other runs. The wound closing scenario reached 90% confluence at 72 hours; and the random seeding case reached 90% coverage in roughly 73 hours. Results did not scale with

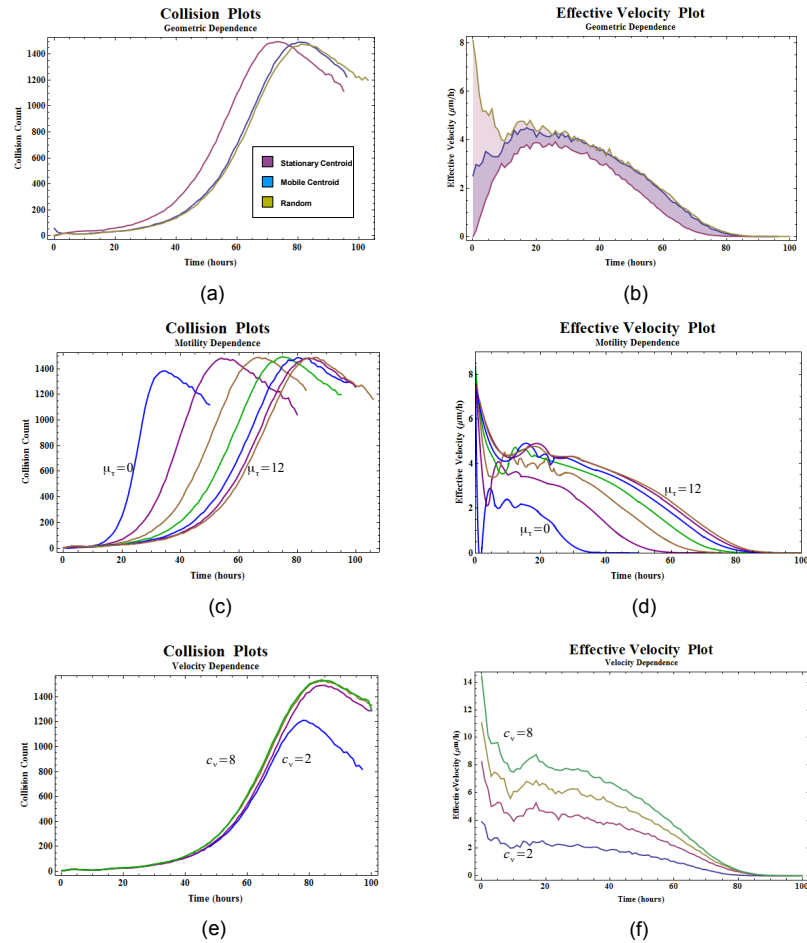


Figure A.6. Plots of effective behaviors displaying influence of: Row 1, different initial seeding conditions; Row 2, different values of μ_T ; and Row 3, different values of c_v . Plots (a), (c) and (e) show the number of collisions within the system; Plots (b), (d) and (f) are of the effective average velocity of the cells. Note, (a) shows the depletion of collision count near the setting phase as more cells are being influenced by contact inhibition and becoming stationary. In (b) the drastic difference in initial effective velocity between the seeding cases at constant c_v . (d) and (f) displays the overall trending behavior is uniform in all cases, just varying time-scales. (e) shows the limiting dependence of the system behavior on c_v as the velocity approaches the motility parameter.

system size, as periodic boundary conditions were employed under constant initial seeding density.

Geometric dependence can be further noted from Figure A.7 as the behavior of the stationary centroid evolution (first column) behaves exactly as Barrandon and Green[63] and later studies[45] have shown. The megacolony, stationary centroid, retains resemblance to its initial geometry as the system evolves and as only cells on the colony's perimeter experience increased proliferation due to superior mobility; this behavior was found, along with the increased proliferation, in response to exposure to growth factors which are known to increase motility. That the stationary centroid case exhibits megacolony behavior to a greater extent than mobile centroid; this establishes the importance of anchorage-induced behaviors and the inclusion of their mechanics within models. The random seeding and wound closing cases, in Figure A.7, are presented as a qualitative validation of statistical behaviors of these systems.

Geometric dependencies in applicable cases can be observed in Figures Fig:allheal and A.4a. In Figure A.4a one should note that total confluence time depends on initial system geometry [37, 44] yet this is a more minor factor than the cell velocity and total motility time. As the stationary centroid case displays an increased division rate; thus generation of a greater number of cells within a less populated region guarantees a decreased rate of collision during diffusion. The mobile centroid case allows cells to diffuse prior to any division-action, this allows a more diffuse environment and minimizes negative effects associated with contact-inhibition. The random seeding case is examined due both to its prevalence in implementation and comparability. The additional time taken to achieve confluence in this case is a coupling of the worse traits of each the mobile centroid and stationary centroid cases. As the cells begin life in the mobile phase they have additional time prior to first division, yet with an initially random distribution the cells have an increasing likelihood of collision as their motion is not pseudo-uniform as in the mobile centroid case. With the total density of the system is placed in only a single direction with respect to the motion

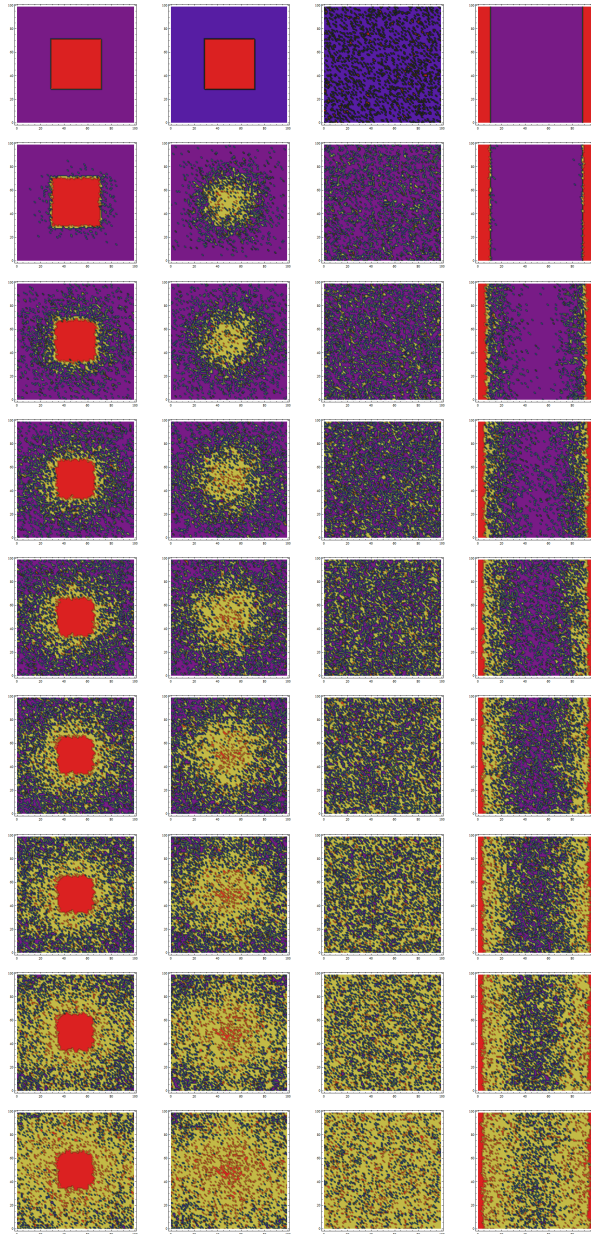


Figure A.7. Four simulations under our model, starting left: Stationary Centroid; Motile Centroid; Random Seeding; Wound Closing. The first row is the initial seeding condition, the second is the system at 20 % coverage and subsequent rows are at increments of 10 % more coverage.

of any individual cell, the centroid cases retain an increase in proliferation with the stationary, again, higher than the mobile due to the initial division.

A.5 Conclusions

We have expanded basic cellular automaton/agent models to accommodate for migration and proliferation of h-ECs within an infinite lattice by allowing a secondary state that determines division while a primary state determines motility. Increasing the total motility time, analogous to weakening the binding between lattice and cell, affects the system in specific and unique ways from increasing the average cellular velocity. Including have positive control over the confluence time of the system, whereas the cellular velocity does not allow for this degree of control. We have examined initial seeding cases where cells were placed with various geometries and in various phases of a cells life-cycle; these seeding states have little effect over the confluence time when compared to lattice binding. Through our expansion to the base model we have more adequately simulated anchorage dependent growth through description of binding affinities of cells to their lattice and this scheme allows for a greater degree of control and specificity in simulations and tissue growth.

A.6 Present and Future Directions

A.6.1 Indtroduction

Hypoxia is indicted as a major problem associated with disorders such as COPD, sleep apnea, hypertension and thromboembolisms. Many of the aforementioned disorders have associations with vascular thickening as well as both covert and overt cardiovascular diseases. Hypoxia in vascular settings triggers a complex signaling process whose end results include neovascularization, angiogenesis and clotting induced by insufficient secretion of heparin-sulfate into the lumen. Hypoxia instigates

a series of vascular-cell responses which promote re-oxygenation through extending transit networks and allow for anaerobic metabolisms forming lactic acid. The hypoxic response has also been found to promote carcinomas through hypoxia-induced apoptosis of vascular cells and to cause cerebral edema due to vascular leakage within the brain.

The hypoxic response is a cascade of gene expression, including that for: HIF-1, cGMP, ET-1, PDGF-B, HO-1 and smooth muscle cell-derived carbon monoxide in vascular cells. These signals can control specific cellular activities, such as Endothelin-1 acting as a mitogen for VSMCs, whose overall effects include angiogenesis, edema and Arteriosclerosis or CO contributing to the manufacturing of cGMP which modulates the coagulant function in Endothelial Cells. Hypoxia also triggers up-regulation of the A2B adenosine receptor phenotype; this up-regulation is accompanied by a down-regulation of the A2A phenotype gene expression and an increase in VEGF concentration. This adenosine signaling pathway was shown to be independent of HIF-1; although HIF-1 does not mediate expression of the A2B phenotype, it has been shown to promote angiogenesis by reducing cellular adhesion and up-regulating VEGF in both Bovine coronary artery and aortic smooth muscle cells.

As mentioned the end results of these hypoxic reactions in vascular cells is the creation of new vessel branches, the generation of new capillary beds as well as the thickening of existing vessels. Exploiting this increase in both proliferation and motility expressed during hypoxia could be of great benefit in the successful generation of engineered tissues for patient transplant in a timely manner. Engineering for the manufacturing of viable transplant tissues is making strides in the generation of bone, skin and vascular tissue culture and generation. It is towards expediting the manufacturing of viable transplant tissue that motivates this work.

A.6.2 Algorithm

These authors have generated a multi-state and multi-layered hybrid simulation of smooth muscle cells within a blood vessel. The hybrid nature of this simulation is the combining of a continuous set of differential equations defining the fluid dynamics within the system as well as a discrete cellular automaton model encompassing the behaviors and expressing the evolution of the smooth muscle cells within the fluid fields. We describe the behaviors of the SMC through a series of varying automaton states such as hypoxic, apoptotic-altered and normoxic. The multi-layered fluid dynamics includes reaction-diffusion mechanics of O₂, VEGF, and Endothelin-1. The constructed simulations follow the path presented in the algorithmic diagrams; Figure A.8 shows the overall simulation, whereas Figure A.9 shows the Automaton calculations for cell behaviors.

The smooth muscle cells being described within our simulations can exist with sets of states describing mobile and proliferating healthy cells, cells which are packed in a confluent manner and mobile and proliferating hypoxic cells. The automaton cell states include all of the aforementioned SMC states with the additional accessible state of being unoccupied. The SMC cells within the simulation will be periodically exposed to durations of hypoxia lasting roughly for 0, 6, 9, 12, 18 and 24 hours. It has been shown that SMC exposed to short duration of hypoxia have expressed lower times to confluence, yet those exposed to chronic hypoxia (periods of roughly 48 hours) have decreased cell populations. Experiments are shown in Table A.3

A.6.2.1. Fluid Dynamics

Herein we have developed a 3-D hybrid model which couples a continuous variable differential fluid dynamic system coupled to a discrete cellular automaton model. The fluid mechanics is described through the diffusion equation:

$$\frac{\partial c}{\partial t} = \nabla \cdot J + R(\rho, c) + S(\rho, c) + D_{\Omega}(c), \quad (\text{A.6})$$

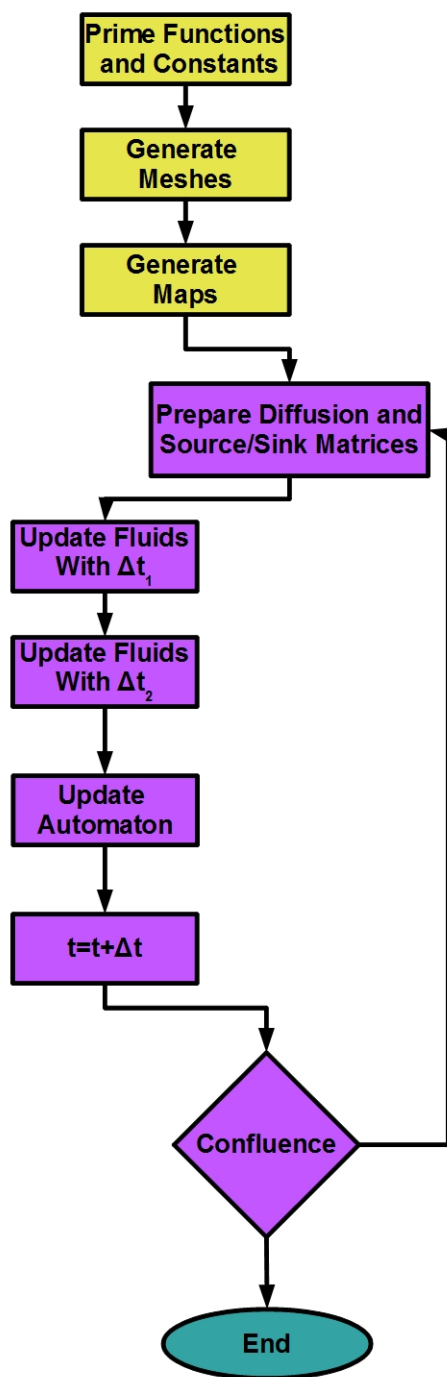


Figure A.8. A schematic representation of the overall algorithm used during the second phase of simulations.

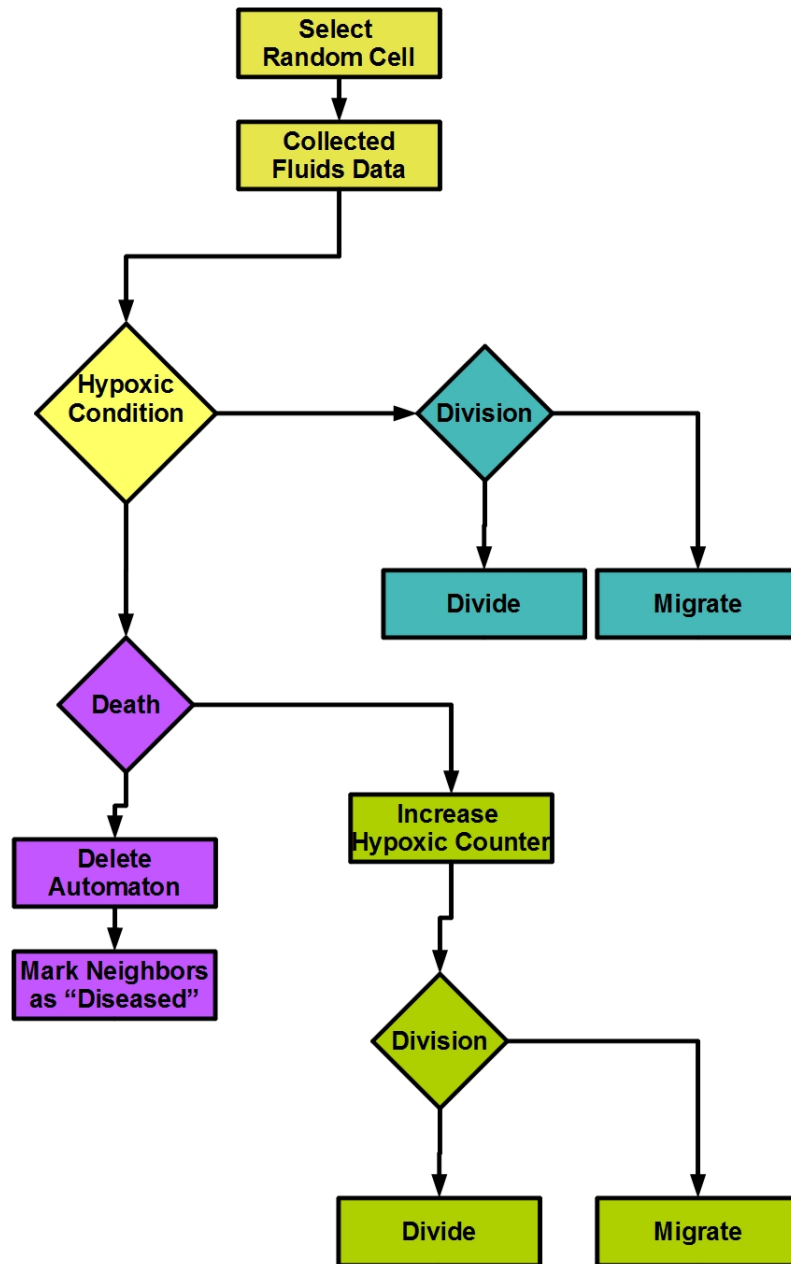


Figure A.9. A schematic representation of the cell specific portion of the algorithm used during the second phase of simulations.

Table A.3

Table containing experimental run data concerning the levels of hypoxia and duration of hypoxia to which cells are exposed.

Experiment Number	Normoxic Duration (h)	Hypoxic Duration (h)	Experiment Duration (days)
1	23.75	6.25	31.25
2	23.75	8.75	32.5
3	23.75	12.5	31.72
4	23.75	17.5	32.66
5	23.75	23.75	33.65
6	720	-	30

This equation is appended with terms describing local source (S) and sink (R) behaviors as well as the boundary condition D on surface Ω . J is the flux of the diffusive material, given by local density gradient:

$$J = (-D \cdot \nabla c). \quad (\text{A.7})$$

Within this work we will be neglecting any remaining drift velocity within the fluid bulk from the luminal flow, otherwise we would require the use of the Smoluchowski Equation; this approximation is likely as the ability for the material to enter into the scaffold requires a high relative velocity in the direction perpendicular to luminal flow and assuming the simulation takes place under dynamic equilibrium.

Equation A.6 will be moved to curvilinear coordinates to conform to the cylindrical geometry of the vascular system. This form is shown here:

$$\frac{\partial c}{\partial t} = D \left(\frac{1}{r} \frac{\partial}{\partial r} \left(r \frac{\partial c}{\partial r} \right) + \frac{1}{r^2} \frac{\partial^2 c}{\partial \varphi^2} + \frac{\partial^2 c}{\partial z^2} \right) + \left(\frac{\partial D}{\partial r} \frac{\partial c}{\partial r} + \frac{1}{r^2} \frac{\partial D}{\partial \varphi} \frac{\partial c}{\partial \varphi} + \frac{\partial D}{\partial z} \frac{\partial c}{\partial z} \right) - R(\rho, c) + S(\rho, c) + D_{\Omega}(c). \quad (\text{A.8})$$

This differential equation will be solved in a discrete manner over a curvilinear grid defining the geometry of the vessel. As terms within Equation A.8 require knowledge of the cell density, ρ , we will approximate the local cell density by γ :

$$\gamma(r, \varphi, z) = \begin{cases} 1, & \text{if cell at}(r, \varphi, z) \\ 0, & \text{if not cell at}(r, \varphi, z) \end{cases}. \quad (\text{A.9})$$

The time discretization is completed through a forward-differences method to prevent density leakage in the reverse-time direction, whereas for the spatial degrees central differencing was selected. Boundary conditions for the system were selected to recreate conditions with the vessel; the inner and outer conditions in the radial direction are dirichlet in nature, and the angular conditions are periodic to simulate a complete vessel. The boundary conditions in the z-direction depend on the seeding

conditions used in the simulation; for a uniform random seeding the z-directional boundary conditions are periodic and during a localizing seeding simulation this boundary condition is taken to be dirichlet.

The vascular system is geometrically modeled as a cylinder possessing an inner diameter and an outer diameter and a length; the diameters can define the thickness of the vessel wall and the diameter of the lumen. A regular grid dividing the solution space in the radial, angular and length directions is used to generate solutions to the diffusion equations governing each of the molecular signals and oxygen via a finite difference scheme.

The cells within the vessel have a constant diameter, d_{cell} , and pack in a confluent manner as the simulation completes; this means that the distance between the cells in the angular degree of freedom is defined by a fixed difference in circumference, Δc . The fluid mechanics is solved on a regular curvilinear grid, and therefore employs a specific $\Delta\varphi$ for all radii. These two grids do not align computational points, as seen in Figure A.10. This misalignment means that the locations of the cells acting as the sources/sinks of Equation A.9 do not agree with the computational points on which Equation A.8 is solved, so we must redistribute the effect of the source/sink amongst the nearest computational points. As Δr and Δz do not suffer from the misalignment as does $\Delta\varphi$, we have redistributed the sources/sinks along the φ -direction through a linear fit of the form:

$$S_i = S_k \frac{\varphi_i - \varphi_k}{\Delta\varphi}; S_j = S_k (1 - S_i). \quad (\text{A.10})$$

The above describes the redistribution of a source/sink, S , within the automaton space at k , where k 's coordinates place it between computational points i and j in the φ -degree of freedom at the same r and z ordinates; this procedure does not change the r and z coordinates for the above mentioned reason. This allows the two grids to agree for the computations required within the hybrid calculation. Examples of the fluid grid are given in Fig. A.11, where (a) is a 15° second of a vascular region defining

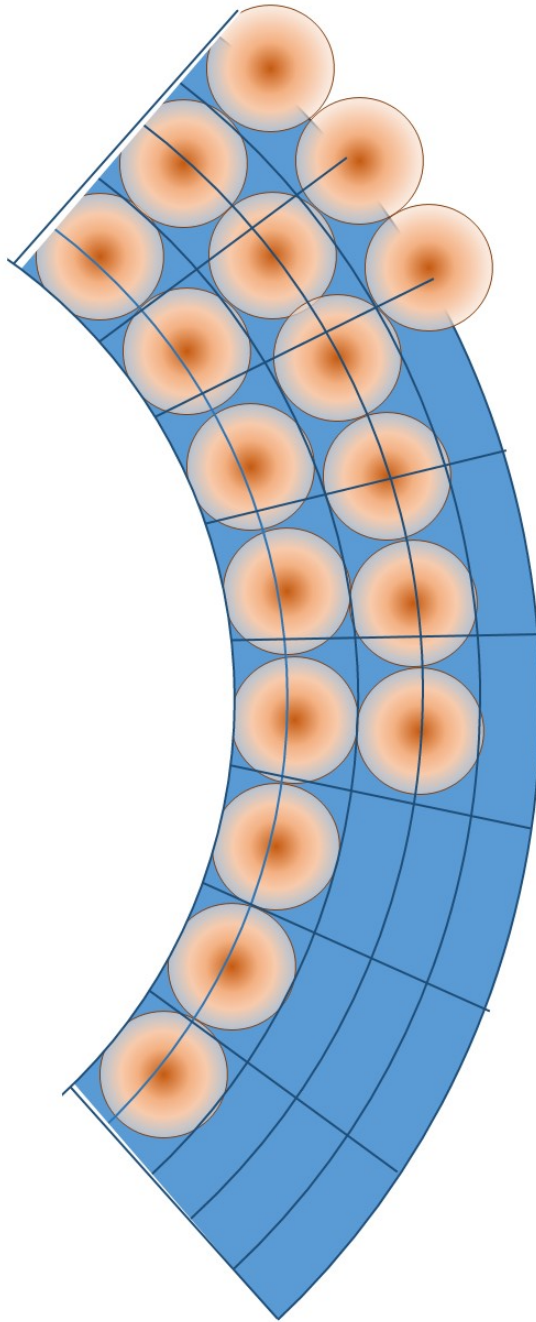


Figure A.10. A schematic representation of disagreement between the fluid dynamic computational grid and the cellular automaton grid.

the solution space, (b) displays the mesh interactions representing fluid computational points and (c) shows fluid diffusion within the mesh system from a single source point.

A.6.3 Cellular Automatons

Cellular automaton are a discrete model first developed by Ulam and Von Neumann at Los Alamos National Laboratory. The facets of CA models include: a discrete grid which is finite in any number of direction, each cell within the grid may exist within a finite number of states, each cell has a defined number of neighbor cells, all cells evolve generationally in time according to sets of pre-defined rules. Typically the rules for updating cells is uniform among the entire populous; these authors have opted to employ a series of possible states with non-uniform evolutionary constants and rules as this best describes the situation existing within the evolving seeded lattice.

Within this model we have opted for the use of the full three dimensional Von Neumann neighborhood consisting of the 26 neighboring automaton. The time-evolution was performed in an asynchronous manner as this is representative of the natural evolution of the system. This asynchronous evolution will be performed by randomly selecting a single occupied automaton at a time for evolution, and cycling through all automata per time-step. The vector directions are assigned through a three-dimensional Markov turner, seen in Figure. A.12.

The automaton grid is initialized with only its index, coordinates and unoccupied state designation. An initial seeding probability of .79% was selected consistent with other works; this seeding probability was employed through a random selection algorithm over all automata thus generating the initial conditions for a random seeding event. A wound-healing scenario is also employed were a confluent seeding layer is placed on the $z = 0$ boundary of the modeling space, the number of seeded layers will conform to the ceiling-round of .79% occupancy. The simulation will begin at the start of a normoxic term within the periodic oxygenation cycle, and as such all

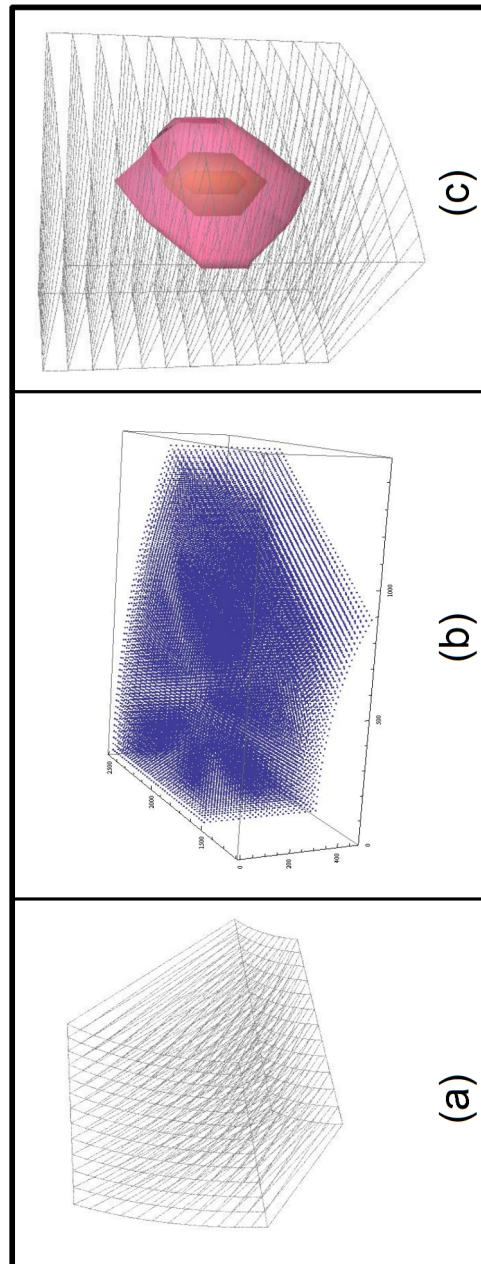


Figure A.11. Visualizations of the solution space for the vascular system. a) the solution space with grid-skeleton. b) computational mesh points for fluid mechanics. c) visualization of fluid diffusion within mesh environment.

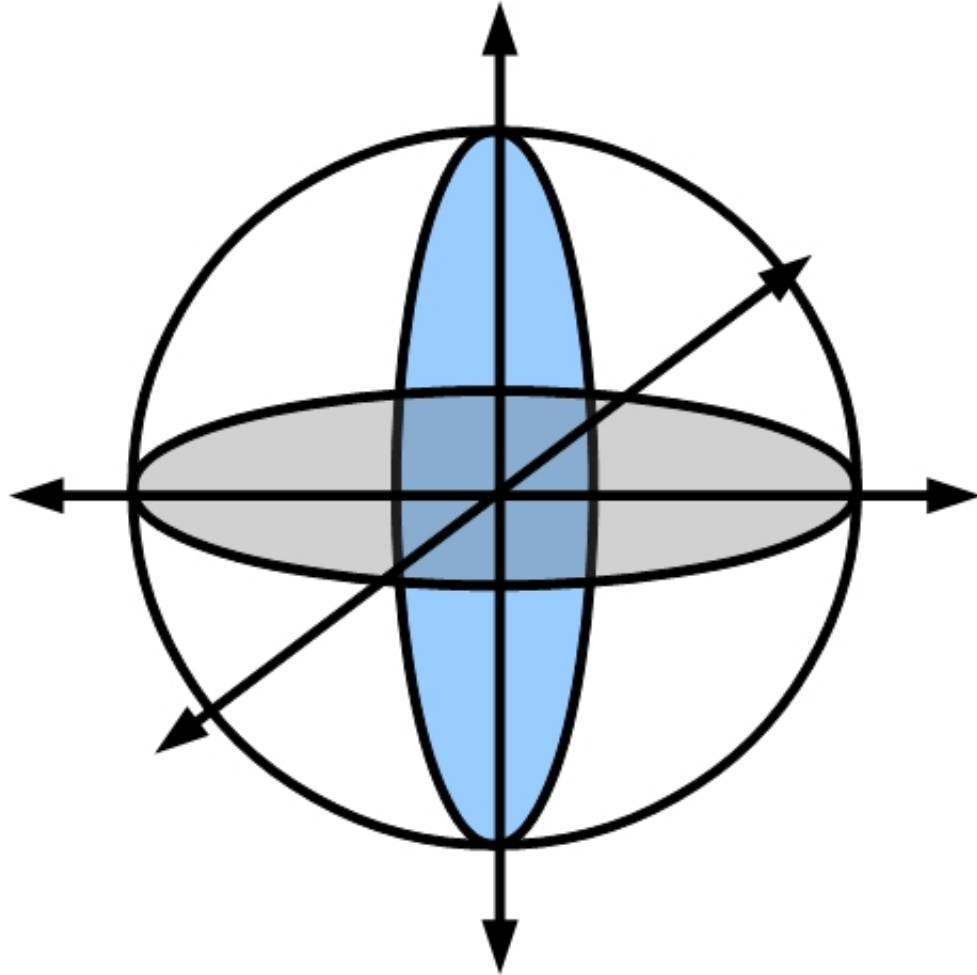


Figure A.12. An example of a three dimensional Markov Turner for the vector definitions within a discrete automaton system.

constants within the automaton vector will be randomly selected through a Gamma Distribution constructed about the average value determined in experiment.

A.7 References

- [1] Langer, R. and Vacanti, J .P. 1993. Tissue Engineering. *Science* 260, 920-926.
- [2] Mooney, D. J. and Mikos, A .G. 1999. Growing New Organs. *Sci. Am.* 280, 60-65.
- [3] Lemon, G., Howard, D. and Tomlinson, M. J. 2009. Mathematical modeling of tissue-engineered angiogenesis *Math. Biosci.* 221. 101-120.
- [4] Harley, B. A. C. and Gibson L. J. 2008. In vivo and in vitro applications of collagen-GAG scaffolds. *Chem. Eng. J.* 137, 102-121.
- [5] Lim, C. T. Zhou, E. H. and Quek, S. T. 2006. Mechanical models for living cells: a review. *J. Biomech.* 39, 195-216.
- [6] Dallon, J. C., Sherratt, J. A. and Maini, P. K. 1999. Mathematical Modeling of Extracellular Matrix Dynamics using Discrete Cells: Fiber Orientation and Tissue Regeneration. *J. Theor. Biol.* 199, 449-471.
- [7] Singh, H., Teoh, S. H. and Low, H. T. 2005. Flow modeling within a scaffold under the influence of uni-axial and bi-axial bioreactor rotation. *J. Biotechnol.* 119, 181-196.
- [8] Stylianopoulos, T., Bashur, C. A. and Goldstein, A. S. 2008. Computational predictions of the tensile properties of electrospun fiber meshes: Effects of fiber diameter and fiber orientation. *J. Mech. Bhvr. Biomed. Mtrls.* 1, 326-335.
- [9] Harley, B. and Kim, H .K. 2008. Microarchitecture of Three-Dimensional Scaffolds Influences Cell Migration Behavior via Junction Interactions. *Biophys. J.* 95, 4013-4024.
- [10] Jacobsen, J. C. B., Hornbech, M. S. and Holstein-Rathlou, N. 2009. A tissue in the tissue: Models of microvascular plasticity. *Pharm. Sci.* 36, 51-61.
- [11] Byrne, D. P., Lacroix, D., Planell, J. A., Kelly, D. J., and Prendergast, P. J. 2007. Simulation of tissue differentiation in a scaffold as a function of porosity, Young's modulus and dissolution rate: Application of Mechanobiological models in tissue engineering. *Biomaterials* 28, 5544-5554.
- [12] Wu, X. and Black, L. 2006. Preparation and assessment of Glutaraldehyde-Crosslinked Collagen-Chitosan Hydrogels for Adipose Tissue Engineering. *J. Biomed. Mater. Res. A.* 81, 59-65.
- [13] Dang, J. M. and Leong, K .W. 2006. Natural Polymers for Gene Delivery and Tissue Engineering. *Adv. Drug Deliv. Rev.* 58, 487-499.
- [14] Eylich, D. and Brandl, F. 2007. Long-Term Stable Fibrin Gels for Cartilage Engineering. *Biomaterials* 28, 55-65.

- [15] Cao, D. and Liu W. 2006. In vitro Tendon Engineering with Avian Tenocytes and Polyglycolic Acids: A preliminary Report. *Tissue Eng.* 12, 1369-1377.
- [16] Fisher, J. P. and Jo, S. 2004. Thermoreversible Hydrogel Scaffolds for Articular Cartilage Engineering *J. Biomed. Mater. Res.* 71, 268-274.
- [17] Sedrakyan, S. and Zhou, Z .Y. 2006. Tissue Engineering of a Small Hand phalanx with a Porously Casted Polylacttic Acid-Polyglycolic Acid Coolymer *Tissue. Eng.* 12, 2675-2683.
- [18] Sengers, B. G., Taylor, M. and Please, C. P. 2007. Computational modeling of cell spreading and tissue regeneration in porous scaffolds. *Biomaterials* 28, 1926-1940.
- [19] Luong, L. N. and Hong, S. I. 2006. Spatial Control of Protein within Biomimetically Nucleated Mineral. *Biomaterials* 27, 1175-1186.
- [20] Yang, X. B. and Roach, H. I. 2001. Human Osteoprogenitor Growth and Differentiation on Synthetic Biodegradable Structures after Surface Modifications. *Bone.* 29, 523-531.
- [21] Tremel, A., Cai, A. and Tirtaatmadja, N. 2009. Cell migration and proliferation during monolayer formation and wound healing. *Chem. Eng. Sci.* 64, 247-253.
- [22] Kladakis, S. and Nerem, R. 2004. Endothelial Cell Monolayer Formation: Effect of Substrate and Fluid Shear Stress. *Endothelium* 11, 29-44.
- [23] Liu, X. and Wei, L. 2005. Surface Engineering of Nanofibrous Poly(l-lactic acid) Scaffolds via Self-Assembly Technique for Bone Tissue Engineering. *Journal of Biomedical Nanotechnology* 1, 54-60.
- [24] Tracqui, P. 1995. From Passive Diffusion to Active Cellular Migration in Mathematical Models of Tumor Invasion. *Acta Biotheor.* 43, 443-464.
- [25] Maini, P. K., McElwain, D. L. S. and Leavesley, D.I. 2004. Traveling Wave Model to Interpret a Wound-Healing Cell Migration Assay for Human Peritoneal Mesothelial Cells. *Tissue Engineering* 10. 475-482.
- [26] Ai, S. 2008. Traveling waves in the modeling of aerosolized skin grafts. *Physica D.* 237, 2761-2766.
- [27] Cai, A. Q., Landman, K. A. and Hughes, B. D. 2007. Multi-scale modeling of a wound-healing cell migration assay. *J. Theor. Biol.* 245, 576-594.
- [28] Merks, R. M. H. and Glazier, J. A. 2006. Dynamic mechanisms of blood vessel growth. *IOP* 10, C1-C10.

- [29] Cavalli, F. and Gamba, A. 2007. 3D Simulations of Early Blood Vessel Formation. *J. Comput. Phys.* 225, 2283-2300.
- [30] Javierre, E., Vermolen, F. J. and Vuijk, C. 2009. A mathematical analysis of physiological and morphological aspects of wound closure. *J. Math. Biol.* 59, 605-630.
- [31] Morel, D., Marcelpoil, R. and Brugal, G. 2001. A Proliferation Control Network Model: The Simulation of Two-Dimensional Epithelial Homeostasis. *Acta Biotheor.* 49, 219-234.
- [32] Forestell, S. P., Milne, B. J. and Kalogerakis, N. 1992. A Cellular Automaton Model for the Growth of Anchorage-Dependent Mammalian Cells Used in Vaccine Production. *Chem. Eng. Sci.* 47, 2381-2386.
- [33] Prez, M. A. and Prendergast, P. J. 2007. Random-walk models of cell dispersal included in mechanobiological simulations of tissue differentiation. *J. Biomech.* 40, 2244-2253.
- [34] Zygourakis, K., Bizios, R. and Markensco, P. 1991. Proliferation of Anchorage-Dependent Contact-Inhibited Cells. I: Development of Theoretical Models Based on Cellular Automata. *Biotechnol. Bioeng.* 38, 459-470.
- [35] Cheng, G., Youssef, B. B., Markensco, P. and Zygourakis, K. 2006. Cell Population Dynamics Modulate the Rates of Tissue Growth Processes. *Biophys. J.* 90, 713-724.
- [36] Chung, C. A., Lin, T. and Chen, S. 2010. Hybrid cellular automation modeling of nutrient modulated cell growth in tissue engineering constructs. *J. Theor. Biol.* 262, 267-278.
- [37] Cheng, G., Markensco P., and Zygourakis, K. 2009. A 3D Hybrid Model for Tissue Growth: The Interplay between Cell Population and Mass Transport Dynamics. *Biophys. J.* 97, 401-414.
- [38] Pisu, M., Concas, A. and Cao, G. 2007. A novel simulation model for stem cells differentiation. *J. Biotechnol.* 130, 171-182.
- [39] Simpson, M. J., Landman, K. A. and Hughes, B. D. 2006. Looking inside an invasion wave of cells using continuum models: Proliferation is the key. *J. Theor. Biol.* 243, 343-360.
- [40] Ferreira, Jr. S. C., Martins, M. L. and Vilela, M. J. 2002. Reaction-diffusion model for the growth of avascular tumor *Phys. Rev. E.* 65, 021907-1-021907-8.
- [41] Moreira, J. and Deutsch, A. 2002. Cellular Automaton Models of Tumor Development: A Critical Review. *ACS.* 5, 247-267.

- [42] Simpson, M. J., Landman, K. A. and Bhaganagarapu, K. 2007. Coalescence of interacting cell populations. *J. Theor. Biol.* 247, 525-543.
- [43] Shirinifard, A., Gens, J. S. and Zaitlen, B. L. 2009. 3D Multi-Cell Simulation of Tumor Growth and Angiogenesis. *PLoS ONE.* 4, 1-11.
- [44] Zygourakis, K., Markensco, P. and Bizios, R. 1991. Proliferation of Anchorage-Dependent Contact-Inhibited Cells. II: Experimental Results and Validation of the Theoretical Models. *Biotechnol. Bioeng.* 38, 471-479.
- [45] Lee, Y., Kouvroukoglou, S. and McIntire, L. V. 1995. A Cellular Automaton Model for the Proliferation of Migrating Contact-Inhibited Cells *Biophys. J.* 69, 1284-1298.
- [46] Zaleskas, J. M. and Kinner, B. 2004. Contractile Forces Generated by Articular Chondrocytes in Collagen-Glycosaminoglycan Matrices *Biomaterials.* 25, 1299-1308.
- [47] Alberts, B. and Bray, D. 1989. *Molecular Biology of the Cell.* Garland Publishing. New York
- [48] Thilo-Korner, D. G. S. and Freshney, R. I. 1983. *The Endothelial Cell A Pluripotent Control Cell of the Vessel Wall.* Karger Publishers. Basel, Switzerland.
- [49] Lee, Y. and Markensco, P. A. 1995. Characterization of Endothelial Cell Locomotion Using a Markov Chain Model. *Biochem. Cell Biol.* 73, 461-472.
- [50] Grotendorst, G. R. and Seppa H. 1981. Attachment of Smooth Muscle Cells to Collagen and their Migration toward platelet-derived Growth Factor. *Proc. Natl. Acad. Sci. USA.* 78, 3669-3672.
- [51] Ross, R. 1993. The Pathogenesis of Atherosclerosis: A Perspective for the 1990s. *Nature.* 1993, 362, 801-809.
- [52] Schwartz, S. M. and Gajdusek, C. M. 1980. Maintenance of Integrity in Aortic Endothelium. *Fed. Proc.* 39, 2618-2625.
- [53] Re, F. and Zanetti, A. 1994. Inhibition of Anchorage-dependent Cell Spreading Triggers Apoptosis in Cultured Human Endothelial Cells. *J. Cell. Biol.* 127, 537-546.
- [54] Frame, K. K. and Hu, W. S. 1988. A model for density-dependent growth of anchorage-dependent mammalian cells. *Biotechnol. Bioeng.* 32, 1061.
- [55] Folkman, J. and Moscona, A. 1978. Role of cell shape in growth control. *Nature.* 273, 345.

- [56] Gottlieb, A. I. and Spector, W. 1984. In vitro reendothelialization: microfilament bundle reorganization in migrating porcine endothelial cells. *Arteriosclerosis*. 4, 91.
- [57] Ashara, T. 1999. Bone Marrow Origin of Endothelial Progenitor Cells Responsible for Postnatal Vasculogenesis in Physiological and Pathological Neovascularization. *Circularization Research* 85, 2218.
- [58] Ruaan, R. C. and Tsai, G. J. 1992. Monitoring and Modeling Density-Dependent Growth of Anchorage-Dependent Cells. *Biotechnol. Bioeng.* 41, 380-389.
- [59] Friedl, Y. and Brocker, E .B. 2000. The Biology of Cell Locomotion within Three-Dimensional Extracellular Matrix. *Cell. Mol. Life Sci.* 57, 41-64.
- [60] Lee, Y. and Green, H. 1994. Computer-assisted Analysis of Endothelial Cell Migration and Proliferation Ph. D. Thesis, Rice University, Houston Texas.
- [61] Lee, Y. and McIntire, L .V. 1994. Analysis of Endothelial Cell Locomotion: Differential Effects of Motility and Contact Inhibition. *Biotechnol. Bioeng.* 43, 622-634.
- [62] Boyrsky, A. and Noble P. B. 1977. A Markov Chain Characterization of Human Neutrophil Locomotion under Neutral and Chemotactic Conditions. *Can. J. Physiol. Pharmacol.* 55, 1-6.
- [63] Barrandon, Y. and Green H., 1987. Cell Migration is Essential for Sustained Growth of Keratinocyte colonies: The Roles of Transforming Growth Factor and Epidermal Growth Factor. *Cell* 50, 1131-1137.
- [64] Jakobsson, L., Kreuger, J. and Claesson-Welsh, L. 2007. Building blood vessels stem cell models in vascular biology. *J. Cell. Biol.* 177, 751-755.
- [65] Ju, Y. M. and Choi, J .S. 2010. Bilayered Scaffolding for Engineering Cellularized Blood Vessels *Biomaterials* 31, 4313-4321.

APPENDIX B. PATENT APPLICATION

The following pages are the formal submission to the United States Patent Office concerning works discussed within the main body of the thesis.

Electronic Acknowledgement Receipt	
EFS ID:	19871469
Application Number:	62037457
International Application Number:	
Confirmation Number:	5515
Title of Invention:	Determination Of The Activation Strength Of Drug Molecules
First Named Inventor/Applicant Name:	Sabre Kais
Customer Number:	11660
Filer:	Pervin Rusi Taleyarkhan
Filer Authorized By:	
Attorney Docket Number:	66840-01
Receipt Date:	14-AUG-2014
Filing Date:	
Time Stamp:	17:31:03
Application Type:	Provisional

Payment information:

Submitted with Payment	yes
Payment Type	Credit Card
Payment was successfully received in RAM	\$ 130
RAM confirmation Number	3937
Deposit Account	
Authorized User	

File Listing:

Document Number	Document Description	File Name	File Size(Bytes)/ Message Digest	Multi Part /.zip	Pages (if appl.)
-----------------	----------------------	-----------	-------------------------------------	------------------	------------------

1	Provisional Cover Sheet (SB16)	66840-01_Provisional_Cover_Sheet.pdf	1477473 1a57587c715e391747c227a292c765fca78e48d6	no	3
Warnings:					
Information:					
2	Specification	66840-01_App_FINAL-995.pdf	5616540 9d0968ba2f5970c2207e4faf6b807c114bd38840	no	26
Warnings:					
Information:					
3	Drawings-other than black and white line drawings	66840-01_FIGURES-995.pdf	12785933 109eb24025abf851c2b0daec9898fa51efff362	no	20
Warnings:					
Information:					
4	Appendix to the Specification	66840-01_Appendix-A-995.pdf	2455212 969453c6aec7eea3965f095395dd1f379c6b1d77	no	6
Warnings:					
Information:					
5	Appendix to the Specification	66840-01_Appendix-B-995.pdf	1061880 16d5c7a9f75ab517f1ea55dcdff83f4847f05e180	no	10
Warnings:					
Information:					
6	Appendix to the Specification	66840-01_Appendix-C-995.pdf	2070999 e3a3089fb408d957ee1e52130000ee487e959dff	no	9
Warnings:					
Information:					
7	Appendix to the Specification	66840-01_Appendix-D-995.pdf	3867555 ae6a2c80c4733adfbef6870eded6647494f3bab84	no	7
Warnings:					
Information:					
8	Appendix to the Specification	66840-01_Appendix-E-995.pdf	8676532 07b0294d0b488b20595a8af78586e80358198751	no	15
Warnings:					
Information:					
9	Fee Worksheet (SB06)	fee-info.pdf	29434 f2541f8da14344ace12fe3c251e7d9fd872390	no	2
Warnings:					
Information:					

Total Files Size (in bytes):	38041558
------------------------------	----------

This Acknowledgement Receipt evidences receipt on the noted date by the USPTO of the indicated documents, characterized by the applicant, and including page counts, where applicable. It serves as evidence of receipt similar to a Post Card, as described in MPEP 503.

New Applications Under 35 U.S.C. 111

If a new application is being filed and the application includes the necessary components for a filing date (see 37 CFR 1.53(b)-(d) and MPEP 506), a Filing Receipt (37 CFR 1.54) will be issued in due course and the date shown on this Acknowledgement Receipt will establish the filing date of the application.

National Stage of an International Application under 35 U.S.C. 371

If a timely submission to enter the national stage of an international application is compliant with the conditions of 35 U.S.C. 371 and other applicable requirements a Form PCT/DO/EO/903 indicating acceptance of the application as a national stage submission under 35 U.S.C. 371 will be issued in addition to the Filing Receipt, in due course.

New International Application Filed with the USPTO as a Receiving Office

If a new international application is being filed and the international application includes the necessary components for an international filing date (see PCT Article 11 and MPEP 1810), a Notification of the International Application Number and of the International Filing Date (Form PCT/RO/105) will be issued in due course, subject to prescriptions concerning national security, and the date shown on this Acknowledgement Receipt will establish the international filing date of the application.

Please wait...

If this message is not eventually replaced by the proper contents of the document, your PDF viewer may not be able to display this type of document.

You can upgrade to the latest version of Adobe Reader for Windows®, Mac, or Linux® by visiting http://www.adobe.com/go/reader_download.

For more assistance with Adobe Reader visit <http://www.adobe.com/go/acrreader>.

Windows is either a registered trademark or a trademark of Microsoft Corporation in the United States and/or other countries. Mac is a trademark of Apple Inc., registered in the United States and other countries. Linux is the registered trademark of Linus Torvalds in the U.S. and other countries.

66840-01

Determination Of The Activation Strength Of Drug Molecules

TECHNICAL FIELD

[0001] The present disclosure generally relates to the determination of the activation strength of drug molecules, and in particular to a method for predicting activation strength of drug molecules with G-Protein Coupled Receptors (GPCRs).

BACKGROUND

[0002] This section introduces aspects that may help facilitate a better understanding of the disclosure. Accordingly, these statements are to be read in this light and are not to be understood as admissions about what is or is not prior art.

[0003] G-Protein Coupled Receptors (GPCRs) are the target for the greatest portion of modern therapeutic small molecule medications. Activation of GPCRs govern many physiological activities, examples of which include olfaction, central nervous system regulation, and maintaining circadian rhythm. Roughly half of all modern small molecule therapeutics target this class of proteins and 50% of all human encoded GPCR genes encode for olfaction alone. Understanding the mechanism by which activation of this class of proteins is achieved is paramount to applications within both the pharmaceutical and the flavor/scent industries.

[0004] Current methods by which the relative activation strength of drug molecules with GPCRs is predicted involve docking studies, which show the binding of the drug with the protein. However, such methods do not provide insight into the mechanism, nor does it provide the

66840-01

ability of the drug to activate the receptor. There is thus an unmet need for methods of predicting the relative strength of drug molecules. Such methods are particularly useful for purpose of predictive ability in silico drug discovery.

66840-01

DETAILED DESCRIPTION

[0005] For the purposes of promoting an understanding of the principles of the present disclosure, reference will now be made to the embodiments illustrated in the drawings, and specific language will be used to describe the same. It will nevertheless be understood that no limitation of the scope of this disclosure is thereby intended.

[0006] Predictability of pharmacological efficacy for new drugs prior to a complex total synthesis may be aided by pharmacore modeling or with either crystal structure or a homology model. The theory of protein/agonist binding has been described through variants of the Lock and Key model, originally proposed by Fisher and the extensions thereof. Although this theory has provided insight into changes of free energy associated with the formation of the activated complex, it has not manifested sufficient capacity for the prediction of ligand activity or a mechanism by which the agonist activates the system.

[0007] A recent resurgence of interest for a vibrational-based theory of protein activation has occurred, featuring inelastic electron tunneling spectroscopy (IETS) as its possible means of detecting the vibrational modes of the bound ligand. The IETS mechanism relies on a field driven electron transfer across an insulating gap situated between two conductive metal plates. The driving field promotes electrons to tunnel from the donor site on one side of the gap to the acceptor site on the other side; this is the elastic process. As the intensity of the driving field is increased, the electrons may donate a quanta of energy to a molecule situated within the gap along their path. This exchange of energy must be equal to a quanta accepted by the molecule's vibrational or electronic transitions. This secondary mechanism provides a new path which

66840-01

enhances the current across the gap. There exist several other mechanisms by which electrons are conveyed across the gap including elastic transfer, inelastic transfer, 2nd order elastic transfer as well as subsequent and less contributing modes of transport. The theoretical description of this mechanism was introduced by Lambe, Jaklevic Scalapino, Hansma and Kirtley and later elucidated by Phillips and Adkins (References [39], [34] – [36], [1], and [50], respectively).

[0008] Calculations of Inelastic Electron Tunneling rates have been performed in various ways throughout the literature. Typically the Barden Transfer Hamiltonian method is employed to allow for the calculation of the elastic contribution from the tunneling wavefunctions across the barrier sides. The WKB approximation is used to describe the wavefunction of the tunneling electrons from each side; the following Equations 1 and 2 are the evanescent wavefunctions describing an electron traversing a gap of length d defined by two conductive plates of area L^2 :

$$\varphi_1 = (A/L)e^{ik_{\parallel}r}e^{-\alpha_0z} \quad (1)$$

$$\varphi_2 = (A/L)e^{ik'_{\parallel}r}e^{-\alpha_0(d-z)} \quad (2)$$

where α_0 is the decay constant of the tunneling electron in the z^{th} direction, k_{\parallel} and k'_{\parallel} are the momentum parallel to the surfaces and A is the normalization constant.

[0009] Referring to FIG. 1a, a cartoon description of the formate ion within the gap is presented. Still referring to FIG. 1a, the distance parameters a and d are shown for clarity, where d represents the total length of the gap and a is the distance between the nearest wall and a particular atom. The experimentally resolved spectra for this system is presented in FIG. 1b.

[0010] As the electrons tunnel through the barrier they may undergo several processes including: elastic transfer, inelastic transfer, 2nd order elastic transfer and subsequent less contributing modes of transfer. The inelastic modes of transport are facilitated through interaction between

66840-01

the tunneling electron and a deposited molecule within the gap; the tunneling electron donates of quanta of energy to the deposited molecule. The donation of energy from the electron to the molecule must obey Fermi's Golden Rule, according to Equation 3:

$$T_{i \rightarrow f} = \frac{2\pi}{\hbar} |\langle \varphi_f | \hat{U} | \varphi_i \rangle|^2 \delta(E_f - E_i \pm \hbar\omega) \quad (3)$$

where $T_{i \rightarrow f}$ is the probability of an electron transferring from state i to state f , with the stationary state wavefunctions φ_i and φ_f ; \hat{U} is the interaction potential to be discussed and δ is the Kronecker delta function depending on the energies of the states and the quanta absorbed by the deposited molecule. The quantum of energy is typically in the range of vibrations for IETS, although electronic excitations have also been achieved experimentally.

[0011] The electronic interaction between the ligand and the molecule treats each atom of the molecule separately; each atom is assigned a partial charge, Z , and sits at its equilibrium positions, R , it vibrates with displacement u . The interaction potential is that of an electron and single dipole and is given by Equation 4:

$$\hat{U}(r, \theta, z) = \left(\frac{Z e^2}{4\pi \epsilon_0 \epsilon_r} \right) \frac{u \cdot (R - r)}{|R - r|^3}. \quad (4)$$

[0012] As the interaction is between the electron and a single atom of the molecule, the contribution to the conductivity found through this calculation must be repeated and summed over all atoms within the molecule.

[0013] To determine the contribution to the conductivity of any mode of transport, the tunneling matrix element is calculated. In the case of the elastic mode the tunneling matrix element, M_e , is calculated as the overlap of the wavefunctions from the donor and acceptor sites over the volume of the gap since this mechanism does not require interaction with the deposited molecule. The

66840-01

calculation of the tunneling matrix element for the inelastic transport to the contribution utilizes both the donor and acceptor wavefunctions and the interaction potential is given by Equation 5:

$$M_{in} = \left(A^2 / L^2 \right) e^{-\alpha_0 d} e^{iq \cdot R} \int_0^\infty \int_0^{2\pi} \int_0^d e^{iq \cdot r} \hat{U}(r, \theta, z) r dz d\theta dr. \quad (5)$$

[0014] Within Equation 5, q is the change in parallel momentum defined as $q = k'_{\parallel} - k_{\parallel}$.

[0015] These tunneling matrix elements act as probability factors in the calculation of the conductivity. IETS's enhancement in the current is related to alterations in the conductivity through the additional transport paths associated with the inelastic transport utilizing the atomic oscillators. The calculation of the ratio between inelastic contribution and the elastic contribution for a single atomic interaction with the electron can be calculated through Equation 6:

$$\frac{\Delta\sigma}{\sigma_e} = \left[\frac{1}{M_e} \right]^2 \int_0^\infty M_A^2 e^{\left(-q^2 d / 4\alpha_0 \right)} \frac{L^2}{2\pi} q \propto \int_0^\infty M_A^2 e^{\left(-q^2 d / 4\alpha_0 \right)} q dq = I_A(a, d) Z_A^2 u_A^2. \quad (6)$$

[0016] The *l.h.s.* (left-hand side) of the proportionality is the integral form proposed by Phillips and Adkins. Whereas the *r.h.s.* (right-hand side) is a simplification through elimination of all constants within the calculation, it is taken as arbitrary units but is proportional to the strict calculation through multiplication of a constant.

[0017] FIG. 2 provides a display of the normal modes of the formate ion for association with the intensities and spectra below. Also included within FIG. 2 is a unit vector indicator as to the direction and magnitude of displacement, given in a.u., and frequency in cm^{-1} (frequencies are displayed beneath the mode to which it belongs).

66840-01

[0018] Point Dipole Approximation:

[0019] The most fundamental expression for the interaction between an electron and a charged dipole is given by Equation 7:

$$V = \frac{z_i(-z_j)e^2}{4\pi\epsilon_0} \frac{1}{|r_j - r_i|} + \frac{z_i z_j e^2}{4\pi\epsilon_0} \frac{1}{|r_j + p_j - r_i|} \quad (7)$$

where r_i is the location of the electron providing a field $z_i e^2$ and r_j is location of a single side of the dipole where both ends provide a field with the magnitude $z_j e^2$; the second term describes the remaining, oppositely charged side of the dipole at a distance p_j from the other end.

Recollection of the terms yields the expression in Equation 8a, and a subsequent Taylor series expansion for the denominator yields Equation 8b.

$$V = \frac{-z_i z_j e^2}{4\pi\epsilon_0} \left(\frac{1}{r_{ji}} - \frac{1}{\sqrt{r_{ji}^2 + 2\vec{r}_{ji} \cdot \vec{p}_j + p_j^2}} \right) \quad (8a)$$

$$\cong \frac{z_j z_i e^2}{4\pi\epsilon_0 r_{ji}} \left(\frac{1}{2} \frac{\vec{r}_{ji} \cdot \vec{p}_j}{r_{ji}^2} + \frac{1}{2} \frac{p_j^2}{r_{ji}^2} - \frac{3}{8} \left(\frac{2\vec{r}_{ji} \cdot \vec{p}_j}{r_{ji}^2} + \frac{p_j^2}{r_{ji}^2} \right)^2 \right) \quad (8b)$$

[0020] After the series expansion, the point dipole approximation is typically employed; this approximation states that the distance between the charge and the dipole is much greater than the displacement between the dipole termini, $r_{ji} \gg p_j$. Under the point dipole approximation, all but the leading terms of Equation 8a drop due to minimal contribution, as seen in Equation 9.

$$V \approx \frac{z_i e}{4\pi\epsilon_0} \frac{\vec{r}_{ji} \cdot \vec{\mu}_j}{r_{ji}^3} = \frac{z_j z_i e^2}{4\pi\epsilon_0} \frac{\vec{r}_{ji} \cdot \vec{u}_j}{r_{ji}^3} \quad (9)$$

[0021] It is important to note that the spatial dimensions of the activation site within this class of proteins has been suggested to be roughly 15Å. The suggested dimensions of the active site,

66840-01

when compared to that of the displacement vector, do not meet the criteria for the point dipole approximation. Considering the system is possibly inappropriate for application of the point dipole approximation, comparing the numerical values for the tunneling matrix elements as calculated by Equation 5 using the interaction potential Equation 4 and the more complete form of the interaction potential in Equation 8a. FIG. 3 shows the relative error associated with using the point dipole approximation with the spatial scale of the active site (i.e., the percent relative error between variations of the interaction potentials given in Equation 4 and Equation 8a; this was completed for several values of θ to emphasize the angular dependence stemming from projection operations in terms eliminated through approximation). It should be noted that the error associated with this misuse of the approximated potential is peaked in the range of the active site length scale. As the point dipole approximation eliminates terms which are dependent upon the projection, $r_{ji} \cdot p_j$, there exists an angular dependence on the magnitude of the tunneling matrix element. This angular dependence can be observed in FIG. 3, and is due to the projector in terms eliminated during application of the point dipole approximation; the magnitude of the relative error is proportional to the cosine of the angle, and then we observe an oscillatory component to the θ dependence.

[0022] Polarizability

[0023] As a method for obtaining information about the vibrational modes of a molecule, IETS does not rely on the interactions between the molecular dipole and the field of the electron. The interaction potential, Equation 4, is that between an electron and a single oscillating dipole, representative of a vibrating atom within the molecule. This interaction does not depend upon the polarizability of the system nor the change in net dipole. The single-dipole nature of the

66840-01

potential requires a summation over the atoms within the molecule to account for all possible interactions.

[0024] The ratio given in Equation 6 is characteristic of the enhancement to the conductivity due to single atom motions. If this were the only responsible contribution to 1st order inelastic conduction than the symmetric modes, corresponding to Raman transitions, would not appear in IETS, yet they do and with roughly the same magnitude as Infrared active modes.

$$\frac{\Delta\sigma}{\sigma_e} \propto \int_0^\infty M_A M_B e^{\left(-q^2 d / 4\alpha_0\right)} F(qb) q dq = I_{AB}(a, d) Z_A Z_B u_A u_B \quad (10)$$

[0025] The above describes the contribution to the conductivity enhancement due to the coherent motion of two atoms. Equation 10 contains a phase factor, $F(qb)$, which is generated through the addition of matrix elements. The advent of this phase factor comes from the addition of the $e^{iq \cdot R}$ terms seen within Equation 5. If the two atoms are identical and their distance from the nearest barrier is the same, the form of the phase factor becomes: $(u_1 + u_2 e^{iq \cdot b})$. In the case that the displacements of each atoms are of equal magnitude and the same direction, $u_1 = u_2$ (IR active), the phase factor becomes $\cos^2\left(q \cdot b / 2\right)$. In the case of Raman active modes, $u_1 = -u_2$, the phase factor simplifies to $\sin^2\left(q \cdot b / 2\right)$.

[0026] It has been shown through experiment that both IR and Raman modes are active within IETS and scale roughly equally. Yet some works within this field authors have chosen to couple the oscillating dipole associated with an entire molecular mode, this would generate the

66840-01

intensities associated with the infrared vibrations of the molecule but not contributions associated with Raman active modes.

[0027] FIG. 4 shows the effects of including intensity contributions of the Raman active modes (standard IETS) (labeled “oscillating atomic dipole plot” in FIG. 4). Specifically, the oscillating atomic dipole plot line in FIG. 4 shows the IETS of the formate ion. The molecular dipole plot line in FIG. 4 shows the spectra where the interaction potential given in Equation 4 is replaced by the interaction potential between the electron and the molecular dipoles. Beside the oscillating atomic dipole plot, the intensity expected if the coupling mechanism were to be only with the molecular dipole moment is provided. The two plots are scaled in reference to each other for convenience of comparison within FIG. 4. It noteworthy that, by comparison between the oscillating atomic dipole plot of FIG. 4 and the experimental plot given in FIG. 1b, the inclusion of Raman mode associated intensities has delivered a better approximation to experiment.

[0028] Orientation

[0029] When considering the charge-dipole interaction potentials it is clear that the leading (point-dipole) term as well as any subsequent terms rely on the projection of the harmonic displacement vector for a specific atomic oscillator (j), u_j , onto the charge-dipole vector, r_{ji} . This projection is of paramount importance within the calculation of the coupling within these systems as it effectively modulates the power of the denominator.

[0030] Orientation effects within IETS intensity calculations have been described as being of such importance as to practically be a selection rule for this type of vibrational characterization. Interaction potentials used within early formulations of IETS calculations has relied on the coupling strength of the electron within the donor site to atomic harmonic oscillators, and did not

66840-01

include any dynamic interactions within the system. More dynamic formulations exist to deal with that rather minute contribution of inelastic tunneling contributions to the current through molecular junctions, such as greens functions approaches. It should be noted that in these cases the inelastic contribution is to the molecular conductance and is attributed to vibronic alteration of electronic levels within the molecule – this second-order coupling (electron-vibrational state-electronic state) is why the inelastic contribution is minute in these cases.

[0031] In maintaining the simplicity of static calculations, one cannot ignore the contributions to the interaction potential from the vector projection. To emphasize the importance of this interaction the IETS of the formate ion is plotted; in FIG. 5a the three angular parameters are shown. The rotation about the z axis does not alter the spectrum of the formate ion as the calculations set the origin of the tunneling junction along this axis and thus this rotation does not alter the projection of the electron onto any molecular modes, merely which component possesses the projection; it should be clearly stated that this is a facet of the formate ion, not of IETS. Rotation about the y and x axes will alter the projections; the effects can be seen in FIG. 5b for rotation about the x-axis and FIG. 5c for rotation about the y-axis. Furthermore, without having calculated these orientation effects one can never achieve modes where the rate of inelastic tunneling is lower than the rate of the elastic process.

[0032] Docking Geometry

[0033] Specifically discussing the activation of olfactory proteins under the odotope theory, the volatile odorant molecule is hypothetically capable of maintaining something akin to its optimized geometry within the activation site. This is due to the fact that only certain sections of the molecule are being determined at once, it may be rationalized that the molecule only loosely enters and is never fully enveloped by the activation site. This rationalization is countered by

66840-01

docking studies of the OR1A1, OR1A2 and OR1G1 human olfactory receptors that do show envelopment of the ligands which dock with the protein.

[0034] Full ligand envelopment may lead to geometric alterations of the ligand during the docking. The alteration of ligand geometry may lead to attenuations in both the modal displacements and the partial charges, which for our example system can roughly generate a 10% by displacement or a 5% by partial charge (where partial charge was calculated through NBO analysis) alteration in the IETS intensity if the molecular geometry group is maintained. Moreover, these attenuations alter the potential interaction between the electron and the dipole through the dot product present in several terms of the non-approximated interaction potential Eq. 8a as well as the standard interaction potential Eq. 4.

[0035] FIGS. 6ai – 6aiii shows the geometry and alignment within the gap of the formate ion as well as variations on the bond angles. FIG. 6ai is the optimized for of the ion, FIG. 6aii is has altered both O-C-H bond angles equally (maintaining both σ planes) and FIG. 6aiii has altered only one of the O-C-H bond angles (maintaining only the σ plane bisecting all bonds). The alterations in the frequencies, displacements and partial charges are shown in Table 1. FIG. 6b gives the IETS for the variations of the formate ion. The frequencies are slightly displaced, and the introduction of asymmetry in the oxygen pair's movement eliminates much of their non-canceling contribution.

66840-01

Table 1. Numerical Values for calculations of the geometric alterations and optimized geometry variants of the formate ions.

	Displacements(Å) (x,y,z)												P	
													C	H
													C _h	C _h
	Mode 1		Mode 2		Mode 3		Mode 4		Mode 5		Mode 6		C	H
Asymm. Variant	(0.01,-0.5,0)	(0.04,-0.45,0)	(0,0,0.24)	(0,0,-0.97)	(-0.02,0.61,0)	(-0.28,0.41,0)	(0.04,0.02,0)	(0.99,0.01,0)	(0.58,0.01,0)	(-0.75,-0.05,0)	(0,-0.07,0)	(-0.02,1,0)	0.39379	0.033
	(0.48,0.21,0)	(-0.48,0.2,0)	(0,0,-0.06)	(0,0,-0.06)	(0.37,-0.26,0)	(-0.34,-0.23,0)	(-0.04,0.05,0)	(-0.06,-0.07,0)	(-0.2,0.08,0)	(-0.2,-0.08,0)	(0,0,0)	(-0.01,-0.01,0)		
Symm. Variant	(0,0,-0.51)	(0,0,-0.45)	(0.23,0,0)	(-0.97,0,0)	(0,0,0.62)	(0,0,0.48)	(0,0.05,0)	(0,0.99,0)	(0,0.56,0)	(0,-0.78,0)	(0,0,-0.07)	(0,0,1)	0.42841	0.000
	(0,0.48,0.21)	(0,-0.48,0.21)	(-0.06,0,0)	(-0.06,0,0)	(0,0.37,-0.25)	(0,0.37,-0.25)	(0,-0.05,0.06)	(0,-0.05,-0.06)	(0,-0.18,0.08)	(0,-0.18,-0.08)	(0,0,0)	(0,0,0)		
Optimized	(0,0,-0.5)	(0,0,-0.45)	(0.26,0,0)	(-0.96,0,0)	(0,0,0.66)	(0,0,0.39)	(0,0.04,0)	(0,0.99,0)	(0,0.62,0)	(0,-0.72,0)	(0,0,-0.07)	(0,0,1)	0.43859	-0.008
	(0,0.48,0.2)	(0,-0.48,0.2)	(-0.07,0,0)	(-0.07,0,0)	(0,0.38,-0.26)	(0,-0.38,-0.26)	(0,-0.05,0.05)	(0,-0.05,-0.05)	(0,-0.21,0.07)	(0,-0.21,-0.07)	(0,0.01,-0.01)	(0,-0.01,-0.01)		

[0036] The feasibility of tunneling electrons being the mechanism behind the activation of has been the subject of recent works. The mechanism by which the electron interacts with a bound ligand has been proposed as being IETS; it is important to consider a more complete description of the IETS model including considerations of the angular dependence between the mode and tunneling vector, alterations in the ligand geometry due to docking and the importance of choosing an appropriate interaction potential considering the confines of the activation site. These facets of the full static IETS calculations have been explored.

[0037] Application of the IETS model for the protein environment requires mapping aspects of the IETS methodology to the biological system. The two-plate setup of the tunneling junction represents the walls of the receptor site. More explicitly, under electron transfer the valence and conductance bands within the juncture become specific highest occupied molecular orbitals (HOMOs) and lowest unoccupied molecular orbital (LUMOs) of the residues making the walls of the receptor. Energy transition detectable by the protein should be the energy difference between electronic levels of residue side-chains. Such alteration of IETS also localizes the source of tunneling electrons to a single residue side-chain. The implication is that electrons are

66840-01

not capable of uniformly tunneling through the molecule. This lack of uniformity indicates the act of tunneling is localized to regions of the agonist molecule and that not all local oscillators of a specific mode contribute to the current enhancement.

[0038] Unlike experimental IETS procedure, the analyte is not deposited upon anything within the activation site. The agonist is encapsulated by the active site. There is no externally applied potential within the receptor site which would allow for the scanning of energies. Yet, an ionic cofactor, likely a calcium ion, may provide this driving field. The implication of this is that the receptor is set to test the vibrational-assisted enhancement to the electron tunneling rate at a specific energy. The electrostatic interactions which govern docking orientation would be a means of orienting the endogenous agonists in such a way that the tunneling junction is appropriately aligned for maximized electron transfer. Non-endogenous agonists would align with residues in a manner which may place energetically appropriate modes in proximity of the tunneling junction, thus activating the receptor.

[0039] Generation of tunneling spectra is completed through the procedure expressed in Equation 11, which represents the approximation of the IETS intensity (I) for a given active mode j :

$$I_j = \sum_{i=1}^N I_{i,j} = \sum_{i=1}^N q_i^2 (\Delta x_{i,j})^2 \quad (11)$$

where the sum is over all atoms within the molecule, q_i is the partial charge of atom i , and $\Delta x_{i,j}$ is the Cartesian displacement of atom i in mode j .

[0040] This procedure has been adapted from procedures reported in earlier IETS literature (Kirtley; Phillips) and similarly uses arbitrary units for the tunneling intensity. The herein disclosed spectral procedure was validated by comparison of the spectra of the formate ion, which is prevalent through experimental and theoretical literature in IETS. These arbitrary units

66840-01

are proportional to the conductance enhancement, as well as the enhancement to the Coulombic interaction probability during tunneling. Necessary information for implementing Equation 15 was collected through quantum chemical calculations. Computations were performed using Density Functional theory (DFT) at 6-311G level of theory. Expanded pseudopotential correlation consistent 5-zeta basis was used for large atoms where necessary. DFT was chosen both due to its high accuracy in transition dipole frequencies and to avoid encroaching error associated with dissimilarity between analyte and parameter molecules in semi-empirical methods. Vibrational calculations utilize reduced modal displacements; proportional to the Cartesian displacement through $\sqrt{\mu}$, μ is the mode's reduced mass. Natural bond order calculations yield the partial charges, q_i in Equation 11. Scaled Kronecker delta functions are plotted at the absorbance frequency of the mode. These functions were convolved with Gaussian functions possessing a full-width at half maximum (FWHM) of 25 cm^{-1} , representing a very narrow thermal distribution. A FWHM of 25 cm^{-1} was selected in the interests of being conservative and yet not allowing for peak additions while avoiding over estimations of peak breadth.

[0041] Referring to FIG. 7, an examination of the endogenous agonist, 5-HT, is shown. Specifically, FIG. 7 shows the IETS spectrum of serotonin. In FIG. 7, the abscissa has units of wave number and the ordinate has units proportional to tunneling probability. Such convention is used for all IETS spectra disclosed herein. Referring still to FIG. 7, the main spectral features are: the OH stretch at 3700 cm^{-1} ; NH_2 bend at 1700 cm^{-1} ; coherent ring motions appearing at both 1500 cm^{-1} and 1150 cm^{-1} ; and indole bending at 530 cm^{-1} . For reasons discussed below the herein disclosure is focused on tunneling in the 1500 cm^{-1} region. Working within Turins theory, this implies that these motions assist in the tunneling and that the tunneling source and sink are

66840-01

in proximity to these motions. Docking studies of homology modeled 5-HT_{2A} show the moieties discussed above are local to F339, F340, S159, and L229 residues, *i.e.*, that one of these residues assists in the tunneling.

[0042] Assessment of vibrational bands for 2A agonists that may be associated with protein activation under Turins vibrational theory is of primary import. Also, agonists of a particular protein share a single IET feature associated with the electron transfer. Herein, we have selected several known 5-HT_{2A} agonists and generated the IETS for each. LSD was selected as it possesses a high potential for activation of serotonin receptors within the cortical interneurons. DOI (2,5-dimethoxy-4-Iodo-amphetamine) was selected due to its high selectivity for the 2A-subtype of the serotonin receptor class. The remaining selected molecules are members of the 2C-X (4-X-2,5-dimethoxyphenethylamine) class of psychedelic phenethylamines. All compounds selected are known hallucinogens.

[0043] Referring to FIG. 8, an IETS of the selected molecules (above the abscissa) is shown. The selection of candidate peaks was performed using a spectral similarity index (SI) similar to that used for comparison of mass spectra, over the entire spectra and then over local regions.

The SI is calculated according to Equation 12:

$$SI = 1 - \sqrt{\frac{|a_i - b_i|}{N}} \quad (12)$$

where, N is a normalization constant (the numerator performed for spectra b); b_i is the value of the spectra being analyzed at discrete location i and a is the spectra being compared against. LSD, as the most potent agonist, was selected as the reference spectra for SI calculations. The SIs associated with each of the IETS are shown in Table 2.

66840-01

Table 2. SI index for several 5-HT_{2A} agonists.

	Spectral Range (cm ⁻¹)					
	0-4200	0-1000	500-1500	1000-2000	3000-4000	1400-1600
LSD	1	1	1	1	1	1
DAM-57	0.89019	0.87090	0.85286	0.87048	0.86997	0.85726
2C-I	0.81664	0.81792	0.75492	0.76284	0.78236	0.70693
2C-T-7	0.83977	0.81371	0.77398	0.80550	0.81748	0.79913
DOI	0.81903	0.80415	0.76196	0.77684	0.78614	0.71396
Aleph-2	0.83233	0.82218	0.77757	0.79102	0.80063	0.77539
DMT	0.84620	0.82282	0.78969	0.80327	0.85075	0.75394
Mescaline	0.82280	0.80003	0.74899	0.77347	0.80797	0.76743
Quipazine	0.82353	0.80820	0.77809	0.79677	0.77694	0.72653
Benzylpiperazine	0.82135	0.79383	0.76929	0.79990	0.79270	0.72390

[0044] Referring to Table 2, the SI is given for the overall spectrum and followed by regional SI's calculated for spans of 1000 cm⁻¹ with 500 cm⁻¹ steps; to emphasize the possible region associated with activation, the final column shows the SI of each compound for 1500±100 cm⁻¹. Regions with large ranges of no intensity have SI's inflated by this spectral facet (these regions have been omitted from the table).when omitting these regions, the SI for the region spanning 1000 – 2000 cm⁻¹ shows enhanced values, and includes the peak at 1500 cm⁻¹. The final column of the table gives the SI for a 100 cm⁻¹ region about this peak to emphasize this heavily shared spectral feature. As a means of reducing minor aspects within the tunneling PDF, the function as squared to exaggerate those energy ranges which exhibit large tunneling amplitudes within the spectra (as shown in FIG. 8 below the energy axis). Application of the SI to the square of the spectra showed similar results (not shown), yet with the expected enhancement of the SI values. The only universally shared spectral aspect were the shared peaks at 1500 cm⁻¹.

[0045] For purposes of this disclosure, DOC (2,5-dimethoxy-4-C-amphetamines) was selected as a prototypical molecule, based on its fairly tractable number of modes, simple geometry,

66840-01

symmetry, and similarities to other agonists. Energy regions associated with an assisted electron transfer would benefit from a large density of vibrational states, implying a greater number of possible states to interact with in this energy range. FIG. 9 shows both the IETS and scaled density states for DOC. Specifically, referring to FIG. 9, the IETS of DOC is plotted alongside a scaled, discrete density of states for the vibrational modes of DOC. The scaling factor is 10 (this scaling factor should be interpreted as a means of lowering the number of modes “step function” (DOS plot) to a readable height with the IETS; that is, the ordinate value of 1 should be interpreted as 10 on the DOS plot). Referring still to FIG. 9, the spectral feature at 1500 cm^{-1} exhibits an enhanced number of vibrational states.

[0046] An isotopologue series is utilized for DAM-57. The series is of variants of deuterated functional groups altering the character in the 1500 cm^{-1} region. It was verified that isotopologues of other atoms do not alter tunneling character in this region. FIGs. 10a -10c show the isotope effects within several groups of the molecule. FIG. 10a shows the effects of replacing the oxygens with ^{18}O 's, which results in little alteration near 1500 cm^{-1} . Substitution of the halide has similar results, with differences appearing at much lower energies. Referring to FIG. 10b, the effects of deuterating the hydrogens on the methoxys is shown. Referring still to FIG. 10b, a large attenuation of the tunneling intensity is observed. FIG. 10c shows the effect of selectively deuterating different functional groups.

[0047] The integral of the tunneling probability was taken for $1500 \pm 35\text{ cm}^{-1}$ and compared to known EC50 data for compounds shown to activate 5-HT_{2A}. The effective concentrations of several phenethylamines were taken from Reference number [7] (see References section below) and compared to the local integrals of the tunneling PDF. This comparison exposes a possible correlation to the inverse of the EC50 data. Results for the 1500 cm^{-1} region are shown in FIGs.

66840-01

11a – 11b and 12a – 12b for the DOI class and 2C-X class molecules computed, respectively.

FIGs. 11a and 12a give the IETS for each molecule, while FIGs. 11b and 12b compare the integral values to the known EC50s.

[0048] Tunneling is a highly local process, where the interaction potential falls off as r^{-3} for non-parallel displacements. Modes that are not local to the electron donor/acceptor sites cannot contribute to the electron transfer responsible for protein activation. Particular modes in 2C-T-2 and in Aleph-2 reside within the thioether (roughly 5 angstrom from the ring system); due to the non-locality of these oscillators, tunneling probability should be examined after removing these contributions from the spectra. FIGs. 11a and 12a present the IETS of 2C-T-2 and Aleph-2, both considering and disregarding these contributions. Excess contribution to the integral due to these modes is shown in FIGs. 11b and 12b. After correction for non-local motion, the integrals are in fair agreement with the inverse EC50.

[0049] FIG. 13 is a high-level diagram showing the components of an exemplary data-processing system for analyzing data and performing other analyses described herein, and related components. The system includes a processor 386, a peripheral system 320, a user interface system 330, and a data storage system 340. The peripheral system 320, the user interface system 330 and the data storage system 340 are communicatively connected to the processor 386. Processor 386 can be communicatively connected to network 350 (shown in phantom), e.g., the Internet or a leased line.

[0050] In one embodiment for implementation of the herein described process, for a molecule of interest, the inputted information includes: the exact location of each atom in the molecule; the energy it would take to excite a harmonic mode of the molecule; the vector displacement of each atom within the molecule; and the particle charge. Such information can be obtained by a

66840-01

structural optimization and normal mode analysis. It should be noted that the units of the information obtained from the structural optimization and normal mode analysis may need to be modified such that their units are in agreement for further calculations (for example, displacement vector information may need to be converted to Cartesian coordinates).

[0051] For each mode, the results from the structural optimization and normal mode analysis (specifically, the magnitude of displacement along any unit vector and partial charge) are inputted into Equation 15 to approximate the IETS intensity for each atom in a particular molecule and for each active mode (for example, if there is only one normal mode and three atoms in the molecule, the computation will be conducted three times for that normal mode). The result is a number respective of the intensity at the peak, which will relay in fundamental terms the transfer rate of electrons using this molecule at a particular normal mode. Scaled Kronecker delta functions are then plotted at the absorbance frequency of the mode. These scaled Kronecker delta functions are convolved with Gaussian functions possessing a full-width at half maximum (FWHM) of 25 cm^{-1} , representing a very narrow thermal distribution. Spectral Index (SI) calculations are then performed. The spectra amongst selected molecules are then compared, and regions where there is no flatlining at zero, resulting in an SI of about 1 (for purposes of the examples shown herein, these regions occurred at about 1800cm^{-1} to about 2000cm^{-1}) are removed to thereby lower the deviation and achieve a higher indexing score. The resulting spectral plots thus allow for determining the relative ability for activation of G-Protein Coupled Receptors of families of agonists.

[0052] Additional disclosure is found in Appendix-A, Appendix-B, Appendix-C, Appendix-D, Appendix-E, and Appendix-F filed herewith, entirety of which are incorporated herein by reference into the present disclosure.

66840-01

[0053] Those skilled in the art will recognize that numerous modifications can be made to the specific implementations described above. The implementations should not be limited to the particular limitations described. Other implementations may be possible.

References:

- [1] C J Adkins and W A Phillips. Inelastic electron tunnelling spectroscopy. *Journal of Physics C: Solid State Physics*, 18(7):1313, 1985.
- [2] Juffmann T. Arndt, M. and V. Vedral. Quantum physics meets biology. *HFSP J.*, 3:386, 2009.
- [3] Philip Ball. The dawn of quantum biology. *NATURE*, 474:272–274, June 2011.
- [4] Sevgi Bayar, Semran Saglam, and Hasan F. Ustundag. Experimental and theoretical studies of the vibrational spectrum of 5-hydroxytryptamine. *Journal of Molecular Structure: THEOCHEM*, 726:225 – 232, 2005. ISSN 0166-1280.
- [5] M. R. Braden and D. E. Nichols. Assessment of the roles of serines 5.43(239) and 5.46(242) for binding and potency of agonist ligands at the human serotonin 5-HT_{2A} receptor. *MOLECULAR PHARMACOLOGY*, 72: 1200–1209, 2007.
- [6] M. R. Braden, J. C. Parrish, J. C. Naylor, and Nichols D. E. Molecular interaction of serotonin 5-HT_{2A} receptor residues phe339 and phe340 with superpotent n-benzyl phenethylamine agonists. *MOLECULAR PHARMACOLOGY*, 70:1956–1964, 2006.
- [7] Michael Robert Braden. Towards a biophysical understanding of hallucinogen action.
- [8] Jennifer C. Brookes, Filio Hartoutsiou, A. P. Horsfield, and A. M. Stoneham. Could humans recognize odor by phonon assisted tunneling? *Phys. Rev. Lett.*, 98:038101, Jan 2007.
- [9] L. Buck and Alex R. A novel multigene family may encode odorant receptors: a molecular basis for odor recognition. *Cell*, 65:175–187, 1991.
- [10] J. M. Cai and M. B. Plenio. Chemical compass model for avian magnetoreception as a quantum coherent device. *PRL*, 111.
- [11] J. J. Chambers and D. N. Nichols. A homology-based model of the human 5-HT_{2A} receptor derived from an in silico activated G-protein coupled receptor. *Journal of Computer-Aided Molecular Design*, 16:511–520, 2002.
- [12] M. S. Choudhary, N. Scabs, A. Uluer, and et al. Differential ergoline and ergopeptine binding to 5-hydroxytryptamine_{2A} receptors: Ergolines require an aromatic residue at position 340 for high affinity binding. *MOLECULAR PHARMACOLOGY*, 47:450–457, 1995.
- [13] A. Christopoulos. Allosteric binding sites on cell surface receptors: novel targets for drug discovery.
- [14] P. C. W. Davies. Does quantum mechanics play a non-trivial role in life? *BioSystems*, 78:69–79, 2004.
- [15] D. Delliou. 4-bromo-2,5-dimethoxyamphetamine: Psychoactivity, toxic effects and analytical methods. *Forensic Science International*.
- [16] E. Fischer. Einfluss der configuration auf die wirkung der enzyme. *Ber. Dt. Chem. Ges.*, 27: 2985–2993, 1894.
- [17] G R Fleming, S F Huelga, and M B Plenio. Focus on quantum effects and noise in biomolecules. *New Journal of Physics*, 13(11): 115002, 2011. URL <http://stacks.iop.org/1367-2630/13/i=11/a=115002>.
- [18] Maria Isabel Franco, Luca Turin, Andreas Merzhin, and Efthimios M. C. Skoulakis. Molecular vibration-sensing component in drosophila melanogaster olfaction. *Proceedings of the National Academy of Sciences*, 2011.
- [19] Simon Gane, Dimitris Georganakis, Kilo Maniati, Manolis Vamvakias, Nikitas Ragoussis, Efthimios M. C. Skoulakis, and Luca Turin. Molecular vibration-sensing component in human olfaction. *PLO SONE*, 8:e55780, Jan 2013.
- [20] Gao J. Karplus M. Garcia-Viloca, M. and D. G. Truhlar. How enzymes work: analysis by modern rate theory and computer simulations. *Science*, 303:186–195, 2004.
- [21] Dyson GM. Some aspects of the vibration theory of odor. *Perfumery and Essential Oil Record*, 19:456–459, 1928.
- [22] T. G. Graeber, J. R. Heath, B. J. Skaggs, M. E. Phelps, R. Remacle, and R. D. Levine. Maximal entropy inference of oncogenicity from phosphorylation signaling. *PNAS*, 107:6112–7, 2010.
- [23] L. J. W. Haffenden, V. A. Yaylayan, and J. Fortin. Investigation of vibrational theory of olfaction with various labelled benzaldehydes. *Food Chem.*, 73:67–72, 2001.
- [24] B. R. Havens and C. D. Melone. The application of deuterated sex pheromone mimics of the american cockroach (*periplaneta americana*, l.), to the study of wright's vibrational theory of olfaction. *Dev. Food. Sci.*, 37:497–524, 1995.
- [25] T. P. Hettinger. Olfaction is a chemical sense, not a spectral sense. *PNAS*, 108.

- [26] Dominik Heyers, Martina Manns, Harald Luksch, Onur Gnrkn, and Henrik Mouritsen. A visual pathway links brain structures active during magnetic compass orientation in migratory birds. *PLoS ONE*, 2(9):e937, 09 2007. doi:10.1371/journal.pone.0000937. URL <http://dx.plos.org/10.1371%2Fjournal.pone.0000937>.
- [27] K. W. Hipps and U. Mazur. *Inelastic Electron Tunneling Spectroscopy*. Handbook of Vibrational Spectroscopy.
- [28] S. F. Huelga and M. B. Plenio. Vibrations, quanta and biology. *Contemporary Physics*, 54: 181, 2013.
- [29] J. G. Iez-Maeso, N. V. Weisstaub, M. Zhou, and et al. Hallucinogens recruit specific cortical 5-HT_{2A} receptor-mediated signaling pathways to affect behavior. *Neuron*, 52:439–452, Feb 2007.
- [30] Hara J. Olfactory discrimination between glycine and deuterated glycine by fish. *Experientia*, 33:6189, 1977.
- [31] Sabre Kais. Entanglement, electron correlation, and density matrices. *Advances in Chemical Physics*, 134:493–535, 2007.
- [32] Karupiah Kanagarajadurai, Manoharan Malini, Aditi Bhattacharya, Mitradas M. Panicker, and Ramanathan Sowdhagini. Molecular modeling and docking studies of human 5-hydroxytryptamine 2a (5-HT_{2A}) receptor for the identification of hotspots for ligand binding. *Mol. BioSyst.*, 5:1877–1888, 2009.
- [33] A. Keller and L. B. Vosshall. A psychophysical test of the vibration theory of olfaction. *NATURE NEUROSCIENCE*, 7, 2004.
- [34] John Kirtley and James T. Hall. Theory of intensities in inelastic-electron tunneling spectroscopy orientation of adsorbed molecules. *Phys. Rev. B*, 22:848–856, Jul 1980.
- [35] John Kirtley and Paul Soven. Multiple-scattering theory of intensities in inelastic electron tunneling spectroscopy. *Phys. Rev. B*, 19: 1812–1817, Feb 1979.
- [36] John Kirtley, D. J. Scalapino, and P. K. Hansma. Theory of vibrational mode intensities in inelastic electron tunneling spectroscopy. *Phys. Rev. B*, 14:3177–3184, Oct 1976.
- [37] A. R. Knight, A. Misra, K. Quirk, K. Benwell, D. Revell, G. Kennett, and M. Bickerdike. Pharmacological characterisation of the agonist radioligand binding site of 5-HT_{2A}, 5-HT_{2B} and 5-HT_{2C} receptors.
- [38] D. E. Koshland. Application of a theory of enzyme specificity to protein synthesis. *Proc. Natl. Acad. Sci.*, 44:98–104, 1958.
- [39] J. Lambe and R. C. Jaklevic. Molecular vibration spectra by inelastic electron tunneling. *Phys. Rev.*
- [40] J. Lambe and S. L. McCarthy. Light emission from inelastic electron tunneling. *Phys. Rev. Lett.*
- [41] Kiminori Maeda, Kevin B. Henbest, Filippo Cintolesi, and et al. Chemical compass model of avian magnetoreception. *NATURE*, 453: 387–U38, May 2008.
- [42] G. J. Marek and G. K. Aghajanian. Lsd and the phenethylamine hallucinogen do are potent partial agonists at 5-HT_{2A} receptors on interneurons in rat piriform cortex.
- [43] H. H. Maurer. Chemistry, pharmacology, and metabolism of emerging drugs of abuse. *Ther Drug Monit*, 32:544–549, Oct 2010.
- [44] J. McFadden. *Quantum Biology*. Norton, 2001.
- [45] J. McFadden and J. Al-Khalili. A quantum mechanical model of adaptive mutations. *BioSystems*, 50:203–211, 1999.
- [46] D. E. Nichols and C. D. Nichols. Serotonin receptors. *Chem. Rev.*, 108:1614–1641, 2008.
- [47] David E Nichols. Hallucinogens. *Pharmacology & Therapeutics*, 101(2):131 – 181, 2004. ISSN 0163-7258.
- [48] A. Patel. Why genetic information processing could have a quantum basis. *J. Biosci.*, 26: 145–151, 2001.
- [49] Y. T. ; Berman G. P. ; Kais S. Pauls, J. A. ; Zhang. Quantum coherence and entanglement in the avian compass. *Phys. Rev. E*, 87:062704, Jun 2013.
- [50] W. A. Phillips and C. J. Adkins. A theory for the intensities of inelastic electron-tunnelling spectra. *Philosophical Magazine Part B*, 52(3): 739–750, 1985.
- [51] R. Remacle, N. Kravchenko-Balasha, A. Levitzki, and R. D. Levine. Information-theoretic analysis of phenotype changes in early stages of carcinogenesis. *PNAS*, 107:10324–9, 2010.
- [52] Mohan Sarovar, Akihito Ishizaki, Graham R. Fleming, and et al. Quantum entanglement in photosynthetic light-harvesting complexes. *NATURE PHYSICS*, 6:462–467, Jun 2010.
- [53] A. Shulgin and A. Shulgin. *PiHKAL: A Chemical Love Story*. Transform Press, 1991.
- [54] A. Shulgin and A. Shulgin. *TiHKAL: The Continuation*. Transform Press, 1997.

66840-01

- [55] A K Sleight, W A Phillips, C J Adkins, and M E Taylor. A quantitative analysis of the inelastic electron tunnelling spectrum of the formate ion. *Journal of Physics C: Solid State Physics*, 19(33):6645, 1986. URL <http://stacks.iop.org/0022-3719/19/i=33/a=013>.
- [56] A K Sleight, M E Taylor, C J Adkins, and W A Phillips. Top-electrode and roughening effects in electron tunnelling spectroscopy. *Journal of Physics: Condensed Matter*, 1(6):1107, 1989.
- [57] Iia A. Solovyov, Po-Yao Changwb, and Klaus Schulten. Vibrationally assisted electron transfer mechanism of olfaction: myth or reality? *Phys. Chem. Chem. Phys.*, 14:13861–13871, Oct 2012.
- [58] Shin-ya Takane and John B. O. Mitchell. A structure-odour relationship study using eva descriptors and hierarchical clustering. *Org. Biol. Chem.*, 2:3250–3255, 2004.
- [59] Ismael Tejero, Nria Gonzalez-Garca, ngels Gonzalez-Lafont, and Jos M. Lluch. Tunneling in green tea: understanding the antioxidant activity of catechol-containing compounds. a variational transition-state theory study. *Journal of the American Chemical Society*, 129(18):5846–5854, 2007.
- [60] L. TURIN. A method for the calculation of odor character from molecular structure. *Journal of Theoretical Biology*, 216(3):367 – 385, 2002. ISSN 0022-5193.
- [61] L. Turin and F. Yoshii. *Handbook of Olfaction and Gustation*. Marcel Dekker, Inc., 2003.
- [62] Luca Turin. A spectroscopic mechanism for primary olfactory reception. *Chemical Senses*, 21(6):773–791, 1996. doi:10.1093/chemse/21.6.773.
- [63] Jonathan D. Urban, William P. Clarke, Mark von Zastrow, David E. Nichols, Brian Kobilka, Harel Weinstein, Jonathan A. Javitch, Bryan L. Roth, Arthur Christopoulos, Patrick M. Sexton, Keith J. Miller, Michael Spedding, and Richard B. Mailman. Functional selectivity and classical concepts of quantitative pharmacology. *Journal of Pharmacology and Experimental Therapeutics*, 320(1):1–13, 2007. doi:10.1124/jpet.106.104463.
- [64] K. X. Wan, I. Vidavsky, and M. L. Gross. Comparing similar spectra: From similarity index to spectral contrast angle. *J Am Soc Mass Spectrom*, 13:85–88, 2002.
- [65] R. H. Wright. Odor and molecular vibration: optical isomers. *Chemical Senses*, 3(1):35–37, 1978.
- [66] R. H. Wright. Molecular vibration and odour blending. *Chemical Senses*, 8:103–106, 1983.
- [67] R.H. Wright. Odor and molecular vibration: Neural coding of olfactory information. *Journal of Theoretical Biology*, 64(3):473 – 502, 1977. ISSN 0022-5193.
- [68] Shu-Hao Yeh, Jing Zhu, and Sabre Kais. Population and coherence dynamics in light harvesting complex ii (lh2). *J. Chem. Phys.*, 137:084110, Aug 2012.
- [69] Jing Zhu, Sabre Kais, Alan Aspuru-Guzik, and et al. Multipartite quantum entanglement evolution in photosynthetic complexes. *J. Chem. Phys.*, 137:074112, Aug 2012.

66840-01

Claims:

1. A method for determining the relative ability for activation of G-Protein Coupled Receptors of families of agonists as shown and described in the specification.
2. A system for determining the relative ability for activation of G-Protein Coupled Receptors of families of agonists as shown and described in the specification.
3. A method for determining the relative activation strength of drug molecules with G-Protein Coupled Receptors (GCPR) using a processor, comprising:
 - structurally optimizing a set of key information regarding a molecule of interest;
 - subjecting the set of key information regarding the molecule to a normal mode analysis;
 - receiving the output from the normal mode analysis;
 - approximating the intensity of the inelastic electron tunneling spectroscopy for the molecule of interest;
 - plotting scaled Kronecker delta functions based on the intensity of the inelastic electron tunneling spectroscopy for the molecule of interest;
 - convolving the scaled Kronecker delta function plots with Gaussian distributions;
 - performing spectral index calculations on the newly convolved Gaussian distribution plots; and
 - comparing the plots of spectral index calculations with at least one additional molecule of interest to thereby determine the relative ability for activation of G-Protein Coupled Receptors of families of agonists.
4. The method of claim 3, the key information regarding a molecule of interest comprises: the exact location of each atom in the molecule; the energy it would take to excite a harmonic

66840-01

mode of the molecule; the vector displacement of each atom within the molecule; and the particle charge.

5. The method of claim 5, further comprising removing flatline regions in the plots of spectral index calculations.

VITA

VITA

Ross Hoehn was born in Corydon, Indiana, United State of America to Cinda and Steve Hoehn in 1984. He graduated Corydon Central High School with honors and entered Purdue University in 2003 for Psychology. He obtained a Bachelors degree in Honors Chemistry with ACS Accredits and minor emphasis in Classics and Philosophy 2008. He took a year after graduation to explore the idea of graduate school in chemistry by taking several classes as well as performing research as a Dreyfus Scholar under the tutelage of Prof. Emt. Jurgen Honig. Ross was admitted to Purdue University in 2009 were he joined the Kais group. He expects to receive a PhD in Physical Chemistry in December 2014.

PUBLICATIONS

Analysis of Irreversible Processes across Narrow Junctions

J.M. HONIG* AND R. HOEHN

Department of Chemistry, Purdue University, West Lafayette, Indiana, 47907, USA

(Received November 17, 2010)

The rectification of the second law of thermodynamics is used to directly relate irreversible heat and work transfers to reversible processes. This permits the construction of thermodynamic functions of state that include entropy contributions due to irreversible processes. A general expression is set up to determine the entropy changes in terms of experimentally accessible parameters when a system is interacting with its surroundings via quasistatic irreversible operations. The procedure is used to determine the entropy changes across a narrow junction in terms of pressure and temperature differences between the system and its surroundings, including cyclic processes.

PACS: 05.70.-a, 05.70.Ln, 44.10.+i

1. Introduction

This article deals with the thermodynamic analysis of irreversible processes across a narrow interface which separates a system from its surroundings (reservoir), the combination forming an isolated unit. We first develop the required fundamental relations that are scattered in the literature and then show how they are applied in specific situations.

At the outset we clarify what is meant by intensive variables that generate irreversible changes. Reference is made to Fig. 1 which illustrates the temperature profile for the compound system under conditions described below. Similar considerations apply to all other intensive variables of interest. The reservoir is assumed to be so large that under all operating conditions its temperature, T_0 , remains constant and uniform over almost its entire extension. The temperature then changes across the small interfacial region, which is a poor thermal conductor, to its value T of the system. In conformity with standard operating procedures we assume all processes in the reservoir to proceed reversibly. All irreversible changes within the system are assumed to proceed sufficiently slowly that its temperature T is uniformly variable over almost the entire extension of the system. Such operations will be termed quasistatic irreversible processes (QSIPs). The system and surroundings are separated by a narrow interface over which the temperature changes from T_0 to T . There is no restriction on the difference between T and T_0 .

The present approach, dealing with entropy changes in irreversible processes, is an extension of earlier work [1-7], and is complementary to the standard theory of ir-

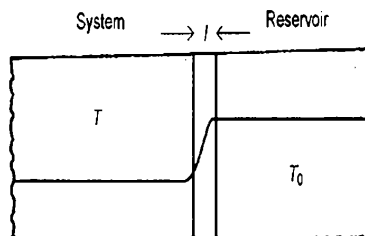


Fig. 1. Sketch of temperature profile for the combined system and reservoir at different temperatures T and T_0 . The temperature in each phase remains essentially constant over almost the entire region; the gradient in temperature develops over only a small region l at the interface.

reversible thermodynamics (e.g., [8-10]) that emphasizes the relation between fluxes and forces.

2. Fundamentals

We first provide a fundamental analysis of irreversible phenomena that is used below. Consider an infinitesimal step in a process that is carried out first reversibly (*a*) and then irreversibly (*b*). For the compound unit the entropy change in the two cases is given by

$$dS + d_a S_0 = 0 \quad (1)$$

and

$$dS + d_b S_0 > 0, \quad (2)$$

where the zero subscript refers to the surroundings, and where the entropy change in the system is identical in the two cases, since S is a function of state of the system. The use of inequalities is awkward; hence, it is

* corresponding author; e-mail: jmh@purdue.edu

opposite to introduce an *entropy deficit function* $d\theta > 0$ that converts Eq. (2) to an equality

$$dS + d_b S_0 - d\theta = 0. \quad (3)$$

Let us note that $d\theta$ is the sum of the entropy changes in the system plus surroundings kept under different conditions; it represents the total entropy change of the universe resulting from the execution of the irreversible process.

We next set $dS = \bar{d}_r Q/T$, where $\bar{d}_r Q$ is the element of heat reversibly absorbed (or released) by the system at temperature T . Since all processes in the reservoir take place reversibly we designate the response of the reservoir as $d_b S_0 = dQ_0/T_0 = -\bar{d}_r Q/T_0$. The second equality is obtained because of the isolation of the compound system; heat gained (lost) by the system is lost (gained) by the reservoir.

3. Heat transfer

When dS and $d_b S_0$ in Eq. (3) are replaced as described above one may relate the heat transferred irreversibly to the heat transferred reversibly as follows:

$$\bar{d}_r Q = (T_0/T) \bar{d}_r Q - T_0 d\theta < (T_0/T) \bar{d}_r Q. \quad (4)$$

This relation was previously derived in Ref. [11]. The inequality may be tightened by noting that it must hold for any value $T < T_0$ when heat is absorbed by the system and for any $T > T_0$ when heat is released; in either case the limiting temperature is $T = T_0$. One thus arrives at the string of inequalities

$$\bar{d}_r Q < \bar{d}_r Q < (T_0/T) \bar{d}_r Q, \quad (5)$$

which either becomes more positive or less negative from left to right. The result $\bar{d}_r Q < \bar{d}_r Q$ is simply a reformulation of the famous Clausius inequality.

It is expedient to rewrite Eq. (4) in the form

$$\bar{d}_r Q = \bar{d}_r Q + (T_0/T - 1) \bar{d}_r Q - T_0 d\theta. \quad (6)$$

Because of the Clausius inequality the last two terms in (6) must be negative. This sets up a lower bound on $d\theta$:

$$d\theta > [(T_0 - T)/T_0 T] \bar{d}_r Q = [(T_0 - T)/T_0] dS > 0, \quad (7)$$

which is positive because the quantity in square brackets has the same sign as dS or $\bar{d}_r Q$, all being positive or negative according as heat is incrementally introduced into or withdrawn from the system. The quantities on the right in principle are experimentally accessible.

4. Work performance

Information on work performance is accessed through the first law of thermodynamics in the form

$$dE = \bar{d}_r Q + \bar{d}_r W = \bar{d}_r Q + \bar{d}_r W, \quad (8)$$

where E is the energy of the system and W indicates the work performance. On substituting from (6) one obtains

a relation between work performed reversibly and irreversibly as

$$\begin{aligned} \bar{d}_r W &= \bar{d}_r W - (T_0/T - 1) \bar{d}_r Q + T_0 d\theta \\ &= \bar{d}_r W - (T_0 - T) dS + T_0 d\theta, \end{aligned} \quad (9)$$

where the last two terms are opposite in sign to those in Eq. (6). It then follows that $\bar{d}_r W > \bar{d}_r W$, known as the *Gouy-Stodola* theorem.

Equation (9) may be rewritten in the form

$$d\theta = (\bar{d}_r W - \bar{d}_r W)/T_0 + (1 - T/T_0) dS. \quad (10)$$

This provides one avenue for determining the incremental contribution of an irreversible process to the entropy of the universe. The quantities on the right are accessible by measurement or calculation. The special cases $d\theta = (1 - T/T_0) dS$ as well as $d\theta = (\bar{d}_r W - \bar{d}_r W)/T_0$ were derived by independent methods in Refs. [12] and [13], respectively.

Here we concentrate on an alternative formulation that provides similar information in terms of the physical properties of the system and its surroundings, as we now show.

5. Functions of state

The energy differential for the *surroundings* takes the customary form

$$dE_0 = T_0 dS_0 - P_0 dV_0 + \sum_i \mu_{0i} dn_{0i}, \quad (11)$$

where P_0 is the prevailing pressure, V_0 — the volume, μ_{0i} — the chemical potential of species i , and n_{0i} — the mole number of species i , all referred to the surroundings, functioning reversibly. We now set $dE = -dE_0$ and $dn_{0i} = -dn_i$, where the unsubscripted quantities refer to the system. We further assume that any volume change of the system is precisely compensated for by the volume change in the surroundings, so that $dV_0 = -dV$. Lastly, we introduce Eq. (3) by setting $dS_0 \equiv d_b S_0 = -dS + d\theta$. This leads to the fundamental expression for the energy of the *system* in the form

$$dE = T_0 dS - P_0 dV + \sum_i \mu_{0i} dn_i - T_0 d\theta, \quad (12)$$

thereby generalizing the conventional relation for the energy differential, so that it may be applied to QSIP processes. This relation was established earlier by Kestin [12], using a different technique. One should note that even for irreversible processes of the system all intensive variables refer to the properties of the surroundings.

For future use it is expedient to rewrite Eq. (12) as

$$\begin{aligned} dE &= (T_0 - T) dS - (P_0 - P) dV + \sum_i (\mu_{0i} - \mu_i) dn_i \\ &\quad + T dS - P dV + \sum_i \mu_i dn_i - T_0 d\theta, \end{aligned} \quad (13)$$

from which we subtract the same energy differential, dE , for the same step executed reversibly,

$$dE = T dS - P dV + \sum_i \mu_i dn_i. \quad (14)$$

This permits us to solve for

$$d\theta = (1/T_0)[(T_0 - T)dS - (P_0 - P)dV + \sum_i(\mu_{0i} - \mu_i)dn_i]. \quad (15)$$

We have thereby expressed the contribution of the infinitesimal step to the entropy generated in executing a QSI process. Equation (15) is consistent with Eq. (3).

For further progress it is expedient to introduce T , P , and n_i as control variables, thereby eliminating the entropy and volume differentials. This is accomplished by specifying $S = S(T, P, n_i)$ and $V = V(T, P, n_i)$ and then taking differentials

$$\begin{aligned} dS &= \frac{\partial S}{\partial T} dT + \frac{\partial S}{\partial P} dP + \sum_i \frac{\partial S}{\partial n_i} dn_i \\ &= \frac{C_{P,n}}{T} dT - \frac{\partial V}{\partial T} dP + \sum_i \bar{S}_i dn_i, \end{aligned} \quad (16)$$

where we have inserted the heat capacity $C_{P,n}$ at constant pressure and composition, the relevant Maxwell relation, and the partial molal entropy, \bar{S}_i . We obtain similarly

$$dV = \frac{\partial V}{\partial T} dT + \frac{\partial V}{\partial P} dP + \sum_i \bar{V}_i dn_i. \quad (17)$$

When these relations are substituted in (15) we generate the fundamental working equation

$$\begin{aligned} d\theta &= \left[\left(1 - \frac{T}{T_0}\right) \frac{C_P}{T} - \frac{1}{T_0} (P_0 - P) \frac{\partial V}{\partial T} \right] dT \\ &\quad - \left[\left(1 - \frac{T}{T_0}\right) \frac{\partial V}{\partial T} + \frac{1}{T_0} (P_0 - P) \frac{\partial V}{\partial P} \right] dP \\ &\quad + \sum_i \left[\left(1 - \frac{T}{T_0}\right) \bar{S}_i - \frac{1}{T_0} (P_0 - P) \bar{V}_i \right. \\ &\quad \left. + \frac{1}{T_0} (\mu_{0i} - \mu_i) \right] dn_i. \end{aligned} \quad (18)$$

6. Special cases

In the above we have specified the incremental contribution to the entropy associated with irreversible quasi-static processes taking place across the interface, in terms of temperature, pressure, and composition of the system as the proper control variables. To obtain the total contribution we must now specify how each of the nonsubscripted variables changes with time t in the overall process, and then integrate the rather formidable expression. For illustrative purposes we therefore introduce a number of reasonable simplifications and special cases that show how to implement the calculation.

We assume that the reservoir is of such huge size that all its variables do not change appreciably during the interaction with the system; then the subscripted quantities are constant. We next specialize to the case of a one-component system at constant composition, which eliminates the third line of Eq. (18). We further divide the calculations into two groups: (a) Systems consisting

of an ideal gas, for which $V = nRT/P$ and $C_P = 5nR/2$, where n is the number of moles of material in the system and R is the gas constant. (b) Condensed phases, where we simulate the modest changes of V with T and P by replacing $\partial V/\partial T$ with $\alpha n\bar{V}_0$, and $\partial V/\partial P$, with $-\beta n\bar{V}_0$. Here α is the isobaric coefficient of thermal expansion, β is the isothermal coefficient of compression, and \bar{V}_0 is a suitably averaged molar volume over the temperature and pressure range of interest. All three of these quantities are assumed to be constant. Lastly, to be definite, we set $T \leq T_0$ and $P \leq P_0$, so that, as the interaction is turned on, the temperature and pressure of the system rises. The volume of the system adjusts in conformity with the equation of state of the material.

(a) For ideal gases the calculation may be subdivided into two categories: integrals that are independent of path, and line integrals that involve more than one variable. In the former case the time dependence is irrelevant. On substituting in (18) for C_P , determining the volume derivatives, and integrating the differentials that involve only one independent variable (T or P) between limits i and f we obtain

$$\theta_{af} = \frac{5}{2} nR \ln \frac{T_f}{T_i} - \frac{3}{2} nR \ln \frac{1}{T_0} (T_f - T_i) - nR \ln \frac{P_f}{P_i}. \quad (19)$$

Here the first and last terms are those encountered for the reversible alteration of temperature and pressure of an ideal gas.

To handle the remainder it is necessary to introduce time as a parameter in the interval $0 \leq t \leq \tau$ and to deal with the line integrals in the form

$$\begin{aligned} \theta_{ad} &\equiv \theta_T + \theta_P = -\frac{P_0}{T_0} nR \int_0^\tau \frac{1}{P(t)} \frac{dT}{dt} dt \\ &\quad + \frac{P_0}{T_0} nR \int_0^\tau \frac{T(t)}{P^2(t)} \frac{dP}{dt} dt. \end{aligned} \quad (20)$$

We now take up two special examples:

Case 1. We set $P = P_i e^{k_P t}$, $T = T_i e^{k_T t}$, $0 \leq t \leq \tau$, where k_P , k_T are time constants, so chosen that at time τ the system has reached the final values T_f and P_f . On inserting these functions into (20) the integrations are straightforward, though lengthy. We obtain

$$\begin{aligned} \theta_T &= -\frac{P_0}{T_0} \frac{T_i}{P_i} nR \frac{1}{1 - k_P/k_T} \left(\frac{T_f/T_i}{P_f/P_i} - 1 \right), \\ \theta_P &= \frac{P_0}{T_0} \frac{T_i}{P_i} nR \frac{1}{k_T/k_P - 1} \left(\frac{T_f/T_i}{P_f/P_i} - 1 \right), \\ \frac{k_P}{k_T} &= \frac{\ln(P_f/P_i)}{\ln(T_f/T_i)}, \end{aligned} \quad (21)$$

which are combined to yield

$$\theta = nR \frac{P_0 T_i}{P_i T_0} \left(1 - \frac{P_i T_f}{P_f T_i} \right) = nR \frac{P_0}{T_0} \left(\frac{T_i}{P_i} - \frac{T_f}{P_f} \right), \quad (22)$$

to which we adjoin Eq. (19). According to Eq. (3), the

resulting expression specifies the entropy increase in the universe arising from the irreversible QSIP interactions between the ideal gas in the system and in the reservoir. Let us note that in addition to the properties of the reservoir only initial and final values of the temperature and pressure of the system appear in the above results.

Case 2. We next take up the particular time dependence $P = P_i e^{k_P t}$, $T = T_i(1 + k_T t)$, $0 \leq t \leq \tau$. Obviously, there is no change in handling the one-variable integrals. Proceeding in the same manner with the path-dependent integrals we obtain the expressions

$$\begin{aligned} \theta_T &= nR \frac{P_0 T_i k_T}{P_i T_0 k_P} \left(\frac{P_i}{P_f} - 1 \right), \\ \theta_P &= nR \frac{P_0 T_i}{P_i T_0} \left[\left(1 - \frac{P_i}{P_f} \right) + \frac{k_T}{k_P} \left(1 - \frac{P_i}{P_f} + \frac{P_i}{P_f} \ln \frac{P_i}{P_f} \right) \right], \\ \frac{k_T}{k_P} &= \frac{T_f/T_i - 1}{\ln(P_f/P_i)}, \end{aligned} \quad (23)$$

which clearly differ from Eq. (21). Nevertheless, on summing these expressions one again recovers Eq. (22) identically. This demonstrates that while the contributions to θ_P and to θ_T differ for the two cases their sum is independent of the choice for the time variation of T and of P . This fact may be rationalized by noting that in the QSIP approximation there is no reference to the path that leads from the initial to the final state. This holds true as long as relaxation effects are ignored. The reader may also verify our finding that a choice in which both P and T vary linearly with time produces yet a different set of θ_P and θ_T integrals that again sum to Eq. (22). Thus, Eqs. (19) and (22) are the final results of interest for the ideal gas.

(b) For the condensed phase we replace the partial derivatives of V in Eq. (18), using the equation of state for condensed phases in the form

$$\begin{aligned} V &= V_0 + \int (\partial V/\partial T) dT + \int (\partial V/\partial P) dP \\ &= V_0(1 + \alpha T - \beta P), \end{aligned} \quad (24)$$

where we later retain the correction terms only to first order in α and β . We then utilize the calorific equation of state for the enthalpy H of the condensed phase in the form

$$(\partial H/\partial T) = V - T(\partial V/\partial T) = V_0(1 - \beta P), \quad (25a)$$

which yields the integrated form as

$$H = H_0 + V_0 P - (1/2)\beta V_0 P^2. \quad (25b)$$

Here $H_0 = 3nRT$ is the arbitrary function of integration for the condensed phase. Accordingly, the heat capacity to first order of smallness is given by $C_P = 3nR$.

We now return to the first line of Eq. (18) and first single out those differentials that involve only one independent variable. On performing that integration we obtain

$$\begin{aligned} \theta_{bi} &= n\tilde{C}_P \ln \frac{T_f}{T_i} - n \frac{\tilde{C}_P}{T_0} (T_f - T_i) - \frac{P_0}{T_0} \alpha n \tilde{V} (T_f - T_i) \\ &\quad - \alpha n \tilde{V} (P_f - P_i) + \frac{P_0}{T_0} \beta n \tilde{V} (P_f - P_i) \\ &\quad - \frac{\beta n \tilde{V}}{2T_0} (P_f^2 - P_i^2). \end{aligned} \quad (26)$$

To the above we adjoin the line integrals

$$\theta_{bd} = \frac{\alpha n \tilde{V}}{T_0} \left[\int_0^\tau P(t) \frac{dT}{dt} dt + \int_0^\tau T(t) \frac{dP}{dt} dt \right]. \quad (27)$$

As was the case earlier, we verified that these also do not depend on the chosen time dependence; we thus adopted Case 1, above, to carry out the integrations to find θ_P and θ_T , which are summed to yield

$$\theta_{bd} = \frac{\alpha n \tilde{V}}{T_0} (P_f T_f - P_i T_i). \quad (28)$$

The final result in the present case involves the sum of Eqs. (26) and (28). The only terms not referring to the expansion properties of the condensed phase are the first two in (26), which depend solely on the temperatures of the system and of the surroundings. Normally, the remaining terms are small compared to those just mentioned.

7. Cyclic processes

Up to now we have assumed a monotonic variation of temperature and pressure with time. Also of interest is a cyclic process in which the intensive variables of the system are changed in the sequence $T_i \rightarrow T_f \rightarrow T_i$ and $P_i \rightarrow P_f \rightarrow P_i$. For this purpose we attach to the system a reservoir at temperature $T_1 < T_i$ and pressure $P_1 < P_i$, while retaining the original reservoir at temperature $T_0 > T_f$ and pressure $P_0 > P_f$. While the system interacts with reservoir 0, reservoir 1 remains sealed off, and vice versa.

(a) In considering the case of the ideal gas the interaction with reservoir for the return process is handled by reversing the indices i and f and replacing subscript 0 by subscript 1 in (19) and (22). When these newly generated expressions are added to (19) and (22) one obtains for the cyclic process

$$\begin{aligned} \theta_c &= \frac{3}{2} nR \left(\frac{1}{T_1} - \frac{1}{T_0} \right) (T_f - T_i) + nR \left(\frac{T_i}{P_i} - \frac{T_f}{P_f} \right) \\ &\quad \times \left(\frac{P_0}{T_0} - \frac{P_1}{T_1} \right) = \frac{3}{2} nR \left(\frac{1}{T_1} - \frac{1}{T_0} \right) (T_f - T_i) \\ &\quad + nR \left(\frac{1}{c_i} - \frac{1}{c_f} \right) (c_0 - c_1), \end{aligned} \quad (29)$$

where c is the concentration of the gas phase. Thus, the second term drops out if the gas concentrations in the two reservoirs are rendered identical. In any case, the principal contribution is shown by the first term in (29), which agrees with the result cited in another derivation [7] where temperature and volume were taken as

the independent variables. If the process had been carried out reversibly there would have been no change in entropy in the system.

(b) For the condensed phase a similar operation involving (26) and (28) leads to the result

$$\begin{aligned} \theta_C = & - \left[n\tilde{c}_P \left(\frac{1}{T_0} - \frac{1}{T_1} \right) + \alpha n\tilde{V} \left(\frac{P_0}{T_0} - \frac{P_1}{T_1} \right) \right] \\ & \times (T_f - T_i) + \alpha n\tilde{V} \left(\frac{1}{T_0} - \frac{1}{T_1} \right) (P_f T_f - P_i T_i) \\ & + \beta n\tilde{V} \left(\frac{P_0}{T_0} - \frac{P_1}{T_1} \right) (P_f - P_i) - \frac{\beta}{2} n\tilde{V} \left(\frac{1}{T_0} - \frac{1}{T_1} \right) \\ & \times (P_f^2 - P_i^2). \end{aligned} \quad (30)$$

Under ordinary laboratory conditions the quantities that involve $\beta\tilde{V}$ and $\alpha\tilde{V}$ will be small relative to \tilde{C}_P and, in zero order approximation, may be ignored. Then the principal contribution to the entropy change of the condensed phase undergoing a cyclic process is given by

$$\theta_c = n\tilde{C}_P (T_f - T_i) \left(\frac{1}{T_1} - \frac{1}{T_0} \right). \quad (31)$$

8. Discussion

By eliminating the commonly used inequalities associated with the second law of thermodynamics we were able to relate differential elements of heat and work transfer carried out irreversibly to those executed reversibly. This permitted us to determine the differential form of the entropy associated with the irreversible transfer of heat and work across a thin boundary separating a reservoir from a system. The control variables governing the dependent variable were temperature, pressure, and composition. To apply these quantities to irreversible processes it was assumed that the latter occurred sufficiently slowly that in the system T , P , and n_i could be altered uniformly over most of the physical extension of the system, but no limits were set between the difference of these quantities and the corresponding fixed ones of the reservoir.

As examples we considered ideal gases as well as condensed phases. When integrating we distinguished between integrals that involve either one or two variables. In the latter set we examined two cases with different time rates of change of temperature and pressure at constant compositions. As expected, the corresponding in-

tegrals depend on the chosen path, but their sum is independent of the selection for the time variations of the independent variables. We also examined cyclic processes to note the net entropy increase in the universe upon irreversibly cycling the ideal gas or condensed phase.

These derivations should serve as a prototype for an analysis of irreversible phenomena. The present approach complements the standard theory of irreversible processes, in which emphasis is placed on the specification of fluxes, such as transport of entropy and matter, in response to external forces either within a system or across boundaries.

Acknowledgments

This research was supported through Award SI-06-021 by the Camille and Henry Dreyfus Foundation.

References

- [1] Dor Ben-Amotz, J.M. Honig, *J. Chem. Phys.* **118**, 5932 (2003).
- [2] J.M. Honig, Dor Ben Amotz, *J. Chem. Ed.* **83**, 132 (2005).
- [3] Dor Ben Amotz, J.M. Honig, *Phys. Rev. Lett.* **96**, 020602 (2006).
- [4] Dor Ben Amotz, J.M. Honig, *J. Phys. Chem. B* **110**, 10066 (2006).
- [5] J.M. Honig, Dor Ben Amotz, *Chem. Educator* **13**, 220 (2008).
- [6] J.M. Honig, *Thermodynamics, Principles Characterizing Chemical and Physical Processes*, 3rd ed., Academic Press, Amsterdam 2008.
- [7] J.M. Honig, R. Hoehn, *Open J. Chem. Thermo.* 2011, in press.
- [8] S.R. de Groot, P. Mazur, *Non-Equilibrium Thermodynamics*, North-Holland, Amsterdam 1962.
- [9] I. Prigogine, *Introduction to Thermodynamics of Irreversible Processes*, Wiley, New York 1967.
- [10] R. Haase, *Thermodynamics of Irreversible Processes*, Dover, New York 1990.
- [11] R.C. Tolman, P.C. Fine, *Rev. Mod. Phys.* **20**, 51 (1948).
- [12] J. Keenan, *A Course in Thermodynamics*, Blaisdell, Waltham MA 1966, Ch. 13.
- [13] A. Bejan, *Advanced Engineering Thermodynamics*, 2nd ed., Wiley, New York 1997, p. 135.

Entropy of Irreversible Processes Across a Boundary

Jurgen Michael Honig* and Ross Hoehn

Department of Chemistry, Purdue University, West Lafayette, Indiana, 47907 USA

Abstract: A novel method for determining the entropy associated with irreversible processes has been provided, differing from the conventional theory of irreversible thermodynamics. It permits the direct relation of heat and work transfers in irreversible processes to those in reversible changes, in terms of measurable properties. The same technique is applied to the construction of thermodynamic state functions that are no longer limited to reversible phenomena. The results are then used to construct line integrals for the contribution of irreversible processes to the entropy associated with the flow of heat, work, and matter across a junction. Specific examples are provided to illustrate the procedure; they relate to changes of temperature and volume and to cycling of systems interacting with a reservoir *via* a thin barrier.

Keywords: Irreversible process/phenomenon, irreversible function of state, quasistatic irreversible processes.

INTRODUCTION

The proper formulation of entropy changes during irreversible processes has been the subject of numerous investigations ever since the formulation of entropy as a function of state. It nevertheless seems appropriate to introduce an unconventional methodology through detailed calculations involving the irreversible exchange of heat and work for a system interacting with a reservoir through a thin intervening barrier. This problem is also of intrinsic interest. For this purpose we first derive fundamental information that is somewhat scattered in the literature, in which the commonly used inequalities in the second law are replaced with equalities. We then apply these concepts to determine the increase in entropy during the irreversible processes in the above-mentioned compound system. Several conclusions of interest are drawn. The present article represents an extension of earlier work in this area [1-5].

At the outset we introduce two basic assumptions. The object under study is an isolated compound unit consisting of a system anchored to its surroundings as sketched in Fig. (1), which shows the temperature profile in both parts of the unit. Corresponding profiles exist for the pressure and the chemical potentials. Processes in both sections are presumed to occur sufficiently slowly that one may assign uniform values T_0, P_0, μ_0 to the temperature, pressure, and chemical potential over almost all the region in the surroundings, and corresponding values T, P, μ over most of the region within the system. The changeover between the two sets of intensive variables is thus limited to a thin boundary region consisting of a poor thermal conductor imbedded in a slowly moving piston that also permits a slow diffusion of matter across its interface. The present situation is thus the exact opposite of the irreversible processes considered in the standard theory of irreversible thermodynamics, where $T, P,$ and μ are locally functions of position within the system, and thereby relate to

the flow of heat, work, and matter through the system as a whole. By contrast, in the present case attention is directed to the transfer of these entities across an interface.

The second restriction involves the commonly employed assumption that all processes in the surroundings (reservoirs) take place reversibly, whether the processes in the system occur reversibly or not. In the absence of this assumption the analysis becomes far more complex. Procedures carried out subject to the above qualifications are termed *Quasistatic Irreversible Processes* (QSIPs).

BASICS

To set up the fundamental expressions, consider an infinitesimal step in an interactive process - involving the system and the reservoir - that is carried out reversibly (*r*) and irreversibly (*i*). Since the entropy, S , is a function of state, the infinitesimal change dS of the system is the same for both processes. However, the entropy change of the reservoir differs in the two cases, which we designate as $dS_0^{(a)}$ and $dS_0^{(b)}$, respectively. Since entropy is conserved in the reversible operation, we set

$$dS + dS_0^{(a)} = 0 \quad (1a)$$

On the other hand, when executing the same process irreversibly, the entropy of the compound system can only increase, so that

$$dS + dS_0^{(b)} > 0 \quad (1b)$$

It is now apposite to introduce an *entropy deficit function* $d\theta > 0$ which converts Eq. (1b) into an equality:

$$dS + dS_0^{(b)} - d\theta = 0 \quad (1c)$$

While this may appear to be simply a bookkeeping operation it has important implications: a trivial rearrangement of the above equation leads to

$$dS_u \equiv dS + dS_0^{(b)} = d\theta \quad (1d)$$

where S_u represents the entropy of the universe, here the compound system. Eq. (1d) shows that the deficit function is equivalent to the entropy increase of the universe resulting from the execution of any (infinitesimal) irreversible proc-

*Address correspondence to these authors at the Department of Chemistry, Purdue University, West Lafayette, Indiana, 47907 USA; Tel: 765 494 5279; Fax: 765 494 0239; E-mail: jmh@purdue.edu

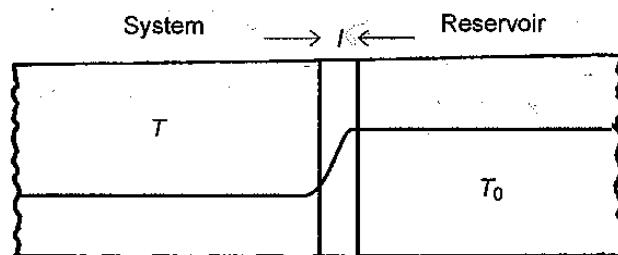


Fig. (1). Sketch of a temperature profile for the combined system and reservoir at different temperatures T and T_0 . The temperature in each phase remains essentially constant over almost the entire region; the gradient in temperature develops over only a small region l at the interface.

ess. Note that dS represents the differential entropy change for the system characterized by intensive variables which differ from those which relate to the surroundings.

We now set $dS = \dot{d}_r Q/T$ and $dS_0^{(b)} = \dot{d}_r Q_0/T_0 = -\dot{d}_i Q/T_0$, where Q signifies the heat transfer into the system and T is its operating temperature. The second relation applies because of heat conservation in the isolated compound system. When these expressions are entered in (1c) one obtains the fundamental result

$$\dot{d}_i Q = (T_0/T) \dot{d}_r Q - T_0 d\theta < (T_0/T) \dot{d}_r Q \quad (2a)$$

The central equality duplicates the expression derived by a different method in Ref. [6].

The constraint on the right may be tightened by noting that the inequality must be satisfied for any value of $T \geq T_0$ ($T \leq T_0$) when heat flows from the system (reservoir) into the reservoir (system). In particular, it must apply to the limiting case $T \rightarrow T_0$. We thereby obtain the string of inequalities

$$\dot{d}_i Q < \dot{d}_r Q < (T_0/T) \dot{d}_r Q \quad (2b)$$

which are self evident for positive values of $\dot{d}_r Q$, where $T_0/T > 1$. Note that in the limiting case discussed above, the quantity $d\theta$ in Eq. (2a) does not necessarily vanish [7]. For example, the reversible heating of a sample may trigger chemical processes totally within the system that cannot be controlled from the outside. However, in the absence of such processes, $\dot{d}_r Q$ is the sole applicable variable.

For heat outflows, with $T_0/T < 1$, the inequalities (2b) still hold; the quantities become progressively less negative from left to right. One should observe that the statement $\dot{d}_i Q < \dot{d}_r Q$ is a reformulation of the well-known Clausius inequality.

Eq. (2a) may also be recast in the familiar form as

$$dS = \dot{d}_i Q/T_0 + d\theta > \dot{d}_i Q/T_0 \quad (2c)$$

Note that it is the experimentally well established temperature of the reservoir that enters the above relations. Eq. (2a) may be rewritten as

$$\dot{d}_i Q = \dot{d}_r Q + (T_0/T - 1) \dot{d}_r Q - T_0 d\theta \quad (2d)$$

which directly relates the two types of heat exchange processes.

LOWER BOUNDS ON THE DEFICIT FUNCTION

In the introduction of the deficit function we had originally set $d\theta > 0$. A greater positive lower bound may be im-

posed by employing the condition $\dot{d}_i Q < \dot{d}_r Q$. Thus, the sum of the last two terms in Eq. (2d) must be negative. This imposes the requirement:

$$d\theta > [(T_0 - T)/T_0 T] \dot{d}_r Q = [(T_0 - T)/T_0] dS \quad (3)$$

The right hand side is always positive. For if $T_0 > T$ ($T_0 < T$), heat flows from the surroundings (system) into the system (surroundings), so that $\dot{d}_r Q$ and dS are both positive (negative). In either case the right hand side is positive, thus establishing a positive lower bound that involves experimentally accessible operating conditions.

INEQUALITIES RELATING TO WORK PERFORMANCE

Information relating to work becomes available via the First Law in the form

$$dE = \dot{d}_r Q + \dot{d}_i W = \dot{d}_i Q + \dot{d}_i W \quad (4)$$

where E is the energy of the system and $\dot{d}_i W$ is the element of work performed in an infinitesimal step of an irreversible process. Eq. (4) holds because E is a function of state. Now introduce Eq. (2d) and solve for

$$\dot{d}_i W = \dot{d}_i W - (T_0/T - 1) \dot{d}_r Q + T_0 d\theta = \dot{d}_i W - (T_0 - T) dS + T_0 d\theta \quad (5)$$

where the last two terms differ in sign from those of Eq. (2d), so that $\dot{d}_i W > \dot{d}_r W$. The irreversible performance of work always exceeds that which is required when the same step is executed reversibly, in accord with intuitive reasoning. The above equation is a reformulation of the Gouy-Stodola theorem.

SPECIFICATION OF THE DEFICIT FUNCTION

To be of use the deficit function must be specified in terms of experimentally accessible quantities. This may be achieved in two ways. The first method involves solving Eq. (5) for $d\theta$:

$$d\theta = (\dot{d}_i W - \dot{d}_r W)/T_0 + (1 - T/T_0) dS \quad (6a)$$

The total performance of work, based on an integration of $\dot{d}_i W$, may be determined experimentally and the integrated value of $\dot{d}_r W$ may be obtained by calculation. The determination of entropy through calorimetric measurements is also well established. Thus, in principle, θ may be found by performing the required integrations. Details concerning this methodology are left to a future publication. We briefly note that in the absence of work Eq. (6a) reduces to

Irreversible Processes

$$d\theta = (1/T - 1/T_0) d_0Q \quad (6b)$$

which is derived by different means in Ref. [8]. If work is processed without heat transfer one obtains the relation obtained by a different approach in Ref. [9] below Eq. (3.53), namely

$$d\theta = (d_0W - d_rW)/T_0 \quad (6c)$$

FUNCTIONS OF STATE FOR IRREVERSIBLE PROCESSES

For future use we now set up the differential form for the energy, E_0 , of the *surroundings*, as appropriate to processes that take place reversibly

$$dE_0 = T_0 dS_0 - P_0 dV_0 + \sum_i \mu_{0i} dn_{0i} \quad (7a)$$

where P_0 is the pressure, V_0 the volume, μ_{0i} the chemical potential of species i , and n_{0i} its mole number, all referred to the surroundings. For the closed entity (system + surroundings) energy and material is conserved, whence $dE = -dE_0$ and $dn_{0i} = -dn_i$, where the nonsubscripted quantities refer to the system. If the volume of the compound unit is held fixed as well, we may set $dV_0 = -dV$. Lastly, we use Eq. (1d) and replace dS_0 in Eq. (7a) with $dS_0^{(b)} = -dS + d\theta$, which is appropriate to irreversible processes in the system. This leads to the expression for the energy of the *system* in the form

$$dE = T_0 dS - P_0 dV + \sum_i \mu_{0i} dn_i - T_0 d\theta \quad (7b)$$

This relation, involving different arguments, was derived by Kestin [8]. Note that it is the intensive variables of the reservoir, different from those of the system, which appear in the above relationship, which applies even to irreversible phenomena. All extensive variables also remain well defined. Conditions of the type introduced here were termed QSIPs.

It is expedient to rewrite the above in the equivalent form

$$dE = (T_0 - T)dS - (P_0 - P)dV + \sum_i (\mu_{0i} - \mu_i) dn_i + TdS - PdV + \sum_i \mu_i dn_i - T_0 d\theta \quad (7c)$$

which explicitly introduces the intensive variables of the system proper. The irreversibilities are subsumed in the last term on the right. The reversible execution of the same step, while retaining the same intensive variables of the system, leads to the customary expression for the same differential energy:

$$dE = TdS - PdV + \sum_i \mu_i dn_i \quad (7d)$$

Since E is a function of state we may subtract (7d) from (7c) to obtain

$$d\theta = (1/T_0)(T_0 - T)dS - (P_0 - P)dV + \sum_i (\mu_{0i} - \mu_i) dn_i \quad (7e)$$

which determines the incremental deficit function in terms of independent variables that are experimentally accessible, namely: S , V , and n_i . Eq. (7e) is consistent with Eq. (1d); when integrated, it relates the entropy increase in the universe to the transfer of entropy (heat), mechanical work, and matter across the interface that connects the system to its surroundings when QSI processes take place. While correct, the above formulation involves S as the independent variable, which is not readily controlled experimentally. An alternate approach is thus desirable.

Toward this end we introduce the Helmholtz free energy $A = E - TS$, with the differential form $dA = dE - TdS - SdT$. When Eq. (7c) is inserted we obtain.

$$dA = (T_0 - T)dS - (P_0 - P)dV + \sum_i (\mu_{0i} - \mu_i) dn_i - SdT - PdV + \sum_i \mu_i dn_i - T_0 d\theta \quad (8a)$$

However, the appropriate control variables for the function, $A = A(T, V, \{n_i\})$, should be temperature, volume, and composition. Accordingly, we reexpress the entropy in terms of these independent variables as $S = S(T, V, \{n_i\})$, with

$$dS = (\partial S/\partial T)_{V, n_i} dT + (\partial S/\partial V)_{T, n_i} dV + \sum_i (\partial S/\partial n_i)_{T, V, n_{i \neq j}} dn_i \quad (8b)$$

We next set $(\partial S/\partial T)_V = C_{V, n_i}/T$, where C_{V, n_i} is the heat capacity at constant volume and composition, introduce the relevant Maxwell relation $(\partial S/\partial V)_T = (\partial P/\partial T)_V$, and set $\hat{S}_i \equiv (\partial S/\partial n_i)_{T, V, n_{i \neq j}}$. Eq. (8a) then reads

$$dA = (T_0 - T)[(C_{V, n_i}/T) dT + (\partial P/\partial T)_{V, n_i} dV + \sum_i \hat{S}_i dn_i] - (P_0 - P) dV + \sum_i (\mu_{0i} - \mu_i) dn_i - SdT - PdV + \sum_i \mu_i dn_i - T_0 d\theta \quad (8c)$$

which is the desired expression for an infinitesimal change in Helmholtz free energy in QSIPs.

Since A is a function of state, we now subtract from the above the standard expression for operations under reversible conditions,

$$dA = -SdT - PdV + \sum_i \mu_i dn_i \quad (8d)$$

to obtain

$$T_0 d\theta = (T_0 - T)[(C_{V, n_i}/T) dT + (\partial P/\partial T)_{V, n_i} dV + \sum_i \hat{S}_i dn_i] - (P_0 - P) dV + \sum_i (\mu_{0i} - \mu_i) dn_i \quad (8e)$$

which relates the differential of the deficit function to temperature, volume, and composition of the system as the appropriate control variables.

The integral formulation requires that we specify how each of the variables changes with time t . We assume that the reservoir is so huge and well mixed that all of its intensive variables remain fixed, so that we set

$$\theta = \int \left[\left(1 - \frac{T(t)}{T_0} \right) \right] \left[\frac{C_{V, n_i}(T(t), V(t), n_i(t))}{T(t)} \frac{dT}{dt} + \frac{\partial P}{\partial T} \frac{dV}{dt} + \sum_i \hat{S}_i \frac{dn_i}{dt} \right] dt$$

$$- \int \frac{P_0}{T_0} \left(1 - \frac{P(t)}{P_0} \right) \frac{dV}{dt} dt + \sum_i \int \frac{\mu_{0i}}{T_0} \left(1 - \frac{\mu_i(t)}{\mu_{0i}} \right) \frac{dn_i}{dt} dt \quad (9)$$

where the integrals are taken between the initial time, $t_i = 0$, and the final time, $t_f = \tau$, as lower and upper limits respectively.

SPECIAL CASES

To illustrate how Eq. (9) is used we now introduce several simplifying, but reasonable, qualifications. First, we already assumed that the reservoir is so huge that none of its intensive properties is significantly altered in any interchange with the system; then T_0 , P_0 , and μ_{0i} remain essentially constant. Second, we restrict consideration to a one-component system of fixed composition, which eliminates the third and fifth integrals in (9). Third, for definiteness assume that the system is initially in a state with $T_i < T_0$ and

$P_i < P_0$. Then as the interaction between the system and its surroundings is turned on, T and P both increase. The latter requirement is satisfied by fulfilling the sufficient condition that the volume of the system should diminish during the interaction. Thus, T and V become the control variables, while P adjusts in accordance with the relevant equation of state of the system. The volume is subject to direct control by the experimenter. Then, during the interaction, the temperature of the system is allowed to increase by heat conduction from its initial value T_i to its final value $T_f < T_0$, and its volume is manipulated to decrease from V_i to V_f , such that at the end of the process the prevailing pressure has increased from P_i to $P_f < P_0$. As will be seen, in the approximation used below, we do not need to specify the path by which T and V are altered; what is important are the specifications of the initial and final states. Fourth, this process also requires forcing an increase in volume of the reservoir to keep the total volume of the compound system constant, as required in setting up Eq. (7b). Fifth, for illustrative purposes, let the system and reservoir consist of a gas which satisfies the Berthelot equation of state [9],

$$P = \frac{nRT}{V-nb} - \frac{n^2a}{TV^2} \approx \frac{nRT}{V} - \frac{n^2a}{TV^2} \quad (10)$$

where a and b are both constants and all other symbols retain their conventional significance; the expansion applies as long as $nb \ll V$.

We now proceed to use Eq. (9) as follows: Introduce the caloric equation of state for the energy E and Eq. (10) to determine

$$\partial E / \partial V = T(\partial P / \partial T) - P = 2n^2a / V^2T \quad (11)$$

and integrate. The arbitrary function of temperature is specified by $3nRT/2$, so that

$$E = 3nRT/2 - 2n^2a / VT; C_{V,i} \\ = 3nR/2 + 2n^2a / VT^2 \quad \dots \quad (12)$$

where $C_{V,n}$ is the heat capacity at constant volume and composition. Now substitute Eqs. (10) – (12) in (8e). At constant composition, changes in temperature and volume of the system produce an infinitesimal change in entropy given by:

$$d\theta = \left(1 - \frac{T}{T_0}\right) \left[\frac{3nR}{2T} + \frac{2n^2a}{VT^3} \right] dT + \left\{ \left(\frac{nR}{V-nb} + \frac{n^2a}{V^2T^2} \right) - \frac{P_0}{T_0} - \frac{2}{T_0} \left(\frac{n^2a}{V^2T} \right) \right\} dV \quad (13)$$

For subsequent ease of handling we next set up contributions under separate headings. (i) We first consider integrals that involve either T or V as the sole integration variable for transitioning the system from its initial state (T_i, V_i) to its final state (T_f, V_f). The corresponding contribution to the entropy is specified by:

$$\theta_{0i} = \frac{3nR}{2} \ln \frac{T_f}{T_i} - \frac{3nR}{2T_0} (T_f - T_i) - nR \ln \left[\frac{V_i - nb}{V_f - nb} \right] + \frac{P_0}{T_0} (V_i - V_f) \quad (14a)$$

(ii) For possible later use we separately study the entropy increase of the reservoir whose volume increases reversibly from V_0 to $V_0 + (V_i - V_f)$ at fixed T_0, P_0 , which matches the volume change of the system, thereby preserving the overall volume. For this purpose we adopt the basic relation $dS_0 = (1/T_0)(dE_0 + P_0dV_0)$, with $dE_0 = (dE_0/dV_0)dV_0$ for fixed T_0 . On introducing (11) and integrating we find that

$$S_{0,f} - S_{0,i} = \frac{2n_0^2a}{T_0^2} \left(\frac{1}{V_{0,i}} - \frac{1}{V_{0,f}} \right) + \frac{P_0}{T_0} (V_{0,f} - V_{0,i}) \quad \dots \\ = \frac{2n_0^2a}{T_0^2} \left(\frac{V_i - V_f}{V_{0,i}^2} \right) + \frac{P_0}{T_0} (V_i - V_f) = \frac{2a}{T_0^2} c_0^2 (V_i - V_f) + \frac{P_0}{T_0} (V_i - V_f) \quad (14b)$$

where we had expanded the denominator for small values of $V_i - V_f$ relative to $V_{0,i}$; also we set $c_0 \equiv n_0/V_0$ as the concentration variable for the reservoir.

(iii) It remains to work with two types of line integrals in Eq. (13) which simultaneously involve both T and V in the integrand. The first deals with temperature changes that accompany heat transfers

$$d\theta_T = \left(1 - \frac{T}{T_0}\right) \left[\frac{2n^2a}{VT^3} \right] dT \quad (14c)$$

and the second relates to volume changes which are produced by work exchange,

$$d\theta_V = \left\{ \frac{n^2a}{V^2T^2} - \frac{2}{T_0} \left(\frac{n^2a}{V^2T} \right) \right\} dV \quad (14d)$$

For their evaluation one must introduce time, t , as a parameter and specify the time dependence of both T and V . We consider two cases at random in conformity with the earlier discussion. Changes in volume and heat flows are adjusted to lead to the following time dependences:

Case 1. Let $V(t) = V_i e^{-k_V t}$, $T(t) = T_i e^{k_T t}$, $0 \leq t \leq \tau$, where k_V and k_T are time constants such that in the time interval $0 \leq t \leq \tau$ the volume (temperature) changes from the initial value V_i (T_i) to the final value V_f (T_f). Insert these two functions of time into (14c) and set $dT = (dT/dt)dt$ to carry out the integrations, which are lengthy though straightforward. One finds that

$$\theta_T = + \frac{2n^2a}{V_i T_i} \left\{ \frac{1}{T_i (k_V/k_T - 2)} \left[\frac{V_i}{V_f} \left(\frac{T_i^2}{T_f^2} \right) - 1 \right] - \frac{1}{T_0 (k_V/k_T - 1)} \left[\frac{V_i}{V_f} \left(\frac{T_i}{T_f} \right) - 1 \right] \right\}; \quad \frac{k_V}{k_T} = \frac{\ln(V_i/V_f)}{\ln(T_f/T_i)} \quad (15a)$$

Proceeding similarly with (14d), using $dV = (dV/dt)dt$ one obtains

$$\theta_V = \frac{n^2a}{V_i T_i} \left\{ \frac{-1}{T_i (1 - 2k_T/k_V)} \left[\frac{V_i}{V_f} \left(\frac{T_i^2}{T_f^2} \right) - 1 \right] + \frac{2}{T_0 (1 - k_T/k_V)} \left[\frac{V_i}{V_f} \left(\frac{T_i}{T_f} \right) - 1 \right] \right\} \quad (15b)$$

If the denominators such as $(k_f/k_T - 1)^{-1}$ or $(2k_T/k_V - 1)^{-1}$ approach zero their multipliers in square brackets do likewise since under these conditions $V_f \rightarrow V_i$, $T_f \rightarrow T_i$; l'Hôpital's rule then shows that the respective products approach zero, as anticipated.

If in its final state the system is equilibrated with its surroundings, then $T_f = T_0$; one then also requires that V_f satisfy Eq. (10) with $P_f = P_0$.

Case 2: We consider the time dependence of the volume $V = V_i / (1 + k_V \tau)$, with the same temperature dependence as before. The upper limit for $k_V \tau$ is determined by the choice for the final volume, V_f . Eqs. (14a) and (14b) are the same as before. On substituting the assumed time dependence for temperature into Eq. (14c) one obtains

$$\theta_T = + \frac{n^2 a}{T_i^2 V_i} \left\{ \left[1 - \frac{T_i^2}{T_f^2} \right] + \frac{k_V}{2k_T} \left[1 - \frac{T_i^2}{T_f^2} + 2 \frac{T_i^2}{T_f^2} \ln \frac{T_i}{T_f} \right] \right\} - \frac{2n^2 a}{T_i T_0 V_i} \left\{ \left[1 - \frac{T_i}{T_f} \right] + \frac{k_V}{k_T} \left[1 - \frac{T_i}{T_f} + \frac{T_i}{T_f} \ln \frac{T_i}{T_f} \right] \right\}, \quad \frac{k_V}{k_T} = \frac{V_i / V_f - 1}{\ln(T_f / T_i)} \quad (16a)$$

Proceeding similarly with Eq. (14d) one finds

$$\theta_V = \frac{n^2 a k_V}{V_i T_i k_T} \left\{ \frac{-1}{2T_i} \left(1 - \frac{T_i^2}{T_f^2} \right) + \frac{2}{T_0} \left(1 - \frac{T_i}{T_f} \right) \right\} \quad (16b)$$

both of which clearly differ from Case 1.

Nevertheless, despite the differences between the two cases, the *total* entropy change associated with step (iii) for the above integrals (on elimination of the k_T/k_V ratios, and summing Eqs. (15a) and (15b) or Eqs. (16a) and (16b)), is exactly the same, namely.

$$\theta_V + \theta_T = \frac{n^2 a}{V_i T_i} \left\{ \frac{2}{T_0} \left[\frac{V_i T_i}{V_f T_f} - 1 \right] - \frac{1}{T_i} \left[\frac{V_i T_i^2}{V_f T_f^2} - 1 \right] \right\} = n^2 a \left\{ \frac{2}{T_0} \left[\frac{1}{V_f T_f} - \frac{1}{V_i T_i} \right] - \left[\frac{1}{V_f T_f^2} - \frac{1}{V_i T_i^2} \right] \right\} \quad (17)$$

This finding may be rationalized by noting that we had selected T_f/T_i and V_f/V_i at the outset for the two cases; in turn this required an adjustment of k_T , k_V , and τ to meet this particular choice. The processes were selected to occur at rates sufficiently slow that the uniformity of temperature and pressure was maintained over almost all the volume of the system. Thus, the final results involve only the initial and final temperatures and volumes of the system; the temperature of the reservoir; the amount of material in the system and reservoir; the parameters appropriate to the Berthelot equation of state; and fundamental constants. In the QSIP approximation, with the assumed uniformly changing properties, no reference is made to pathways by which the system changes from its initial to its final configuration. What Eqs. (15) and (16) do show is a difference in the contributions of heat and work to θ_V and θ_T respectively, but they sum to the same final result. Further, if $V_f = V_i$, $T_f = T_i$ the above equations

show, as they should, that there is no entropy change in the system and surroundings. We have examined other changes of control variables with time and again obtain results fully in accordance with the above findings.

The total entropy change of the compound system under the assumed conditions is the sum of Eqs. (14a) and (17); the entropy change of the reservoir responding to the irreversible processes is given by (14b).

For an ideal gas as a working substance Eq. (17) drops out and Eq. (14a) simplifies to

$$\theta_{ig} = \frac{3nR}{2} \ln \frac{T_f}{T_i} - \frac{3nR}{2T_0} (T_f - T_i) - nR \ln \left[\frac{V_i}{V_f} \right] + \frac{P_0}{T_0} (V_i - V_f) \quad (18)$$

Here the first and third terms agree with the entropy change accruing to the system under reversible operations.

CYCLIC PROCESSES

So far we have considered only monotonic changes in T and V . Also of interest is the execution of a circular process in which the initial state of the system is restored. To explore this situation we attach to the system a second reservoir at temperature $T_1 < T_i$, pressure $P_1 < P_i$, that initially remains sealed off while the interaction between the system and the first reservoir proceeds as shown above. After the end point T_f and V_f has been reached the first reservoir is sealed off and the interaction between the system and the second reservoir is initiated and maintained until the initial state of the system has been restored.

Assume again that the reservoirs and system are comprised of a Berthelot gas; then, for the return path the subscripts f and i in Eqs. (14a) must be interchanged and the subscript 0 must be replaced by 1. On adding this modified equation to (14a) for the forward process, one obtains (in the approximation $nb \ll V$) the net contribution associated with (i) the path-independent integrals as:

$$\theta_1 = \frac{3}{2} nR (T_f - T_i) \left(\frac{1}{T_1} - \frac{1}{T_0} \right) + R (V_i - V_f) [(c_0 - c_1) + (c_1^2 - c_0^2) b] \quad (19a)$$

We proceed similarly (ii) with the same index alterations to Eq. (14b) to deal with the entropy contribution for the volume change of reservoir 1 in the reverse process. We also again expand P_1/T_1 and add the resultant to Eq. (14b) to obtain

$$\theta_2 = a (V_i - V_f) \left(\frac{c_0^2}{T_0^2} - \frac{c_1^2}{T_1^2} \right) + R (V_i - V_f) [(c_0 - c_1) + (c_0^2 - c_1^2) b] \quad (19b)$$

as the overall change in entropy of the two reservoirs.

(iii) Lastly, we must evaluate the line integrals. To handle the exchange between the system and reservoir 1 we must repeat the mathematical operations that led to Eqs. (15), but with $V(t) = V_i e^{+k_V t}$, $T(t) = T_i e^{-k_T t}$, $0 \leq t \leq \tau$. It turns out that we then recover Eq. (17) with the indices once more interchanged. When this resultant is added to (17) we obtain

$$\theta_3 = 2n^2 a \left[\frac{1}{V_f T_f} - \frac{1}{V_i T_i} \right] \left(\frac{1}{T_0} - \frac{1}{T_1} \right) \quad (19c)$$

The total entropy change during the cyclic process is the sum of (19a), and (19c).

The major contribution to the entropy changes in the cyclic process of the compound system is in the form

$$\theta = \frac{3}{2} nR (T_f - T_i) \left(\frac{1}{T_1} - \frac{1}{T_0} \right) \quad (19d)$$

In fact, if matters are arranged such that $c_0 = c_1$, Eq. (19d) is the only contribution. In a strictly reversible process the total entropy change would add up to zero.

Eqs. (19a) and (19c) specify the increase in entropy of the compound unit when the system is cycled through the changes $T_i \rightarrow T_f \rightarrow T_i$ and $V_i \rightarrow V_f \rightarrow V_i$. The results depend on the difference between the initial and final temperatures and volumes of the system, the temperatures of the hot and cold reservoir, the concentration of the gases in the reservoirs, the number of moles of gas in the system, and on the parameters of the Berthelot equation of state. Remarkably, the major contribution, Eq. (19d), is independent of the constitution of the gas phases, and depends only on the indicated temperatures.

CONCLUSIONS

By generalizing the standard thermodynamic theory pertaining to irreversible phenomena it is possible to determine changes in the state of a system during an irreversible transfer of heat or irreversible execution of work in terms of measurable quantities. The theory was extended to set up thermodynamic functions of state when irreversible changes take place, as shown by Eqs. (7c) and (8c). One can then specify the entropy associated with QSI processes across the boundary of a system attached to a reservoir, as shown by Eq. (9), in terms of changes in temperature, volume, and composition. The theory is applicable to QSIPs no matter how big the initial difference between the intensive properties of the reservoir and the system. Whenever two or more of the independent variables are simultaneously changed the relevant integrals require the specification of the time dependence of T , V and n . Specific examples have been provided to show how to determine the contributions of irreversible processes to the entropy when different kinds of changes in temperature and volume are maintained across a thin boundary between a system and its surroundings at fixed composition. As is verified by explicit calculations, or by general considerations, in the QSIP approximation the total entropy change associated with the irreversible processes does not depend on the chosen pathway. The entropy change in QSIPs, as specified by temperature and volume as inde-

pendent variables, are specified by Eqs. (14a,b) and (17). Also investigated was the entropy change in the universe when the system executes a cyclic change, as specified by Eqs. (19a,b,c).

This analysis should serve as a prototype study of irreversible phenomena under specified initial assumptions. It complements the standard theory of irreversible processes, in which emphasis is placed on the specification of fluxes, such as transport of entropy and matter, in response to external forces either within a system or across boundaries.

ACKNOWLEDGEMENTS

The authors are indebted to Professor Dor Ben Amotz of Purdue University for many insightful discussions. They also acknowledge contributions by Ms. Kasi Rubadue; both she and the junior author of this paper were undergraduate students at Purdue University. The research was supported by Award SI - 06 - 021 of the Dreyfus Foundation.

NOTES:

1. The notation is now somewhat confusing. What is meant by $d_r Q$ in the limiting case is actually a reversible heat transfer while additional irreversible processes are triggered totally within the system; $d_r Q$ represents the reversible transfer in the absence of such additional events.
2. Actually, it is only necessary to demand that the volume change of the surroundings be exactly the negative of that of the system. This allows the surroundings to assume other volume changes not associated with the irreversible process of the system.

REFERENCES

- [1] J.M. Honig, and D.B. Amotz, "The analysis of spontaneous processes using equilibrium thermodynamics", *J. Chem. Ed.*, vol. 83, pp. 132-7, 2005.
- [2] D.B. Amotz, and J.M. Honig, "Average entropy dissipation in irreversible mesoscopic processes", *Phys. Rev. Lett.*, vol. 96, pp. 1-4, 2006.
- [3] D.B. Amotz, and J.M. Honig, "The rectified second law of thermodynamics", *J. Phys. Chem. B.*, vol. 110, pp. 10066-72, 2006.
- [4] J.M. Honig, and D.B. Amotz, "Rectification of thermodynamic inequalities as a means of characterizing irreversible phenomena", *Chem. Educator.*, vol.13, pp. 220-6, 2008.
- [5] J.M. Honig, "Thermodynamics, principles characterizing chemical and physical processes". 3rd ed. Academic Press: Amsterdam 2008.
- [6] R.C. Tolman, and P.C. Fine, "On the irreversible production of entropy", *Rev. Mod. Phys.*, vol. 20: pp. 51-77, 1948.
- [7] J. Kestin, "A course in thermodynamics", Blaisdell: Waltham MA 1966, Chap. 13.
- [8] A. Bejan. "Advanced engineering thermodynamics". 2nd ed., Wiley: New York 1997, p. 135.
- [9] R.S. Berry, S.A. Rice, and Ross J. "Physical chemistry" 2nd ed. Oxford University Press: New York 2000, p. 553.

Received: December 20, 2010

Revised: February 10, 2011

Accepted: March 03, 2011

© Honig and Hoehn; licensee *Bentham Open*.

This is an open access article licensed under the terms of the Creative Commons Attribution Non-Commercial License (<http://creativecommons.org/licenses/by-nc/3.0/>) which permits unrestricted, non-commercial use, distribution and reproduction in any medium, provided the work is properly cited.

Dimensional scaling treatment with relativistic corrections for stable multiply charged atomic ions in high-frequency super-intense laser fields

Ross D. Hoehn,¹ Jiaxiang Wang,² and Sabre Kais^{1,a)}

¹*Departments of Chemistry and Physics, Purdue University, West Lafayette, Indiana 47907, USA*

²*State Key Laboratory of Precision Spectroscopy, Institute of Theoretical Physics, Department of Physics, East China Normal University, Shanghai 200241, China*

(Received 29 August 2011; accepted 8 December 2011; published online 19 January 2012)

We present a theoretical framework which describes multiply charged atomic ions, their stability within super-intense laser fields, and also lay corrections to the systems due to relativistic effects. Dimensional scaling calculations with relativistic corrections for systems: H, H⁻, H²⁻, He, He⁻, He²⁻, He³⁻ within super-intense laser fields were completed. Also completed were three-dimensional self consistent field calculations to verify the dimensionally scaled quantities. With the aforementioned methods the system's ability to stably bind "additional" electrons through the development of multiple isolated regions of high potential energy leading to nodes of high electron density is shown. These nodes are spaced far enough from each other to minimize the electronic repulsion of the electrons, while still providing adequate enough attraction so as to bind the excess electrons into orbitals. We have found that even with relativistic considerations these species are stably bound within the field. It was also found that performing the dimensional scaling calculations for systems within the confines of laser fields to be a much simpler and more cost-effective method than the supporting D = 3 SCF method. The dimensional scaling method is general and can be extended to include relativistic corrections to describe the stability of simple molecular systems in super-intense laser fields. © 2012 American Institute of Physics. [doi:10.1063/1.3673317]

I. INTRODUCTION

The generation of stable, multiply charged atomic ions via exposure to super-intense laser fields is a topic which challenges preconceived notions for ionic atoms and is, therefore, of fundamental importance in atomic and molecular physics.¹⁻³ Over the past decades, advancements in spectroscopic methods have yielded verification of mono-charged calcium and strontium atomic anions^{4,5} and various gas-phase poly-charged molecular ions.⁶⁻⁸ However, without the large charge volume which is provided by the heavy atoms—above—or small molecules it is unlikely that species would be able to bind more than one excess electron; this can be noted by the relative stability of O⁻² in the liquid-phase, yet it is unstable within the gas-phase.⁶ Theoretical works have developed an absolute upper-limit to the number of electrons which may be bound to a atomic center:⁹ $N_c \geq 2Z$, with N_c being the number of electrons and Z being the Coulomb charge of the nucleus. Within the context of Lieb's frameworks, hydrogen would therefore be disallowed any excess electrons beyond that which yields the hydride state, thusly H²⁻ is unstable.^{10,11} Supporting theoretical works have come later^{12,13}—some including implementation of finite-sized scaling¹³—and have conclusively determined at gas-phase that dianionic atoms are unstable.

It has been shown that stable, multiply charged atomic ions may be developed within extremely strong laser fields on the order of 10¹⁶ W/cm² and above.^{14,15} Within the field, the electron density—still being bound to the nucleus—has been

found to be nodal in nature as the Coulomb potential splinters under the influence of the field into distinct, localized regions whose positions are governed by the field parameters of the laser. This phenomenon is most easily—and best—discussed within the context of the Kramers Henneberger (KH) reference frame, electron centric frame, where the electron is treated as the stationary body and the nucleus traverses the path of the applied field; in this context the local nodes of electron density are located at the turning points on the path of the nucleus. These are the location at which the angular velocity of the nucleus decreases and thus spends more time in a local area—thus generating a greater pull in that area. Within these nodal regions, the bound electrons maintain a great enough distance from one another to minimize their Coulomb repulsion while also giving each a center with which to bind. In this field, the electrons—which intuition tells us would be completely ionized—are capable of stably binding into multiply charged atomic ions. The field strength allows one to manipulate the location and pull of the nodal centers, thus generating a method of control over the potential, and therefore establishing the ability to push the electrons into and past their most stable state by means of manipulating laser parameters, frequency, and intensity.

The contained theoretical works are concerned with high-frequency Floquet theory (HFFT) which allows for a time-independent treatment of the coupling of the static Coulomb potential with a time-varying electromagnetic field. This is possible by exploiting highly oscillatory fields in which the electrons would be prohibited from coupling with the periodic nature of the field due to extremely short periods (large frequencies) of oscillation, thus the system's electrons would

^{a)}Electronic mail: kais@purdue.edu.

feel a period average of the applied potential coupled with the static Coulomb potential, again this is best discussed within the KH frame. This time-average allows generation of the aforementioned nodal structure, and therefore permits the stability of the subsequent states and allows the system to forgo autoionization. The above discussed methodology was introduced to atomic systems by Pont *et al.*,¹⁶ van Duijn *et al.*,¹⁷ and was used again by Wei *et al.*^{14,15,18,19} to describe non-relativistic, multiply charged atomic ions. Herein, we shall propose a framework utilizing HFFT as a backbone for applying relativistic corrections to atomic ions in a time-independent manner.

The procedure enclosed is not only a search for the stability of multiply charged ions, but also that in concert with an explicit utilization and validation of the dimensional scaling procedure and the fourthfold installment in such works. Multiple electrons in bound state configurations under either the Dirac or Klein-Gordon equations are both open questions in dimensional scaling, and thus we resort such augmentations to the time independent Schrodinger equation (TISE) at the large-dimensional limit as most relativistic effects can be appended to the Schrodinger equation through first-order perturbation theory.

Also, Kaminski had proposed a relativistic Kramers-Henneberger frame based on the three-dimensional Dirac equation,²⁰ which however, is rather impractical for numerical purposes as the electron momenta appear in the argument of the potential of the KH-transformed Hamiltonian. Krstic also discussed the relativistic corrections starting from Dirac equation and showed the same orbital corrections as used in our work,²¹ although we present it in a phenomenological way. Protopapas *et al.*²² discussed the relativistic mass shift effects from Klein-Gordon equation in stabilization with respect to the non-relativistic prediction and demonstrated in KH frame the feasibility of using the relativistic effective mass.

To derive the atom-intense laser interaction directly from Dirac equation is a demanding work both theoretically and numerically; and, as of yet, the use of such method in search for stable multiply charged ions is open. The most sensible way is to start from Schrodinger equation by including the relativistic corrections in a perturbative way. Physically, the main relativistic corrections in atom-laser interactions include the magnetic component of the laser field, the relativistic mass shift, the invalidity of the dipole approximation and spin and retardation effects. The effects of retardation, the dipole approximation and spin, have been shown by Latinne to be small in general.²³

II. RELATIVISTIC CORRECTIONS

A. Non-relativistic methodology

Consideration within the non-relativistic cases lies no longer with both the mass and the magnetic coupling, but with the time dependent electric field coupling with the system's Coulomb potential; this work was performed by Wei *et al.*^{14,15,18,19} and produced stably bound multiply charged ions for small atomic centers utilizing the field parameter (α_0), discussed later, and finding detachment energies on or-

ders of 0.1 eV to 1.0 eV. The enclosed works, here, expound upon this by adding the necessary relativistic corrections to the previous framework. A free electron within an oscillating electric field shall undergo oscillatory motions which are governed by a coupling to the field; the electron is said to be "quivering" with a motion defined by a trajectory, $\vec{\alpha}_0(t)$, and a quiver amplitude, α_0 . A bound electron within the same situation shall feel a new potential, which is a stacking of the applied field and the Coulomb potential of the central charge; the total potential for the system is said to be a Coulomb potential dressed by the laser, denoted as a dressed potential, V_{dres} .

Under the auspices of HFFT, introduced above and here,¹⁶ by applying a highly oscillatory laser field with an extremely short period the electrons will lack the ability to oscillate synchronously with the applied field. In this manner, the potential felt by the electrons is a period average of the oscillatory field, this new potential is a dressed potential under the HFFT approximation, V_{dres}^{HFFT} . In all cases addressed within this paper the laser-coordinates are: laser fired in y-direction, electronic component linearly polarized in the z-direction, and the magnetic component in the x-direction.

The situation of the dressed potential, V_{dres}^{HFFT} , is a time independent problem as the field has been period averaged, due to this the full Hamiltonian can be treated within the time independent Schrodinger equation:

$$\epsilon_i \Psi_i = \hat{H} \Psi_i = \frac{-\hbar^2}{2m_e} \nabla^2 \Psi_i + V_{dres}^{HFFT} \Psi_i. \quad (1)$$

Accurate solutions to the equation are difficult for systems of more than one electron due to many-body interactions, but approximate solutions can be obtained in a self-consistent method (SCF) through Hartree-Fock (RHF/UHF), density functional theory (DFT), or post-Hartree-Fock methods.

B. The relativistic mass gauge

Mass—as a fundamental—is conceptualized in two different manners within physics, these being the rest mass and the relativistic mass. Rest mass, or invariant mass, is for a specific body, a constant, measurable quantity denoted m_0 . In opposition to the rest mass is the variant quantity: relativistic mass, m_r . The relativistic mass depends upon the velocity of the observer. The variant nature of m_r is a correction to the rest mass which accounts for a non-zero kinetic energy for the measured system. This means that the relativistic mass increases in magnitude as the velocity of the system increases, and shall reach infinite mass as the system reaches the speed of light.

This portrayal of the mass shall be implemented within the TISE for the enclosed work. We shall now need to express alterations to the rest mass in terms of the system's laser parameters.

We are now called to introduce the concept of ponderomotive energy, U_p ; this being the cycle average kinetic energy of a quivering electron, i.e., electron undergoing oscillatory motion due to an external field and also qualifying under the dipole approximation. This is quantity discussed in context of

such systems by Joachain, Dörr, and Klystra:²⁴

$$U_p = \frac{e^2 \mathcal{E}_0^2}{4m_e \omega^2}. \quad (2)$$

In the above, \mathcal{E}_0 is the peak strength of the electric field, ω is the angular frequency of the applied field and both e and m_e retain their conventional meanings: of magnitude of electron charge and electron mass, respectively. This quantity aides in the evolution of the rest mass to the relativistic mass as:

$$m_r = m^{\text{dressed}} = m_e \left(1 + 2 \frac{U_p}{m_e c^2} \right)^{\frac{1}{2}} \quad (3a)$$

$$= m_e (1 + 2q)^{\frac{1}{2}}. \quad (3b)$$

As can be seen, the quantity q begins to shift the mass and becomes the dominant factor within the expression as it approaches unity.²⁵ The form of Eq. (3b) was found by Brown and Kibble²⁶ and later verified by Eberly and Sleeper²⁷ via the Hamilton-Jacobi equation.

Below we shall discuss the above mass concept as it applies to the TISE for one electron (which can then be generalized to N electrons), these lines shall be discussed stepwise:

$$\text{Eq. (1)} \rightarrow \frac{-\hbar^2}{2m_e(1+2q)^{\frac{1}{2}}} \nabla^2 \Psi_i + V \Psi_i, \quad (4)$$

$$\rightarrow \frac{-\hbar^2}{2m_e \left(1 + 2 \frac{e^2 \alpha^2 \omega^2}{4m_e^2 c^2} \right)^{\frac{1}{2}}} \nabla^2 \Psi_i + V \Psi_i, \quad (5)$$

$$\rightarrow \frac{-\hbar^2}{2(1 + 2.66 \times 10^{-5} \alpha^2 \omega^2)^{\frac{1}{2}}} \nabla^2 \Psi_i + V \Psi_i. \quad (6)$$

The first line, Eq. (4), shows the form of the TISE as it appears accounting for the mass gauge, which is tuned by the quantity q . Second, we have introduced and employed the field coefficient, $\alpha = \mathcal{E}_0/\omega^2$, as a means of defining q in terms of known laser parameters. Last, we express all quantities in $\hbar = m_e = 1$ units (atomic units), this allows us to maintain the relativistic alterations as a unitless multiplier, Eq. (6). As the multiplier which transforms invariant mass to relativistic mass is a unitless quantity, the resultant energies from the final line, Eq. (6), shall be in Hartree E_H , as they would be if one ignored the mass gauge entirely. In all cases considered within this paper the potential function, V , shall be dressed under HFFT, making $V = V_{dres}^{\text{HFFT}}$

C. Trajectory corrections

High-frequency Floquet theory was first introduced to similar systems by Pont *et al.*,¹⁶ it relies on the frequency of the externally applied electromagnetic field so quickly oscillating such that even the electrons are incapable of coupling their motions to the field. In this manner the D-dimensional dressed Coulomb potential—which is in essence a time-dependent problem is simplified to a time-independent problem:

$$V_{dres}^{\text{HFFT}} = \frac{Z}{2\pi} \int_0^{2\pi} \left(\frac{d(\omega t)}{\sqrt{\sum_i^D (x_i + \alpha_i)^2}} \right). \quad (7)$$

To apply the above period average to a system one must develop an interest in the trajectory, $\vec{\alpha}(t)$, of the laser's path as its components are required in the above averaging as α_i along with the i th Cartesian component, x_i . Earlier works^{14,15,18,19} have concentrated upon non-relativistic systems, and thus the laser trajectory is equivalent to the path taken by a free electron undergoing influence by a time-dependent external electric field (or laser field where no magneto-coupling is considered); the up and down oscillatory motion of the electric field governs the trajectory of the electron, seen in Eq. (8), where the polarization is as discussed in Sec. II A:

$$\vec{\alpha}(t) = \langle \alpha_x, \alpha_y, \alpha_z \rangle \quad (8a)$$

$$= (0, 0, \alpha_0 \cos(\omega t)). \quad (8b)$$

Now concerning ourselves with the electronic-magnetic coupling within relativistic regimes, this shall be described analogously for the non-relativistic case above by the path taken by a free electron in an electromagnetic field with the electronic-magneto coupling accounted. Within a plane-wave laser field, the electron classical trajectory can be obtained analytically. For a linearly polarized laser field, the non-zero field components can be written as

$$E_z = E_0 \cos \eta, \quad (9)$$

$$cB_x = E_0 \cos \eta, \quad (10)$$

where $\eta = \omega t - ky$ is the phase of the field. By using Newton-Lorentz equation,

$$\frac{d\vec{P}}{dt} = -e(\vec{E} + \vec{v} \times \vec{B}), \quad (11)$$

we have,

$$\begin{aligned} \frac{d\vec{P}}{dt} &= \left\{ \frac{dP_x}{dt}, \frac{dP_y}{dt}, \frac{dP_z}{dt} \right\} \\ &= \{-eE_0 \beta_x \cos \eta, 0, -eE_0(1 - \beta_z) \cos \eta\} \end{aligned} \quad (12)$$

$$m_e c^2 \frac{d\gamma}{dt} = -eE_0 \cos \eta \cdot v_x, \quad (13)$$

where $\gamma = \sqrt{1 + \vec{P}^2/(m_e^2 c^2)}$ is the Lorentz factor. For an electron initially at rest, from Eqs. (12) and (13), we obtain:

$$\vec{P} = \{P_x, P_y, P_z\} = \left\{ \frac{e^2 E_0^2}{2m_e c \omega^2} \sin^2 \eta, 0, -\frac{eE_0}{\omega} \sin \eta \right\}. \quad (14)$$

From the above, an electron's trajectory can be acquired,

$$\vec{\alpha} = \left\{ -\frac{c}{8\omega} Q_0^2 \sin(2\eta), 0, \frac{c}{\omega} Q_0 \cos \eta \right\}, \quad (15)$$

where $Q_0 = eE_0/(m_e \omega c)$ and electron drift motion has been neglected. Within dipole approximation,

$$\vec{\alpha} = \left\{ 0, -\frac{c}{8\omega} Q_0^2 \sin(2\omega t), \frac{c}{\omega} Q_0 \cos(\omega t) \right\}, \quad (16)$$

which means

$$\begin{aligned} \frac{d^2 \vec{\alpha}}{dt^2} &= \{\ddot{\alpha}_x, \ddot{\alpha}_y, \ddot{\alpha}_z\} \\ &= \left\{ \frac{1}{2} c \omega Q_0^2 \sin(2\omega t), 0, -c \omega Q_0 \cos(\omega t) \right\}. \end{aligned} \quad (17)$$

Equation (17) tells us that we can approximately take the above relativistic trajectory as an equivalent one for the electron moving in the following effective electric fields,

$$\vec{E} = \left\{ \frac{\omega m_e c}{2e} Q_0^2 \sin(2\omega t), 0, -\frac{\omega m_e c}{e} Q_0 \cos(\omega t) \right\}, \quad (18)$$

which will be used in HK theory. In atomic units, the trajectory can be written as,

$$\vec{\alpha} = \{-\alpha_0^2 \alpha_f \sin(2\omega t), 0, \alpha_0 \cos(\omega t)\}. \quad (19)$$

By comparing with the non-relativistic trajectory, we have an extra oscillation motion along the laser propagation direction, which comes from the magnetic coupling, also introduced is the fine structure constant which mediates the magnetic-electronic coupling term, α_f . This results in the famous figure-8 motion. To illustrate the effects of this correction in HK effective potential, we will first take a 1D box potential as an example in Sec. II D.

It should be noted that the KH expansion²⁸ committed to allow for this above expressions was developed by Gilary *et al.*²⁹ In our previous work¹⁵ it was seen that the higher order terms, those with the leading ω^{-2} , provided additional stability such that a system with a bound state under the dis-inclusion of the higher ordered terms would still be bound under the inclusion of said terms. The total value of the potential scales with respect to α_0 in a similar manner and thus the same arguments contained within the above reference hold here. Inclusion of the mass gauge provides a small alteration to the system, but in a destabilizing manner; thus bound states and their limitations under the methods of this paper are of a more conservative estimation.

D. 1D particle in a box

For simplicity, we take the 1D box potential as follows:

$$V(z) = \begin{cases} \pi, & |z| \leq 1, \\ 0, & \text{elsewhere.} \end{cases} \quad (20)$$

Then the HK effective potential can be acquired analytically by the following integration:

$$V_{\text{eff}}(z) = \frac{1}{2\pi} \int_0^{2\pi} V(z + \alpha_0 \cos(\Omega)) d\Omega. \quad (21)$$

When $0 \leq \alpha_0 \leq \frac{1}{2}$,

$$V_{\text{eff}}(z) = \begin{cases} ar \cos \left[\frac{-z+1}{\alpha_0} \right], & -\alpha_0 \leq z \leq -1 + \alpha_0, \\ ar \cos \left[\frac{z-1}{\alpha_0} \right], & 1 - \alpha_0 \leq z \leq 1 + \alpha_0, \\ \pi, & -1 - \alpha_0 \leq z \leq 1 - \alpha_0, \\ 0, & \text{elsewhere.} \end{cases} \quad (22)$$

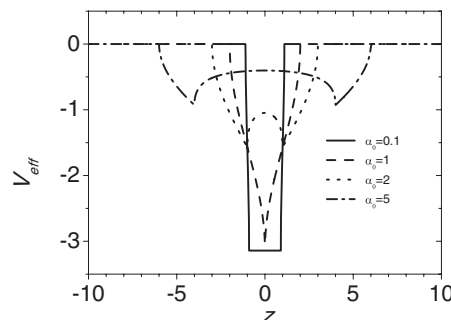


FIG. 1. Non-relativistic effective potential for a 1D particle in a box under different laser intensity, measured by α_0 .

When $\alpha_0 \geq \frac{1}{2}$,

$$V_{\text{eff}}(z) = \begin{cases} ar \cos \left[\frac{-z+1}{\alpha_0} \right], & -\alpha_0 \leq z \leq 1 - \alpha_0, \\ ar \cos \left[\frac{z-1}{\alpha_0} \right], & 1 - \alpha_0 \leq z \leq -1 + \alpha_0, \\ ar \cos \left[\frac{z-1}{\alpha_0} \right], & -1 + \alpha_0 \leq z \leq 1 + \alpha_0, \\ 0, & \text{elsewhere.} \end{cases} \quad (23)$$

Figure 1 shows how the box potential is modified by the external laser field. It is clear to see that as the laser intensity increases above certain value, the original potential will evolve into a double well. Moreover, the two wells will become more separate and more shallow if α_0 is further increased. This indicates two important features for the ground state in this potential. First, the electrons will become less bound or the potential might have higher ground state energy. Second, if we have two electrons in this effective potential, they will have more space in which to avoid each other, which means the electron repulsion energy will tend to be smaller for un-paired electrons. Hence, the final ground state energy for multi-electron systems should depend upon the competition of these two factors.

Once we introduce the relativistic corrections to the electron trajectory, the effective potential along z -axis will become:

$$V_{\text{eff}}(z) = \frac{1}{2\pi} \int_0^{2\pi} d\Omega (\sqrt{(z + \alpha_0 \cos \Omega)^2 + \alpha_0^2 \alpha^2 \sin^2 2\Omega}), \quad (24)$$

in which the integral will be calculated numerically. From Fig. 2, it is interesting to note that, when α_0 is large enough, for example $\alpha_0 = 10$ as in Fig. 2(b), the effective potential will have three local minima. Qualitatively, this should result from the relativistic figure-8 motions, which helps the electron maintain a position nearer the orbit center for a greater period of time. Another characteristic is that the three separate minima become much shallower for higher laser intensity. These drastic changes over the effective potential will

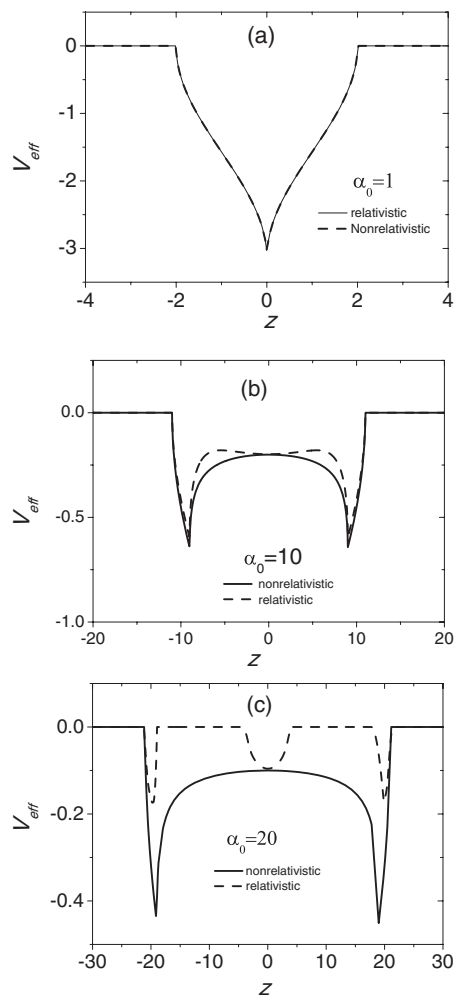


FIG. 2. Relativistic corrections to the effective potential for different laser fields.

be expected to have influences over the many-electron states bound by the potential. It seems that the relativistic effect provides us another way to engineer the potential. Based upon the observations over Eq. (24), we can even think about using lasers with different colors superposed together to have more freedom modifying the effective potentials. Figure 3 shows us one example with two alternating electric fields as follows:

$$\vec{a}(t) = \alpha_0 \cos(\omega t) \hat{e}_x + \alpha_1 \sin(4\omega t) \hat{e}_z. \quad (25)$$

E. Potential under consideration

Beginning with the spherically symmetric Coulomb potential, the applied external fields shall morphologically alter this potential to conform to the trajectory discussed in

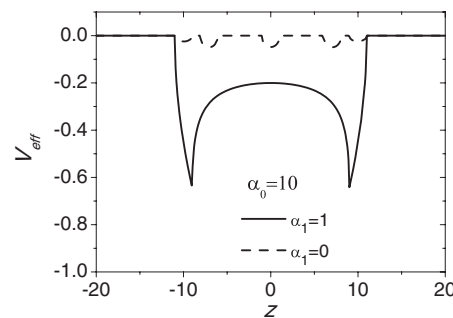


FIG. 3. Effective potential for two alternating electric fields superposed along \hat{e}_x and \hat{e}_z , respectively, with different colors.

Sec. II B. In doing this, there are three main regimes in which the potential may exist: first, the spherical; second, the pseudo-linear; and finally, the parametric. The potential only exists within the spherical regime when there is no applied external field, as the field begins to evolve the coupling of the external field and the Coulomb potential becomes apparent with the electric field component dominating; this creates a regime where the system maintains an almost linear behavior as if there were no relativistic corrections to the trajectory. Distortion of the pure linear nature exists but has a small effect compared to the primary electric effect.

As the intensity of applied field increases the magnitude of the magnetic field begins to compensate for the dampening effect of the fine structure constant, α_f ; as this takes place, the magnetic contributions to the field coupling begin to dominate the system, whose character now exhibits the hourglass figure of the parametric regime. Figure 4 shows a series of

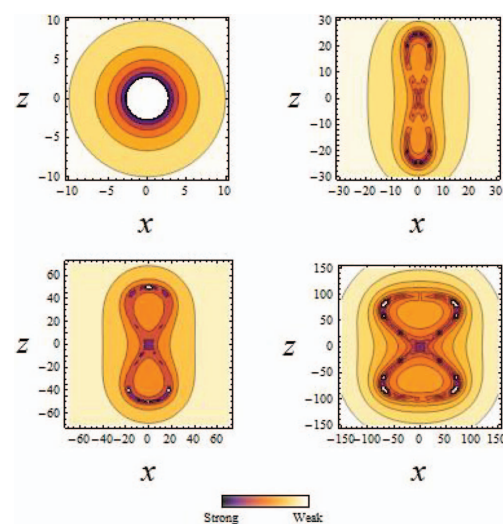


FIG. 4. Contour plots of dressed potential for (clockwise) $\alpha_0 = 0, 25, 100, 50$. Note both the shift in regime as α_0 grows and the key below the plots for the interpretation of the intensity of the contours.

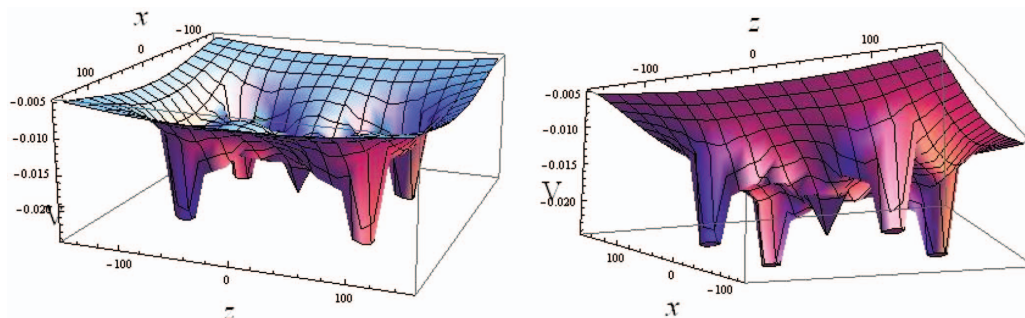


FIG. 5. Three dimensional plots of the potential energy, V_{dres}^{HFFT} , as a function of x and z coordinates for the case $\alpha_0 = 100$. Left and right of above are two different angles of the same surface.

contour plots of the potential energy plotted in the x - z directions for a series of field intensities, α_0 ; the behavior of the system and its development through the previously discussed regimes should be obvious. A three-dimensional plot of the potential energy surface for $\alpha_0 = 100$ is also enclosed as Fig. 5, this plot only considers displacements in the spatial x - z directions for reasons introduced in Sec. II A, where the vertical axis describes the magnitude of the potential energy at this x - z location.

This potential is ideal for attempting to develop multiply charged ionic system from small nuclei, as it maintains a potential well at the center of the system along with four other locations along the parametric trajectory; this allows bound electrons to attach to the individual potential wells while maintaining a large enough distance from each other to minimize electron-electron repulsions.

III. METHODOLOGY FOR $D = 3$ CALCULATIONS

Three-dimensional calculations which describe our systems were executed as a means of verifying the simpler dimensional scaling approach discussed later. The methodology consisted of unrestricted Hartree-Fock (UHF) utilizing the Pople-Nesbot equations—which allow for the accommodation of basis sets—to complete calculations for a series of total electron counts, N , per single value of the field intensity parameter, α_0 . The calculations were dependent both upon appropriate choice of basis set and upon the locations selected as the centers for these basis sets; for the determination of the locations of probable electron density we deferred both to “exact” locations of the electrons from the limit $D \rightarrow \infty$ calculations and to contour plots of the potentials for a given field intensity value, see Fig. 4 for example. Upon discerning from the above information the locations of the pseudo-centers within the system-space, a basis set was selected which could describe these nodes. There exist, at minimum, 5 distinct nodes of electron density within the system, these being at the center coexisting with the origin of our coordinate systems—and at four pseudo-centers residing upon the parametric curve described by the relativistic trajectory

used within the HFFT potential:

$$\begin{Bmatrix} x \\ y \\ z \end{Bmatrix} = \begin{Bmatrix} -\left(\frac{\alpha_0^2}{\alpha_f}\right) \sin(2t) \\ 0 \\ \alpha_0 \cos(t) \end{Bmatrix}. \quad (26)$$

The orbital centers were selected to satisfy the above curve and to coincide with the “hottest” locations displayed within the contour plots of potential energy. A basis set was selected, which allowed for significant description of both polarized and diffused phenomenon residing on small centers. The centers of potential electron density which do not reside at origin were described by basis sets optimized to describe the atom of the nucleus at the system’s origin, i.e., all five centers on hydrogen use a hydrogen-fit basis set. Overlap and kinetic integrals were performed with variations on the integrals described by McMurchie and Davidson in their seminal paper here.³⁰ Numerical integration methods were appropriate for the more challenging, non-analytic potential integrals. A global adaptive method was applied to the system which performs admirably with Gaussian functions placed at the coordinate origin; but as the method relies on sampling points within the equation-space to find non-zero areas of the function, Gaussians placed distances away from the origin were sometimes so small relative to the distance from origin so as to be invisible. For this reason two-centered integral includes the cost of shifting the coordinate-origin to the center of the product Gaussian as defined by³¹

$$\begin{aligned} & \phi_{1s}^{GF}(\alpha_A, r - R_A) \times \phi_{1s}^{GF}(\alpha_B, r - R_B) \\ &= \exp\{-[\alpha_A(r - R_A) + \alpha_B(r - R_B)]\} \\ &= \exp\{-\alpha_A \alpha_B (\alpha_A + \alpha_B)^{-1} |R_A - R_B|^2\} \\ & \quad \times \phi_{1s}^{GF}(\alpha_A + \alpha_B, r - R_P). \end{aligned} \quad (27)$$

In this way the chosen method of numerical integration was capable of adequately describing the three-dimensional potential energy integrals. Single electron cases were verified prior to enacting the self-consistent field calculations, as the energies of the single electron system may be revealed as the eigenvalues of the canonically orthogonalized $H_{\mu,\nu}^{core}$ matrix alone, $H_{\mu,\nu}^{core} = T_{\mu,\nu} + V_{\mu,\nu}$. The four-centered integrals

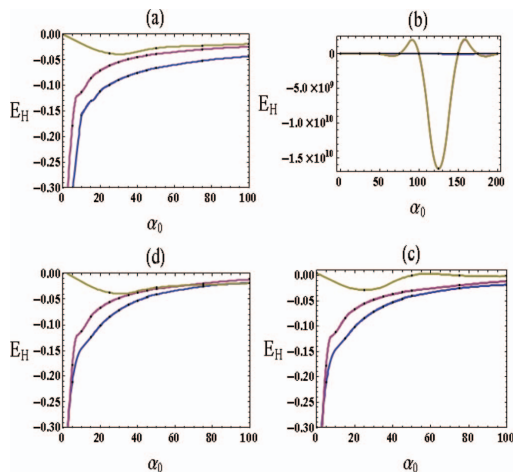


FIG. 6. Plots of both molecular energies and binding energy for (clockwise): \mathcal{H}_{DA} with non-relativistic trajectory; \mathcal{H}_{DA} , relativistic trajectory; \mathcal{H}_P , relativistic trajectory; and \mathcal{H}_P with non-relativistic trajectory. All may be read as yellow: Binding energy; blue: Hydrogen energy; purple: H^- energy.

needed for the self-consistency were generated by exploiting the auxiliary function defined by Boyes.³² The calculations for the multi-electron energies were performed self-consistently with a convergence set to six decimals of accuracy, as chemical accuracy is defined as 1.6 mE_H, this set limit should suffice.

A plot of the square of the linear combination of atomic orbitals which comprised the set describing the appropriate eigenvalue yields semblance to the wave function of the system, whose probability density ($|\Psi|^2$) is shown in Fig. 6 for H^- and for He^- , a two and a three electron case. It should be noted, as the $D = 3$, UHF calculations were employed to verify the results of the dimensional scaling approach, that the locations of electron density shown in the aforementioned probability density plots speak to the validity of the dimensional scaling approach as the locations of the delta functions, see discussion provided in Sec. V, which describe the seemingly stationary locations of the electrons in the limit of $D \rightarrow \infty$ calculations that are very near to those locations which are of highest probability density to find electrons given by the $D = 3$ calculations. Three-dimensional verification was performed for both the H^- and He^- species, as the regions of high potential energy become very delocalized for the remaining high-field species. Aside from the high level of delocalization prohibiting the species from being described sufficiently with an appropriate number of Gaussians, the potential also spans a region of space on the order of 100 Bohr radii, yet optimized Gaussian basis sets for atomic centers span an order of 1–10 Bohr radii; this prohibits overlap of these species forcing the use of more and more Gaussians. This acts prohibitively as the matrices required for UHF calculations are $n \times n$, where n scales as the number of centers by the number of basis contractions; this obviously limits the achievable

intensities applied to systems which can be calculated in this manner, especially on stand alone machines.

IV. DIMENSIONAL SCALING: CALCULATIONS AND CONSIDERATIONS

A. Methodology

Many body interactions are something which has troubled computational methodologies within quantum mechanics since inception; throughout the years the physical and chemical communities have made great advances in the field of electronic structure theory to help account for these electron-electron interaction through variational practices such as the Hartree Fock method or density functional theory. The alternative method to the aforementioned is a dimensional scaling treatment pioneered by Herschbach,³³ discussed in Refs. 34–38, and is briefly introduced here for the central force problem.³⁴ Given the TISE for the simple central force problem in D-dimensions:

$$\left[-\frac{1}{2}\nabla_D^2 + V(r) \right] \Psi_D = \epsilon_D \Psi_D. \quad (28)$$

If we were to employ polar coordinates to the above, we would require

$$r \equiv \left[\sum_{k=1}^D x_k^2 \right]^{\frac{1}{2}} \quad (29a)$$

$$\nabla_D^2 = \frac{1}{r^{D-1}} \frac{\partial}{\partial r} \left(r^{D-1} \frac{\partial}{\partial r} \right) - \frac{L_{D-1}^2}{r^2}, \quad (29b)$$

where Eq. (29a) gives the definition of the radial coordinate in a generic D-scaled space, and Eq. (29b) is the polar Laplacian in this D-scaled space, L_{D-1}^2 is the term which retains all angular dependencies. These angular and radial terms shall be dealt with in a divide and conquer treatment reminiscent to the radial and angular terms of the rigid rotor/harmonic oscillator approximations for the simple diatomic. We first write the wave function in D-dimensions to be the product: $\Psi_D = r^\ell \mathcal{Y}(\Omega_{D-1})$, where all radial dependencies are in the r^ℓ term and the $D-1$ remaining angular dimensions are described through $\mathcal{Y}(\Omega_{D-1})$. Now solving the angular terms for the form Eq. (30), and the recognizing that the $V(r)$ term in Eq. (28) can be set to equal magnitude as the ϵ_D term, thus making Eq. (28) reduce to the Laplace equation shown in Eq. (31):

$$L_{D-1}^2 \mathcal{Y}(\Omega_{D-1}) = C \mathcal{Y}(\Omega_{D-1}), \quad (30)$$

$$\nabla_D^2 r^\ell \mathcal{Y}(\Omega_{D-1}) = 0, \quad (31a)$$

$$\{\ell(\ell + D - 2) - C\} r^{\ell-2} \mathcal{Y}(\Omega_{D-1}). \quad (31b)$$

This means: $C = \ell(\ell + D - 2)$; and the Hamiltonian operator in Eq. (28) is now of the form

$$\hat{H}_D = -\frac{1}{2} K_{D-1}(r) + \frac{\ell(\ell + D - 2)}{2r^2} + V(r). \quad (32)$$

In the above, $K_{D-1}(r)$ is the single non-angular term from the polar Laplacian in Eq. (29b). We may now pass the system through a unit Jacobian, making: $J_D|\Psi_D|^2 = \Phi_D$, where J_D is the radial part of the unit Jacobian and is of the form: $r^{(D-1)}$. This would mean, $\Psi_D = r^{-\frac{1}{2}(D-1)}\Phi_D$. All leading to the form of K_{D-1} as seen here:

$$K_{D-1}(r) = r^{-\frac{1}{2}(D-1)} \left\{ \frac{\partial^2 \Phi_D}{\partial r^2} - \frac{D-1}{2} \frac{D-3}{2} \frac{\Phi_D}{r^2} \right\}. \quad (33)$$

Reassembling all the above, and placing them appropriately back into Eq. (28), one shall—after menial simplification—get:

$$\left\{ -\frac{1}{2} \frac{\partial^2}{\partial r^2} + \frac{\Lambda(\Lambda+1)}{2r^2} + V(r) \right\} \Phi_D = \epsilon_D \Phi_D. \quad (34)$$

Equation (34) is the radial, D-scaled form of Eq. (28), where the only dimensional dependencies lay within the Λ terms as: $\Lambda = \ell + 1/2(D-3)$. The above leads to the minimization problem defined by the Hamiltonian discussed in Sec. II B.

B. Planar infinite-D Hamiltonian

Prior works published^{14,19} have also described systems both by infinite dimensional limit and then verified with three-dimensional self consistent methods. The dimensional scaled Hamiltonian presented in previous works was diatomic in nature and of the form³⁹

$$\mathcal{H}_{DA} = \frac{1}{2} \sum_{i=1}^N \frac{1}{\rho_i^2} + \sum_{i=1}^N V(\rho_i, z_i) + \sum_{i=1}^N \sum_{j=i+1}^{N-1} \frac{1}{\sqrt{(z_i - z_j)^2 + \rho_i^2 + \rho_j^2}} \quad (35)$$

and relied on previous works in which D-scaled Hamiltonians for diatomic systems were constructed, these diatomic Hamiltonians are also of the form above, and denoted \mathcal{H}_{DA} .

Hamiltonians of this form are applicable to the previous works as those non-relativistic systems, this is due to the consideration in absence of the second degree of symmetry breaking in the linear potential systems.

The diatomic-based Hamiltonian performed well on linear systems, but when attempting to use the above described Hamiltonian on a relativistically corrected trajectory, it was found that the equation behaved erratically with a smoothly evolving intensity as seen in Fig. 7, and was in disagreement with the early 3D calculations. Although this Hamiltonian does not work well, overall it was found to be in good agreement while the potential was in the spherical and pseudo-linear regimes, failing only as the system approached and entered the parametric regime.

As dimensionally scaled Hamiltonians are not unique in nature, they are not singular in form. We relied on arguments based on the breaking of spherical and then cylindrical symmetries to generate the following assumed Hamiltonian for systems with broken radial and cylindrical symmetries, yet maintaining three orthogonal planes of symmetry.

As the dimensional-scaled, single electron central force problem yields as it is Hamiltonian \mathcal{H}_{CF} ,

$$\mathcal{H}_{CF} = \frac{1}{2r^2} + V(r). \quad (36)$$

One can see from above the spherical nature of all terms within the Hamiltonian, as the potential is radial. This equation predicts the ground state hydrogen energy to be at $-1/2E_H$, exactly where it should be, and predicts the inter-atomic distance between the electron and the proton to be 1 in unit of R_{Bohr} . If one were to alter the above potential to conform with either the relativistic or non-relativistic cases discussed in this paper, the energies obtained would possess no physical significance and would overall behave similarly to the diatomic equation with the relativistic trajectory. The addition of multiple electrons to the spherical symmetric problem yields

$$\mathcal{H}_{CF} = \frac{1}{2} \sum_{i=1}^N \frac{1}{r_i^2} + \sum_{i=1}^N V(r_i) + \sum_{i=1}^N \sum_{j=i+1}^{N-1} \frac{1}{\sqrt{r_i + r_j}}. \quad (37)$$

Now we examine the diatomic case shown in Eq. (35). This equation has been designed to allow for potential which are of a cylindrical nature, as it must for a diatomic system. Reevaluating the equation in Cartesian coordinates yields

$$\mathcal{H}_{DA} = \frac{1}{2} \sum_{i=1}^N \frac{1}{x_i^2 + y_i^2} + \sum_{i=1}^N V(x_i, y_i, z_i) + \sum_{i=1}^N \sum_{j=i+1}^{N-1} \frac{1}{\sqrt{(z_i - z_j)^2 + x_i^2 + x_j^2 + y_i^2 + y_j^2}}. \quad (38)$$

Reevaluation of the spherically symmetrical case in Cartesian coordinates gives

$$\mathcal{H}_{CF} = \frac{1}{2} \sum_{i=1}^N \frac{1}{x_i^2 + y_i^2 + z_i^2} + \sum_{i=1}^N V(x_i, y_i, z_i) + \sum_{i=1}^N \sum_{j=i+1}^{N-1} \frac{1}{\sqrt{x_i^2 + x_j^2 + y_i^2 + y_j^2 + z_i^2 + z_j^2}}. \quad (39)$$

As can be seen from the above, the orthogonal coordinate which is being cleaved from spherical symmetry has been removed from the kinetic evaluation and have been treated as a difference in the electron-electron term. Continuing to use Cartesian coordinates, as it is this coordinate system which makes the relations apparent, we can move to an equation where the x-coordinate is now allowed to deviate from radial symmetry. This again would remove the symmetry breaking

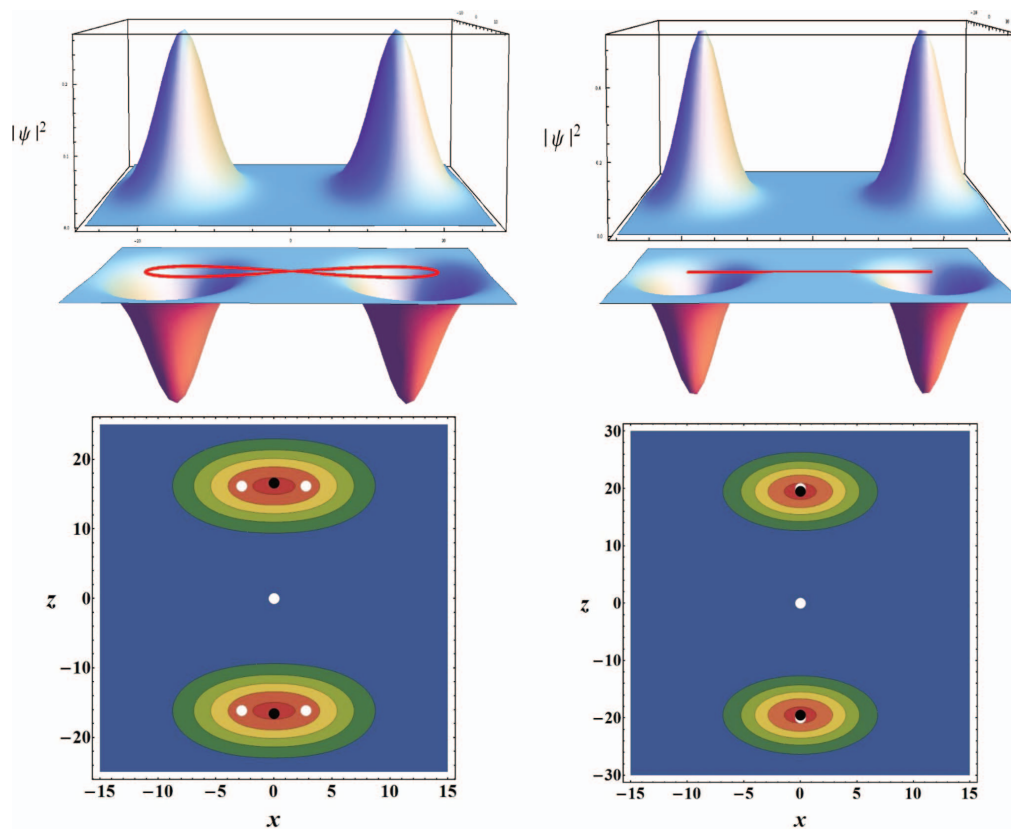


FIG. 7. Top: Probability distribution for H^- , a two electron system. Bottom: Probability distribution for He^- , a three electron system.

coordinate from the kinetic term and utilize it as a difference in the electron-electron term. This Hamiltonian is shown in Eq. (40). Its energies completely agree with those of the radial and cylindrical cases, and by allowing this symmetry to break in the x -coordinate can be used for the potential discussed in Sec. II E.

This planar Hamiltonian, \mathcal{H}_P :

$$\mathcal{H}_P = \frac{1}{2} \sum_{i=1}^N \frac{1}{y_i^2} + \sum_{i=1}^N V(x_i, y_i, z_i) + \sum_{i=1}^N \sum_{j=i+1}^{N-1} \frac{1}{\sqrt{(z_i - z_j)^2 + (x_i - x_j)^2 + y_i^2 + y_j^2}} \quad (40)$$

was found to allow—but not require—the breaking of symmetry, as it was applied to the previously discussed linear systems and had extremely good agreement, as shown in Fig. 7. The relation between the Cartesian coordinates used in the above and the geometry of the system is shown in Fig. 8. When applied to our system, containing the corrected trajectory, this new Hamiltonian performs both smoothings with

smoothly evolving trajectories—as seen in Fig. 9. This planar dimensional scaled Hamiltonian was capable of adequate description of the system in all three of the regimes discussed earlier.

V. RESULTS AND DISCUSSION

We shall concern ourselves with a discussion of the binding energies (B.E.) for the following species: H^- , H^{-2} , He^- , He^{-2} , He^{-3} ; where the B.E. is the negative of the detachment energy for a single “excess” electron shown in Eq. (41), where N signifies the number of electrons for a species:

$$B.E. = E_H(N) - E_H(N-1). \quad (41)$$

Figure 10 displays the binding energies for the two species, $Z = 1$ and $Z = 2$. From this figure we can see a clear maximum binding energy for the H^- species (top left) at, roughly, $\alpha_0 = 10$; this energy shows a stability of the second electron of 0.047 Hartree (1.28 eV). Also shown in Fig. 10 the B.E. curve for H^{2-} (top right), showing a stable binding of 0.00012 Hartree (0.0033 eV). This, the B.E. of H^{2-} , reaches

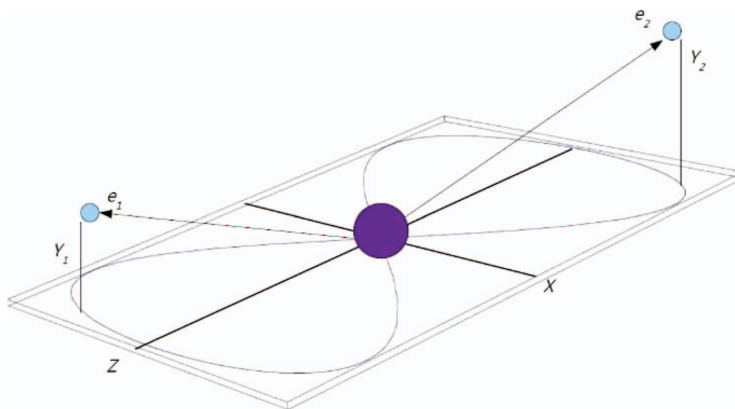


FIG. 8. The above displays the relationship between the system's geometry with respect to the electrons and the coordinates use in Eq. (40).

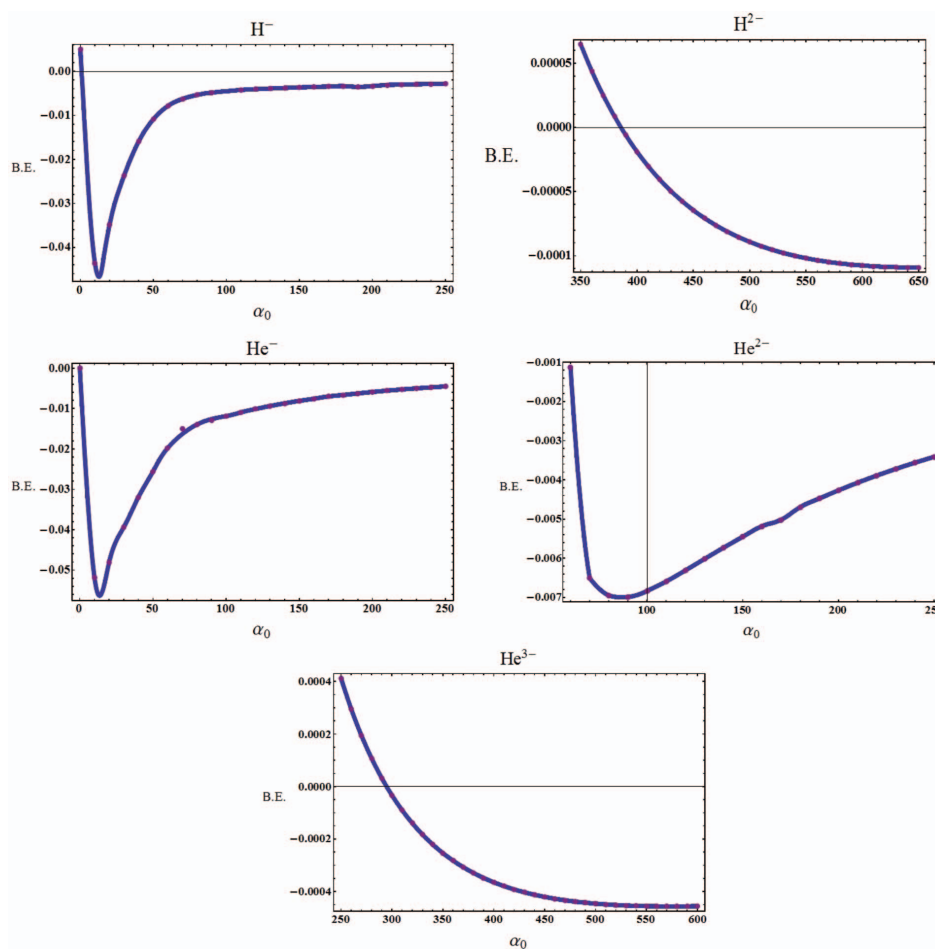


FIG. 9. Above are plots of the binding energies of, from left to right and top to bottom: H^- , H^{2-} , He^- , He^{2-} , and He^{3-} .

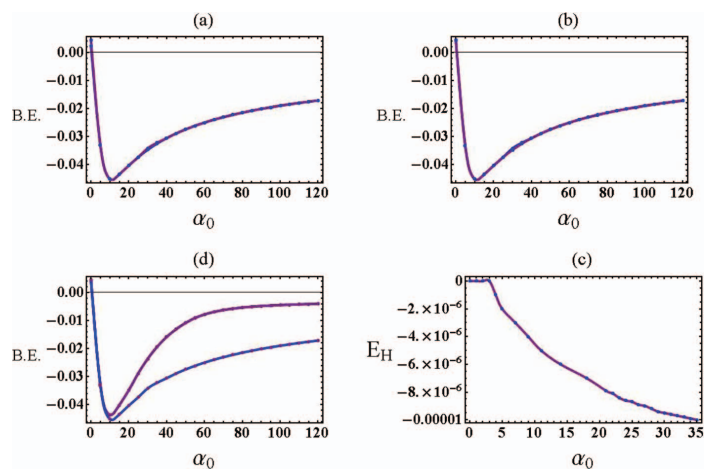


FIG. 10. Plots of binding energy comparisons for (clockwise): comparison plot of \mathcal{H}_{DA} versus \mathcal{H}_P , non-relativistic trajectory; \mathcal{H}_P with relativistic trajectory m_0 and m_r , differences value of Hydrogen energy between use of m_0 and m_r ; and a comparison of relativistic trajectory (both m_0 and m_r) with non-relativistic trajectory both using \mathcal{H}_P .

it's minimal value asymptotically with increasing α_0 implying the addition of any further electrons will not be allowed; this fact was verified by performing the requisite minimization, and if the mass gauge was not applied to the system the number of allowed additional electrons would increase unre-

alistically and seemingly without bound as the laser intensity is increased.

The middle left plot in Fig. 10 shows the binding of a third electron to Helium at α_0 equalling, roughly, 10 again; the binding energy for this species at it's greatest magnitude

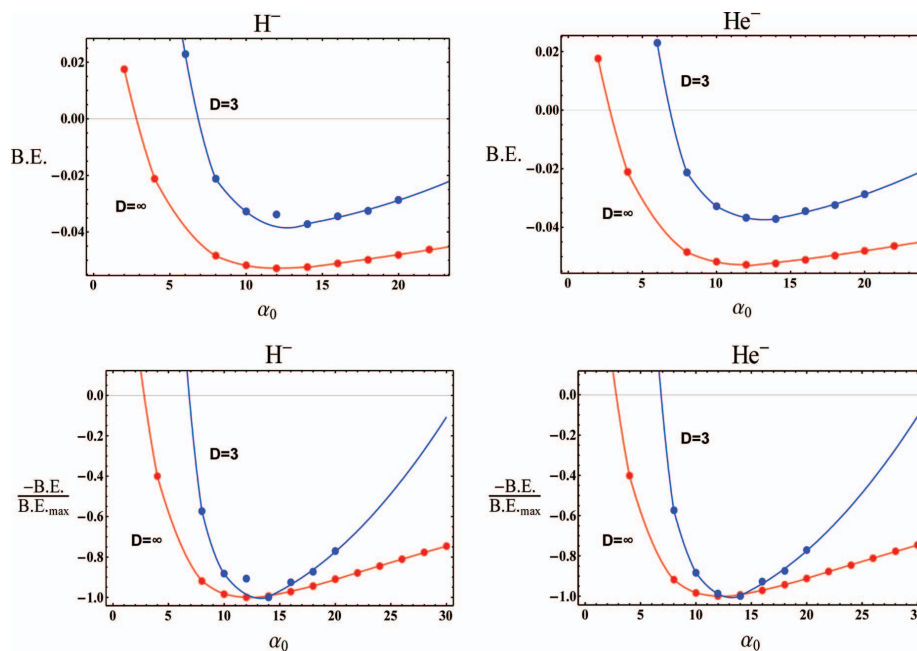


FIG. 11. Plots of binding energy for the H^- (left) and He^- (right) systems. Top, Non-normalized plots of the calculation data showing agreement between the methods. Bottom, $-B.E./B.E._{max}$ to emphasize the qualitative similarity between the methods as they share minima for the B.E. curves.

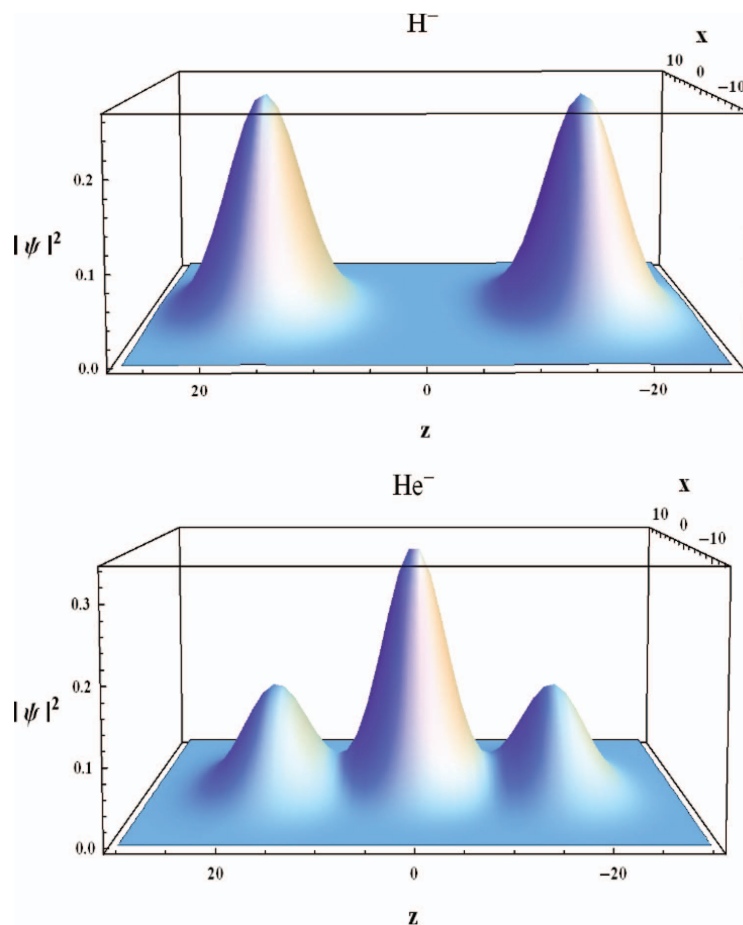


FIG. 12. Top row: Plots of the probability distribution for the corrected (left) and non-corrected (right) H^- system, directly below is a superimposition of the trajectory upon the probability density function plot to emphasize their relation. Bottom row: Contour plots of the H^- system, both corrected (left) and non-corrected (right), note the different scales on the vertical (z) axis and the more diffuse behavior of the corrected system.

is extrapolated to be 0.057 Hartree (1.55 eV). The second “additional” electron to Helium (middle right) is most stable at $\alpha_0 = 90$, with a B.E. of 0.007 Hartree (0.19 eV). The fifth and final electron which can stably bind to a $Z = 2$ center (bottom center) is, similarly to the H^{2-} species, a terminal binding that reaches an asymptotic stability with increasing α , the B.E. is 0.0004 Hartree (0.011 eV). Table II contains the maximum binding energies and their respective intensities for each system described within this work; it contains also, the non-relativistic binding energies and intensities as comparison.

Of the two relativistic corrections accounted for in the above framework, the trajectory is the paramount addition. An examination of Figs. 9 and 7 shall be required for the subsequent discussions. The introduction of the planar large-D Hamiltonian, \mathcal{H}_P , for the systems was a boom which aligns itself in agreement with the previous works—see Fig. 9(a) and compare plots a and c in Fig. 7—and yet out performs the pre-

vious equation when this relativistic trajectory is introduced, to see this compare plots b and c in Fig. 7.

By comparing plots a and d of Fig. 7 it can be seen that the raw energies and the binding energies between the non-relativistic trajectory (plotted with \mathcal{H}_{DA}) and the relativistic trajectory are not extreme. This can be verified

TABLE I. Results of Mulliken population analysis, note that there are four outer orbitals the table contains one of the four values.

Species	Inner orbital population	Outer orbital population (each)	Total electron count (N)
H	0.01645	0.24576	1
H^-	0.000524	0.49987	2
He	0.000432	0.499892	2
He^-	1.00001	0.499999	3

TABLE II. Differences present when relativistic considerations are undertaken for these multiply charged ions. The non-relativistic values were taken from Ref. 14.

Species	D= ∞				D=3			
	Non-Relativistic		Relativistic		Non-Relativistic		Relativistic	
	α_0^{max}	BE (eV)	α_0^{max}	BE (eV)	α_0^{max}	BE (eV)	α_0^{max}	BE (eV)
H ⁻	10	-1.2	12	-1.28	17	-1.1	12	-0.98
H ²⁻	500	-0.019	>600 *	-0.003	400	-0.026	-----	-----
He ⁻	12	-1.4	12	-1.55	26	-1.2	14	-1.03
He ²⁻	160	-0.14	85	-0.19	180	-0.12	-----	-----

and more clearly seen by examination of Fig. 9(c), wherein both the non-relativistic and relativistic binding energies are shown; although the energies become quite different with increasing α_0 , the field intensity which yields the most stable binding energy is same and the most stable binding energy deviates only in the thousandth of a Hartree. Consideration of the mass gauge for this system provides a very slight correction within the values of α_0 examined here; where although these values of α_0 indicate laser field strengths on the order of atomic units and greater (in competition with the Coulomb potential of the center), they are in no way strong enough to generate quivering electron masses, m_r , which deviate significantly from the invariant mass, m_0 . The deviation of the binding energies due to the consideration of m_r over m_0 is also slightly less than breath-taking, this can be seen in Fig. 9(b) and again impressed by the examination of the deviation of the raw energies of hydrogen in Fig. 9(d). To be gleaned from this is that within the examined field strengths, m_r deviates very little from m_0 , but more significant is the fact that the overall consideration of relativistic effects does destabilize the system, but not by an appreciable amount.

Figure 11 helps emphasise the differences between the corrected and non-corrected systems. The top level of the figure is the probability density, $|\psi|^2$, of corrected (left) and non-corrected (right), the density in the outer orbital centers is lower due to a more diffused spread of probability density at these locations compared to the non-corrected. The mid-level of the plot is the negative probability density, superimposed on the probability density function is the trajectory of the system which it describes. Below all else is a contour plot of each system, again emphasis is merited on the more diffuse spread in the corrected system due to the evolution of the parametric trajectory as opposed to the linear oscillating trajectory of the non-corrected system.

Figure 12 shows a plot of the B.E. For the H⁻ (left) and He⁻ (right) systems from both the SCF (blue) and D-Scaled (red) methods. The lower B.E. plots in Fig. 12 have been normalized to the minimum value to show the tight agreement between the qualitative assessment of the scaling procedure and the SCF method. The Dimensionally Scaled minimization problem bore "exact" position of the electrons as $(x_1, y_1, z_1; \alpha_0) = (4.1660 \times 10^{-10}, 5.4461, -12.2387; 20)$ for the Z = 1, N = 1 system and $(x_1, y_1, z_1; x_2, y_2, z_2; \alpha_0) = (6.4472 \times 10^{-8}, 5.0386, 16.5852; -6.4472 \times 10^{-8}, 5.0386, -16.5852; 20)$ for the Z = 1, N = 2 system; these localized

electron positions are similarly predictable as they attempt to bind to regions where the angular velocity of the nucleus is lowest in the KH frame; these locations would be most notable at the $\frac{\pi}{4}$'s trajectory. With a single electron the central point of the parametric curve, sets a origin in our calculations, binds the electron strongly; as more electrons are introduced they are situated at locations which minimize the electron-electron repulsion of the system. A Mulliken population analysis of the system shows that the orbitals about the central charge typically possess a smaller number of electrons, except in the N = 3 (and assumably the N=5 case); the results of such population assessments can be seen in Table I. In this way we are able to verify not only the energetic behavior of the D-scaled Hamiltonian but its treatment of the electrons in space.

VI. CONCLUSION

It has been shown that even under conditions of relativity multiply charge atomic ions should still be achievable within the confines of an intense laser field. The stability of several atomic-anions has been found and discussed, some ions are on the order of an entire electron volt and are more stable than the ionized system. The importance of the general dimensional scaling procedure was verified not only via the energetics, but with a comparison of the "exact" locations of the electrons as predicted by the dimensional scaling as they compare to the probability densities from the standard SCF procedure. These species were found to be stable and should, therefore, be experimentally realizable. Stability of simple molecular systems in super-intense laser fields have been previously discussed here.⁴⁰⁻⁴² This dimensionally scaled framework with relativistic corrections yields itself easily to a description of molecules and molecular ions within the confines of super-intense laser fields, which shall be undertaken next.

ACKNOWLEDGMENTS

We would like to thank the Army Research Offices for funding this project. Jiayang Wang would like to thank National Science Foundation (NSF) China for the support by Grant No. 10974056. We would also like to thank Professor Dudley Herschbach of stimulating discussion of the materials within this paper.

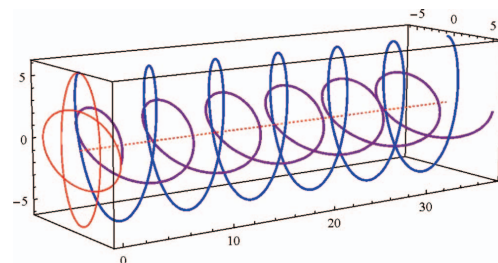


FIG. 13. The electronic elliptical contribution can be seen as the function whose major axis lies in the z -direction (vertical) and the magnetic contribution has an orthogonal orientation.

APPENDIX: BRIEF NOTES ON THESE RELATIVISTIC CORRECTIONS WITH ELLIPTICAL AND CIRCULAR POLARIZATIONS

1. Elliptical and circular polarizations

Within the above, concern was only given to the relativistically corrected linear polarized light, this is because similar corrections placed on elliptical polarized light yielded no new—or interesting—phenomenon. Following similar mathematics as to achieve an analogous relativistically considered trajectory would consider the electronic coupling as before and consider a minor weighted coupling to the magnetic field, as in the linear case before. An elliptically polarized laser fired in the y -direction with the electronic major (minor) axis oriented in the $x(z)$ -direction yields the trajectories

$$\vec{\alpha}_{\tilde{E}, \text{Elliptical}}(t) = \{\epsilon_1 \cos(\phi), 0, \epsilon_2 \sin(\phi)\}, \quad (\text{A1})$$

$$\vec{\alpha}_{\tilde{B}, \text{Elliptical}}(t) = \{-\beta_2 \sin(\phi), 0, \beta_1 \cos(\phi)\}. \quad (\text{A2})$$

Within Eqs. (A1) and (A2) the amplitude in each, the major and minor axis is denoted by the subscript 1 and 2, respectively, and the ϵ and β are the coefficients of the electronic and magnetic components. The trajectory generated by both the above biases applied to free particle merely generates a new ellipse with a major and minor amplitude mediated between those of the above and tilted by an angle respective to the coefficients:

$$\vec{\alpha} = \{\epsilon_1 \cos(t) - \beta_2 \sin(t), 0, \epsilon_2 \sin(\phi) + \beta_1 \cos(\phi)\}. \quad (\text{A3})$$

This can be seen graphically in Fig. 13 which displays the individual electronic and magnetic trajectories and then in Fig. 14 which displays the combined trajectory which would

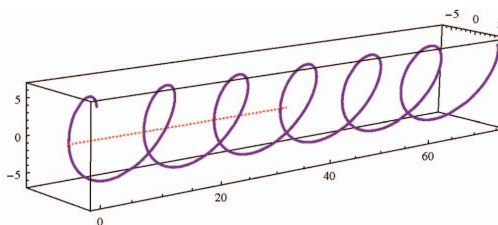


FIG. 14. Within the above plot, the total trajectory can be seen, the amplitude of the major and minor axes are mediated in value between those from the electronic and magnetic components and the orientation is set off by an angle whose value respects the same coefficients as the relative amplitudes.

be followed by a free particle traveling within this electromagnetic field.

If this scheme is applied to a circularly polarized field the same mathematics will appear but the coefficients within the trajectories will be reduced to $\epsilon_1 = \epsilon_2 = \epsilon$ and $\beta_1 = \beta_2 = \beta$. This will yield the same uninteresting phenomenon, but merely present it as the mediate of two circles with no change in the orientation angle as there is no unique point of reference on a circle.

- ¹M. Gavrilu, *J. Phys. B* **35**, R147 (2002).
- ²M. Gavrilu, *Atoms in Intense Laser Fields* (Academic, NY, 1992).
- ³J. H. Eberly and K. C. Kulander, *Science* **262**, 1229 (1993).
- ⁴D. J. Pegg, J. S. Thompson, R. N. Compton, and G. D. Alton, *Phys. Rev. Lett.* **59**, 2267 (1987).
- ⁵D. Berkovits, E. Boaretto, S. Ghelberg, O. Heber, and M. Paul, *Phys. Rev. Lett.* **75**, 414 (1995).
- ⁶M. K. Scheller, R. N. Compton, and L. S. Cederbaum, *Science* **270**, 1160 (1995).
- ⁷J. Simons, *Ann. Rev. Phys. Chem.* **62**, 107 (2011).
- ⁸J. Simons, *J. Phys. A* **112**, 6401 (2008).
- ⁹E. H. Lieb, *Phys. Rev. A* **29**, 3018 (1984).
- ¹⁰K. H. Chang, R. D. McKeown, R. G. Milner, and J. Labrenz, *Phys. Rev. A* **35**, 3949 (1987).
- ¹¹D. R. Bates, *Negative Ions: Structure and Spectra*, Advances In Atomic, Molecular, and Optical Physics Vol. 27, edited by S. D. Bates and B. Bederson (Academic, New York/London, 1990), pp. 1–80.
- ¹²A. V. Sergeev and S. Kais, *J. Phys. A* **32**, 6891 (1999).
- ¹³P. Serra and S. Kais, *Chem. Phys. Lett.* **372**, 205 (2003).
- ¹⁴Q. Wei, S. Kais, and D. Herschbach, *J. Chem. Phys.* **127**, 094301 (2007).
- ¹⁵Q. Wei, S. Kais, and N. Moiseyev, *J. Chem. Phys.* **124**, 201108 (2006).
- ¹⁶M. Pont, N. R. Walet, M. Gavrilu, and C. W. McCurdy, *Phys. Rev. Lett.* **61**, 939 (1988).
- ¹⁷E. van Duijn, M. Gavrilu, and H. G. Muller, *Phys. Rev. Lett.* **77**, 3759 (1996).
- ¹⁸Q. Wei, S. Kais, and N. Moiseyev, *Phys. Rev. A* **76**, 013407 (2007).
- ¹⁹Q. Wei, S. Kais, and D. Herschbach, *J. Chem. Phys.* **129**, 214110 (2008).
- ²⁰J. Z. Kaminski, *J. Phys. A* **18**, 3365 (1985).
- ²¹P. S. Krstic and M. H. Mittleman, *Phys. Rev. A* **42**, 4037 (1990).
- ²²M. Protopapas, C. H. Keitel, and P. L. Knight, *J. Phys. B* **29**, L591 (1996).
- ²³C. J. Joachain, O. Latinne, and M. Dörr, *Europhys. Lett.* **26**, 333 (1994).
- ²⁴C. Joachain, M. Dorr, and N. Kylstra, *High-Intensity Laser-Atom Physics*, Advances In Atomic, Molecular, and Optical Physics, Vol. 42, edited by B. Bederson and H. Walther (Academic, New York/London, 2000), pp. 225–286.
- ²⁵C. J. Joachain and N. J. Kylstra, *Phys. Scr.* **68**, C72 (2003).
- ²⁶L. S. Brown and T. W. B. Kibble, *Phys. Rev.* **133**, A705 (1964).
- ²⁷J. H. Eberly and A. Sleeper, *Phys. Rev.* **176**, 1570 (1968).
- ²⁸W. C. Henneberger, *Phys. Rev. Lett.* **21**, 838 (1968).
- ²⁹I. Gilary and N. Moiseyev, *Phys. Rev. A* **66**, 063415 (2002).
- ³⁰L. E. McMurchie and E. R. Davidson, *J. Comput. Phys.* **26**, 218 (1978).
- ³¹A. Szabo and N. S. Ostlund, *Modern Quantum Chemistry: Introduction to Advanced Electronic Structure Theory* (Dover, New York, 1996), p. 480.
- ³²S. F. Boys, *Proc. R. Soc. London, Ser. A* **200**, 542 (1950).
- ³³D. R. Herschbach, *J. Chem. Phys.* **84**, 838 (1986).
- ³⁴D. Herschbach, J. Aver, and O. Gosinkis, *Dimensional Scaling in Chemical Physics* (Kluwer Academic Publishers, Norwell, MA, 1993), p. 480.
- ³⁵A. Svidzinsky, S. Chin, G. Chen, M. Kim, D. Ma, R. Murawski, A. Sergeev, M. O. Scully, and D. Herschbach, *Int. Rev. Phys. Chem.* **27**, 665 (2008).
- ³⁶S. Kais and D. R. Herschbach, *J. Chem. Phys.* **100**, 4367 (1993).
- ³⁷M. Dunn, T. C. Germann, D. Z. Goodson, C. A. Traynor, J. D. Morgan, D. K. Watson, and D. R. Herschbach, *J. Chem. Phys.* **101**, 5987 (1994).
- ³⁸J. Avery, D. Z. Goodson, and D. R. Herschbach, *Theor. Chim. Acta* **81**, 1 (1991).
- ³⁹C. Tsipis, V. Popov, D. Herschbach, and J. Avery, *New Methods in Quantum Theory* (Kluwer Academic Publishing, Norwell, MA, 1996), pp. 33–54.
- ⁴⁰N. A. Nguyen and T.-T. Nguyen-Dang, *J. Chem. Phys.* **112**, 1229 (2000).
- ⁴¹T. Yasuike and K. Sameda, *J. Phys. B* **37**, 3149 (2004).
- ⁴²B. Rotenberg, R. Taieb, V. Veniard, and A. Maquet, *J. Phys. B* **35**, L397 (2002).

Harmonic generation from free electrons in intense laser fields: classical versus semi-classical theory

A K Li¹, J X Wang¹, N Ren¹, W J Zhu², X Y Li², Ross Hoehn^{3,4} and Sabre Kais^{3,4}

¹ State Key Laboratory of Precision Spectroscopy and Department of Physics, East China Normal University, Shanghai 200062, People's Republic of China

² National Key Laboratory of Shock Wave and Detonation Physics, Mianyang 621900, Sichuan, People's Republic of China

³ Departments of Chemistry and Physics, Purdue University, West Lafayette, IN 47907, USA

⁴ Qatar Environment and Energy Research Institute, Qatar Foundation, Doha, Qatar

E-mail: jxwang@phy.ecnu.edu.cn

Received 14 August 2013, revised 31 October 2013

Accepted for publication 31 October 2013

Published 11 December 2013

Abstract

In this paper, a detailed numerical comparison of the high-harmonic generation (HHG) from free electrons in intense laser fields in both classical and semi-classical frameworks has been presented. These two frameworks have been widely used in the literature. It has been found that the HHG spectra display distinct quantitative differences for high-energy electrons. In some special situations, qualitative differences appear. Even if the radiation reaction is included in the electron classical dynamics, no consistent result can be obtained. Hence it should be of critical importance to submit the present HHG theory for high-precision experimental tests, which can help us not only to justify the present theories, but also to check the QED predictions in the high-intensity regime.

(Some figures may appear in colour only in the online journal)

1. Introduction

High-harmonic generation (HHG) plays an important role in generating coherent light sources in the UV, EUV, XUV or x-ray frequency regime [1, 2]. The traditional way to achieve high harmonics mainly focuses upon the interaction between atomic vapours and intense laser fields [3, 4]. However, due to the saturation and cutoff effects in atomic systems, much work has been recently carried out on HHG from solid-density plasma [5, 6]. With this method it is now possible to produce harmonics as high as the 3200th order with multi-keV photon energy by using intense high-contrast-ratio lasers [7, 8]. Moreover, these harmonics can be coherent in phase, which is a very important condition for the generation of ultra-short attosecond light pulses [9]. Another similar technique for HHG, which was put forward as early as the 1960s [10], is

based upon free electron interactions with intense laser fields in vacuum. Compared with harmonic generation from plasma, this method is much simpler in experimental setup since no control of plasma-related processes is involved. Its problem lies in the requirements of high-intensity laser fields ($I \gtrsim 10^{18} \text{ W cm}^{-2}$) and high-energy electrons ($E \sim \text{MeV-GeV}$). The former is necessary for the nonlinear electron dynamics to appear and the latter is necessary for the electron to overcome the ponderomotive barrier in order to reach the focus of the laser beam. It is not easy to meet both requirements at the same time in an experiment. Hence the corresponding experimental work progresses slowly [11–15]. Until now, the highest order of the observed harmonic is four, produced on SLAC [12]. Two recent experimental developments deserve our attention. First, the laser intensity has reached as high as $10^{22} \text{ W cm}^{-2}$ [16]. Second, the electron acceleration by

plasmas has made enormous progress [17–19]. It is now possible to produce a high-quality electron beam of GeV energy with a tabletop laser system [18, 20, 21]. These developments provide us with great opportunities to study the HHG from free electrons with an all-optical system. It is the anticipation of these opportunities that motivates us to check the related underlying theories in more details.

There are two main theoretical methods to deal with the HHG by free electrons in the literature. One is to obtain the harmonic spectrum from the electron's classical trajectory acquired by solving the Lorentz equation [22–24]. For high-intensity lasers, this process is the so-called nonlinear Thomson scattering (NTS). The other is to treat the HHG as a spontaneous emission of one photon from the Volkov state of an electron in a classical plane-wave laser field [25–30]. This is the well-known nonlinear Compton scattering (NCS). We refer the reader to the review [37] for an overview of the literature relevant for the interaction between the quantum systems and intense laser fields. Although both methods have been widely used to describe the HHG spectrum, they are basically derived from two different theoretical frameworks with different approximations. For example, the recoil effect is absent from the NTS. The NCS is in essence only a first-order result in the Furry picture [31], which is semi-classical since the strong field is treated classically. Hence it should be of great interest to make a detailed comparison between the results from these two methods in order to pave the way for the future developments of both the basic theories and the related experiments.

Actually, the comparisons have already been made in several published papers and some qualitative conclusions have been established [32–37]. For example, in Goreslavski's work [32], the classical energy and angular distribution of radiation have been derived by taking the classical limit of quantum results in the case of circularly polarized monochromatic radiation. The applicability of the classical limit for weak fields and for very intense fields has been discussed. Recently, Heinzl also made the quantum calculations and obtained the Thomson limit for the particular conditions relevant to experiments planned at the Forschungszentrum Dresden-Rossendorf (FZD) [34]. However, on the whole, a complete quantitative analysis of the two theories is still lacking, especially from the viewpoint of HHG with radiation reaction effect included in the classical framework.

In section 2, we shall briefly review the basic formulae of HHG in both the classical and semi-classical frameworks. Then in section 3, the detailed numerical comparisons are presented and discussed. In section 4, the influences of the classical radiation reaction effect on the scattering will be displayed. Finally, section 5 is devoted to the summaries.

2. Review of the HHG theory of free electrons in plane wavefields

The configuration of the electron–laser interaction is shown in figure 1. The plane wavefield is described by a vector

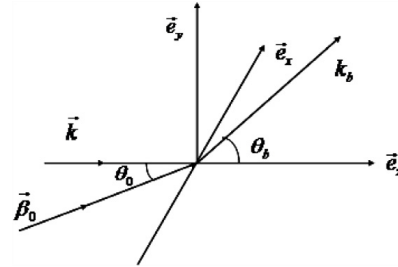


Figure 1. The configuration of the laser–electron interaction. The electron is moving in the x – z plane with incident four-momentum $p_{in} = mc\gamma_0(1, \beta_0)$. θ_0 is the crossing angle between β_0 and the z -axis. The laser propagates along the positive z -axis. The scattering angle of the emitted photon k' is denoted by θ_b . The azimuthal dependence of the interaction has not been considered in this paper.

potential A ,

$$A = A_0[\delta \cos \phi e_x + (1 - \delta^2)^{1/2} \sin \phi e_y], \quad (1)$$

with the phase factor $\phi = k^\mu x_\mu$, in which x^μ is the space–time coordinate and $k^\mu = \omega_0 n_k^\mu / c$ with $n_k = (1, e_k)$ to be a unit four vector. ω_0 represents the laser circular frequency. The electron is moving in the x – z plane with the initial four-momentum $p_{in} = mc\gamma_0(1, \beta_0)$, in which $\beta_0 = \beta_0(\cos \theta_0 e_z + \sin \theta_0 e_x)$ is the electron initial speed in the unit of c with θ_0 the crossing angle between β_0 and e_x . The laser intensity can be easily estimated by a dimensionless parameter $Q = eA_0/(mc^2)$, which is called the laser intensity parameter here. In the nonrelativistic regime, the characteristic velocity and energy for an electron moving in such an electromagnetic field are $v \sim eA_0/(mc)$ and $E \sim e^2 A_0^2 / (mc^2)$, so relativistic treatment is necessary if $v \sim c$ and $E \sim mc^2$ are satisfied. That is to say, the motion of the electron will become relativistic for $Q \sim 1$. In the optical regime ($\hbar\omega \approx 1$ eV), the corresponding laser intensity is about 10^{18} W cm $^{-2}$ for $Q \sim 1$, which has been achieved in the last decade.

2.1. Harmonic generation based upon nonlinear Thomson scattering in classical theory

In classical physics, the radiated energy from the free electrons per unit solid angle $d\Omega$ and per unit frequency interval $d\omega$ can be obtained with the following expression [38]:

$$\frac{dP^2}{d\omega d\Omega} = \frac{e^2 \omega^2}{4\pi^2 c} \lim_{T \rightarrow \infty} \frac{1}{T} \left| \int_{-\infty}^{\infty} e_{k'} \times (e_{k'} \times \beta) e^{ik'x} dt \right|^2, \quad (2)$$

where $e_{k'}$ denotes the direction of the emitted photon, and $k'^\mu = \omega n_{k'}^\mu / c$ with $n_{k'} = (1, e_{k'})$. β is acquired by solving the Lorentz equation,

$$mc \frac{du^\mu}{ds} = -\frac{e}{c} F^{\mu\nu} u_\nu, \quad (3)$$

in which $F^{\mu\nu} = \partial^\mu A^\nu - \partial^\nu A^\mu$ is the electromagnetic tensor.

In case of the plane wavefield described by equation (1), equation (3) can be solved analytically as follows [39, 40]:

$$u^\mu = u_{\text{in}}^\mu - a^\mu + \frac{a \cdot u_{\text{in}}}{k \cdot u_{\text{in}}} k^\mu - \frac{a^2}{2k \cdot u_{\text{in}}} k^\mu, \quad (4)$$

$$x^\mu = x_{\text{in}}^\mu + \frac{1}{k \cdot u_{\text{in}}} \left[u_{\text{in}}^\mu \phi - \int_0^\phi a^\mu d\phi' + \frac{1}{k \cdot u_{\text{in}}} \int_0^\phi [2(a \cdot u_{\text{in}}) - a^2] k^\mu d\phi' \right], \quad (5)$$

where $a^\mu = eA^\mu/(mc^2)$, $u = \gamma(1, \beta)$, $u_{\text{in}} = \gamma_0(1, \beta_0)$. Substituting equation (4) into (2), we can get the angular distribution of the n th-order harmonic power,

$$\frac{dP_n^{\text{NTS}}}{d\Omega} = \alpha \hbar \omega_n \frac{\omega_n mc}{2\pi q_{\text{in}}^0} \frac{mc}{p_{\text{in}} \cdot n_k} (|J_n|^2 - |e_k' \cdot J_n|^2), \quad (6)$$

where q_{in}^0 denotes the zeroth component of q_{in}^μ with the frequency being

$$\omega_n^{\text{NTS}} = \frac{n\omega_0 p_{\text{in}} \cdot n_k}{p_{\text{in}} n_k' + n_k \cdot n_k' \frac{Q^2 m^2 c^2}{4p_{\text{in}} n_k}}, \quad (7)$$

in which α is the fine structure constant and $q = p + \frac{e^2 A_0^2}{4c^2 (p_{\text{in}} \cdot n_k)} k$, $J_n = (J_{n,x}, J_{n,y}, J_{n,z})$ is a vector of the following form:

$$J_{n,x} = u_{\text{in},x} G_n^0 \left(B_1 \frac{\omega_n}{\omega_0}, B_2 \frac{\omega_n}{\omega_0}, \varphi \right) + \frac{Q}{2} \delta G_n^1 \left(B_1 \frac{\omega_n}{\omega_0}, B_2 \frac{\omega_n}{\omega_0}, \varphi \right), \quad (8)$$

$$J_{n,y} = \frac{Q}{2i} (1 - \delta^2)^{1/2} G_n^2 \left(B_1 \frac{\omega_n}{\omega_0}, B_2 \frac{\omega_n}{\omega_0}, \varphi \right), \quad (9)$$

$$J_{n,z} = \left(u_{\text{in},z} + \frac{Q^2}{4(n_k u_{\text{in}})} \right) G_n^0 \left(B_1 \frac{\omega_n}{\omega_0}, B_2 \frac{\omega_n}{\omega_0}, \varphi \right) + \frac{Q}{2(n_k u_{\text{in}})} u_{\text{in},x} \delta G_n^1 \left(B_1 \frac{\omega_n}{\omega_0}, B_2 \frac{\omega_n}{\omega_0}, \varphi \right) + \frac{Q^2}{2(n_k u_{\text{in}})} (1 - \delta^2)^{1/2} G_n^3 \left(B_1 \frac{\omega_n}{\omega_0}, B_2 \frac{\omega_n}{\omega_0}, \varphi \right), \quad (10)$$

where

$$B_1 = \sqrt{B_3^2 + B_4^2}, \quad (11)$$

$$B_2 = -\frac{Q^2 (n_k \cdot n_k')}{4(n_k \cdot u_{\text{in}})^2} \left(\delta^2 - \frac{1}{2} \right), \quad (12)$$

$$B_3 = \frac{Q}{n_k \cdot u_{\text{in}}} \delta \left[(e_k' \cdot e_x) - \frac{(n_k \cdot n_k') (p_{\text{in}} \cdot e_x)}{n_k \cdot p_{\text{in}}} \right], \quad (13)$$

$$B_4 = \frac{Q}{n_k \cdot u_{\text{in}}} (1 - \delta^2)^{1/2} (e_k' \cdot e_y), \quad (14)$$

$$\varphi = \arctan \frac{B_4}{B_3}. \quad (15)$$

The generalized Bessel function in equations (8)–(10) is defined as

$$G_s^0(\alpha, \beta, \varphi) = \sum_n J_{2n-s}(\alpha) J_n(\beta) e^{i(s-2n)\varphi},$$

$$G_s^1(\alpha, \beta, \varphi) = \frac{1}{2} (G_{s+1}^0(\alpha, \beta, \varphi) + G_{s-1}^0(\alpha, \beta, \varphi)),$$

$$G_s^2(\alpha, \beta, \varphi) = \frac{1}{2i} (G_{s+1}^0(\alpha, \beta, \varphi) - G_{s-1}^0(\alpha, \beta, \varphi)),$$

$$G_s^3(\alpha, \beta, \varphi) = \frac{1}{2} (G_{s+2}^0(\alpha, \beta, \varphi) + G_{s-2}^0(\alpha, \beta, \varphi)). \quad (16)$$

2.2. Harmonic generation based upon nonlinear Compton scattering in semi-classical theory

By solving the Dirac equation with the external plane-wave laser field as shown in equation (1), we can get the Volkov state as [41]

$$\psi_{p,r} = \sqrt{\frac{mc}{q^0}} \left(1 + \frac{e k A}{2p \cdot k} \right) u_r(p) e^{iS}, \quad (17)$$

where $u_r(p)$ is the free Dirac spinor and

$$S = -\frac{qx}{\hbar} - \frac{e^2 A_0^2}{8\hbar c^2} (2\delta^2 - 1) \sin(2k \cdot x) + \frac{eA_0}{\hbar c p \cdot k} [\delta(p \cdot e_x) \sin(k \cdot x) - (1 - \delta^2)^{1/2} (p \cdot e_y) \cos(k \cdot x)] \quad (18)$$

in which p is the four-momentum of the electron and q is the quasi-momentum mentioned before. The scattering matrix can be calculated by considering the first-order Feynman diagram based upon the Volkov state,

$$S_{\text{fi}} = -\frac{ie}{\hbar c} \int dx^4 \bar{\psi}_{p_f, r_f} A_c \psi_{p_i, r_i} \quad (19)$$

where the subscript f denotes the electron in the final state and $A_{c,\mu} = \sqrt{\frac{2\pi\hbar}{\omega}} c \varepsilon_{c,\mu} e^{ik \cdot x}$ is the quantized electromagnetic field. ε_c is the polarization four vector satisfying $\varepsilon_c^2 = -1$.

With S_{fi} , the differential rate for emitting a single photon of frequency ω can be written as

$$dW = \lim_{T \rightarrow \infty} \frac{1}{2T} \sum_{r_i, r_f, \varepsilon_c} |S_{\text{fi}}|^2 \frac{d^3 q_f}{(2\pi\hbar)^3} \frac{d^3 k'}{(2\pi)^3} \quad (20)$$

from which the differential power scattered per unit solid angle of the n th-order harmonic is obtained,

$$\frac{dP_n^{\text{NCS}}}{d\Omega} = \alpha \hbar \omega_n \frac{\omega_n mc}{2\pi q_{\text{in}}^0} \frac{mc}{p_{\text{in}} \cdot n_k} \frac{M_n(\chi_1, \chi_2, \vartheta)}{m^2 c^2} \quad (21)$$

in which the dimensionless function $M_n(\chi_1, \chi_2, \vartheta)$ is expressed as

$$M_n = \left[p_{\text{in}} \cdot p_f - 2m^2 c^2 - \frac{e^2 A_0^2}{2c^2} \right] |G_n^0|^2 + \frac{e^2 A_0^2}{2c^2} \left[\frac{p_{\text{in}} \cdot k}{p_f \cdot k} + \frac{p_f \cdot k}{p_{\text{in}} \cdot k} \right] \times (\delta^2 |G_n^1|^2 + (1 - \delta^2) |G_n^2|^2)$$

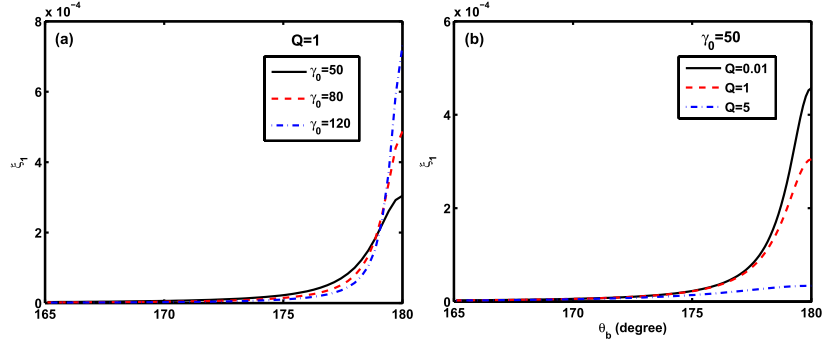


Figure 2. Relative differences of the fundamental harmonic frequency between NTS and NCS under different conditions. (a) $Q = 1$ with the incident electron energies being $\gamma_0 = 50, 80$ and 120 . (b) $\gamma_0 = 50$ with the laser intensities being $Q = 0.01, 1$ and 5 .

$$\begin{aligned}
 & - (1 - \delta^2) \frac{e^2 A_0^2}{2c^2} \operatorname{Re}(G_n^0 * G_n^3) \\
 & + \frac{e A_0}{c} k(p_{\text{in}} + p_{\text{f}}) \left[\delta \left(\frac{p_{\text{in}} \cdot e_x}{k \cdot p_{\text{in}}} - \frac{p_{\text{f}} \cdot e_x}{k \cdot p_{\text{f}}} \right) \right. \\
 & \times \operatorname{Re}(G_n^0 * G_n^1) + (1 - \delta^2)^{1/2} \\
 & \left. \times \left(\frac{p_{\text{in}} \cdot e_y}{k \cdot p_{\text{in}}} - \frac{p_{\text{f}} \cdot e_y}{k \cdot p_{\text{f}}} \right) \operatorname{Re}(G_n^0 * G_n^2) \right], \quad (22)
 \end{aligned}$$

where

$$\chi_1 = \chi_3^2 + \chi_4^2, \quad (23)$$

$$\chi_2 = \frac{Qm^2 c^2}{8\hbar} (2\delta - 1) \left(\frac{1}{k \cdot p_{\text{in}}} - \frac{1}{k \cdot p_{\text{f}}} \right), \quad (24)$$

$$\chi_3 = Qmc\delta \left(\frac{p_{\text{f}} \cdot e_x}{\hbar k \cdot p_{\text{f}}} - \frac{p_{\text{in}} \cdot e_x}{\hbar k \cdot p_{\text{in}}} \right), \quad (25)$$

$$\chi_4 = Qmc(1 - \delta^2)^{1/2} \left(\frac{p_{\text{f}} \cdot e_y}{\hbar k \cdot p_{\text{in}}} - \frac{p_{\text{in}} \cdot e_y}{\hbar k \cdot p_{\text{in}}} \right), \quad (26)$$

$$\vartheta = \arctan \frac{\chi_2}{\chi_1}. \quad (27)$$

The generalized Bessel functions are the same as those in the classical calculations except that the arguments become χ_1 , χ_2 and ϑ .

The expression for the n th harmonic frequency is

$$\omega_n^{\text{NCS}} = \frac{n\omega_0 p_{\text{in}} \cdot n_k}{p_{\text{in}} \cdot n_{k'} + n_k \cdot n_{k'} [n\hbar k + Q^2 m^2 c^2 / (4p_{\text{in}} \cdot n_k)]}. \quad (28)$$

3. Comparison of the classical and semi-classical results

In this section we shall compare the result from NTS with those of the NSC with emphasis placed upon effects in the strong field regime. In our opinion, the comparison is more complete and rigorous than that of the previous work. There are two main reasons: first, we achieve the classical

results by direct calculation in the framework of classical electrodynamics rather than just taking the classical limit (i.e., $\hbar \rightarrow 0$). We think this is a formal way because not every quantum process has its classical correspondence. Second, the comparison is made by considering a large parameter space rather than a few special cases. So it may be beneficial to recognize the discrepancy between results of NTS and NSC under the conditions for a certain experiment. The laser frequency involved in all the numerical calculations is chosen to be $\omega_0 = 1.17$ eV (Nd laser).

3.1. Frequency shift

From equations (7) and (28), we could define the relative difference of the harmonic frequency for NTS and NCS,

$$\xi_n = \frac{\omega_n^{\text{NTS}} - \omega_n^{\text{NCS}}}{\omega_n^{\text{NTS}}} = \frac{n\hbar\omega}{n\hbar\omega + \frac{Q^2 m c}{4p_{\text{in}} \cdot n_k} m c^2 + \frac{p_{\text{in}} \cdot n_{k'}}{n_k \cdot n_{k'} c}}. \quad (29)$$

It is easy to see that ξ_n depends upon several factors, such as the harmonic order n , laser intensity Q , electron initial energy γ_0 and interaction configurations among the electrons and incident and outgoing photons. Although ξ_n does not represent direct measurable quantities in experiment, it does offer information about how large the discrepancy of harmonic frequency is between NTS and NCS under certain conditions. So how these factors influence ξ_n is definitely of potential importance to a clear-cut experimental verification of HHG theories.

For simplicity, we shall first consider the head-on collisions with $\theta_0 = 180^\circ$. Figure 2 shows the results for the fundamental harmonic ($n = 1$) as a function of the emitting angle θ_b . We should mention here that the electron energy is 0.511 MeV for $\gamma_0 = 1$. It is obvious that the relative difference increases with the emitting angle θ_b . The maximum difference occurs in the electron running direction ($\theta_b = \theta_0 = 180^\circ$), or the backscattering direction if viewed along the laser propagation direction. Moreover, the relative difference becomes larger when increasing the

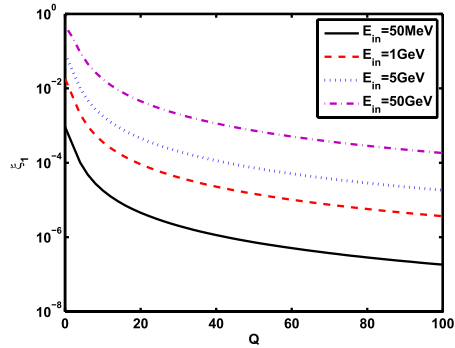


Figure 3. Variations of the relative differences between the NTS and NCS frequency of the fundamental harmonic with the laser intensity for different incident electron energies: $E_{in} = 50$ MeV (black solid line), 1 GeV (red dashed line), 5 GeV (blue dotted line), 50 GeV (purple dash-dotted line). $\theta_b = 180^\circ$.

electron energy. This is consistent with our usual physical intuition since high-energy electrons will greatly upshift the frequency of the counter-propagating laser by the Doppler effect. This means that the quantum recoil of the emitted photons will begin to influence the electron motion, which has not been considered in the classical framework. With the same logic, we can explain the decrease of ξ_1 when increasing the laser intensity as seen from figure 2(b), since the electrons are more decelerated by the light pressure of a stronger counter-propagating laser field. It should be noted that the photon recoil will be less significant with the increase of the laser intensity in a head-on configuration for the reason that the energy of the radiated photon will be small in a strong laser field (see equation (7)).

Figure 3 gives the scaling of ξ_1 against Q at $\theta_b = 180^\circ$ for different electron energies, from which we can observe two extreme situations.

- (i) When the electron energy reaches 50 GeV under low-intensity lasers, ξ_1 is almost as high as 60%. This is a truly quantum regime. The corresponding frequency might be so upshifted that even the Dirac sea might be excited, as happened in the SLAC experiment [42] ($E_{in} = 46.6$ eV, $Q = 0.4$, $\xi_1 \approx 43\%$).
- (ii) With extra-intense lasers, for example if $Q \approx 100$ ($I \approx 10^{22}$ W cm $^{-2}$), the electron will be so heavily decelerated that ξ_1 is reduced by nearly three orders of magnitude compared with the case when $Q \ll 1$. Hence, for head-on collisions with extra-intense lasers, there should not be much difference in the shift of fundamental frequency from NTS and NCS, especially if the electron energy is not extremely high.

It should be emphasized that the large relative frequency difference for high-energy electrons is mainly in the backscattering direction. In this direction, equation (29) can

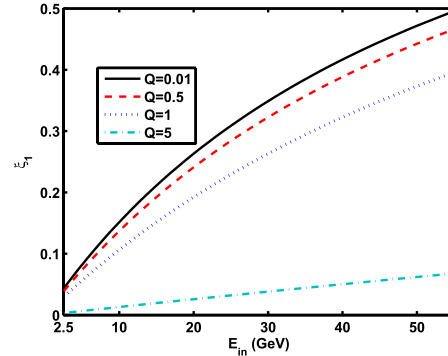


Figure 4. Variations of the relative differences between the NTS and NCS frequencies of the fundamental harmonic with the incident electron energy for different laser intensities: $Q = 0.01$ (black solid line), $Q = 0.5$ (red dashed line), $Q = 1$ (blue dotted line), $Q = 5$ (indigo dash-dotted line). $\theta_b = 180^\circ$.

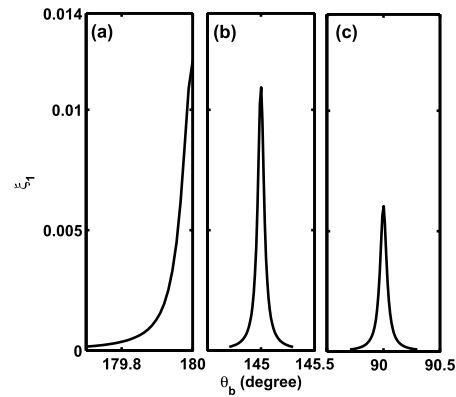


Figure 5. Variations of the relative differences between the NTS and NCS frequencies of the fundamental harmonic against different incident angles of the electron. (a) $\theta_b = 180^\circ$. (b) 145° . (c) 90° .

be simplified as

$$\xi_1(\theta_b = \pi) = \frac{\hbar\omega}{\hbar\omega + \gamma_0(1 - \beta_0)\left(1 + \frac{Q^2}{4}mc^2\right)}, \quad (30)$$

from which scaling with the initial electron energy is more transparent, as depicted in figure 4.

Next, for a non-head-on collision, i.e. $\theta_b \neq \pi$, the relative difference peak will occur at $\theta_b = \theta_0$ or in the electron running direction. Away from the direction of θ_0 , it decreases rapidly as shown in figure 5. The explanation is the same as for the above head-on collision case.

As to the radiation of higher-order harmonics, we shall only focus on head-on collisions, since these are typical configurations in which to expect a large relative difference

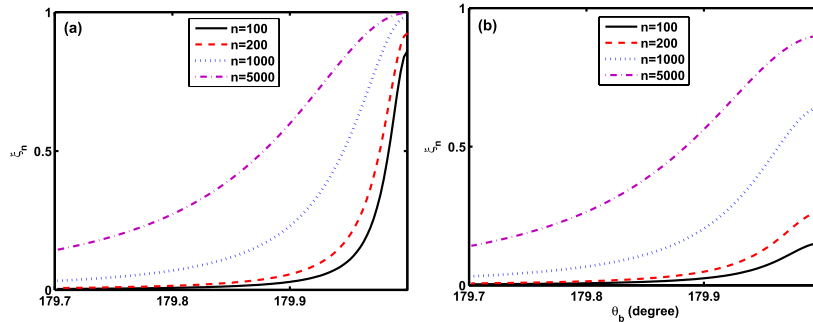


Figure 6. Angular dependence of the relative differences between the NTS and NCS frequencies of high-order harmonics with $n = 100, 200, 500, 1000,$ and 5000 for (a) $Q = 1$ and (b) $Q = 10$.

between NTS and NCS. Figure 6 presents the angular distribution of ξ_n for different n . It is interesting to note that ξ_n covers a much larger angular range than ξ_1 . For higher n , this feature is more obvious, although the maximum relative difference still occurs in the backscattering direction ($\theta_b = 180^\circ$). In the case with $Q = 1$, for n starting at 100, we already have a relative frequency shift of more than 70%. Even if a higher-intensity laser is used, for example $Q = 10$ as shown in figure 6(b), not much reduction has been found. This is because higher-order harmonics have a larger recoil effect. This effect can lead to a totally different scaling relationship of ω_n against n . In NTS,

$$\lim_{n \rightarrow \infty} \omega_n^{\text{NCS}} \sim n. \quad (31)$$

But in NCS, ω_n will saturate, i.e.

$$\lim_{n \rightarrow \infty} \omega_n^{\text{NCS}} = \frac{n_k \cdot p_{in}}{\hbar k \cdot n_b} \sim \text{constant}. \quad (32)$$

Hence, the larger relative difference will always come from higher-order harmonics. Even for the superintense fields ($Q \gg 1$), it is always significant so long as the order of the harmonic meets the condition

$$n \gtrsim \frac{Q^2 m^2 c^2}{(n_k \cdot p_{in})(n_b \cdot \hbar k)}. \quad (33)$$

But to have a larger relative difference does not guarantee its observability in experiments, since we also need to consider the corresponding radiation energy or transition probability, which will be the topic of section 3.2.

3.2. Harmonic spectrum

From equations (11)–(15) and (23)–(27), it is easy to see that

$$\lim_{\hbar \rightarrow 0} \chi_1 = B_1 \frac{\omega_n^{\text{NTC}}}{\omega_0}, \quad (34)$$

$$\lim_{\hbar \rightarrow 0} \chi_2 = B_2 \frac{\omega_n^{\text{NTC}}}{\omega_0}, \quad (35)$$

$$\lim_{\hbar \rightarrow 0} \vartheta = \varphi. \quad (36)$$

It can also be proved from equations (8)–(10) and (22) that

$$\lim_{\hbar \rightarrow 0} \frac{M_n(\chi_1, \chi_2, \vartheta)}{m^2 c^2} = |J_n|^2 - |e_{k'} \cdot J_n|^2, \quad (37)$$

as given in Avetissian's book [43]. So the classical harmonic spectrum can be taken as a limit of the semi-classical one by taking $\hbar \rightarrow 0$. As a tractable example, for a circularly polarized plane wave with $\delta = 1/\sqrt{2}$ in equations (6) and (21), we can obtain

$$\begin{aligned} \frac{dP_n^{\text{NTS}}}{d\Omega} &= \alpha \frac{\hbar (\omega_n^{\text{NTS}})^2}{8\pi} \frac{mc}{q_{in}^0} \frac{\omega_n^{\text{NTS}}}{n\omega_0} \frac{mc}{p_i \cdot n_k} \\ &\times \left\{ -4J_n^2 \left(B_1 \frac{\omega_n^{\text{NTS}}}{\omega_0} \right) + Q^2 \left[J_{n+1}^2 \left(B_1 \frac{\omega_n^{\text{NTS}}}{\omega_0} \right) \right. \right. \\ &\left. \left. + J_{n-1}^2 \left(B_1 \frac{\omega_n^{\text{NTS}}}{\omega_0} \right) - 2J_n^2 \left(B_1 \frac{\omega_n^{\text{NTS}}}{\omega_0} \right) \right] \right\} \quad (38) \end{aligned}$$

$$\begin{aligned} \frac{dP_n^{\text{NCS}}}{d\Omega} &= \alpha \frac{\hbar (\omega_n^{\text{NCS}})^2}{8\pi} \frac{mc}{q_{in}^0} \frac{\omega_n^{\text{NCS}}}{n\omega_0} \frac{mc}{p_{in} \cdot n_k} \left\{ -4J_n^2(\chi_1) \right. \\ &+ Q^2 \left[1 + \frac{\hbar(k \cdot k')^2}{2(p_{in} \cdot k)(p_f \cdot k)} \right] \left[J_{n+1}^2(\chi_1) \right. \\ &\left. \left. + J_{n-1}^2(\chi_1) - 2J_n^2(\chi_1) \right] \right\}. \quad (39) \end{aligned}$$

It is obvious, by using equation (34), that the above two equations give the same results. In addition, if the quantum effect is small, we can neglect the difference in the variables of the Bessel function in equations (38)–(39) and acquire the following simplified expression:

$$\frac{dP_n^{\text{NTS}}}{d\Omega} / \frac{dP_n^{\text{NCS}}}{d\Omega} = \left(\frac{\omega_n^{\text{NTS}}}{\omega_n^{\text{NCS}}} \right)^3. \quad (40)$$

From section 3.1, we already know $\omega_n^{\text{NTS}} > \omega_n^{\text{NCS}}$. Hence one can expect that the ratio of the radiation energies from NTS and NCS should be much larger than the ratio of the harmonic frequencies, which means that the quantum effect will be more

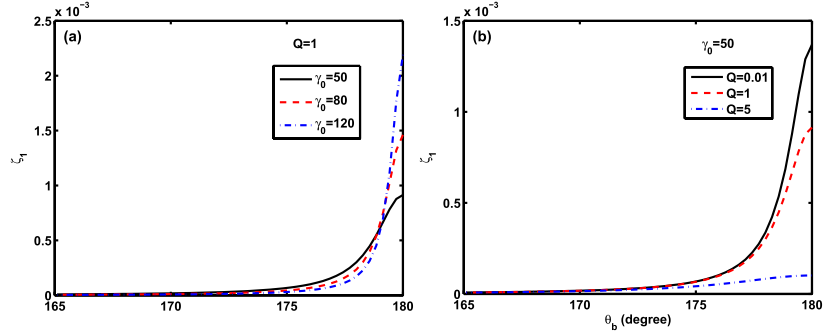


Figure 7. Angular dependence of the relative differences between the NTS and NCS radiation power of the fundamental harmonic under different electron incident energies (a) and laser intensities (b).

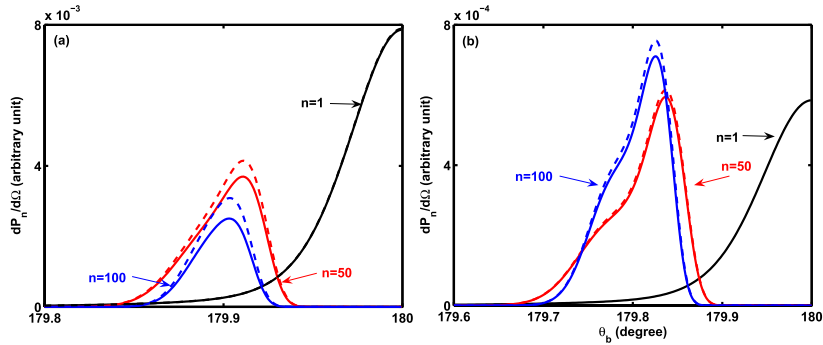


Figure 8. Angular distribution of the harmonic radiation power from NTS (solid line) and NCS (dotted line) for different laser intensities. (a) $Q = 5$. (b) $Q = 10$. The electron energy is 1 GeV.

prominent in studying the energy spectrum. To measure the relative difference of the power distribution, we introduce the following parameter:

$$\zeta_n = \left(\frac{dP_n^{\text{NTS}}}{d\Omega} - \frac{dP_n^{\text{NCS}}}{d\Omega} \right) / \frac{dP_n^{\text{NTS}}}{d\Omega}, \quad (41)$$

which is similar to the definition in equation (29) for the frequency shift.

First, let us consider the situation with circular polarized laser fields. The dependence of ζ_n upon the emission angle of the fundamental harmonic is shown in figure 7, which shows almost the same variations as the frequency shift in figure 2, but with much larger values. This tells once again that the angular distribution of the power is a much better index with which to measure the relative differences between NTS and NCS.

Compared with the fundamental harmonic, the high-order harmonic ($n > 1$) shows a different pattern of angular distribution as displayed in figure 8. One notes that there is

no high-order harmonic radiation around the backscattering direction ($\theta_b = 180^\circ$) in both the classical and semi-classical framework. It is called a ‘dead cone’ in the work of Heinzl [34] since no scattered photons will be detected within the cone. The size of the dead cone increases with harmonic order and laser intensity. Away from the dead zone, there is an angle with maximum radiation, whose position is dependent upon n . The higher is n , the more the peak will move away from the backscattering direction. In addition, from the comparisons between figures 8(a) and (b), we can also see that, as the laser intensity increases, the radiated energy tends to move from lower harmonics to higher harmonics. So stronger laser fields will result in higher harmonic generations, which is easy to understand and is consistent with former results [44]. For example, when Q is increased from 5 to 10, the peak power of $n = 100$ has already been bigger than that of $n = 1$. As for ζ_n , it increases with n , but decreases with Q as can be observed from figures 9(a) and (b). For example, if Q is increased from 5 to 100, ζ_n will decrease by almost two orders of magnitude. This is also due to the deceleration effect

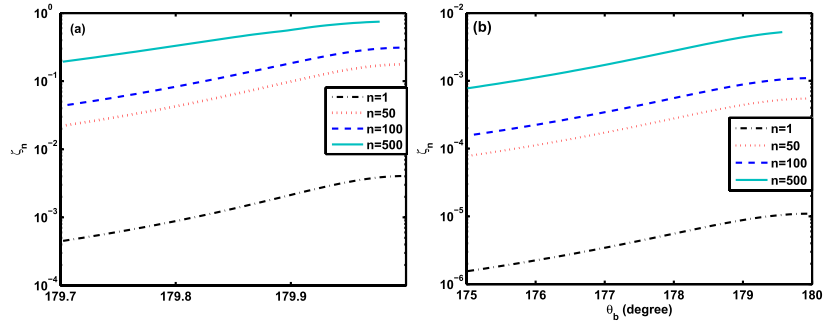


Figure 9. The relative difference between angular distribution of the high-harmonic radiations from NTS and NCS under different laser intensities. (a) $Q = 1$. (b) $Q = 100$. The electron energy is 1 GeV.

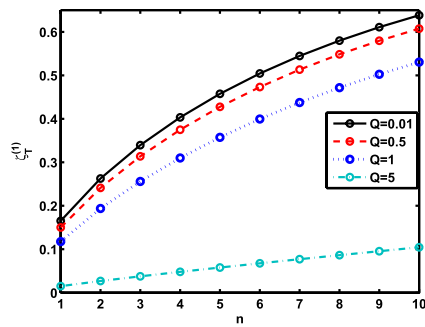


Figure 10. Relative difference between the total power from high-order harmonic radiation under different laser intensities. The electron energy is 5 GeV.

of the electron during head-on collisions, as discussed in the study of the frequency shift.

Figure 10 demonstrates the variations of relative difference of the total power ζ_T against the harmonic order for different laser intensities. ζ_n is defined as follows:

$$\zeta_T^{(1)} = \left(\int \frac{dP_n^{\text{NTS}}}{d\Omega} d\Omega - \int \frac{dP_n^{\text{NCS}}}{d\Omega} d\Omega \right) / \int \frac{dP_n^{\text{NTS}}}{d\Omega}. \quad (42)$$

From figure 10, one may see that ζ_T decreases with the laser intensity just as the radiation does in a definite emitting angle. But it should be noted that, as $Q \lesssim 1$, the radiation ζ_T increases much faster with the harmonic order than $Q = 5$. This again implicates that the large relative difference of the total power always comes from the case of not-so-strong field intensity and high-order harmonic radiation.

As to the other laser polarizations, we find that the difference of the power distribution is almost the same as that of the circularly polarization whatever the laser intensity and incident electron energy. The only exception occurs in the case of linear polarization with $\delta = 1$. In this situation, there is a

special direction where no classical emission in fundamental frequency exists as shown in figure 11, in which there is an obvious dip around $\theta_b = 179.97^\circ$. From equation (6), we find that this happens when J is parallel to e_k . This is in sharp contrast to the NCS result, which is smooth in this direction.

4. The comparison of the radiation damping and quantum recoil

A basic difference between NTS and NCS is the recoil effect of the emitted photons. It is natural to get this effect in the quantum theory, but there is a lot of controversy on how to include it in the classical electron dynamics. In 1938 [45], Dirac put forward the following Lorentz–Abraham–Dirac (LAD) equation [46, 45], which is one of the most controversial equations in the history of physics [47]:

$$mc \frac{du^\alpha}{ds} = \frac{e}{c} F^{\mu\nu} U_\nu + \frac{2e^2}{3c^3} \left(\frac{d^2 u^\alpha}{ds^2} - u^\alpha u^\nu \frac{d^2 u_\nu}{ds^2} \right), \quad (43)$$

where $ds = \sqrt{dx^\mu dx_\mu}$ refers to the four-dimensional distance and $F^{\mu\nu} = \partial_\mu A^\nu - \partial_\nu A^\mu$ is the electromagnetic field tensor. The LAD formula on a point charge suffers from two notorious defects: runaways and preacceleration. In the past seven decades, many new proposals have been put forward, trying to overcome the inherent difficulties, such as the equations from Landau–Lifshitz (LL) [48], Caldirola [49], Mo–Papas [50], Eliezer [51] and Caldirola–Yaghjian [52]. But each time a promising idea appears, there will be some objections. For example, Rohrlich [53, 54] has presented a revised LAD equation, which involves much discussion [55–57]. Later, O’Connell [58] claimed that their equation is actually for structured particles. Then in 1990, Herrera [59] gave another radiation reaction equation. Hence the problem is still open.

If the damping force is much smaller than the Lorentz force, from the first-order perturbation of the LAD equation,

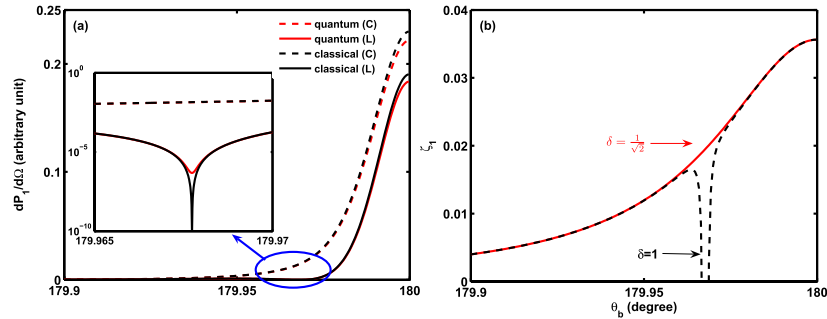


Figure 11. (a) Comparisons between the angular distribution of the radiation power for fundamental harmonic frequency from NTS (black) and NCS (red) under circularly (dashed line) or linearly polarized laser fields. The inset is the enlargement of the details. (b) The same as (a) but for the comparison of the relative differences. In both cases, the electron energy is 1 GeV and the laser intensity is $Q = 5$.

we can get the Landau–Lifshitz (LL) equation [48],

$$mc \frac{du^\mu}{ds} = \frac{e}{c} F^{\mu\nu} u_\nu + g^\mu$$

$$g^\mu = \frac{2e^2}{3c} \left[\frac{e}{c^2} u_\lambda \partial^\lambda F^{\mu\nu} + \frac{e^2}{mc^4} F^{\mu\nu} F_{\nu\lambda} u^\lambda \right. \\ \left. - \frac{e^2}{mc^4} (F_{\nu\rho} u^\nu)(F_{\rho\lambda} u_\lambda) u^\mu \right], \quad (44)$$

which does not admit runaways or preacceleration and can be analytically solved for a plane wavefield [60]. Recently it has been shown that LL can also be obtained with no reference to the size of the particle [61]. So it is not clear which is superior between LDA and LL. To check this problem, Griffiths [62] has compared the LL and LAD results as the limiting cases of a spherical shell of finite size, but no definite answer has yet been acquired.

Generally, for a tightly focused intense laser beam, the LAD or LL equations can only be solved numerically, especially in a so-called radiation-dominated regime [63, 64]. In this paper, we shall use the LL equation to determine the trajectory of the accelerated electron.

For a circularly polarized plane wave, the four-vector potential can be written as

$$A^\mu = a_1^\mu \psi_1(\phi) + a_2^\mu \psi_2(\phi), \quad (45)$$

with

$$a_1 = (0, 1, 0, 0), \quad a_2 = (0, 0, 1, 0), \quad (46)$$

$$\psi_1 = \frac{A_0}{\sqrt{2}} \cos \phi, \quad \psi_2 = \frac{A_0}{\sqrt{2}} \sin \phi. \quad (47)$$

The solution of the LL equation can be obtained as follows [60]:

$$u^\mu(\phi) = \frac{1}{h} \left[u_0^\mu + \frac{k^\mu}{2\Phi_0} (h^2 - 1) + \frac{1}{\Phi_0} (f_1^{\mu\nu} I_1 + f_2^{\mu\nu} I_2) u_{0,\nu} \right. \\ \left. + \frac{k^\mu}{2\Phi_0} (q_1^2 I_1^2 + q_2^2 I_2^2) \right], \quad (48)$$

where

$$\Phi_0 = k \cdot u_0 \quad f_j^{\mu\nu} = k^\mu a_j^\nu - k^\nu a_j^\mu \\ (j = 1, 2)$$

$$h(\phi) = 1 + \frac{\Phi_0 Q^2 e^2}{3mc^2} \phi$$

$$I_1(\phi) = \left[1 + \frac{2\Phi_0 e^2}{3mc^2} Q^2 \phi \right] \cos \phi - \frac{2\Phi_0 e^2}{3mc^2} (Q^2 + 1) \sin \phi, \quad (49)$$

$$I_2(\phi) = \left[1 + \frac{2\Phi_0 e^2}{3mc^2} Q^2 \phi \right] \sin \phi - \frac{2\Phi_0 e^2}{3mc^2} (Q^2 + 1) \cos \phi.$$

Here we assume the interaction is switched on and off adiabatically and neglect the edge effect. By substituting the above equations into equation (2), the energy radiated per unit solid angle $d\Omega$ per unit frequency $d\omega$ can be calculated. Unlike the case without radiation reaction, no explicit analytical results can be found. So we still need to resort to numerical calculations.

First, we shall consider an electron initially at rest in a strong circularly polarized plane wave with $Q = 100$. During the numerical calculations, the time interval corresponding to a phase change of $\Delta\phi = 300\pi$ will be used for the interaction since the electron motion is highly damped.

According to section 2, the relative differences of the frequency spectra between the classical results without radiation reactions and the semi-classical results will be less than 10^{-6} in such a strong laser field. But in figure 12, as we plot the differential spectrum of the fundamental harmonic with different emitting angles, it is easy to see that there is an obvious downshift in the spectrum from the result in equation (7). The difference becomes larger with the increase of the emitting angle. This shift can be attributed to the strong radiation reaction effect. It is expected that this shift will be enhanced by increasing the laser field intensity, which does not occur for the NCS under the same condition. Besides the frequency shift, the broadening of the spectrum is another feature of the influence from the classical damping effect. For the emitting angle of $\theta_b = 3.5^\circ$, we can observe about

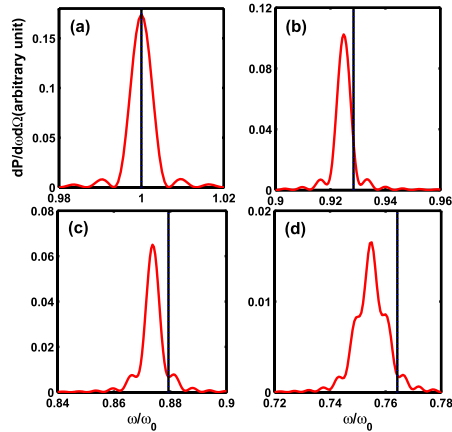


Figure 12. Differential spectrum from NTS (black), NCS (blue) and NTS with radiation damping (red) for a plane laser field with different emitting angles. (a) $\theta_0 = 0^\circ$. (b) 1.41° . (c) 1.88° . (d) 2.82° . The electron is initially at rest in a plane wavefield and the laser intensity is $Q = 100$.

2% downshift and broadening of the fundamental frequency. This could be observed with high-precision measurements in experiments.

Next we consider a Gaussian laser pulse described by the following vector potential:

$$A = A_0 \exp\left(-\frac{\phi^2}{\tau^2}\right) (\cos \phi e_x + \sin \phi e_y) \quad (50)$$

with τ being the dimensionless pulse length normalized by $1/\omega_0$. Figure 13 presents the differential spectrum for the classical damped, undamped and semi-classical cases with $\tau = 50$ cycles (the corresponding pulse duration is 177 fs) and $Q = 100$. It is apparent that similar downshift and broadening of the fundamental harmonic also happen as in the plane wavefield. The downshift of the spectrum also increases with the duration of the pulse as well as the laser intensity. To further illustrate the difference between the quantum recoil and classical radiation reaction, we shall consider head-on collision for an relativistic electron with a Gaussian radiation pulse. In figure 14, the differential spectra of the fundamental harmonic for emitting angles $\theta_0 = \pi$ are represented, the two plots corresponding to (a) $\gamma_0 = 100$ ($E_{in} = 50$ MeV), $Q = 20$, and (b) $\gamma_0 = 2000$ ($E_{in} = 1$ GeV), $Q = 0.5$. The pulse duration is $\tau = 50$ cycles as the previous case. In figure 14(a), the frequency downshift is clear and the radiation intensity is largely suppressed by the radiation reaction (this can be explained by the energy lost for the electron) while the effect of the quantum recoil seems to be negligible. For a lower laser intensity and increased electron energy in figure 14(b), the discrepancy between the quantum and classical results becomes large as we expect in section 3. At the same time the classical radiation damping does not have a dramatic impact

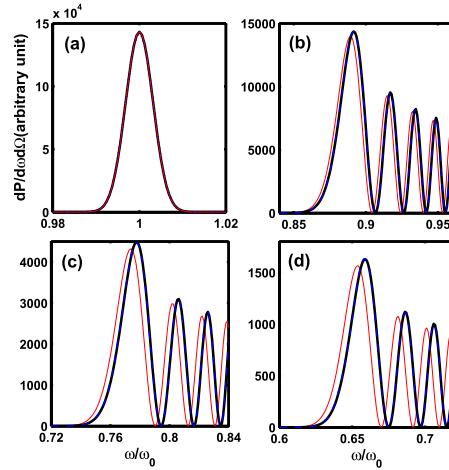


Figure 13. The same as in figure 12 but for a pulsed laser field with $\tau = 50$ cycles. The emitting angles are (a) $\theta_0 = 0^\circ$, (b) 1.88° , (c) 2.82° and (d) 3.76° .

on the differential spectrum for a small damping force in such a weak field.

Finally, we need to emphasize here that the NTS and the NCS come from two different frameworks. Both have been used in studying the HHG from free electrons. In most cases, they coincide with each other very well, but distinct quantitative differences exist and in some situations a qualitative difference appears. Even if we include the classical recoil effect embodied in the radiation reactions in the classical framework, no quantitatively consistent result has been found in the considered cases. Here several possible reasons for the inconsistency can be put forward. First, the present semi-classical theory based upon NCS is not enough and we need more higher-order corrections. Second, the LL equation has not covered the full story of the radiation reaction effect and needs more improvement. Third, the recoil effect from classical radiation reaction is basically of a different nature from the semi-classical one and an extra radiation reaction force obtained from QED is required for a complete classical theory. But this last reason brings about another deep physical question, namely, what is the essence of classical radiation reactions? Does the classical radiation reaction have quantum correspondence and if so what is it? To delve into these questions and problems is already out of the scope of this paper. It is hoped that future high-precision strong-field experiments could give us more data to justify which theory is nearer the truth.

5. Summary

In this paper, based upon NTS, NCS and LL equations, we have performed a detailed numerical investigation of the

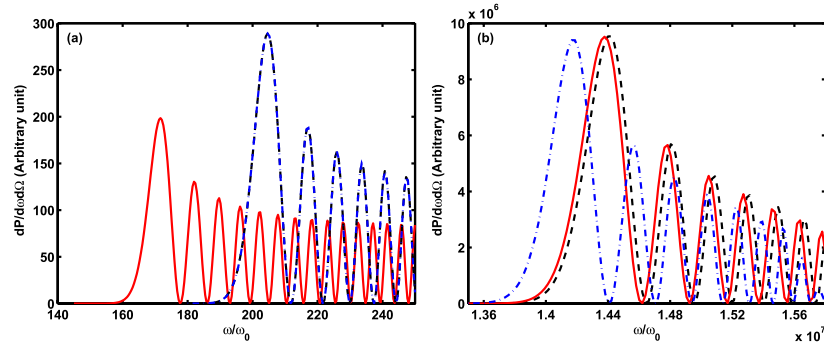


Figure 14. Differential spectrum from NTS (black dashed line), NCS (blue dash-dotted line) and NTS with radiation damping (red solid line) for the electron head-on collision with a pulsed laser field. The pulse duration is $\tau = 50$ cycles and the emitting angle is $\theta_0 = 180^\circ$. The initial energy of the electron and the peak intensity of the pulse are (a) $\gamma_0 = 100$, $Q = 20$, and (b) $\gamma_0 = 2000$, $Q = 0.5$.

differences between the classical and semi-classical results for free electron high-harmonic generations in intense laser fields. The focus is mainly upon the differences between the frequency and the angular power distribution of the harmonic radiation in a plane wave or a pulsed laser field. To maximize the differences, only the head-on collision is considered. The conclusions can be summarized as follows.

- (i) The frequency differences in NTS and NCS will increase with the electron energy. For GeV electrons, the relative frequency difference in the backscattering direction for the fundamental harmonic can be as high as 40–50% in a laser field with $Q \sim 1$.
- (ii) For stronger laser intensity ($Q \gtrsim 1$), the importance of the higher-order harmonic radiation begins to emerge. If we take $Q = 5$ and $n = 500$, the relative frequency difference can reach 10%.
- (iii) Generally, as the laser intensity is increased, more radiation energy will go to higher-order harmonics. The relative differences in both the frequency and radiation energy tend to increase with harmonic order, yet decrease with the laser intensity. This implies that the most prominent differences appear around $Q \sim 1$ –10 for GeV-energy electrons, which is readily in reach of the present experimental technology.
- (iv) The differences are independent of the field polarizations except for a linearly polarized laser, which shows a dip in the relative angular distribution of radiation power for the fundamental harmonic along the direction just a little away from the backscattering direction. The width of the dip is smaller than 0.1° , which would be a big challenge for a high-precision experimental test.
- (v) With the classical radiation reactions included by using the LL equation, NTS demonstrates bigger differences from NCS in both the shift and the widening of the fundamental frequency. Moreover, these differences depend upon the pulse length. Hence it is utterly desirable to check more deeply the underlying physics in the

classical and quantum recoil effects. According to the recent study [36], it has been identified that the quantum radiation reaction corresponds to the consecutive photon recoils in multiple incoherent single-photon emissions by the laser-driven electron. So the single-photon emission may not include the radiation reaction. Hence it is utterly desirable to check more deeply the underlying physics in the classical and quantum recoil effects in order to get a consistent physical picture and elucidate the present theories for free electron harmonic generation in strong laser fields.

Acknowledgment

This work is supported by the National Natural Science Foundation of China under Grant No. 11274117.

References

- [1] Zeitoun Ph *et al* 2004 A high-intensity highly coherent soft x-ray femtosecond laser seeded by a high harmonic beam *Nature* **431** 426–9
- [2] Sekikawa T, Kosuge A, Kanai T and Watanabe S 2004 Nonlinear optics in the extreme ultraviolet *Nature* **432** 605–8
- [3] Eden J G 2004 High-order harmonic generation and other intense optical field–matter interactions: review of recent experimental and theoretical advances *Prog. Quantum Electron.* **28** 197–246
- [4] L’Huillier A, Lompre L A, Mainfray G and Manus C 1992 High-order harmonic generation in rare gases *Atoms in Intense Laser Fields* ed M Gavrilu (New York: Academic) p 139
- [5] Tarasevitch A, Orisch A, von der Linde D, Balcou Ph, Rey G, Chambaret J-P, Teubner U, Klöpfel D and Theobald W 2000 Generation of high-order spatially coherent harmonics from solid targets by femtosecond laser pulses *Phys. Rev. A* **62** 023816
- [6] Teubner U and Gibbon P 2009 High-order harmonics from laser-irradiated plasma surfaces *Rev. Mod. Phys.* **81** 445
- [7] Dromey B *et al* 2007 Bright multi-keV harmonic generation from relativistically oscillating plasma surfaces *Phys. Rev. Lett.* **99** 085001

- [8] Thaury C *et al* 2007 Plasma mirrors for ultrahigh-intensity optics *Nature Phys.* **3** 424–9
- [9] Quéré F, Thaury C, Monot P, Dobosz S, Martin Ph, Geindre J-P and Audebert P 2006 Coherent wake emission of high-order harmonics from overdense plasmas *Phys. Rev. Lett.* **96** 125004
- [10] Vachaspati 1962 Harmonics in the scattering of light by free electrons *Phys. Rev.* **128** 664–6
- [11] Englert T J and Rinehart E A 1983 Second-harmonic photons from the interaction of free electrons with intense laser radiation *Phys. Rev. A* **28** 1539–45
- [12] Bula C *et al* 1996 Observation of nonlinear effects in Compton scattering *Phys. Rev. Lett.* **76** 3116–9
- [13] Chen S-Y, Maksimchuk A and Umstadter D 1998 Experimental observation of relativistic nonlinear Thomson scattering *Nature* **396** 653–5
- [14] Chen S-Y, Maksimchuk A, Esarey E and Umstadter D 2000 Observation of phase-matched relativistic harmonic generation *Phys. Rev. Lett.* **84** 5528–31
- [15] Kumita T *et al* 2006 Observation of the nonlinear effect in relativistic Thomson scattering of electron and laser beams *Laser Phys.* **16** 267–71
- [16] Yanovsky V *et al* 2008 Ultra-high intensity- 300-tw laser at 0.1 Hz repetition rate *Opt. Express* **16** 2109–14
- [17] Geddes C G R, Toth Cs, van Tilborg J, Esarey E, Schroeder C B, Bruhwiler D, Nietzer C, Cary J and Leemans W P 2004 High-quality electron beams from a laser wakefield accelerator using plasma-channel guiding *Nature* **431** 538–41
- [18] Faure J, Rechatin C, Norlin A, Lifschitz A, Glinec Y and Malka V 2006 Controlled injection and acceleration of electrons in plasma wakefields by colliding laser pulses *Nature* **444** 737–9
- [19] Mangles S P D *et al* 2004 Monoenergetic beams of relativistic electrons from intense laser–plasma interactions *Nature* **431** 535–8
- [20] Geddes C G R, Nakamura K, Plateau G R, Toth Cs, Cormier-Michel E, Esarey E, Schroeder C B, Cary J R and Leemans W P 2008 Plasma-density-gradient injection of low absolute-momentum-spread electron bunches *Phys. Rev. Lett.* **100** 215004
- [21] Leemans W P, Nagler B, Gonsalves A J, Toth Cs, Nakamura K, Geddes C G R, Esarey E, Schroeder C B and Hooker S M 2006 GeV electron beams from a centimetre-scale accelerator *Nature Phys.* **2** 696–9
- [22] Sarachik E S and Schappert G T 1970 Classical theory of the scattering of intense laser radiation by free electrons *Phys. Rev. D* **1** 2738–53
- [23] Salamin Y I and Faisal F H M 1996 Harmonic generation by superintense light scattering from relativistic electrons *Phys. Rev. A* **54** 4383–95
- [24] Hartemann F V and Kerman A K 1996 Classical theory of nonlinear Compton scattering *Phys. Rev. Lett.* **76** 624
- [25] Narozhnyi N B and Fofanov M S 1996 *J. Exp. Theor. Phys.* **83** 14
- [26] Panek P, Kamiński J Z and Ehlötzky F 2002 Laser-induced Compton scattering at relativistically high radiation powers *Phys. Rev. A* **65** 022712
- [27] Ehlötzky F, Krajewska K and Kaminski J Z 2009 Fundamental processes of quantum electrodynamics in laser fields of relativistic power *Rep. Prog. Phys.* **72** 046401
- [28] Harvey C, Heinzl T and Ilderton A 2009 Signatures of high-intensity Compton scattering *Phys. Rev. A* **79** 063407
- [29] Boca M and Florescu V 2009 Nonlinear Compton scattering with a laser pulse *Phys. Rev. A* **80** 053403
- [30] Mackenroth F and Di Piazza A 2011 Nonlinear Compton scattering in ultrashort laser pulses *Phys. Rev. A* **83** 032106
- [31] Furry W H 1951 On bound states and scattering in positron theory *Phys. Rev.* **81** 115–24
- [32] Goreslavski S P, Popruzhenko S V and Shcherbachev O V 1999 *Laser Phys.* **9** 1039
- [33] Gao J 2004 Thomson scattering from ultrashort and ultraintense laser pulses *Phys. Rev. Lett.* **93** 243001
- [34] Heinzl T, Seipt D and Kämpfer B 2010 Beam-shape effects in nonlinear Compton and Thomson scattering *Phys. Rev. A* **81** 022125
- [35] Boca M and Florescu V 2010 Thomson and Compton scattering with an intense laser pulse *Eur. Phys. J. D* **61** 449–62
- [36] Di Piazza A, Hatsagortsyan K Z and Keitel C H 2010 Quantum radiation reaction effects in multiphoton Compton scattering *Phys. Rev. Lett.* **105** 220403
- [37] Di Piazza A, Müller C, Hatsagortsyan K Z and Keitel C H 2012 Extremely high-intensity laser interactions with fundamental quantum systems *Rev. Mod. Phys.* **84** 1177
- [38] Jackson J D 1976 *Classical Electrodynamics* (New York: Wiley)
- [39] Meyer J W 1971 Covariant classical motion of electron in a laser beam *Phys. Rev. D* **3** 621
- [40] Heinzl T and Ilderton A 2009 A Lorentz and gauge invariant measure of laser intensity *Opt. Commun.* **282** 1879–83
- [41] Volkov D M 1935 Über eine Klasse von Lösungen der Diracschen Gleichung *Z. Phys.* **94** 250
- [42] Burke D L *et al* 1997 Positron production in multiphoton light-by-light scattering *Phys. Rev. Lett.* **79** 1626–9
- [43] Avezissian H K 2010 *Relativistic Nonlinear Electrodynamics: Interaction of Charged Particles with Strong and Super Strong Laser Fields* (Berlin: Springer)
- [44] Wang J X and Ho Y K 1999 Energy-exchange characteristics in ordinary and nonlinear Compton scattering *Phys. Rev. A* **59** 4522–9
- [45] Dirac P A M 1938 Classical theory of radiating electrons *Proc. R. Soc. Lond. A* **167** 148
- [46] Poisson Eric 1999 An introduction to the Lorentz–Dirac equation arXiv:gr-qc/9912045v1
- [47] Rohrlich F 1965 *Classical Charged Particles* (Reading, MA: Addison-Wesley)
- [48] Landau L D 1962 *The Classical Field* (Oxford: Pergamon)
- [49] Caldirola P 1979 A relativistic theory of the classical electron *Riv. Nuovo Cimento* **2** 1–49
- [50] Mo T C and Papas C H 1971 New equation of motion for classical charged particles *Phys. Rev. D* **4** 3566–71
- [51] Eliezer C J 1948 On the classical theory of particles *Proc. R. Soc. Lond. A* **194** 543–55
- [52] Yaghjian A D 1992 *Relativistic Dynamics of a Charged Sphere* (New York: Springer)
- [53] Rohrlich F 2001 The correct equation of motion of a classical point charge *Phys. Lett. A* **283** 276–8
- [54] Rohrlich F 2002 Dynamics of a classical quasi-point charge *Phys. Lett. A* **303** 307–10
- [55] Ribaric M and Sustersic L 2002 Qualitative properties of an equation of motion of a classical point charge *Phys. Lett. A* **295** 318–9
- [56] Rohrlich F 2002 The validity limits of physical theories: response to the preceding letter *Phys. Lett. A* **295** 320–2
- [57] Baylis W E and Huschilt J 2002 Energy balance with the Landau–Lifshitz equation *Phys. Lett. A* **301** 7–12
- [58] O’Connell R F 2003 The equation of motion of an electron *Phys. Lett. A* **313** 491–7
- [59] Herrera L 1990 The equation of motion for a radiating charged particle without self-interaction term *Phys. Lett. A* **145** 14–8
- [60] Di Piazza A 2008 Exact solution of the Landau–Lifshitz equation in a plane wave *Lett. Math. Phys.* **83** 305–13
- [61] Medina R 2006 Radiation reaction of a classical quasi-rigid extended particle *J. Phys. A: Math. Gen.* **39** 3801
- [62] Griffiths D J, Proctor T C and Schroeter D F 2010 Abraham Lorentz versus Landau Lifshitz *Am. J. Phys.* **78** 391
- [63] Koga J, Esirkepov T Zh and Bulanov S V 2005 Nonlinear Thomson scattering in the strong radiation damping regime *Phys. Plasmas* **12** 093106
- [64] Wang J X, Ho Y K and Feng L 1998 Radiation corrections to the electron inelastic scattering by an intense stationary laser beam *Phys. Lett. A* **244** 523–6



The interference effect of laser-assisted bremsstrahlung emission in Coulomb fields of two nuclei

Ankang Li,¹ Jiaxiang Wang,^{1,a)} Na Ren,¹ Pingxiao Wang,² Wenjun Zhu,³ Xiaoya Li,³ Ross Hoehn,⁴ and Sabre Kais^{4,5}

¹State Key Laboratory of Precision Spectroscopy and Department of Physics, East China Normal University, Shanghai 200062, China

²Applied Ion Beam Physics Laboratory, Key Laboratory of the Ministry of Education, China and Institute of Modern Physics, Department of Nuclear Science and Technology, Fudan University, Shanghai 200433, China

³National Key Laboratory of Shock Wave and Detonation Physics, Mianyang 621900, Sichuan, China

⁴Departments of Chemistry and Physics, Purdue University, West Lafayette, Indiana 47907, USA

⁵Qatar Environment and Energy Research Institute, Qatar Foundation, Doha, Qatar

(Received 3 August 2013; accepted 11 September 2013; published online 27 September 2013)

In this paper, the spontaneous bremsstrahlung emission from an electron scattered by two fixed nuclei in an intense laser field is investigated in detail based upon the Volkov state and the Dirac-Volkov propagator. It has been found that the fundamental harmonic spectrum from the electron radiation exhibits distinctive fringes, which is dependent not only upon the internucleus distance and orientation but also upon the initial energy of the electron and the laser intensity. By analyzing the differential cross section, we are able to explain these effects in terms of interference among the electron scattering by the nuclei. These results could have promising applications in probing the atomic or molecular dressed potentials in intense laser fields. © 2013 AIP Publishing LLC. [<http://dx.doi.org/10.1063/1.4822317>]

I. INTRODUCTION

High-order harmonic generation (HHG)¹⁻⁴ is a process in which high-order harmonics of the fundamental laser frequency are coherently radiated when an intense laser pulse is focused into an atomic or molecular gas. This process is not only used to generate UV or XUV lights but also be applied to explore molecular structures, recently. The first breakthrough was the discovery of a double-slit-type interference effect from the simplest diatomic molecules H_2^+ and H_2 .⁵⁻⁸ The experimental confirmation was first realized for aligned CO_2 in 2005.^{9,10} The next major development was the so-called molecular orbital tomography proposed by Itatani *et al.* in 2004.¹¹ Namely, once the HHG spectra and phases are known for various orientation of molecular axis, a 2D projection of the initial electron orbital can be reconstructed through a tomographic algorithm. Now, the work has been generalized to include orbital symmetry influences upon HHG and quantum tomography with 2D calculations.¹²

In all the above-mentioned works, the HHG originates from the electrons bound by the atoms or molecules and the calculation usually involves the time-dependent Schrodinger equation (TDSE) with dipole approximation. But when the field is so strong that the ponderomotive energy of the free electron reaches the same order of the rest energy of the electron, there will be a different picture. Namely, the dipole approximation may not be a good choice and the TDSE should be replaced by the Dirac equation. Moreover, some electrons may be ionized to be free particles, whose dynamics will be predominated by the intense laser fields instead of

the Coulomb potentials. Now, the principle process is the so-called laser-assisted bremsstrahlung, which has been studied previously by several authors. In the early works, the analytic expression for the radiation spectrum of laser-assisted bremsstrahlung in a plane monochromatic has been derived by Karapetyan and Fedorov for nonrelativistic regime.¹³ Within the framework of the Born approximation, Roshchupkin^{14,15} has developed a general relativistic expression for the amplitude of the scattering of an electron by a nucleus in an external field with arbitrary intensity. Recently, the numerical evaluation of the laser-assisted bremsstrahlung process has been carried out for both circularly polarized and linearly polarized laser field.^{16,17}

Motivated by the molecule HHG in non-relativistic case, in this paper, we will consider an electron scattering by two nuclei in strong laser fields. This model differs from one-nucleus case mentioned above by providing more than one center for the electron scattering, which will allow for dynamics, for example, the emission spectra of the electron may depend on the internuclear distance and orientation, just as in the situation of molecule HHG. This model could provide us a method to explore some special potentials, which exists only in intense laser fields, such as the dressed Kramer-Henneberg potential in high-frequency laser fields, which plays an important role in guaranteeing the existence of multiply charged negative ions in the fields.

The notations used in this paper are as follows. The four-vector product is denoted by $a \cdot b = a^0 b^0 - \mathbf{ab}$. For the Feynman dagger, we use the following notation: $\hat{A} = \gamma \cdot A$. The Dirac adjoint is denoted by the standard notation $\bar{u} = u^\dagger \gamma^0$ for a bispinor u and $\bar{F} = \gamma^0 F^\dagger \gamma^0$ for a matrix F .

The outline of this paper is as follows. First, we will introduce the laser-assisted bremsstrahlung model and derive

^{a)}Author to whom correspondence should be addressed. Electronic mail: jxwang@phy.ecnu.edu.cn

the theoretical expression for the cross section of the emission in Sec. II. Then, the numerical estimation of the cross section and the corresponding analyses will be provided in Sec. III. Concluding remarks are reserved for Sec. IV.

II. THEORETICAL DERIVATION OF THE BREMSSTRAHLUNG CROSS SECTION

Consider two nuclei with charge number Z fixed in the x - z plane with an internucleus distance R_0 in a strong laser field. We assume that, in the laboratory frame of reference, the laser can be described by a plane wave propagating in the positive direction of the z -axis with a vector potential A^μ

$$A^\mu = A_0[\delta\cos\phi\epsilon_1^\mu + (1 - \delta^2)^{1/2}\sin\phi\epsilon_2^\mu]. \quad (1)$$

The approximation is acceptable if the number of laser photons is large enough so that an arbitrary amount of energy and momentum can be taken from or emitted into the field without changing it. The plane wave depends only on the phase factor $\phi = k \cdot x$, in which x is the position vector, and $k^\mu = \frac{\omega_0}{c}(1, 0, 0, 1)$ the four wave vector with ω_0 denoting the laser frequency. The laser is circularly polarized for $\delta = 1/\sqrt{2}$ and linearly polarized for $\delta = 0, \pm 1$. We define two polarization vectors ϵ_1, ϵ_2 , satisfying $\epsilon_i \cdot k = 0$, $\epsilon_i \cdot \epsilon_j = \delta_{ij}$ ($i, j = 1, 2$). The laser intensity can be easily described by a dimensionless parameter $Q = eA_0/(mc^2)$, which is usually called laser intensity parameter. It should be mentioned that in the nonrelativistic regime, the characteristic velocity and energy for an electron moving in such an electromagnetic field is $v \sim eA_0/(mc)$ and $E \sim e^2A_0^2/(mc^2)$, so a relativistic treatment is necessary if $v \sim c$ and $E \sim mc^2$ is satisfied, which means the motion of the electron will become relativistic when $Q \sim 1$.

The angle between the orientation of two nuclei and the laser propagation direction is denoted by ϑ . For convenience of calculation, here we set the origin of the coordinate at the middle of two nuclei. So we can easily introduce a vector $\mathbf{R} = R_0(\sin\vartheta\mathbf{e}_x + \cos\vartheta\mathbf{e}_z)/2$ to describe the location of the two nuclei.

Now we begin to derive the differential cross section of the electron-nucleus bremsstrahlung. Consider the scattering geometry that an incoming electron moving along the negative z -axis has a head-on collision of the laser photons while scattering by two nuclei. The configuration is shown in Fig. 1. The whole process can be described by two Feynman diagrams displayed in Fig. 2. In the first one, the initial electron first interacts with two nuclei and then emits a bremsstrahlung photon. The situation is reversed in the second diagram. In Feynman diagrams, the electron is denoted by a zigzag line on top of a straight line since it is dressed by a strong laser. Also, here the free electron propagator is replaced by the Dirac-Volkov propagator.¹⁸

Actually, the electron will interact with three external fields during the process, namely, the laser field described by Eq. (1), the Coulomb field of two nuclei, and the field of the emitted bremsstrahlung photon. As usual, we treat the laser-electron interaction exactly and nonperturbatively by using Volkov states as the initial and final wave functions

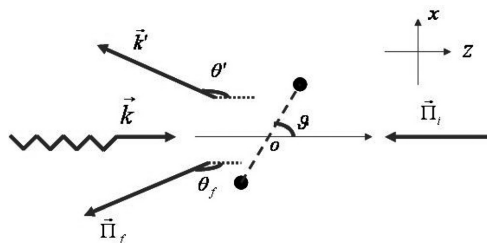


FIG. 1. The scattering geometry: The incoming electron with laser-dressed four momentum Π_f counterpropagates with the laser, while scattering by two fixed nuclei. ϑ is an angle between internucleus axis and the laser propagating direction. The final electron with Π_f' and the bremsstrahlung photon with k' are projected onto the xz plane in this figure; so, only the polar angles θ_f and θ' are displayed. The azimuthal angles are denoted by Ω_f and Ω' , respectively.

$$\psi_{p,r} = \sqrt{\frac{mc}{\Pi^0 V}} \zeta_p(x) u_r(p), \quad (2)$$

$$\zeta_p(x) = \left(1 + \frac{e\mathbf{k}\cdot\mathbf{A}}{2p \cdot k}\right) e^{iS}, \quad (3)$$

$$S = -\frac{\Pi \cdot x}{\hbar} - \frac{e^2 A_0^2}{8\hbar c^2 (p \cdot k)} (2\delta^2 - 1) \sin 2\phi + \frac{eA_0}{\hbar c (p \cdot k)} \times [\delta(p \cdot \epsilon_1) \sin \phi - (1 - \delta^2)^{1/2} (p \cdot \epsilon_2) \cos \phi]. \quad (4)$$

Here, p is the four-momentum of the electron outside the field, and $\Pi = p + \frac{e^2 A_0^2}{4c^2 (p \cdot k)}$ is the corresponding laser-dressed four-momentum, $u_r(p)$ the free Dirac spinor. Here, we employ a box normalization with a normalized volume V .

The interaction with the emitted radiation and Coulomb field is taken to the first perturbation, in which the interaction between electron and nuclei is considered under Born approximation: $v_i/c \ll \alpha Z$. Here, α is fine structure constant and v_i is the initial velocity of the electron. As to the Coulomb field of the nuclei, we use a Yukawa potential with a screen length l_0 instead of the conventional Coulomb potential to avoid possible singularity at resonance. The four-vector potential of the two fixed nuclei can be written as

$$A_Y^\mu(\mathbf{r}) = -\frac{Ze\delta^{\mu 0}}{|\mathbf{r} - \mathbf{R}|} e^{|\mathbf{r} - \mathbf{R}|/l_0} - \frac{Ze\delta^{\mu 0}}{|\mathbf{r} + \mathbf{R}|} e^{|\mathbf{r} + \mathbf{R}|/l_0}. \quad (5)$$

The corresponding Fourier transform is

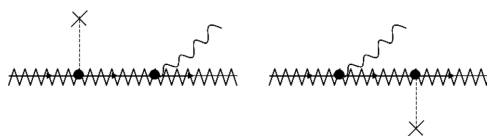


FIG. 2. Feynman diagrams describing laser-assisted bremsstrahlung. The laser-dressed electron and laser-dressed electron propagator are denoted by a zigzag line on top of the straight line. The Coulomb field photon is drawn as a dashed line, and the bremsstrahlung photon as a wavy line.

$$A_Y^\mu(\mathbf{q}) = -\frac{4\pi Ze}{q^2 + l_0^2} (e^{i\mathbf{q}\mathbf{R}} + e^{-i\mathbf{q}\mathbf{R}}). \quad (6)$$

As we can see, the Fourier transform of the potential depends on the inter-distance and the orientation of the two nuclei. This is the origin of the interference effect on the radiation spectrum. The four-vector potential of the emitted bremsstrahlung photon has the form

$$A_c^\mu(x) = \sqrt{2\pi\hbar/\omega'} c e_c^\mu e^{ikx}. \quad (7)$$

The wave vector of the emitted photon with polarization is described by $k' = \frac{\omega'}{c}(1, \mathbf{e}_{k'})$, $\mathbf{e}_{k'} = \cos\phi' \sin\theta' \mathbf{e}_x + \sin\phi' \sin\theta' \mathbf{e}_y + \cos\theta' \mathbf{e}_z$. So, the transition amplitude of an electron scattering by two fixed nuclei in a strong laser field can be specified by the following expression:

$$S_{fi} = -\frac{e^2}{\hbar^2 c^2} \int dx^4 dy^4 \bar{\psi}_{p_f, r_f}(x) [A_c(x) iG(x-y) A_Y(y) + A_Y(x) iG(x-y) A_c(y)] \psi_{p_i, r_i}(y). \quad (8)$$

Here, $iG(x-y)$ is the laser-dressed propagator of the electron, which can be written as

$$iG(x-y) = -\int \frac{dp^4}{(2\pi\hbar)^3} \frac{\bar{\psi}_p(x)}{(2\pi i)^3} \frac{\not{p} + mc}{p^2 - m^2 c^2} \bar{\psi}_p(y). \quad (9)$$

Since we are not interested in investigating polarization or spin properties, we average over the spin of the incoming electron, and sum over the spin and polarization of the final electron. The differential cross section is calculated with the formula

$$d\bar{\sigma} = \frac{1}{2JT} \sum_{r_i, r_f, s_c} |S_{fi}|^2 \frac{V d^3 \Pi_f}{(2\pi\hbar)^3} \frac{d^3 k'}{(2\pi)^3}. \quad (10)$$

Here, T is the long observation time and $J = \frac{c}{V} \frac{\Pi_f}{\Pi_i}$ stands for the incoming particle flux. We have $d^3 \Pi_f = |\mathbf{\Pi}_f|^2 d\Omega_f$, $d^3 k' = \frac{\omega'^2}{c^2} d\Omega' = \frac{\omega'^2}{c^2} \sin\theta' d\theta' d\phi'$, where Ω' and Ω_f are solid angle for the emitted photon and electron, respectively. Finally, we can derive the expression of the average differential cross section for emission or absorption of n photons as (for details, see Appendix)

$$\frac{d\bar{\sigma}}{d\omega' d\Omega' d\Omega_f} = \frac{\alpha(Z\alpha)^2}{8\pi^2 c^2} \sum_{n, s_c} \frac{|\mathbf{\Pi}_f|}{|\mathbf{\Pi}_i|} |e^{i\mathbf{q}\mathbf{R}} + e^{-i\mathbf{q}\mathbf{R}}|^2 \times \frac{\omega'}{(q^2 + l_0^2)^2} \text{Tr}[\bar{R}_{f_i, n}(p_f + mc) R_{f_i, n}(p_i + mc)], \quad (11)$$

where

$$R_{f_i, n} = \sum_s M_{-n-s}(\not{\epsilon}_c, \eta_{\Pi, \Pi_f}^1, \eta_{\Pi, \Pi_f}^2) \frac{i}{\not{p} - mc} \times \bar{M}_{-s}(\gamma^0, \eta_{\Pi, \Pi_i}^1, \eta_{\Pi, \Pi_i}^2) + \sum_{s'} M_{-n-s'}(\gamma^0, \eta_{\Pi', \Pi_f}^1, \eta_{\Pi', \Pi_f}^2) \frac{i}{\not{p}' - mc} \times \bar{M}_{-s'}(\not{\epsilon}_c, \eta_{\Pi', \Pi_i}^1, \eta_{\Pi', \Pi_i}^2), \quad (12)$$

with the argument defined as

$$\eta_{p_1, p_2}^1 = \frac{eA_0}{\hbar c} \delta \left[\frac{p_2 \cdot \epsilon_1}{k \cdot p_2} - \frac{p_1 \cdot \epsilon_1}{k \cdot p_1} \right], \eta_{p_1, p_2}^2 = -\frac{eA_0}{\hbar c} (1 - \delta^2)^{1/2} \left[\frac{p_2 \cdot \epsilon_1}{k \cdot p_2} - \frac{p_1 \cdot \epsilon_1}{k \cdot p_1} \right]. \quad (13)$$

The four-momentum transfer onto the Coulomb field by two fixed nuclei is denoted by $q^\mu = (0, \mathbf{q})$, and the two laser-dressed four-momenta of the virtual electrons in the Feynman diagrams by Π, Π' . They are given by the energy-momentum conserving relation during the scattering process

$$\begin{aligned} \Pi &= \pi_f - (n+s)\hbar k + \hbar k', \\ \Pi' &= \pi_i - s\hbar k - \hbar k', \\ \hbar q &= \pi_f - \pi_i + \hbar k' - n\hbar k. \end{aligned} \quad (14)$$

M is a 4×4 matrix with five arguments

$$M_s(F, \eta_{p_1, p_2}^1, \eta_{p_1, p_2}^2) = \left[F + \frac{e^2 A_0^2}{8c^2} \frac{\not{k} \not{F} \not{k}}{(p_i \cdot k)(p_2 \cdot k)} \right] G_s^0(\alpha, \beta, \varphi) + \frac{eA_0}{2c} \delta \left[\frac{\not{\epsilon}_1 \not{k} \not{F}}{(p_1 \cdot k)} + \frac{\not{F} \not{k} \not{\epsilon}_1}{(p_2 \cdot k)} \right] G_s^1(\alpha, \beta, \varphi) + \frac{eA_0}{2c} (1 - \delta^2)^{1/2} \left[\frac{\not{\epsilon}_2 \not{k} \not{F}}{(p_1 \cdot k)} + \frac{\not{F} \not{k} \not{\epsilon}_2}{(p_2 \cdot k)} \right] G_s^2(\alpha, \beta, \varphi) + \left(\delta^2 - \frac{1}{2} \right) \frac{e^2 A_0^2}{4c^2} \frac{\not{k} \not{F} \not{k}}{(p_i \cdot k)(p_2 \cdot k)} G_s^3(\alpha, \beta, \varphi). \quad (15)$$

The generalized Bessel functions are given by

$$G_s^0(\alpha, \beta, \varphi) = \sum_n J_{2n-s}(\alpha) J_n(\beta) e^{i(s-2n)\varphi}, G_s^1(\alpha, \beta, \varphi) = \frac{1}{2} (G_{s+1}^0(\alpha, \beta, \varphi) + G_{s-1}^0(\alpha, \beta, \varphi)), G_s^2(\alpha, \beta, \varphi) = \frac{1}{2i} (G_{s+1}^0(\alpha, \beta, \varphi) - G_{s-1}^0(\alpha, \beta, \varphi)), G_s^3(\alpha, \beta, \varphi) = \frac{1}{2} (G_{s+2}^0(\alpha, \beta, \varphi) + G_{s-2}^0(\alpha, \beta, \varphi)). \quad (16)$$

With the corresponding argument,

$$\begin{aligned} \alpha &= \left[(\eta_{p_1, p_2}^1)^2 + (\eta_{p_1, p_2}^2)^2 \right]^{1/2}, \\ \beta &= \frac{Qm^2 c^2}{8\hbar} (2\delta - 1) \left(\frac{1}{k \cdot p_1} - \frac{1}{k \cdot p_2} \right), \\ \varphi &= \arctan \left(-\frac{\eta_{p_1, p_2}^2}{\eta_{p_1, p_2}^1} \right). \end{aligned} \quad (17)$$

The differential cross section in Eq. (11) is evaluated for both the direction of the final electron and the bremsstrahlung photon. Here, we are more interested in the influence by the internuclear distance and orientation on the bremsstrahlung photon spectrum, so we integrate the differential cross section over the solid angle Ω_f of the outgoing electron and obtain a cross section differential only in the direction of the emitted bremsstrahlung photon and its energy

$$\frac{d\sigma}{d\omega'd\Omega'} = \int \frac{d\bar{\sigma}}{d\omega'd\Omega'd\Omega_f} d\Omega_f. \quad (18)$$

It is well known that the resonance occurs when the intermediate electron falls within the mass shell.^{14–17} That is because the lower order processes (here refers to the nonlinear Compton scattering) are allowed in the field of a light wave. Although the resonance is a characteristic feature of the second-order process like bremsstrahlung, but it will not draw much of our attention here since the cross section (18) at resonance will not be affected by the internuclear distance or orientation, for which the screening length need not be discussed here. More details will be given in Sec. III.

III. NUMERICAL RESULTS

In this section, we will present some examples of the cross section in Eq. (18) for different internuclear distance or orientation. We consider the internuclear distance of two fixed proton ($Z = 1$) is about several atom units. To observe the effect of the Coulomb field of two fixed nuclei on the spectra, we have to choose the laser frequency in an X-rays order: the wavelength is 0.2 nm. The intensity of the laser is $Q = 17.8$ and circularly polarized. First, we consider the electron has an initial energy of $E_i = 5$ MeV and the orientation of the two nuclei is parallel to the direction of laser propagation. The cross section of the fundamental harmonic for scattering angle $\theta' = 1^\circ$ is shown in Fig. 3. The most remarkable feature of the spectrum is that there are minima at some frequencies for large internuclear distance.

The mechanism behind this phenomenon is two-centre interference during the scattering process, which is described by the term $\zeta(\mathbf{q}, \mathbf{R}) = |e^{i\mathbf{q}\cdot\mathbf{R}} + e^{-i\mathbf{q}\cdot\mathbf{R}}|^2 \sim \cos^2(\mathbf{q} \cdot \mathbf{R})$ in the cross section. So when the momentum transfer from the Coulomb field is so large that $\mathbf{q} \cdot \mathbf{R} \sim 1$, the differential cross section in Eq. (11) will be suppressed for some special condition. Since most of the contribution to the integrand (18)

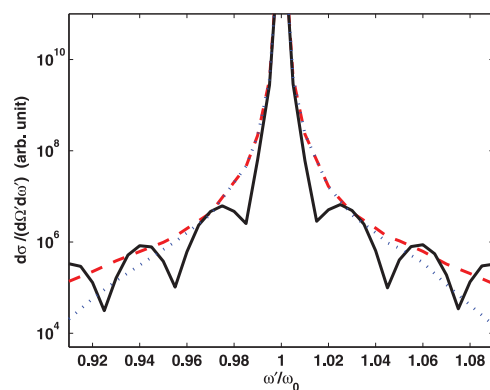


FIG. 3. The cross section for the fundamental harmonic at $\theta' = 1^\circ$. Here, we consider an electron with initial energy 5 MeV head-collide with a circularly polarized laser with intensity parameter $Q = 17.8$ and is scattered by two fixed nuclei. The internuclear distance is 1 nm for the full line, 0.152 nm for the dotted line, and 0.1 nm for the dashed line.

comes from a small cone in the forward direction of the ingoing electron ($\theta_f = \pi$), the positions of the minima found in the spectra are largely determined by the parameter $\zeta(\mathbf{q}, \mathbf{R})$ in the backscattering direction. This can be confirmed in Fig. 4, which plots $\zeta(\mathbf{q}, \mathbf{R})$ as a function of harmonic frequency for emission angle $\theta_f = \pi$. The positions of the minima in the spectra are almost coincident with those of $\zeta(\mathbf{q}, \mathbf{R})$, which can be expected for the condition

$$R_0 \cdot \cos \vartheta/2 = 2\pi(l + \frac{1}{2})/|q|, \quad l = (1, 2, 3, \dots). \quad (19)$$

That is interesting because we can deduce the internuclear distance by estimating the momentum transfer through the conservation relationship (14). It is obvious that $\zeta(\mathbf{q}, \mathbf{R})$ is at its peak at the resonances regardless of the internuclear distance. This can be explained by considering that the momentum transfer onto the nucleus is almost zero when the resonance condition is satisfied (i.e., the intermediate electron becomes real). That is to say, the resonance peak of the spectrum carries little information about the internuclear distance or orientation, for which we will not pay much attention to the phenomenon of resonance.

The dependence of the differential cross section in Eq. (18) on the electron emission angle θ_f at frequency $\omega' = 0.955\omega_0$ is plotted in Fig. 5. It is located close to one of the minima in the spectrum. We observe a clear suppression of the emission at small angle around the direction of the ingoing electron for $R_0 = 1$ nm, which result in the minimum of the spectrum. As can be expected from Eq. (19), if we increase the angle between the orientation of the two nuclei and the direction of the laser propagation, the two-centre interference will be less effective. Finally, we even could not find a pronounced minimum in the spectrum when the internuclear orientation is perpendicular to the direction of the laser propagation ($\vartheta = \frac{\pi}{2}$). In order to corroborate this idea, we plot the full cross section for $\vartheta = \pi/2$ in comparison with that of $\vartheta = 0$ for the same internuclear distance in

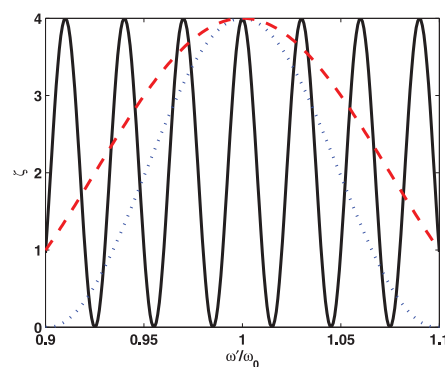


FIG. 4. The relation between the parameter $\zeta(\mathbf{q}, \mathbf{R})$ and the bremsstrahlung photo frequency ω' at $\theta_f = \pi$ for absorbing 1 photon in the whole process ($n = 1$). The parameter of the electron and laser is the same with Fig. 3. The internuclear distance is 1 nm for the full line, 0.152 nm for the dotted line, and 0.1 nm for the dashed line.

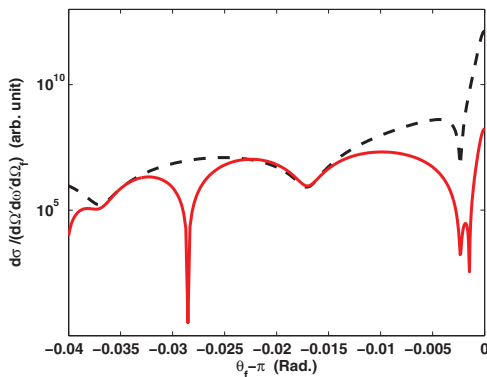


FIG. 5. The differential cross section as a function of the electron emission angle θ_f for the fundamental harmonic for absorbing 1 photon in the whole process ($n = 1$). The parameter of the electron and laser is the same with Fig. 3. The internucleus distance is 1 nm for the full line and 0.1 nm for the dashed line.

Fig. 6. The explanation for this phenomenon is that the momentum transfer from the Coulomb field \mathbf{q} is mainly in the backscattering direction according to the conservation relationship (14), thus $\mathbf{q} \cdot \mathbf{R} \approx 0$. We can conclude that the more projection of the internucleus distance onto the laser propagating direction, the more oscillation occurs for the parameter $\zeta(\mathbf{q}, \mathbf{R})$, which leads to the appearance of the minima in spectrum. The initial velocity of the ingoing electron also has a large effect on this two-centre interference phenomenon. That is because it will influence the momentum transfer from the Coulomb field to the electron. Here, we still set ($\vartheta = 0$) to maximize the two-centre interference. To have a clear idea of the relation between the initial velocity v_i and the momentum transfer from the Coulomb field on the internucleus orientation q^4 , we shall calculate the derivative

dq^4/dv_i for fundamental harmonics. From the conservation relationship, we have (here we set $\hbar = m = c = 1$)

$$\frac{dq^4}{dv_i} = \left[\frac{1 - \frac{1 + Q^2/2}{(\pi_i^0)^2}}{1 - \frac{1 + Q^2/2}{(\pi_i^0 + \Delta\omega)^2}} \right]^{1/2} \cos(\theta_f - \pi) - 1. \quad (20)$$

Here, $\Delta\omega = \omega' - \omega_0$. For $\theta_f \approx \pi$, we could learn there will be more momentum transfer for smaller initial velocity based on Eq. (19). Remembering the interference is in connection with the term $\zeta(\mathbf{q}, \mathbf{R}) \sim \cos^2(\mathbf{q} \cdot \mathbf{R})$, so we expect there will be more minima on the spectrum for “slow” electron but still satisfying the Born approximation, as can be seen from Fig. 7. Here, we compare the spectrum for initial electron energy $E_i = 3.5$ MeV with that of $E_i = 5$ MeV. The locations of the minima on the spectrum are different and the interval is smaller for $E_i = 3.5$ MeV, which confirms our opinion. For the same reason, we expect this will also happen with the increasing laser intensity since the electron is more decelerated by the light pressure of a counterpropagating laser.

It has to be mentioned that the parameter ($Q = 17.8$ with a wavelength of 0.2 nm) we choose in the paper will correspond to an X-ray laser with intensity up to $I = 10^{28}$ W/cm², which, according to an optimistic view,¹⁹ could be reached with future upgrades of the FLASH facility in Hamburg. On the other hand, considering a neodymium laser with a frequency of 1.17 eV and $Q = 17.8$ (corresponding to an intensity $I = 10^{28}$ W/cm²), the clear interference effect of laser-assisted bremsstrahlung emission also could be found when $\mathbf{q} \cdot \mathbf{R} \sim 1$ is satisfied. That is to say, the corresponding internucleus distance has to be on an order of micrometer ($R \sim 10^{-6}$ m) according to our calculation. Moreover, it is true that the interference modulations may be also found in the Bethe-Heitler cross section generated by the electron scattering in multi-center potentials in the absence of a laser field.

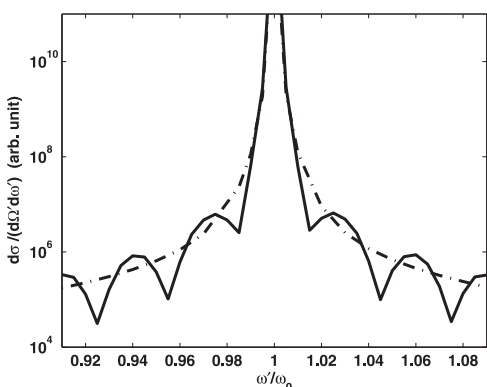


FIG. 6. The cross section for the fundamental harmonic at $\theta' = 1^\circ$. The parameter of the electron and laser is the same with Fig. 3. The internucleus distance is 1 nm and the orientation is ($\vartheta = 0$) for the full line and ($\vartheta = \pi/2$) for the dashed line.

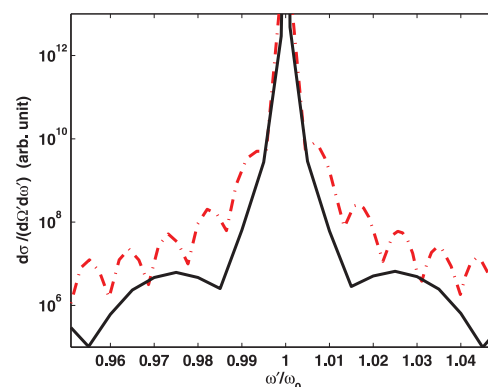


FIG. 7. The cross section for the fundamental harmonic at $\theta' = 1^\circ$. The parameter of the electron and laser is the same with Fig. 3 except that the initial energy of the electron reduces to 3.5 MeV for the dotted-dashed line and 5 MeV for the full line. The internucleus distance is 1 nm.

Considering the appearance of the resonances, we may expect a great difference between the interference modulations of the laser-free spectrum from those of the laser-assisted spectrum we found in this paper (i.e., there will not be minima located symmetrically on each side of the resonance in the laser-free spectrum). Further discussion of the detail about the differences between the two spectrums is beyond the topic of this paper. Furthermore, it is possible to modulate the intensity and the interference diagram of the electron radiation spectrum by controlling the laser field in an actual experiment, for which we think the laser field is helpful in observing a clear interference effect in the spectrum.

IV. CONCLUSION

In this paper, we have investigated the scattering of an electron by the screened Coulomb field of two fixed nuclei in a highly intense laser field and then emit a bremsstrahlung photon. As a result, we found that the spectrum may exhibit minima away from the resonant frequency. This may be explained by the interference between contributions from two fixed nuclei. It was shown that the positions of the interference minima are characteristic of both the internuclear distance and orientation for given laser and electron. On the other hand, the laser intensity and wavelength and the initial electron energy are also responsible for the observed minima. It is shown that the interference effect is remarkable for slow electrons counter-propagating with the laser field. That is due to the large momentum transfer from the Coulomb field. This interference effect is very general in highly intense laser field in which the drift motion of the electron cannot be neglected. Choosing proper laser wavelength, one can obtain information about the molecule structure by detecting the corresponding photon spectrum.

Finally, we must point out that the idea discussed in this paper about the two-center potential can be generalized to more complex potentials to find its important practical applications. For example, the existence of multiply charged negative ions in intense high-frequency laser fields has been studied theoretically for a long time.²⁰ Recently, by including relativistic corrections, the ions have been found to be able to bind more electrons.²¹ How to detect these exotic ions existing only in intense laser fields has posed a great challenge to present experimentalists. Our next work will focus upon analyzing the characteristics of the radiation spectrum when the free electrons are injected upon the negative ions inside the laser fields, for these ions have a very special dressed potential structure just like a many-atom molecule.

ACKNOWLEDGMENTS

This work was supported by the National Natural Science Foundation of China under Grant Nos. 10974056 and 11274117. One of the authors, Wenjun Zhu, thanks the support by the Science and Technology Foundation of National Key Laboratory of Shock Wave and Detonation Physics (Grant No. 077110).

APPENDIX A: DERIVATION OF EQ. (11)

Considering expressions (2), (3), (4), and (9), the transition amplitude of an electron scattering (8) reads as

$$S_{fi} = -\frac{e^2 c}{\hbar^2 c^2} \sqrt{\frac{m^2 c^2}{\Pi_i^0 \Pi_f^0 V}} \sqrt{2\pi\hbar/\omega'} T_{fi}.$$

Here,

$$\begin{aligned} T_{fi} &= T_{fi}^{(1)} + T_{fi}^{(2)}, \\ T_{fi}^{(1)} &= \int dx^4 dy^4 \overline{u_{r_j}(p_f)} [\bar{\zeta}_{p_j}(x) \not{\epsilon}_c \zeta_{p_i}(x)] iS(x-y) \\ &\quad \times [\bar{\zeta}_{p_i}(y) \not{A}_Y(y) \zeta_{p_i}(y)] u_{r_i}(p_i) e^{ikx}, \\ iS(x-y) &= -\frac{1}{2\pi i} \int \frac{d^4 p}{(2\pi\hbar)^3} \frac{1}{\not{p} - mc}. \end{aligned} \quad (\text{A1})$$

$T_{fi}^{(2)}$ can be obtained from $T_{fi}^{(1)}$ by interchanging: $x \rightarrow y$, $\not{\epsilon}_c \rightarrow \not{A}_Y$.

With the definition of $\zeta_p(x)$ in Eq. (3), it follows the relation

$$\begin{aligned} \bar{\zeta}_{p_j}(x) \not{\epsilon}_c \zeta_{p_i}(x) &= \sum_{s_1} M_{s_1}(\not{\epsilon}_c, \eta_{\Pi, \Pi_f}^1, \eta_{\Pi, \Pi_f}^2) \\ &\quad \times e^{i(\Pi_f - \Pi + s_1 \hbar k)x/\hbar}, \\ \bar{\zeta}_{p_i}(y) \not{A}_Y(y) \zeta_{p_i}(y) &= \sum_{s_2} \bar{M}_{s_2}(\not{A}_Y(y), \eta_{\Pi, \Pi}^1, \eta_{\Pi, \Pi}^2) \\ &\quad \times e^{i(\Pi_i - \Pi + s_2 \hbar k)y/\hbar}. \end{aligned} \quad (\text{A2})$$

During the calculation, the following expression will be useful

$$\begin{aligned} \exp(ix \sin(kx - \varphi) - i\beta \sin 2kx) &= \sum_s G_s^0(\alpha, \beta, \varphi) e^{iskx}, \\ \cos(kx) \exp(ix \sin(kx - \varphi) - i\beta \sin 2kx) &= \sum_s G_s^1(\alpha, \beta, \varphi) e^{iskx}, \\ \sin(kx) \exp(ix \sin(kx - \varphi) - i\beta \sin 2kx) &= \sum_s G_s^2(\alpha, \beta, \varphi) e^{iskx}, \\ \sin(2kx) \exp(ix \sin(kx - \varphi) - i\beta \sin 2kx) &= \sum_s G_s^3(\alpha, \beta, \varphi) e^{iskx}. \end{aligned} \quad (\text{A3})$$

All integrations can be taken in the expression of $T_{fi}^{(1)}$, leaving the energy-conserving delta function: $\delta(\Pi_f - \Pi + s_1 \hbar k + \hbar k')$ and $\delta(\Pi_i - \Pi + s_2 \hbar k + \hbar q)$, which leads to the energy-momentum conserving relation (14). Finally, the expression for $T_{fi}^{(1)}$ reads

$$\begin{aligned} T_{fi}^{(1)} &= (\hbar^2) \sum_{s,n} A_Y^0(q) \overline{u_{r_j}(p_f)} M_{-n-s}(\not{\epsilon}_c, \eta_{\Pi, \Pi_f}^1, \eta_{\Pi, \Pi_f}^2) \\ &\quad \times \frac{i}{\not{p} - mc} \times \bar{M}_{-s}(\not{\gamma}^0, \eta_{\Pi, \Pi}^1, \eta_{\Pi, \Pi}^2) u_{r_i}(p_i) \\ &\quad \times \delta(\Pi_f^0 - \Pi^0 - n\hbar k^0 - \hbar k'^0). \end{aligned} \quad (\text{A4})$$

The expression of $T_{fi}^{(2)}$ is similar to that of $T_{fi}^{(1)}$ by substitutions as follows:

$$\Pi \rightarrow \Pi', \ell_c \rightarrow \gamma^0.$$

Taking the square of the transition amplitude S_{fi} , we will finally have expression (11).

¹A. McPherson *et al.*, *J. Opt. Soc. Am. B* **4**, 595 (1987).

²A. L'Huillier, K. J. Schafer, and K. C. Kulander, *J. Phys. B* **24**, 3315 (1991).

³P. B. Corkum, *Phys. Rev. Lett.* **71**, 1994 (1993).

⁴M. Lewenstein, Ph. Balcou, M. Yu. Ivanov, A. L'Huillier, and P. B. Corkum, *Phys. Rev. A* **49**, 2117 (1994).

⁵M. Lein, N. Hay, R. Velotta, J. P. Marangos, and P. L. Knight, *Phys. Rev. Lett.* **88**, 183903 (2002).

⁶M. Lein, N. Hay, R. Velotta, J. P. Marangos, and P. L. Knight, *Phys. Rev. A* **66**, 023805 (2002).

⁷R. Kopold, W. Becker, and M. Kleber, *Phys. Rev. A* **58**, 4022 (1998).

⁸G. Lagmago Kamta and A. D. Bandrauk, *Phys. Rev. A* **70**, 011404 (R) (2004); **71**, 053407 (2005).

⁹T. Kanai, N. Minemoto, and H. Sakai, *Nature (London)* **435**, 470 (2005).

¹⁰C. Vozzi *et al.*, *Phys. Rev. Lett.* **95**, 153902 (2005).

¹¹J. Itatani *et al.*, *Nature (London)* **432**, 867 (2004).

¹²G. N. Gibson and J. Biegert, *Phys. Rev. A* **78**, 033423 (2008).

¹³P. V. Karapetyan and M. V. Fedorov, *Zh. Eksp. Teor. Fiz.* **75**, 816 (1978).

¹⁴S. P. Roshchupkin, *Laser Phys.* **6**, 837 (1996).

¹⁵S. P. Roshchupkin, *Laser Phys.* **12**, 498 (2002).

¹⁶E. Lotstedt, U. D. Jentschura, and C. H. Keitel, *Phys. Rev. Lett.* **98**, 043002 (2007).

¹⁷S. Schnez, E. Lotstedt, U. D. Jentschura, and C. H. Keitel, *Phys. Rev. A* **75**, 053412 (2007).

¹⁸H. Mitter, *Acta Phys. Austriaca, Suppl.* **14**, 397 (1975).

¹⁹A. Ringwald, *Phys. Lett. B* **510**, 107 (2001).

²⁰T. Andersen, *Phys. Rep.* **394**, 157 (2004).

²¹R. D. Hoehn, J. X. Wang, and S. Kais, *J. Chem. Phys.* **136**, 034114 (2012).

Jet-Cooled Spectroscopy of the α -Methylbenzyl Radical: Probing the State-Dependent Effects of Methyl Rocking Against a Radical Site

Nathanael M. Kidwell,[†] Neil J. Reilly,^{‡,§,||} Ben Nebgen,[†] Deepali N. Mehta-Hurt,[†] Ross D. Hoehn,[†] Damian L. Kokkin,^{‡,§,⊥} Michael C. McCarthy,^{‡,§} Lyudmila V. Slipchenko,[†] and Timothy S. Zwier^{*,†}

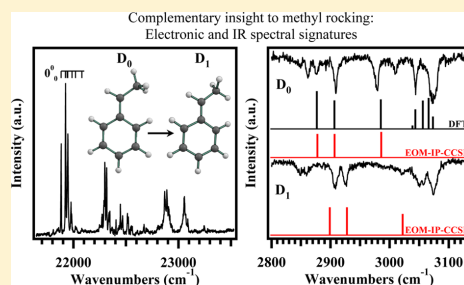
[†]Department of Chemistry, Purdue University, West Lafayette, Indiana 47907-2084, United States

[‡]Harvard-Smithsonian Center for Astrophysics, 60 Garden Street, Cambridge, Massachusetts 02138, United States

[§]School of Engineering & Applied Sciences, Harvard University, 29 Oxford Street, Cambridge, Massachusetts 02138, United States

Supporting Information

ABSTRACT: The state-dependent spectroscopy of α -methylbenzyl radical (α -MeBz) has been studied under jet-cooled conditions. Two-color resonant two-photon ionization (2C-R2PI), laser-induced fluorescence, and dispersed fluorescence spectra were obtained for the D_0 – D_1 electronic transition of this prototypical resonance-stabilized radical in which the methyl group is immediately adjacent to the primary radical site. Extensive Franck–Condon activity in hindered rotor levels was observed in the excitation spectrum, reflecting a reorientation of the methyl group upon electronic excitation. Dispersed fluorescence spectra from the set of internal rotor levels are combined with the excitation spectrum to obtain a global fit of the barrier heights and angular change of the methyl group in both D_0 and D_1 states. The best-fit methyl rotor potential in the ground electronic state (D_0) is a flat-topped 3-fold potential ($V_3'' = 151 \text{ cm}^{-1}$, $V_6'' = 34 \text{ cm}^{-1}$) while the D_1 state has a lower barrier ($V_3' = 72 \text{ cm}^{-1}$, $V_6' = 15 \text{ cm}^{-1}$) with $\Delta\varphi = \pm \pi/3, \pi$, consistent with a reorientation of the methyl group upon electronic excitation. The ground state results are compared with calculations carried out at the DFT B3LYP level of theory using the 6-311+G(d,p) basis set, and a variety of excited state calculations are carried out to compare against experiment. The preferred geometry of the methyl rotor in the ground state is *anti*, which switches to *syn* in the D_1 state and in the cation. The calculations uncover a subtle combination of effects that contribute to the shift in orientation and change in barrier in the excited state relative to ground state. Steric interaction favors the *anti* conformation, while hyperconjugation is greater in the *syn* orientation. The presence of a second excited state close by D_1 is postulated to influence the methyl rotor properties. A resonant ion-dip infrared (RIDIR) spectrum in the alkyl and aromatic CH stretch regions was also recorded, probing in a complementary way the state-dependent conformation of α -MeBz. Using a scheme in which infrared depletion occurs between excitation and ionization steps of the 2C-R2PI process, analogous infrared spectra in D_1 were also obtained, probing the response of the CH stretch fundamentals to electronic excitation. A reduced-dimension Wilson G-matrix model was implemented to simulate and interpret the observed infrared results. Finally, photoionization efficiency scans were carried out to determine the adiabatic ionization threshold of α -MeBz (IP = $6.835 \pm 0.002 \text{ eV}$) and provide thresholds for ionization out of specific internal rotor levels, which report on the methyl rotor barrier in the cation state.



I. INTRODUCTION

Combustion processes involve a myriad of complex reaction pathways that connect smaller precursors to larger polyaromatic hydrocarbons (PAHs), many of which are still poorly characterized. In particular, resonance-stabilized radicals (RSRs) play an important role in combustion due to their high relative concentrations and effects on reaction kinetics and product distributions. The prototypical aromatic RSR is the benzyl radical, which has a rich history of theoretical and experimental studies.^{1–8} One of the important aspects of the electronic spectroscopy of benzyl radical is its prominent vibronic coupling due to closely lying electronic states. Other studies have investigated the implications of substitution on the benzyl

radical ring or radical site, and observed significant changes in the electronic state behavior.^{4,9–11}

Methyl substituents are known to serve as sensitive probes of local electronic structure, responding to changes in electronic state with changes to the orientation and barrier height of the methyl group.^{12–14} Furthermore, the chemical dynamics of methylated compounds are affected in higher energy environments as a result of the accelerated onset of intramolecular

Special Issue: Terry A. Miller Festschrift

Received: July 14, 2013

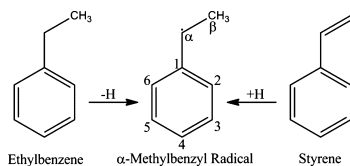
Revised: August 20, 2013

Published: August 21, 2013



vibrational redistribution (IVR) due to the higher density of accessible vibrational states at a given energy.^{15,16} Substituting a methyl group at different sites on the benzyl radical ring, Lin and co-workers¹⁰ observed strikingly different barriers to internal rotation among the *ortho*-, *meta*-, and *para*- isomers in the ground and excited states due to influences from their electronic structures which are different from the benzyl radical as evidenced in the excitation spectra. Additionally, Lee et al.¹¹ observed vibronic emission from discharge products of several precursors, one of which they ascribed to the α -methylbenzyl radical (α -MeBz) arising from the cleavage of the C $_{\alpha}$ -CH₃ or C $_{\alpha}$ -H bond in isopropylbenzene or ethylbenzene, respectively.

In a typical mixture of gasoline, ethylbenzene comprises 1.7–2.5% of the total,¹⁷ while styrene is also known to be ubiquitous in combustible fuels, making it a target of considerable interest.^{18–22} Whether by H-atom abstraction of ethylbenzene or H-atom addition to styrene, α -MeBz may be generated, pointing to its potential importance as a key resonance-stabilized intermediate from which larger PAHs can be made.



Motivated by the fact that benzyl-type radicals are involved in the principal pathways of formation and destruction of fused-ring aromatics, there have been several recent efforts to characterize related resonance-stabilized radicals suspected to promote PAH formation, including phenylpropargyl, phenylallyl, benzylallenyl, naphthylmethyl, and hydronaphthyl radicals.^{23–28} In each of these cases, vibronic spectroscopy has played a significant role in this characterization, with ground to first excited state transitions occurring in the middle of the visible region (~450–550 nm).

The present study of α -MeBz radical represents another contribution to this growing foundation of spectroscopic characterization of benzyl-like RSRs, this one a simple derivative in which the methyl group is substituted in place of hydrogen on the benzylic carbon. This placement of the methyl group gives the α -MeBz radical fundamental interest due to the position of the methyl group immediately adjacent to a primary radical site which belongs to the extended π -network of the benzyl radical motif. Simpler alkyl radicals such as the ethyl radical have been studied in detail^{29–33} where the methyl group interacts through hyperconjugation with the radical π -orbital, but these systems typically do not possess easily accessible excited electronic states. However, α -MeBz affords the opportunity to examine the hindered rotation of a methyl group with electronic state specificity, which is made more interesting because of the vibronic coupling known to be pervasive in the spectroscopy of the benzyl radical.

In this paper, we describe the results of a detailed spectroscopic analysis of α -MeBz radical. We report vibronic spectra and rotational band contour analysis of the D₀–D₁ transition of α -MeBz, paying special attention to the effect that methyl substitution on the benzyl radical site has on the electronic states and the extent of vibronic coupling. The extensive internal rotor structure identified in the 2C-R2PI and dispersed fluorescence spectra are analyzed to determine the potentials

for methyl internal rotation in the D₀ and D₁ states, providing insight into the properties of a methyl group attached directly to the primary radical site. Finally, the repercussions that hyperconjugation and steric interactions impose on the alkyl stretch vibrations of the methyl group, and their response to electronic excitation, are studied using infrared depletion spectroscopy.

II. METHODS

A. Experimental Section. The experimental apparatus used for the work carried out at Purdue has been described in detail elsewhere.³⁴ Briefly, the samples used in the experiments were either isopropylbenzene (99%, Sigma Aldrich) or 1-phenylethanol (98%, Sigma Aldrich), which were heated to 338 K, entrained in an Ar buffer gas with a stagnation pressure of approximately 2 bar, and subsequently introduced into a reaction channel (2 mm ID \times 15 mm long) via a pulsed valve (R.M. Jordan, 800 μ m orifice). Timing an electric discharge to intersect the gas pulse just prior to expansion, discharge products such as α -MeBz were generated and collisionally cooled upon expansion into a vacuum chamber. For two-color, resonant two-photon ionization (2C-R2PI), the tunable output of a Nd:YAG pumped dye laser operating in the 425–465 nm region was set perpendicular to the free-jet expansion and provided the resonant photon source. The doubled output of another Nd:YAG pumped dye laser fixed at 235 nm counter-propagated the preceding laser and subsequently ionized α -MeBz. Radical ions produced were accelerated in a Wiley–McLaren type time-of-flight mass spectrometer,³⁵ and detected by a microchannel plate ion detector. Finally, the ion signal was amplified 25 times, averaged by a boxcar gated integrator (Stanford Research System, model SR250), and then recorded on a personal computer.

Rotational band contours (RBCs) were taken by scanning the resonant photon at a higher resolution (0.04 cm⁻¹) over individual bands to gather rotational constants and transition dipole moment directions. The excited-state lifetime of the radical was measured by incrementally increasing the temporal separation between the resonant and ionizing lasers and observing the eventual decay in ion signal. Furthermore, the adiabatic ionization threshold of the radical was experimentally determined using two-color, photoionization efficiency (PIE) scans. To do this, the resonant photon laser was fixed on the D₀–D₁ origin of the radical and the ionizing laser was scanned over the threshold for ionization out of the intermediate level. Thresholds for ionization out of hindered rotor or vibronic levels in the D₁ state were determined similarly, providing data on the internal rotor levels of the cation.

Laser-induced fluorescence/dispersed fluorescence (LIF/DFL) studies of α -MeBz were undertaken using a vacuum chamber in the laboratory in Cambridge. The radical of interest was produced in a pulsed discharge of ethylbenzene (Sigma-Aldrich, 99%) seeded in Ar (1% with stagnation pressure 7 bar). The discharge source is similar to that previously described.³⁶ Optimal LIF signal was obtained with a voltage of 1 kV applied to the outer electrode (farthest from the valve orifice) through a ballast resistance of 10 k Ω . The chamber base pressure was 2×10^{-7} Torr, and typical operating pressure was 3×10^{-5} Torr. Supersonically cooled α -MeBz radicals were interrogated several centimeters downstream of the discharge orifice by the tunable output of a Nd:YAG-pumped dye laser (typical pulse energy 5 mJ, line width 0.4 cm⁻¹) operated in the range 450–460 nm.

Fluorescence was imaged using f -number-matched optics onto the entrance slit of a 1m monochromator equipped with a 1200 lines/mm grating and a photomultiplier tube (PMT) at the exit. Signal from the PMT was amplified 25 times and passed to an oscilloscope and personal computer for gated integration of the decay profile using custom software. For LIF excitation scans, the monochromator slits were opened fully to give a bandpass of approximately 120 cm^{-1} , and the laser and monochromator were simultaneously scanned with the latter at a constant Stokes shift of approximately 600 cm^{-1} , which was revealed in a survey DFL spectrum to be a region of strong Franck–Condon activity. Simultaneous scanning of the monochromator bandpass in this manner facilitated selective detection of α -MeBz with limited spectral interference from the numerous benzylic radical discharge products that absorb throughout this region, including benzyl radical, 1-phenylpropargyl radical, and an OH-containing species (indicated in the inset in Figure 1) formed from residual water

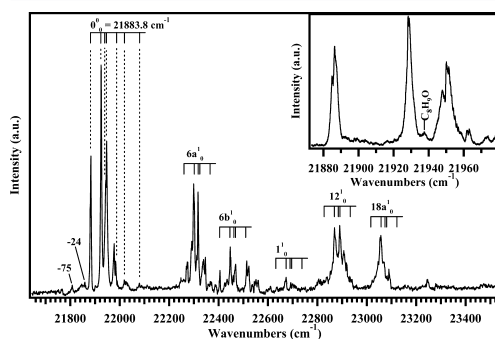


Figure 1. 2C-R2PI spectrum of α -MeBz radical (m/z 105). The inset displays the low-frequency region of the LIF spectrum.

contamination in the sample line (this species will be the subject of a future article from the Harvard-Smithsonian group).

Subsequently, the α -MeBz origin and nearby internal rotor transitions were studied in detail by DFL, with particular attention paid to ground state vibrational energies below 300 cm^{-1} , corresponding primarily to internal rotor levels. Because of the small energy intervals in the excited state, DFL spectra from these levels were particularly prone to collisional de-excitation in the jet, manifesting as a “copy” of the origin DFL spectrum appearing in emission spectra from higher levels, and a characteristic rising and falling fluorescence decay profile. To mitigate this effect, it was necessary to reduce the stagnation pressure to 2 bar, and use a nozzle-laser distance equivalent to approximately 200 nozzle diameters. Fluorescence lifetimes were also monitored for all features appearing in the DFL spectra, and were determined, by comparison with the origin decay profile (which is immune to such effects), to be unaffected by collisional de-excitation, with the exception of two weak bands designated with asterisks in Figure 5. For DFL scans, the monochromator slits were set to 0.25 mm , yielding a bandpass of approximately 15 cm^{-1} at full width at half-maximum (fwhm). Wavelength calibration of the monochromator was performed using a mercury lamp.

State-selected infrared spectra of the α -MeBz radical were obtained using resonant ion-dip infrared spectroscopy (RIDIRS),

requiring a three-laser arrangement.²³ First, D_0 -RIDIRS was taken with the output of a Nd:YAG pumped LaserVision OPO/OPA system acting as the holeburning laser, which was spatially overlapped with and temporally preceded ($\Delta t = 200\text{ ns}$) the origin-resonant probe and ionizing lasers, which operate at twice the repetition rate. As the infrared laser is tuned across the alkyl and aromatic CH stretch regions ($2800\text{--}3150\text{ cm}^{-1}$), whenever its wavelength is resonant with an IR active vibration, depletion of the ground-state population occurs, leading to a decrease in ion signal, which is detected as the difference in ion signal produced by the IR laser using active baseline subtraction. Therefore, an infrared spectrum is recorded by plotting the ion depletion signal as a function of infrared wavelength, which yields the ground-state IR spectrum of the radical of interest. Similarly, D_1 -RIDIRS was taken using the same scheme with the exception that the infrared laser is temporally placed between the resonant and ionizing lasers and subsequently scanned to deplete the population that was initially excited into a well-defined vibronic state. In order to observe depletion in the excited state, the infrared laser is scanned, and when it becomes resonant with an IR transition, excited state levels are reached, which are less readily ionized, likely through enhanced internal conversion to D_0 .

B. Computational. As an aid to the analysis of the experimental spectra, *ab initio* calculations using the Gaussian09 suite of programs³⁷ at the B3LYP/6-311+G(d,p) level of theory^{38,39} were used to determine the optimized ground-state geometry and harmonic vibrational frequencies. The predicted ground-state CH stretch frequencies with respect to the methyl rotor torsional angle coordinate ($\varphi = [\angle = 1, \alpha, \beta, \text{H}]$) were generated by incrementing the dihedral angle by 5° . Additionally, Natural Bond Order^{40,41} (NBO) calculations were performed for the D_0 electronic state for different methyl group orientations to describe the intramolecular donor/acceptor electrostatic interactions.

Excited state calculations on α -MeBz and benzyl radicals were carried out with a variety of correlated single-reference excited state methods within the equation of motion coupled cluster (EOM-CC) family^{42–44} using the Q-Chem⁴⁵ electronic structure package. Excited state properties (vertical excitation energies, transition dipole moment (TDM) components, oscillator strengths, and the D_1 – D_2 energy splitting) for the benzyl radical and α -MeBz were determined using EOM-CC for ionization potentials (EOM-IP-CCSD)^{46,47} in the 6-311+G(d,p) basis.^{48,49} Vertical excitation energies for the D_1 and D_2 states were further refined by adding perturbative triple corrections as in the EOM-IP-CCSD(dT) method.⁵⁰ The EOM-CC method for excitation energies with single and double excitations (EOM-EE-CCSD)^{42–44,51} in the aug'-cc-pVDZ basis (aug-cc-pVDZ^{52,53} without diffuse p functions on hydrogen atoms and diffuse d functions on carbon atoms) was also employed. EOM-EE-CCSD calculations used an open-shell doublet reference, while all IP calculations used the closed shell anion state as the reference determinant.

In order to determine the preferred methyl rotor orientation in α -MeBz, the ground state and the D_1 excited state geometries were determined for the (fixed) *anti* and *syn* orientations of the methyl rotor with respect to the aromatic ring. CCSD and EOM-EE-CCSD (for the ground and excited states, respectively) in aug'-cc-pVDZ and the ionization potential configuration interaction with single and double excitations (IP-CISD) method⁵⁴ in aug-cc-pVDZ were used for the geometry optimizations. Calculations with more accurate EOM-IP-CCSD

and EOM-IP-CC(2,3) (EOM-IP method with single and double excitations for the reference state and single, double, and triple excitations for the excited state)⁵⁵ were additionally performed at the IP-CISD optimized geometries of the D₀ and D₁ states.

Additionally, a set of multiconfigurational calculations with multiconfigurational self-consistent field (MCSCF)⁵⁶ and multiconfigurational quasi-degenerate perturbation theory (MCQDPT)⁵⁷ were performed using the GAMESS electronic structure software.^{58,59} Equilibrium geometries of the D₀ and D₁ states in *anti* and *syn* orientations were optimized at the MCSCF/6-31G*^{60,61} level of theory. Single-point energy calculations at the optimized geometries were performed at the MCSCF/cc-pVTZ⁶² and MCQDPT/cc-pVTZ levels. Seven active orbitals (six π orbitals at the benzene ring and a radical π orbital on the CH₂ moiety) with seven electrons comprised the active space for the benzyl radical. σ and σ^* CH orbitals on the methyl rotor were added to the active space of α -MeBz, bringing the active space to nine orbitals and nine electrons. State averaging of the three lowest states (D₀, D₁, and D₂) was employed in the MCSCF and MCQDPT energy calculations.

Finally, geometry optimizations of the α -MeBz cation in *anti* and *syn* configurations of the methyl rotor were performed at the B3LYP/6-311+G**^{39,48,49} level. Single point energies at these geometries were obtained at the coupled CCSD(T)⁶²/cc-pVTZ level of theory.

III. SPECTROSCOPIC BACKGROUND

A. Symmetry Considerations. Throughout much of what follows, the benzyl radical will serve as a point of comparison for the present results on α -MeBz. Previous studies of the vibronic spectroscopy of benzyl radical uncovered the presence of two close-lying excited states. The rotational structure from these vibronic transitions was analyzed to determine the TDM directions^{63,64} of the origin and a triad of vibronic bands above the origin. The D₀–D₁ origin has a pure B-type band contour, while the vibronic transitions are A-type, confirming that vibronic coupling to the D₂ state was responsible for their intensity. Based on the C_{2v} symmetry of the benzyl radical, the D₀–D₁ and D₀–D₂ transitions were inferred to have TDMs perpendicular and parallel to the 2-fold symmetry axis (xz plane), respectively. By virtue of methyl substitution on the benzyl radical site, the symmetry of α -MeBz is lowered to C_s if the methyl group is in a configuration in which one methyl CH bond is in the plane of the aromatic ring. However, in the presence of methyl internal rotation, the permutations and permutation inversions of the methyl hydrogens must be considered.⁶⁵ Accordingly, methyl rotor transitions must be cast into the G₆ molecular symmetry group, which is isomorphic with the C_{3v} point group.

In the G₆ molecular symmetry group, the D₀, D₁, and D₂ electronic states for α -MeBz are all of ²A₂ symmetry, equivalent to ²A'' in C_{3v}, making the D₀–D₁ transition allowed and polarized to form a hybrid AB-type band. Additionally, the methyl rotor levels are given the symmetry labels a₁, a₂, and e in which the symmetry-allowed transitions follow a₁ ↔ a₁, a₂ ↔ a₂, and e ↔ e selection rules. The nuclear spin symmetries of the three methyl group hydrogens are different for 'a' and 'e' symmetry internal rotor levels. Under the conditions of a jet-cooled environment, the population is funneled toward the lowest possible energy levels of each nuclear spin symmetry type (0a₁ and 1e levels), which have identical nuclear spin

statistical weights and do not interconvert efficiently via collisions on the time scale of the expansion cooling.

B. Torsional Simulations and Fitting to Spectral Data. The methyl torsional structure found in the excitation and DFL spectra is governed by Franck–Condon factors involving the torsional rotor levels in D₀ and D₁ states, which, in turn, reflect the methyl rotor potentials for the two electronic states. These potentials were simulated according to the procedure used by Laane and co-workers,⁶⁶ in which overall rotation and torsion-rotation coupling are neglected, and the one-dimensional, hindered rotor Hamiltonian is written as

$$H\Psi_v = \left[-F \frac{\partial^2}{\partial \varphi^2} + V(\varphi) \right] \Psi_v = E_v \Psi_v \quad (1)$$

where φ is the torsional angle about which the methyl group rotates. We define $\varphi = 0$ (π or $\pm \pi/3$) when a methyl CH is in-plane, *anti* (*syn*) to the phenyl ring. In order to emphasize the switch in direction of the in-plane CH group, we will refer to $\varphi = \pi$ as the *syn* configuration from this point forward. The methyl rotational constant F is given by

$$F = \frac{h}{8\pi^2 I_r} \quad (2)$$

with I_r as the reduced moment of inertia as defined by Pitzer.⁶⁷ Using the calculated geometries for D₀ and D₁, the internal rotational constants were determined to be $F = 5.540$ cm⁻¹ for D₀ and 5.527 cm⁻¹ for D₁. The potential form $V(\varphi)$ and thus the barrier to internal rotation can be approximated from the Fourier expansion of the form

$$V(\varphi) = \frac{1}{2} \sum_6^{n=1} V_n (1 - \cos n\varphi) \quad (3)$$

which for 3-fold symmetric internal rotors only requires V_n with $n = 3, 6, \dots$ to be considered.

The set of free rotor wave functions $\{\psi_i\}$ is then used as a basis set for variational diagonalization of the hindered rotor Hamiltonian to obtain eigenvalues E_v and eigenfunctions

$$\Psi_v = \sum_N^{i=1} c_{iv} \psi_i \quad (4)$$

To ensure the eigenvalues converged, a basis set size of $N = 200$ was employed although convergence was achieved for $N = 50$. Agreement between the simulated and experimental eigenvalues was optimized by minimizing a linear least-squares fitting function. Finally, the fit to experiment was checked by calculating the intensities of the hindered rotor transitions, and comparing the results with the intensities observed in the excitation and DFL spectra. To that end, the Franck–Condon factors for individual hindered rotor transitions were computed as

$$I = |\langle \psi_j'(\varphi) | \psi_i'(\varphi + \Delta\varphi) \rangle|^2 \quad (5)$$

where $\Delta\varphi$ is the phase shift between the ground and excited state potential energy forms, $V(\varphi)$.

IV. RESULTS AND ANALYSIS

A. 2C-R2PI and LIF Excitation Spectra. As a first step in characterizing α -MeBz, a mass-resolved two-color resonant two-photon ionization spectrum (2C-R2PI) was recorded. The first 1900 cm⁻¹ of this spectrum is shown in Figure 1.

Table 1. Ring-Mode Transitions in the First Excited (D_1) and Ground (D_0) Electronic States with a Comparison to S_1 and S_0 Frequencies in Ethylbenzene, Respectively

assignment	D_1		assignment	D_0	
	expt. freq. ^a	ethylbenzene (S_1) ^b		expt. freq. ^a	ethylbenzene (S_0) ^c
$6a_1^1$	389.9	-	$6a_1^0$	549.0	560
$6b_1^1$	522.7	530.3	$6b_1^0$	617.4	627
1_1^1	754.0	727.7/739.6	1_1^0	785.3	778
12_1^1	969.2	931.9	12_1^0	971.6	1016
$18a_1^1$	1138.6	970.6	$18a_1^0$	-	1042

^aWavenumber shifts relative to the $0a_1-0a_1$ transition, in cm^{-1} . ^bReference 68. ^cReference 70.

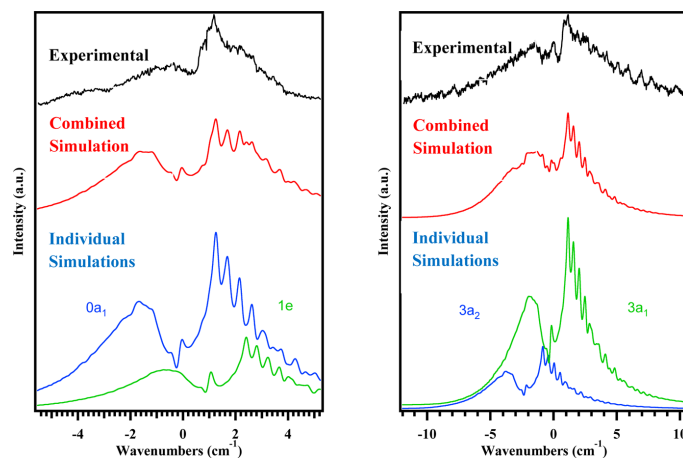


Figure 2. RBCs of the (a) origin and (b) $+61/63 \text{ cm}^{-1}$ transitions. The black trace shows the experimental results with the simulated results given underneath. The individual simulated RBC transitions are shown as blue and green traces, which are combined as the red trace and compared to experiment.

The spectrum displays a prominent D_0-D_1 origin at 21884 cm^{-1} , -115 cm^{-1} from the corresponding benzyl radical origin (21999.8 cm^{-1}).² Additionally, extensive Franck-Condon activity in several ring modes is also present, as expected for a $\pi-\pi^*$ transition. Table 1 shows the observed positions and assignments of the main D_0-D_1 ring mode transitions for α -MeBz, comparing these results with those in ethylbenzene.⁶⁸

Vibronic effects appear to be less pronounced in α -MeBz than they are in the benzyl radical, where vibronic coupling involving the ν_{6a}/ν_{6b} modes dominates the spectrum. The inset in Figure 1 portrays a magnified version of the low-frequency portion of the LIF spectrum, highlighting the fact that a non-harmonic progression is built off of the origin. This structure is also observed built off of the ring mode fundamentals, marking it as potentially ascribable to methyl internal rotor transitions. Their large intensity points to a change in the orientation of the methyl group between ground and excited states.

B. Rotational Band Contours. In order to analyze the low-frequency internal rotor structure further, RBCs taken at higher resolution were obtained for the origin and the $+61/+63 \text{ cm}^{-1}$ peaks. In both cases, these RBCs have complicated band profiles arising from overlapping transitions. Using the predicted D_0-D_1 TDM direction from EOM-IP-CCSD calculations (see Section V), the origin and $+61/+63 \text{ cm}^{-1}$ band contours were simulated using the JB95⁶⁹ program for a rigid rotor. A comparison with the experimental spectra is shown in Figure 2a,b,

demonstrating close agreement between the two. The calculated rotational constants are given in Table S1. The band contours of individual a and e internal rotor transitions are shown in blue and green, while the sum of the components shown as the red trace is displayed underneath the respective experimental spectra. The close correspondence between experiment and calculation establishes that the first transitions in the excited state spectra involve transitions to the D_1 electronic state, producing a 53%:47% a:b hybrid band. By comparison, the corresponding D_0-D_2 transition would be pure a-type, inconsistent with the experimental data. The RBC for the $+41 \text{ cm}^{-1}$ ($1e''-2e'$) transition is shown in Figure S1. It was not fit due to the presence of internal rotation/overall rotation coupling.

The significant change in TDM direction in the D_0-D_1 transition of α -MeBz radical (53:47 a:b hybrid) relative to the benzyl radical (pure b-type) cannot be accounted for simply by inertial effects, since the inertial axes rotation under methyl substitution is only 20° . As a result, electronic effects are also at play, as is discussed further in Section V.

C. Origin Dispersed Fluorescence Spectrum. Figure 3 presents the first 1200 cm^{-1} of the DFL spectrum of the D_1 $0_0^0(0a_1/1e)$. The spectrum bears some resemblance to the excitation spectrum, displaying irregular structure in the low-frequency region, which is also built off of each of the ring mode fundamentals. The observed ring modes are tabulated

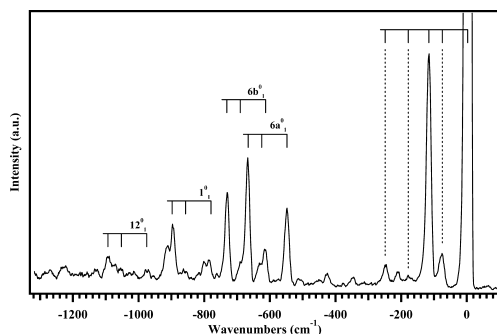


Figure 3. DFL spectrum of the D_0 - D_1 origin of α -MeBz radical. The spectrum contains contributions from the $0a_1'$ and $1e'$ excited state levels.

and compared to ethylbenzene⁷⁰ in Table 1, which are in relatively good agreement with each other. The lack of mirror symmetry with respect to the excitation spectra is also consistent with a change in the preferred methyl conformation between ground and excited states.

D. Methyl Rotor Torsional Potentials. The internal rotor structure was simulated for both the ground and first electronic states using the torsional formalism described in Section III.B. Figure 4 compares the 2C-R2PI spectrum with the best-fit

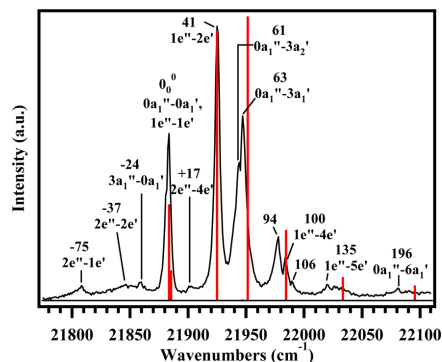


Figure 4. Close-up view of the 2C-R2PI spectrum near the D_0 - D_1 origin. The experimental spectrum is compared with the best-fit simulations of the internal rotor structure, shown as a stick diagram in red. See text for further discussion.

methyl rotor simulation, with the relative wavenumber positions and internal rotor labels attached to individual transitions. The optimized wavenumber positions of the simulation are compared with experimental frequencies in Table 2, yielding the best fit excited state potential parameters $V_3' = 72 \text{ cm}^{-1}$ and $V_6' = 15 \text{ cm}^{-1}$. The predicted intensities using a phase shift of $\Delta\varphi = \pi$ are in good overall agreement with experiment, although the predicted intensity for the $0a_1''$ - $3a_1'$ transition is somewhat overestimated. However, such anomalous internal rotor intensities have been observed in previous work,^{71,72} where they were assigned based on a careful analysis to Coriolis coupling between the $3a_1$ and $3a_2$ levels. In the G_6 molecular

Table 2. Best Fit between the Experimental and Simulated Internal Rotor Results in the First Excited (D_1) and Ground (D_0) Electronic States

assignment	excitation spectrum		dispersed fluorescence	
	expt. freq. ^a	sim. freq. ^a	assignment	expt. freq. ^a
$2e''$ - $1e'$	-75	-79	$0a_1''$ - $0a_1''$	0
$2e''$ - $2e'$	-37	-37.3	$1e'$ - $1e''$	0
$3a_1''$ - $0a_1'$	-24	-23.9	$1e'$ - $2e''$	-79.4
$0a_1''$ - $0a_1'$	0	0	$0a_1''$ - $3a_2''$	-84
$2e''$ - $4e'$	17	21.8	$0a_1''$ - $3a_1''$	-117.4
$1e''$ - $1e'$	1.5	1.7	$1e'$ - $4e''$	-136.8
$1e''$ - $2e'$	41.3	41.4	$1e'$ - $5e''$	-174.9
$0a_1''$ - $3a_2'$	60.5	63.3	$0a_1''$ - $6a_1''$	-247.6
$0a_1''$ - $3a_1'$	63.4	67.9	$0a_1''$ - $6a_2''$	-247.6
$1e''$ - $4e'$	100.1	100.8	44_2°	2×-121.2
$1e''$ - $5e'$	134.9	149.8	30_1°	-212.7
$0a_1''$ - $6a_1'$	196.2	211.9		
$0a_1''$ - $6a_2'$	196.5	212		

^aWavenumber shifts from the $0a_1$ - $0a_1$ transition in cm^{-1} .

symmetry group, the Coriolis selection rules⁷³ are met with $\Gamma(\psi_{3a_2}) \times \Gamma(\psi_{3a_1}) \rightarrow \Gamma(J_p)$, where J_p is the torsional momentum operator with the correct symmetry to mix $3a_1$ and $3a_2$.⁶⁵ This mixing between methyl rotor levels manifests itself experimentally in the appearance of the $0a_1''$ - $3a_2'$ transition as a peak with a fraction of the $0a_1''$ - $3a_1'$ intensity, in a manner similar to that in the *ortho*-fluorotoluene isomer.⁷² The broad rotational envelope of the +61/+63 RBC indicates that the $0a_1''$ - $3a_2'$ transition lies just on the low-frequency edge of the dominant $0a_1''$ - $3a_1'$ transition leading to the composite rotational band contour shown in Figure 2b. Furthermore, contained in the low-frequency structure located at -75, -37, -24 and +17 cm^{-1} with respect to the origin are "hot bands" that are attributed to the $2e''$ - $1e'$, $2e''$ - $2e'$, $3a_1''$ - $0a_1'$, and $2e''$ - $4e'$ methyl rotor transitions, respectively.

Figure 5a-d shows the DFL spectra taken from the origin, $2e'$, $3a_2'$, and $3a_1'$ torsional levels in the excited state, respectively. Due to symmetry restrictions, only those levels that share the same spin-state symmetry of the excited state rotor level are visible in the spectrum. As a result of their partial overlap in the excitation spectrum, the $0a_1''/1e'$ DFL spectrum (Figure 5a) has contributions both from *a* and *e* levels. Since the DFL spectrum was recorded with excitation laser fixed at a wavelength where both $0a_1'$ and $1e'$ levels contribute, the relative intensities of the $0a_1'$ and $1e'$ components of the spectrum were adjusted to match experiment. The best fit was obtained with $1e'$ intensities multiplied by a factor of 0.4. All four spectra contain contributions from scattered laser light at the resonance frequency, which masks the intensity of this band. In order to assess the intensities in the absence of such interference, Figure 5e presents the $0a_1''/1e'$ spectrum in the region of the $6a_1^0$ transition (-549 cm^{-1} from resonance), where no such interference occurs. Using the same phase shift ($\Delta\varphi = \pi$) as deduced from the excitation spectrum, the simulated DFL spectra are in good agreement with the experimental spectra, with the best-fit internal rotor energy levels shown in Table 2. From the analysis, the ground state potential terms are $V_3'' = 151 \text{ cm}^{-1}$ and $V_6'' = 34 \text{ cm}^{-1}$. The best-fit internal rotor potentials in ground and excited states are shown pictorially in Figure 6.

While methyl rotor transitions account for most of the observed transitions, there are two transitions at -213 and

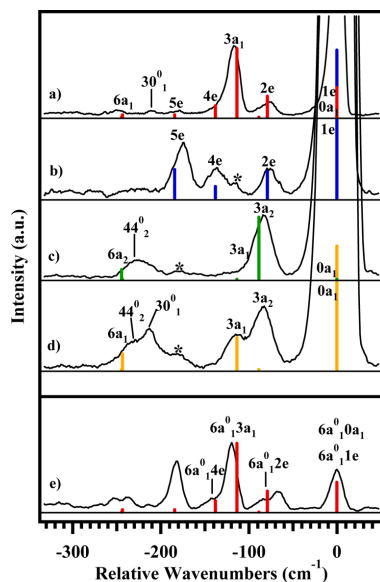


Figure 5. DFL spectra along with the simulated results for emission from the (a) $0a_1'/1e'$, (b) $2e'$, (c) $3a_2'$, and (d) $3a_1'$ excited state levels. Scattered light masks intensities at '0' relative wavenumbers. (e) Internal rotor structure built off the $6a_1^0$ vibronic band in the $0a_1'/1e'$ DFL spectrum, which has no interference from scattered light. In (a) and (e), the relative intensities of transitions out of $0a_1'$ and $1e'$ were adjusted to match experiment, due to overlap of these transitions at the excitation wavelength used for the DFL spectra. Asterisks indicate the features affected by collisional quenching verified from fluorescence lifetime measurements.

-229 cm^{-1} that are not assignable as such. Based on the calculated ground state frequencies for α -MeBz, we tentatively assign the band at -213 cm^{-1} as an in-plane fundamental (30^0_1), while the band at -229 cm^{-1} has a wavenumber position consistent with assignment as the first overtone of the out-of-plane vibration $\nu_{44^0_2}$; that is, 44^0_2 . The forms of these vibrations are shown in Figure S2.

E. Photoionization Efficiency Scans. The adiabatic ionization threshold of α -MeBz was determined from a PIE scan recorded with the D_1 zero-point level as the intermediate state. The results are shown in Figure 7. A sharp onset was observed at $6.835 \pm 0.002\text{ eV}$, indicating that there is little geometry change from D_1 to the radical cation ground state (S_0). Since the PIE scans were carried out in an extraction field of only 70 V/cm , the ionization threshold is likely to underestimate the true adiabatic threshold by no more than 20 cm^{-1} (0.002 eV). The calculated ionization potential (IP = 6.764 eV) agrees well with the experimental value. As we shall see in Section V, the calculations also predict that the methyl group prefers a *syn* orientation in the cation, the same as that in D_1 , consistent with the sharp ionization threshold observed. The experimental IP of α -MeBz is lower than that obtained for the benzyl radical (IP = $7.2477 \pm 0.00017\text{ eV}$) by 0.41 eV , as one might anticipate based on hyperconjugation of the methyl group with the π cloud, similar to the IP reduction from benzene (9.245 eV) to toluene (8.828 eV).⁷⁴

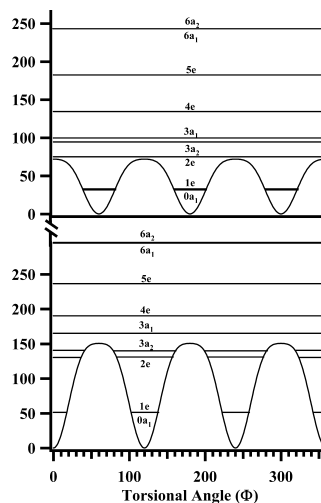


Figure 6. Potential energy curves and eigenvalues for D_0 and D_1 states based on the best-fit parameters from the methyl rotor simulations. D_0 : $V_3'' = 151\text{ cm}^{-1}$, $V_6'' = 34\text{ cm}^{-1}$. D_1 : $V_3' = 72\text{ cm}^{-1}$, $V_6' = 15\text{ cm}^{-1}$, and $\Delta\varphi = \pi$.

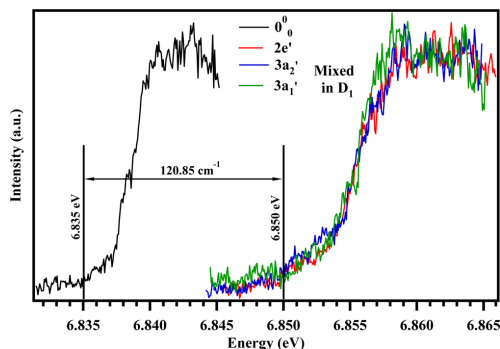


Figure 7. Adiabatic ionization threshold for the $0a_1''-0a_1'/1e''-1e'$ transition (left, black) and a series of PIE scans (on right) using the indicated D_1 internal rotor levels as intermediate states. See text for further discussion.

Ionization threshold scans were also obtained using the $2e'$, $3a_2'$, and $3a_1'$ D_1 methyl rotor levels as intermediate states. Based on the expected near-vertical nature of the D_1 -ion transition, these scans are anticipated to map out the positions of the $2e$, $3a_2$, and $3a_1$ levels of the cation. The threshold out of the $D_1(2e')$ intermediate state is $121 \pm 15\text{ cm}^{-1}$ above the adiabatic threshold, consistent with a significant increase in the barrier to methyl rotation in the cation. The near-coincidence of the $2e$ and $3a_2$ levels of the cation is consistent with this notion. However, the similar threshold for ionization out of $3a_1'$ is anomalous as it should be paired with $4e'$ in the high barrier limit, well separated from the $2e'/3a_2'$ pair. Nevertheless, if the Coriolis coupling involving $3a_1'/3a_2'$ invoked to explain the intensity of the $0a_1''-3a_2'$ transition in the 2C-R2PI spectrum is

correct, this mixing will produce Franck–Condon activity to the $3a_1$ level of the cation, as observed. Based on the fitting of the PIE scans taken from D_1 rotor levels, a tentative methyl internal rotor barrier of $V_3^+ = 360 \text{ cm}^{-1}$ was deduced for the cation.

F. State-Selected Infrared Spectra. The alkyl CH stretch region of the infrared is particularly useful as an alternative, complementary probe of the methyl group and its electronic state dependent effects on the spectroscopy of α -MeBz. As a result, both ground state (D_0) and excited state (D_1) RIDIR spectra were recorded for α -MeBz in the alkyl and aromatic CH stretch regions ($2800\text{--}3150 \text{ cm}^{-1}$). The results are shown in Figures 8a,b, respectively. The changes in the IR spectrum with

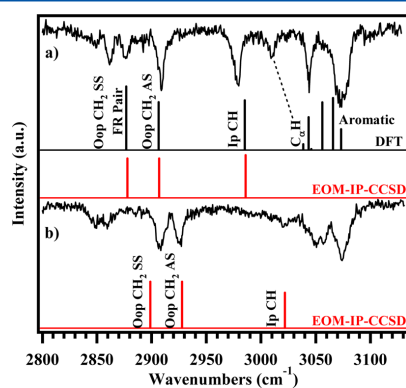


Figure 8. (a) D_0 -RIDIR spectrum compared to IR frequencies and intensities calculated at the B3LYP/6-311+G(d,p) (black sticks, scaling factor: 0.9635) and at the EOM-IP-CCSD/6-311+G(d,p) level of theory (red sticks, scaling factor: 0.9414). (b) D_1 -RIDIR spectrum compared to IR transitions calculated at the EOM-IP-CCSD/6-311+G(d,p) level of theory (red sticks, scaling factor: 0.9414). The EOM-IP-CCSD results were obtained upon implementing the Wilson G-matrix formulated by Häber et al. (ref 32). See text for further discussion.

electronic excitation are striking, suggesting a sensitivity of the spectrum to the orientation of the methyl group and/or its changed electronic environment.

The predictions of the calculations for the ground state are included as a stick diagram in the figure, calculated at the B3LYP/6-311+G(d,p) level of theory. There is generally good correspondence between calculation and experiment, although the experimental spectrum is complicated by the presence of stretch/bend Fermi resonances. Based on the internal rotor structure in the vibronic spectrum, the calculated CH stretch modes give guidance as to how to interpret the methyl group's CH stretch spectrum. By symmetry, the methyl CH stretch modes divide into a CH stretch mode localized on the in-plane CH group, and a pair of out-of-plane CH stretch modes associated with the symmetric/asymmetric motions of the out-of-plane CH_2 group. The prediction of the calculation is that this pair of transitions appear with small at the low-frequency end of the spectrum, while the in-plane CH is much higher in frequency, appearing as a strong transition at 2980 cm^{-1} . We tentatively assign the transition at 2909 cm^{-1} as the out-of-plane asymmetric CH_2 stretch, while the symmetric stretch mode is split by a Fermi resonance with an even overtone of

the CH_2 bend of the same CH_2 group, which is calculated, after scaling, to be in close proximity ($1435 \times 2 = 2870 \text{ cm}^{-1}$). This mixed set of levels appears at 2862 and 2876 cm^{-1} in the experimental spectrum. Finally, we tentatively assign the C_6H stretch to the weak transition at 3009 cm^{-1} . The aromatic CH stretch region is notorious for undergoing extensive anharmonic mixing.^{44,46} In this region, the agreement between experiment and theory is insufficient to make confident assignments.

Full normal mode calculations at the EOM-IP-CCSD/6-311+G(d,p) level of theory were deemed too computationally intensive for the D_1 excited state. Instead, the CH stretch transitions were treated in the reduced set of internal coordinates associated with stretching the three CH bonds of the methyl group. Numerical second derivatives were calculated using standard formulas, serving as input to a reduced-dimension Wilson G-matrix formalism from Häber et al.,³² here generalized to the less symmetric potential present in the α -MeBz radical to compute the frequencies and forms of the three CH stretch normal modes of D_1 α -MeBz radical. More detailed information regarding this model is given in Section VI.C. As a check, the ground state CH stretch modes were also calculated in this way, reproducing the normal mode result at the B3LYP/6-311+G(d,p) level of theory, as is shown in Figure 8a, using a scale factor of 0.9414. The parameters from the model to obtain the ground state EOM-IP-CCSD results are given in Table S2. In order to calculate the infrared intensities of the normal modes, dipole derivatives along the three CH bonds were also calculated, and used to compute the IR intensities.

Upon electronic excitation, the experimental data indicate that the methyl group orientation rotates relative to the ground state configuration so that the in-plane CH now points in the opposite direction. This methyl reorientation is consistent with an angular change $\Delta\varphi = \pi$ based on the best fit to the observed internal rotor structure in the excitation and DFL spectra. One consequence of this change is that the excited state RIDIR spectrum of Figure 8b is strikingly different than its ground state counterpart, most notably in the highest frequency methyl CH stretch (labeled "in-plane CH" in Figure 8a) being shifted and/or reduced in intensity in the D_1 state to the point that it is difficult to locate. We tentatively assign it to the weak transition at 3021 cm^{-1} , although it could also be part of the clump of transitions near 3050 cm^{-1} . In either case, the experimental and calculated CH stretch fundamentals retain the same pattern as in D_0 , with two low and one high frequency CH stretch transition, with all three shifted to higher frequency than their ground state counterparts. We postulate that this increase in frequency shifts the symmetric CH_2 stretch located at 2909 cm^{-1} out of resonance with the bend overtones, so that they now undergo only minor Fermi resonance coupling with the bend overtones. The weak bands at 2850 cm^{-1} are therefore tentatively assigned as the remnant of this Fermi resonance, which is now less pronounced. The band at 2926 cm^{-1} is assigned to the out-of-plane asymmetric CH_2 stretch. As in the D_0 state, the aromatic ring and C_6H stretch fundamentals form a set of transitions in the $3040\text{--}3090 \text{ cm}^{-1}$ region. No attempt was made to further analyze this region.

V. COMPARISON WITH CALCULATIONS

The spectral data and analysis just presented have provided experimentally derived shapes, barrier heights, and change in preferred orientations for the methyl group upon electronic excitation. However, a direct measure of the preferred

orientation of the methyl rotor in either state is missing. Thus, we performed a set of ab initio calculations aiming to predict the preferred methyl orientations in D_0 and D_1 states. We also sought additional insight into the methyl CH stretch region of the infrared, and the observed changes that accompanied electronic excitation there.

To calibrate various levels of theory, we have carried out calculations on the excited states of the benzyl radical. Since the TDM directions and relative oscillator strengths of the D_0 – D_1 and D_0 – D_2 transitions are known for the benzyl radical,^{63,64} it provides a benchmark for decisions on the level of theory needed to correctly describe the excited states of α -MeBz. In the benzyl radical, the D_0 – D_1 transition is known to be a very weak, pure *B*-type band, while the vibronically induced transitions are pure *A*-type peaks associated with the D_0 – D_2 transition with much greater oscillator strength. Based on their analysis of this vibronic coupling, Cossart-Magos and Leach surmised that the D_2 state is only 430–485 cm^{-1} above D_1 .¹

While MCSCF provides a qualitatively correct description of the first two excited states in benzyl and α -MeBz (discussed more thoroughly in Supporting Information), it misses dynamic correlation effects which leads to the wrong order of the two states, as shown in Table 3, consistent with the calculations of

Table 3. Comparison of the Vertical Energy Splittings (cm^{-1}) between the D_1 and D_2 States of Benzyl and α -MeBz Radicals Provided by Different Levels of Theory^a

level of theory	benzyl	α -methylbenzyl
EOM-EE-CCSD/ aug'-cc-pVDZ ^b	-229.0	563.8
EOM-IP-CCSD/ 6-311+G(d,p) ^c	1197.2	742.8
EOM-IP-CCSD (dT)/ 6-311+G(d,p) ^c	592.2	478.6
MCSCF/cc-pVTZ ^d	-1288.8	-1666.6
MCQDPT/cc-pVTZ ^d	1209.3	1138.1

^aPositive values correspond to the state with TDM along *b* axes (2A_2 state of the benzyl radical) being the lowest one. All calculations are performed at the ground state geometries (geometry of the *anti* isomer is used for α -methylbenzyl). ^bG.S. geometry optimized at EOM-EE-CCSD/aug'-cc-pVDZ. ^cG.S. geometry optimized at EOM-IP-CCSD/6-311+G(d,p). ^dG.S. geometry optimized at MCSCF(9,9)/6-31G(d). State averaging for the three lowest states (D_0 , D_1 , D_2) was employed for energy calculations.

Rice et al.⁷⁵ Introducing dynamic correlation through configuration interaction as was done by Negri et al.⁸ or using multiconfigurational perturbation theory recovers the correct order of the excited states (see Table 3). Even though the 1^2A_2 state in benzyl is the second excited state at the ground state geometry at the MCSCF level, it becomes the lowest excited state near its own equilibrium geometry. As a result, it is possible to find the optimized geometry of this state and its vibrational frequencies as needed. However, it was not possible to find an optimal geometry of the corresponding (*B*-type) state in α -MeBz using MCSCF, due to a destabilizing steric repulsion of the methyl group with the aromatic ring and stronger mixing of the two excited states. On the contrary, MCSCF geometry optimizations in α -MeBz always converge to the equilibrium structure of the other (*A*-type) state. Since the MCQDPT analytic gradients are not available, it becomes very challenging to obtain accurate values of the methyl rotor barrier

and the preferred orientation for the first excited state at the MCSCF/MCQDPT level of theory.

Not surprisingly, low-correlated single-reference methods like CIS⁷⁶ and TDDFT (our own preliminary calculations) also fail to produce a correct ordering of the excited states in benzyl and yield a D_1 – D_2 energy splitting with significant error. EOM-EE-CCSD in the aug'-cc-pVDZ basis inverts the order of the D_1 and D_2 states for benzyl, but gives the correct order in α -MeBz (see Table 3). We found, however, that EOM-EE-CCSD produces the correct order of states adiabatically if the larger cc-pVTZ basis is employed. Fortunately, EOM-EE-CCSD/aug'-cc-pVDZ gives the correct state ordering both vertically and adiabatically in α -MeBz. On the other hand, the EOM-IP-CCSD method matches with experiment for the benzyl radical, giving D_0 – D_1 and D_0 – D_2 transitions with the correct TDM directions, relative oscillator strengths, and approximate energy splittings (see Tables 3 and 4). The approximate vertical

Table 4. Calculated Properties of the D_1 and D_2 States of Benzyl and α -MeBz Radicals at the EOM-IP-CCSD/6-311+G(d,p) Level of Theory

parameter	benzyl	α -methylbenzyl
$D_1(\mu_a^2;\mu_b^2;\mu_c^2)$	0:100:0	53:47:0
$D_2(\mu_a^2;\mu_b^2;\mu_c^2)$	100:0:0	99:1:0
$f_{D_1:D_2}$	0.0179:0.1218	0.0416:0.1030

D_0 – D_1 and D_0 – D_2 energy splittings at the EOM-IP-CCSD level with and without perturbative triple corrections are given in Table 3.

Additional complexity in describing D_1 / D_2 splittings arises due to nonadiabatic effects and vibronic interactions between these states. While investigating these topics is beyond the scope of this paper, we note that the vibronic couplings in α -MeBz are stronger and the adiabatic states are more strongly mixed than the corresponding states in the benzyl radical. This is because D_1 and D_2 belong to the same symmetry representation in α -MeBz and are allowed to mix. At the same time, the presence of the methyl group rotates the TDMs of D_1 and D_2 toward each other.

We found that the orientations and magnitudes of the TDMs for the D_0 – D_1 and D_0 – D_2 transitions in α -MeBz are extremely sensitive to the electronic structure method, basis set, and the geometry of the molecule. Tables 3 and 4 provide a representative set of data comparing calculated properties of the D_1 and D_2 states in benzyl and α -MeBz. The EOM-IP-CCSD calculations predict greater oscillator strength (by ~ 2.5 times) for the D_0 – D_1 transition in α -MeBz than in benzyl. The D_2 state is predicted to be less than 500 cm^{-1} above D_1 in α -MeBz, and still carries a greater oscillator strength in its transition from D_0 , with $f_{02} = 0.103$ compared to $f_{01} = 0.042$. As a result, it is somewhat surprising that the effects of vibronic coupling between D_1 and D_2 are not more readily apparent in the 2C-R2PI spectrum.

Taking into account the complexity of the electronic structure of α -MeBz and the intrinsic limitations of the suite of computational methods used in describing its electronic states, determining the preferred orientation of the methyl rotor in the ground and first excited states is a challenging task. Table 5 summarizes the rotational barriers obtained at different levels of theory.

All methods except IP-CISD predict the ground state to be more stable in the *anti* geometry than in *syn*, with the methyl

Table 5. The Barrier Heights between the *syn* and *anti* Conformations of α -MeBz in the Ground and the First Excited State^a

method	geometry	D ₀ barrier (cm ⁻¹)	D ₁ barrier (cm ⁻¹)	rotation
IP-CISD/ aug-cc-pVDZ	IP-CISD/ aug-cc-pVDZ	-61	336	yes ^b
EOM-IP-CCSD/ aug-cc-pVDZ	IP-CISD/ aug-cc-pVDZ	124	316	no
EOM-IP-CC(2,3)/ 6-31G(d)	IP-CISD/ aug-cc-pVDZ	185	294	no
CCSD/EOM-EE- CCSD/ aug'-cc-pVDZ	CCSD/EOM-EE- CCSD/ aug'-cc-pVDZ	146	-377	yes
MCSCF/cc-pVTZ ^{c,d}	MCSCF/6-31G(d) ^c	179	-123	yes
MCQDPT/cc- pVTZ ^{c,d}	MCSCF/6-31G(d) ^c	166	-253	yes

^aThe positive value of the barrier means that the *anti* conformation is preferred. The rotation column indicates whether the method predicts methyl rotation between the ground and excited state. ^bPredicts D₀ as *syn* and D₁ as *anti*. ^cThe active space comprised of 9 orbitals and 9 electrons. ^dState averaging for the three lowest states (D₀, D₁, D₂) was employed for energy calculations. D₀ geometries were used for estimating rotational barriers in the D₁ state.

rotor barrier between 120 and 190 cm⁻¹. Rather misleadingly, IP-CISD in diffuse basis sets gives lower energy for the *syn* configuration. This suggests that even in the ground electronic state, the molecular structure is very sensitive to the level of theory employed.

All IP methods suggest that the *anti* conformation is preferred in the first excited state (see Table 5). However, this would imply that the methyl group is not rotated upon excitation, in contradiction with the experimental evidence. The calculations with EOM-EE-CCSD and multiconfigurational methods show that the *syn* conformation is lower in energy for the experimentally observed D₁ (*B*-type) state. As discussed above, we believe EOM-EE-CCSD provides a more balanced description of the excited states in α -MeBz than the IP methods. Additionally, the calculations at the ground state geometry with MCSCF and MCQDPT also provide a hint that the *B*-type state prefers the *syn* conformation; however, more precise analysis was not possible due to a failure of these methods to find the optimal geometry of the *B*-type state.

The experimental observation of a sharp ionization threshold in the PIE scans suggests that the D₁ state has the same orientation as the S₀ state of the cation. Optimized geometries at the B3LYP/6-311+G** level of theory predict a *syn* ground state geometry of the cation, with a barrier of 597 cm⁻¹. CCSD(T)/cc-pVTZ calculations of the cation (at the B3LYP/6-311+G** geometries) are consistent with this conclusion, with a *syn* structure 575 cm⁻¹ lower than the *anti* configuration. These data agree with EOM-EE-CCSD and MCSCF/MCQDPT predictions that the methyl group is in an *anti* orientation in the ground state, rotates to a *syn* position in the excited state, and retains this preference for the *syn* orientation in the cation. The calculated geometries for the D₀, D₁, and S₀ electronic states are shown in Figure 9a–c.

VI. DISCUSSION

A. The Effect of the Methyl Group on the Benzyl Radical Excited States. Given the close structural and electronic similarity of the α -MeBz radical to its parent benzyl radical, it is natural to compare the two in assessing the effects of methyl substitution at the C _{α} position. The vibronic spectroscopy of benzyl radical has been studied in some detail previously.^{1–3} This spectrum is striking in that the D₀–D₁ transition, while allowed, is quite weak, with strong vibronic coupling leading to a triad of intense vibronic bands about 300–400 cm⁻¹ above the D₀–D₁ origin. This strong vibronic coupling is facilitated by the close proximity of the D₂ and D₃ states to D₁, and their large oscillator strengths out of D₀. Analysis of vibronic coupling by Eiden et al. led to the conclusion that the ν_{6a} fundamental gains its intensity from vibronic coupling to D₃, while the ν_{6b} fundamental and its Fermi resonant partner (a $\nu_{17} + \nu_{36}$ combination band) are vibronically coupled to D₂.²

The vibronic spectrum of α -MeBz is, by contrast, much less affected by vibronic coupling than benzyl radical. The vibronic spectrum of Figure 1 is dominated by a strong origin transition, with the most intense Franck–Condon activity involving the methyl rotor levels built off it, which can be explained by the change in preferred orientation of the methyl rotor, without direct reference to higher excited states. Vibronic activity in the ν_{6a} , ν_{6b} , ν_{12} , and ν_{18a} fundamentals (using Varsanyi notation for substituted benzenes) is similar to what one might expect for a substituted benzene. However, much like the benzyl radical, the ν_{6a} ring mode decreases by ~ 100 cm⁻¹ relative to typical ν_{6a} modes in the ground state.²

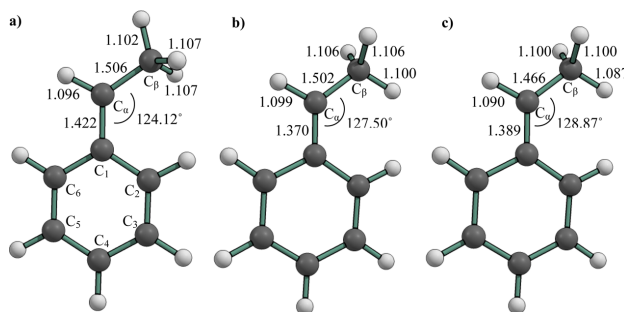


Figure 9. Structural parameters for the (a) D₀ and (b) D₁ states of the neutral radical at the EOM-EE-CCSD/aug'-cc-pVDZ level of theory, and the (c) S₀ electronic state of the ion at the EOM-EE-CCSD(T)/cc-pVTZ level of theory. Bond lengths are given in Angstroms and angles are given in degrees.

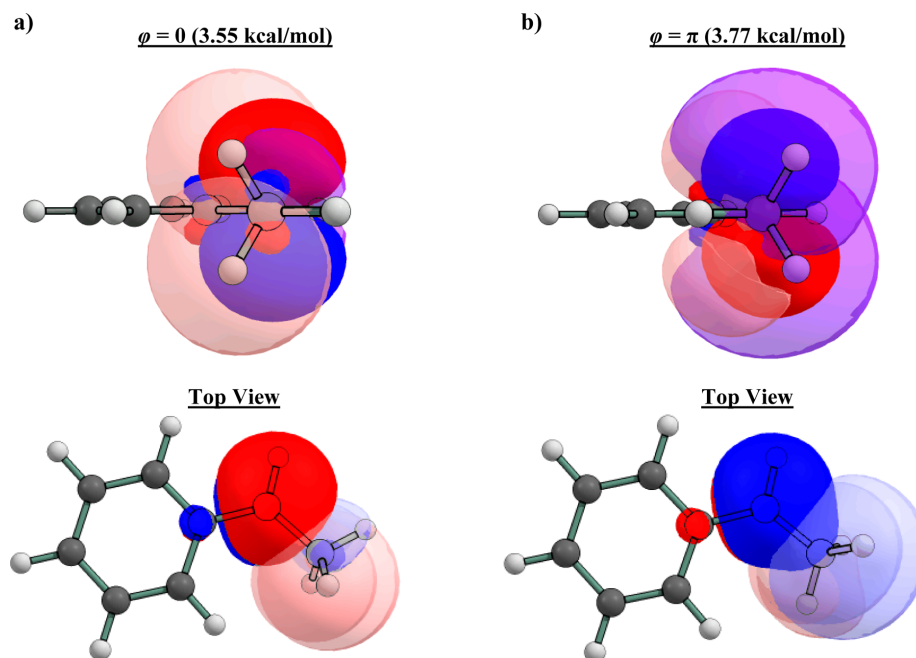


Figure 10. Illustrations depicting the NBO orbitals and their hyperconjugation in the D_0 ($\varphi = 0$ and π) electronic state of the neutral radical for (a) $\varphi = 0$ and (b) $\varphi = \pi$. The solid red/blue surfaces depict the radical π orbital and the light red or blue are the methyl σ_{CH} orbitals. When the in-plane CH is *anti* to the aromatic ring, both σ_{CH} orbitals stabilize the configuration by interacting with the radical π orbital by 3.55 kcal/mol. In the *syn* orientation, both σ_{CH} orbitals interact with the radical π orbital with 3.77 kcal/mol stabilization energy.

Despite the apparent weakening of the vibronic coupling, it is plausible that it still may be present in the spectrum and influencing it. Since vibronic coupling of the D_1 state to D_2 and D_3 occurs through the same totally symmetric ring modes (ν_{6a} , ν_{6b} , ν_{11} , ν_{12} , ν_{18a}) that already have Franck–Condon activity, the effects of the vibronic coupling may manifest themselves by modifying the intensities of these transitions. In particular, as a totally symmetric mode (a_1), the ν_{6a} ring mode can couple D_1 and D_2 , which are of the same symmetry (A_2) in G_6 . The ratio of the $6a_1^0/0_0^0$ intensities in the 2C-R2PI spectrum (Figure 1) can be compared with those for $6a_1^0$ relative to resonance fluorescence in the 0_0^0 DFL spectrum (Figure 3). In this and the other Franck–Condon active modes, modest changes in intensity are apparent, but not dramatic, pointing again to the diminished effect of vibronic coupling in the spectrum.

Finally, it is worth noting that the excited state lifetimes of the vibronic levels of α -MeBz (480 ns) are similar to those in the benzyl radical (400 ns). While only a single exponential decay is distinguishable for α -MeBz, the benzyl radical demonstrates a biexponential decay with a fast component of 400 ns and a slow component of 1.86 μs whose source is still under debate.⁴ In the present case, we do not clearly see a weak long-lived component to the decay.

B. Electronic State Dependence of the Internal Rotation Barriers. In our discussion in the preceding section, we have been considering the effect of methyl substitution on the electronic states of the benzyl radical. In this section, we discuss the way in which the methyl group responds to the

electronic state structure of the benzyl radical via changes in its orientation and the barrier to its internal rotation.

In this context, it is helpful to view α -MeBz as a phenyl-substituted ethyl radical. In the absence of substitution, the ethyl radical has a hindered rotor ground state potential dictated by a pure V_6 term due to the symmetric nature of the $-\text{CH}_2$ group against which the methyl group internally rotates. The major effect of phenyl substitution, then, is to break this “left/right” symmetry, leading to a hindered rotor potential dominated by a V_3 term that distinguishes whether the methyl group has its in-plane CH group *syn* or *anti* to the aromatic ring. As previously summarized, the frequencies of the hindered rotor structure present in the D_0 – D_1 excitation and DFL spectra can be fit with a D_0 potential with $V_3'' = 151 \text{ cm}^{-1}$ and $V_6'' = 34 \text{ cm}^{-1}$, and a D_1 potential with a barrier about half that size ($V_3' = 72 \text{ cm}^{-1}$ and $V_6' = 15 \text{ cm}^{-1}$). Furthermore, the intensities were best fit with $\Delta\varphi = \pi$, proving that there is a switch in the preferred orientation between D_0 and D_1 states. Based on the calculations, we surmise that the α -MeBz radical prefers the *anti* orientation in D_0 and *syn* orientation in D_1 .

This electronic “switch” for the methyl rotor is an effect observed in other circumstances in which the methyl rotor is directly bonded to the electronic chromophore. The 1- and 2-methylvinoxy radicals studied by Williams et al.^{77–79} are especially instructive in this regard. Here, as in the present case, the methyl group rocks against a planar radical framework that is asymmetric, with the V_3 term dominating and shifted between the ground and first excited state by $\Delta\varphi = \pi$. In general,

the orientation for a methyl group is affected by a delicate balance between electrostatic donor/acceptor (hyperconjugation) and steric interactions.⁸⁰ If steric effects are negligible, such is the case for the methylvinoxy radical isomers, the methyl group consistently favors an orientation in which the in-plane methyl CH orients *syn* to the vicinal bond with higher bond order to optimize hyperconjugative overlap between occupied and vacant orbitals. The role of hyperconjugation in dictating the orientational preference of the methyl group was first noted in propene,⁸¹ as explained in the seminal work of Pople and co-workers.⁸²

In the present case of α -MeBz, the two vicinal bonds are the C_α -H and C_1 - C_α bonds, only the latter of which has any double bond character (see Figure 9). This leads to a prediction that in the ground state the in-plane methyl CH should be *syn* to the ring, counter to the calculated *anti* configuration (Figure 9a). Steric effects, in fact, suggest the opposite preference in the ground state because the aromatic C_2 -H group and in-plane methyl hydrogen are unfavorably close in the *syn* configuration (2.1 Å) relative to the sum of their van der Waals' radii (~ 2.4 Å). According to calculations, the C_1 - C_α - C_β angle also increases slightly from 124.12° in the *anti* configuration (D_0) to 127.50° for *syn* (D_1 , Figure 9b), consistent with the notion that steric hindrance counteracts hyperconjugation in the ground state. On this basis, we deduce that steric hindrance dictates the barrier to methyl internal rotation in D_0 , yielding a barrier two times that of D_1 .

In the D_1 excited state, the in-plane CH is oriented *syn* to the ring (Figure 9b). Here the in-plane methyl CH now eclipses the vicinal C_1 - C_α bond since its bond order increases upon excitation as predicted by calculations. We surmise on this basis that hyperconjugation effects now outweigh steric hindrance. Natural bond orbital (NBO) analysis^{40,41} can be used to describe the electronic structure in terms of hyperconjugative interactions. The NBO wave functions give a Lewis structure picture of the localized orbitals in the molecule and describe the donor/acceptor charge transfer contributions arising from orbital overlap between neighboring groups. Figures 11a,b illustrate the NBO results for the *anti* and *syn* geometries in the ground state, depicting the methyl σ_{CH} orbitals (semi-transparent) back-donating electron density to the partially filled radical π orbital (solid), resulting in the *syn* configuration having a slightly larger stabilization energy (3.77 kcal/mol) than the *anti* geometry (3.55 kcal/mol). The conformational change in the D_1 geometry may be ascribed to the fact that upon excitation, there is stronger overlap between the out-of-plane σ_{CH} orbitals and the C_α π orbital. Although steric hindrance still plays a role, albeit less pronounced, hyperconjugation is now suspected to control the D_1 barrier height and the preferred methyl group orientation.

While we do not have a detailed characterization of the cation methyl rotor states, the near-vertical excitation thresholds in the PIE scans point clearly to the cation having the same preferred methyl orientation as the D_1 excited state; namely, *syn*. Removal of the radical π electron upon ionization dramatically changes the local π -bonding. The calculated geometry in Figure 9c suggests retention of significant C_1 - C_α double bond character and a slight increase in the C_1 - C_α - C_β angle to 128.87° , further reducing steric effects. Thus, the correct prediction that the in-plane methyl CH lies toward the vicinal C_1 - C_α bond agrees with calculations. As a consequence of ionization, the delocalized positive charge induces greater hyperconjugation between these orbitals, and the barrier to

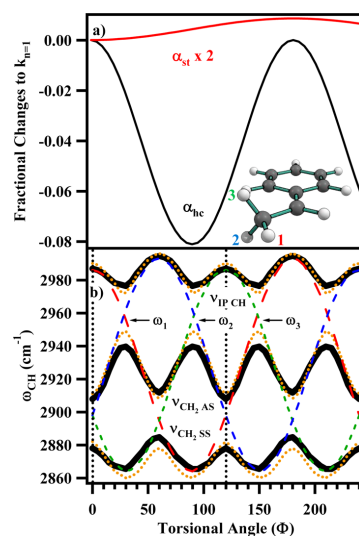


Figure 11. Methyl CH stretch modeling results for the D_0 ground electronic state of α -MeBz. (a) The changes to the spring constant of CH(1) ($k_{CH=1}$) shown as the constituent components α_{st} and α_{hc} for a single CH oscillator as a function of the torsional angle. (b) Calculated frequencies of the CH stretch normal modes at the B3LYP/6-311+G(d,p) level of theory (solid black traces, scaling factor: 0.9635), with the best-fit results for the diabatic local mode CH(n) stretch frequencies shown as the broken red (ω_1), blue (ω_2) and green (ω_3) traces, and the adiabatic CH stretches shown as dotted gold traces. The vertical dotted line indicates the optimized D_0 geometry torsional angle.

internal rotation tentatively deduced based on the photoionization thresholds (~ 360 cm^{-1}) reflects this overall behavior.

C. Coupling Between the Alkyl CH Stretches and Methyl Rotation. Having characterized the methyl rotor orientations and the detailed shapes of the methyl rotor potentials of α -MeBz in both D_0 and D_1 states, we conclude the Discussion section with an analysis of the methyl CH stretch infrared spectrum. Particular attention is focused on the coupling of methyl rotation with the methyl CH stretch modes, and how the orientation and shapes of the methyl rotor potentials manifest themselves in the methyl CH stretch results. One of the intriguing aspects of the present work is that it reports CH stretch spectra in both D_0 and D_1 states (Figure 8) using the three-laser technique of excited state RIDIR spectroscopy.⁴² In Section IV.F, the B3LYP (D_0) and EOM (D_1) calculations were used to describe the pattern of transitions observed experimentally, notably, in having the methyl CH stretch transitions split into a pair of transitions due to the out-of-plane CH groups at low frequency and a single CH stretch due to the in-plane CH at higher frequency. The EOM calculations also predicted the observed shift up in frequency of the set of three alkyl CH bands in D_1 relative to D_0 .

To provide a simple physical picture for the frequency pattern and shift in the experimental IR spectra, we present an analysis of the torsion–vibration coupling using a Wilson G-matrix model, which treats the three CH stretches as local harmonic oscillators with optional finite kinetic coupling.⁸³

This treatment generalizes that outlined in the seminal work of Häber et al. on the ethyl radical³² where hyperconjugation acts as a stabilizing force between the partially filled radical site and the methyl group that has implications on the methyl CH stretch modes. For α -MeBz, the methyl CH bond force constants k_n oscillate periodically as

$$k_n(\varphi) = k_0[1 - \alpha_{\text{hc}} + \alpha_{\text{st}}] \quad (6)$$

where

$$\alpha_{\text{hc}} = \frac{\Delta k_{\text{hc}}}{k_0} \sin^2(\varphi + (n-1)\pi/3),$$

$$\alpha_{\text{st}} = \frac{\Delta k_{\text{st}}}{k_0} \sin^2(\varphi/2 + [(n-1)2\pi]/3) \quad (7)$$

for each of the three CH(n , $n = 1-3$) bonds with α_{hc} and α_{st} representing the hyperconjugation-induced and sterically hindered fractional changes to the force constant k_0 , respectively, as a function of the torsional angle φ . The α_{hc} and α_{st} terms of eq 6 are plotted individually for D_0 in Figure 11a with the latter multiplied by 2 to more easily see its form. The α_{hc} term represents the major factor due to hyperconjugation lowering the force constant k_0 , and it is maximized when a CH(n) bond becomes parallel to the adjacent radical π orbital (e.g., CH($n = 1$) for $\varphi = \pi/2$). Figure 10a,b show this hyperconjugation in D_0 for methyl group orientations $\varphi = 0$ and $\varphi = \pi$ providing a useful visualization of the overlap between

Table 6. Best Fit Parameters for Modeling the Methyl CH Stretch Frequencies in the Ground Electronic State at the B3LYP/6-311+G(d,p) Level of Theory

parameter	D_0
k_0	1.269×10^4 dyn/cm
α_{hc}	0.0811
α_{st}	0.0043
M_0	34.1 amu

the methyl σ_{CH} orbitals and the respective π orbital that leads to a reduction in the force constant for the CH bond, thereby lowering its frequency.

The α_{st} term provides a counteracting force that is greatest/lowest when a CH(n) bond is eclipsed/staggered relative to the aromatic C₂-H group, leading to a “left-right” in-plane asymmetry as the degree of steric hindrance changes. The α_{st} term was not included in the original model of Häber et al. The addition of this term makes it possible to include the effects of steric crowding from the aromatic ring for different methyl group torsional angles. Overall, both α_{hc} and α_{st} provide physical insight into the electronic structure of α -MeBz and its repercussions on the CH stretches as the methyl group rotates about the asymmetric environment of the benzyl radical motif.

At any fixed methyl group orientation, the oscillating CH(n) bond constants (k_n) obtained from eq 6 can be incorporated into the ethyl radical Hamiltonian,³² with the CH stretch matrix constructed as

$$\begin{pmatrix} \frac{(3\omega_1 + \omega_2 + \omega_3)}{2} & \sqrt{\omega_1\omega_2} \left(\frac{\mu_{\text{HC}}}{M_0} \cdot \frac{\cos(\theta)}{2} \right) & \sqrt{\omega_1\omega_3} \left(\frac{\mu_{\text{HC}}}{M_0} \cdot \frac{\cos(\theta)}{2} \right) \\ \sqrt{\omega_1\omega_2} \left(\frac{\mu_{\text{HC}}}{M_0} \cdot \frac{\cos(\theta)}{2} \right) & \frac{(\omega_1 + 3\omega_2 + \omega_3)}{2} & \sqrt{\omega_2\omega_3} \left(\frac{\mu_{\text{HC}}}{M_0} \cdot \frac{\cos(\theta)}{2} \right) \\ \sqrt{\omega_1\omega_3} \left(\frac{\mu_{\text{HC}}}{M_0} \cdot \frac{\cos(\theta)}{2} \right) & \sqrt{\omega_2\omega_3} \left(\frac{\mu_{\text{HC}}}{M_0} \cdot \frac{\cos(\theta)}{2} \right) & \frac{(\omega_1 + \omega_2 + 3\omega_3)}{2} \end{pmatrix} \quad (8)$$

where ω_n are the uncoupled CH stretch frequencies ($\omega_n = (kn/\mu_{\text{HC}})^{1/2}$), μ_{HC} is the reduced mass, M_0 is the effective mass of the central atom, and θ is the angle between CH groups of approximately 109°. Upon diagonalization, the results yield the changes in the CH stretch normal-mode frequencies with torsional angle, which were initially generated for the diabatic limit in the absence of kinetic coupling (or $M_0 = \infty$). Minimizing a linear least-squares function, the k_0 , α_{hc} and α_{st} parameters were optimized for the best agreement between the diabatic and ab initio CH stretch frequencies' extrema. The diabatic CH(n) results for D_0 are plotted with their respective broken lines (ω_n) in Figure 11b and compared to the calculated CH stretch frequencies at the B3LYP/6-311+G(d,p) level of theory (solid black lines). However, the final fit was obtained for the adiabatic limit by incorporating coupling between the CH stretch modes. To do so, M_0 was varied to optimize the agreement between the adiabatic (broken gold lines) and the full ab initio results, both of which closely agree with the ground state experimental alkyl CH stretches for a $\varphi = 0$ configuration marked with a vertical dotted line. The final fit parameters are tabulated in Table 6. Notably, the best-fit M_0 value is 34.1 amu, close to the effective mass used for the ethyl

radical simulations (31 amu) or the mass of the CCH₂ subunit. The slight increase in M_0 for α -MeBz results from the phenyl ring adding only incrementally to the effective counter-mass to methyl internal rotation, due to the methyl rotor axis being oriented 120° relative to the C₁-C _{α} axis.

As a particular simulated diabatic CH(n) stretch rotates about the torsional angle φ , the “left-right” asymmetry leads to a periodic representation such that a minimum and two inequivalent maxima are obtained with a phase of π . As referred to earlier, the minima correspond to full hyperconjugation between the methyl σ_{CH} orbitals and the radical π orbital, and the maxima convey the degree of steric hindrance experienced by the in-plane methyl CH group. Relative to each other, the local mode CH(n) stretches have a 120° phase shift between equivalent points on the diagram. The experimentally observed pattern of CH stretch normal modes, with two low- and one high-frequency stretch for $\varphi = 0$ and π , is understandable within this model in that the in-plane methyl CH encounters no hyperconjugation so remains unperturbed and the out-of-plane CH bonds undergo some electrostatic interaction from the adjacent radical π orbital thereby decreasing their vibrational frequencies. Similar to the ethyl radical, the sites

in the diagram where the $\text{CH}(n)$ frequencies intersect are characterized as conical intersections in the diabatic limit, but become avoided crossings when finite kinetic coupling is allowed (adiabatic).

However, the optimized geometry for ethyl radical orients the methyl group at $\varphi = \pi/2$ with respect to its $-\dot{\text{C}}\text{H}_2$ neighbor, and the barrier is determined by a $V_6'' = 18 \text{ cm}^{-1}$ term due to the torsional environment symmetry. The $\text{CH}(n)$ frequencies are, consequently, unaffected by different steric-hindering locations. The phenyl substitution introduces a V_3'' term in $\alpha\text{-MeBz}$, which is about an order of magnitude higher ($\sim 151 \text{ cm}^{-1}$) than the ethyl radical barrier in the ground state. This distinction may not only be due to steric effects, but may possibly be credited to dissimilar extents of hyperconjugation arising from different electronic structures.

Reflecting on the analysis presented for the electronic and infrared data sets in the ground state, we are now in a position to directly compare how these two are connected. In D_0 , if one compares the dependence of the adiabatic in-plane CH stretch with torsional angle in the Wilson G-matrix results (Figure 11b) with the shape of the methyl torsional potential energy curve (Figure 6), the maxima in the model's in-plane CH stretch frequencies occur at the same angles as the maxima in the torsional PES. Thus, this suggests that the steric crowding experienced by the in-plane CH bond is primarily responsible for the ground state barrier to internal rotation. Hyperconjugation may also play a role, where Figure 10a,b shows that the stabilization energy is greater for $\varphi = \pi$ than $\varphi = 0$. As a result, this greater interaction between the σ_{CH} orbitals and the radical π orbital at this particular methyl group orientation may increase the D_0 internal rotation barrier.

In the excited state for $\alpha\text{-MeBz}$, the methyl group switches orientation due to changes in the degree of steric hindrance and/or hyperconjugation accompanying the $\pi\text{-}\pi^*$ excitation. We anticipate with an increase in the CH stretch frequencies in the excited state that k_0 should become larger. Additionally, for $\Delta\varphi = \pi$, we expect that α_{st} and α_{hc} will change in such a way as to decrease the D_1 barrier to internal rotation to half that of the D_0 barrier. More information on the modeling of the excited state CH stretch spectrum is given in the Supporting Information.

VI. CONCLUSIONS

We have presented a multifaceted spectroscopic characterization of the $\alpha\text{-MeBz}$ radical, a resonance-stabilized radical that may form by H-atom loss from ethylbenzene or H-atom addition to styrene. The spectra provide a unique opportunity to study the response of a methyl group to the presence of a radical site immediately adjacent to it, and to follow the changes that accompany electronic excitation.

The $\text{D}_0\text{-D}_1$ $\pi\text{-}\pi^*$ transition of $\alpha\text{-MeBz}$ has its origin transition at 21884 cm^{-1} , with an extensive set of low-frequency transitions due to hindered rotation of the methyl group. DFL spectra help identify analogous transitions due to methyl internal rotation in the ground electronic state. Fits to the frequencies and intensities of these transitions have provided the form of the methyl hindered rotor potentials in D_0 and D_1 states. Both states are dominated by a V_3 term, which in the excited state is 72 cm^{-1} , and increases to 151 cm^{-1} in D_0 . Ground state calculations predict that the preferred orientation for the methyl group is with one CH group in the plane of the aromatic ring, pointing toward the vicinal $\text{C}_\alpha\text{-H}$ bond. Arguments have been made that the major interaction dictating this choice is in minimizing steric repulsions between the methyl CH and the

ortho ring CH group, opposing hyperconjugation which would prefer the opposite orientation. In the D_1 state, the experimental data point to a switching of the methyl conformation with minimized steric repulsions from a larger $\text{C}_1\text{-C}_\alpha\text{-C}_\beta$ angle and from favorable hyperconjugative overlap between the $\text{C}_1\text{-C}_\alpha$ π orbital and the out-of-plane methyl σ_{CH} orbitals. High-level ab initio excited state calculations support this conclusion.

Finally, we have recorded resonant ion-dip infrared spectra of the radical in the alkyl and aromatic CH stretch regions, varying the timing of the IR, visible, and UV laser pulses to obtain IR spectra in both D_0 and D_1 states. These spectra provide complementary insight into the methyl group orientation and hyperconjugation-induced effects on the methyl CH stretch absorptions. Extending a model first introduced by Häber and co-workers for the ethyl radical,³² we show that the pattern of methyl CH stretch transitions and their frequency shifts with electronic excitation reflect a change in the balance of effects due to hyperconjugation and steric interactions.

■ ASSOCIATED CONTENT

■ Supporting Information

Details of the rotational band contour for the $+41 \text{ cm}^{-1}$ transition and rotational constants, form of the low-frequency vibrational modes, explanation of the excited state alkyl CH stretch analysis, the simulation results, and the best-fit parameters from the analysis for both the ground and excited states, and full citation for references 37 and 45. This material is available free of charge via the Internet at <http://pubs.acs.org>.

■ AUTHOR INFORMATION

Corresponding Author

*E-mail: zwier@purdue.edu.

Present Addresses

^{||}Department of Chemistry, University of Louisville, 2320 South Brook Street, Louisville, KY 40292, U.S.A.

[†]IRAP, UPS; CNRS; 9 Av. du Colonel Roche, BP 44346, 31028 Toulouse cedex 4, France.

Notes

The authors declare no competing financial interest.

■ ACKNOWLEDGMENTS

N.M.K. and T.S.Z. gratefully acknowledge support for this research from the Department of Energy Basic Energy Research, Chemical Sciences Division under Grant No. DE-FG02-96ER14656. L.V.S. acknowledges support from the National Science Foundation (Grant CHE-0955419) and Purdue University. The work in Cambridge was supported by the National Science Foundation (Grant CHE-1058063). N.M.K. and T.S.Z. also thank the Purdue Rosen Center for Advanced Computing for the computational resources. Assistance from David F. Plusquellic in implementing the JB95 modeling package is gratefully acknowledged as well.

■ REFERENCES

- (1) Cossart-Magos, C.; Leach, S. Two-Mode Vibronic Interaction Between Neighboring 1^2A_2 and 2^2B_2 Excited Electronic States of the Benzyl Radical. *J. Chem. Phys.* **1976**, *64*, 4006–4019.
- (2) Eiden, G. C.; Weisshaar, J. C. Vibronic Coupling Mechanism in the $\text{A } ^2\text{A}_2\text{-B } ^2\text{B}_2$ Excited States of Benzyl Radical. *J. Chem. Phys.* **1996**, *104*, 8896–8912.
- (3) Selco, J. L.; Carrick, P. G. Jet Cooled Emission Spectra of Toluene and the Benzyl Radical. *J. Mol. Spectrosc.* **1989**, *137*, 13–23.

- (4) Fukushima, M.; Obi, K. Jet Spectroscopy and Excited-State Dynamics of Benzyl and Substituted Benzyl Radicals. *J. Chem. Phys.* **1990**, *93*, 8488–8497.
- (5) Im, H. S.; Bernstein, E. R. Mass Resolved Excitation Spectroscopy of Radicals - Benzyl and Phenylnitrene. *J. Chem. Phys.* **1991**, *95*, 6326–6329.
- (6) Fukushima, M.; Obi, K. Jet Spectroscopy of Benzyl and Benzyl- d_2 . *J. Chem. Phys.* **1992**, *96*, 4224–4232.
- (7) Orlandi, G.; Poggi, G.; Zerbetto, F. Vibronic Coupling in the Benzyl Radical. *Chem. Phys. Lett.* **1985**, *115*, 253–258.
- (8) Negri, F.; Orlandi, G.; Zerbetto, F.; Zgierski, M. Z. Quantum Chemical and Vibronic Analysis of the $1^2B_2 \leftrightarrow 1^2A_2$, 2^2B_2 Transition in Benzyl- h , and Benzyl- d_7 Radicals. *J. Chem. Phys.* **1990**, *93*, 600–608.
- (9) Yao, J.; Bernstein, E. R. On the Formation and Vibronic Spectroscopy of α -Halobenzyl Radicals in a Supersonic Expansion. *J. Chem. Phys.* **1997**, *107*, 3352–3362.
- (10) Lin, T.-Y. D.; Miller, T. A. Measurement of Methyl Torsional Barriers in the Ground and Excited States of the o -, m -, and p -Methylbenzyl Radicals. *J. Phys. Chem.* **1990**, *94*, 3554–3559.
- (11) Lee, G. W.; Ahn, H. G.; Kim, T. K.; Lee, S. K. Spectroscopic Evidence of α -Methylbenzyl Radical in the Gas Phase. *Chem. Phys. Lett.* **2008**, *465*, 193–196.
- (12) Tomer, J. L.; Spangler, L. H.; Pratt, D. W. Difference in the Methyl-Group Conformational Preferences of T_1 and S_1 Acetophenone - A Probe of the Orbital Character of Excited Electronic States. *J. Am. Chem. Soc.* **1988**, *110*, 1615–1617.
- (13) Murakami, J. I.; Ito, M.; Kaya, K. The Multi-Photon Ionization Spectrum of Toluene in a Supersonic Free Jet - Internal-Rotation of the Methyl-Group. *Chem. Phys. Lett.* **1981**, *80*, 203–206.
- (14) Breen, P. J.; Warren, J. A.; Bernstein, E. R.; Seeman, J. I. A Study of Nonrigid Aromatic-Molecules by Supersonic Molecular Jet Spectroscopy 0.1. Toluene and the Xylenes. *J. Chem. Phys.* **1987**, *87*, 1917–1926.
- (15) Parmenter, C. S. Vibrational-Energy Flow within Excited Electronic States of Large Molecules. *J. Phys. Chem.* **1982**, *86*, 1735–1750.
- (16) Moss, D. B.; Parmenter, C. S. Acceleration of Intramolecular Vibrational Redistribution of Methyl Internal-Rotation - A Chemical Timing Study of p -Fluorotoluene and p -Fluorotoluene- d_3 . *J. Chem. Phys.* **1993**, *98*, 6897–6905.
- (17) Diehl, J. W.; Finkbeiner, J. W.; Disanzo, F. P. Determination of Benzene, Toluene, Ethylbenzene, and Xylenes in Gasolines by Gas-Chromatography Deuterium-Isotope Dilution Fourier-Transform Infrared-Spectroscopy. *Anal. Chem.* **1993**, *65*, 2493–2496.
- (18) Hollas, J. M.; Ridley, T. The C_1 - C_α Torsional Potential Function in the Ground Electronic State of Styrene Obtained from the Single Vibronic Level Fluorescence and Other Spectra. *Chem. Phys. Lett.* **1980**, *75*, 94.
- (19) Schaefer, T.; Penner, G. H. Calculations of the C_1 - C_α Torsional Barrier in Styrene. Comparison with Experiment. *Chem. Phys. Lett.* **1985**, *114*, 526–528.
- (20) Bock, C. W.; Trachtman, M.; George, P. A. Molecular-Orbital Study of the Rotation About the C–C Bond in Styrene. *Chem. Phys.* **1985**, *93*, 431–443.
- (21) Syage, J. A.; Aladel, F.; Zewail, A. H. Jet-Cooled Styrene - Spectra and Isomerization. *Chem. Phys. Lett.* **1983**, *103*, 15–22.
- (22) Nunn, A. D. G.; Minns, R. S.; Spesyvtsev, R.; Bearpark, M. J.; Robb, M. A.; Fielding, H. H. Ultrafast Dynamics Through Conical Intersections and Intramolecular Vibrational Energy Redistribution in Styrene. *Phys. Chem. Chem. Phys.* **2010**, *12*, 15751–15759.
- (23) Sebree, J. A.; Kidwell, N. M.; Buchanan, E. G.; Zgierski, M. Z.; Zwier, T. S. Spectroscopy and Ionization Thresholds of p -Isoelectronic 1-Phenylallyl and Benzylallyl Resonance Stabilized Radicals. *Chem. Sci.* **2011**, *2*, 1746–1754.
- (24) Sebree, J. A.; Kidwell, N. M.; Selby, T. M.; Amberger, B. K.; McMahon, R. J.; Zwier, T. S. Photochemistry of Benzylallene: Ring-Closing Reactions to Form Naphthalene. *J. Am. Chem. Soc.* **2012**, *134*, 1153–1163.
- (25) Reilly, N. J.; Nakajima, M.; Gibson, B. A.; Schmidt, T. W.; Kable, S. H. Laser-Induced Fluorescence and Dispersed Fluorescence Spectroscopy of Jet-Cooled 1-Phenylpropargyl Radical. *J. Chem. Phys.* **2009**, *130*, 144313.
- (26) Sebree, J. A.; Kislov, V. V.; Mebel, A. M.; Zwier, T. S. Spectroscopic and Thermochemical Consequences of Site-Specific H-atom Addition to Naphthalene. *J. Phys. Chem. A* **2010**, *114*, 6255–6262.
- (27) Chalyavi, N.; Troy, T. P.; Nakajima, M.; Gibson, B. A.; Nauta, K.; Sharp, R. G.; Kable, S. H.; Schmidt, T. W. Excitation and Emission Spectra of Jet-Cooled Naphthylmethyl Radicals. *J. Phys. Chem. A* **2011**, *115*, 7959–7965.
- (28) Troy, T. P.; Chalyavi, N.; Menon, A. S.; O'Connor, G. D.; Fockel, B.; Nauta, K.; Radom, L.; Schmidt, T. W. The Spectroscopy and Thermochemistry of Phenylallyl Radical Chromophores. *Chem. Sci.* **2011**, *2*, 1755–1765.
- (29) Sears, T. J.; Johnson, P. M.; Jin, P.; Oatis, S. Infrared Laser Transient Absorption Spectroscopy of the Ethyl Radical. *J. Chem. Phys.* **1996**, *104*, 781–792.
- (30) Sears, T. J.; Johnson, P. M.; BeeBe-Wang, J. Infrared Spectrum of the CH_2 Out-of-Plane Fundamental of C_2H_5 . *J. Chem. Phys.* **1999**, *111*, 9213–9221.
- (31) Davis, S.; Uy, D.; Nesbitt, D. J. Laser Spectroscopy of Jet-Cooled Ethyl Radical: Infrared Studies in the CH_2 Stretch Manifold. *J. Chem. Phys.* **2000**, *112*, 1823–1834.
- (32) Haber, T.; Blair, A. C.; Nesbitt, D. J.; Schuder, M. D. CH Stretch/Internal Rotor Dynamics in Ethyl Radical: High-Resolution Spectroscopy in the CH_3 -Stretch Manifold. *J. Chem. Phys.* **2006**, *124*, 054316.
- (33) Raston, P. L.; Agarwal, J.; Turney, J. M.; Schaefer, H. F.; Doublerly, G. E. The Ethyl Radical in Superfluid Helium Nanodroplets: Rovibrational Spectroscopy and ab initio Computations. *J. Chem. Phys.* **2013**, *138*.
- (34) Frost, R. K.; Zavarin, G. S.; Zwier, T. S. Ultraviolet Photochemistry of Diacetylene - Metastable $C_4H_2^* + C_2H_2$ Reaction in Helium and Nitrogen. *J. Phys. Chem.* **1995**, *99*, 9408–9415.
- (35) Wiley, W. C.; McLaren, I. H. Time-of-Flight Mass Spectrometer with Improved Resolution. *Rev. Sci. Instrum.* **1955**, *26*, 1150–1157.
- (36) McCarthy, M. C.; Chen, W.; Travers, J.; Thaddeus, P. Microwave Spectra of 11 Polyyne Carbon Chains. *Astrophys. J., Suppl. Ser.* **2000**, *129*, 611–623.
- (37) Frisch, M. J. et al. *Gaussian 09*; Gaussian, Inc.: Wallingford, CT, 2009. The full citation is found in the Supporting Information.
- (38) Lee, C. T.; Yang, W. T.; Parr, R. G. Development of the Colle-Salvetti Correlation-Energy Formula into a Functional of the Electron Density. *Phys. Rev. B* **1988**, *37*, 785–789.
- (39) Becke, A. D. Density-Functional Thermochemistry. III. The Role of Exact Exchange. *J. Chem. Phys.* **1993**, *98*, 5648–5652.
- (40) Foster, J. P.; Weinhold, F. Natural Hybrid Orbitals. *J. Am. Chem. Soc.* **1980**, *102*, 7211–7218.
- (41) Reed, A. E.; Curtiss, L. A.; Weinhold, F. Intermolecular Interactions from a Natural Bond Orbital, Donor-Acceptor Viewpoint. *Chem. Rev.* **1988**, *88*, 899–926.
- (42) Sekino, H.; Bartlett, R. J. A Linear Response, Coupled-Cluster Theory for Excitation-Energy. *Int. J. Quantum Chem.* **1984**, *18*, 255–265.
- (43) Koch, H.; Jensen, H. J. A.; Jorgensen, P.; Helgaker, T. Excitation-Energies from the Coupled Cluster Singles and Doubles Linear Response Function (CCDlr) - Applications to Be, CH^+ , CO, and H_2O . *J. Chem. Phys.* **1990**, *93*, 3345–3350.
- (44) Stanton, J. F.; Bartlett, R. J. The Equation of Motion Coupled-Cluster Method. A Systematic Biorthogonal Approach to Molecular Excitation Energies, Transition Probabilities, and Excited State Properties. *J. Chem. Phys.* **1993**, *98*, 7029–7039.
- (45) Shao, Y. e. a. Advances in Methods and Algorithms in a Modern Quantum Chemistry Program Package. *Phys. Chem. Chem. Phys.* **2006**, *8*, 3172–3191.

- (46) Stanton, J. F.; Gauss, J. Analytic Energy Derivatives for Ionized States Described by the Equation-of-Motion Coupled-Cluster Method. *J. Chem. Phys.* **1994**, *101*, 8938–8944.
- (47) Stanton, J. F.; Gauss, J. A Simple Scheme for the Direct Calculation of Ionization Potentials with Coupled-Cluster Theory that Exploits Established Excitation Energy Methods. *J. Chem. Phys.* **1999**, *111*, 8785–8788.
- (48) Krishnan, R.; Binkley, J. S.; Seeger, R.; Pople, J. A. Self-Consistent Molecular Orbital Methods. XX. A Basis Set for Correlated Wave Functions. *J. Chem. Phys.* **1980**, *72*, 650–654.
- (49) Clark, T.; Chandrasekhar, J.; Spitznagel, G. W.; Schleyer, P. V. Efficient Diffuse Function-Augmented Basis Sets for Anion Calculations. III. The 3-21 + G Basis Set for First-Row Elements, Lithium to Fluorine. *J. Comput. Chem.* **1983**, *4*, 294–301.
- (50) Manohar, P. U.; Stanton, J. F.; Krylov, A. I. Perturbative Triples Correction for the Equation-of-Motion Coupled-Cluster Wave Functions with Single and Double Substitutions for Ionized States: Theory, Implementation, and Examples. *J. Chem. Phys.* **2009**, *131*, 114112.
- (51) Krylov, A. I. Equation-of-Motion Coupled-Cluster Methods for Open-Shell and Electronically Excited Species: The Hitchhiker's Guide to Fock Space. *Annu. Rev. Phys. Chem.* **2008**, *59*, 433–462.
- (52) Dunning, T. H. Gaussian Basis Sets for Use in Correlated Molecular Calculations. I. The Atoms Boron Through Neon and Hydrogen. *J. Chem. Phys.* **1989**, *90*, 1007–1023.
- (53) Woon, D. E.; Dunning, T. H. Gaussian Basis Sets for Use in Correlated Molecular Calculations. V. Core-Valence Basis Sets for Boron Through Neon. *J. Chem. Phys.* **1995**, *103*, 4572–4585.
- (54) Golubeva, A. A.; Pieniazek, P. A.; Krylov, A. I. A New Electronic Structure Method for Doublet States: Configuration Interaction in the Space of Ionized 1h and 2h1p Determinants. *J. Chem. Phys.* **2009**, *130*, 124113.
- (55) Slipchenko, L. V.; Krylov, A. I. Spin-Conserving and Spin-Flipping Equation-of-Motion Coupled-Cluster Method with Triple Excitations. *J. Chem. Phys.* **2005**, *123*, 84107.
- (56) Roos, B. O.; Taylor, P. R.; Siegbahn, P. E. M. A complete active space SCF method (CASSCF) using a density matrix formulated super-CI approach. *Chem. Phys.* **1980**, *48*, 157–173.
- (57) Nakano, H. Quasidegenerate perturbation theory with multi-configurational self-consistent-field reference functions. *J. Chem. Phys.* **1993**, *99*, 7983–7992.
- (58) Gordon, M. S.; Schmidt, M. W. In *Theory and Applications of Computational Chemistry*; Dykstra, C. E., Frenking, G., Kim, K. S., Scuseria, G. E., Eds.; Elsevier: New York, 2005.
- (59) Schmidt, M. W.; Baldridge, K. K.; Boatz, J. A.; Elbert, S. T.; Gordon, M. S.; Jensen, J. H.; Koseki, S.; Matsunaga, N.; Nguyen, K. A.; Su, S. J.; Windus, T. L.; Dupuis, M.; Montgomery, J. A. General Atomic and Molecular Electronic-Structure System. *J. Comput. Chem.* **1993**, *14*, 1347–1363.
- (60) Hehre, W. J.; Ditchfield, R.; Pople, J. A. Self-Consistent Molecular Orbital Methods. XII. Further Extensions of Gaussian-Type Basis Sets for Use in Molecular Orbital Studies of Organic Molecules. *J. Chem. Phys.* **1972**, *56*, 2257–2261.
- (61) Hariharan, P. C.; Pople, J. A. The Influence of Polarization Functions on Molecular Orbital Hydrogenation Energies. *Theor. Chim. Acta* **1973**, *28*, 213–222.
- (62) Raghavachari, K.; Trucks, G. W.; Pople, J. A.; Head-Gordon, M. A Fifth-Order Perturbation Comparison of Electron Correlation Theories. *Chem. Phys. Lett.* **1989**, *157*, 479–483.
- (63) Cossart-Magos, C.; Leach, S. Determination of the Symmetry of the First Excited Electronic State of Benzyl by Rotational Contour Analysis of Vibronic Bands of the Emission Spectra of C₆H₅CH₂, C₆H₅CD₂, and C₆D₅CD₂. *J. Chem. Phys.* **1971**, *56*, 1534–1545.
- (64) Heaven, M.; Dimauro, L.; Miller, T. A. Laser-Induced Fluorescence Spectra of Free-Jet Cooled Organic Free Radicals. Vinyloxy, Cyclopentadienyl, and Benzyl. *Chem. Phys. Lett.* **1983**, *95*, 347–351.
- (65) Bunker, P. R.; Jensen, P. *Molecular Symmetry and Spectroscopy*; 2nd ed.; NRC Research Press: Ottawa, Ontario, Canada, 1998.
- (66) Lewis, J. D.; Malloy, T. B.; Chao, T. H.; Laane, J. Periodic Potential Functions for Pseudorotation and Internal Rotation. *J. Mol. Struct.* **1972**, *12*, 427–449.
- (67) Pitzer, K. S. Energy Levels and Thermodynamic Functions for Molecules with Internal Rotation: II. Unsymmetrical Tops Attached to a Rigid Frame. *J. Chem. Phys.* **1946**, *14*, 239–243.
- (68) Hopkins, J. B.; Powers, D. E.; Smalley, R. E. Vibrational-Relaxation in Jet-Cooled Alkylbenzenes 0.1. Absorption-Spectra. *J. Chem. Phys.* **1980**, *72*, 5039–5048.
- (69) Plusquellic, D. F.; Suenram, R. D.; Mate, B.; Jensen, J. O.; Samuels, A. C. The Conformational Structures and Dipole Moments of Ethyl Sulfide in the Gas Phase. *J. Chem. Phys.* **2001**, *115*, 3057–3067.
- (70) Hopkins, J. B.; Powers, D. E.; Mukamel, S.; Smalley, R. E. Vibrational-Relaxation in Jet-Cooled Alkylbenzenes 0.2. Fluorescence-Spectra. *J. Chem. Phys.* **1980**, *72*, 5049–5061.
- (71) Richard, E. C.; Walker, R. A.; Weisshaar, J. C. Hindered Internal Rotation and Torsion-Vibrational Coupling in Ortho-Chlorotoluene (S₁) and Ortho-Chlorotoluene⁺ (D₀). *J. Chem. Phys.* **1996**, *104*, 4451–4469.
- (72) Okuyama, K.; Mikami, N.; Ito, M. Internal Rotation of the Methyl Group in the Electronically Excited State: o-, m-, and p-Fluorotoluene. *J. Phys. Chem.* **1985**, *89*, 5617–5625.
- (73) Hollas, J. M. *High Resolution Spectroscopy*; 2nd ed.; John Wiley & Sons: Chichester, England, 1998.
- (74) Watanabe, K. Ionization Potential of Some Molecules. *J. Chem. Phys.* **1957**, *26*.
- (75) Rice, J. E.; Handy, N. C.; Knowles, P. J. An MCSCF Study of the X²B₂, ²A₂ and 2²B₂ States of Benzyl. *J. Chem. Soc., Faraday Trans.* **1987**, *83*, 1643–1649.
- (76) Maurice, D.; Head-Gordon, M. On the Nature of Electronic Transitions in Radicals: An Extended Single Excitation Configuration Interaction Method. *J. Phys. Chem.* **1996**, *100*, 6131–6137.
- (77) Williams, S.; Zingher, E.; Weisshaar, J. C. B-X Vibronic Spectra and B-State Fluorescence Lifetimes of Methylvinyloxy Isomers. *J. Phys. Chem. A* **1998**, *102*, 2297–2301.
- (78) Williams, S.; Harding, L. B.; Stanton, J. F.; Weisshaar, J. C. Barrier to Methyl Internal Rotation of 1-Methylvinyloxy Radical in the X(2A⁺) and B(2A⁺) States: Experiment and Theory. *J. Phys. Chem. A* **2000**, *104*, 10131–10138.
- (79) Williams, S.; Harding, L. B.; Stanton, J. F.; Weisshaar, J. C. Barrier to Methyl Internal Rotation of cis and trans-Methylvinyloxy Radical in the X(2A⁺) and B(2A⁺) States: Experiment and Theory. *J. Phys. Chem. A* **2000**, *104*, 9906–9913.
- (80) Liu, S. B. Origin and Nature of Bond Rotation Barriers: A Unified View. *J. Phys. Chem. A* **2013**, *117*, 962–965.
- (81) Herschbach, D. R.; Krisher, L. C. Microwave Spectrum of CH₂DCH:CH₂ - Equilibrium Conformation of Propylene. *J. Chem. Phys.* **1958**, *28*, 728–729.
- (82) Hehre, W. J.; Pople, J. A.; Devaquet, A. J. P. Torsional Potentials of Methyl Rotors Attached to Polar Linkages. *J. Am. Chem. Soc.* **1976**, *98*, 664–668.
- (83) Wilson, J., E.B.; Decius, J. C.; Cross, P. C. *Molecular Vibrations*; Dover Publications, Inc.: Mineola, NY, 1955.

Influence of the intensity gradient upon HHG from free electrons scattered by an intense laser beam

Ankang Li · Jiaxiang Wang · Na Ren ·
Pingxiao Wang · Wenjun Zhu · Xiaoya Li ·
Ross Hoehn · Sabre Kais

Received: 13 August 2013 / Accepted: 11 October 2013
© Springer-Verlag Berlin Heidelberg 2014

Abstract When an electron is scattered by a tightly focused laser beam in vacuum, the intensity gradient is a critical factor to influence the electron dynamics. In this paper, we have further investigated its influence upon the electron high-harmonic generation (HHG) by treating the spacial gradient of the laser intensity as a ponderomotive potential. Based upon perturbative quantum electrodynamics calculations, it has been found that the main effect of the intensity gradient is the broadening of the originally line HHG spectra. A one-to-one relationship can be built between the beam width and the corresponding line width. Hence, this finding may provide us a promising way to

measure the beam width of intense lasers in experiments. In addition, for a laser pulse, we have also studied the different influences from transverse and longitudinal intensity gradients upon HHG.

1 Introduction

Since the availability of high-power lasers, high-harmonic generation (HHG) based upon nonlinear Compton scattering (NLCS) from free electrons in strong laser fields has drawn considerable attention [1–14]. This is not only because it is a fundamental non-perturbative laser-induced phenomena, but also because it is a prospective X-ray or gamma-ray source [15–18] with remarkable performances in terms of tunability. Moreover, the free-electron laser interaction is very clean without other uncontrollable physical processes such as ionizations and collisions, which happen in the interaction between lasers and atoms or plasmas. In recent years, the observation of NLCS in some experiments [19–22] also renew the interest in its theoretical study.

The main aim of this paper is to investigate how the effect of the laser intensity gradients change the radiation of free electron in strong laser field. It is well-known that there is a cycle-averaged force on a charged particle in a spatially inhomogeneous laser field. It is associated with a time-independent potential energy called ponderomotive potential, which is due to the laser intensity gradient in an oscillatory field. After the presence of such ponderomotive potential was first proposed in 1957 by Boot and Harvie [23, 24], it is well-known for the last four decades that the potential could have a significant effect on the matter interacting with the laser field, such as particle acceleration [25], trapping and cooling of the atoms [26],

A. Li · J. Wang (✉) · N. Ren
State Key Laboratory of Precision Spectroscopy, East China
Normal University, Shanghai 200062, China
e-mail: jxwang@phy.ecnu.edu.cn

P. Wang
Applied Ion Beam Physics Laboratory, Key Laboratory of the
Ministry
of Education, Shanghai, China

P. Wang
Department of Nuclear Science and Technology, Institute
of Modern Physics, Fudan University, Shanghai 200433, China

W. Zhu · X. Li
National Key Laboratory of Shock Wave and Detonation
Physics, Mianyang 621900, Sichuan, China

R. Hoehn · S. Kais
Departments of Chemistry and Physics, Purdue University,
West Lafayette, IN 47907, USA

R. Hoehn · S. Kais
Qatar Environment and Energy Research Institute,
Qatar Foundation, Doha, Qatar

high-field photoionization of atoms [27], self-focusing in plasma [28] and HHG [29, 30]. In the classical framework, the mechanical motion of electrons in a strong laser field will be changed if the ponderomotive potential is taken into account due to the limited spatial dimensions of the laser focus, which leads to the ponderomotive broadening of the radiation spectrum [29]. But, so far few works are done to study the role of the ponderomotive effects on the radiation spectrum based on a quantum theory [29, 30, 37].

To gain a clear idea of the influence by the laser intensity gradients on the HHG spectrum from free electrons in strong laser fields, we start from the scattering of the electron Volkov state by the ponderomotive potential of the laser beam. The corresponding cross section is calculated as a second-order quantum electrodynamics (QED) laser-assisted process similar to laser-assisted bremsstrahlung, where a charged particle scatters by the field of a nucleus in a background strong laser field [31–36].

For notations in this paper, the four-vector product is denoted by $a \cdot b = a^0 b^0 - \mathbf{a} \cdot \mathbf{b}$ and the Feynman dagger is $\bar{A} = \gamma \cdot A$. The Dirac adjoint is denoted by $\bar{u} = u^\dagger \gamma^0$ for a bispinor u and $\bar{F} = \gamma^0 F^\dagger \gamma^0$ for a matrix F .

The outline of this paper is the following. First, we will introduce the scattering model and derive the theoretical expression for the cross section of the electron radiation. Then, the numerical estimation of the cross section and the corresponding analyses will be provided in Sect. 3. Concluding remarks are reserved for Sect. 4.

2 Theoretical derivation of the scattering cross section

We begin by introducing our scattering mode: Consider there are two monochromatic laser pulse in space. The first one propagates along z axis, of which the duration is long enough and the field intensity so strong that it can be modeled by a background classical plane wave field, described by a four-dimension vector potential A^μ :

$$A^\mu = A_0[\delta \cos \phi \epsilon_1^\mu + (1 - \delta^2)^{1/2} \sin \phi \epsilon_2^\mu], \quad (1)$$

Here, with the phase factor $\phi = k \cdot x$, in which x is the position vector, and the four wave vector is related to $k^\mu = \frac{\omega_0}{c}(1, 0, 0, 1)$ with ω_0 denoting the wave propagation direction and laser frequency, respectively. The laser is circularly polarized for $\delta = 1/\sqrt{2}$ and linearly polarized for $\delta = 0, \pm 1$. We define two polarization vectors ϵ_1, ϵ_2 , satisfying $\epsilon_i \cdot k = 0$, $\epsilon_i \cdot \epsilon_j = \delta_{ij}$ ($i, j = 1, 2$). The laser intensity can be easily described by a dimensionless parameter $Q = eA_0/(mc^2)$, which is usually called laser intensity parameter. In the nonrelativistic regime, the

characteristic velocity and energy for an electron moving in such an electromagnetic field is $v \sim eA_0/(mc)$ and $E \sim e^2 A_0^2/(mc^2)$, so relativistic treatment is necessary if $v \sim c$ and $E \sim mc^2$ is satisfied. That is to say the motion of the electron will become relativistic for $Q \sim 1$. In the optical regime ($\hbar\omega \approx 1\text{eV}$), the corresponding laser intensity is about 10^{18}W/cm^2 for $Q \sim 1$, which has been achieved in the last decade.

The second field is a tightly focused laser pulse propagating opposite the first one, which can be described by the lowest-order axicon Gaussian fields with a envelop factor $g(\phi) = e^{(-\phi^2/(\Delta\phi))}$. It is far less intense than the first one (the intensity is described by another dimensionless parameter Q_G) but much rapidly oscillatory. The electron will be assumed to be moving with a momentum p in the direction perpendicular to z axis, say, x axis. When the electron is placed in the two laser wave field, it will be mainly driven by the longer-wavelength laser. The interaction of the electron with the plane wave laser will be treated exactly by introducing the well-known Volkov state. That is to say, the “dressed” electron will have an effective momentum $\Pi = p + \frac{e^2 A_0^2}{4c^2(p \cdot k)}$ with a corresponding effective mass $m' = m\sqrt{1 + \frac{Q^2}{2}}$. While the main effect of the Gaussian laser pulse on the electron can be described by an time-averaged potential in view of its low intensity and fast oscillation (here, we do not care about the high-frequency part of the radiation caused by the fast oscillation). We assume that the relativistic electron moves so fast that the envelop factor is almost time independent. The effective ponderomotive potential can be described by:

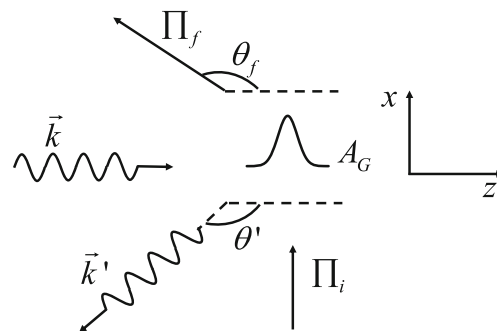


Fig. 1 The scattering geometry: the incoming electron with four momentum p_i have a 90° collision with a plane laser field while scattering by a time-independent ponderomotive potential A_G . The final electron with Π_f and the emitted photon with k' are projected onto the xz plane in this figure; θ_f and θ' denotes the scattering angle of the outgoing electron and the emitted photon, respectively

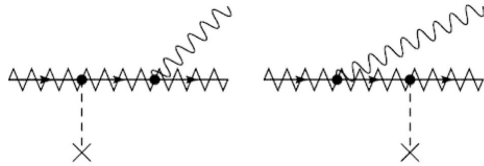


Fig. 2 Feynman diagrams describing laser-assisted bremsstrahlung. The laser-dressed electron and laser-dressed electron propagator are denoted by a zigzag line on top of the straight line. The Coulomb field photon is drawn as a dashed line, and the bremsstrahlung photon as a wavy line

$$U_p = \frac{mc^2}{4} Q_G^2 e^{-\frac{r_\perp^2}{b_0^2} - \frac{z^2}{b_1^2}} \quad (2)$$

The corresponding four-vector potential can be written as:

$$A_p^\mu = \frac{U_p}{e} \delta^{\mu 0} \quad (3)$$

where the Fourier-transformed pondermotive potential is given by:

$$A_p^\mu(\mathbf{q}) = \frac{mc^2 \pi^{3/2}}{4e} Q_G^2 b_0^2 b_1 \delta^{\mu 0} e^{-\frac{b_0^2}{4} q_\perp^2 - \frac{b_1^2}{4} q_z^2} \quad (4)$$

Here, \mathbf{r}_\perp and \mathbf{q}_\perp refers to the position and momentum in the plane perpendicular to the propagation direction, respectively, while z is related to the beam waist and is decided by the pulse duration. Considering the high-frequency character of the pulse, which means a small wavelength, the paraxial approximation of the laser pulse can be acceptable confidently. Since $Q_G \ll Q$, we will treat the pondermotive potential as perturbation. The whole scattering configuration can be seen in Fig. 1, and it can be described by two Feynman diagrams shown in Fig. 2.

It is obvious that the interaction of electron with the intense plane laser wave will lead to discrete lines at a given harmonic on the spectrum if the second weak pulse is absent. The scattering process is called laser-induced Compton scattering, or NLCS for its nonlinear nature, which has been widely studied since the invention of laser in 1960 [13–16]. The frequencies of the emitted harmonics are determined from the energy-momentum conservation laws, which involve both the incident electron condition and laser parameters. Here, we wonder the effect of the pondermotive potential on the discrete radiation spectrum.

In order to calculate the differential cross section of the second-order laser-assisted process, we begin by employing the well-known Volkov state to describe the initial and final electron state:

$$\psi_{p,r} = \frac{1}{\sqrt{V}} \sqrt{\frac{mc}{\Pi}} \zeta_{p,r}(x) u_r(p) \quad (5)$$

$$\zeta_p(x) = \left(1 + \frac{e\mathbf{k}\cdot\mathbf{A}}{2p\cdot\mathbf{k}}\right) e^{iS} \quad (6)$$

$$S = -\frac{\Pi\cdot x}{\hbar} - \frac{e^2 A_0^2}{8\hbar c^2 (p\cdot k)} (2\delta^2 - 1) \sin 2\phi + \frac{eA_0}{\hbar c (p\cdot k)} \times [\delta(p\cdot\epsilon_1) \sin \phi - (1 - \delta^2)^{1/2} (p\cdot\epsilon_2) \cos \phi]. \quad (7)$$

Here, $u_r(p)$ the free Dirac spinor. Here, we employ a box normalization with a normalization volume V .

Then, the corresponding transition amplitude can be written as:

$$S_{fi} = -\frac{e^2}{\hbar^2 c^2} \int d^4x d^4y \bar{\psi}_{p_f, r_f}(x) [A_c(x) iG(x-y) A_G(y) + A_G(x) iG(x-y) A_c(y)] \psi_{p_i, r_i}(y) \quad (8)$$

$A_c^\mu(x) = \sqrt{\frac{2\pi\hbar}{\omega}} \epsilon_\mu e^{ik\cdot x}$ stands for the four momentum of the emitted photon during the scattering process with ϵ_μ the photon polarization vector and $k' = \frac{\omega'}{c} (1, \mathbf{e}_{k'})$ the wave vector, respectively. As the previous work [34, 35], here, we use the Dirac-Volkov propagator instead of the free-electron propagator in view of the strong laser field:

$$iG(x-y) = -\int \frac{d^4p}{(2\pi\hbar)^3 (2\pi i)} \zeta_p(x) \frac{\not{p} + mc}{p^2 - m^2 c^2} \bar{\zeta}_p(y) \quad (9)$$

It has been proven [34] that the use of the Dirac-Volkov propagator is crucial to obtain correct numerical results in laser-modified QED processes.

Here, we take average on the initial electron spin (i.e., the electron is unpolarized) and sum over the both final electron spin and emitted photon polarization. The differential cross section is calculated with the formula:

$$d\tilde{\sigma} = \frac{1}{2JT} \sum_{r_i, r_f, \epsilon_c} |S_{fi}|^2 \frac{V d^3\Pi_f d^3k'}{(2\pi\hbar)^3 (2\pi)^3}. \quad (10)$$

Here, T is the long observation time and $J = \frac{c}{V} \Pi_f$ stands for the incoming particle flux. We have $d^3\Pi_f = |\Pi_f|^2 d\Omega_f = |\Pi_f|^2 \sin\theta_f d\theta_f d\varphi_f$, $d^3k' = \frac{\omega'^2}{c^2} d\Omega' = \frac{\omega'^2}{c^2} \sin\theta' d\theta' d\varphi'$, where Ω' and Ω_f stands for the solid angle of the emitted photon and electron, respectively. After a long but straightforward deriving process, we finally write down the differential cross section as:

$$\frac{d\tilde{\sigma}}{d\omega' d\Omega' d\Omega_f} = \frac{\alpha Q_G^4 b_0^4}{8(4\pi)^4 c^2} \left(\frac{m^2 c^2}{\hbar^2} b_1^2\right) \times \sum_{n, \epsilon_c} \frac{|\Pi_f|}{|\Pi_i|} e^{-\frac{b_0^2}{4} q_\perp^2 - \frac{b_1^2}{4} q_z^2} Tr[\bar{R}_{f_i, n}(p_f + mc) R_{f_i, n}(p_i + mc)] \quad (11)$$

where:

$$R_{fi,n} = \sum_s M_{-n-s}(\Pi_f, \Pi, \not{\epsilon}_c, \eta_{\Pi, \Pi_f}^1, \eta_{\Pi, \Pi_f}^2) \frac{i}{\not{p} - mc} \bar{M}_{-s}(\Pi_i, \Pi, \gamma^0, \eta_{\Pi, \Pi_i}^1, \eta_{\Pi, \Pi_i}^2) + \sum_{s'} M_{-n-s'}(\Pi_f, \Pi', \gamma^0, \eta_{\Pi', \Pi_f}^1, \eta_{\Pi', \Pi_f}^2) \frac{i}{\not{p}' - mc} \bar{M}_{-s'}(\Pi_i, \Pi', \not{\epsilon}_c, \eta_{\Pi', \Pi_i}^1, \eta_{\Pi', \Pi_i}^2) \tag{12}$$

With the argument is defined as:

$$\eta_{p_1, p_2}^1 = \frac{eA_0}{\hbar c} \delta \left[\frac{p_2 \cdot \epsilon_1}{k \cdot p_2} - \frac{p_1 \cdot \epsilon_1}{k \cdot p_1} \right] \eta_{p_1, p_2}^2 = -\frac{eA_0}{\hbar c} (1 - \delta^2)^{1/2} \left[\frac{p_2 \cdot \epsilon_1}{k \cdot p_2} - \frac{p_1 \cdot \epsilon_1}{k \cdot p_1} \right] \tag{13}$$

Π, Π' is the four momentum of the intermediate electron in the Feynman diagrams shown in Fig. 2. They are determined by the conservation law, together with the four momentum q transfer from the ponderomotive potential, which is given by the corresponding functions during the calculation process:

$$\begin{aligned} \Pi &= \pi_f - (n + s)\hbar k + \hbar k' \\ \Pi' &= \pi_i - s\hbar k - \hbar k' \\ \hbar q &= \pi_f - \pi_i + \hbar k' - n\hbar k \end{aligned} \tag{14}$$

M is a 4×4 matrix with five arguments:

$$\begin{aligned} M_s(p_1, p_2, F, \eta_{p_1, p_2}^1, \eta_{p_1, p_2}^2) &= \left[F + \frac{e^2 A_0^2}{8c^2} \frac{\not{k} F \not{k}}{(p_i \cdot k)(p_2 \cdot k)} \right] G_s^0(\alpha, \beta, \varphi) \\ &+ \frac{eA_0}{2c} \delta \left[\frac{\not{\epsilon}_1 \not{k} F}{(p_1 \cdot k)} + \frac{F \not{k} \not{\epsilon}_1}{(p_2 \cdot k)} \right] G_s^1(\alpha, \beta, \varphi) \\ &+ \frac{eA_0}{2c} (1 - \delta^2)^{1/2} \left[\frac{\not{\epsilon}_2 \not{k} F}{(p_1 \cdot k)} + \frac{F \not{k} \not{\epsilon}_2}{(p_2 \cdot k)} \right] G_s^2(\alpha, \beta, \varphi) \\ &+ \left(\delta^2 - \frac{1}{2} \right) \frac{e^2 A_0^2}{4c^2} \frac{\not{k} F \not{k}}{(p_i \cdot k)(p_2 \cdot k)} G_s^3(\alpha, \beta, \varphi) \end{aligned} \tag{15}$$

The generalized Bessel functions are given by:

$$\begin{aligned} G_s^0(\alpha, \beta, \varphi) &= \sum_n J_{2n-s}(\alpha) J_n(\beta) e^{i(s-2n)\varphi}, \\ G_s^1(\alpha, \beta, \varphi) &= \frac{1}{2} (G_{s+1}^0(\alpha, \beta, \varphi) + G_{s-1}^0(\alpha, \beta, \varphi)), \\ G_s^2(\alpha, \beta, \varphi) &= \frac{1}{2i} (G_{s+1}^0(\alpha, \beta, \varphi) - G_{s-1}^0(\alpha, \beta, \varphi)), \\ G_s^3(\alpha, \beta, \varphi) &= \frac{1}{2} (G_{s+2}^0(\alpha, \beta, \varphi) + G_{s-2}^0(\alpha, \beta, \varphi)). \end{aligned} \tag{16}$$

With the corresponding argument:

$$\begin{aligned} \alpha &= [(\eta_{p_1, p_2}^1)^2 + (\eta_{p_1, p_2}^2)^2]^{1/2} \\ \beta &= \frac{Qm^2 c^2}{8\hbar} (2\delta - 1) \left(\frac{1}{k \cdot p_1} - \frac{1}{k \cdot p_2} \right) \\ \varphi &= \arctan \left(-\frac{\eta_{p_1, p_2}^2}{\eta_{p_1, p_2}^1} \right) \end{aligned} \tag{17}$$

The above differential cross section is related to the spontaneous photon in the frequency interval $d\omega'$ within the solid angle Ω' and the final electron within the solid angle Ω_f . But it is difficult to detect the photon and electron in the same time during an actual experiment. So we integrate the differential cross section over the scattering electron direction, by which leads to the doubly differential cross section only differential in the direction of the radiated photon and its frequency:

$$\frac{d\sigma}{d\omega' d\Omega'} = \int \frac{d\tilde{\sigma}}{d\omega' d\Omega' d\Omega_f} d\Omega_f \tag{18}$$

As one of the characteristic feature of a second-order process, the resonance will happen when the intermediate electron fall within the mass shell. The physical interpretation, according to Roshchupkin [36], may be that the considered second-order process effectively reduces to two sequential first-order processes under certain resonance condition. In the paper, the two sequential lower processes are NLCS and static ponderomotive potential scattering, respectively. The corresponding resonance condition may be written as $\Pi^2 = m'^2 c^2$ or $\Pi'^2 = m'^2 c^2$. When resonance occurs, the scattering cross section will be divergent, which indicates that the perturbation method is not applicable in such situation. To avoid the problem, one has to introduce a small imaginary part of the mass which results from the high radiative correction, i.e., the self-energy of the laser-dressed electron, which is determined by the total probability of the Compton scattering in a laser wave $W_c(k \cdot p)$: $\Gamma_m(k \cdot p) = \frac{\Pi^0}{2m} W_c(k \cdot p)$. Then, the shifted propagator reads:

$$\begin{aligned} &\frac{1}{p - mc} \\ &= \frac{\Pi + m'c}{\Pi^2 - m'^2 c^2 - i \frac{m}{\Gamma_m^0} (\hbar\omega' - (n + s)\hbar\omega_0) \Gamma_m(k \cdot \Pi_f) + im\Gamma_m(\hbar k \cdot k')} \\ &\frac{1}{p' - mc} \\ &= \frac{\Pi' + m'c}{\Pi'^2 - m'^2 c^2 + i \frac{m}{\Gamma_m^0} (\hbar\omega' - s\hbar\omega_0) \Gamma_m(k \cdot \Pi_i) - im\Gamma_m(\hbar k \cdot k')} \end{aligned} \tag{19}$$

The inclusion of the imaginary part of the electron mass eliminates the resonance singularity, which enable us to evaluate the cross section numerically. Then, the resonance peak altitude is determined by the lifetime of the immediate electron. Actually, the calculation of Γ_m has been discussed in many papers, and we can easily obtain the imaginary mass by taking advantage of the corresponding results of our previous study.

3 Numerical results

In this section, we will present the numerical results of the differential cross section referring to the case of 90° laser–electron interaction geometry shown in Fig. 1. We consider the plane wave laser to be circularly polarized with a frequency of $\omega = 1.17$ eV and the dimensionless parameter $Q = 17.8$, which is related to a laser intensity of 7.58×10^{22} W/cm². It should be emphasized that the numerical results in our presentation are more exploratory than systematic since we shall focus on the influence of ponderomotive potential due to the intensity gradients on the photon radiation. First, we start with the results for a tightly focused laser pulse with the parameters $b_0 = 5$ μm , $b_1 = 100$ μm , which means the pulse duration is very long (i.e., for a pulse with wavelength 0.1 μm , the duration is about 0.3 ps). The corresponding differential cross section of the radiated photon for an emission angle $\theta' = 1^\circ$ is

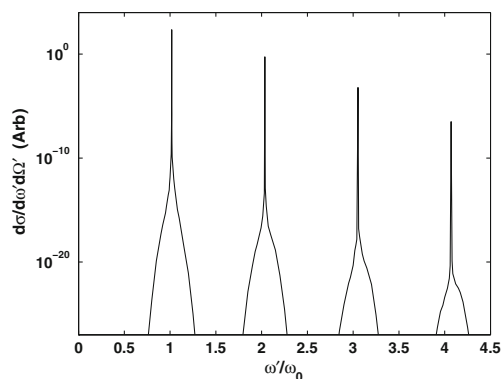


Fig. 3 The cross section for the low-order harmonics at emission angle $\theta' = 1^\circ$. Here, we consider an electron with initial energy 5 MeV collide with a circularly polarized laser with intensity parameter $Q = 17.8$ and is scattered by an effective ponderomotive potential for a 90° geometry. The ponderomotive potential is characterized by two parameter: $b_0 = 5$ μm , $b_1 = 100$ μm , describing the beam waist size and duration of the tightly focused laser pulse, respectively

shown in Fig. 3. As expected, high harmonics are generated and the positions of the resonances located in the spectrum coincide with those for NLCS. This is due to the fact that the resonant second-order process can effectively reduce to two sequent lower-order processes as mentioned before while the mechanism responsible for radiation of photons is the NLCS process. Furthermore, the main contribution of the cross section comes from $q \approx 0$ at a resonance, which means there is nearly no momentum transfer between the electron and the ponderomotive potential. It is easy to find that the main influence due to the ponderomotive potential is the broadened spectrum compared with that of NLCS, which is in accordance with the conclusion based on a classical theory [30]. The magnitude of the spectrum drops fast when the energy of photon is away from resonance. From a mathematical point of view, that is because the differential cross section is subject to an exponential decay with respect to the transfer momentum q . So the spectrum broadening effects is determined both the parameter b_0 and b_1 , or the pulse duration and the beam waist size.

Now, we proceed to investigate how the broadening effect depends on the laser pulse duration and the beam waist size. In Fig. 4, we compare the spectrum of fundamental harmonics for different beam waist size with same pulse duration. The cross section with $b_0 = 5$ μm is denoted by full line, whereas the dotted-dashed line denote the cross section with $b_0 = 10$ μm . Here, the magnitude of the cross section near resonance is a little larger for a broader beam waist size. This is probably because a laser with certain intensity has a great energy with the increase in the beam waist size. We can also see from the expression (11) that the differential cross section is proportional to the quartic of b_0 . But the peak falls off much more quickly for a larger beam waist size. This can be understood by

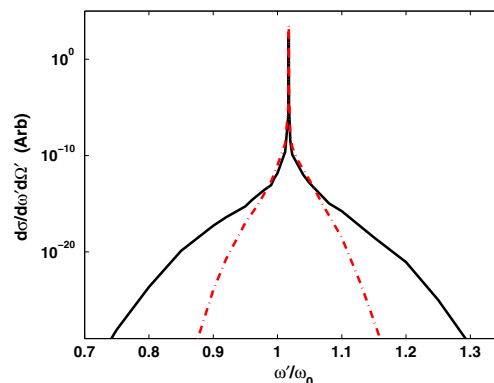


Fig. 4 The cross section for the fundamental harmonic at emission angle $\theta' = 1^\circ$. The condition is same with Fig. 3 except the parameter b_0 : 5 μm for full line and 10 μm for dot-dashed line

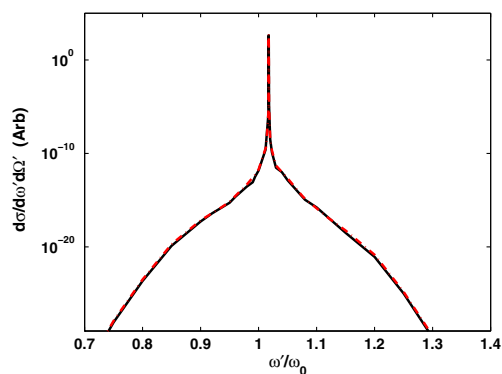


Fig. 5 The cross section for the fundamental harmonic at emission angle $\theta' = 1^\circ$. The condition is same with Fig. 3 except the parameter b_1 : $b_1 = 100 \mu\text{m}$ for full line and $b_1 = 150 \mu\text{m}$ for dot-dashed line

considering that the differential cross section is determined exponentially by b_0 . The physical interpretation may be that the large beam waist leads to a less field gradient, which means a small ponderomotive potential effect. When the beam waist is so large that we can neglect the spatial gradient if we consider the interaction of the electron with laser field near its focus place, there will be almost no ponderomotive broadening at all. In the following, we shall refer to the spectra of different laser pulse by changing the parameter b_1 , as shown in Fig. 5. The difference is so small that it can be hardly visible. We thus find that the pulse duration plays only a minor role in the spectrum. That is probably because there is far less momentum transfer from the electron onto the ponderomotive potential in the laser propagation direction (i.e., $q_z^2 \approx 0 \ll q_\perp^2$) for a 90° interaction geometry. Hence, there is almost no ponderomotive potential scattering in this direction.

Finally, we compare the results of different laser intensity of the circularly polarized plane wave field. The corresponding spectra are displayed in Fig. 6. It shows that the radiation for the plane wave field $Q = 5$ (corresponds to a intensity of $3 \times 10^{19} \text{W/cm}^2$) is several magnitudes smaller than that for $Q = 17.8$ (corresponds to a intensity of $7.58 \times 10^{20} \text{W/cm}^2$). But the broadening width of the spectra is similar for two different laser strengths. It confirmed the conclusion that the broadening effect has almost nothing to do with the plane wave field, but caused by the ponderomotive potential.

4 Summary

In this paper, we study the role of the field intensity gradients on the radiation spectrum emitting from the electron

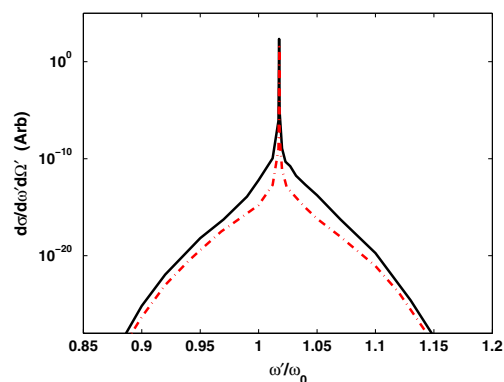


Fig. 6 The cross section for the fundamental harmonic at emission angle $\theta' = 1^\circ$. The condition is same with Fig. 3 except the intensity of the plane wave laser: $Q = 17.8(7.58 \times 10^{20} \text{W/cm}^2)$ for full line and $Q = 5(3 \times 10^{19} \text{W/cm}^2)$ for dot-dashed line

in the laser field. The whole scattering process is calculated as a laser-modified second-order QED process with resonances addressed. Consequently, it shows that the spectrum is broadening due to the ponderomotive effects compared with that of NLCS, with the positions of the resonance peak corresponding to the discrete harmonic frequencies of NLCS. Because the broadening of the spectrum line contains important information about the laser intensity gradient, it might provide us a feasible way to measure the width of the intense laser beam. In addition, the broadening effect is determined far more by the beam waist size than the pulse duration for the case of 90° incidence scattering geometry. Since the parameters of the corresponding laser field is readily accessible in the lab, it is hoped that these results could be submitted to the experiment test in the near future.

Acknowledgments This work is supported by the National Natural Science Foundation of China under Grant Nos. 10974056 and 11274117. One of the authors, Wenjun Zhu, thanks the support by the Science and Technology Foundation of National Key Laboratory of Shock Wave and Detonation Physics (Grant No. 077110).

References

1. L.S. Brown, T.W.B. Kibble, Phys. Rev. **133**, 3 (1964)
2. Z. Fried, J.H. Eberly, Phys. Rev. **136**, B871 (1964)
3. E.S. Sarachik, G.T. Schappert, Phys. Rev. D **1**, 10 (1970)
4. Y.I. Salamin, F.H.M. Faisal, Phys. Rev. A **54**, 4383 (1996)
5. Y.I. Salamin, F.H.M. Faisal, Phys. Rev. A **55**, 3678 (1997)
6. Y.I. Salamin, F.H.M. Faisal, Phys. Rev. A **55**, 3964 (1997)
7. Y.I. Salamin, F.H.M. Faisal, J. Phys. B **31**, 1319 (1998)
8. C. Harvey, T. Heinzl, A. Ilderton, Phys. Rev. A **79**, 063407 (2009)
9. P. Panek, Phys. Rev. A **65**, 022712 (2002)

10. P. Panek, *Phys. Rev. A* **65**, 033408 (2002)
11. D.Y. Ivanov, G.L. Kotkin, V.G. Serbo, *Eur. Phys. J. C* **36**, 127 (2004)
12. M. Boca, V. Florescu, *Phys. Rev. A* **80**, 053403 (2009)
13. T. Heinzl, D. Seipt, B. Kampfer, *Phys. Rev. A* **81**, 022125 (2010)
14. F. Mackenroth, A. Di Piazza, *Phys. Rev. A* **83**, 032106 (2011)
15. R.W. Schoenlein, W.P. Leemans, A.H. Chin, P. Volfbeyn, *Science* **274**, 236 (1996)
16. R.W. Schoenlein, W.P. Leemans, A.H. Chin, P. Volfbeyn, *Phys. Rev. Lett.* **77**, 4182 (1996)
17. P.F. Lan, P.X. Lu, W. Cao, X.L. Wang, *Phys. Rev. E* **72**, 066501 (2005)
18. P. Paneka, J.Z. Kaminskia, F. Ehlötzkyb, *Opt. Commun.* **213**, 121 (2002)
19. C. Bula et al., *Phys. Rev. Lett.* **76**, 3116 (1996)
20. C. Bamber et al., *Phys. Rev. D* **60**, 092004 (1999)
21. T. Kumita et al., *Laser Phys.* **16**, 267 (2006)
22. M. Inuma et al., *Phys. Lett. A* **346**, 255 (2005)
23. H.A.H. Boot, R.B.R.-S. Harvie, *Nature* **180**, 1187 (1957)
24. T.W.B. Kibble, *Phys. Rev. Lett.* **16**, 1966 (1954)
25. Y.I. Salamin, C.H. Keitel, *Phys. Rev. Lett.* **88**, 095005 (2002)
26. F. Dierich, E. Peick, J.M. Chen, W. Quint, H. Walther, *Phys. Rev. Lett.* **79**, 2931 (1987)
27. E. Wells, I. Ben-Itzhak, R.R. Jones, *Phys. Rev. Lett.* **93**, 023001 (2002)
28. T. Afshar-rad, L.A. Gizzi, M. Desselberger, F. Khattak, *Phys. Rev. Lett.* **86**, 942 (1992)
29. G.A. Krafft, *Phys. Rev. Lett.* **92**, 204802 (2004)
30. G.A. Krafft, *Phys. Rev. E* **72**, 056502 (2005)
31. S.P. Roshchupkin, *J. Nucl. Phys.* **41**, 1244 (1985)
32. S.P. Roshchupkin, *Laser Phys.* **6**, 837 (1996)
33. S.P. Roshchupkin, *Laser Phys.* **12**, 498 (2002)
34. E. Lotstedt, U.D. Jentschura, C.H. Keitel, *Phys. Rev. Lett.* **98**, 043002 (2007)
35. S. Schnez, E. Lotstedt, U.D. Jentschura, C.H. Keitel, *Phys. Rev. A* **75**, 053412 (2007)
36. A.A. Lebed, S.P. Roshchupkin, *Phys. Rev. A* **83**, 033413 (2009)
37. F.V. Hartemann, S.S.Q. Wu, *Phys. Rev. Lett.* **111**, 044801 (2013)

Using Quantum Games To Teach Quantum Mechanics, Part 1

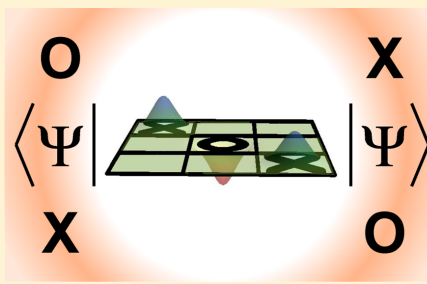
Ross D. Hoehn,^{*,†} Nick Mack,[†] and Sabre Kais^{†,‡}

[†]Department of Chemistry and [‡]Department of Physics, Purdue University, West Lafayette, Indiana 47907, United States

Supporting Information

ABSTRACT: The learning of quantum mechanics is contingent upon an understanding of the physical significance of the mathematics that one must perform. Concepts such as normalization, superposition, interference, probability amplitude, and entanglement can prove challenging for the beginning student. Several class activities that use a nonclassical version of tic-tac-toe are described to introduce several topics in an undergraduate quantum mechanics course. Quantum tic-tac-toe (QTTT) is a quantum analogue of classical tic-tac-toe (CTTT) and can be used to demonstrate the use of superposition in movement, qualitative (and later quantitative) displays of entanglement, and state collapse due to observation. QTTT can be used to aid student understanding in several other topics with the aid of proper discussion.

KEYWORDS: First-Year Undergraduate/General, High School/Introductory Chemistry, Upper-Division Undergraduate, Physical Chemistry, Humor/Puzzles/Games, Hands-On Learning/Manipulatives, Quantum Chemistry, Student-Centered Learning



Classical mechanics, whose approach was developed based on Newton's new mathematics, was contemporaneously formulated alongside calculus. Both topics moved from academic investigation into undergraduate lecture halls, and in the case of Newtonian mechanics, earlier still, with its concepts being introduced prior to high school. Quantum mechanics, developed in the 20th century, was required to adequately describe such experimental phenomena as black-body radiation, the photoelectric effect, and the atomic spectrum of hydrogen. The development of quantum mechanics has led to description of phenomena such as the superposition principle, the ability of an unobserved quantum object to exist in a superposition of multiple states simultaneously; entanglement, spooky action at a distance where the state of one system affects that of another without a direct observable relationship connecting them; and interference, as matter exists in both particle and waveform within quantum theory, matter interactions present wave phenomenon such as diffraction and the properties of constructive and destructive matter–wave addition. Just as a rudimentary understanding, at minimum, of classical mechanics became necessary for so many fields, an introduction into the concepts of quantum mechanics is of growing importance.

A student's first excursion into quantum mechanics can be both overwhelming and daunting, even to an upper-division science student. Understanding such concepts as wave functions, overlap integrals, and probability amplitudes are vital in mastering the subsequent material within the course. A typical first semester course in quantum mechanics focuses on the Schrödinger picture and equation.^{1–3} Herein we present several activities using quantum tic-tac-toe (QTTT), which is a quantum analogue of classical tic-tac-toe (CTTT), presented by

Allen Goff,^{4–6} as a means of introducing and enforcing early topics in an introductory quantum mechanics course. The activities allow for introduction and discussion of probability amplitude, probability density, normalization, overlap, the inner product, and separability of states. It is the belief of the authors that QTTT can be used as an approachable, fun, and intuitive means of introducing these topics. It is the hope of the authors that this tool could act as a companion throughout instruction; after the students have been taught the game, the instructor can use it as a stepping-stone to new topics and as an avenue for intuitive activities.

The activities described, as well as other similar activities, have been used to assist the understanding of various audiences in anything from a brief understanding of concepts necessary to quantum computing to furthering a student's understanding of topics in their quantum mechanics classroom. The bulk of the material was used as assignments and Supporting Information in an undergraduate quantum mechanics classroom to great avail with students who did not grasp some early concepts within the course.

PHYSICAL CONCEPTS AND GAME PLAY

Board

The tic-tac-toe board is square and is divided into nine square subspaces. These subspaces will be referred to as principal squares and will each carry a number to denote the particular square being referenced. The numbering pattern of the principal squares on the board is shown in Figure 1. Prior to discussing the game play, some vocabulary and concepts are

Published: January 29, 2014

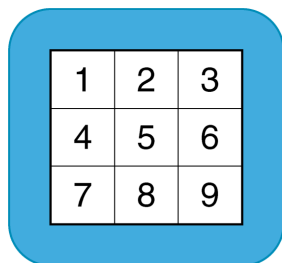


Figure 1. The layout of the game board for either classical or quantum tic-tac-toe. This figure also displays the enumeration scheme that is used throughout this paper.

introduced. The following four elements are underlying physical concepts that are necessary for game play and thus their use is weaved within the description of the game.

Spooky Marker. Named after Einstein's reference to entanglement and hidden variable interactions as "spooky action at a distance".⁷ This is a direct consequence to the system being completely described through a finite number of basis functions of an observable. A coupled pair of electrons exist within a 0-spin state; that is to say that the wave function of the pair is of the form: $\psi = 1/\sqrt{2}(|\uparrow\downarrow\rangle + |\downarrow\uparrow\rangle)$. If one observes the state of a single electron within the pair, say it is in the up-state, that observer incidentally knows the state of the other spin within the pair. Like CTTT markers, the spooky marker represents a single move of a single player during one turn, yet a spooky marker exists within two separate principal squares simultaneously.

Superposition. As players have placed a pair of spooky markers that represents their move for that turn, this move can be said to exist as a superposition of the states (board positions) in which it may be realized. If player one, referred to as Alice, places spooky markers for her first move into squares 1 and 5, then the state of that move is the superposition of the two states: square 1 and square 5. All player moves within QTTT are superposition moves. A typical teaching example of this is the superposition of spins separated through observation in the Stern–Gerlach^{8–10} experiments, which are typically discussed in introductory quantum mechanics courses. A further example, to which the students may have already been exposed, is the superposition of ammonia states by tunneling; the students may have discussed this already in their organic chemistry course with reference to nitrogen inversions¹¹ and the topic can be expounded through a discussion of the MASER problem.¹²

Cyclic Entanglement. Entanglement is the correlation between parts of a system, induced through an interaction and maintained in separation, which is independent of factors such as position and momentum.¹³ In QTTT this would consist of a group of spooky markers whose board positions are all self-referencing; as an example, Alice's first move (X_1) exists in both squares 1 and square 5; the second player's, referred to as Bob, first move (O_2) exists both within square 5 and square 7; and Alice's second move (X_3) is within both square 7 and square 1. In this way, the possible states of these moves are dependent upon each other in a similar fashion as to the spin states of paired electrons. The cyclic reference here is that X_1 shares principal square 1 with X_3 , X_3 shares principal square 7 with O_2 , and finally O_2 shares principal square 5 with X_1 . This series of

moves is shown in Figure 2 and will be made clearer in a sample game.

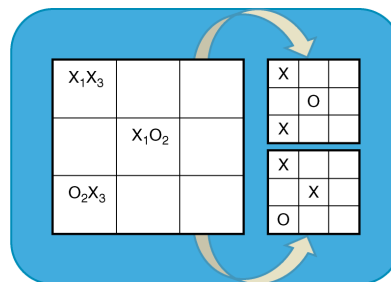


Figure 2. The effect of "measurement" on the system of cyclic entanglement can yield, at minimum, a pair of classical states corresponding to the state in which X_3 was observed.

State Collapse. A quantum system may exist in a superposition of several states. Only one subordinate state is observed when the state of the system is measured. An example of this would be a doublet spin system; the state of the single electron would be a superposition of up-spin and down-spin, yet when observed, a single electron will present only either an up-spin or a down-spin state. When a state collapse occurs through observation within the game, spooky markers collapse into CTTT marks.

General Structure of the Game

The general structure of the game is similar to that of CTTT. The few caveats and expansions to the rules can be most easily fleshed-out through an example game. Game play begins as Alice places her first pair of spooky markers on the board; any such move within the game will be denoted by $|\psi_i^\eta\rangle_j$, where η represents the player to whom the marker belongs and will thus take on the values X or O, i denotes the turn when this marker was placed, and j is the location on the board where the marker was placed. She places her markers in principal squares 1 and 5. This means that her first move, $|\psi_1^X\rangle$, is a super position with the form: $|\psi_1^X\rangle = 1/\sqrt{2}(|\varphi_1^X\rangle_1 + |\varphi_5^X\rangle_5)$. Let us now have Bob place his markers in principal squares 5 and 7; unlike the classical tic-tac-toe game, the placement of a spooky marker in QTTT does not prevent either player from placing subsequent markers in a particular square. Alice retorts with markers in principal squares 7 and 1. With this last move, our game board is now consistent with that in Figure 2. It can now be seen that the state of each of the spooky markers is a linear combination of the two squares that it occupies and each position within this linear combination is a position within a linear combination describing another spooky marker. In Figure 2 it can now be seen that we have generated a cyclic entanglement between markers placed for $|\psi_1^X\rangle$, $|\psi_2^O\rangle$ and $|\psi_3^X\rangle$ through their possible states (squares 1, 5, and 7).

As a cyclic entanglement has been generated, it is time for a player to make an observation on the system that will cause a state collapse of our spooky markers into classical markers. As Alice's last move was that which sealed the cyclic entanglement, it will be Bob's right to decide in which way the states will collapse; this reciprocation of closure and observation was developed in hope to generate a fair game, although it was an ad hoc rule implemented for the sake of fair game play (a more

quantum mechanically accurate rule would be flipping a coin to decide the collapse). When an observation is made on the system, the states of the markers involved with the cyclic entanglement will collapse. Unlike a spooky marker, when a classical marker occupies a board position, no other marker (neither classical nor quantum) may occupy that position.

The two possible pathways that an observation could take are also shown in Figure 2. We will first state completely the logic of the upper path and then that of the lower path. If Bob chooses that Alice's most recent move, $|\varphi_3^x\rangle = 1/\sqrt{2}(|\varphi_3^x\rangle_1 + |\varphi_3^x\rangle_7)$, should be observed in square 7, this would imply that the only state that $|\varphi_2^o\rangle = 1/\sqrt{2}(|\varphi_2^o\rangle_5 + |\varphi_2^o\rangle_7)$ could take is that of square 5 and thus the only state $|\varphi_1^x\rangle = 1/\sqrt{2}(|\varphi_1^x\rangle_1 + |\varphi_1^x\rangle_5)$ can manifest is that of square 1; all this due to the fact that this observation turns these spooky markers into classical markers and thus exclusively occupy their observed site.

If Bob had chosen the other path, ψ_3^x would collapse in square 1 forcing ψ_2^o in square 1 and finally ψ_1^o in square 5. The lower board is that which would occur if Bob chose to observe ψ_3^o in square 1. It should also be noted that if a situation arises consistent with Figure 3, there exist a pair (or more) or spooky

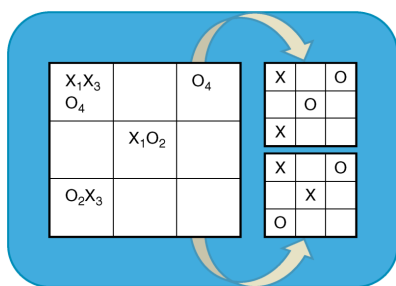


Figure 3. The “measurement” on a specific board can have observable ramifications even for game pieces that are not members of the cyclic entanglement; these pieces are referred to as dangling markers.

markers that are entangled with the cycle without both of its states being enveloped by the cycle. In these cases, the observation will also effect a collapse upon the “dangling” marker; the subsequent collapse of dangling markers can also be seen in Figure 3.

Game play will continue in this manner until one of the players has generated a “three-in-a-row” consisting of only classical markers. It is possible that two players will simultaneously win the game through the same observation. When this occurs, the player with the most recent Spooky Makers generating one of their winning classical markers loses; which is, in a way, to say “first in, first out”. When playing a volley of games, Goff^{4–6} does propose that the winning player during a simultaneous victory be awarded 1 point and the loser 1/2 point.

■ ACTIVITY

We present the following work as an instructor-guided inquiry activity^{14,15} with the students divided into groups of two. We present specific board examples as a means of discussion and instructional guidance examples, as introductory courses have been shown to benefit from strong instructor guidance.¹⁶ A more natural experience would be allowing the students (postinstruction on the rules and teaching a specific

phenomenon) to play the game and come across these phenomena on their own in an inductive learning style similar to a lab exercise.^{17–20} QTTT could also be used as a continuing-themed homework exercise as it can be used to exemplify many of the introductory topics in quantum mechanics.

Introducing the game rules and running a small example game can take up to 15 min, whereas the average time to play a single game is roughly 4 min. In the experience of these authors, the use of quantum tic-tac-toe lowers the level of fear associated with introducing these early concepts, as it both builds student confidence and gives them a foothold on the material through a familiar mechanism. Students took to the game enthusiastically and divorced of the quantum mechanical concepts, learning the game rules comes quickly. The most difficult part in learning the game is recognizing the closed loops; it is suggested that the instructor select a student to act as a representative for all the students as the class plays against the instructor for a game; this method seems to reveal the present thought processes of the students, which can benefit instruction. These authors also found that the notions to be discussed within the following sections of this paper benefitted from introduction through QTTT as they are, at times, early signs of student understanding of quantum mechanics.

We will maintain the use of Alice as player X and Bob as player O, which is appropriate as the groups are of two players. Player names, Alice and Bob, were purposefully chosen, as discussion of pairs entangled particles uses the notation particles A and B; from this notation, observers at each end of the system are often referred to as Alice (for A) and Bob (for B).¹³

■ PROBABILITY AMPLITUDE, SIGN SYMMETRY, AND PROBABILITY DENSITY

The fundamental quantity within the Schrödinger picture of quantum mechanics is the wave function, $\Psi(x)$. $\Psi(x)$ are the solutions to the second-order differential wave equation describing the total system energy of a particle.²¹ The use of either QTTT or CTTT does not lend itself to the introduction of the Schrödinger equation as there are no intuitive nor appropriate methods for the student to connect game play to energy. Yet use of QTTT has proven beneficial in the explanation and discussion of several properties of the wave function, especially topics such as normalization and sign symmetry of the probability amplitude.

Wave functions, as stated by the first postulate of quantum mechanics,¹ show how the state of their system evolves in time. The use of Gaussian-type functions in the description of moves lends itself immediately as a means of emphasizing the sign invariance of the probability density. We will begin by defining:

$$g_j^\eta(x, y) = \alpha e^{[(x-\mu_j^x)^2 + (y-\mu_j^y)^2]/2\sigma^2} \quad (1)$$

where j denotes the board space in which the Gaussian function resides ($j \in [1, 9]$), α is the normalization constant of the function, η denotes which player's move is described by the Gaussian, μ is the full width at half max of the Gaussian function and $x_{0,j}$ is the center of the board square j . Defining each board square to be of unit length, then $\mu_j^x \in \{0.5, 1.5, 2.5\}$; $\mu_j^y \in \{0.5, 1.5, 2.5\}$; $\sigma = 0.2$; and $\alpha = 1/[\sigma(2\pi)^{1/2}]$. In this scheme the center of the fifth board square would be $(\mu_5^x, \mu_5^y) = (1.5, 1.5)$. By using Gaussian functions to represent the wave function describing a player's move, we afforded an opportunity

to teach the Gaussian integrals that are vital in quantum chemistry²² while exploiting the ease of the integral forms.²³ Students seem to take to this introduction to the use of Gaussian functions more so than a typical introduction in atomic or molecular calculations. This may be due to the less intimidating or esoteric application.

One could assign to Alice a normalized wave function that is a Gaussian-type function for her pieces with a negative (−) leading sign and to Bob a Gaussian-type wave function with positive (+) leading sign. Beginning a classical game of tic-tac-toe, allow both Alice and Bob to make their first move. Both players will recognize that the X and O represent game pieces, yet they have opposing signs. This will frame a discussion of the sign invariance of the wave function. During this discussion, these authors have found it appropriate to emphasize that it is the magnitude of the function's displacement from zero that is of significance and draw an analogue to waves in fluids while pointing out that the Laplacian term of the Schrödinger equation is used to describe fluid waves as well.

As these probability amplitudes can differ in both sign and complexity (real vs imaginary), it is here that these authors have introduced the magnitude (in fact, the squared magnitude) to the students as the valuable and physically interpretable quantity. As the function is possibly complex, one should remind the student that magnitude of a general complex number is given by $|z| = (z \cdot z^*)^{1/2}$ and that the wave function acts in a similar fashion. We may now introduce the probability density, $|\Psi|^2$, of the system as the physical quantity.

In both the quantum and classical analogues of tic-tac-toe, the system could either be described through a series of single player's moves, $|\psi^i\rangle_j$, or the total state of the board, Ψ . In terms of the classical game, each move represents a complete particle on the board. These single particles each inhabit a principal square within the board, in this manner any function describing a specific particle would be linearly independent of a function describing another. This example can be seen in Figure 4A; this linearly independent set of moves can be described through the following function for the total state of the board:

$$\Psi = |\psi_1^X\rangle_1 |\psi_2^O\rangle_2 |\psi_3^X\rangle_3 \quad (2)$$

Similarly, a spooky marker represents a single particle that exists in two different board square simultaneously and the

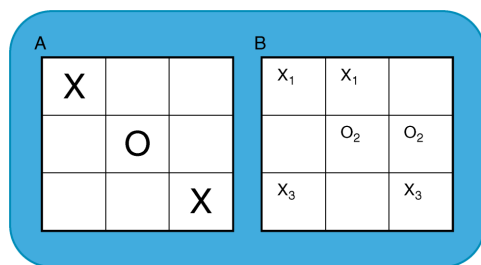


Figure 4. (A) Board shows a series of classical markers; by their nature of classical markers, any wave function describing one is linearly independent with any other marker's wave function. (B) Board shows a series of spooky markers. The wave function describing this series of moves reveals that these partials are linearly independent with each other.

moves seen in Figure 4B can be described through a total board wave function:

$$\begin{aligned} \Psi &= |\psi_1^X\rangle_1 |\psi_2^O\rangle_2 |\psi_3^X\rangle_3 \\ &= \frac{1}{\sqrt{8}} (|\varphi_1^X\rangle_1 + |\varphi_1^X\rangle_2) (|\varphi_2^O\rangle_5 + |\varphi_2^O\rangle_6) (|\varphi_3^X\rangle_7 + |\varphi_3^X\rangle_8) \end{aligned} \quad (3)$$

We reserve explaining the factor of $1/\sqrt{8}$ to the student until later.

Our decision to use Gaussian functions lends itself to instruction of these introductory concepts through CTTT alone; this allows the instructor to choose to reserve the use of QTTT for times when it is more comprehensible to the student and more necessary for the course material. The instructor can choose to show that a classical game piece is representable by a Gaussian function that can be of either sign. Both signs equally represent a particle and lead to a properly signed (+) probability density for the system. At this point it is also at the instructor's discretion to employ imaginary exponents in the Gaussian functions to show a properly signed magnitude for the probability density and proving the need for taking the complex conjugate of the wave function.

■ THE INNER PRODUCT, NORMALIZATION, AND OVERLAP

Extending the discussions framed within the previous section allows for the introduction of the inner product whose general form is:

$$\langle \Psi(\vec{\tau}) | \Psi(\vec{\tau}) \rangle = \int^{\Omega_c} \Psi^*(\vec{\tau}) \Psi(\vec{\tau}) d\vec{\tau} \quad (4)$$

where $\vec{\tau}$ refers to all coordinates within the function and Ω_c is the bounds of the space defined by a specific problem. The inner product may be exercised within the confines of the game in ways that exemplify its two early uses: the normalization and the overlap.

Many early students beginning their studies in quantum mechanics find that the first hurdle to their understanding is normalization. We have used this game and presented methods to successfully introduce this topic to students who are struggling in their undergraduate quantum mechanics course; the authors feel that the student benefits from the initial removal of the concept from atomic and molecular systems. This allows the student to understand the concept intuitively, learn the mathematical statement and then transplant all of this back into quantum mechanics. Starting with the boards expressed in Figure 5, we have used a series of activities to test the student's comprehension of normalization.

Students, from experience, recognize that when a classical marker is placed in a square of the game board the marker is completely contained within that space and does not exist within any other space on the board. In an effort to prove that which the student already knows, we can perform the following inner product using the wave function for just the X in Figure 5A:

$$\langle \psi^X(\vec{\tau}) | \psi^X(\vec{\tau}) \rangle_{5,A} = \int^{\Omega_c} (g_5(x, y))^* g_5(x, y) dx dy \quad (5)$$

The inner product will be evaluated three times for Figure 5A. For the first evaluation of eq 4 we shall define $\Omega_c = \Omega_{\text{board}}$; in this instance the student's intuition that the marker is somewhere within the board is verified through the value of the

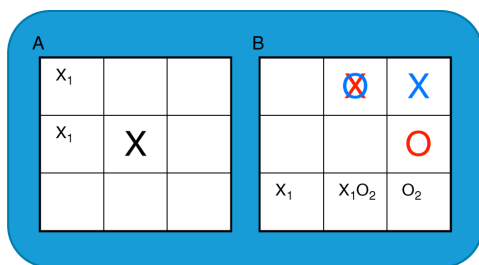


Figure 5. Boards that can be used during class activities: (A) a board giving a brief pair of activities that can be used to enforce the concept of normalization as the student integrates the board over each of the markers and then the pair of spooky markers and (B) a board yielding several activities that can be used as a means of both enforcing the concept of overlap and allow the student to numerically evaluate the overlap integral of Gaussian-type functions.

integral being 1, thus permitting the student to solve for α by following intuition. We can further impress upon the student this point by the reevaluation of eq 4 with $\Omega_c = \Omega_3$ and then again with $\Omega_c = \Omega_9$. The first of these evaluations again leads the student to accept that the marker is exactly where they think it should be, in square 5. The later of these two activities merely shows the student that the marker that is not in square 9.

Shifting focus to evaluations of eq 3 on the board shown in Figure 5A, we can now generate the linear combination, $\psi_1^X = 1/\sqrt{2}(|\varphi_1^X\rangle_1 + |\varphi_1^X\rangle_4)$ describing the state of spooky marker in a manner consistent with eq 3. Reverting to Dirac notation and the student's intuition, we can complete the following simplifications and evaluations with $\Omega_c = \Omega_{\text{Board}}$:

$$\begin{aligned} \langle \psi_1^X | \psi_1^X \rangle &= \frac{1}{\sqrt{4}} (\langle \varphi_1^X |_1 + \langle \varphi_1^X |_4) (|\varphi_1^X \rangle_1 + |\varphi_1^X \rangle_4) \\ &= \frac{1}{2} (\langle \varphi_1^X | \varphi_1^X \rangle_{1,1} + \langle \varphi_1^X | \varphi_1^X \rangle_{1,4} + \langle \varphi_1^X | \varphi_1^X \rangle_{4,1} + \langle \varphi_1^X | \varphi_1^X \rangle_{4,4}) \\ &= \frac{1}{2} (1 + 0 + 0 + 1) = 1 \end{aligned} \quad (6)$$

The students by now have recognized that a spooky marker has the same weight as a classical marker in the totality of the board. These authors also chose to commit the inner product of the spooky marker in Figure 5 with $\Omega_c = \Omega_4$, revealing that square 4 contains half of the spooky marker.

In a similar fashion, the instructor can impress both the meaning and mechanism of the overlap integral onto the student through activities definable on game boards. Here, the use of the Spooky Marker in this exercise is highlighted as they are capable of overlapping with other spooky markers. The provided board and marker combinations in Figure 5 hold the potential for a variety of activities for the student. Board 5A works as an example of the difference between spooky markers and classical markers. Board 5B can be used to instruct overlap of both types of markers.

SEPARABILITY AND ENTANGLEMENT

If an instructor wishes to introduce the concept of entanglement within the course, as we did, they may do so by introducing the most fundamental necessity for entanglement: inseparability of wave functions.^{24–26} To this end, a series of moves can be shown to the student, such as those seen

in Figure 6. As the game hinges on the generation of the entangled cycles through generation of inseparable states

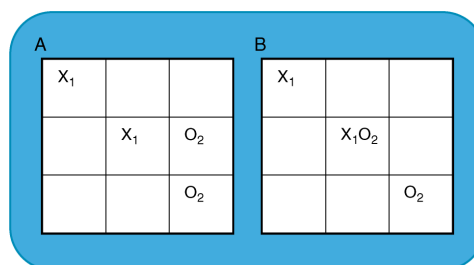


Figure 6. (A) A pair of moves are placed in such a way, that the overall wave function of the board is separable; this can be shown through an expansion of the product of the wave functions for each spooky marker and then the subsequent concretion back to the original product. (B) A pair of moves are placed whose total board wave function is inseparable; there exist members of the product expansion who are exclusionary to other members.

through marker placement, this is a great opportunity to forge into this topic.

It can be shown that the moves in Figure 6 are linearly independent as the series of moves fails to generate a state whose collapse into classicality is forbidden. This is clarified by example, observe Figure 6A; this series of moves can be described by the following expression for the wave function of the board (Ψ):

$$\begin{aligned} \Psi &= \psi_1^X \psi_2^O \\ &= \frac{1}{\sqrt{2}} (|\varphi_1^X \rangle_1 + |\varphi_1^X \rangle_5) \frac{1}{\sqrt{2}} (|\varphi_2^O \rangle_6 + |\varphi_2^O \rangle_9) \\ &= \frac{1}{\sqrt{4}} (|\varphi_1^X \rangle_1 |\varphi_2^O \rangle_6 + |\varphi_1^X \rangle_1 |\varphi_2^O \rangle_9 + |\varphi_1^X \rangle_5 |\varphi_2^O \rangle_6 + |\varphi_1^X \rangle_5 |\varphi_2^O \rangle_9) \end{aligned} \quad (7)$$

Here we pointed out to the students that the density of particle X is not cohabitating with any fraction of the density of particle O; this indicates that the classically collapsed state of particle X has no effect on the classically collapsed state of particle O. The expanded total state expression seen in equality 3 of eq 6 can be recollected back into equality 2; this state function can be said to display the property of separability imbued on systems comprised of states that are linearly independent of each other. This linear independence is forfeit if density fractions of the two particles share the same state (or position on the board), as seen in Figure 6B and whose functional description is here:

$$\begin{aligned} \Psi &\neq \psi_1^X \psi_2^O \\ &= \frac{1}{\sqrt{3}} (|\varphi_1^X \rangle_1 |\varphi_2^O \rangle_5 + |\varphi_1^X \rangle_1 |\varphi_2^O \rangle_9 + |\varphi_1^X \rangle_5 |\varphi_2^O \rangle_9) \end{aligned} \quad (8)$$

It is clearly noted that the expanded form of the states describing the board in eq 8 includes states that are forbidden on the board, noted by the loss of the $|\varphi_1^X \rangle_5 |\varphi_2^O \rangle_5$ state, which is classically forbidden. Due to the loss of this mathematical state, the expression cannot be recollected as a product of the two individual moves; this is referred to as inseparability of functions is a fundamental property for systems that possess and exhibit entanglement. Similarly, individual electrons can be

in the $|\uparrow\rangle$ state or the $|\downarrow\rangle$ state, yet when in a coupled pair, the electron system can only be in the $|\uparrow\downarrow\rangle$ state or the $|\downarrow\uparrow\rangle$ state, noting the loss of the $|\uparrow\uparrow\rangle$ state and the $|\downarrow\downarrow\rangle$ state.

CONCLUSION

In summary, we have presented a series of activities that may be used during introductory quantum mechanics and physics courses. These activities have, through the experience of these authors, aided students in their understanding of quantum mechanics by providing a degree of intuition to the mathematics of the topic. This intuition provided by both classical and quantum versions of a children's game with which most student have had some experience has benefited the instruction simple topics within the course, especially normalization and simple statements described through the use of wave functions. Furthermore, by exploiting the game we have found this method lowers the degree of fear some students possess toward quantum mechanics. It is the hope of these authors that utilizing such intuitive examples may become as widely accepted as has the use of the particle-in-a-box problem. These authors also hope that the armory of quantum games used in the classroom will be expanded to include other versions of tic-tac-toe²⁷ and furthered to a larger variety of games.^{6,28} A playable online version, which includes an AI player, for use by the students or practice for the instructor can be found on the Web.²⁹

ASSOCIATED CONTENT

Supporting Information

Board and example activities. This material is available via the Internet at <http://pubs.acs.org>.

AUTHOR INFORMATION

Corresponding Author

*E-mail: rhoehn@purdue.edu.

Notes

The authors declare no competing financial interest.

ACKNOWLEDGMENTS

This work is supported by the NSF Centers for Chemical Innovation: Quantum Information for Quantum Chemistry, CHE-1037992. The authors would also like to thank George Bodner of Purdue University for critical reading.

REFERENCES

- Messiah, A. *Quantum Mechanics*; Dover: New York, 1999.
- Messiah, A. *Quantum Mechanics*; Dover: New York, 1999; Vol. II.
- McQuarrie, D. A.; Simon, J. D. *Physical Chemistry: A Molecular Approach*, 1st ed.; University Science Books: Sausalito, CA, 1997.
- Goff, A.; Lehmann, D.; Seigel, J. Quantum TicTacToe as Metaphor for Quantum Physics. *AIP Conf. Proc.* **2004**, *699*, 1152.
- Goff, A. Quantum Tic-Tac-Toe: A Teaching Metaphor for Superposition in Mechanics. *Am. J. Phys.* **2006**, *74*, 962.
- Goff, A.; Lehmann, D.; Siegel, J. Quantum Tic-Tac-Toe, Spooky-Coins & Magic-Envelopes, as Metaphors for Relativistic Quantum Physics. *AIAA Pap.* **2002**, No. AIAA-2002-3763.
- Einstein, A.; Podolsky, B.; Rosen, N. Can Quantum-Mechanical Description of Physical Reality Be Considered Complete? *Phys. Rev.* **1935**, *47* (10), 777–780.
- Stern, O. Ein Weg zur experimentellen Prüfung der Richtungsquantelung im Magnetfeld. *Z. Phys.* **1921**, *7*, 249–253.
- Gerlach, W.; Stern, O. Das magnetische Moment des Silberatoms. *Z. Phys.* **1922**, *9*, 353–355.
- Bernstein, J. The Stern Gerlach Experiment. 2010, arXiv:1007.2435v1. arXiv.com e-Print archive.
- Loudon, M. *Organic Chemistry*, 4th ed.; Oxford University Press: New York, 2002; pp 37–38.
- Feynman, R.; Leighton, R.; Sands, M. *The Feynman Lectures on Physics*; Addison-Wesley: Reading, MA, 1964; p 1966, 3 volumes; Library of Congress Catalog Card No. 63-20717.
- Nielsen, M. A.; Chuang, I. L. *Quantum Computation and Quantum Information (Cambridge Series on Information and the Natural Sciences)*; Cambridge University Press: New York, 2004.
- Domin, D. A Review of Laboratory Instruction Styles. *J. Chem. Educ.* **1999**, *76*, 543–547.
- Prince, M. J.; Felder, R. M. Inductive Teaching and Learning Methods: Definitions, Comparisons, And Research Bases. *J. Eng. Educ.* **2006**, *95*, 123–138.
- Kirschner, P. A.; Sweller, J.; Clark, R. E. Why Minimal Guidance during Instruction Does Not Work: An Analysis of the Failure of Constructivist, Discovery, Problem-Based, Experiential and Inquiry Based Teaching. *Educ. Psychol.* **2006**, *41*, 75–86.
- Briggs, M.; Long, G.; Owens, K. Qualitative Assessment of Inquiry-Based Teaching Methods. *J. Chem. Educ.* **2011**, *88*, 1034–1040.
- Spencer, J. New Approaches to Chemistry Teaching. *J. Chem. Educ.* **2006**, *83*, 538–533.
- Farrell, J. J.; Moog, R. S.; Spencer, J. N. A Guided Inquiry General Chemistry Course. *J. Chem. Educ.* **1999**, *76*, 570–574.
- Ditzler, M. A.; Ricci, R. W. Discovery Chemistry: Balancing Creativity and Structure. *J. Chem. Educ.* **1994**, *71*, 685–688.
- Schrödinger, E. An Undulatory Theory of the Mechanics of Atoms and Molecules. *Phys. Rev.* **1926**, *28* (6), 1049–1070.
- Szabo, A.; Ostlund, N. S. *Modern Quantum Chemistry: Introduction to Advanced Electronic Structure Theory*; Dover Publications: Mineola, NY, 1996.
- McMurchie, L. E.; Davidson, E. R. One-and Two-Electron Integrals over Cartesian Gaussian Functions. *J. Comput. Phys.* **1978**, *26*, 218.
- Schrödinger, E. Discussion of Probability Relations between Separated Systems. *Math. Proc. Cambridge Philos. Soc.* **1935**, *31*, 555–563, DOI: 10.1017/S0305004100013554.
- Schrödinger, E. Probability Relations between Separated Systems. *Math. Proc. Cambridge Philos. Soc.* **1936**, *32*, 446–452, DOI: 10.1017/S0305004100019137.
- Kias, S. Entanglement, Electron Correlation and Density Matrices. *Adv. Chem. Phys.* **2007**, *134*, 493–535.
- Leaw, J. N.; Cheong, S. A. Strategic Insights from Playing Quantum Tic-Tac-Toe. *J. Phys. A: Math. Theor.* **2010**, *43*, 455304.
- Meyer, D. A. Quantum Strategies. *Phys. Rev. Lett.* **1999**, *82* (5), 1052–1055.
- Quantum Tic-Tac-Toe at <http://www.paradigmpuzzles.com/QT3Play.htm> (accessed Jan 2014).

Using Quantum Games To Teach Quantum Mechanics, Part 2

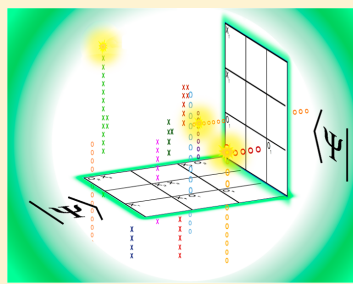
Ross D. Hoehn,^{*,†} Nick Mack,[†] and Sabre Kais^{†,‡}

[†]Department of Chemistry and [‡]Department of Physics, Purdue University, West Lafayette, Indiana 47907, United States

Supporting Information

ABSTRACT: Introductory courses in computational and quantum chemistry introduce topics such as Hilbert spaces, basis set expansions, and observable matrices. These topics are fundamental in the practice of quantum computations in chemistry as most computational methods rely on basis sets to approximate the true wave function. The mechanics of these topics can easily and intuitively be shown through the use of the game quantum tic-tac-toe (QTTT). Herein we propose a series of activities, using the mechanics of both classical tic-tac-toe (CTTT) and QTTT, intended to assist in the student's understanding of these quantum chemistry topics by exploiting their intuitive comprehension of the game. Quantum tic-tac-toe QTTT is a quantum analogue of CTTT and can be used to demonstrate the use of superposition in movement, qualitative (and later quantitative) displays of entanglement, and state collapse due to observation. QTTT can be used for the benefit of the student's comprehension in several other topics with the aid of proper discussion. This paper is the second in a series on the topic published in this *Journal*.

KEYWORDS: First-Year Undergraduate/General, High School/Introductory Chemistry, Upper-Division Undergraduate, Physical Chemistry, Humor/Puzzles/Games, Hands-On Learning/Manipulatives, Quantum Chemistry, Student-Centered Learning



Computational chemistry methods are of vital importance in areas such as materials science and drug design due to their predictive capacities, which may aid researchers in the prevention of generating failed targets. During the advent of quantum mechanics two schools of thought began to emerge: the Schrödinger picture and the Heisenberg picture.¹ The numerical results and physical significance taken from these schools are the same; however, they differ in where the time-dependency is exhibited (operators vs states). From the Heisenberg picture, Born and Heisenberg generated the matrix methods that are prevalent in modern computation chemistry;^{2,3} methods such as the Hartree–Fock method, density functional theory, and configuration interaction methods.

Discussion of basis-set methods is something that is normally avoided in undergraduate courses. This paper provides discussion and activities by which topics in matrix methods can be approached in undergraduate courses or as an early assessment or introduction to computational methods in a graduate course. This paper is the second in a series;⁴ for an introduction to the game, please see the papers by Hoehn et al.⁴ and Goff et al.^{5–7}

We also briefly discuss density matrices so that we may introduce entanglement and concurrence to the students. We have chosen to introduce entanglement as it has proved to be a vital element in the future studies of quantum computing^{8,9} and quantum biology.^{10,11}

ACTIVITY

We provide a series of example activities focusing on the matrix methods commonly used within computational chemistry. The activities presented here are not encompassing, and thus this paper is meant to inspire the instructor to use the tools of classical

tic-tac-toe (CTTT) and quantum tic-tac-toe (QTTT) in any way applicable to their classroom. Introduction of the game to audience with undergraduate-level of understanding in science has taken roughly 15 min; extending this topic to a graduate level course should take less time. The average length of time to play a single game is 4 min. Students take to the game enthusiastically. Instruction in the topics below has not been tested using quantum games, unlike those in the previous paper; but student understanding to both concept and clarity is expected.

These activities are intended to be used in inquiry-based classroom and take-home capacities. These authors have found that assigning these types of problems after instructional guidance and discussion of topics is best.¹² These methods allow the student to explore new topics after a framework has been laid, which affords an exploration with confidence due to the student's pre-existing intuition for several aspects of both CTTT and QTTT. In this manner these activities are akin to lab exercises in that they exploit elements of inductive learning^{13–16} and guided inquiry.^{17,18}

HILBERT SPACE AND BASIS FUNCTIONS

The matrix formulation is typically avoided in early quantum mechanics courses geared toward undergraduate students,¹⁹ where preference is given to the Schrödinger equation due to the *Anschaulichkeit* of the latter (which has historically been a primary positive aspect of this formulation).¹ Although matrix formulations have been relegated to graduate-level courses, they are extensively used in quantum chemistry methods.^{20–23}

Published: January 29, 2014

We began by introducing the game briefly and then defining a clear and finite set of basis vectors spanning the space of the game board. This set can be used as a means of formulating a vector describing any particular move within the game. Noting as a sensible preliminary to further discussion that the basis that spans and describes the spaces on board is the set of nine basis vectors conforming to the completeness relation

$$\sum_i^9 |q_i\rangle\langle q_i| = I_9 \quad (1)$$

by noting that $|q_i\rangle$ is the i th dimensional principle Cartesian vector where each dimension in the vector is representative of a principal square on the board. Each player's move can be described as a column vector constructed of weighted basis vectors spanning the totality of possible (finite) states within the board:

$$|\psi\rangle = \sum_{i=1}^9 v_i |q_i\rangle \quad (2)$$

In this manner, the move X_1 shown in Figure 1A can be described in the aforementioned manner and is given by either of the following equivalent statements:

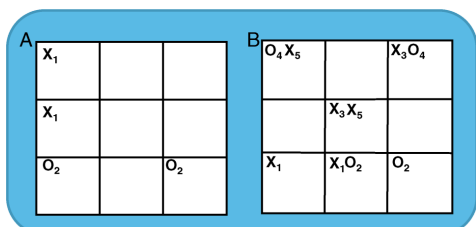


Figure 1. Boards displaying several possible activities: (A) a brief series of exercises for the expansion of moves in terms of basis functions and (B) several possible exercises for the topics of normalization and overlap.

$$\begin{aligned} \psi_1^X = & \frac{1}{\sqrt{2}} \begin{pmatrix} 1 \\ 0 \\ 0 \\ 0 \\ 0 \\ 0 \\ 0 \\ 0 \\ 0 \end{pmatrix} + 0 \begin{pmatrix} 0 \\ 1 \\ 0 \\ 0 \\ 0 \\ 0 \\ 0 \\ 0 \\ 0 \end{pmatrix} + 0 \begin{pmatrix} 0 \\ 0 \\ 1 \\ 0 \\ 0 \\ 0 \\ 0 \\ 0 \\ 0 \end{pmatrix} + \frac{1}{\sqrt{2}} \begin{pmatrix} 0 \\ 0 \\ 0 \\ 1 \\ 0 \\ 0 \\ 0 \\ 0 \\ 0 \end{pmatrix} + 0 \begin{pmatrix} 0 \\ 0 \\ 0 \\ 0 \\ 1 \\ 0 \\ 0 \\ 0 \\ 0 \end{pmatrix} \\ & + 0 \begin{pmatrix} 0 \\ 0 \\ 0 \\ 0 \\ 0 \\ 1 \\ 0 \\ 0 \\ 0 \end{pmatrix} + 0 \begin{pmatrix} 0 \\ 0 \\ 0 \\ 0 \\ 0 \\ 0 \\ 1 \\ 0 \\ 0 \end{pmatrix} + 0 \begin{pmatrix} 0 \\ 0 \\ 0 \\ 0 \\ 0 \\ 0 \\ 0 \\ 1 \\ 0 \end{pmatrix} + 0 \begin{pmatrix} 0 \\ 0 \\ 0 \\ 0 \\ 0 \\ 0 \\ 0 \\ 0 \\ 1 \end{pmatrix} \quad (3) \end{aligned}$$

$$= \frac{1}{\sqrt{2}} s_1 + 0s_2 + 0s_3 + \frac{1}{\sqrt{2}} s_4 + 0s_5 + 0s_6 + 0s_7 + 0s_8 + 0s_9 \quad (4)$$

Noting that the coefficients provide weight to each basis vector, we may now represent the probability amplitude of a particle in a board space defined by the basis vector (S_i).

We can now easily show students the importance of normalization in a manner divorced of the use of integrals. In this way, the student is exposed to the material from several vantages (as they have seen the overlap integral method in earlier courses and coursework); this allows the student to achieve a full perspective and decide which picture they find most insightful. The student needs only to recognize that a single classical move represents a single particle placed within the board; thus, the following statement makes the connection between common sense and quantum mechanics:

$$\sum_{i=1}^9 |v_i|^2 = 1 \quad (5)$$

where the evaluation, at this point, can be shown to the student as the dot product of two vectors (in this case is X_1 from Figure 1):

$$\langle \psi_1^{X_1} | \psi_1^{X_1} \rangle = \begin{pmatrix} \frac{1}{\sqrt{2}} & 0 & 0 & \frac{1}{\sqrt{2}} & 0 & 0 & 0 & 0 & 0 \end{pmatrix} \begin{pmatrix} \frac{1}{\sqrt{2}} \\ 0 \\ 0 \\ \frac{1}{\sqrt{2}} \\ 0 \\ 0 \\ 0 \\ 0 \\ 0 \end{pmatrix} = 1 \quad (6)$$

Just as the mathematics of normalization and overlap are nearly identical in the Schrödinger picture, so it is in the Heisenberg picture. The act of describing the overlap integral of two moves in vector notation can be performed for the pair of spooky marker moves seen in Figure 1B and yields the same solution as the use of the Gaussian functions presented in⁴

$$\langle \psi_1^{X_1} | \psi_1^{O_1} \rangle = \begin{pmatrix} 0 & 0 & 0 & 0 & 0 & 0 & \frac{1}{\sqrt{2}} & \frac{1}{\sqrt{2}} & 0 \end{pmatrix} \begin{pmatrix} 0 \\ 0 \\ 0 \\ 0 \\ 0 \\ 0 \\ \frac{1}{\sqrt{2}} \\ \frac{1}{\sqrt{2}} \\ 0 \end{pmatrix} = \frac{1}{2} \quad (7)$$

We have now shown the student how to describe a move, normalization, and overlap integral within the matrix formulation; now we may guide our discussions into the direction of observables in quantum mechanics.

CHANGE OF BASIS, PROJECTORS, AND OBSERVATIONS

The student, now being able to describe both the board and the individual moves in terms of vector spaces, is prepared to start making observations within those spaces. We first introduce the concept of change of basis. To the student the phrase, "there are two sides to every story", may be trite but is exemplary in the description of basis for a vector space. The phrase merely implores the listener to look at the problem in another perspective; this is the fundamental concept in change of basis.

We have until now described our vectors through a weighted sum of Cartesian basis vectors (which are shorthanded by the *s*-basis for site-basis). At this point we introduce a new basis by which to describe our system. Victory in both classical and quantum versions tic-tac-toe can be obtained through generating a three-in-a-row on any of the three vertical columns defined by the board. We define a normalized set of spanning vectors starting with a three-in-a-row in each of the columns:

$$\begin{pmatrix} \frac{1}{\sqrt{3}} & 0 & 0 & \frac{1}{\sqrt{2}} & 0 & 0 & -\frac{1}{\sqrt{6}} & 0 & 0 \\ 0 & \frac{1}{\sqrt{3}} & 0 & 0 & \frac{1}{\sqrt{2}} & 0 & 0 & -\frac{1}{\sqrt{6}} & 0 \\ 0 & 0 & \frac{1}{\sqrt{3}} & 0 & 0 & \frac{1}{\sqrt{2}} & 0 & 0 & -\frac{1}{\sqrt{6}} \\ \frac{1}{\sqrt{3}} & 0 & 0 & -\frac{1}{\sqrt{2}} & 0 & 0 & -\frac{1}{\sqrt{6}} & 0 & 0 \\ 0 & \frac{1}{\sqrt{3}} & 0 & 0 & -\frac{1}{\sqrt{2}} & 0 & 0 & -\frac{1}{\sqrt{6}} & 0 \\ 0 & 0 & \frac{1}{\sqrt{3}} & 0 & 0 & -\frac{1}{\sqrt{2}} & 0 & 0 & -\frac{1}{\sqrt{6}} \\ \frac{1}{\sqrt{3}} & 0 & 0 & 0 & 0 & 0 & \sqrt{\frac{2}{3}} & 0 & 0 \\ 0 & \frac{1}{\sqrt{3}} & 0 & 0 & 0 & 0 & 0 & \sqrt{\frac{2}{3}} & 0 \\ 0 & 0 & \frac{1}{\sqrt{3}} & 0 & 0 & 0 & 0 & 0 & \sqrt{\frac{2}{3}} \end{pmatrix} \quad (8)$$

that is referred to as the Victory basis (*v*-basis). *V*-basis was defined by generating the vector describing the three-in-a-row along the columns of a board; the subsequent vectors can be solved for analytically or by any canonical orthogonalization method. The *v*-basis is not the only other basis that could be defined that spans our board, so we would encourage the reader to form any basis that is appropriate for their class.

We are capable of constructing a matrix from this basis that allows for vectors from one basis to be transformed to the other basis.²⁴ The creation of such a matrix (**P**) is a simple matter of defining the target basis vectors *B'*, in terms of the source basis, *B*, and constructing a matrix from these definitions. Consider a pair of basis sets, *B* and *B'*, each spanning the space of a problem and consisting of vectors **u** and **w** in basis *B* as well as *u'* and *w'* in *B'*:

$$\mathbf{u} = \begin{pmatrix} a \\ b \end{pmatrix} \text{ and } \mathbf{w} = \begin{pmatrix} c \\ d \end{pmatrix} \quad (9)$$

where the vector elements are found from:

$$\mathbf{u} = au' + bw' \text{ and } \mathbf{w} = cu' + dw' \quad (10)$$

These allow the construction of our **P** matrix:

$$\mathbf{P} = \begin{pmatrix} a & c \\ b & d \end{pmatrix} \quad (11)$$

whose properties are such that: $Pv = v'$. Following this standard method, we can define a **P'** matrix allowing the translation from site basis to victory basis. This matrix is identical to that of eq 8.

We can now use the column vectors of the **P'** matrix to start making observations on our system. We begin by defining a projection operator, $\hat{\Xi} = |v\rangle\langle v|$, using the first column vector of our **P** matrix to generate **P'** and then employ that operator within $\langle \psi | \hat{\Xi} | \psi \rangle$. We make our observation on the three moves shown in Figure 2. Starting with the classical marker, we can see that our

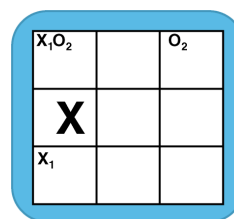


Figure 2. A board presenting possible exercises that may be used to introduce the mathematics of observations of moves in several different basis.

observation of its state made with the projector defined from the first vector of the victory basis would be:

$$\langle \psi^X | v_1 \rangle \langle v_1 | \psi^X \rangle = \frac{1}{3} \quad (12)$$

The value of 1/3 for the observation is due to the weight of the spooky marker within the vector space of v_1 being 1/3; when summing over all the spanning vectors of the basis, the student is able to recover the total density of the marker, 1. Completing the same act for the spooky markers of $\langle \psi^O |$, we get the numerical value of 2/3 because the spooky marker pair has greater weight within v_1 than has the classical marker of Figure 2.

When we complete the final example in Figure 2, that of $\langle \psi^O |$, we can see the observation is 1/6, which is to say half that of the previous two measurements because this time the particles are only half within the space of the measurement, v_1 . The sum over all the vectors within the basis yields a density of 1, but the sum over v_1 , v_2 , and v_3 yields 1/2; this value is due to only have of the superposition defining the state being within the region of the basis defined by these vectors.

As we have now made a measurement, we may begin defining a density matrix for our system and show the student how they can make their first measurement of entanglement.

DENSITY MATRIX AND CONCURRENCE

Now, we show the student how one can make a measurement of entanglement. Entanglement is the correlation between parts of a system, induced through an interaction and maintained in separation, which is independent of factors such as position and momentum.²⁵ Entanglement was introduced by Schrödinger^{26,27} and was the focus of the famous EPR paper.²⁸ We do this by measuring the concurrence, which gives a measurement of pairwise entanglement of particles within our system; the method was developed by Wootters.^{29,30} The calculation of concurrence is a brief five-step process:³¹

1. Construction of a density matrix: $\rho = |\psi\rangle\langle\psi|$.
2. Construction of a flipped density matrix: $\tilde{\rho}$.
3. Product matrix: $\rho\tilde{\rho}$.
4. Determine the eigenvalues of $\rho\tilde{\rho}$: $\lambda_1, \lambda_2, \lambda_3, \dots$.
5. Calculate concurrence: $C = \max[0, \sqrt{\lambda_1} - \sqrt{\lambda_2} - \dots]$.

We start by generating a density matrix for our system; this is typically done by generating and subsequently diagonalizing the Hamiltonian matrix for the system, but we have no energies associated with our board or moves so we choose marker location as our observable. Let us construct an observation matrix, O , by using the site basis for the board and a projector, $|\psi_1^X\rangle\langle\psi_1^X|$, described by the spooky markers seen in Figure 1A:

$$|\psi_1^X\rangle = \begin{pmatrix} \frac{1}{\sqrt{2}} \\ 0 \\ 0 \\ \frac{1}{\sqrt{2}} \\ 0 \\ 0 \\ 0 \\ 0 \end{pmatrix} \quad (13)$$

$$\begin{aligned} O_{i,j} &= \langle\psi_i|\psi_1^X\rangle\langle\psi_1^X|\psi_j\rangle \\ &= \langle s_i|\psi_1^X\rangle\langle\psi_1^X|s_j\rangle \end{aligned} \quad (14)$$

This allows us to generate a general observation matrix over the space of the board, not unlike a Hamiltonian matrix generated with a finite basis set. This matrix O is of the form:

$$O = \begin{pmatrix} \frac{1}{2} & 0 & 0 & \frac{1}{2} & 0 & 0 & 0 & 0 \\ 0 & 0 & 0 & 0 & 0 & 0 & 0 & 0 \\ 0 & 0 & 0 & 0 & 0 & 0 & 0 & 0 \\ \frac{1}{2} & 0 & 0 & \frac{1}{2} & 0 & 0 & 0 & 0 \\ 0 & 0 & 0 & 0 & 0 & 0 & 0 & 0 \\ 0 & 0 & 0 & 0 & 0 & 0 & 0 & 0 \\ 0 & 0 & 0 & 0 & 0 & 0 & 0 & 0 \\ 0 & 0 & 0 & 0 & 0 & 0 & 0 & 0 \end{pmatrix} \quad (15)$$

Now we construct a density matrix from the above. We first diagonalize the O matrix and select the state of the system we will use for the generation of the density matrix. We use the first eigenvectors of the system, the vector corresponding to the eigenvalue of 1. This vector may be seen in eq 16 as it is being used to generate the density matrix:

$$\rho = |O_1\rangle\langle O_1| = \begin{pmatrix} \frac{1}{\sqrt{2}} & & & \frac{1}{\sqrt{2}} \\ 0 & & & 0 \\ 0 & & & 0 \\ \frac{1}{\sqrt{2}} & & & \frac{1}{\sqrt{2}} \end{pmatrix} \quad (16)$$

In generating ρ , we note that most of the space in which this system lives is superfluous, and thus, we can reduce the

space of our calculations into a 4×4 region; this simplification yields a ρ :

$$\rho = \begin{pmatrix} \frac{1}{2} & 0 & 0 & \frac{1}{2} \\ 0 & 0 & 0 & 0 \\ 0 & 0 & 0 & 0 \\ \frac{1}{2} & 0 & 0 & \frac{1}{2} \end{pmatrix} \quad (17)$$

From the above we may now start to generate the spin-flip density matrix, $\tilde{\rho}$, for this state of the system. The generation of $\tilde{\rho}$ is completed by:

$$\tilde{\rho} = (\sigma_y \otimes \sigma_y)\rho(\sigma_y \otimes \sigma_y) \quad (18)$$

where ρ is the density matrix discussed above and the σ_y is the y th Pauli spin matrix. The use of the Kronecker product (\otimes) on the series of Pauli spin matrices is to generate a rotation matrix in the same dimensions of the system. As our ρ is a 4×4 matrix, the Kronecker product of two Pauli spin matrices is sufficient to generate a four dimensional rotation matrix for our system. Following the above procedural step our $\tilde{\rho}$ happens to, again, generate:

$$\tilde{\rho} = \begin{pmatrix} \frac{1}{2} & 0 & 0 & \frac{1}{2} \\ 0 & 0 & 0 & 0 \\ 0 & 0 & 0 & 0 \\ \frac{1}{2} & 0 & 0 & \frac{1}{2} \end{pmatrix} \quad (19)$$

Armed with both ρ and $\tilde{\rho}$, we can now complete the fourth procedural step: finding the Eigenvalues of the $\rho\tilde{\rho}$ matrix-product:

$$\rho\tilde{\rho} = \begin{pmatrix} \frac{1}{2} & 0 & 0 & \frac{1}{2} \\ 0 & 0 & 0 & 0 \\ 0 & 0 & 0 & 0 \\ \frac{1}{2} & 0 & 0 & \frac{1}{2} \end{pmatrix} \quad (20)$$

with Eigenvalues $\{1, 0, 0, 0\}$. Using these Eigenvalues within the expression for concurrence: $C = \max[0, \sqrt{1 - \sqrt{0 - \sqrt{0 - \sqrt{0}}}}]$. This would yield a concurrence of 1; this is the maximum value that the concurrence can yield for pairwise entanglement. The value implies that the two parts of the spooky marker are maximally entangled. This is a sensible finding as these markers are entangled (as per the rules) and unencumbered by interaction with other markers.

CONCLUSION

We have herein presented an introduction to the possible uses of both classical and quantum tic-tac-toe as a means of instruction in the matrix methods of quantum chemistry. These authors have also found that a brief introduction in quantum entanglement is beneficial to students and have presented a brief series of activities using QTTT as a means of intruding entanglement. It is the experience of these authors that students can benefit from their previous experience in CTTT in the teaching of quantum mechanical topics. Students also further their knowledge of these

topics through learning and exercising with QTTT. Other quantum games exist^{32–34} and their introduction into the classroom as teaching tools and metaphors is encouraged.

■ ASSOCIATED CONTENT

📄 Supporting Information

Example activity. This material is available via the Internet at <http://pubs.acs.org>.

■ AUTHOR INFORMATION

Corresponding Author

*E-mail: rhoehn@purdue.edu.

Notes

The authors declare no competing financial interest.

■ ACKNOWLEDGMENTS

This work is supported by the NSF Centers for Chemical Innovation: Quantum Information for Quantum Chemistry, CHE-1037992. The authors would also like to thank George Bodner of Purdue University for critical reading.

■ REFERENCES

- (1) Beller, M. The Conceptual and the Anecdotal History of Quantum Mechanics. *Found. Phys.* **1996**, *26* (4), pp545–557.
- (2) Born, M.; Heisenberg, W.; Jordan, P.; Zur Quantenmechanik, I. I. *Z. Phys.* **1936**, *35* (8–9), pp557–615.
- (3) Hilbert, D.; Ewald, W. B.; Hallett, M.; Majer, U.; Sieg, W. *David Hilbert's Lectures on the Foundations of Mathematics and Physics, 1891–1933*; Springer: New York, 2004; Volume 5.
- (4) Hoehn, R.; Kais, S. Using Quantum Games to Teach Quantum Mechanics, Part 1. *J. Chem. Educ.* **2014**, DOI: 10.1021/ed400385k.
- (5) Goff, A.; Lehmann, D.; Siegel, J. Quantum TicTacToe as Metaphor for Quantum Physics. *AIP Conf. Proc.* **2004**, *699*, 1152.
- (6) Goff, A. Quantum Tic-Tac-Toe: A Teaching Metaphor for Superposition in Mechanics. *Am. J. Phys.* **2006**, *74*, 962.
- (7) Goff, A.; Lehmann, D.; Siegel, J. Quantum Tic-Tac-Toe, Spooky-Coins & Magic-Envelopes, as Metaphors for Relativistic Quantum Physics. *AIAA Pap.* **2002**, No. AIAA-2002-3763.
- (8) Feynman, R. P. Simulating Physics with Computers. *Int. J. Theor. Phys.* **1982**, *21*, 6/7.
- (9) Lloyd, S. Universal Quantum Simulators. *Science* **1996**, *273* (5278), 1073–1078.
- (10) Zhu, J.; Kais, S.; Aspuru-Guzik, A.; Rodrigues, S.; Brock, B.; Love, P. J. Multipartite Quantum Entanglement Evolution in Photosynthetic Complexes. *J. Chem. Phys.* **2012**, *137*, 074112.
- (11) Gauger, E. M.; Rieper, E.; Morton, J. J. L.; Benjamin, S. C.; Vedral, V. Sustained Quantum Coherence and Entanglement in the Avian Compass. *Phys. Rev. Lett.* **2011**, *106*, 040503.
- (12) Kirschner, P. A.; Sweller, J.; Clark, R. E. Why Minimal Guidance during Instruction Does Not Work: An Analysis of the Failure of Constructivist, Discovery, Problem-Based, Experiential and Inquiry Based Teaching. *Educ. Psychol.* **2006**, *41*, 75–86.
- (13) Briggs, M.; Long, G.; Owens, K. Qualitative Assessment of Inquiry-Based Teaching Methods. *J. Chem. Educ.* **2011**, *88*, 1034–1040.
- (14) Spencer, J. New Approaches to Chemistry Teaching. *J. Chem. Educ.* **2006**, *83*, 538–533.
- (15) Farrell, J. J.; Moog, R.; Spencer, J. N. A Guided Inquiry General Chemistry Course. *J. Chem. Educ.* **1999**, *76*, 570–574.
- (16) Ditzler, M. A.; Ricci, R. W. Discovery Chemistry: Balancing Creativity and Structure. *J. Chem. Educ.* **1994**, *71*, 685–688.
- (17) Domin, D. A Review of Laboratory Instruction Styles. *J. Chem. Educ.* **1999**, *76*, 543–547.
- (18) Prince, M. J.; Felder, R. M. Inductive Teaching and Learning Methods: Definitions, Comparisons, And Research Bases. *J. Eng. Educ.* **2006**, *95*, 123–138.
- (19) McQuarrie, D. A.; Simon, J. D. *Physical Chemistry: A Molecular Approach*, 1st ed.; University Science Books: Sausalito, CA, 1997.
- (20) Szabo, A.; Ostlund, N. S. *Modern Quantum Chemistry: Introduction to Advanced Electronic Structure Theory*; Dover Publications: Mineola, NY, 1996.
- (21) Messiah, A. *Quantum Mechanics*; Dover: New York, 1999.
- (22) Messiah, A. *Quantum Mechanics*; Dover: New York, 1999; Vol. II.
- (23) Levine, I. N. *Quantum Chemistry*, 5th ed.; Prentice Hall: Upper Saddle River, NJ, 2000.
- (24) Schneider, H.; Baker, G. P. *Matrices and Linear Algebra*, 2nd ed.; Dover Publishing: New York, 1989.
- (25) Nielsen, M. A.; Chuang, I. L. *Quantum Computation and Quantum Information (Cambridge Series on Information and the Natural Sciences)*; Cambridge University Press: New York, 2004.
- (26) Schrödinger, E. Discussion of Probability Relations between Separated Systems. *Math. Proc. Cambridge Philos. Soc.* **1935**, *31*, 555–563, DOI: 10.1017/S0305004100013554.
- (27) Schrödinger, E. Probability Relations between Separated Systems. *Math. Proc. Cambridge Philos. Soc.* **1936**, *32*, 446–452, DOI: 10.1017/S0305004100019137.
- (28) Einstein, A.; Podolsky, B.; Rosen, N. Can Quantum-Mechanical Description of Physical Reality Be Considered Complete? *Phys. Rev.* **1935**, *47* (10), 777–780.
- (29) Hill, S.; Wootters, W. K. Entanglement of a Pair of Quantum Bits. *Phys. Rev. Lett.* **1997**, *78* (26), 5022–5025.
- (30) Wootters, W. K. Entanglement of Formation and Concurrence. *Quantum Inf. Comput.* **2001**, *1* (1), 27–44.
- (31) Kias, S. Entanglement, electron correlation and Density Matrices. *Adv. Chem. Phys.* **2007**, *134*, 493–535.
- (32) Leaw, J. N.; Cheong, S. A. Strategic Insights from Playing Quantum Tic-Tac-Toe. *J. Phys. A: Math. Theor.* **2010**, *43*, 455304.
- (33) Meyer, D. A. Quantum Strategies. *Phys. Rev. Lett.* **1999**, *82* (5), 1052–1055.
- (34) Schmidt, A. G. M.; da Silva, L. Quantum Russian Roulette. *Physica A* **2013**, *392*, 400–410.

IN SUBMISSION

Neuroreceptor Activation by Vibration-Assisted Tunneling

Ross D. Hoehn,¹ David Nichols,² Hartmut Neven,³ and Sabre Kais^{4,*}

¹*Department of Chemistry, Purdue University, West Lafayette, IN 47907 USA*

²*Department of Medicinal Chemistry and Molecular Pharmacology, Purdue University, West Lafayette, IN 47907 USA*

³*Google Los Angeles, Venice, CA 90291 USA*

⁴*Departments of Chemistry and Physics, Purdue University, West Lafayette, IN 47907 USA*

(Dated: August 6, 2014)

G protein-coupled receptors (GPCRs) constitute a large family of receptors that sense molecules outside of a cell and activate signal transduction pathways inside the cell. Modeling how an agonist activates such a receptor is important for understanding a wide variety of physiological processes and it is of tremendous value for pharmacology and drug design. Inelastic electron tunneling spectroscopy (IETS) has been proposed as the mechanism by which olfactory GPCRs are activated by an encapsulated agonist. In this note we apply this notion to GPCRs within the mammalian nervous system using *ab initio* quantum chemical modeling. We found that non-endogenous agonists of the serotonin receptor share a singular IET spectral aspect both amongst each other and with the serotonin molecule: a peak that scales in intensity with the known agonist activities. We propose an experiential validation of this model by utilizing lysergic acid dimethylamide (DAM-57), an ergot derivative, and its isotopologues in which hydrogen atoms are replaced by deuterium. If validated our theory may provide new avenues for guided drug design and better *in silico* prediction of ecacies.

Significance Statement

This project provides a scheme by which the activity of small molecule drugs at their target transmembrane receptor may be predicted. This is a vital task as it allows for the development of new drug technologies for pharmaceuticals and suggests a mechanism by which these proteins are activated through a quantum mechanical process.

I. INTRODUCTION

Quantum activity within biological systems and information theory applied therein have drawn much recent attention¹⁻⁵. Examples of systems that exploit such phenomenon are: quantum coherence and entanglement in photosynthetic complexes⁶⁻¹⁵, quantum mutations^{16,17}, information theory and thermodynamics of cancers^{18,19}, the avian magnetic compass²⁰⁻²³, tunneling behavior in the antioxidant breakdown of catechols present in green tea²⁴, enzymatic action²⁵, olfaction²⁶, and genetic coding²⁷. G Protein-Coupled Receptors (GPCR) are the target for the greatest portion of modern therapeutic small molecule medications²⁸. Predictability of pharmacological efficacy for new drugs prior to a complex total synthesis can be aided by pharmacophore modeling, crystal structure or a homology model. The theory of protein/agonist binding has been described through variants of the Lock and Key model, originally proposed by Fischer²⁹ and the extensions thereof³⁰. Although this theory has provided insight into changes of free energy associated with the formation of the activated complex, it has not manifested sufficient capacity for the prediction ligand activity or a mechanism by which the agonist activates the system.

Early models attempting to account for predictability of agonist classification beyond shape were those of odorant binding^{31,32}; these works proposed a vibra-

tional theory of activation and effect. Vibrational theories were eventually disregarded for reasons that include a lack of conceived mechanism and the inability of the protein (which is vibrating) to detect the continuum of thermally-activated, classical vibrations of the odorant. A recently suggested a theory of olfactory activation consisting of a physical mechanism closely resembling Inelastic Electron Tunneling Spectroscopy (IETS)^{26,33,34}. The plausibility of time scales associated with this process was verified through Marcus theory³⁵. Electron tunneling rates for the olfaction system have been calculated and support the theory³⁶. Furthermore, eigenvalue spectral analysis of odorant molecules has shown a high correlation between the vibrations and odorant classification³⁷.

We focus on an initial examination of the viability of the vibrational theory of protein activation in cases involving protein-agonist binding within the central nervous system and as a predictor of intrinsic efficacy as defined within³⁸. Activation of the 5-HT_{1A} and 5-HT_{2A} receptors is implicated as being associated with human hallucinogenic responses^{39,40}. We utilize a model of inelastic electron tunneling to describe the protein-agonist complex in a manner that will utilize the vibrational frequencies of the bound agonist to facilitate electron transfer within the activation site of the protein. The prerequisite agonist information was collected through molecular quantum mechanics calculations utilizing density function theory as well as normal mode analysis and

natural bonding order methods; necessary were the harmonic displacements, frequencies and partial charges of each constituent atom. In Section II, we will first present a qualitative discussion of the relationship between the tunneling model and the protein-agonist complex. Section III will discuss the tunneling features of several 5-HT_{1A} and 5-HT_{2A} agonists, and how these correlate with efficacy of these molecules. We conclude with a proposed set of molecules that could be employed in experimental validation of the vibrational theory’s applicability in the central nervous system.

II. MAPPING THE MODELS

Application of the IETS model for the protein environment requires mapping several aspects of the IETS methodology to the biological system. The two-plate setup of the tunneling junction represent the walls of the receptor site; more explicitly, under electron transfer the valance and conductance bands within the juncture become specific HOMOs and LUMOs of the residues making the walls of the receptor. This dictates that energy transition detectable by the protein should be the energy difference between electronic levels of residue side-chains or any bound cofactors such as a metal ion. This alteration of IETS also localizes the source of tunneling electrons to a single residue side-chain; the implication is that electrons are not capable of uniformly tunneling through the molecule. This lack of uniformity suggests that the act of tunneling is localized to regions of the agonist molecule and that not all local oscillators of a specific mode fully contribute to the current enhancement.

Secondly, unlike the experimental IETS procedure, the analyte is not deposited upon a surface, being encapsulated by the active site. There is no externally applied potential within the receptor site which would have allowed for the scanning of energies; yet, it has been suggested that an ionic cofactor, likely a calcium ion, could provide this driving field. The implication of this is that the receptor is set to test the vibrational-assisted enhancement to the electron tunneling rate at a specific energy. The electrostatic interactions which govern docking orientation would be a means of orienting the endogenous agonists in such a way that the tunneling junction is appropriately aligned for maximized electron transfer across the atoms responsible for the inelastic contribution. Non-endogenous agonists would align with residues in a manner which may place energetically appropriate modes in proximity of the tunneling junction, thus allow for the activation of the receptor.

III. RESULTS

Generation of tunneling spectra is completed through the procedure described in^{26,41}, and outlined within the Supplementary Material. This procedure was adapted

from earlier inelastic tunneling literature^{42,43} and similarly uses arbitrary units (a.u.) for the tunneling intensity. Our spectral procedure was validated by comparison of the spectra of the formate ion, which is prevalent throughout experimental and theoretical literature in IETS. These a.u. are proportional to the conductance enhancement, as well as the enhancement to the probability of Coulombic interactions during tunneling. Necessary information for implementing the calculations outlined in the Supplementary Material was collected through quantum chemical calculations. Computations were performed using Density Functional theory at 6-311G level utilizing the B3LYP functional; in contrast to similar previous works^{26,41}. Expanded pseudopotential correlation consistent 5-zeta basis was used for large atoms where necessary. DFT was chosen both due to its high accuracy in transition dipole frequencies and to avoid encroaching error associated with dissimilarity between analyte and parameter molecules in semi-empirical methods; initial use of Hartree-Fock theory display the characteristic .8 factor shift to the vibrational frequencies. Vibrational calculations utilize reduced modal displacements, μ ; proportional to the Cartesian displacement through a factor of $\sqrt{\mu}$. These arising due to the center of mass coordinates within the classical theory after using the harmonic approximation to calculate the normal modes. Natural bond order calculations yield the partial charges, q_i . Scaled Kronecker delta functions are plotted at the absorbance frequency of the mode; these functions were convolved with Gaussian functions possessing a conservative FWHM of 25 cm⁻¹, representing a very narrow thermal distribution. 25cm⁻¹ to allow for peak additions while avoiding over estimations of peak breadth.

Assessment of vibrational bands of the 5-HT_{2A} agonists that could facilitate the inelastic transfer of electrons within the protein environment is of primary import. Agonists of a particular protein would share a single spectral feature associated with the inelastic transfer, as the same ligands would be responsible for the electron donation and acceptance in a particular protein. Tunneling spectrum of several selected 5-HT_{2A} agonists have been generated. LSD, was selected as it possesses a high potential for activation at this particular serotonin receptor within the cortical interneurons⁴⁴. DOI (2,5-dimethoxy-4-Iodo-amphetamine) was selected due to its high selective for the 2A-subtype receptor⁴⁵. The remaining selected molecules are members of the 2C-X (4-X-2,5-dimethoxyphenethylamine) class of psychedelic phenethylamines. All compounds selected are known hallucinogens⁴⁶⁻⁴⁸ some first characterized by Alexander Shulgin in the compendia works PiHKAL and TiHKAL^{49,50}.

Figure 1 shows the tunneling spectra of select agonists (above the axis). The selection of candidate peaks, possibly responsible for facilitating inelastic transfer, was performed using the spectral similarity index (SI), similar to that used for comparison of mass spectra⁵¹. The SI

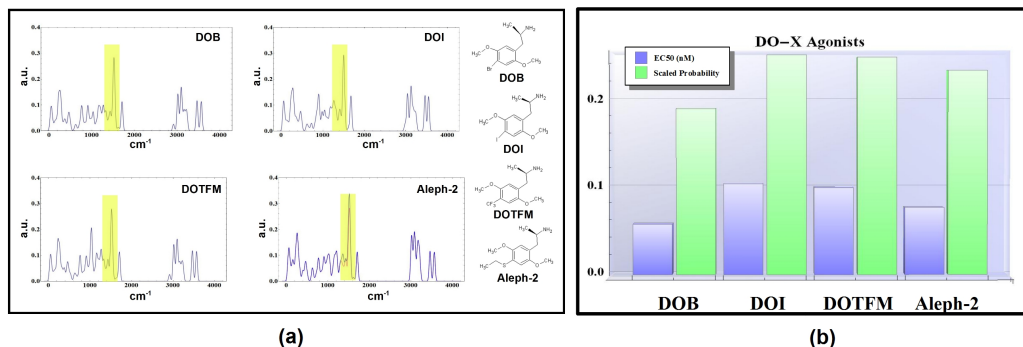


FIG. 2. (a) The tunneling spectra of several DOX class agonists as well as their molecular structures. (b) The inverse of the median effective concentration for the DOX class agonists plotted against the tunneling probability within the region in question. The trend of tunneling intensity follows roughly the trend of the agonist's efficacy at the 5-HT_{2A} receptor.

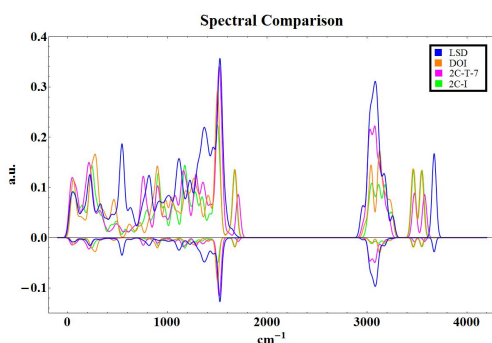


FIG. 1. The tunneling spectrum of several known 5-HT_{2A} agonists as well as the square of the tunneling PDF reflected below the energy axes; the square is used to highlight major spectral aspects. The Spectral Similarity index of each plot given in the inset, noting that these similarity indices allude to good spectral mapping.

was taken over the entire spectral region and repeated for local regions. The SI is given by:

$$SI = 1 - \sqrt{\frac{|a_i - b_i|}{N}} \quad (1)$$

Where N is the normalization constant (the numerator performed for spectra b); b_i is the value of the spectra being analyzed at discrete location i and a is the spectra being the reference spectra; being the most potent agonist, LSD was selected as the reference spectra for our SI calculations. The SIs associated with each of the tunneling spectra can be found in the provided Supplementary Material. To highlight major aspects of the tunneling PDF, we squared the function; this exaggerated aspects which exhibit large tunneling amplitudes within the spectra (Figure 1 reflected below energy axis). The only broadly shared spectral aspects were those at 1500cm^{-1} . For a more thorough discussion of the spectral aspects, isotopic effects and density of states for these systems, please see the provided Supplementary Materials.

The integral of the tunneling probability density was taken around the $1500 \pm 35\text{cm}^{-1}$ region and compared to known EC50 data for compounds shown to activate 5-HT_{2A}. The effective concentrations of several phenethylamines were taken from⁵² and compared to the local integrals of the tunneling PDF. This comparison exposes a possible correlation to the inverse of the EC50 data, taken to represent the efficacy of the agonist at a receptor. Results for the 1500cm^{-1} region are shown in Figures 2 and 3 for the DOI class and 2C-X class molecules computed, respectively. Figures 2a and 3a give the tunneling spectra for each molecule, Fig. 2b and 3b compare the integral values to the known EC50s.

As tunneling is a highly local process were the inter-

action potential falls-off as r^{-3} for non-parallel displace-

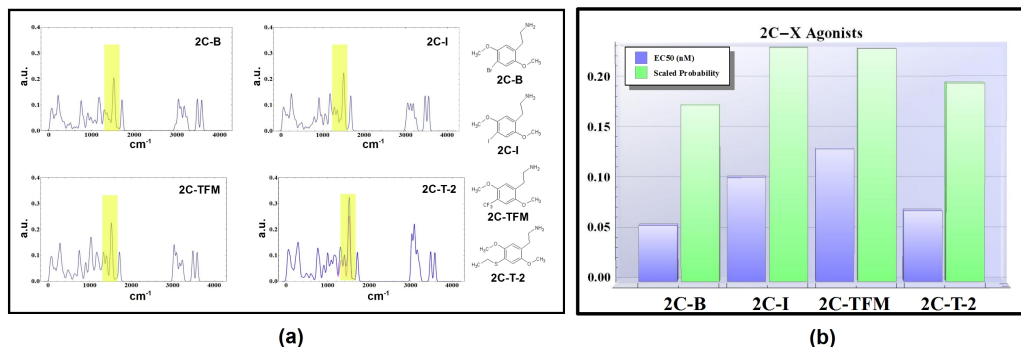


FIG. 3. (a) The tunneling spectra of several 2C-X class agonists as well as their molecular structures. (b) The inverse of the median effective concentration for the 2C-X class agonists plotted against the tunneling probability within the region in question. The trend of tunneling intensity follows roughly the trend of the agonist’s efficacy at the 5-HT_{2A} receptor.

ments. Modes not local to the electron donor/acceptor sites will not maximally contribute to the electron transfer responsible for protein activation. Particular modes in 2C-T-2 and in Aleph-2 reside within the thioether (roughly 5 angstrom from the ring system); due to the non-locality of these oscillators, tunneling probability should be examined after having removed their contributions from the spectra. Figures 2a and 3a present the tunneling spectrum of 2C-T-2 and Aleph-2 both considering and disregarding these contributions; the additional contribution to the tunneling probability due to these modes is shown in orange of Fig. 2b and 3b. After correction for non-local motions, the integrals are in good qualitative agreement with the inverse EC50. This preliminary information supports a quantum mechanical origin for the activation of these proteins, we propose an experimental validation of the theory in the following section.

IV. EXPERIMENT

Early findings suggest that both the lake whitefish and the American cockroach can identify isotopologues

Using 1500 cm^{-1} as a central point, and recalling the applied FWHM, the modes contributing to inelastic transfer are those at $1500 \pm 50 \text{ cm}^{-1}$. Modes within that range have motions associated with (in order of contribution): stretching of the amide methyl hydrogen; stretching of the phenyl and indole hydrogens; and bending of the methyl hydrogen of the tertiary amine.

Dueteration of the three phenyl hydrogens (DAM-57-i) yields a marginal attenuation in intensity near 1500 cm^{-1} , and small change in tunneling probability. DAM-

of amino acids and pheromones, respectively^{53,54}. Recent experiments using the common fruit fly present both naive bias to and potential for trained aversion towards isotopologues of acetophenone⁵⁵, and repute⁵⁶. Recent works featuring human subjects shows that naive participants cannot discern between dueterated acetophenone⁵⁷; a second study⁵⁸ presented evidence suggesting human capability at discerning dueterated variants of musk odorants. Other works have attempted to identify the characteristic vibrations associated with particular odors⁵⁹, yet have not explicitly considered an electron tunneling mechanism.

DAM-57 (N,N-dimethyllysergamide) is an ergot derivative with a mild hallucinogen with activity at the 5-HT_{2A} receptor. As it activates the same receptor, the above discussed candidate peak should, and does, appear in the tunneling spectrum of DAM-57. Figure 4 shows the tunneling spectra for various isotope labeled DAM-57 variants. Each spectrum is accompanied by a molecular structure highlighting the isotope exchanges; the candidate peak is highlighted in yellow.

57-ii displays a reduction in the 3700 cm^{-1} region, N-H stretch, shifting weight to 2700 cm^{-1} . Deuteration of the indole amine results in almost no character change near the active region. Pro-deuteration of a single amide methyl (DAM-57-iii) significantly decreases the tunneling intensity in the 1500 cm^{-1} region. Continued deuteration of the amide system (DAM-57-vi), reduces this peak to roughly one-half the pro-protium intensity. DAM-57-vi and DAM-57-v, moiety co-deuteration scenarios, present very small alterations of the peak intensity when com-

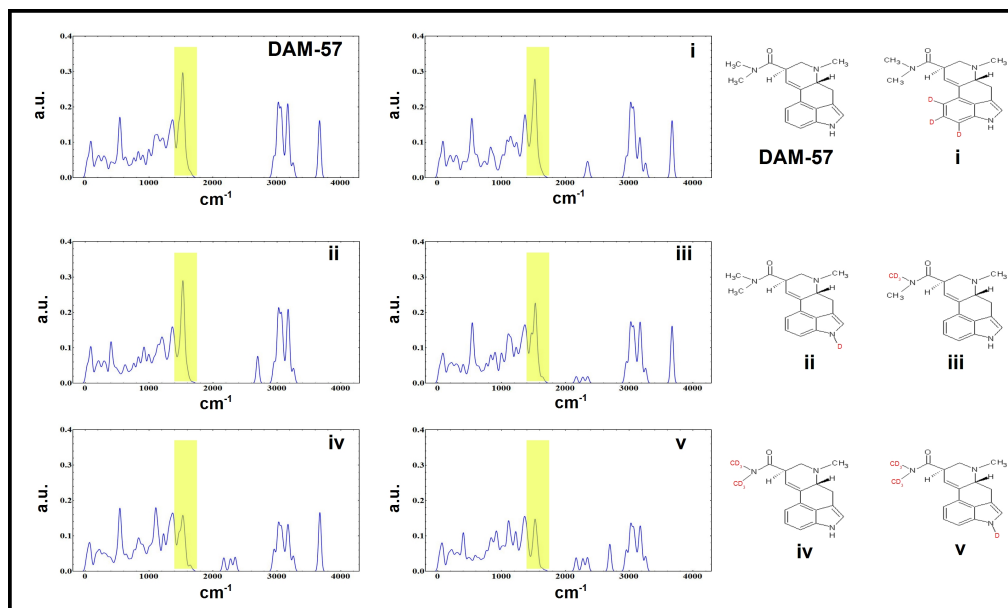


FIG. 4. The tunneling spectrum of several deuterium-isotopologues of DAM-57. Yellow highlights have been given to the energy region which is assumed to be the active energy region for inelastic tunneling transfer. Specific deuterations deplete the tunneling probability within this region, and may effectively eliminate the agonism of the molecule within the 5-HT_{2A} receptor.

pared to DAM-57-iii and DAM-57-vi, respectively.

Within the tunneling model, deuteration of the amide side chains should dampen the activity of the molecule at the 5-HT_{2A} receptor. This conclusion is supported by the relative activity between DAM-57 and LSD. The flexible ethyl amide of LSD has been found to be essential to its high activity^{39,40,60,61}, and that the methyl analogue (DAM-57) is far less potent; the tunneling probability at the 1500 cm^{-1} region of DAM-57 is depleted when compared to that of LSD. Following this, a prediction that further depletion of the tunneling probability within this region should continue to diminish the efficacy at the receptor may be entertained. The intensity of the tunneling spectrum of DAM-57 is roughly a third the pro-protium, and the probability density of tunneling is roughly tented this implies an extreme loss of activity associated with deuteration of the amide side-chains.

V. CONCLUSIONS

Herein we describe the agonist-protein system by an electron tunneling junction coupled to a field of oscillating dipoles, representative of the constituent atoms of the agonist. The oscillator field provides a secondary path for

electron transfer been the donor and acceptor states of the junction; this secondary, inelastic path facilitates the transfer if and only if the electron can donate a quantum of energy to the oscillator field. Using this method we tested classes of agonists for the 5-HT_{2A} receptor and found that all agonist, to varying degrees, facilitate electron transfer within the same energy region. The degree to which this tunneling is facilitates correlates roughly to the efficacy of the agonist within our test cases. We examined the tunneling characteristics of isotopologues of these agonists and predict that one could modulate and quench their agonist properties though the isotope exchange of specific atoms. Also included is a proposed experimental path to text the model herein described. We conclude that this mechanism is a candidate for the activation step for some transmembrane proteins, allowing for better prediction of candidate drug molecules and the possible ability to control agonism of molecules.

VI. ACKNOWLEDGEMENTS

This work is supported by the NSF Centers for Chemical Innovation: Quantum Information for Quantum Chemistry, CHE-1037992

- * kais@purdue.edu
- ¹ J. T. Arndt, M. and V. Vedral, HFSP J. **3**, 386 (2009).
 - ² P. C. W. Davies, BioSystems **78**, 69 (2004).
 - ³ P. Ball, Nature **474**, 272 (2011).
 - ⁴ S. F. Huelga and M. B. Plenio, Contemporary Physics **54**, 181 (2013).
 - ⁵ S. Lloyd, M. Mohseni, A. Shabani, and H. Rabitz, arXiv:1111.4982 [quant-ph] (2011).
 - ⁶ G. S. Engel, T. R. Calhoun, E. L. Read, T.-K. Ahn, T. Mancal, Y.-C. Cheng, R. Blankenship, and G. R. Fleming, Nature **446**, 782 (2007).
 - ⁷ G. R. Fleming, S. F. Huelga, and M. B. Plenio, New Journal of Physics **13**, 115002 (2011).
 - ⁸ S. Kais, Advances in Chemical Physics **134**, 493 (2007).
 - ⁹ S.-H. Yeh, J. Zhu, and S. Kais, J. Chem. Phys. **137**, 084110 (2012).
 - ¹⁰ M. Sarovar, A. Ishizaki, G. R. Fleming, and et al., NATURE PHYSICS **6**, 462 (2010).
 - ¹¹ J. Zhu, S. Kais, A. Aspuru-Guzik, and et al., J. Chem. Phys. **137**, 074112 (2012).
 - ¹² T. Fujita, J. C. Brookes, S. K. Saikin, and A. Aspuru-Guzik, J Phys Chem Lett **3**, 2357 (2012).
 - ¹³ A. Shabani, M. Mohseni, H. Rabitz, and S. Lloyd, arXiv:1103.3823 [quant-ph] (2012).
 - ¹⁴ E. Collini, C. Y. Wong, K. E. Wilk, P. M. G. Curmi, P. Brumer, and G. D. Scholes, Nature **463**, 782 (2010).
 - ¹⁵ A. Olaya-Castro and G. D. Scholes, Int. Nat. Revs. in Phys. Chem. **30**, 49 (2011).
 - ¹⁶ J. McFadden, *Quantum Biology* (Norton, 2001).
 - ¹⁷ J. McFadden and J. Al-Khalili, BioSystems **50**, 203 (1999).
 - ¹⁸ R. Remacle, N. Kravchenko-Balasha, A. Levitzki, and R. D. Levine, PNAS **107**, 10324 (2010).
 - ¹⁹ T. G. Graeber, J. R. Heath, B. J. Skaggs, M. E. Phelps, R. Remacle, and R. D. Levine, PNAS **107**, 6112 (2010).
 - ²⁰ D. Heyers, M. Manns, H. Luksch, O. Gntrkn, and H. Mouritsen, PLOS ONE **2**, e937 (2007).
 - ²¹ K. Maeda, K. B. Henbest, F. Cintolesi, and et al., NATURE **453**, 387 (2008).
 - ²² J. A. Pauls, Y. T. Zhang, G. P. Berman, and S. Kais, Phys. Rev. E **87**, 062704 (2013).
 - ²³ J. M. Cai and M. B. Plenio, PRL **111**, 230503 (2013).
 - ²⁴ I. Tejero, N. Gonzalez-Garca, A. Gonzalez-Lafont, and J. M. Lluch, Journal of the American Chemical Society **129**, 5846 (2007).
 - ²⁵ M. Garcia-Viloca, J. Gao, M. Karplus, and D. G. Truhlar, Science **303**, 186 (2004).
 - ²⁶ L. Turin, Journal of Theoretical Biology **216**, 367 (2002).
 - ²⁷ A. Patel, J. Biosci. **26**, 145 (2001).
 - ²⁸ A. Christopoulos, Nat Rev Drug Discov **1**, 198 (2002).
 - ²⁹ E. Fischer, Ber. Dt. Chem. Ges. **27**, 2985 (1894).
 - ³⁰ D. E. Koshland, Proc. Natl. Acad. Sci. **44**, 98 (1958).
 - ³¹ G. M. Dyson, Perfumery and Essential Oil Record **19**, 456 (1928).
 - ³² R. Wright, Journal of Theoretical Biology **64**, 473 (1977).
 - ³³ L. Turin, Chemical Senses **21**, 773 (1996).
 - ³⁴ L. Turin and F. Yoshii, *Handbook of Olfaction and Gustation* (Marcel Dekker, Inc., 2003).
 - ³⁵ J. C. Brookes, F. Hartoutsiou, A. P. Horsfield, and A. M. Stoneham, Phys. Rev. Lett. **98**, 038101 (2007).
 - ³⁶ I. A. Solovvov, P.-Y. Changwb, and K. Schulten, Phys. Chem. Chem. Phys. **14**, 13861 (2012).
 - ³⁷ S.-Y. Takane and J. B. O. Mitchell, Org. Biolol. Chem. **2**, 3250 (2004).
 - ³⁸ J. D. Urban, W. P. Clarke, M. von Zastrow, D. E. Nichols, B. Kobilka, H. Weinstein, J. A. Javitch, B. L. Roth, A. Christopoulos, P. M. Sexton, K. J. Miller, M. Spedding, and R. B. Mailman, Journal of Pharmacology and Experimental Therapeutics **320**, 1 (2007).
 - ³⁹ D. E. Nichols, Pharmacology & Therapeutics **101**, 131 (2004).
 - ⁴⁰ D. E. Nichols and C. D. Nichols, Chem. Rev. **108**, 1614 (2008).
 - ⁴¹ A. K. Sleight, W. A. Phillips, C. J. Adkins, and M. E. Taylor, Journal of Physics C: Solid State Physics **19**, 6645 (1986).
 - ⁴² W. A. Phillips and C. J. Adkins, Philosophical Magazine Part B **52**, 739 (1985).
 - ⁴³ J. Kirtley, D. J. Scalapino, and P. K. Hansma, Phys. Rev. B **14**, 3177 (1976).
 - ⁴⁴ G. J. Marek and G. K. Aghajanian, JPET **278**, 1373 (1996).
 - ⁴⁵ A. R. Knight, A. Misra, K. Quirk, K. Benwell, D. Revell, G. Kennett, and M. Bickerdike, Naunyn-Schmiedeberg's Arch Pharmacol **370**, 114 (2004).
 - ⁴⁶ D. Delliou, Forensic Science International **21**, 259 (1983).
 - ⁴⁷ H. H. Maurer, Ther Drug Monit **32**, 544 (2010).
 - ⁴⁸ J. G. Iez-Maeso, N. V. Weisstaub, M. Zhou, and et al., Neuron **52**, 439 (2007).
 - ⁴⁹ A. Shulgin and A. Shulgin, *PiHKAL: A Chemical Love Story* (Transform Press, 1991).
 - ⁵⁰ A. Shulgin and A. Shulgin, *TiHKAL: The Continuation* (Transform Press, 1997).
 - ⁵¹ K. X. Wan, I. Vidavsky, and M. L. Gross, J Am Soc Mass Spectrom **13**, 85 (2002).
 - ⁵² M. R. Braden, Thesis Purdue University (2007).
 - ⁵³ J. Hara, Experientia **33**, 6189 (1977).
 - ⁵⁴ B. R. Havens and C. D. Melone, Dev. Food. Sci. **37**, 497 (1995).
 - ⁵⁵ M. I. Franco, L. Turin, A. Mershin, and E. M. C. Skoulakis, PNAS **108**, 3797 (2011).
 - ⁵⁶ T. P. Hettinger, PNAS **108**, E349 (2011).
 - ⁵⁷ A. Keller and L. B. Vosshall, NATURE NEUROSCIENCE **7** (2004).
 - ⁵⁸ S. Gane, D. Georganakis, K. Maniati, M. Vamvakias, N. Ragoussis, E. M. C. Skoulakis, and L. Turin, PLO SONE **8**, e55780 (2013).
 - ⁵⁹ L. J. W. Haffenden, V. A. Yaylayan, and J. Fortin, Food Chem. **73**, 67 (2001).
 - ⁶⁰ K. Kanagarajadurai, M. Malini, A. Bhattacharya, M. M. Panicker, and R. Sowdhamini, Mol. BioSyst. **5**, 1877 (2009).
 - ⁶¹ S. Bayar, S. Saglam, and H. F. Ustundag, Journal of Molecular Structure: THEOCHEM **726**, 225 (2005).

Supplemental Material

I. TUNNELING THEORY

Inelastic Electron Tunneling Spectroscopy is a well-founded experimental method utilizing a simplistic laboratory set-up that can deliver the vibrational spectra of an analyte. The mechanism of action is semi-classical and not optical, particular selection rules are derivable with IETS¹ but in general this method allows for forbidden transitions, thus all vibrational modes are addressable². The method is implemented by the application of a potential across a two-plate junction with a spatial separation between the plates. High energy electrons from the valence band of one plate will tunnel across the junction into the conduction band of the other. When the tunneling process occurs in the absence of analyte molecules, the process is elastic in nature and electron energy is maintained throughout the process, thus the electrons energy must be respective of the energy between the valence and conductance band.

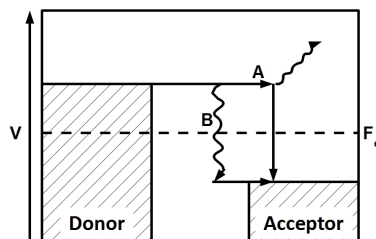


FIG. 1: Cartoon displaying the competing processes during IETS where V is potential energy and F_e is the Fermi Level. Path A is radiative^{1,3}, requiring the tunneling electron to spontaneously lose energy to meet the energy of the conductive band. Path B shows the electron losing energy via a non-radiative process; it is implicit that the energy lost is to a normal mode of a deposited molecule within the gap - such is our case.

Depositing an analyte molecule onto the electron source plate, as the tunneling electrons enter the gap they may interact with the deposited analyte molecules; in doing so they are effectively given a springboard, shortening their tunneling path. This interaction comes at a cost of energy; the electron will lose energy to the analyte molecule, where the amount of lost energy is equal to that of a vibrational mode of the molecule. This process may be seen in Figure 1. This method has been well described theoretically⁴⁻⁶ and expanded to include such considerations as molecular orientation⁷ and short-ranged higher harmonics⁸. Here we shall review the theoretical description of the elastic process as seen in^{9,10}. It is a fair starting assumption that the wave function is oscillatory in the x - and y -directions and evanescent in the z -direction. In this manner the decay constant for such a function is spatially dependent and thus the function is anisotropic; the wave functions used were described

through WKB theory and are provided here:

$$\begin{cases} \psi_i = \left(\frac{A}{L}\right) e^{i\mathbf{k}'_{\parallel}\cdot\mathbf{r}} e^{-\alpha_0 z} \\ \psi_f = \left(\frac{A}{L}\right) e^{i\mathbf{k}_{\parallel}\cdot\mathbf{r}} e^{-\alpha_0(d-z)} \end{cases} \quad (1)$$

From the above it should be noted that L is the dimension of the square plate. k_x , k_y and k_z are the wave vectors in the appropriate directions. Similarly, A is a collection of constants, α_0 is the decay rate of the evanescent wave in the z direction and assuming cylindrical symmetry the wave vectors in the \hat{x} and \hat{y} directions are identical and are combined into the radial wave vector k_{\parallel} , noting that this is the wave vector components parallel to the plate surface.

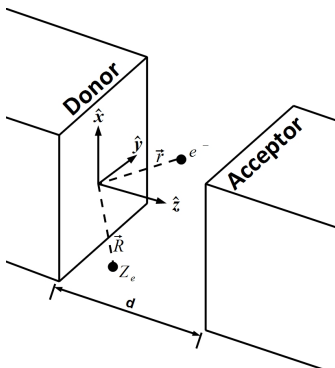


FIG. 2: A cartoon displaying the physical relations and significance of variables within the problem. e^- is the tunneling electron with vector displacement of \vec{r} and Z_e is the partial charge associated with a molecular mode with displacement \vec{R} , and d is the distance between the two plates.

We shall use the wave functions in Eq. 1 to attain the average value of the current

for the system, via the current operator, M_e . The elastic process yields:

$$\langle \psi_i | \hat{M}_e | \psi_f \rangle = M_e = \left(\frac{A^2}{L^2} \right) \int_0^L dS e^{i\mathbf{q}\cdot\mathbf{r}} \left(\frac{\hbar^2 \alpha_0}{m} \right) e^{-\alpha_0 d} \quad (2)$$

$$= \left(\frac{A^2 \hbar^2 \alpha_0}{m} \right) \cdot e^{-\alpha_0 d}, \quad (3)$$

where \mathbf{q} is the difference between \mathbf{k}'_{\parallel} and \mathbf{k}_{\parallel} . The inelastic process for a single specified normal mode is governed by the following interaction potential:

$$U(r') = \frac{Z_e e^2}{4\pi\epsilon_0\epsilon_r} \cdot \frac{\mathbf{u} \cdot (\mathbf{R} - \mathbf{r})}{(|\mathbf{R} - \mathbf{r}|)^3}, \quad (4)$$

where all symbols retain their standard definitions, including ϵ_r being the permittivity of the generic real media, \mathbf{r} and \mathbf{R} are made clear by Figure 2 and \mathbf{u} is the vector representing the displacement of the atom within the molecule with partial charge Z_e . This potential allows us to calculate the inelastic contributions in a manner similarly to the above:

$$M_{in} = \left(\frac{A^2}{L^2} \right) e^{-\alpha_0 d} e^{i\mathbf{q}\cdot\mathbf{R}} \int_0^\infty \int_0^{2\pi} \int_0^d r e^{i\mathbf{q}\cdot\mathbf{r}} U(r, \theta, z) dz d\theta dr. \quad (5)$$

Where the integral in Equation 5 can be performed analytically for cases where the vector directions of \mathbf{u} are either parallel or perpendicular to the plate surfaces. For \mathbf{u} along the z direction (parallel to gap):

$$M_{in}^z = M_0 \frac{1}{qd} (e^{-q\alpha_0} - e^{-q(d-\alpha_0)}); \quad (6)$$

and for \mathbf{u} parallel to the plates:

$$M_{in}^x = iM_0 \frac{1}{qd} \{ (1 - e^{-q\alpha_0}) + (1 - e^{-q(d-\alpha_0)}) \}. \quad (7)$$

Where, in both the above, the quantity M_0 is given by:

$$M_0 = e^{i\mathbf{q}\cdot\mathbf{R} - \alpha_0 d} \left(\frac{A^2 Z e^2 u d}{L^2 2\epsilon_0 \epsilon_r} \right). \quad (8)$$

The decay constants for each of ψ_i and ψ_f should conform with the statement:

$$E_c - E = \frac{\hbar^2}{2m}(\alpha^2 - k_{\parallel}^2) \quad (9)$$

where E is the energy of the tunneling electron, E_c is the energy of the conductive band and m is the mass of the electron (effective mass is typically used). The above yields two unique decay constants consistent with the difference in electron energies at the conduction band and during tunneling. With these two unique decay constants we must append a factor of

$$e^{(\alpha_i + \alpha_f)d/2} e^{(\alpha_i - \alpha_f)z} \quad (10)$$

to our matrix elements due to the difference in α 's. Carrying this factor through we note there is a depletion of tunneling probability equivalent to:

$$e^{-q^2/4(\alpha_0 d)}; \quad (11)$$

and finally placing this into an expression for the relative conductivities associated with the inelastic and elastic processes, $\frac{\Delta\sigma}{\sigma_e}$, and finally including a 2-D density of states representative of the plate surface areas:

$$\frac{\sigma_{in}}{\sigma_e} = \left\{ \frac{1}{M_e} \right\}^2 \int_0^\infty (M_{in}^z)^2 e^{-q^2/4(\alpha_0/d)} \left(\frac{qL^2}{2\pi} \right) dq. \quad (12)$$

The above allows us to make the statement:

$$\frac{\sigma_{in}}{\sigma_e} \propto Z_e^2 u_z^2, \quad (13)$$

as those quantities on the R.H.S. of Eq. 12 are the only quantities dependent on molecular characteristics and thus are featured in Eq. 13. As the elastic tunneling process occurs with or without the presence of the analyte molecules, the experimental observable is the ratio between the known elastic contribution, $\sigma_e = M_e^2$, to the current at a given applied potential (found through a zeroing process with a

non-deposited gap) and the deposited gap current at the same potential; this ratio quantity is denoted as $\frac{\Delta\sigma}{\sigma_e}$. Armed with the above, the IETS intensity for a given active mode j can be approximated by^{6,11}:

$$I_j = \sum_{i=1}^N I_{i,j} = \sum_{i=1}^N q_i^2 (\Delta x_{i,j})^2, \quad (14)$$

where the sum is over all atoms within the molecule, q_i is the partial charge of atom i , and $\Delta x_{i,j}$ is the Cartesian displacement of atom i in mode j .

II. DISCUSSION OF TUNNELING SPECTRAL ASPECTS

An examination of the edrogenous agonist 5-HT is given in Figure 3. The main spectral features are (quantities are in cm^{-1}): the OH stretch at 3700; NH_2 bend at 1700; coherent ring motions appear at both 1500 and 1150; and indole bending at 530. For reasons discussed below, we will focus our discussion on tunneling in the 1500 cm^{-1} region. Working within Turins theory, this implies that these motions assist in the tunneling and that the tunneling source and sink are in proximity to these motions. Docking studies of homology modeled 5-HT_{2A} show that the moieties discussed above are local to F339, F340, S159 and L229 residues¹²⁻¹⁵, alluding that one of these residues may facilitate the tunneling process.

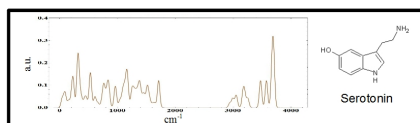


FIG. 3: Serotonin's tunneling spectrum used as a comparator throughout the discussion. Here the abscissa has units of wavenumber and the ordinate has units proportional to tunneling probability; this conversion holds for all tunneling spectrum to follow.

The spectral indices are given for the overall spectrum and followed by regional SI's calculated for spans of 1000cm^{-1} with 500cm^{-1} steps, to emphasize the possible region associated with activation the final column shows the SI of each compound for $1500\pm 100\text{cm}^{-1}$. Regions with large ranges of zero intensity have SI's inflated by this spectral facet, these regions have been disincluded within the table. When disincluding these regions, the SI for the region spanning $1000\text{-}2000\text{cm}^{-1}$ shows enhanced values, and includes the peak at 1500cm^{-1} . The final column of the table gives the SI for a 100cm^{-1} region about this peak to emphasis this heavily shared spectral feature. Application of the SI to the square of the spectra yielded similar results (not shown), yet with the expected enhancement of the SI values (not shown).

	Spectral Range (cm^{-1})					
	0-4200	0-1000	500-1500	1000-2000	3000-4000	1400-1600
LSD	1	1	1	1	1	1
DAM-57	0.89019	0.87090	0.85286	0.87048	0.86997	0.85726
2C-I	0.81664	0.81792	0.75492	0.76284	0.78236	0.70693
2C-T-7	0.83977	0.81371	0.77398	0.80550	0.81748	0.79913
DOI	0.81903	0.80415	0.76196	0.77684	0.78614	0.71396
Aleph-2	0.83233	0.82216	0.77757	0.79102	0.80063	0.77539
DMT	0.84620	0.82282	0.78969	0.80327	0.85075	0.75394
Mescaline	0.82280	0.80003	0.74899	0.77347	0.80797	0.76743
Quipazine	0.82353	0.80820	0.77809	0.79677	0.77694	0.72653
Benzylpiperazine	0.82135	0.79383	0.76929	0.79990	0.79270	0.72390

TABLE I: Table contains the SI indexes for several 5-HT_{2A} agonists. The procedure was applied to the total spectra, and several sections of 1000cm^{-1} which march with an overlapping pattern and shifted by 500cm^{-1} . The region of interest is also performed with a calculated SI for the region of $1500\pm 100\text{cm}^{-1}$

In the next few sections we have selected DOC (2,5-dimethoxy-4-C-amphetamines) as a prototypical molecule for discussion, this selection was based on its fairly tractable number of modes, simple geometry, symmetry and similarities to other agonists. Energy regions associated with an assisted electron transfer would benefit from a large density of vibrational states; implying a greater number of possible states to interact with in this energy range. Figure 4 shows both the IETS and scaled

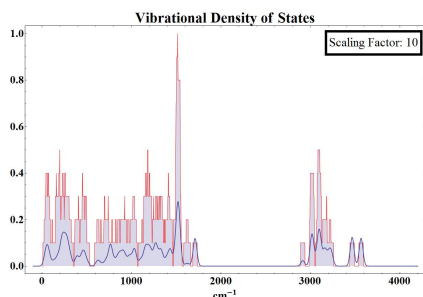


FIG. 4: The tunneling spectrum of DOC (Blue) is plotting alongside a scaled, discrete density of states for the vibrational modes of DOC. The scaling factor is given in the inlay. Note the enhanced number of states associated with 1500cm^{-1} region. This large number of states reflects a large density of possible vibrational modes within this energy range that are capable of accepting a quanta of energy from the tunneling electron.

density of states for DOC; the spectral feature at 1500cm^{-1} exhibits an enhanced number of vibrational states.

In the main body of the paper we propose an isotopologue series for DAM-57; the series is of variants are deuterated functional groups altering the character in the 1500cm^{-1} region. We verified that isotopologues of other atoms do not to alter tunneling character in this region. Figure 5 shows the isotope effects within several groups of the molecule. Fig. 5 a) shows the effects of replacing the oxygens with ^{18}O 's, this results in little alteration near 1500cm^{-1} ; substitution of the halide has similar results, with differences appearing at much lower energies. Fig. 5 b) displays the effects of deuterating the hydrogens on the methoxys, this show a large attenuation of the tunneling intensity; finally, Fig. 5 c) shows the effect of selectively deuterating different functional groups.

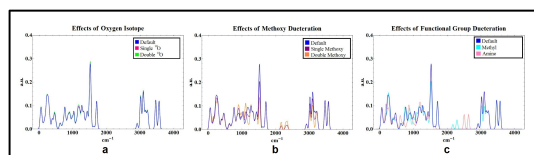


FIG. 5: Plots of the isotopologues of oxygen with the DOC molecules. The isotope exchanges has no effect on the region in question. This means that it is not vibration of the oxygen atoms which are most heavily responsible for the tunneling features within our candidate region.

BIBLIOGRAPHY

- ¹J. Lambe and R. C. Jaklevic, Phys. Rev. **165**, 821 (1968).
- ²K. W. Hippias and U. Mazur, *Inelastic Electron Tunneling Spectroscopy*, Handbook of Vibrational Spectroscopy.
- ³J. Lambe and S. L. McCarthy, Phys. Rev. Lett..
- ⁴A. K. Sleight, M. E. Taylor, C. J. Adkins, and W. A. Phillips, Journal of Physics: Condensed Matter **1**, 1107 (1989).
- ⁵C. J. Adkins and W. A. Phillips, Journal of Physics C: Solid State Physics **18**, 1313 (1985).
- ⁶A. K. Sleight, W. A. Phillips, C. J. Adkins, and M. E. Taylor, Journal of Physics C: Solid State Physics **19**, 6645 (1986).
- ⁷J. Kirtley and J. T. Hall, Phys. Rev. B **22**, 848 (1980).
- ⁸J. Kirtley and P. Soven, Phys. Rev. B **19**, 1812 (1979).
- ⁹J. Kirtley, D. J. Scalapino, and P. K. Hansma, Phys. Rev. B **14**, 3177 (1976).
- ¹⁰W. A. Phillips and C. J. Adkins, Philosophical Magazine Part B **52**, 739 (1985).
- ¹¹L. Turin, Journal of Theoretical Biology **216**, 367 (2002).
- ¹²M. R. Braden and D. E. Nichols, Molecular Pharmacology **72**, 1200 (2007).

- ¹³M. S. Choudhary, N. Scabs, A. Uluer, and et al., *Molecular Pharmacology* **47**, 450 (1995).
- ¹⁴M. R. Braden, J. C. Parrish, J. C. Naylor, and N. D. E., *Molecular Pharmacology* **70**, 1956 (2006).
- ¹⁵J. J. Chambers and D. N. Nichols, *Journal of Computer-Aided Molecular Design* **16**, 511 (2002).

On the Theory of Vibrational Assisted Tunneling in GPCR Activation

Ross D. Hoehn,¹ Hartmut Neven,² and Sabre Kais^{3,*}

¹*Department of Chemistry, Purdue University, West Lafayette, IN 47907 USA*

²*Google Los Angeles, Venice, CA 90291 USA*

³*Departments of Chemistry and Physics, Purdue University, West Lafayette, IN 47907 USA
Qatar Environment and Energy Research Institute, Doha, Qatar*

(Dated: June 16, 2014)

Attention has recently been given to a particular theory governing the activation of G-Protein Coupled Receptors (GPCRs) within the olfactory cavity by means of an electron transfer process across the proteins activation site. This theory prescribes mechanisms similar to those governing Inelastic Electron Tunneling Spectroscopy (IETS), a method of spectroscopic determination of molecular vibrational and electronic transitions, to the protein/agonist complex. This theory has been used to reassert odorant compounds within their known odor classes; agreement was established, possibly bolstering the applicability of this theory. There are several facets within the framework of inelastic electron tunneling theory that should be further considered and included within future works surrounding this topic. Herein we elucidate several considerations and to what degree these influence calculations: spatial dimensions of the activation site, orientation effects of the odorant within the site, modulation of the geometry of docked ligands, and the importance of both Infrared and Raman active modes.

I. INTRODUCTION

The activation of G-Protein Coupled Receptors (GPCRs) governs many physiological activities examples of which include: olfaction¹, central nervous system regulation² and maintaining circadian rhythm³. Roughly half of all modern small molecule therapeutics target this class of proteins⁴ and roughly 50% of all human encoded GPCR genes encode for olfaction alone⁵. Understanding the mechanism by which GPCRs are activated is paramount to applications within both the pharmaceutical and the flavor/scent industries.

A recent resurgence of interest for a vibrational-based theory of protein activation has occurred⁶⁻⁸, featuring the mechanisms surrounding Inelastic Electron Tunneling Spectroscopy (IETS) as its possible means of detecting the vibrational modes of the bound ligand⁹, while activating the protein through an electron transfer process. The IETS mechanism relies on a field driven electron transfer across an insulating gap situated between two conductive metal plates. The driving field promotes electrons to tunnel from the donor site on one side of the gap to the acceptor site on the other side, this being the elastic process. As the intensity of the driving field is increased, the electrons may donate a quanta of energy to a molecule situated within the gap along their path, this being the inelastic process. This secondary conductive path promotes an enhancement to the current across the gap. The donated quanta of energy is equal to a quanta accepted by the molecules vibrational or electronic transitions. There exist several other mechanisms by which electrons are conveyed across the gap including elastic transfer, inelastic transfer, 2nd order elastic transfer as well as subsequent and less contributing modes of transport including modes displaying photon emission^{10,11}. Theoretical descriptions of this mechanism were introduced by Kirtley et al¹² and later elucidated

by Phillips and Adkins¹³.

To exemplify the effects of several factors on the measurable IETS intensities, we have selected the formate ion for our example system. This ionic system is both small and simple enough to allow for easily observed emphasis of effects of the IETS mechanism discussed within this paper as it possesses a very tractable number of vibrational modes and a simple geometry. This example also has the added benefit of being a classical example within the IETS theory and experimental literature^{12,14}.

II. RESULTS AND DISCUSSION

Calculations of Inelastic Electron Tunneling rates have been performed in various ways throughout the literature^{12,13}. Typically the Barden Transfer Hamiltonian method is employed to allow for the calculation of the elastic contribution from the tunneling wavefunctions across the barrier sides. The WKB approximation is used to describe the wavefunction of the tunneling electrons from each side; the following are the evanescent wavefunctions describing an electron traversing a gap of length d defined by two conductive plates of area L^2 :

$$\varphi_1 = \left(\frac{A}{L}\right) e^{ik_{\parallel} \cdot r} e^{-\alpha_0 z} \quad (1)$$

$$\varphi_2 = \left(\frac{A}{L}\right) e^{ik'_{\parallel} \cdot r} e^{-\alpha_0(d-z)} \quad (2)$$

Where a_0 is the decay constant of the tunneling electron in the z^{th} direction, $k_{parallel}$ and k'_{\parallel} are the momentum parallel to the surfaces and A is the normalization constant. As a reference, a cartoon description of the formate ion within the gap is given in Figure 1a and the

experimentally resolved spectra for this system is in Figure 1b¹⁴.

As the electrons tunnel through the barrier they may undergo several processes including: elastic transfer, inelastic transfer, 2^{nd} order elastic transfer and subsequent less contributing modes of transfer. The inelastic modes of transport are facilitated through interaction between the tunneling electron and a deposited molecule within the gap¹¹; the tunneling electron donates of quanta of energy to the deposited molecule. In the case where there are a non-continuum of acceptor and donor energy levels, the donation of energy from the electron to the molecule must obey Fermis Golden Rule:

$$T_{i \rightarrow f} = \frac{2\pi}{\hbar} \left| \langle \varphi_2 | \hat{U} | \varphi_1 \rangle \right|^2 \delta(E_f - E_i \pm \hbar\omega) \quad (3)$$

Where $T_{i \rightarrow f}$ is the probability of an electron transferring from state i to state f , with the stationary state wavefunctions φ_i and φ_f ; \hat{U} is the interaction potential to be discussed and δ is the Kronecker delta function depending on the energies of the states and the quanta absorbed by the deposited molecule. The quanta of energy is typically in the range of vibrations for IETS, although electronic excitations have also been achieved experimentally¹⁵. The electronic interaction between the ligand and the molecule treats each atom of the molecule separately; each atom is assigned a partial charge, Z , and sits at its equilibrium positions, R , it vibrates with a displacement u . The interaction potential is that of an electron and single dipole:

$$\hat{U}(r, \theta, z) = \left(\frac{Ze^2}{4\pi\epsilon_0\epsilon_r} \right) \frac{u \cdot (R - r)}{|R - r|^3} \quad (4)$$

As the interaction is between the electron and a single atom of the molecule, the contribution to the conductivity found through this calculation must be repeated and summed over all atoms within the molecule.

To determine the contribution to the conductivity of any mode of transport, one must first calculate the tunneling matrix element. In the case of the elastic mode the tunneling matrix element, M_e , is calculated as the overlap of the wavefunctions from the donor and acceptor sites over the volume of the gap since this mechanism does not require interaction with the deposited molecule. The calculation of the tunneling matrix element for the inelastic transport to the contribution utilizes the both donor and acceptor wavefunctions and the interaction potential:

$$M_{in} = \left(\frac{A^2}{L^2} \right) e^{-\alpha_0 d} e^{iqR} \int_0^\infty \int_0^{2\pi} \int_0^d \hat{U}(r, \theta, z) r dz d\theta dr. \quad (5)$$

Within the above, q is the change in parallel momentum defined as $q = k'_\parallel - k_\parallel$.

The tunneling matrix elements act as probability factors in the calculation of the conductivity. IETSS enhancement in the current is related to alterations in the conductivity through the additional transport paths associated with the inelastic transport utilizing the atomic oscillators as energy syncs. The ratio between inelastic contribution and the elastic contribution for a single atomic interaction with the electron can be calculated through:

$$\begin{aligned} \frac{\sigma_{in}}{\sigma_e} &= \left[\frac{1}{M_e} \right]^2 \int_0^\infty M_A^2 e^{-\frac{q^2 d}{4\alpha_0}} \frac{L^2}{2\pi} q dq \quad (6a) \\ &\propto \int_0^\infty M_A^2 e^{-\frac{q^2 d}{4\alpha_0}} q dq = I_A(a, d) Z_A^2 u_A^2. \quad (6b) \end{aligned}$$

The *l.h.s.* of the proportionality is the integral form proposed by Phillips and Adkins¹³. Whereas the *r.h.s.* is a simplification through elimination of all constants within the calculation, it is taken to be in arbitrary units, *a. u.*, while being proportional to the strict calculation through multiplication of a constant.

Figure 2 is provided as a useful reference for subsequent sections; it gives the normal modes of the formate ion for association with the intensities and spectra to be discussed. Within this figure, the displacements in *a.u.*, the directional unit vector and the frequency in cm^{-1} are all given; oxygens are depicted in red, carbon in black and hydrogen in grey.

A. Point Dipole Approximation

The most fundamental expression describing electromagnetic interactions between an electron and a charged dipole is given here¹⁶:

$$V = \frac{z_i(-z_j)e^2}{4\pi\epsilon_0} \frac{1}{|r_j - r_i|} + \frac{z_i z_j e^2}{4\pi\epsilon_0} \frac{1}{|r_j + p_j - r_i|} \quad (7)$$

Where r_i is the location of the electron providing a field $z_i e^2$ and r_j is location of a single side of the dipole where both ends provide a field with the magnitude $z_j e^2$; the second term describes the remaining, oppositely charged side of the dipole at a distance p_j from r_j . Recollection of the terms yields the expression in Eq. 8a, and a subsequent Taylor series expansion for the denominator yields Eq. 8 line 2.

$$V = \frac{-z_i z_j e^2}{4\pi\epsilon_0} \left(\frac{1}{r_{ij}} - \frac{1}{\sqrt{r_{ij}^2 + 2\vec{r}_{ij} \cdot \vec{p}_j + p_j^2}} \right) \quad (8a)$$

$$\cong \frac{z_i z_j e^2}{4\pi\epsilon_0 r_{ji}} \left(\frac{1}{2} \frac{\vec{r}_{ji} \cdot \vec{p}_j}{r_{ji}^2} + \frac{1}{2} \frac{p_j^2}{r_{ji}^2} - \frac{3}{8} \left(\frac{2\vec{r}_{ji} \cdot \vec{p}_j}{r_{ji}^2} + \frac{p_j^2}{r_{ji}^2} \right)^2 \right) \quad (8b)$$

After the series expansion, the point dipole approximation is typically employed; this approximation states

that the distance between the charge and the dipole is much greater than the displacement between the dipole termini, $r_{ji} \gg p_j$. Under the point dipole approximation all but the leading terms of Eq. 8 (line 1) drop due to minimal contribution, seen in Eq. 9.

$$V \approx \frac{z_j e}{4\pi\epsilon_0} \frac{\vec{r}_{ji} \cdot \vec{\mu}_j}{r_{ji}^3} = \frac{z_j z_i e^2}{4\pi\epsilon_0} \frac{\vec{r}_{ji} \cdot \vec{u}_j}{r_{ji}^3} \quad (9)$$

It is important to note that it has been suggested that the spatial dimensions of the activation site within this class of proteins is to be on the order of 15\AA ¹⁷. This suggested dimension of, when compared to order of magnitude of the normal mode displacement vector, does not meet the criteria for the point dipole approximation. Considering that the system is possibly inappropriate for application of the point dipole approximation, we compare the numerical values for the tunneling matrix elements as calculated through Eq. 5 using the interaction potential Eq. 4 and the more complete form of the interaction potential in Eq. 8 (line 1). Figure 3 shows the relative error associated with using the point dipole approximation with the spatial scale of the active site; it should be noted that the error associated with this misuse of the approximated potential is peaked in the range of the active site length scale. Within this regime the dipole approximation eliminates terms which are dependent upon the projection, $r_{ji} \cdot p_j$, there exists an angular dependence on the magnitude of the tunneling matrix element. This angular dependence can be observed in Figure 3, and is due to the projector terms which are eliminated during application of the point dipole approximation; the magnitude of the relative error is proportional to the cosine of the angle, and then we observe an oscillatory component to the error in the θ -dependences.

B. Polarizability

Inelastic electron tunneling, a method for obtaining information about the vibrational modes of a molecule, does not rely on the interactions between the molecular dipole and the field of the electron^{12,13}. The interaction potential, Eq. 4, describes the interaction between an electron and a single oscillating dipole, representing a single vibrating atom within the molecule; this interaction depends neither upon the polarizability of the system nor the change in net dipole. The single-dipole nature of the potential requires a summation over the atoms within the molecule to account for each independent electron-atom interaction.

The ratio given in Eq. 6b is characteristic of the enhancement to the conductivity due to single atom motions. If this were the only responsible contribution to 1st order inelastic conduction then the symmetric modes, corresponding to Raman transitions, would not appear in IETS, yet they do and with roughly the same magnitude as Infrared active modes.

$$\frac{\sigma_{in}}{\sigma_e} \propto \int_0^\infty M_A M_B e^{-\frac{a^2 d}{4\alpha_0}} F(qb) q dq = I_{AB}(a, d) Z_A Z_B u_A u_B \quad (10)$$

The above describes the contribution to the conductivity enhancement due to the coherent motion of two atoms. Eq. 10 contains a phase factor, $F(qb)$, which is generated through the addition of matrix elements. The advent of this phase factor comes from the addition of the $e^{iq \cdot R}$ terms seen within Eq. 5. If the two atoms are identical and their distance from the nearest barrier is the same, the form of the phase factor becomes: $(u_1 + u_2 e^{iq \cdot b})$. In the case that the displacements of each atom are of equal magnitude and the same direction, $u_1 = u_2$ (IR active), the phase factor becomes $\cos^2\left(\frac{q \cdot b}{2}\right)$. In the case of Raman active modes, $u_1 = -u_2$, the phase factor simplifies to $\sin^2\left(\frac{q \cdot b}{2}\right)$.

It has been experimentally observed that both IR and Raman modes are active within IETS and scale roughly equally. Yet some works within this field have chosen to couple the oscillating dipole associated with an entire molecular mode¹⁷, this would generate the intensities associated with the infrared vibrations of the molecule but not contributions associated with Raman active modes.

Figure 5 shows the effects of including intensity contributions of the Raman active modes (standard IETS), blue plot. Alongside the blue plot, we have provided the intensity expected if the coupling mechanism were to be only with the molecular dipole moment. The two plots are scaled to each other for convenience of comparison. It is clear to note, by comparison between the blue plot of Figure 5 and the experimental plot given in Figure 1, that the inclusion of Raman mode associated intensities has delivered a better approximation to experiment.

C. Orientation

When considering the charge-dipole interaction potentials it is clear that the leading (point-dipole) term as well as any subsequent terms rely on the projection of the harmonic displacement vector for a specific atomic oscillator (j), u_j , onto the charge-dipole vector, r_{ji} . This projection is of paramount importance within the calculation of the coupling within these systems as it effectively modulates the power of the denominator.

Orientation effects within IETS intensity calculations have been described as being of such importance as to practically be a selection rule for this type of vibrational characterization^{9,12,18}. Interaction potentials used within early formulations of IETS calculations rely on the coupling strength of the electron within the donor site to atomic harmonic oscillators, and did not include any dynamic interactions within the system. More dynamic formulations exist to deal with that rather minute contribution of inelastic tunneling contributions to

the current through molecular junctions, such as green's functions approaches. It should be noted that in these cases the inelastic contribution is to the molecular conductance and is attributed to vibronic alteration of electronic levels within the molecule - this second-order coupling (electron-vibrational state-electronic state) is why the inelastic contribution is minute in these cases¹⁹.

In maintaining the simplicity of static calculations, one cannot ignore the contributions to the interaction potential from the vector projection. To emphasize the importance of this interaction we have plotted the IETS of the formate ion; in Figure ??a you can see the three angular parameters and their relation to the molecular geometry of the formate ion. The rotation about the red (z) axis does not alter the spectrum of the formate ion as the calculations set the origin of the tunneling junction along this axis, and thus this rotation does not alter the projection of the electron onto any molecular modes - merely which component (x or y) possesses the projection; it should be clearly stated that this is a facet of the formate ions C_2 rotational symmetry, not of inelastic tunneling. Rotation about the green (y) and blue (x) axes will alter the projections, the effects can be seen in Figure ??b for rotation about the x-axis and Figure ??c for rotation about the y-axis. Furthermore, without having calculated these orientation effects one can never achieve modes where the rate of inelastic tunneling is lower than the rate of the elastic process, which is vital in inelastic tunneling spectrum.

D. Docking Geometry

Specifically discussing the activation of olfactory proteins under the odotope theory, the volatile odorant molecule is hypothetically capable of maintaining something akin to its optimized geometry within the activation site²⁰. This is due to the fact that only certain sections of the molecule are being determined at once suggestive of a soft or partial docking; it could be rationalized that the molecule only loosely enters and is never fully enveloped by the activation site. This rationalization would be countered by docking studies of the OR1A1, OR1A2 and OR1G1 human olfactory receptors that do show envelopment of the ligands which dock with the protein^{21,22}.

Full ligand envelopment can lead to geometric alterations of the ligand during the docking as the protein-

agonist complex reaches its energy minimum states. The alteration of ligand geometry can lead to attenuations in both the modal displacements and the partial charges, which for our example system can roughly generate a 10% alteration by displacement or a 5% alteration by partial charge (where partial charge was calculated through NBO analysis) in the tunneling intensity if the molecular geometry group is maintained. Moreover, these attenuations alter the potential interaction between the electron and the dipole through the dot product present in several terms of the non-approximated interaction potential Eq. 8 (line 1) as well as the standard interaction potential Eq. 4.

Figure 6a shows the geometry and alignment within the gap of the formate ion as well as variations on the bond angles. Fig. 6ai is the optimized for of the ion, Fig. 6aii is has altered both O-C-H bond angles equally (maintaining both σ planes) and Fig. 6aiii has altered only one of the O-C-H bond angles (maintaining only the σ plane bisecting all bonds). The alterations in the frequencies, displacements and partial charges are shown in Table I. Figure 6b gives the inelastic tunneling intensities for the variations of the formate ion. For obvious reasons the frequencies are slightly displaced, and the introduction of asymmetry in the oxygen pairs movement eliminates much of their non-canceling contribution.

III. CONCLUSION

The feasibility of tunneling electrons being the mechanism behind the activation of has been the subject of recent works. The mechanism by which the electron interacts with a bound ligand has been proposed as being IETS; for future works in this direction it is important to consider a more complete description of the IETS model including considerations of the angular dependence between the mode and tunneling vector, alterations in the ligand geometry due to docking and the importance of choosing an appropriate interaction potential considering the confines of the activation site. These facets of the full static IETS calculations have been explored here and these authors iterate their importance. Future works should not only consider the aspects discussed within this paper, as these aspects are mandatory consideration, but could also explore mode coupling of residue chains within the activation site itself or thermal line broadening at biological temperatures.

* kais@purdue.edu

¹ I. Gaillard, S. Rouquier, and D. Giorgi, *Cell. Mol. Life Sci.* **61**, 456 (2004).

² D. Hoyer, D. E. Clarke, J. R. Fozard, P. R. Hartig, G. R. Martin, E. J. Mylecharane, P. R. Saxena, and P. P. Humphrey, *Pharmacol. Rev.* **46**, 157 (1994).

³ S. M. Reppert, *J Biol Rhythms* **12**, 528 (1997).

⁴ D. Filmore, *Modern Drug Discovery*.

⁵ Y. Niimura and M. Nei, *PNAS* **100**, 12235 (2003).

⁶ L. Turin, *Chemical Senses* **21**, 773 (1996).

⁷ L. Turin, *Journal of Theoretical Biology* **216**, 367 (2002).

⁸ J. C. Brookes, F. Hartoutsiou, A. P. Horsfield, and A. M. Stoneham, *Phys. Rev. Lett.* **98**, 038101 (2007).

⁹ J. Lambe and R. C. Jaklevic, *Phys. Rev.* **165**, 821 (1968).

- ¹⁰ J. Lambe and S. L. McCarthy, Phys Rev Lett **37**, 923 (1976).
- ¹¹ M. Reed, MaterialsToday **11**, 46 (2008).
- ¹² J. Kirtley, D. J. Scalapino, and P. K. Hansma, Phys. Rev. B **14**, 3177 (1976).
- ¹³ W. A. Phillips and C. J. Adkins, Philosophical Magazine Part B **52**, 739 (1985).
- ¹⁴ A. K. Sleight, W. A. Phillips, C. J. Adkins, and M. E. Taylor, Journal of Physics C: Solid State Physics **19**, 6645 (1986).
- ¹⁵ S. K. Khanna and J. Lambe, Science **220**, 1345 (1983).
- ¹⁶ H. W. Wyld, *Mathematical Methods for Physics* (Westview Press, 1987).
- ¹⁷ I. A. Solovyov, P.-Y. Changwb, and K. Schulten, Phys. Chem. Chem. Phys. **14**, 13861 (2012).
- ¹⁸ J. Kirtley and J. T. Hall, Phys. Rev. B **22**, 848 (1980).
- ¹⁹ M. Galperin, M. A. Ratner, and A. Nitzan, arXiv , 1 (2004).
- ²⁰ A. Rinaldi, EMBO Rep **8**, 629 (2007).
- ²¹ K. Schmiedeberg, E. Shirokova, H.-P. Wber, B. Schilling, W. Meyerhof, and D. Krautwurst, J. Struct. Biol. **159**, 400 (2007).
- ²² K. Schmiedeberg, E. Shirokova, H.-P. Wber, B. Schilling, W. Meyerhof, and D. Krautwurst, J. Struct. Biol. **159**, 400 (2007).

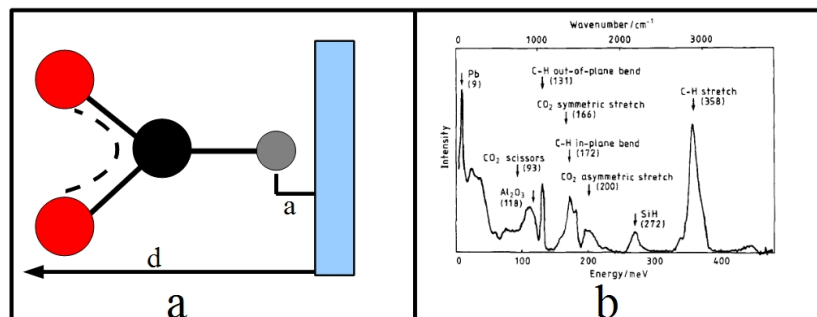


FIG. 1. a) A cartoon schematic of the formate ion within its gap, distance parameters d and a are shown within the figure for clarity. b) The IETS spectra of the formate ion taken from¹⁴, provided as reference.

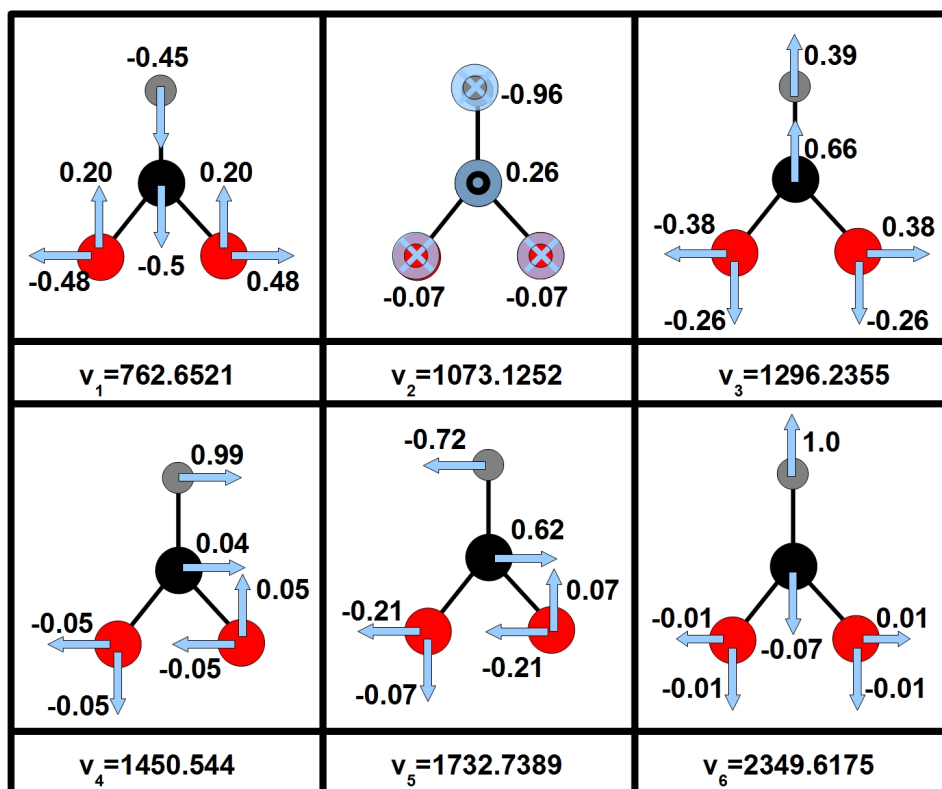


FIG. 2. A display of the normal modes associated with the formate ion. Also included are a unit vector indicator as to the direction of displacement and the magnitude is shown beside it. Distances are in $a.u.$ Frequencies are also displayed in cm^{-1} beneath the mode to which it belongs.

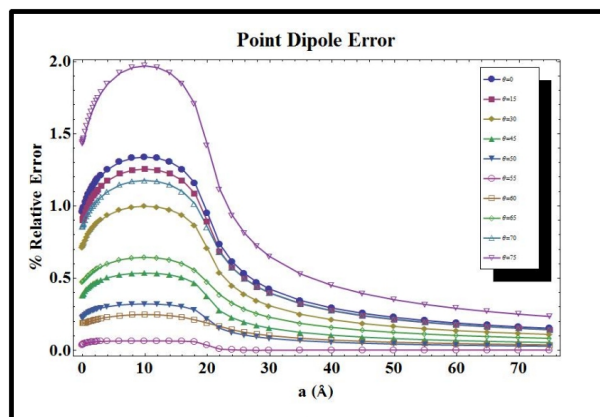


FIG. 3. The percent relative error between variations of the interaction potential given in Eq. 4 and Eq. 8a. This was completed for several values of θ to emphasize the angular dependence stemming from projection operations in terms eliminated through approximation.

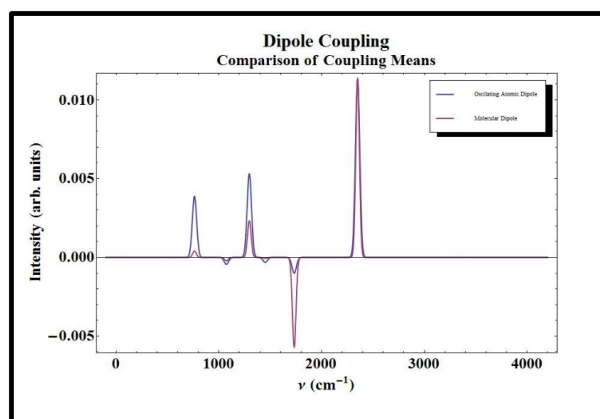


FIG. 4. The blue line shows the IETS of the formate ion; the maroon line shows the spectra where the interaction potential given Eq. 4 is replaced by the interaction potential between the electron and the molecular dipole. The two plots have been scaled so to be comparable.

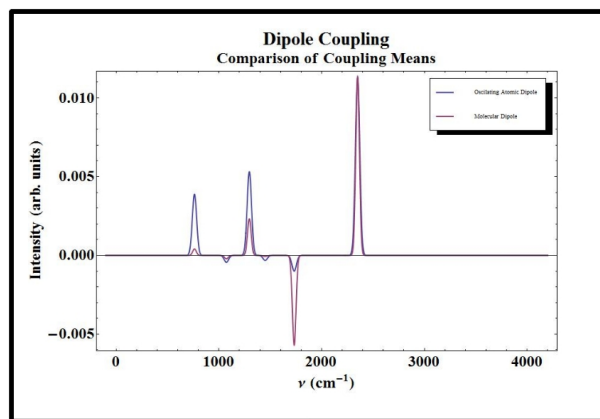


FIG. 5. The blue line shows the IETS of the formate ion; the maroon line shows the spectra where the interaction potential given Eq. 4 is replaced by the interaction potential between the electron and the molecular dipole. The two plots have been scaled so to be comparable.

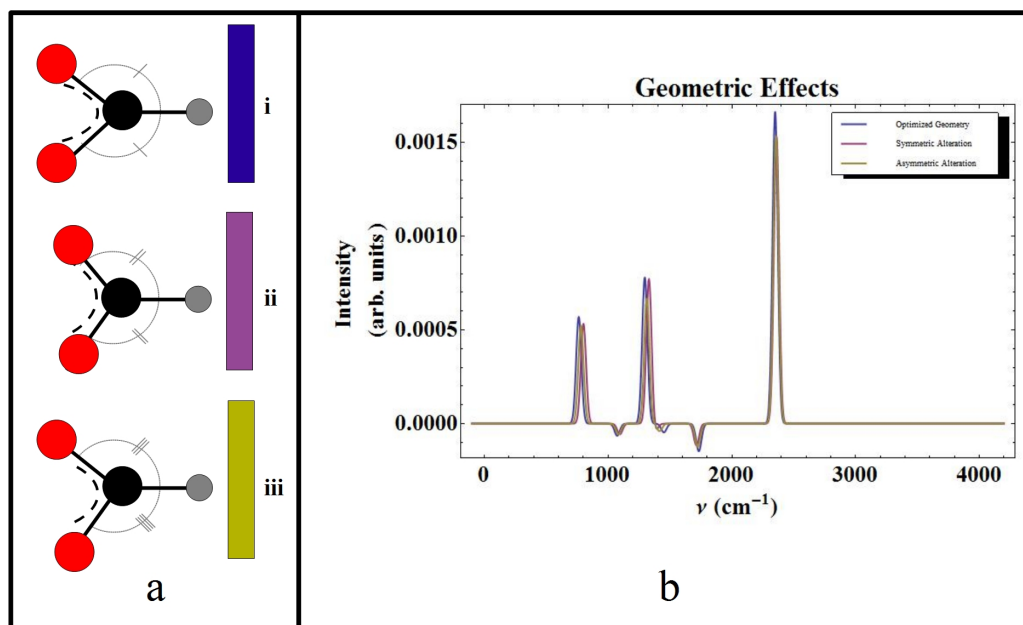


FIG. 6. Effects of alterations of the geometry of a system on the IETS. Subfigure (a) shows cartoons of the geometries of concern: optimized geometry, symmetric alteration and asymmetric alteration, respectively. Subfigure (b) shows the IETS of the formate ion variants

	Displacement (\AA) (x, y, z)						C		H		Partial Charges					
	Mode 1		Mode 2		Mode 3		Mode 4		Mode 5		Mode 6		C	H	O _a	O _b
	x	y	x	y	x	y	x	y	x	y	x	y				
Asymm. Variant	(0.01, -0.5, 0)	(0.04, -0.45, 0)	(0, 0, 0.24)	(0, 0, -0.97)	(-0.02, 0.61, 0)	(-0.29, 0.41, 0)	(0.04, 0.02, 0)	(0.99, 0.03, 0)	(0.59, 0.04, 0)	(-0.75, -0.05, 0)	(0, -0.07, 0)	(-0.02, 1, 0)	0.39379	0.03396	-0.71387	-0.71387
Optimized	(0, 0, -0.51)	(-0.48, 0.2, 0)	(0, 0, -0.09)	(-0.97, 0, 0)	(0.37, -0.26, 0)	(-0.34, -0.23, 0)	(-0.04, 0.05, 0)	(-0.05, -0.07, 0)	(-0.2, 0.08, 0)	(-0.2, -0.08, 0)	(0, 0, 0)	(-0.01, -0.01, 0)	0.42941	0.00053	-0.71447	-0.71447
Symm. Variant	(0, 0, 0.5)	(0, 0, -0.45)	(-0.06, 0, 0)	(-0.06, 0, 0)	(0, 0, 0.09)	(0, -0.37, -0.29)	(0, -0.05, 0.05)	(0, -0.05, -0.05)	(0, -0.18, 0.08)	(0, -0.18, -0.08)	(0, 0, 0)	(0, 0, 0)	0.43099	-0.00063	-0.71281	-0.71714

TABLE I. Numerical Values for calculations of the geometric alterations and optimized geometry variants of the formate ions.